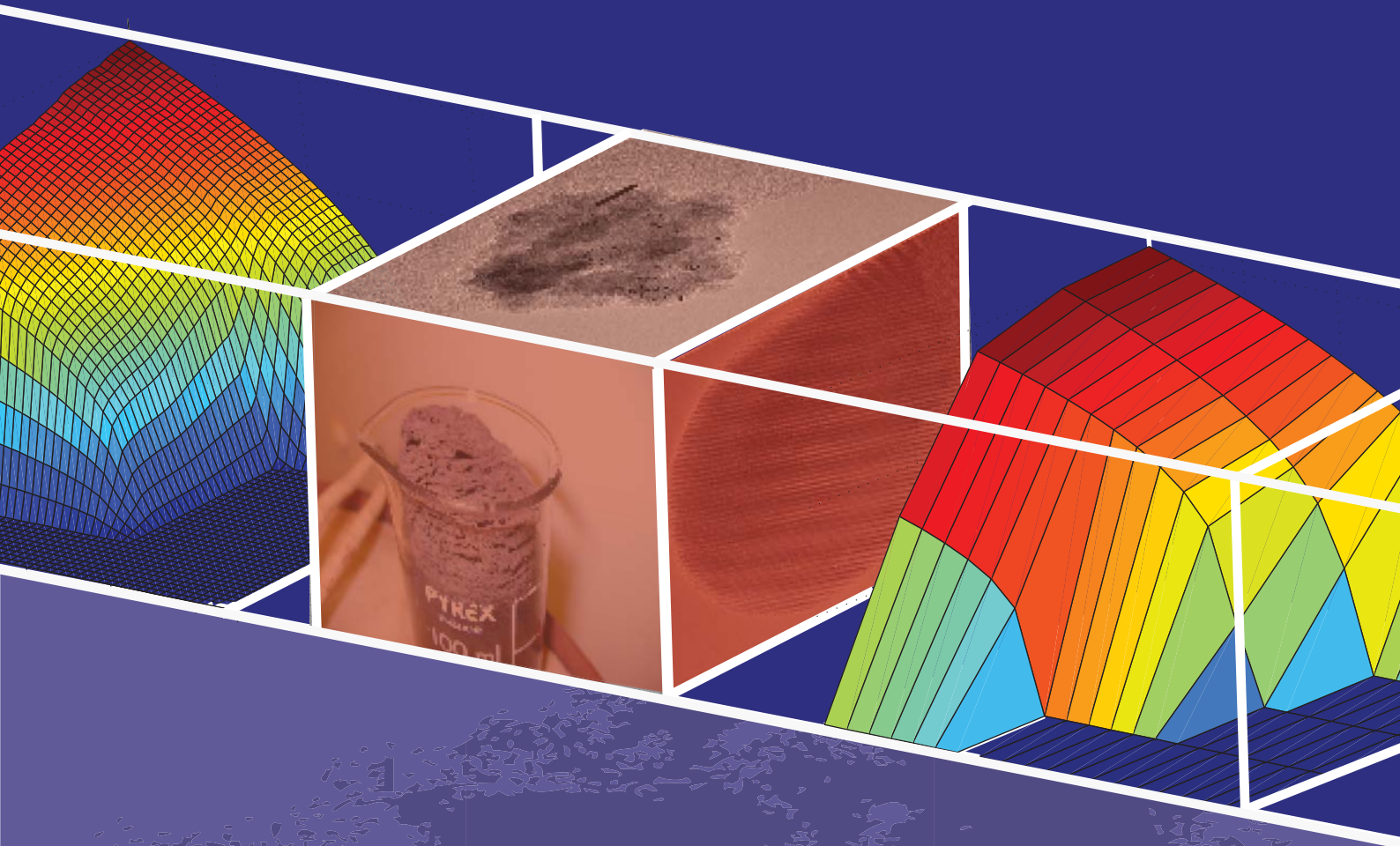


# Antiferromagnetism in YBCO and CoO Nanoparticles

Jari í Hjøllum

Ph.D. Thesis  
University of Copenhagen



## Supervisors:

Morten Bo Madsen, Earth & Planetary Physics, Niels Bohr Institute,  
Christof Niedermayer, Paul Scherrer Institute & ETH Zürich,  
Kim Lefmann, AFM, Risø National Laboratory, DTU



# Antiferromagnetism in YBCO and CoO Nanoparticles

Jari í Hjøllum

Ph.D. Thesis  
University of Copenhagen  
August 2008

Supervisors: Morten Bo Madsen, Earth & Planetary Physics, Niels Bohr Institute,  
Christof Niedermayer, Paul Scherrer Institute & ETH Zürich,  
Kim Lefmann, AFM, Risø National Laboratory, DTU



*Dedicated to my family who have made everything possible.*



# Abstract

By means of a variety of techniques, including neutron scattering and muon spin rotation, the antiferromagnetism in two very different nanoparticle systems, the high-temperature superconductor YBCO ( $\text{YBa}_2\text{Cu}_3\text{O}_{6+x}$ ) and the 3D Ising antiferromagnet CoO, have been studied. With its complex chemical structure and magnetic properties YBCO is far from well-understood and the magnetic behavior of the system under different conditions is investigated. In contrast, the Ising magnetism in CoO makes it a simple system to study and the critical behavior of the system in a magnetic phase transition is investigated.

Utilizing the advantages of both neutron diffraction and muon spin rotation techniques we have for the first time mapped out the staggered magnetization of disc-shaped 30 nm YBCO nanoparticles as a function of temperature as well as oxygen-doping.

A significant reduction of the Néel temperature is found at low doping. The reduction is strongest at low doping, and is diminished with increasing hole doping. Neutron scattering measurements also show a more linearly-shaped magnetic order parameter behavior compared to bulk. These observations are attributed to the confined dimensionality of the disc-shaped system. Our findings agree with a similar study of NiO nanoparticles for which the reported reduction of the Néel temperature was found to stem from finite-size effects [86].

Furthermore, a possible spin canting or spin flop mechanism is observed in neutron scattering measurements as a weak response to an applied magnetic field.

Muon spin rotation measurements reveal a distribution of Néel temperatures, seen as an increasing number of non-ordered spins, coexisting with a bulk-like behavior of the magnetic order parameter versus temperature. This exotic finite-size effect could be due to superparamagnetic relaxation, surface spin melting or a combination of these, all of which are phenomena exclusively observed in nanoparticles.

Even more exciting, our muon spin rotation data show that reemergence of the native-like Néel state [33] at low temperature also exists in YBCO nanoparticles. The reemergence is seen as a distinct rise of the staggered magnetization at low temperature in a doped sample and is caused by changes in the internal field distribution due to the localization of holes. This removes the frustration on most spins, allowing these to form a Néel-like state with a staggered magnetization approaching that of the undoped system [20]. This observation along with previous observations in bulk YBCO [165],  $\text{Y}_{1-x}\text{Ca}_x\text{Ba}_2\text{Cu}_3\text{O}_6$  [130] and LSCO [33], strongly supports the view that the reemergence of the native-like Néel state is an intrinsic property of cuprate systems.

To study nanoscale critical phenomena, we have performed neutron scattering measurements on the simple 3D Ising antiferromagnet CoO in a novel type of experimental setup. By running a triple-axis spectrometer in two-axis mode, we have utilized a large 2D Position Sensitive Detector, to collect diffraction data with a markedly enhanced intensity around the antiferromagnetic  $(\frac{1}{2} \frac{1}{2} \frac{1}{2})$  reflection.

For bulk- and nano- sized powders, we determine the Néel temperature ( $T_N$ ) and measure the critical magnetic scattering below and above this temperature. From the integrated intensity and shape of the magnetic diffraction peak we extract the magnetic order parameter,  $M \propto (T_N - T)^\beta$ . The observed bulk value of  $\beta=0.28(5)$  agrees relatively well with the numerical prediction  $\simeq 0.33$  for a 3D Ising system [64], whereas the values for nanoparticles are strongly size-dependent and

found to be as large as  $\beta=0.46(3)$ . Furthermore, comparison between X-Ray diffraction and neutron scattering results on the nanoparticles indicates that the structural size is larger than the statically ordered magnetic particle size (*e.g.* 19.3(8) nm and 12.87(11) nm respectively), likely because the spins at the surface are canted or disordered.

Intriguingly, we observe a distinct cut-off in the critical correlation length  $\xi \propto (T - T_N)^{-\nu}$  for nanoparticles over a large temperature interval around the critical temperature. In this temperature region the critical intensity and correlation length of bulk are extremely temperature sensitive, whereas the nanoparticle system shows little or no change of either. Furthermore, the cut-off level of the correlation length clearly scales with the structural particle size.

Presented are the first-ever observations of exotic magnetic behavior of two nanosized systems and it is shown how the observed phenomena are strongly affected by the finite size of these systems.

# Contents

<b>1</b>	<b>Introduction</b>	<b>3</b>
1.1	Motivation . . . . .	4
1.1.1	Antiferromagnetic Order Parameter in YBCO Nanoparticles . . . . .	4
1.1.2	Critical Phenomena in Nano-Sized CoO Particles . . . . .	5
<b>2</b>	<b>Antiferromagnetism and Superconductivity</b>	<b>7</b>
2.1	Antiferromagnetism . . . . .	7
2.1.1	Heisenberg and Ising Interaction Models . . . . .	8
2.1.2	Phase Transitions . . . . .	8
2.1.3	Critical Exponents . . . . .	9
2.2	Superconductivity . . . . .	10
2.2.1	The Meissner Effect . . . . .	11
2.2.2	Type I and Type II Superconductors . . . . .	11
2.3	The Cuprate High- $T_C$ Phase Diagram . . . . .	11
2.4	Introduction to YBCO . . . . .	13
2.4.1	Crystal Structure . . . . .	13
2.4.2	Electronic, Magnetic and Superconducting Properties . . . . .	15
2.4.3	Oxygen Doping and Hole Doping . . . . .	16
2.5	Finite Size Effects . . . . .	18
2.6	Introduction to CoO . . . . .	20
<b>3</b>	<b>Experimental methods</b>	<b>23</b>
3.1	Introduction . . . . .	23
3.2	Neutron scattering . . . . .	24
3.2.1	Theory . . . . .	24
3.2.2	The Correlation Function and Critical Scattering . . . . .	27
3.2.3	Spin Dynamics . . . . .	29
3.2.4	Triple Axis Spectroscopy . . . . .	29
3.2.5	RITA-2 Modes . . . . .	32
3.2.6	Using Monochromatic Imaging Mode . . . . .	34
3.2.7	Two-Axis Mode . . . . .	34
3.2.8	Instrumental Resolution Function . . . . .	36
3.3	Muon Spin Rotation . . . . .	37
3.3.1	Spin Polarization . . . . .	37
3.3.2	Muon Decay . . . . .	38
3.3.3	Detected Signal . . . . .	39
3.3.4	Apparatus . . . . .	39
3.3.5	Measurement Time Scales . . . . .	40
3.3.6	Asymmetry . . . . .	41
3.3.7	Analysis methods . . . . .	42

<b>4</b>	<b>Sample Preparation and Characterization</b>	<b>45</b>
4.1	Diffraction . . . . .	45
4.1.1	The Scherrer Formula . . . . .	46
4.1.2	The Debye-Scherrer Cone . . . . .	46
4.1.3	Line Shapes . . . . .	47
4.2	Magnetic Susceptibility . . . . .	48
4.2.1	Apparatus . . . . .	49
4.2.2	Magnetic Susceptibility of an Antiferromagnet . . . . .	50
4.3	Transmission Electron Microscopy . . . . .	51
4.4	YBCO Sample Preparation . . . . .	52
4.4.1	Nanoparticle Preparation . . . . .	52
4.4.2	Bulk Preparation . . . . .	55
4.5	YBCO Doping . . . . .	56
4.6	YBCO Sample Doping Overview . . . . .	58
4.7	YBCO Sample Characterization . . . . .	58
4.7.1	YBCO XRD Phase Characterization . . . . .	58
4.7.2	Magnetic Susceptibility Measurements . . . . .	60
4.7.3	TEM Size Measurements . . . . .	61
4.7.4	AFM Size Measurements . . . . .	62
4.7.5	Particle Shape from Neutron Diffraction . . . . .	66
4.8	CoO Nanoparticle Preparation . . . . .	67
4.9	CoO Sample Characterization . . . . .	68
4.9.1	XRD Size Determination . . . . .	68
4.9.2	TEM Size Measurements . . . . .	68
4.9.3	Magnetic Susceptibility . . . . .	70
<b>5</b>	<b>Nano-sized YBCO particles</b>	<b>73</b>
5.1	Neutron Scattering Data Analysis . . . . .	73
5.1.1	Calibration of Magnetic Scattering Intensity . . . . .	74
5.1.2	Analyzer Blade Normalization . . . . .	77
5.1.3	Discussion of Line Shapes . . . . .	77
5.1.4	Simulation of Line Shapes . . . . .	78
5.1.5	Preliminary Analysis . . . . .	79
5.1.6	Simple Model Analysis . . . . .	80
5.1.7	Simple Model Results . . . . .	82
5.1.8	Advanced Model - <i>hkl</i> Model . . . . .	86
5.1.9	<i>hkl</i> Model Results . . . . .	87
5.1.10	Applied Magnetic Field Experiments . . . . .	91
5.1.11	Bulk YBCO Analysis . . . . .	94
5.2	Muon Spin Rotation Data Analysis . . . . .	95
5.2.1	Calibration . . . . .	96
5.2.2	Fitting models . . . . .	96
5.2.3	Analysis . . . . .	99
5.2.4	Discussion . . . . .	106
5.3	Conclusion . . . . .	112
5.3.1	Magnetic Field Response . . . . .	112
5.3.2	Nano and Bulk Magnetization from Neutron Diffraction . . . . .	112
5.3.3	Nano and Bulk Magnetization from $\mu$ SR . . . . .	114
5.3.4	Magnetization from Neutron Diffraction and $\mu$ SR . . . . .	114
5.3.5	The $\mu$ SR Magnetization in the General Phase Diagram . . . . .	116
5.3.6	Spin Freezing . . . . .	118
5.3.7	Outlook and Perspectives . . . . .	119

<b>6</b>	<b>Critical Phenomena in Cobalt Oxide Nanoparticles</b>	<b>121</b>
6.1	Critical Fluctuations . . . . .	121
6.1.1	Studies of Finite-Size Criticality . . . . .	122
6.1.2	Critical Exponents in CoO . . . . .	123
6.1.3	Critical Exponents in CoO . . . . .	123
6.2	Strategy of Measurements . . . . .	123
6.2.1	Two-Axis Measurements and PSD Data Analysis . . . . .	123
6.2.2	Choice of Sample Container . . . . .	125
6.3	Preliminary Analysis . . . . .	125
6.3.1	Detector Normalization . . . . .	125
6.3.2	Observations . . . . .	126
6.3.3	Models . . . . .	126
6.3.4	Particle Length Scales . . . . .	129
6.3.5	Outline of Analysis . . . . .	129
6.3.6	Determining the Néel Temperature . . . . .	130
6.4	Bulk Sample Analysis . . . . .	131
6.5	Nanosized Sample Analysis . . . . .	133
6.5.1	20 nm Sample Analysis Details . . . . .	133
6.5.2	30 nm Sample Analysis Details . . . . .	137
6.5.3	10 nm Sample Analysis Details . . . . .	138
6.6	Discussion and Conclusion . . . . .	139
6.6.1	Consistency Check . . . . .	139
6.6.2	The Cut-Off in the Correlation Length . . . . .	140
6.6.3	Néel Temperature and Critical Exponents . . . . .	144
6.6.4	Mesoscopic Range Order . . . . .	146
6.6.5	Perspectives and Outlook . . . . .	147
<b>7</b>	<b>Summary and Outlook</b>	<b>149</b>
7.1	Summary . . . . .	149
7.2	Outlook . . . . .	150
<b>A</b>	<b>SICS Implementation</b>	<b>153</b>
A.1	Implementation of SICS on RITA-2 . . . . .	153
<b>B</b>	<b>YBCO Preparation Logs</b>	<b>155</b>
B.1	Nano YBCO Fabrication Logs . . . . .	155
B.1.1	Titration of Yttrium solution . . . . .	155
B.1.2	Titration of Barium solution . . . . .	156
B.1.3	Titration of Copper solution . . . . .	156
<b>C</b>	<b>Calculations and Implementations</b>	<b>157</b>
C.1	Calculations of Magnetic Moments in YBCO . . . . .	157
<b>D</b>	<b>YBCO Islands on Semiconductor Substrates</b>	<b>159</b>
D.1	YBCO Islands on Si Substrate . . . . .	160
D.2	YBCO Islands on SrTiO <sub>3</sub> Substrate . . . . .	161
<b>E</b>	<b>YBCO Extra Analysis Material</b>	<b>163</b>
E.1	Neutron Scattering Data . . . . .	163
E.1.1	Sample 1 ( $x=0.20$ ) - Simple Model Details . . . . .	163
E.1.2	Sample 3 ( $x=0.35$ ) - Simple Model Details . . . . .	164
E.1.3	Sample 4 ( $x=0.25$ ) - Simple Model Details . . . . .	164
E.1.4	Sample 5 ( $x=0.30$ ) - Simple Model Details . . . . .	165
E.2	$\mu$ SR Data . . . . .	166
E.2.1	Calibration . . . . .	166

E.2.2	Sample 3 ( $x=0.35$ ) Fit Results . . . . .	169
E.2.3	Sample 4 ( $x=0.25$ ) Fit Results . . . . .	170
E.2.4	Sample 5 ( $x=0.30$ ) Fit Results . . . . .	172
E.3	XRD Data . . . . .	176
E.4	Susceptibility Data and Measurements . . . . .	177
E.4.1	Sample 5 ( $x=0.30$ ) Applied Field Dependence . . . . .	178
E.4.2	Bulk Doping Problems . . . . .	178
E.4.3	Chasing a Phantom... . . . .	179
<b>F</b>	<b>Calculations and Simulations on CoO</b>	<b>181</b>
F.1	Structure Factor Calculations for CoO . . . . .	181
F.2	PSD Debye-Scherrer Calculations . . . . .	182
F.3	PSD Debye-Scherrer Simulations . . . . .	183
<b>G</b>	<b>Physical and Chemical data tables</b>	<b>185</b>
G.1	Fundamental Physical Constants . . . . .	185
G.2	Properties of Selected Elements . . . . .	185
G.3	Neutron Scattering Properties for Selected Elements . . . . .	186
G.4	Crystal Data for Selected Compounds . . . . .	186
G.5	Tables of Reflections for Selected Materials . . . . .	187
G.5.1	$Y_2Cu_2O_5$ at 20 K . . . . .	187
G.5.2	$Y_2Cu_2O_5$ at 50 K . . . . .	187
G.5.3	$Y_2Cu_2O_5$ at 80 K . . . . .	188
G.5.4	$Y_2Cu_2O_5$ at 296 K . . . . .	188
G.5.5	$Y_2BaCuO_5$ (Green Phase) . . . . .	189
G.5.6	$BaCuO_2$ #1 . . . . .	190
G.5.7	$BaCuO_2$ #2 . . . . .	191
G.5.8	$Y_2O_3$ . . . . .	191
<b>H</b>	<b>Publications</b>	<b>193</b>
H.1	Submitted Papers . . . . .	193
H.1.1	Paper I . . . . .	193
H.1.2	Paper II . . . . .	195
H.1.3	Paper III . . . . .	197
H.2	Papers in Preparation . . . . .	199
H.2.1	Paper IV . . . . .	199
H.2.2	Paper V . . . . .	200
H.3	Conference Contributions . . . . .	201
H.4	Awards . . . . .	201

# Acknowledgements

This thesis would not have been completed without the help and assistance, support and good will of the people and institutions, which I in one way or another have had a cooperation with during the work of the project.

Most part of my work has been done at Risø National Laboratory, DTU, Roskilde in Denmark, and at the Niels Bohr Institute at Copenhagen University. However, a good third of the time I have spent at the Paul Scherrer Institute (PSI), Villigen, Switzerland. I have spent shorter periods at the University of Turku in Finland.

As mentioned I have accumulatively spent around a year and a half at the PSI, and I owe my thanks to many there. First, I would like to thank Heinz Heer and Uwe Filges for welcoming me and making the start of my stay there very pleasant.

During the implementation of SICS on the RITA-2 spectrometer, I worked very closely with Mark Könnecke, the main architect of SICS and I would like to thank him for a productive cooperation.

During my work with characterization of YBCO I had great help from Dr. Kazimierz Conder and Dr. Ekaterina Pomjakushina, in baking YBCO powder, and through performing Thermo-Gravimetric Analysis (TGA).

Niels Bech Christensen and Christof Niedermayer, instrument responsables at RITA-2, have provided great help with measurements on the RITA-2 instrument, for which I would like to thank them. I also owe Henrik M. Rønnow thanks for his help with measurements.

The instrument responsables of the Physical Properties Measurement System (PPMS), Johan Chang and in particular Krunoslav Prsa have always been helpful when I have needed assistance using the instrument or in providing me with measurement time on a short notice.

I would also like to mention my fellow Ph.D. students from PSI, Johan Chang, Yasmine Sassa, Krunoslav Prsa and Beni Thielemann, and thank them for their enjoyable company and occasional discussions.

While working on the YBCO part of my project I have had a close and fruitful collaboration with Jussi Raittila, Hannu Huhtinen and Petriina Paturi from the solid state physics department at the University of Turku, Finland. During my stay there in the spring of 2006 they made sure that I felt welcome. Especially I would like to thank Jussi for help with the manufacturing of YBCO nano powder, good ideas and helpful discussions, and Hannu for good cooperation on the YBCO nano-islands project, where he is the expert on Pulsed Laser Deposition (PLD) and with whom I made the first AFM measurements on YBCO nano islands.

From the Physics Department at the Technical University of Denmark, I have had a good cooperation with Cathrine Frandsen, Helge Rasmusen and Lis Lilleballe during the manufacturing and preparation of samples.

Furthermore I would like to thank Kenny Ståhl, Lise Lotte Berring and Astrid Schöneberg from the X-Ray group at the Chemical Institute at the Technical University of Denmark, for giving Jonas O. Birk and me access their X-Ray diffraction equipment, with very short notice.

During my Ph.D. I have also had dealings with people from the H. C. Ørsted Intitute, Niels Bohr Institute. While doing some AFM measurements I had assistance from master student Anders Eliassen and Ph.D. student Jonas Hauptmann which they deserve thanking for.

As a interdisciplinary trial, I participated in an experiment where we were studying the distribution of minerals in primitive meteorites using neutron imaging/tomography, time of flight and

powder diffraction, at the instruments Neutra, Poldi and HRPT [65]. This experiment was very interesting and yielded some very exciting results, but has yet to converge into publications or a conclusion.

Last but not least I would like to thank the people of the Mars group at Niels Bohr Institute for good company during my days at the Rockefeller Institute, Niels Bohr Institute.

Morten Bo Madsen, head of the Mars Group at the Niels Bohr Institute, has been my formal university supervisor. However he has done much more than that, I would like to express my gratitude for our friendship, as well as I would like to thank him for a super supervisor, even through tough times.

From the Department of Materials Science at Risø National Laboratory I would like to thank all my colleagues for good cooperation and support. Especially Christian R. H. Bahl and Luise Theil Kuhn for help with TEM imaging, nice discussions and good friendship. Linda Udby and Peter K. Willendrup for fruitful discussions and for being great friends, and for help with McStas simulations. Asger B. Abrahamsen for helpful discussions, sharp observations and help with the doping of YBCO powder and ideas for the analysis of the results of my measurements. Sonja Rosenlund Hansen for discussions and comments to the manuscript. Erik Johnson for discussion of and reviewing of papers, and for his positive support. Niels Hessel Andersen for good advice and many motivating and inspiring discussions. Bente Lebech for help with analysis and discussion of XRD results, and for always being inspiring and smiling. Jean-Claude Grivel for help with making YBCO bulk powder and Finn Willy Poulsen, Lene Knudsen and Stinus Jeppesen for help with XRD measurements.

During a significant part of my Ph.D. period I have been working with Jonas Okkels Birk in a very good collaboration on the CoO project, and I would like to thank him for this. The students from the 'Neutron course' at University of Copenhagen (A. Tønnesen, A. D. Givskov, J. Garde, J. Larsen, A. P. L. Böttiger M. Glyvradal, L. P. Sperling) which were involved in some of the measurements also deserve a thanks.

I would also like to thank my brother Ottar who, although far away, has given me good assistance with the design of the front page for the thesis.

Jørn Bindslev who has been co-supervisor since the branch of my project related to him dried out, deserves thanks for his continued help with advice and sharp observations.

Luise Theil Kuhn most definitely deserves a second mentioning for being a fantastic co-supervisor. Even though she has had no formal obligation, and defying a very busy schedule, she has been a very reliable support. Her ability to say things, which are in need of being said, but always doing so in an encouraging manner, is fantastic. All in all it has been a pleasure and I owe her many thanks.

Finally I owe my biggest thanks to my main supervisor Kim Lefmann for being a very patient, competent, supporting and a good supervisor. I would not have made it without him.

Last, but not least, I would sincerely like to give my thanks to my supervisor and contact at the PSI, Christof Niedermayer, for being a great supervisor! He has with his always positive, yet realistic attitude, provided me with many very fruitful discussions, and good support. Leaving his office, I have always felt a little bit wiser and a bit more certain of things – and often with a smile on my face.

Lastly I owe thanks to all my friends and family for support and long-lasting understanding while I have completed this work.

# Preface

This thesis appears in partial fulfillment of the requirements for the Ph.D. degree at the Niels Bohr Institute, Copenhagen University.

Chapter 1 contains an introduction to the subject of the thesis, *magnetic order in nano-scale antiferromagnetic materials*. The introduction is followed by the motivation to the subject of this thesis.

Chapter 2 gives a brief introduction to high temperature superconductivity and antiferromagnetism before continuing to introduce critical phenomena in phase transitions and finite size effects. Furthermore the chapter contains introductions to the studied systems YBCO and CoO.

Chapter 3 gives an introduction to the two main experimental techniques employed in this work, namely neutron scattering and muon spin rotation.

Chapter 4 contains details on the preparation, doping and characterization of the studied samples of YBCO and CoO, as well as it briefly introduces the techniques used.

Chapter 5 contains the analysis of YBCO results obtained using neutron scattering and muon spin rotation, followed by a conclusion in which the results are presented, inter-compared and compared to literature.

Chapter 6 contains the analysis of the results from the measurements of the critical phenomena in CoO nanoparticles, followed by a discussion, conclusion and outlook on the studied system.

Chapter 7 gives a brief summary and conclusion of the results from the previous chapters, followed by an outlook on potential areas in relation to the systems studied during the course of this thesis work.

Appendix A is a résumé of the implementation of the SICS instrument operating system on the triple axis spectrometer RITA-2 at the Paul Scherrer Institute, which was performed by me during the course of my Ph.D. time.

Appendix B contains selected logs from the synthesis of the YBCO nanoparticles.

Appendix C contains calculations and implementations performed in relation to the analysis of the data.

Appendix D contains manufacturing details and AFM images of PLD-produced YBCO islands on semiconductor substrates.

Appendix E contains in raw form extra analysis and characterization material, which is not included in the analysis chapters.

Appendix F provides details on calculations and simulations used in the analysis of the CoO results in chapter 6.

Appendix G contains a range of physical and chemical data tables, with values used in the present work.

Appendix H contains the papers both submitted and in progress, which I have written or co-authored during my Ph.D. time.

Copenhagen, August 15, 2008

Jari í Hjøllum

# Chapter 1

## Introduction

The understanding of nano-structured materials is in present day society becoming increasingly important. In this thesis investigations of two very different antiferromagnetic material nanoparticle systems is presented. The first of these is a complex material, the high temperature superconductor YBCO, with a potentially very important usage in technological advancement. In high contrast to this, the second material is a simple and well understood material, which has the potential to cast light on the universal phase transition phenomena.

Common to these two materials is the long range magnetic order in bulk material, and the question thus arises: How do these systems, in which long range order is intrinsic, respond, when the system is spatially highly confined?

The famous high-temperature superconductor (HTSC)  $\text{YBa}_2\text{Cu}_3\text{O}_{6+x}$  (YBCO), discovered by Wu *et al.* [207] in 1987, was the first superconductor with a critical temperature ( $T_C \simeq 93\text{K}$  [53]), which was above the boiling temperature of nitrogen. It is part of a large family of cuprate HTSC's where the superconductivity resides in conducting  $\text{CuO}_2$ -planes separated by insulating  $\text{CuO}$ -planes, as shown in figure 2.4.1.

The fundamental properties of YBCO are determined by the hole doping, which determines whether the material is in an antiferromagnetically (AFM) ordered or a superconducting (SC) state. This hole doping  $p$  can be controlled through oxygen doping  $x$ , which can be varied within  $0 < x < 1$ . YBCO is an antiferromagnet at doping levels  $x < x_C$  ( $x_C \simeq 0.35$ <sup>1</sup>), and a superconductor at  $x > x_C$ . YBCO is special in the sense that the AFM and the SC phases are very close in the phase diagram – and might even be coexisting, as shown in figure 2.4.4.

This stands in strong contrast to conventional superconductors (*e.g.* metals) where SC and magnetism are antagonistic, and a moderate magnetic field will destroy SC.

The superconductivity of the cuprates is still not entirely understood, but an increasing amount of work indicate [32, 40, 121, 122, 200] that AFM spin fluctuations are related to the SC. There are also indications, that the AFM order is intimately related to the superconductivity of the system. For instance, in the superconductor  $\text{La}_{2-x}\text{Sr}_x\text{CuO}_4$  (LSCO), there is a 1/8-anomaly ( $p=1/8$ ), where superconductivity decreases significantly and antiferromagnetism is greatly enhanced [98]. One interpretation of this is that superconductivity and magnetism are competing phases, where another – as mentioned with the spin fluctuations – is that the mechanisms behind the superconductivity and the magnetic ordering are related [169].

Simple antiferromagnetically ordered materials, have been thoroughly investigated, and are believed to be well understood. Even the understanding of phase transitions, and more specifically, of the behavior very close to a phase transition, in the critical region, the so-called critical phenomena are well understood theoretically [204, 205, 206] and have been verified experimentally [3, 13, 178]. The Nobel Prize in physics was awarded to Kenneth G. Wilson in 1982 [204, 205, 206]

---

<sup>1</sup>The exact doping value of the transition varies somewhat in the literature [159, 164, 182, 183, 188].

'for his theory for critical phenomena in connection with phase transitions' [133].

However, the theory of critical phenomena applies to infinite systems, as well as the experimental verifications have been conducted on large, close to infinitely-sized single crystals. The importance of the length scale of the infinite systems becomes evident when considering for instance the correlation length of the magnetically ordered spins in an antiferromagnet, which diverges at the phase transition (at the critical point).

It is therefore an open question what the critical behavior of a finite sized system would be. Or taking this to the extreme, do systems, with dimensions of only a few hundred ions across, show the behavior of a phase transition, and if so, what is the behavior of such a nanosized system? To elucidate on this question, I have performed experiments, where the magnetic order parameter and the correlation length has been measured in the simple antiferromagnet CoO.

Many physical systems have a long range order or exhibit behavior which is related to the large dimensionality of the system. Static magnetic order in, *e.g.* antiferromagnetic systems, display a long range order, described by the magnetic order parameter. Close to the magnetic transition, critical fluctuations with infinite correlation length dominate the system.

The cuprate HTSC systems have a short coherence length, but have as an intrinsic part of the system a long penetration depth of magnetic fields. The interplay between these two phenomena on a large scale, determines to a large extent the superconducting properties and macroscopic behavior of the cuprate superconductors. Below  $x_C$  a highly anisotropic long range antiferromagnetic order arises.

## 1.1 Motivation

The present work is divided into two main parts, *Antiferromagnetic Order Parameter in YBCO Nanoparticles* and *Critical Phenomena in Nano-Sized CoO Particles*. The former deals with a complex and far from well-understood HTSC-system, the latter presents first-ever measurements of nano-sizing the critical phenomena in an otherwise well-understood system. The two very different system, we have investigated, come together in this study of phase transitions in antiferromagnetic nano-sized systems.

### 1.1.1 Antiferromagnetic Order Parameter in YBCO Nanoparticles

The fact that the antiferromagnetic and superconducting regions in YBCO (in contrast to other HTSC's) intersect and possibly overlap suggests that the superconductivity and the antiferromagnetism are intimately related and possibly not just competing phases.

The original idea was to experimentally investigate, with particle size, temperature and doping, whether the magnetic properties of the system were affected when one of the length scales in the superconducting phase, the correlation length or the penetration depth, were approached. In particular, it was thought interesting to investigate the magnetic order behavior, in YBCO particles comparable in size to the coherence length of the YBCO Cooper-pairs ( $\xi_{ab}=2.5$  nm,  $\xi_c=0.5$  nm [53]). During the course of this project it was, however, discovered that size control of the particles was not possible with present technique, which yielded a distribution of particle sizes larger than  $\xi_{ab}$ .

As size control was beyond reach I decided to stay with the investigations of the magnetic order parameter of the nanoparticles. This is still interesting as there are open and interesting issues regarding the nanosized scale. The particles are disc-shaped, and the very narrow dimensions along the short  $c$  axis, can be conceived to give rise to nano-effects, as those previously observed in NiO by Klausen *et al.* (2002) [86].

The parameters have been characterized using a range of methods, including X-Ray Diffraction (XRD), Transmission Electron Microscopy (TEM), Atomic Force Microscopy (AFM) and magnetic AC susceptibility. The magnetic order parameter of the samples was investigated using triple axis

neutron scattering and zero field muon spin rotation – two techniques which are complementary and provide different types of information.

### 1.1.2 Critical Phenomena in Nano-Sized CoO Particles

The behavior of phase transitions in bulk materials is well understood, is accurately described theoretically and has been thoroughly verified experimentally.

However, the rise of studies of nano-systems in the light of the nano-revolution, has lead us to the question: What happens to phenomena related to length scales when we make the systems as small or smaller than the length scale in question? Does the bulk behavior break down entirely, is it altered or do new phenomena arise?

To study this, we have utilized the two-axis mode of a triple axis neutron spectrometer with a large position sensitive detector to investigate the properties, in particular the correlation length, of the magnetic critical fluctuations in CoO nanoparticles in comparison to bulk results.

CoO has a simple structure, is 3D antiferromagnetically ordered, and is described well with the simple Ising magnetic interaction. Furthermore, it has been extensively studied (in *e.g.* refs. [60, 79, 117, 150, 151, 152, 153, 154, 162, 186, 194]).

In our study of the antiferromagnetic-paramagnetic transition critical phenomena in CoO, we have employed neutron scattering which through the magnetic scattering approach is a very powerful tool for studying magnetic critical phenomena.



## Chapter 2

# Antiferromagnetism and Superconductivity

### 2.1 Antiferromagnetism

Understanding antiferromagnetism requires understanding of ferromagnetism. Figure 2.1.1 shows the two types of magnetic ordering, the ferromagnet and the antiferromagnet, in which the spins are oriented parallel and antiparallel respectively. The main ordering mechanism of magnetism is the exchange interaction, of which a simple Heisenberg hamiltonian can be written as

$$\mathcal{H} = \sum_{\langle i,j \rangle} -J_{i,j} \mathbf{S}_i \cdot \mathbf{S}_j, \quad (2.1.1)$$

where  $\sum_{\langle i,j \rangle}$  is the sum over all combinations of spins in the system (crystal),  $J_{i,j}$  is the interaction between the spins  $i$  and  $j$  and  $\mathbf{S}_i$  and  $\mathbf{S}_j$  are the spin operators of the spins  $i$  and  $j$  respectively.

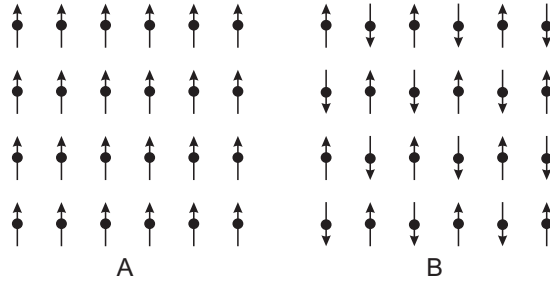


Figure 2.1.1: *Schematic representation of two types of magnetic ordering in solids (material with a crystal structure). A) Ferromagnetic, all spins are aligned parallel. B) Antiferromagnetic, the spins in the different sublattices have antiparallel spins, and cancel each other resulting in a zero net magnetic moment.*

In a ferromagnet the sign of  $J_{i,j}$  is positive, dictating a parallel orientation as the energetically most favorable organization of the atomic spins. However, in a ferromagnet this creates a large external dipolar field, which comes enters the equation of energy, forcing the creation of domains, to minimize the stray field energy.

The third factor which has to be considered is the spin-orbit interaction which links the electronic spin direction to the crystal axis, thereby causing preferred directions (easy axis) of magnetization in a crystal.

The antiferromagnet is the case where the resulting exchange integral is negative, causing an antiparallel orientation of the spins. If the antiparallel sub-lattices are equal in magnitude, we have an antiferromagnet with no net external magnetic moment.

Although the origin of the spin ordering is the same as in ferromagnets, antiferromagnets are quite different. An example of this is, that as the antiferromagnet does not have a macroscopic magnetic dipolar field and that the formation of magnetic domains therefore is not driven by minimization of the field energy, as in ferromagnets, but rather by the nucleation of the spin ordering with multiple nucleation sites. Another example is the existence of complex ground states, as the Néel state, where the spins are aligned antiparallel, is not an eigenstate of (2.1.1). This is often described by the quantum fluctuations.

As the antiferromagnet does not have a macroscopic magnetic moment, only a few techniques, such as neutron scattering and muon spin rotation, can probe the staggered magnetization in the sublattices. However, other techniques such as susceptibility and heat capacity measurements can provide information on *e.g.* phase transitions of the system.

### 2.1.1 Heisenberg and Ising Interaction Models

Eq. (2.1.1) is the hamiltonian for a system interaction with 3D order parameter. However, far from all systems have dimensionality  $D$  of 3. The most common models are the Heisenberg model ( $D=3$ ), the XY model ( $D=2$ ) and the Ising model ( $D=1$ ). The XY model is not relevant for the remainder of this thesis. The hamiltonian for the Heisenberg exchange interaction as mentioned is given by (2.1.1). The Heisenberg interaction takes the spin components in all 3 directions into account.

The Ising model interaction is expressed by the hamiltonian

$$\mathcal{H} = - \sum_{\langle i,j \rangle} J_{i,j} S_i^z S_j^z, \quad (2.1.2)$$

where  $J_{i,j}$  is the exchange constant between the  $z$ -component spins ( $\mathbf{S}_i^z$  and  $\mathbf{S}_j^z$ ). In opposition to the Heisenberg hamiltonian, the spins in the Ising model are only allowed to point up or down (along  $z$ ), although they may have more than 2 values if  $S > \frac{1}{2}$ .

### 2.1.2 Phase Transitions

Phase transitions and phases are a most central concept in describing the behavior and properties of matter. It has for instance been proposed that the evolution of the early universe contained a series of phase transitions [59]. Many phase transitions are continuous in nature, and can be associated with an order parameter, that changes continuously to reach zero just at the order transitions. These transitions, which go through a critical point are called second order. These well known phase transitions are also called critical phase transitions [38].

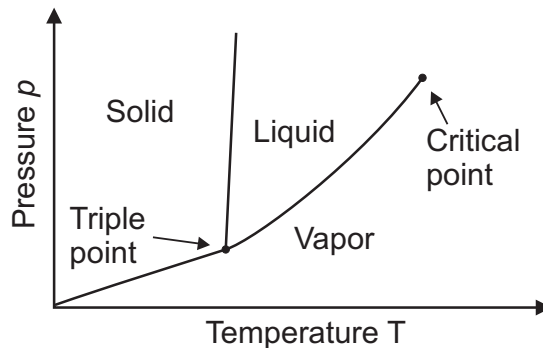


Figure 2.1.2: *Pressure-temperature diagram for a typical gas-liquid-solid system. The solid lines represent phase-borders, where the phase transitions are first order. Only phase transition going through the critical point are of second order. Modified from ref. [38].*

If we consider the well known solid/liquid/gas phase diagram (*e.g.* in figure 2.1.2), it has a triple point and a critical point. These familiar phase transitions (solid/liquid/gas), which cross the phase boundaries, are all first order as they involve the abrupt change of state from one phase to another. Expressed in terms of Gibbs free energy  $G(P, t)$ , it means that  $\partial G/\partial P$  and  $\partial G/\partial T$  are discontinuous at the phase boundaries in figure 2.1.2.

Opposed to the first order transitions, the second order transitions have a continuous transition from one phase to the other. In these transitions the above derivatives are continuous and the transition does not have any latent heat associated with it.

Critical phase transition phenomena or just critical phenomena cover the behavior of matter at, or very close to, the phase transition. In critical region, the thermodynamical properties (herein the behavior of the order parameter(s)) can be described in universal power law behavior. Our understanding of these second order phase transitions comes largely from the theory of critical phenomena [204, 205].

The critical exponents by which the critical phenomena are characterized, are universal, *i.e.* the value depends on the very overall features of the system, such as dimensionality of the system and of the order parameter, but not on its detailed features. For example, the microscopic magnetization  $m$  of a system can be described as  $m \propto \left(\frac{T_C - T}{T_C}\right)^\beta$  where  $\beta$  is a universal critical exponent,  $T$  is temperature and  $T_C$  is the transition temperature (Curie or Néel temperature).

The systems to which this universality applies ranges from dimensionality  $N=0$  (*e.g.* polymers), over  $N=1$  (*e.g.* Ising systems),  $N=2$  (*e.g.* superfluid helium and binary mixtures),  $N=3$  (*e.g.* real ferromagnets) [210], to higher dimensions. The theory of criticality is well developed, and many of the critical exponents have been calculated, either through exact solutions or through numerical calculations [63, 64, 99, 210, 211].

### 2.1.3 Critical Exponents

The theoretical study of the magnetic order phase transition, started with Ising's analysis of the 1D ordered system [25], and was followed by Onsager's exact solutions [135] of the two dimensional Ising model in the 1940's, and evolved over the approximate solutions to the three dimensional systems as no exact solution seemed forthcoming. Later the idea of describing the systems with critical exponents arose. Further development of theory yielded first the scaling approach and later the renormalization group approach as ways of describing the critical exponents [38].

A wide range of critical exponents exist, and below I will list these without any further derivation. There are several very good derivations in the literature, *e.g.* [14, 19, 38, 111]. The properties and their critical exponents can be expressed [14, 38] as:

$$\text{Reduced temperature } \epsilon = \frac{T - T_N}{T_N} \quad (2.1.3)$$

$$\text{Magnetic order } M \propto (-\epsilon)^\beta \quad T < T_N \quad (2.1.4)$$

$$\text{Correlation length } \xi \propto (-\epsilon)^{-\nu'} \quad T < T_N \quad (2.1.5)$$

$$\xi \propto (\epsilon)^{-\nu} \quad T > T_N \quad (2.1.6)$$

$$\text{Correlation function } \Gamma \propto \frac{e^{-r/\xi}}{r^{2-d-\eta}} \quad \text{where } r \text{ is large, close to } T_N \quad (2.1.7)$$

$$\text{Magnetic susceptibility } \chi \propto (-\epsilon)^{-\gamma'} \quad T < T_N \quad (2.1.8)$$

$$\chi \propto (\epsilon)^{-\gamma} \quad T > T_N \quad (2.1.9)$$

$$\text{Heat capacity } C_V \propto (-\epsilon)^{-\alpha'} \quad T < T_N \quad (2.1.10)$$

$$C_V \propto (\epsilon)^{-\alpha} \quad T > T_N \quad (2.1.11)$$

The values of the exponents depends on the dimensionality of the physical system ( $d$ ), the dimensionality of the order parameter ( $D$ ) and of the size of the system. The correlation function (2.1.7) defined as

$$\Gamma_{i,j} = \langle \mathbf{s}_i \cdot \mathbf{s}_j \rangle - \langle \mathbf{s}_i \rangle \cdot \langle \mathbf{s}_j \rangle, \quad (2.1.12)$$

can under certain conditions, be expressed [38] as

$$\Gamma(\epsilon) \propto \chi \propto (\epsilon)^{-\gamma}, \quad T > T_N. \quad (2.1.13)$$

The correlation function will be treated further in section 3.2.2.

For 3D Ising systems no analytical derivation of the exponents is known, and the exponents in table 2.1.1 are found numerically [64]<sup>1</sup>.

Property	Exp.	Value
Magnetic order	$\beta$	0.3258(14) $\simeq \frac{5}{16}$
Magnetic susceptibility	$\gamma$	1.2396(13) $\simeq \frac{5}{4}$
Correlation length	$\nu$	0.6304(13) $\simeq \frac{5}{8}$
Heat capacity	$\alpha$	0.109(4) $\simeq \frac{1}{8}$
Correlation function	$\eta$	0.0335(25) $\simeq 0$

Table 2.1.1: Numerically found 3D Ising exponents. From ref. [64].  $\simeq$  is only intended to indicate a fraction close to the found value.

### Critical Exponent Scaling Laws

Scaling law calculations, of which the details will not be treated here, give four relations linking the critical exponents of a system. These relations state that the different exponents are *not* independent of each other, and are given [52] as

$$\alpha + 2\beta + \gamma = 2 \quad \text{Rushbrooke,} \quad (2.1.14)$$

$$\beta(\delta - 1) = \gamma \quad \text{Widom,} \quad (2.1.15)$$

$$(2 - \eta)\nu = \gamma \quad \text{Fisher,} \quad (2.1.16)$$

$$2 - \alpha = d\nu \quad \text{Josephson,} \quad (2.1.17)$$

where (2.1.17) for instance is obeyed by both the Onsager results for  $d = 2$  as well as by the mean field theory result for  $d = 4$ . The scaling laws furthermore predict that  $\nu = \nu'$ ,  $\gamma = \gamma'$  and  $\alpha = \alpha'$  for 3D Ising systems [38].

### Universality

As briefly mentioned in section 2.1.2, the behavior of the critical systems and more importantly the values of the critical exponents, do not depend on details of the physical system being considered. The values and thus the behavior, does only depend on the dimensionality of the interactions (the Hamiltonian), and of the dimensionality of the space of the system being considered, and are thus universal. Due to the universality, the critical exponents are of tremendous interest, as the universality actually allows the solution to the physical problem to be reapplied to totally different physical systems, which will exhibit the same critical exponents due to the universality.

### Experimental Verification of Critical Exponents

Experimental verification of the theory on critical phenomena is ongoing and is conducted using a multitude of techniques on a range of systems. These include for instance X-Ray studies on structural transitions (correlation length  $\nu_{L2}$ ) [115], calorimetry measurements of heat capacity ( $\alpha, \alpha'$ ) [162] and neutron scattering on antiferromagnets ( $\nu, \gamma, \eta, \eta', \beta$ ) [3, 13, 178].

The neutron scattering technique is one of few able to probe the correlation length (as well as other critical exponents) in antiferromagnets [3], and is therefore widely used.

## 2.2 Superconductivity

Superconductivity describes a conductor with zero resistance. However, a superconductor is fundamentally different from an perfect conductor of *e.g.* an ordinary metal with zero impurities and at 0K. The physics driving these states is the formation of Cooper pairs of electrons. The

<sup>1</sup>Other works [63, 99, 210, 211] support the findings in this paper.

Cooper pairs which form a Bose-Einstein-like condensate below the critical temperature  $T_C$ , will flow without resistance through the superconducting material.

### 2.2.1 The Meissner Effect

One of the most spectacular properties of a superconductor is the Meissner effect, which is the phenomenon of total expulsion of magnetic flux from the superconductor. This implies that in the Meissner state ( $B \equiv 0$ ) a superconductor is a perfect diamagnet with a susceptibility  $\chi = -1$ . This will hold with increasing applied field until a certain value, where it is no longer energetically favorable to uphold the Meissner state.

### 2.2.2 Type I and Type II Superconductors

Two types of superconductors exist - type I and type II. Type I usually has quite low  $T_C$ , and will uphold the Meissner state, up to a critical field  $H_C$  at which the superconducting state breaks down completely.

Type II will as type I expel the magnetic field up to a certain field  $H_{C1}$ , where it is energetically favorable to allow flux penetration in the form of flux lines. The density of flux lines will increase with the applied field to a field  $H_{C2}$  where there is no more room for the superconductivity, as the distance between the flux lines is less than the Cooper pair coherence length.

The distinction between type I and type II is given with  $\kappa$

$$\text{Type I: } \kappa = \frac{\lambda}{\xi} < \frac{1}{\sqrt{2}} \quad (2.2.1)$$

$$\text{Type II: } \kappa = \frac{\lambda}{\xi} > \frac{1}{\sqrt{2}}, \quad (2.2.2)$$

where  $\lambda$  is the London penetration depth and  $\xi$  is the coherence length of the Cooper pairs [53].  $\lambda$  characterizes the distance which a weak magnetic field penetrates a superconductor, or in other words, how the penetration of an external field into the superconductor will be damped with distance  $r$  as  $e^{-\frac{r}{\lambda}}$ .

$\xi$  characterizes the minimum length over which the quantum mechanical phase can be changed with  $\pi$  without destroying the superconductivity, or equivalently the length scale over which the superconducting order parameter  $\psi$  is unchanged

Metallic elements which are superconducting are typical type I superconductors, with large coherence lengths and small penetration depths. Type II superconductors have large penetration depths and small coherence lengths. The cuprate high- $T_C$  superconductors are extreme type II superconductors, typically with  $\lambda \sim 2000 \text{ \AA}$ , and  $\xi \sim 25 \text{ \AA}$  [53].

Another distinction in superconductivity is whether the superconductor can be described by the Bardeen, Cooper and Schrieffer (BCS) theory [12]. The BCS theory, in which the superconductivity is phonon-mediated, which means that the phonons mediate an electron-electron coupling allowing the electrons to form a Cooper-pair. The Cooper-pairs are bosons and Bose-condensate below a certain temperature. BCS theory can explain superconductivity in most type I and several type II materials, but is, however, not applicable to the cuprate superconductors, which are still far from being understood. The mechanism behind superconductivity in these materials is something different, and several explanations such as charge stripes have been proposed.

## 2.3 The Cuprate High- $T_C$ Phase Diagram

The cuprate superconductors exhibit several very special features. Observing the phase diagram in figure 2.3.2 we see that common to the cuprates is that they are antiferromagnetic and insulating at low doping, with the antiferromagnetic order being located in the  $\text{CuO}_2$  planes. However, a small degree of hole doping causes a transition from an insulator into a metallic state, which, however, has a poor conductivity. When cooled, this poor metal becomes a superconductor with

a very high  $T_C$ . When doped further the material becomes very metallic-like with a Fermi liquid state.

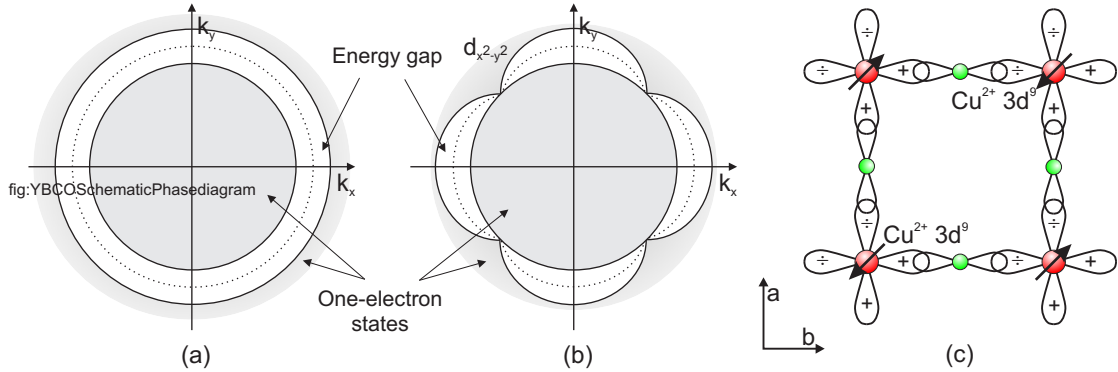


Figure 2.3.1: Schematic illustration of the difference of the energy gap in  $s$ -wave and  $d$ -wave superconductors, and the relation to the magnetic order in the  $d$ -wave superconductors. (a)  $s$ -wave superconductor energy gap. The dashed lines indicate the Fermi surface in the normal state, and inner and outer surfaces represent the borders of the allowed electronic states. (b)  $d$ -wave superconductor. For illustrative purposes the inner surface, limiting the allowed states, is depicted as a sphere. The energy gap is seen to go to zero in certain directions in reciprocal space. (c) The spatial arrangement of the Cu<sup>2+</sup> (red)  $d$ -orbitals and the oxygen (green)  $p$ -orbitals in real space. Also shown is the spin arrangement of the Cu spins, dictated by the orbital arrangement.

In contrast to the conventional superconductors (e.g. metals), which usually are  $s$ -wave superconductors with an isotropic superconducting energy gap or band gap in reciprocal space, the cuprates are  $d$ -wave superconductors where the superconducting energy gap is anisotropic, and actually closes in some directions, as illustrated in figure 2.3.1.

The orientation of the bands in reciprocal space is closely linked to the spatial orientation of the  $d$ -orbitals, like the orientation of the Cu-spins is also related to the  $d$  orbital orientation as illustrated in figure 2.3.1.

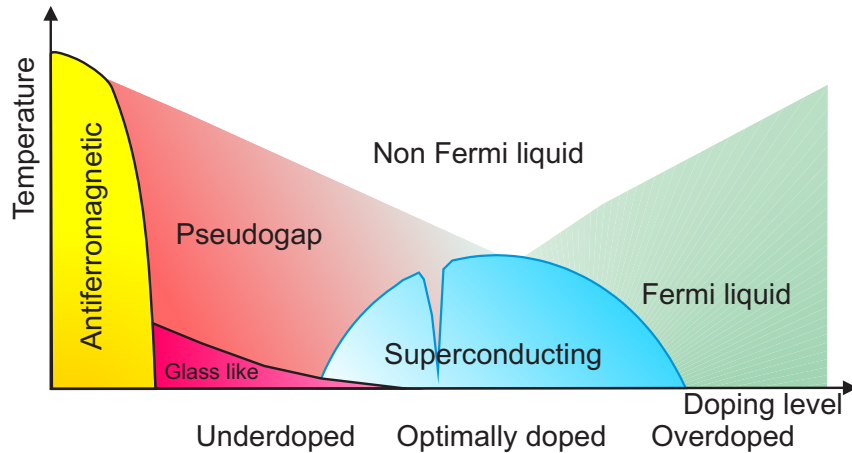


Figure 2.3.2: The generic phase diagram of the cuprate high  $T_C$  superconducting materials.

Another very interesting feature of the cuprates, is the close competition of the different phases. This is seen from figure 2.3.2, where different ordered phases are bordering each other. Considering the phase diagram, from the left, we have the antiferromagnetically ordered phase, and a magnetically non-ordered phase, which, however, exhibits a pseudo-gap. The fact that the system

has a pseudo-gap, indicates that the system has an internal short ranged order, which by some is interpreted as preformed Cooper-pairs [134].

Below the pseudo-gap there is a glass like phase, with short range magnetic correlations, which extends into the superconducting dome. In the superconducting dome the transition temperature  $T_C$  increases with doping up to optimal doping, before decreasing again. The discontinuity on the underdoped/optimally doped border, is the so-called 1/8'th feature, present in LSCO, where superconductivity disappears and magnetic order reemerges [29]. The subject of this study, YBCO, has a plateau in the same region (see figure 2.4.4). Recently, indications of the 1/8'th feature in YBCO have been published [71].

The coexistence of the spin-glass state and superconductivity, and the 1/8'th feature, are indications of the competition of the order parameters of magnetism and superconductivity. The observations close to 1/8'th doping by Lake *et al.* (2002) [98] and others [29, 84], that the antiferromagnetic order is enhanced by an applied magnetic field supports this view.

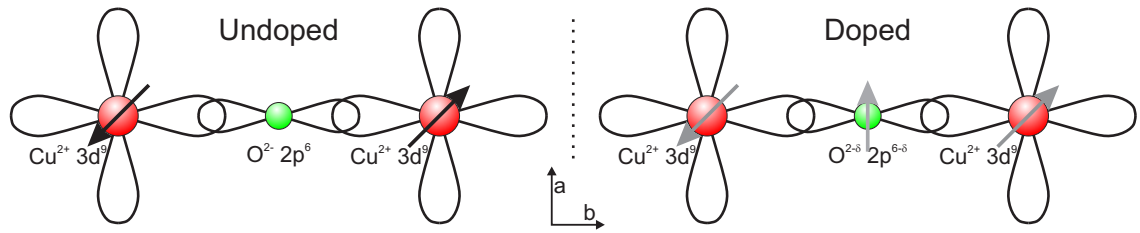


Figure 2.3.3: *Schematic illustration of the antiferromagnetic order of the Cu-O-Cu bond in the conduction plane of a cuprate superconductor. Left: The un-doped ( $x=0$ ) and non-frustrated state. Right: The doped and frustrated state. At low doping, the hole introduces a spin at the oxygen atom, frustrating the Cu spins.  $\delta$  is hole concentration per Cu plane. The gray Cu spins indicate a frustrated spin.*

The break-down of antiferromagnetic order is in itself remarkable. The  $T_N$  of the un-doped system is high,  $\sim 400$  K, indicating relatively strong exchange interactions, however, a very small amount of hole doping ( $\sim 2\%$  in LSCO and  $\sim 6\%$  in YBCO) causes the entire antiferromagnetic order to break down. The explanation is frustration. As illustrated in figure 2.3.3, the un-doped system has a non-frustrated spin lattice, and the antiferromagnetic coupling is carried by the interstitial oxygen atom. However, as holes are introduced at low doping, these go into the interstitial oxygen atom ( $\delta$  in figure 2.3.3), the orbitals are no longer full and a spin moment arises here. This causes frustration of the Cu spins, as there is no longer any preferred spin orientation and the 'ground state' has been destroyed [131, 188].

The doping can be done in several ways, for instance, in LSCO the hole concentration is  $x$ , as each Sr ion introduces a hole into the  $\text{CuO}_2$  plane. In YBCO, the oxygen doping causes a complicated charge transfer from the conduction layer to the charge reservoir layer, introducing holes into the conduction layer, so that  $x$  is not proportional to  $\delta$ . This will be treated further in section 2.4.3.

## 2.4 Introduction to YBCO

This section will be used to give a brief introduction to crystal structure and the electronic, magnetic and superconducting properties of YBCO.

### 2.4.1 Crystal Structure

As the formula  $\text{YBa}_2\text{Cu}_3\text{O}_{6+x}$  ( $0 \leq x \leq 1$ ) indicates, YBCO is a structure in which the oxygen content can be varied. At the lowest doping,  $x = 0$ ,  $\text{YBa}_2\text{Cu}_3\text{O}_6$ , is a simple symmetrical structure, in which the O(4) oxygen position in figure 2.4.1 is empty. At the highest doping,  $x = 1$ ,

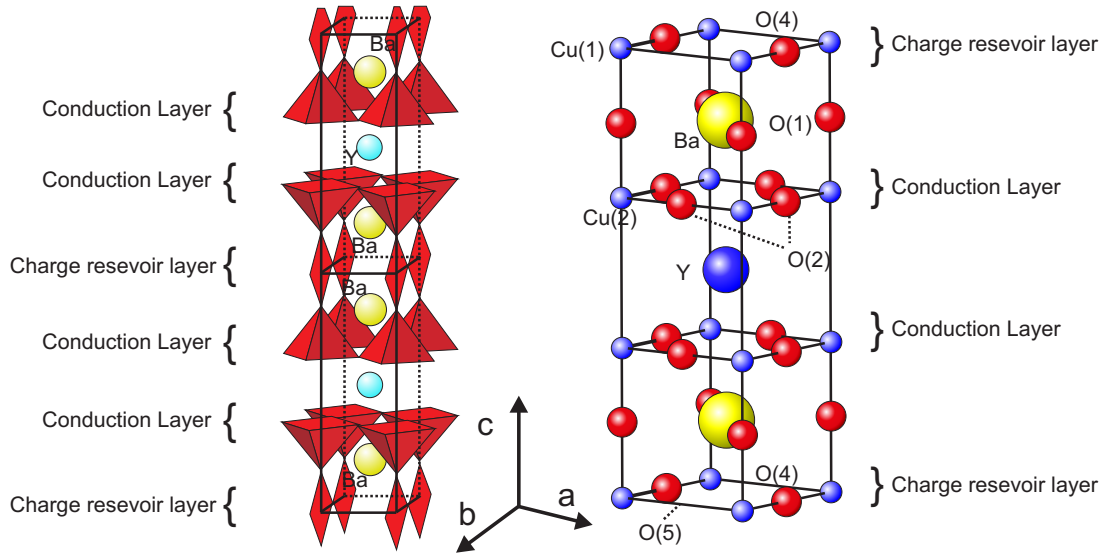


Figure 2.4.1: *Schematic illustrations of the atomic structure of  $YBa_2Cu_3O_{6+x}$ . Left: Schematic illustration of the chemical bonds. Displayed are 2 stacked unit cells. The base plane of the half-octahedra are part of the conduction layers, and the rhombi are centered around the charge reservoir layers. Right: One schematic unit cell with the conduction layers (Cu(2), O(1) and O(2)) and charge reservoir layers (Cu(1), O(4) and O(5)) marked. Modified from refs. [131, 145].*

$YBa_2Cu_3O_7$  has a more complex structure, as discussed below. In this structure the O(4) oxygen position is fully occupied. The oxygen doping  $x$  of YBCO can not be lowered below 0 or raised to above 1, without in both cases causing decomposition of the structure.

$YBa_2Cu_3O_{6+x}$  has depending on oxygen doping  $x$  two different crystal structures, tetragonal and orthorhombic. In the tetragonal state the  $a$  and  $b$  axes are equal ( $\sim 3.8 \text{ \AA}$ ), whereas they in the orthorhombic state have slightly different lengths ( $\sim 3.8 \text{ \AA}$  and  $\sim 3.9 \text{ \AA}$ ). The  $c$  axis is close to 3 times as long,  $\sim 11.8 \text{ \AA}$ . The factor of 3 is easily understood considering that the YBCO structure along the  $c$  axis essentially consists of 3 stacked perovskite unit cells.

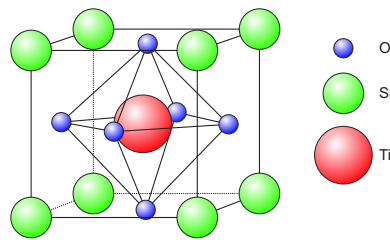


Figure 2.4.2: *The cubic perovskite  $ABX_3$  structure, here  $SrTiO_3$ . Reproduced from ref. [53].*

The general perovskite unit cell is given by  $ABX_3$  (e.g.  $SrTiO_3$  in figure 2.4.2), and YBCO is produced by removing some atoms, and substituting others. The perovskite octahedra have been split by the Y atoms, thus forming the double layer, and Ba substitutes Y in two of the cells [53].

Turning back to the oxygen doping and starting at  $x = 0$ , YBCO has as mentioned a tetragonal structure (space group  $P4/mmm$ , no. 123) with  $a = b$ , and the O(4) position is void of oxygen atoms. Increasing the oxygen content, oxygen atoms settle into the O(4) position and the equivalent O(5) position, randomly. At  $x \simeq 0.35$  [28, 80] ( $x \simeq 0.4$  [145]) at room temperature an ordering of the oxygen atoms occur, and they tend to form chains along the  $b$  axis, occupying only the O(4) site. This causes a transition (the T/O transition) to the orthorhombic structure (space

group Pmmm, no. 47), with  $a \neq b$ <sup>2</sup>. The oxygen ordering and structural transition is illustrated in figure 2.4.3.

The orthorhombic order is in itself not simple, as it is divided into several phases with different oxygen ordering of which Ortho-I and Ortho-II are the most well known. These two differ in the order of the oxygen chains. Ortho-I has identical oxygen chains along the  $b$  axis, *i.e.* every  $b$ -axis chain is occupied. The Ortho-II phase has only every 2nd  $b$  occupied by oxygen atoms [140].

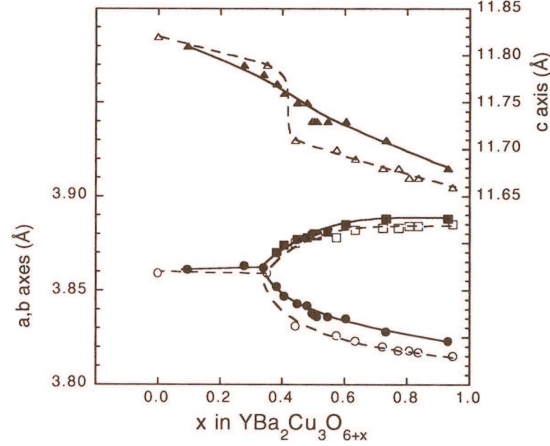


Figure 2.4.3: The development of the YBCO unit cell axes versus doping, as determined by Cava *et al.* (1990) [28] (open symbols and dotted lines) and by Jorgensen *et al.* (1990) [80] (filled symbols and solid lines). Note how Cava's data show a step-like  $c$ -axis anomaly, which is absent in Jorgensen's data. Reproduced from ref. [145].

## 2.4.2 Electronic, Magnetic and Superconducting Properties

Coinciding in doping with the structural phase transition changes happen in the electronic nature of YBCO. Generally the phase diagram of YBCO can be divided into two regions, the antiferromagnetically (AFM) ordered and the superconducting (SC) region as showed in figure 2.4.4.

YBCO is an antiferromagnet with oxygen doping  $x \leq 0.35$  and a superconductor when  $x \geq 0.35$  [182]. As with the structural T/O transition, the exact location of the AFM/SC transition is under debate. For instance Stock *et al.* (2006) [183], found in a  $x = 0.353$  sample no long range antiferromagnetism, whereas Tranquada *et al.* (1988) [188] found the transition at  $x \simeq 0.4$ . Sanna *et al.* (2004) [164] report 0.32.

Whether the T/O transition and the AFM/SC transition dopings are exactly the same, is uncertain, but that the mentioned oxygen chain formation is related to the T/O transition is widely accepted. The AFM/SC transition is also most likely caused, at least indirectly, by the oxygen chain ordering, as the chain ordering introduces a new order in the charge reservoir layer, which in return creates a more ordered hole doping in the conduction layers.

In the AFM phase the Néel temperature ranges from as high as  $T_N \geq 500$  K for  $x=0$ , over  $T_N=400 \pm 10$  ( $x=0.15 \pm 0.05$ ) [187] and 350 K ( $x=0.32$ ) [188], before dropping quickly to 0 K at the AFM/SC transition doping [188] as showed in figure 2.4.4.

The magnetic spin structure is that the spins are oriented along the  $(\frac{1}{2}\frac{1}{2}0)$  direction (*i.e.* in the  $a,b$ -plane), and the planes are antiferromagnetically coupled. The structure is illustrated in figure 2.4.5. The magnetic unit cell has the same  $c$ -axis as the chemical cell, but the  $a$  and  $b$  axis have the double length.

<sup>2</sup>There are slight disagreements in literature and in the communities regarding the transition doping between tetragonal and orthorhombic structure. For instance Cava *et al.* (1990) report YBCO( $x=0.35$ ) as tetragonal [28], although they in a previous paper [27] report it to be orthorhombic. Manca *et al.* (2001) [112] report a T-OII transition  $x \simeq 0.28-0.32$ .

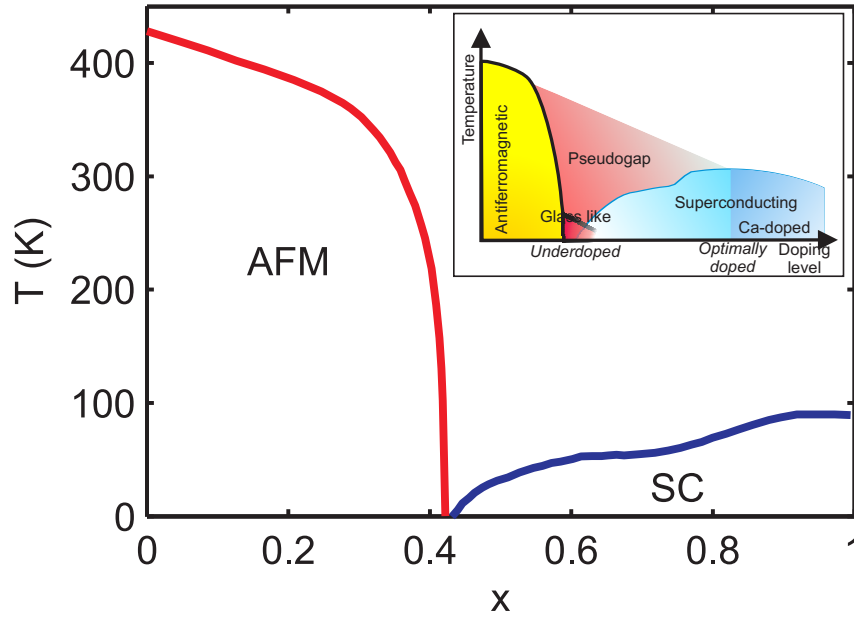


Figure 2.4.4: Measured phase diagram of YBCO. On the left, the antiferromagnetically ordered phase and on the right the superconducting phase, where the superconducting transition temperature  $T_C$  increases with doping up to optimal doping. The plateau is in the same region as the  $1/8$ 'th LSCO feature (see figure 2.3.2), and exhibits signs of incommensurate magnetic order [71, 123]. The solid lines show  $T_N$  (red) and  $T_C$  (blue) versus oxygen doping  $x$ . Modified from ref. [188]. Inset: Schematic phase diagram of YBCO. From the left, the antiferromagnetically ordered phase and the spin glass like phase. Above the glass like phase is the magnetically non-ordered phase, which exhibits a spin gap. The glass like state extends into the superconducting dome [164], where the superconducting transition temperature  $T_C$  increases with doping up to optimal doping, before decreasing again. YBCO can not be doped with oxygen to above  $x=1$ , and further hole doping is therefore done using Ca-Y replacement doping. Figure modified from ref. [131].

In the SC phase (see figure 2.4.6) the  $T_C$  rises rapidly as  $x$  goes beyond 0.35, settles on a semi-plateau (the  $T_C=60$  K plateau) for  $x = 0.50 - 0.65$  before climbing again, to reach the maximum  $T_C$  of  $\approx 93$  K at  $x \approx 0.93$  which is the optimal doping for YBCO. Poulsen *et al.* (1991) [140] have performed calculations which link the behavior of  $T_C$  versus  $x$  to the formation of coexisting domains of the Ortho-II and Ortho-I phases.

### 2.4.3 Oxygen Doping and Hole Doping

As previously mentioned the role of the oxygen doping in the charge reservoir layer is to introduce holes into the conduction planes. Simply put the  $O^{2-}$  ions, draw negative charge from the conduction planes, thereby introducing holes. However, the oxygen ordering in the reservoir layer causes this to be a non-trivial process, and the relation between oxygen doping  $x$  and conduction layer hole doping  $p$  is rather complicated. I will not go further into the mechanisms behind this here, as this is beyond the scope of this thesis. Instead I will use the experimental results described below in chapter 5.

Tallon *et al.* (1995) [185] studied the oxygen doping versus hole doping, but focused more on the superconducting region. They use Bond Valence Sums (BVS) to estimate the hole doping as a function of oxygen doping, using  $p \approx V_- = 2 + V_{Cu} - V_{O(2)} - V_{O(3)}$  displayed in figure 2.4.7. Here  $V_{Cu}$ ,  $V_{O(2)}$  and  $V_{O(3)}$  are the BVS of the Cu, O(2) and O(3) ions, respectively.  $V_-$  is just a band valence sum parameter defined through the above equation. As seen from the figure  $V_- \approx p$  goes below 0, for  $YBa_2Cu_3O_6$ , hence the authors note that the curve should be shifted upwards

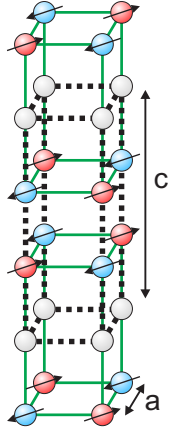


Figure 2.4.5: The magnetic structure of YBCO. Only the Cu ions are displayed. The red and blue ions indicate antiparallel spin orientations. The grey atoms are non-magnetic Cu ions. The green lines connect Cu ion pairs bridged by oxygen ions. The dotted black line shows the chemical unit cell. The arrows on the ions indicate the spin direction. Figure reproduced from ref. [187].

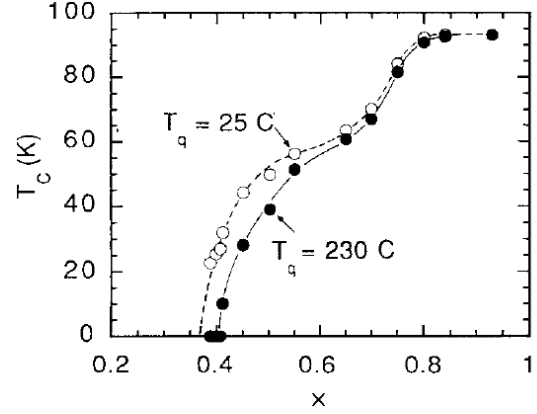


Figure 2.4.6: An example of the  $T_C$  versus  $x$ , for a sample quenched from  $230^\circ\text{C}$  ( $T_q=230^\circ\text{C}$ ), and a sample equilibrated at  $25^\circ\text{C}$  ( $T_q=25^\circ\text{C}$ ). These samples are oxygen disordered and have ordered chains respectively. Modified from ref. [35].

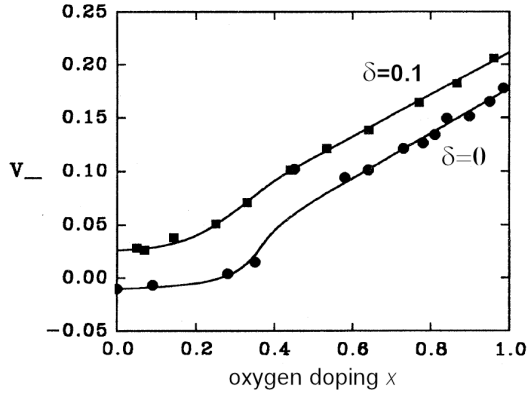


Figure 2.4.7: The bond valence parameter  $V_- = 2 + V_{Cu} - V_{O(2)} - V_{O(3)} \approx p$  plotted versus oxygen doping  $x$  for  $Y_{1-\delta}Ca_\delta Ba_2 Cu_3 O_{6+x}$  with  $\delta = 0$  and  $\delta = 0.1$ . Modified from ref. [185].

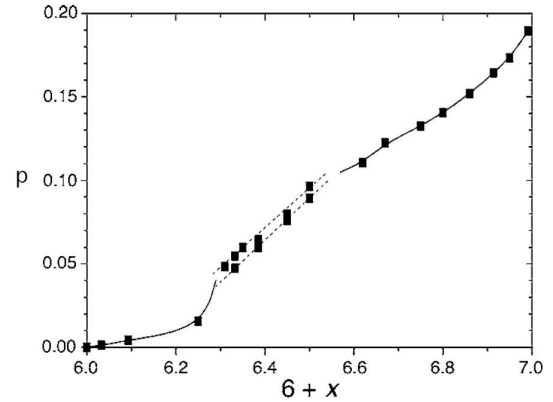


Figure 2.4.8:  $CuO_2$  plane hole doping  $p$  versus oxygen doping  $x$  in YBCO. The lines are guides to the eye. The upper dashed line indicates the Ortho-II phase (with the best oxygen ordering) behavior, and the lower indicates the Ortho-I phase (quenched from above the Ortho-II transition temperature). Modified from ref. [109].

by 0.01, causing  $p$  to be 0 for  $YBa_2Cu_3O_6$ .

A more direct relation is provided by Liang *et al.* (2006) [109] who calculated the relationship between the oxygen doping  $x$  and the hole doping  $p$ . This is presented in figure 2.4.8. The calculations used the  $c$ -axis lattice expansion dependence of oxygen doping as bridge to hole doping, using an empirical formula linking  $c$ -axis expansion to hole doping.

## 2.5 Finite Size Effects

In all regions of solid state physics, the understanding is mainly based on dealing with ideal systems, infinitely sized systems or systems with periodic boundary conditions which allow translational symmetry. In many cases, this approximation is valid, as the systems are so large that any boundary effects are non-existing in the bulk of the sample or system.

There are several types of nanosized systems, which are not described by the infinite system approach. Films, rods or particles which have effective dimensionality of 2, 1 and 0 respectively, all exhibit properties highly affected by the dimensionality [49]. Common to many of the finite sized systems is that the physical properties change compared to bulk or infinitely sized systems. In some cases, the change is continuous with decreasing size, *e.g.* the average magnetization or X-Ray diffraction line width, whereas in other cases, *e.g.* superparamagnetism the effect is more dramatic.

### Magnetic Nanoparticles

If we consider a very small crystal, the number of ions and crystal planes becomes finite, and the system can no longer be considered infinite *i.e.* the periodic boundary conditions are no longer valid. If, for instance, we have a small crystallite, it also becomes important for the physical properties, where in the unit cell the particle 'ends', and whether there is any systematics or pattern in the particle's choice of border.

In recent years with the advances in technology, and in particular in microelectronics, an increased focus has been put on the behavior of finite size and nanosized magnetic systems. The increased capacity of data storage devices, is continuously pushing the border of superparamagnetism, in which the entire magnetic orientation of a particle randomly flips, with a time scale which is a function of the particle size. The time  $\tau$  between the collective flipping of the spins of the particle can for non-interacting particles with uniaxial magnetic anisotropy be approximated with the Néel-Brown [125, 128] expression

$$\tau = \tau_0 e^{\frac{KV}{k_B T}}, \quad (2.5.1)$$

where  $\tau_0$  is a time constant (typically of the order  $10^{-10}$ - $10^{-12}$  s),  $K$  is the anisotropy constant,  $V$  is the volume of the particle,  $k_B$  is Boltzmann's constant and  $T$  is temperature [124]. If the time  $\tau$  is less than the characteristic time scale of the measurement technique, the local magnetization will likely have flipped, and no net local magnetization is detected.

For antiferromagnetic nanoparticles, Néel proposed that [129], any antiferromagnetically ordered nanoparticle would have a finite number of uncompensated surface spins. The number of uncompensated spins  $\delta$  in a cube varies from  $\delta \simeq n_s^{1/3}$  to  $\delta \simeq n_s^{2/3}$  depending on the arrangement of the missing spins, from randomly missing surface spins to an odd number of antiferromagnetically ordered layers, respectively [11].

As seen from the expressions for  $\delta$ , size of the particles becomes important when we consider the number of relative uncompensated spins, which amount to

$$\delta_s = \frac{\delta}{n_s} = n_s^{-\frac{2}{3}}, \quad (2.5.2)$$

in the most conservative above case. Linking the particle diameter to the number of (random,  $\delta \simeq n_s^{1/3}$ ) uncompensated spins ( $d^3 \propto n_s$ ) we get

$$\delta_s \propto d^{-1}. \quad (2.5.3)$$

From the above equations we see that when approaching very small sizes, the surface spins play an increasing large role in the behavior of the system. A common phenomena considering uncompensated spins is spin canting (figure 5.1.24), in which the uncompensated spins are canted with respect to the bulk spins within their sublattice, due to the missing neighbor interactions.

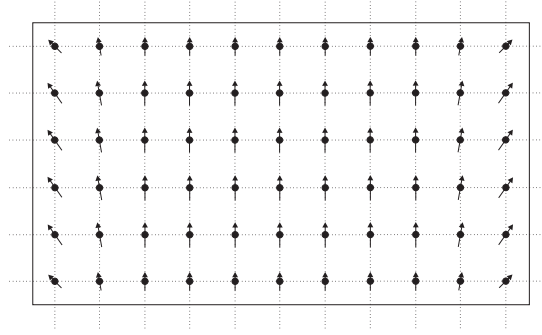


Figure 2.5.1: A schematic illustration of spin canting in a nanoparticle. The dashed lines indicate exchange interactions, and the box indicates the boundary of the particle.

Examples of the significant role of the surface spins in very small particles is reported by Frandsen *et al.* (2004 & 2005) [55, 54], showing interparticle interactions, and oriented attachment and exchange coupling respectively.

Nanosized systems may also exhibit reduced magnetic moment and Néel temperature, such as that found in nano-crystalline Cr [48, 49]. Similar effects are, as mentioned, also found in disc-shaped NiO nanoparticles [86].

A phenomena related to nanoparticle systems, superparamagnetism and interparticle interactions, is the stabilization of the magnetic moment of nanoparticles, in magnetic recording devices. In the size limit of superparamagnetism, the magnetic orientation of a layer of nanoparticles is stabilized against thermal excitations through an antiferromagnetic interaction with an underlying layer of magnetic nanoparticles [1, 49, 56].

### Mermim-Wagner Theorem

The Mermim-Wagner theorem [120] states that there can be no ferro- or antiferromagnetic order in an isotropic 1D or 2D Heisenberg system for  $T=0$ . In an 1D system long-range order is even forbidden in an anisotropic Heisenberg system [49]. However, as all magnetic system in reality exist in 3 dimensions, systems with reduced dimensions may still exhibit magnetic order.

### Magnetic Thin Films

The anisotropy of the system also plays a role, and in the extreme and more moderate 2D cases, thin films and discs, the magnetic order may be significantly altered from that of bulk. In very thin films the orientation of the spins is typically out of plane, and reorients to being in-plane with growing film thickness, due to changes in anisotropy and due to demagnetization fields. There are, however, exceptions, where the behavior is opposite [49, 174].

The reduced dimensionality also acts to reduce the magnetic ordering temperature,  $T_N$  or  $T_C$ . This is a finite size effect, as the individual layers are strongly perturbed by the local coupling at the interfaces [49, 110, 173]. There are studies directly showing that the Néel temperature of antiferromagnetic systems is related to the magnetic correlation length and thus the system size [6, 82]. Furthermore the finite size/reduced dimensionality along with the geometry and structure of the system may act to reduce the magnitude of the ordered magnetic moment [108, 49].

The coupling of the individual layers also has a dramatic effect on the transition temperature, where for instance  $T_N$  of CoO in  $\text{Fe}_3\text{O}_4/\text{CoO}$  multi layers, increases beyond that of bulk due to the coupling with the  $\text{Fe}_3\text{O}_4$  which has a much higher transition temperature [49, 75].

### Superconductivity

Considering the nano-scale lengths in superconductivity, the coherence length  $\xi_0$  and the London penetration depth  $\lambda_L$ , the idea that approaching these length, would lead to changes in the superconductivity, is close. Similarly the magnetic correlation length  $\chi$ , is a length scale which can

be approached to investigate finite size effects.

Raittila *et al.* (2002-2003) [138, 146, 148], used a citrate-gel method to manufacture the nanosized YBCO powder studied in this thesis. They studied the morphology of the powder using atomic force microscopy (AFM), as well as they studied the physical properties using X-Ray diffraction and SQUID magnetometry, finding the particles to be disc-shaped with a significant diameter-distribution, crystalline with a slightly reduced  $c$ -axis and exhibiting a gradual Meissner effect.

Other studies of small particle YBCO systems, focusing on structure and oxygen ordering, such as Weyl *et al.* (1995) [201] have been performed.

However, the antiferromagnetic phase of YBCO nanosized systems has to our knowledge not been explored.

### Criticality in Nanosized Systems

The theory of critical phenomena is in principle valid only for 'infinitely' large systems. For atomic and molecular systems the behavior can be quite different, as a relatively large portion of the elements (*e.g.* spins) of the system, as mentioned, do not have periodic boundary conditions.

For CoO systems in the mesoscopic (or nano-) length scale, the behavior is in some cases predicted from numerical simulations, but very few experiments are performed. However, Flipse *et al.* (1999) [51] and Golosovsky *et al.* (2005) [60] have successfully studied 4 nm CoO nanoparticles using magnetic circular X-Ray dichroism and 10 nm CoO nanoparticles using neutron scattering, respectively. They report observing significant finite size effects such as superparamagnetism and a significant surface-atom related magnetic contribution [51] and a reduced Néel temperature compared to bulk [60], respectively.

## 2.6 Introduction to CoO

The CoO structure is traditionally considered a cubic NaCl structure with a Co and O in the places of Na and Cl respectively shown in figure 2.6.1. It is a 3D-Ising antiferromagnet [153, 154, 162], with a bulk Néel temperature  $T_N=288.98(10)$  K [153]. Studies show, however, that the fundamental magnetic order is retained above  $T_N$  [152].

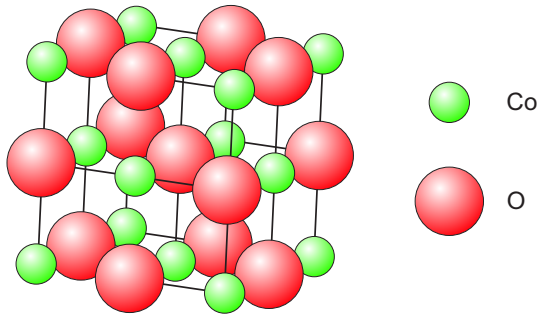


Figure 2.6.1: The structure of CoO. The size of the unit cell is  $4.263(1)$  Å [166]. Created from ref. [166] using *Crystallographica*.

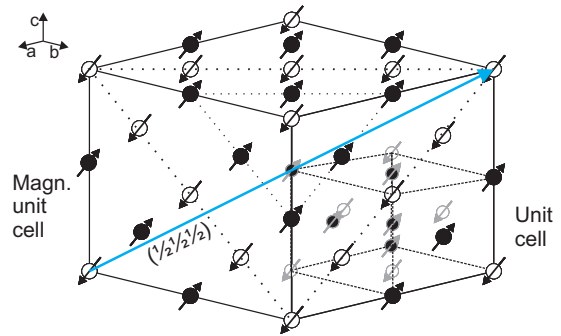


Figure 2.6.2: The magnetic structure of CoO. Only the Co ions are shown. In part from ref. [186].

At temperatures close to  $T_N$  the Ising model gives a good representation of the long range magnetic order, albeit, other models give a better representation in other temperature-regions of the magnetic phase [151]. Spin-wave theory describe the magnetic interactions well at low temperatures, whereas Green function's theory come the closest to describing the interactions at the intermediate temperature region.

Although the structure is close to cubic, CoO has a structural phase transition at  $T_N$  where the unit cell is tetragonally elongated below  $T_N$  [150], reaching a minimum  $c/a=0.988$  at  $\sim 93$  K. The

picture of a complex structure is supported by recent studies by Tomiyasu *et al.* (2004) [186] and Jauch *et al.* (2001) [79], as they report that the unit cell is distorted monoclinically below  $T_N$  with the magnetic order along the triclinic axis. The CoO structure is monoclinic with  $a=5.18190(6)$ ,  $b=3.01761(3)$ ,  $c=3.01860(3)$  Å and  $\beta=125.5792(9)^\circ$ , which in the face-centered picture corresponds to  $89.962^\circ$  between the  $c$  and  $a$  axes [79]. However, as the distortion is small and since our investigations focus on the  $T_N$ -close region, we treat the system as cubic.

The magnetic structure of CoO is that of a slightly distorted AF-II order [186]. AF-II means that the spins are ordered antiferromagnetically along the (111) unit cell direction [79] as shown in figure 2.6.2. However, the magnetic unit cell has a double axis length, and the reflection is therefore denoted  $(\frac{1}{2}\frac{1}{2}\frac{1}{2})$  as illustrated in the figure.



# Chapter 3

## Experimental methods

### 3.1 Introduction

In this and the following chapter the experimental techniques that have been employed during my thesis work will be introduced. The vast majority of my experimental work has been carried out utilizing neutron scattering and Muon Spin Rotation ( $\mu$ SR). Furthermore, techniques such as X-Ray diffraction, magnetic AC susceptibility, Transmission Electron Microscopy (TEM) and Atomic Force Microscopy (AFM) have been employed.

The emphasis of this thesis is on results obtained using neutron scattering and  $\mu$ SR. These two techniques are a good match, since they complement each other, and measure different aspects of magnetic ordering.

Magnetic neutron scattering is scattering from the magnetic moment of ions, or more precisely from the spin component perpendicular to the neutron momentum transfer. The technique enables the measurement of the correlations between spins throughout a sample. Neutron scattering does not, however, provide information on the local environment.

Muon spin rotation on the other hand, provides this information, as each muon senses the local hyperfine field and delivers information about it. Due to its local character it is a very sensitive probe to short range order phenomena. Furthermore, muon spin rotation samples the local magnetic environment of all magnetic ions in a sample, where neutron scattering, due to the Bragg condition, is only able to probe long range order in the scattering directions actively being investigated.

The third magnetism sensing technique, magnetic susceptibility, complements both neutrons and muons by measuring the overall (macroscopic) magnetic properties of a sample. Using this technique, diamagnetic or paramagnetic components of the sample composition may be investigated.

For structural and morphological characterization of the nanoparticles X-Ray Diffraction (XRD), Transmission Electron Microscopy (TEM) and Atomic Force Microscopy (AFM) have been employed. These techniques are also complementary, as XRD provides the weighed average of the structural properties such as chemical compound composition and crystallite size and shape.

TEM directly provides information on particle size, size distribution and morphology, and can be employed as a tool for both direct imaging and diffraction of individual particles. Through TEM size distributions can be produced and individual chemical phase identifications can be made. Even lattice planes can be imaged directly, providing direct crystal structure information, such as lattice distances. The limitations of TEM lie in that TEM only provides local information on the sample, and that it is limited to give 2D projections.

AFM may be considered a complementary technique to TEM, as it using a tapping tip is able to give 3D-information such as thickness on materials (including particles), on a substrate.

Of the mentioned techniques, neutron scattering and  $\mu$ SR, which are the central techniques, are presented in this chapter, whereas the other mentioned techniques are introduced in chapter 4.

## 3.2 Neutron scattering

Neutron scattering has been the main experimental technique used throughout this thesis work. I will therefore in this section first provide a short introduction to solid state physics, and to the basics of neutron scattering. Then I will proceed to present the RITA-2 triple axis spectrometer (TAS) at Paul Scherrer Institute which I have used for my measurements. As I have made measurements on this spectrometer in both triple axis and 2-axis mode both of these will be discussed. The theory part of this section is based in large on refs. [176, 181].

### The Neutron

The properties of the neutron, shown in table 3.2.1, make it a very well suited probe for a variety of investigations. The charge of 0 gives it a large penetration depth as it does not interact with other charged particles. On the other hand, it has spin  $\frac{1}{2}$  and does therefore interact with the spins in a material. These two properties make for instance the neutron very well suited for investigations of magnetic materials through magnetic Bragg scattering.

Mass	$m$	$=$	$1.674928(1) \cdot 10^{-27} \text{ kg}$
Charge	$q$	$=$	0
Spin	$s$	$=$	$\hbar/2$ (1/2)
Magnetic moment	$\mu_n$	$=$	$-1.913 \mu_N = -\gamma \mu_N$ $= -9.6491783(18) \cdot 10^{-27} \text{ JT}^{-1}$
$\beta$ -decay lifetime	$\tau$	$=$	$885.9 \pm 0.9 \text{ s}$
Confinement radius	$R$	$=$	0.7 fm
Quark structure			u d d

Table 3.2.1: *The main properties of the neutron. From ref. [43].*

### 3.2.1 Theory

Neutron scattering utilizes that the neutron has wave-properties. The de Broglie wavelength  $\lambda$  of the neutron and the wave vector  $k$  of the neutron are given as

$$\lambda = \frac{h}{mv} \quad k = \frac{2\pi}{\lambda}. \quad (3.2.1)$$

From these expressions the momentum  $\mathbf{p}$  and the energy  $E$  are calculated as

$$\mathbf{p} = \hbar \mathbf{k} \quad (3.2.2)$$

$$E = \frac{\hbar^2 k^2}{2m} \quad (3.2.3)$$

$$= \frac{h^2}{2m\lambda^2}. \quad (3.2.4)$$

The conservation laws for momentum and energy are central to neutron scattering and these will therefore be introduced here. Consider an incoming neutron with momentum  $\mathbf{p}_i = \hbar \mathbf{k}_i$  being scattered from a medium, which after the scattering event will have the momentum  $\mathbf{p}_f = \hbar \mathbf{k}_f$ . The change in momentum, transferred to the scattering medium, is given as

$$\mathbf{q} = \boldsymbol{\kappa} = \mathbf{k}_i - \mathbf{k}_f, \quad (3.2.5)$$

where  $\mathbf{q}$  (or  $\boldsymbol{\kappa}$ ) is the scattering vector. Similarly, energy conservation dictates that the energy transfer  $\Delta E = \hbar\omega$  to the scattering medium is given by

$$\Delta E = \hbar\omega = \frac{\hbar^2}{2m}(k_i^2 - k_f^2). \quad (3.2.6)$$

### 3.2.1.1 Scattering Cross Section

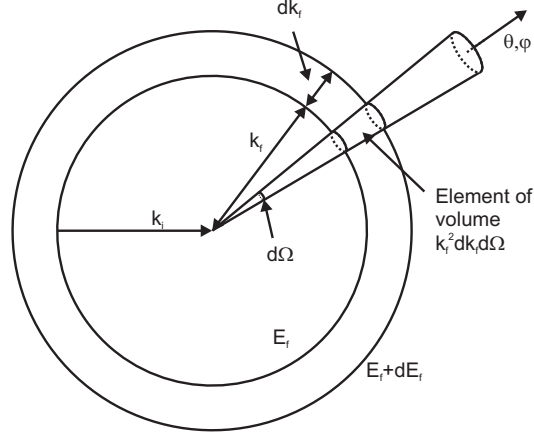


Figure 3.2.1: Illustration of the scattering cross section. Reproduced from ref. [181].

I will in this section briefly present some neutron scattering theory, in order to introduce equations which will be utilized through this thesis. The purpose is not to give an introduction to neutron scattering, as there exist many good and fulfilling introductions to neutron scattering, such as refs. [176, 181].

Consider an incident neutron beam with neutron energy  $E$  on some material by which a fraction of the incoming neutrons are scattered. The likelihood of a neutron being scattered, and more specific, of it being scattered into a solid angle  $\Omega$  with a energy  $E'$  is related to the *scattering cross-section* or more specifically to the *partial differential cross-section scattering* which is given [181] as

$$\frac{d^2\sigma}{d\Omega dE'} = \frac{I(d\Omega, \theta, \phi, E', E' + dE')}{\Phi d\Omega dE'}, \quad (3.2.7)$$

where  $\Phi$  is the flux of the incident neutrons and  $I(d\Omega, \theta, \phi, E', E' + dE')$  is the number of scattered neutrons per second into a small solid angle  $d\Omega$  in the direction  $\theta, \phi$  with final energy between  $E'$  and  $E' + dE'$ . Similarly we may define [181] the *differential cross-section* as

$$\frac{d\sigma}{d\Omega} = \frac{I(d\Omega, \theta, \phi)}{\Phi d\Omega}, \quad (3.2.8)$$

where  $I(d\Omega, \theta, \phi)$  is the number of scattered neutrons per second into a small solid angle  $d\Omega$  in the direction  $\theta, \phi$ . Finally, we define the *total scattering cross-section* as

$$\sigma_{tot} = \frac{I}{\Phi} \quad (3.2.9)$$

where  $I$  is the total number of neutrons scattered per second, and we integrate over all solid angles. We now rewrite (3.2.7) as

$$\left. \frac{d^2\sigma}{d\Omega dE'} \right|_{\lambda_i \rightarrow \lambda_f} = \frac{k_f}{k_i} \left( \frac{m_n}{2\pi\hbar^2} \right)^2 |\langle \mathbf{k}_f \lambda_f | V | \mathbf{k}_i \lambda_i \rangle|^2 \delta(\hbar\omega + E_i - E_f), \quad (3.2.10)$$

where  $k_i, k_f$  and  $E_i, E_f$  are the wave vectors and energies of the incoming and scattered neutrons respectively and  $\lambda_i, \lambda_f$  are the initial and final states of the scattering system.  $V$  is the interaction operator for the neutron with the sample [176]. Treating the incoming and outgoing neutrons as plane waves and the nuclear potential as a delta function (3.2.10) can be transformed into

$$\frac{d^2\sigma}{d\Omega dE'} = N \frac{k_f}{k_i} b^2 S(\mathbf{q}, \omega), \quad (3.2.11)$$

where  $N$  is the number of nuclei and  $b$  is the scattering length, described further by (3.2.13) below. The scattering function  $S(\mathbf{q}, \omega)$  is given by

$$S(\mathbf{q}, \omega) = \frac{1}{2\pi\hbar N} \sum_{ll'} \int_{-\infty}^{\infty} dt \langle e^{-i\mathbf{q}\cdot\mathbf{r}_{l'}(0)} e^{i\mathbf{q}\cdot\mathbf{r}_l(t)} \rangle e^{-i\omega t}, \quad (3.2.12)$$

where  $t$  is time and  $\langle \dots \rangle$  denotes the thermal average. The scattering length is related to the scattering cross sections by

$$\sigma_c = 4\pi b_c^2 \quad \sigma_i = 4\pi b_i^2 \quad \sigma_t = \sigma_c + \sigma_i, \quad (3.2.13)$$

where  $\sigma_c$  is the coherent scattering cross section,  $\sigma_i$  is the incoherent scattering cross section and  $\sigma_t = \sigma_{scatt}$  is the total scattering cross section. The scattering length is in principle a complex number, a large imaginary part of which would indicate that the nucleus is likely to absorb the incoming neutron. In most cases however, the imaginary part is small, and we shall therefore henceforth ignore it. Ignoring the incoherent nuclear scattering, we write up the coherent partial differential scattering cross section as

$$\left. \frac{d^2\sigma}{d\Omega_f dE_f} \right|_{coh} = N \frac{k_f}{k_i} \frac{\sigma_{coh}}{4\pi} S(\mathbf{q}, \omega), \quad (3.2.14)$$

where the scattering function for elastic scattering is given by

$$S(\mathbf{q}, \omega) = \delta(\hbar\omega) \frac{1}{N} \left\langle \sum_{ll'} e^{i\mathbf{q}\cdot(\mathbf{r}_l - \mathbf{r}_{l'})} \right\rangle. \quad (3.2.15)$$

For a Bravais lattice this can be rewritten as

$$S(\mathbf{q}, \omega) = \delta(\hbar\omega) \frac{(2\pi)^3}{v_0} \sum_{\mathbf{G}} \delta(\mathbf{q} - \mathbf{G}), \quad (3.2.16)$$

where  $v_0$  is the volume of the unit cell and  $\mathbf{G}$  are reciprocal lattice vectors. We can now write up the coherent, elastic differential scattering cross section as

$$\left. \frac{d\sigma}{d\Omega} \right|_{coh}^{el} = N \frac{(2\pi)^3}{v_0} (\bar{b})^2 \sum_{\mathbf{G}} \delta(\mathbf{q} - \mathbf{G}), \quad (3.2.17)$$

for a perfectly rigid lattice. Taking into account the thermal atomic displacements, more than one atom in the unit cell, different positions and different nuclei, the above equation can be generalized to

$$\left. \frac{d\sigma}{d\Omega} \right|_{coh}^{el} = N \frac{(2\pi)^3}{v_0} \sum_{\mathbf{G}} \delta(\mathbf{q} - \mathbf{G}) |F_N(\mathbf{G})|^2, \quad (3.2.18)$$

where  $|F_N(\mathbf{G})|^2$  is called the structure factor and is given by

$$|F_N(\mathbf{G})|^2 = |F_N(hkl)|^2 = \left| \sum_j \bar{b}_j e^{i\mathbf{G}\cdot\mathbf{d}_j} \right|^2 e^{-2W_j}. \quad (3.2.19)$$

In the above expression  $-2W_j$  is the Debye-Waller factor.

### 3.2.1.2 Magnetic Bragg Scattering

The general expression for the *magnetic partial differential cross section* is given as

$$\left( \frac{d^2\sigma}{d\Omega dE'} \right)_{\mathbf{s}_i \lambda_i \rightarrow \mathbf{s}_f \lambda_f} = \frac{k_f}{k_i} \left( \frac{m}{2\pi\hbar^2} \right)^2 |(\mathbf{k}_f \mathbf{s}_f \lambda_f | V_m | \mathbf{k}_i \mathbf{s}_i \lambda_i)|^2 \delta(E_i - E_f + \hbar\omega), \quad (3.2.20)$$

where  $\mathbf{s}_i, \mathbf{s}_f$  are the neutron spin states before and after scattering and  $V_m$  is the potential between the neutron and all electrons in the scattering system [181]. After some calculation the *coherent elastic differential cross section* from an ordered crystal can be written as

$$\left. \frac{d\sigma}{d\Omega_f} \right|_{coh}^{el} = N_M \frac{(2\pi)^3}{v_M} \sum_{\mathbf{G}_M} \delta(\mathbf{q} - \mathbf{G}_M) |F_M(\mathbf{G}_M)|^2, \quad (3.2.21)$$

where  $v_M$  is the volume of the magnetic unit cell,  $N_M$  is the number of magnetic unit cells and  $\mathbf{G}_M$  is the magnetic reciprocal lattice vectors. The magnetic structure factor  $F_M(\mathbf{G}_M)$  is given as

$$F_M(\mathbf{G}_M) = \sum_j p_j \mathbf{S}_{\perp j} e^{i\mathbf{G}_M \cdot \mathbf{d}_j} e^{W_j}, \quad (3.2.22)$$

where  $\mathbf{S}$  is the spin of an atom and  $p$  through the expression  $pS$  gives the amplitude for the magnetic scattering.  $p$  is given as

$$p = \left( \frac{\gamma r_0}{2} \right) g f(\mathbf{q}), \quad (3.2.23)$$

where  $r_0$  is the electron radius,  $g$  is the Landé splitting factor and  $\gamma$  is the neutron magnetic moment  $\mu_n$  to nuclear magneton  $\mu_N$  ratio (see table 3.2.1). The magnetic form factor  $f(\mathbf{q}) = \int \rho_s(\mathbf{r}) e^{i\mathbf{q} \cdot \mathbf{r}}$  is the Fourier transform of the normalized unpaired spin density on an atom, as only the unpaired electrons contribute to the magnetic moment and thus to the scattering. The term  $\mathbf{S}_{\perp}$  is the component of  $\mathbf{S}$  perpendicular to the scattering vector  $\mathbf{q}$ , and is given as

$$\mathbf{S}_{\perp} = \hat{\mathbf{q}} \times (\mathbf{S} \times \hat{\mathbf{q}}), \quad (3.2.24)$$

where  $\hat{\mathbf{q}}$  is a unit vector along  $\mathbf{q}$ ,  $v$  is . From (3.2.24) it can be seen, that only the perpendicular component of the spin  $\mathbf{S}$  contributes to the scattering cross section, and from insertion of (3.2.22) and (3.2.24) into (3.2.21), we see that the scattering cross section scales with  $|\mathbf{S}_{\perp}|^2$ . When scattering on multi-domain magnetic samples, we redefine the magnetic form factor  $\mathbf{F}_M$  as

$$\mathbf{F}_M = \mathbf{S}_{\perp} \tilde{F}_M \quad \text{where} \quad \tilde{F}_M = \sum_j p_j e^{-W_j} e^{i\mathbf{q} \cdot \mathbf{d}_j}, \quad (3.2.25)$$

and  $p_j$  is now set to  $\pm|p_j|$  depending on the relative spin directions. The  $p_j^{\mathbf{S}}$ 's define the configurational symmetry of the magnetic structure. When averaged over domains the expression for  $|\mathbf{F}_M|^2$  becomes

$$\langle |\mathbf{F}_M(\{hkl\})|^2 \rangle = \langle |\mathbf{S}_{\perp}|^2 \rangle |\tilde{F}_M(\{hkl\})|^2, \quad (3.2.26)$$

and  $\langle |\mathbf{S}_{\perp}|^2 \rangle$  can be rewritten as

$$\langle |\mathbf{S}_{\perp}|^2 \rangle = S^2 (1 - \langle \cos^2 \eta \rangle), \quad (3.2.27)$$

where  $\eta$  is the angle between  $\mathbf{S}$  and  $\mathbf{q}$ . Therefore the magnetic form factor over domains is now only dependent on evaluating  $\langle \cos^2 \eta \rangle$  over the domains.

## 3.2.2 The Correlation Function and Critical Scattering

As magnetic scattering in effect is scattering from correlated spins, the spin-spin correlation function is important. The correlation function  $\Gamma_{i,j}$  between two spins is defined as

$$\Gamma_{i,j} = \Gamma(\mathbf{r}_{i,j}, \epsilon, h) = \langle \mathbf{s}_i \cdot \mathbf{s}_j \rangle - \langle \mathbf{s}_i \rangle \cdot \langle \mathbf{s}_j \rangle, \quad (3.2.28)$$

$$= \langle (\mathbf{s}_i - \langle \mathbf{s}_i \rangle) \cdot (\mathbf{s}_j - \langle \mathbf{s}_j \rangle) \rangle \quad (3.2.29)$$

where  $\mathbf{s}_i, \mathbf{s}_j$  are the  $i$ 'th and  $j$  spins respectively,  $\mathbf{r}_{i,j}$  is the distance between the spins,  $\epsilon = \frac{T-T_C}{T_C}$  is the reduced temperature and  $h = \frac{g\mu_B H_e}{k_B T}$  is the reduced magnetic field [38, 52].  $H_e$  comes from the scaling approach, and is the effective field between cells of spins [38].

In this context  $\mathbf{s}_i - \langle \mathbf{s}_i \rangle$  is the deviation from the average spin direction,  $\langle \mathbf{s}_i \cdot \mathbf{s}_j \rangle$  is a measure of how parallel the spins are and  $\langle \mathbf{s}_i \rangle \cdot \langle \mathbf{s}_j \rangle$  is a measure of the long range order. From this expression it can be seen that the correlation function can yield a finite result in a system with no long range order, if there are correlations between the individual spins, i.e. if the  $\langle \mathbf{s}_i \cdot \mathbf{s}_j \rangle \neq 0$ .

This becomes relevant close to a magnetic phase transition, where the thermal energy is comparable to the magnetic energy, and the long range order is small or zero. In this temperature region, the critical region, the spins fluctuate, but are still correlated with the surrounding spins. The spatial extent of these correlations is given with a correlation length, which in an infinite system diverges at the transition temperature.

Figure 3.2.2 shows a schematic of the neutron scattering intensity from critically correlated spins along with scattering from static long range order versus temperature.

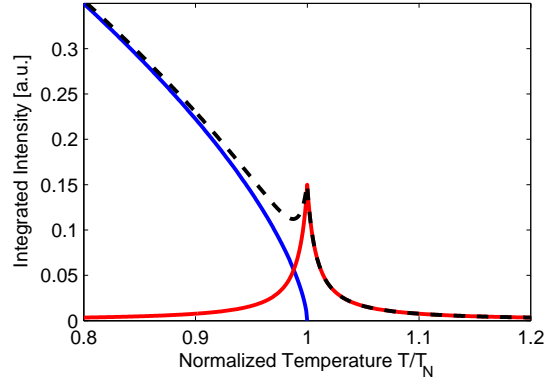


Figure 3.2.2: Schematic illustration of the scattering intensity close to the Néel temperature. The blue line is scattering from static long range ordered spins, the red line is scattering from critically correlated spins and the black line is total scattering intensity. The static and critical intensities are not to scale.

The correlation length  $\xi$  is defined through the correlation function, and is for a large spin system given [38, 47, 52] as

$$\Gamma(\mathbf{r}_{i,j}, \epsilon, 0) \propto |\mathbf{r}_{i,j}|^{(1-d)/2} \xi^{(3-d)/2-\eta} \exp\left(\frac{-|\mathbf{r}_{i,j}|}{\xi}\right) \quad (3.2.30)$$

$$\propto \frac{e^{-r_{i,j}/\xi}}{r_{i,j}^{d-2-\eta}}, \quad (3.2.31)$$

where  $d$  is the dimensionality of the system. The critical exponent for the correlation function is  $\eta$ . The correlation length can be expressed as

$$\xi \propto \left(\frac{T-T_C}{T_C}\right)^{-\nu} = (\epsilon)^{-\nu}, \quad T > T_C \quad (3.2.32)$$

where  $T_C$  is the transition temperature. The correlation length has the critical exponent  $\nu$  [52].

The scattering rate or differential cross section  $\frac{d\sigma}{d\Omega}$  for neutrons with the initial incoming momentum  $\mathbf{p}_i$  ( $\mathbf{k}_i$ ) and outgoing momentum  $\mathbf{p}_f$  ( $\mathbf{k}_f$ ) is related to the spin density matrix element as

$$\frac{d\sigma}{d\Omega} \propto \left| \left\langle \int dV e^{-i\mathbf{k}_f \cdot \mathbf{r}} \mathbf{s}(\mathbf{r}) e^{i\mathbf{k}_i \cdot \mathbf{r}} \right\rangle \right|^2 \quad (3.2.33)$$

$$\propto \int dV_i dV_j \langle \mathbf{s}_i \cdot \mathbf{s}_j \rangle e^{-i\mathbf{q} \cdot \mathbf{r}_{ij}} \quad (3.2.34)$$

in the Born approximation. The Fourier transform of the real space correlation function is

$$\Gamma(q) = V^{-1} \int dV \Gamma(\mathbf{r}) e^{-i\mathbf{q}\cdot\mathbf{r}} \quad (3.2.35)$$

$$= V^{-1} \int dV_i dV_j \langle \mathbf{s}_i \cdot \mathbf{s}_j \rangle e^{-i\mathbf{q}\cdot(\mathbf{r}_{ij})} + \langle \mathbf{s}_i \rangle \cdot \langle \mathbf{s}_j \rangle \delta(\mathbf{q} - \mathbf{G}_M), \quad (3.2.36)$$

where the last term is zero except when  $\mathbf{q}$  coincides with a reciprocal lattice point, giving a Bragg peak. The Fourier space correlation function  $\Gamma$  can be related to the neutron differential scattering cross section using

$$\Gamma(\mathbf{q}) = V^{-1} \int dV_i dV_j \langle \mathbf{s}_i \cdot \mathbf{s}_j \rangle e^{-i\mathbf{q}\cdot\mathbf{r}_{ij}} \quad (3.2.37)$$

where  $V$  is the volume of the material. Combining the above equations (3.2.34) and (3.2.37) we get

$$\frac{d\sigma}{d\Omega} \propto \Gamma(q), \quad (3.2.38)$$

which in other words says that the correlation function is proportional to the differential scattering cross section.

### 3.2.3 Spin Dynamics

Spins fluctuations or spin dynamics in a system with long range order consists of wave-like deviations of the individual spin orientations from the equilibrium orientation. These deviations are called spin waves or magnons, and have properties similar to those of phonons in solids. For instance, the spin waves follow  $E$ - $q$  dispersion relations.

In a magnetic system at finite temperature, the thermal fluctuations thus consist of excited spin waves, which cause the spins to deviate from the equilibrium position, yielding a reduced magnetic moment. At the magnetic transition temperature (the Curie or the Néel temperature), the average thermal energy is equal to the magnetic exchange energy of the spin system.

The spin dynamics of a magnetic system can be probed with inelastic neutron scattering, for instance by investigating the dispersion relation of the system. However, as no inelastic neutron scattering has been performed in this project, the theory of spin waves will not be pursued further here.

### 3.2.4 Triple Axis Spectroscopy

Neutron scattering experiments performed during this thesis have been made using the cold neutron RITA-2 (ReInvented Triple Axis) spectrometer [144], which as the name indicates is a triple axis spectrometer with a modified design (see figure 3.2.4).

The concept of cold neutrons is usually used on neutrons with wavelengths of 3-10 Å, whereas for instance thermal neutrons have wavelengths of 1-3 Å.

#### 3.2.4.1 Producing Neutrons

The neutrons for RITA-2 are produced at the Swiss spallation neutron source (SINQ), by leading a proton beam into a target. During the my Ph.D. time there have been two targets in use, a solid state target made of lead, and a new liquid eutectic<sup>1</sup> lead-bismuth beam target, the MegaPie [139]. In both cases protons are either exciting existing nuclei and causing them to decay, or they are absorbed in the nucleus and causing it to decay while emitting neutrons. The neutrons are emitted in arbitrary directions and are after being slowed down to specific energies (in a cold source thermalizing the neutrons to liquid H<sub>2</sub> at  $T=20$ -25 K), transmitted towards the instruments via neutron guides.

<sup>1</sup>An eutectic mixture is a mixture with such proportions, that the melting point is as low as possible.

### 3.2.4.2 Triple-Axis Neutron Spectrometers

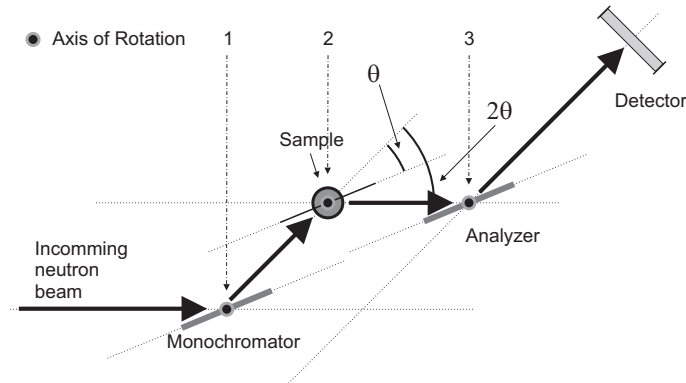


Figure 3.2.3: *Schematic illustration of the principle of a triple axis neutron scattering instrument.*

Conventional triple-axis neutron spectroscopy was developed by Brockhouse over forty years ago [24, 36, 37]. Triple axis spectrometers have as the name says 3 axes of rotation, as shown in the schematic in figure 3.2.3. The neutron beam flowing through the neutron guide is 'white' (compared to what is desired) e.g. it contains a wide distribution of wave lengths.

To select a specific energy, a monochromator is located at the first axis, (1) in figure 3.2.3, which utilizes Bragg's law (see section 4.1) to select neutrons with a wave length which fulfills the Bragg condition. The monochromator is made of a material which has a good neutron reflectivity, and suitable mosaicity [102]. Common materials used as monochromators include pyrolytic graphite (PG), Ge, Si and Cu. The RITA-2 monochromator is composed of PG.

What is meant by using the term 'suiting mosaicity', is that the mosaicity (and thus material) is chosen considering the divergence of the raw beam, and considering desired divergence of the monochromatic beam. The divergences are weighed off versus intensity loss. The lower divergence, the lower intensity. Depending on the experiment (instrument, sample, subject of measurement), monochromators can be chosen for either low divergence or high intensity, but usually a monochromator is seldom changed. Rather collimators are used for creating a less divergent beam.

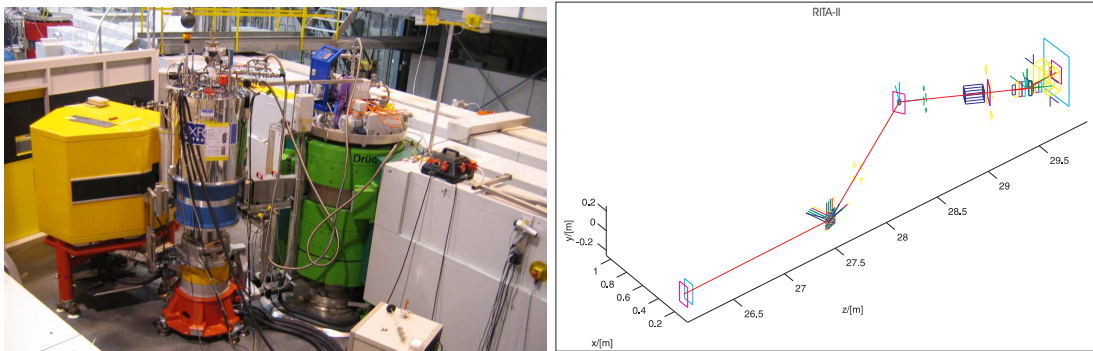


Figure 3.2.4: Left: *Image of the RITA-II spectrometer. From the left, the yellow detector tank containing the analyzer assembly and the PSD. The sample is located further right, inside the blue cryo magnet. The monochromator is located inside the green tank. The grey box to the right of the monochromator tank contains the neutron guide.* Right: *A simulation schematic of RITA-II. From ref. [104].*

The neutrons scattered from the monochromator, are directed towards the sample located at the second (2) axis. The second axis is used to rotate the sample so as to reach the specific

crystal reflection which one wishes to measure on. TAS' have beyond the rotating axes several displacement motors and tilting axes, through which the sample can be rotated into the scattering plane.

When studying powder samples the angle of the second axis is irrelevant, as there always is an equal fraction of powder grains which lies oriented so as to fulfill any possible scattering condition (assuming random grain orientation), and the neutrons are scattered in Debye-Scherrer cones (see section 4.1.2) from each reflection.

A fraction of the neutrons scattered from the sample arrive at the the third axis (3) – the analyzer. The analyzer scatters, as the monochromator, neutrons with a specific energy. Finally, the scattered neutrons directed towards the detector.

Depending on whether the scattering energy of the monochromator and analyzer are equal, the spectrometer can perform inelastic neutron scattering measurements *i.e.* study of dynamics in materials *e.g.* spin waves and phonons, or elastic scattering measurements, where either nuclear or magnetic Bragg scattering, is used to study structure.

### 3.2.4.3 The RITA-2 Analyzer and Detector

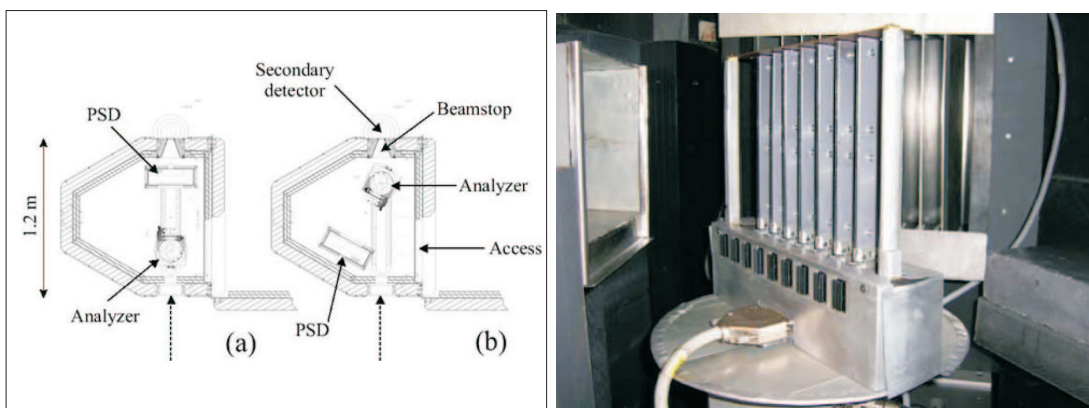


Figure 3.2.5: Left: *Drawing of the detector tank from above, in two configurations. (a) Two-axis configuration, where the neutrons are scattered directly into the detector. (b) Triple-axis configuration where the neutrons are scattered via an analyzer onto the detector. From ref. [34].* Right: *An image of the RITA-2 analyzer blade rack. From ref. [105].*

RITA-2 differs from other TAS' by the environment around the 3rd axis. The analyzer and the detector are located inside a detector housing (the detector tank). The detector tank is shown in figure 3.2.4 (left), and a schematic is shown in figure 3.2.5 (left). The detector tank is coated (shielded) with Boron-plastic<sup>2</sup>, which absorbs stray neutrons both from outside and inside the tank.

Neutrons scattered from the sample enter the tank through a relatively small hole in the shielding (dashed arrows in figure 3.2.5 (left)). To reduce background-neutrons further, the opening of the hole can be reduced further through setting of slits, and by use of a neutron funnel.

Instead of the conventional setup with a single analyzer blade, RITA-2 has an analyzer blade assembly, seen in figure 3.2.5 (right) and figure 3.2.7 (left), on which 7 analyzer blades are mounted. The assembly and the analyzer blade can rotate individually, giving rise to a vast number of different possible measurement configurations, many of which have still to be explored. The assembly has room for 9 blades, but at present only the blades 2-8 are installed. The configurations will be treated further in section 3.2.5 and appendix A.

Where many TAS' have a single detector, RITA-2 has a large, approximately 30x50 cm position sensitive detector (PSD) with 128x128 pixel resolution. The PSD is an equally important part

<sup>2</sup>Boron has a very high absorption cross section, see table G.3.1

of the RITA-2 concept as the multiple analyzer blades are. Through the use of software, it is possible to select neutron counts registered in specific regions of the PSD, thereby further lowering the number of background neutrons in the final datasets. As a last detail even the PSD can be equipped with a collimator, to eliminate neutrons, not scattered perpendicular onto the surface.

All in all, the many background-lowering features make RITA-2 an excellent instrument for studying weak phenomena, within a limited  $q$ -range, where a low background level is crucial.

### Instrumental Resolution

The instrumental  $q$ -resolution is very good compared to e.g. powder diffractometers. An early attempt was made to measure on the magnetic  $(\frac{1}{2}\frac{1}{2}1)$  peak in YBCO, which is studied in section 5.1, on the two axis diffractometer DMC. This was, however, unsuccessful, as not even see the much stronger impurity reflections close to it could be seen. Using RITA-2 however, this region can be studied in high detail.

The resolution of the instrument, however good, is very dependent on correct settings of the monochromator, as an incorrect setting will result in a divergent beam scattered towards the sample. The resolution is also very dependent on the monochromator collimator (vertical). However, using too tight collimation has a dramatic effect upon the neutron flux, so there is always the trade-off between resolution and intensity.

In the area around the sample, the monochromator slit settings, the dimensions and material of a sample container and the sample environment all affect the background level. In most all measurements a cooled BeO filter, filtering out second order neutrons<sup>3</sup> is used. The filter prevents these neutrons from entering the tank.

### 3.2.5 RITA-2 Modes

When doing triple axis experiments RITA-2 can, as mentioned, run in different configurations or modes. Within each of these modes there are wide degrees of freedom in settings of  $E_i$ ,  $E_f$  and  $q$ , which are well described in ref. [104]. At present RITA-2 is implemented to run in 3 modes [10, 104, 132]. These are presented in figure 3.2.6 and described below.

**Standard TAS mode (Flat)** In flat mode all the analyzer blades are set parallel at  $0^\circ$ , and the assembly is rotated, as one would do on a standard TAS (*i.e.* assembly angle  $a_5 = a_6/2$ ). The entire PSD can be used as a single detector. However, each blade will scatter neutrons with slightly different  $q$  and  $E_f$ . A schematic of this mode is shown in figure 3.2.6 (top).

**Monochromatic point-to-point focusing mode (Focusing mode)** In focusing mode, all the blades are set such that they reflect neutrons monochromatically with different  $q$  values onto the same region on the PSD, acting as a focusing analyzer. This mode may be used when focusing upon  $E_f$ , where high  $q$  resolution has second priority. In practise only the central 3 blades are used, due to  $q$ -resolution considerations. A schematic is shown in figure 3.2.6 (middle).

**Monochromatic  $q$ -dispersive mode (Monochromatic Imaging Mode)** Monochromatic imaging mode or imaging mode, is the most used configuration at RITA-2. It is also in contrast to the other two modes a specific mode for RITA-type spectrometers *e.g.* RITA-2 and SPINS (NIST). In imaging mode each blades will scatter neutrons monochromatically with different  $q$  values onto different region on the PSD, such that they can be differentiated. The spectrometer will in this configuration therefore function as 7 spectrometers scanning in parallel but with a small analyzer area per spectrometer. Furthermore this mode has the advantage that the previously mentioned detector-collimation can be applied eliminating cross-talk and providing narrow detector channels for the neutrons reflected from each blade. Imaging mode can be used in both elastic and inelastic mode. A simple schematic is presented

<sup>3</sup>Second order neutrons are neutrons with higher energy, fulfilling the same scattering conditions as the desired neutrons, as  $n > 1$  in (4.1.2).

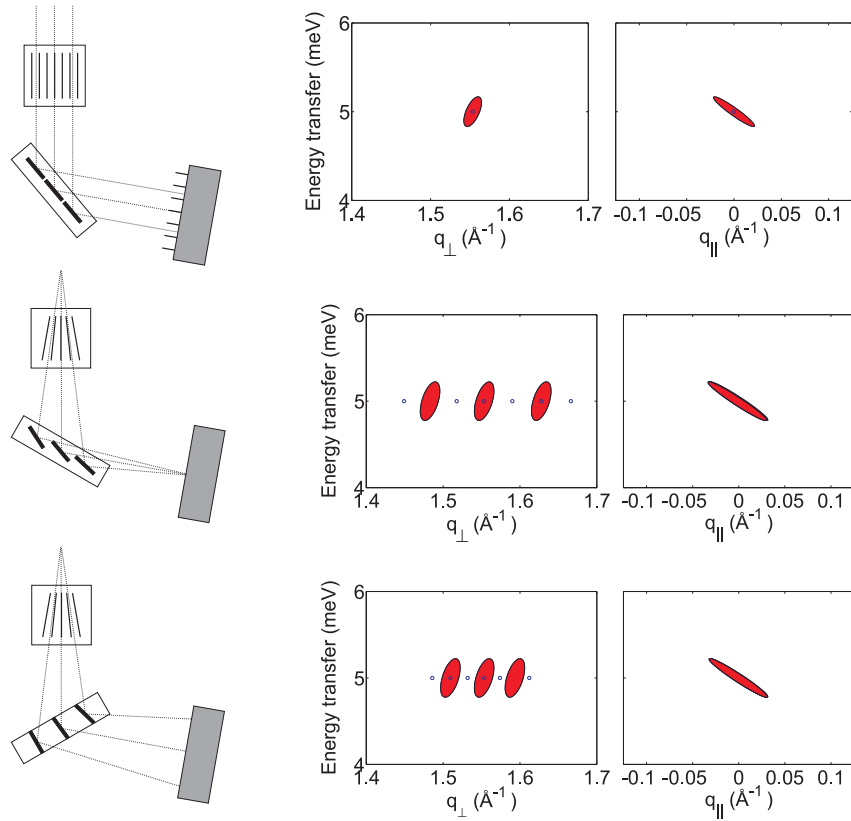


Figure 3.2.6: The implemented RITA-2 scattering modes. On the left side schematics of the orientations of assembly, analyzer blades, and detector. On the right plot showing the regions in  $(q_{\perp}, q_{\parallel}, E)$  space which are measured. Top: The standard TAS mode, or flat mode. Middle: Monochromatic point-to-point focusing mode. Bottom: Monochromatic  $q$ -dispersive (monochromatic imaging) mode. Figures from ref. [104].

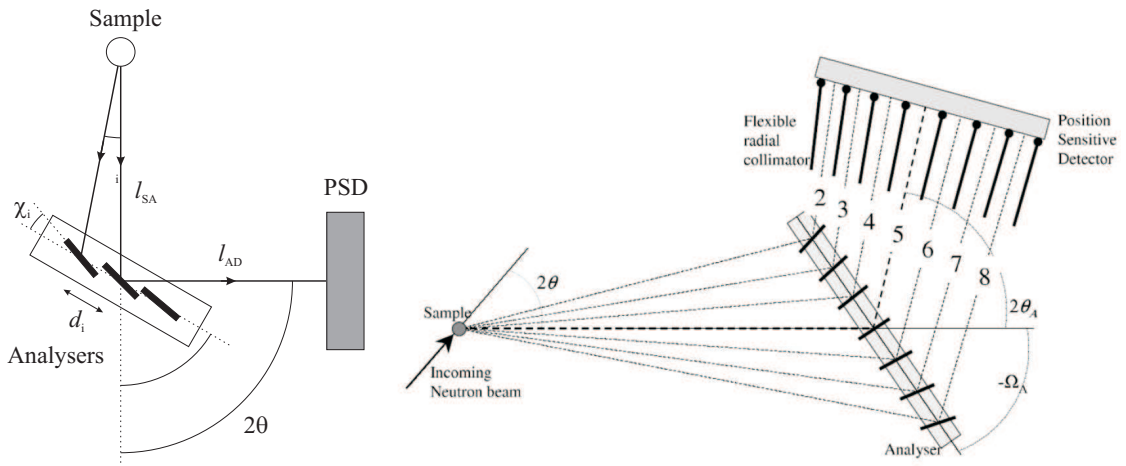


Figure 3.2.7: Left: The essential parts of the RITA-2 analyzer assembly. The analyzer blade assembly, with the analyzer blades. The blades which are spaced by  $d_i$ , are oriented in an angle of  $\xi_i$  with respect to the assembly. Figure from ref. [104]. Right: A schematic of the analyzer-collimator setup of the RITA-2 in monochromatic  $q$ -dispersive mode. From ref. [34].

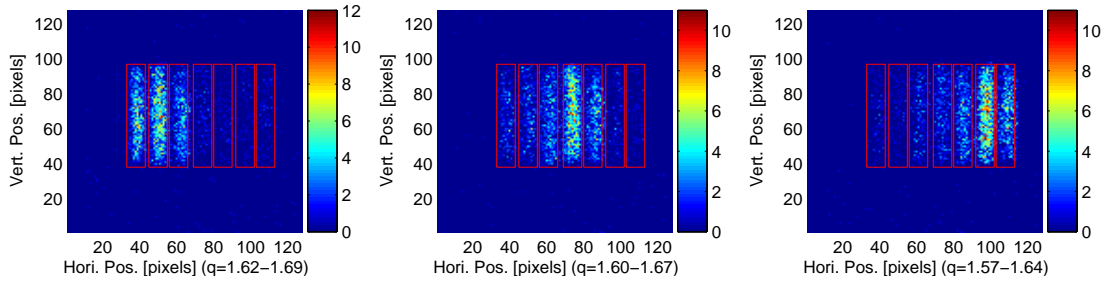


Figure 3.2.8: *Examples of the PSD images. From a scan across the (003)-(100) peak region in nanosized YBCO ( $x=0.25$ ). The software windows are marked with red frames. Left: Image no. 35. Center: Image no. 45. Right: Image no. 55.*

in figure 3.2.6 (bottom) and a more detailed schematic with detector collimation is shown in figure 3.2.7 (right).

### 3.2.6 Using Monochromatic Imaging Mode

All triple axis experiments in this thesis involve elastic scattering in the monochromatic imaging mode at  $E=3.7\text{meV}$  ( $\lambda=4.7022\text{\AA}$ ,  $k=1.3363\text{\AA}^{-1}$ ), with a 80' collimator inserted between the monochromator and the sample. The energy and collimation have been chosen to give the best resolution at a reasonable flux.

When extracting data from the 7 individual blades, it is done through defined software windows, which are indicated in figure 3.2.8. When combing the data, normalization is crucial. The neutron intensity varies between the analyzer blades, for a number of reasons. The blades are located at different angles with respect to the entry to the detector tank, and have different distances to the sample, and will therefore receive different neutron flux, as seen from figure 3.2.5 (right) and figure 3.2.7 (right).

The different reflectivity and mosaicity of the blades together with variations of the PSD collimator, filter collimator and slit settings, will skew the homogeneity of the detected neutron further. The combination of these factors results in an effective reflectivity for the individual analyzer blades, which needs to be corrected for, such that the scattering data from the individual blades can be combined into one dataset.

The normalization is performed by fitting a suitable line shape to a broad Bragg peak for each individual blade. From the total integrated intensity of the peak, the normalization factors  $n_i$  of the individual blades are derived as

$$n_i = A_i \left( \sum_{i=2}^8 A_i \right)^{-1}, \quad (3.2.39)$$

where  $A_i$  is the integrated intensity from the  $i$ 'th analyzer blade.

Alternatively to performing the normalization to a broad Bragg peak, the normalization could be performed to the incoherent scattering from a vanadium sample or from the sample background.

### 3.2.7 Two-Axis Mode

As mentioned in section 3.2.4.3 the two-axis diffractometer DMC was not suitable for studying magnetic order in my nano-YBCO samples, as the signal is weak and the background is high.

In this thesis work I have along with J. O. Birk, K. Lefmann and two groups of students from the University of Copenhagen, performed measurements on the magnetic order in CoO, using the RITA-2 instrument in two-axis mode, as shown in figure 3.2.9. In these measurements, we have studied magnetic critical phenomena in CoO nanoparticles, *e.g.* with the purpose of determining

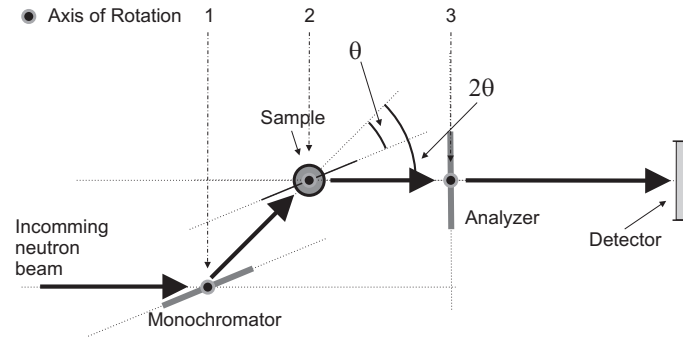


Figure 3.2.9: Schematic illustration of the setup of triple axis neutron scattering instrument in two-axis mode. In the schematic, the analyzer is still present, but set perpendicular to the beam. Alternative it can be removed.

the magnetic correlation length. The CoO samples, which are powders, can be studied in this mode, as they compared to the YBCO samples are clean and have a strong magnetic signal.

In two-axis mode the third axis, the analyzer, is not used, and the scattering angle at the analyzer  $2\theta$  is set to zero. The PSD is thus set in a straight-through configuration (see figure 3.2.9), and the neutrons from the sample are scattered directly onto the PSD. To eliminate the analyzer, it can either be set perpendicular to the beam direction, such that the neutron will fly through it, or it can be taken out entirely.

The advantage with two-axis mode is that the flux is very high, as no neutrons are wasted by not being scattered by the analyzer. Furthermore, we get a uniquely high  $q$  resolution, as the sample to PSD distance is larger than the sample to analyzer distance, 154.8 cm and 120.9 cm, respectively and we can use the pixelation of the PSD to our advantage.

The first main disadvantage of the two-axis configuration is that the lack of energy selection from the analyzer will allow inelastically scattered neutrons to be counted. However, studying elastic phenomena, the inelastic processes are often negligible.

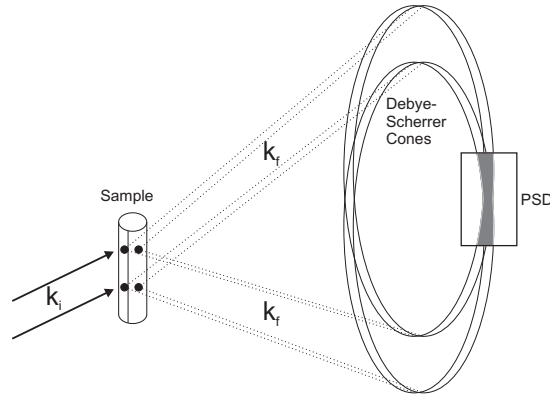


Figure 3.2.10: Illustration of the contribution to instrumental line broadening due to finite sample size, in a two-axis experimental setup. Each volume element of the sample scatters neutrons in an individual Debye-Scherrer cone (left), shifted in space relative to other volume elements. The overlap of shifted Debye-Scherrer cones on the PSD results in a smeared signal, as illustrated on the right, and hence the scattering from a sharp Bragg peak will be smeared on a PSD. The smearing significantly depends on sample size as illustrated in figure F.3.1.

Secondly, due to the finite size of the sample there is smearing of the  $q$ -resolution. This smearing comes from neutrons scattered from different parts of the sample (and thus with different  $q$ 's) onto the same position on the PSD, or in other words from the overlap of Debye-Scherrer cones from

the different parts of the sample as illustrated in figure 3.2.10. The Debye-Scherrer scattering cone will be treated further later in the thesis, *e.g.* in section 4.1.2.

The mentioned disadvantages with the two-axis mode are, however, minor, and the advantage with high flux in the CoO case far outweighed the disadvantages, and we were successfully able to perform the measurements (with nice results), presented in chapter 6.

### 3.2.8 Instrumental Resolution Function

A prerequisite to the data analysis is knowledge about the instrument resolution function, *i.e.* the instrument peak broadening, which is being convoluted onto the broadening originating from the sample, as will be discussed in section 4.1.3. For this purpose, a scan was made (in monochromatic

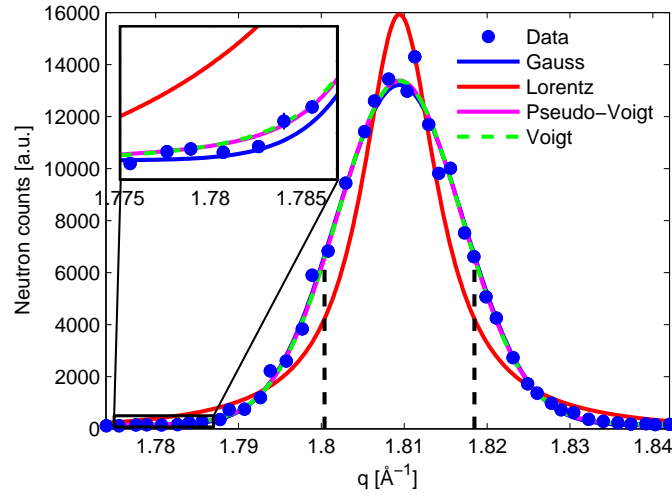


Figure 3.2.11:  $Al_2O_3$  (102) bulk powder peak, fitted with different line shapes. The Pseudo-Voigt and Voigt are nearly coinciding. The dashed lines indicate FWHM.

Line shape	$I_0$ $10^4$	$W$ FWHM	$\eta$	$W_G$ FWHM	$W_L$ FWHM	$B$ $10^2$	$\chi^2$
Gauss	1.309(5)	0.01809(5)				1.25(2)	5.41
Lorentz	1.609(8)	0.01107(6)				-1.59(3)	117.01
Pseudo-Voigt	1.330(6)	0.01777(6)	0.064(7)			0.88(4)	4.36
Voigt	1.41(12)			0.0172(10)	0.0011(11)	0.93(4)	4.28

Table 3.2.2:  $Al_2O_3$  (102) bulk powder peak, fitted with different line shapes. Notice the lower  $\chi^2$  of the Pseudo-Voigt and Voigt line shapes. Symbols:  $I_0$ : amplitude.  $\eta$ : The Pseudo-Voigtian parameter.  $W_G$ : Gaussian  $W$ .  $W_L$ : Lorentzian  $W$ .  $B$ : Background

imaging mode), across the (102) peak ( $q \sim 1.81 \text{ \AA}^{-1}$ ) of bulk  $Al_2O_3$  powder. The peak is fitted with different line shapes in figure 3.2.11, and the results are presented in table 3.2.2. In this procedure it is assumed that the diffraction peak is close to a  $\delta$ -function, whence the convolution with the instrumental resolution function gives the instrumental resolution function again. Convolution of line shapes is discussed further in section 4.1.3.

As seen from the plot and the table the instrumental broadening is very close to Gaussian. The resolution function, however, has small Lorentzian tails, which is evident from the fitting results (Pseudo-Voigt and Voigt fits). Firstly the  $\chi^2$  is smaller than in the Gaussian fit, and secondly the Lorentzian contributions ( $\eta$  and  $W_L$ , respectively) deviate significantly from zero. The tails are weak, and will not affect the fitting result for strong peaks, but may become significant when analyzing overlapping weak and strong peaks.

### 3.3 Muon Spin Rotation

$\mu$ SR measurements were performed on YBCO nano-powder on the PSI General Purpose Surface-Muon Instrument (GPS).

As described in section 3.1,  $\mu$ SR is a technique which allows one to study static and dynamic internal magnetic fields in materials, fields in solids in with an unmatched sensitivity and an interesting time scale which extends the neutron scattering time scale into the  $\mu$ s range. Below a short introduction to the theory of  $\mu$ SR, mainly based on [91, 131, 170], is given.

#### The Muon<sup>+</sup> ( $\mu^+$ )

Spin	1/2
Mass	105.659 MeV/c <sup>2</sup> (206.769 m <sub>e</sub> )
Gyromagnetic ratio	8.5161 · 10 <sup>8</sup> $\frac{\text{rad}}{\text{sT}}$
Decay	$\mu^+ \rightarrow e^+ + \nu_e + \bar{\nu}_\mu$
Mean lifetime $\tau = t_{1/2} \ln(2)$	2.197 · 10 <sup>-6</sup> s
Polarization in rest-system	100 %
Angle distribution (averaged over e <sup>+</sup> -energies)	$1 + \frac{1}{3} \cos(\theta)$
Nature	Light proton
Larmor Frequency	0.01355 MHz/G or 135.5 MHz/T

Table 3.3.1: *Main properties of the muon<sup>+</sup>. From ref. [170].*

#### 3.3.1 Spin Polarization

The muons are a product of the collision of a proton beam with a low-Z (e.g. Li, Be, C) target, in which the reaction,

$$p + p \rightarrow p + n + \pi^+ \quad (3.3.1)$$

where  $p$  is a proton,  $n$  is a neutron,  $\pi^+$  is a pion, is one of many to take place. This is interesting as the pion after 26 ns decays into a positive muon and a muon neutrino:

$$\pi^+ \rightarrow \mu^+ + \nu_\mu, \quad (3.3.2)$$

where  $\mu^+$  is the positive muon (the  $\mu$  equivalent of the positron) and  $\nu_\mu$  is the  $\mu$  neutrino. The energy of the emitted muon is 4.12 MeV.

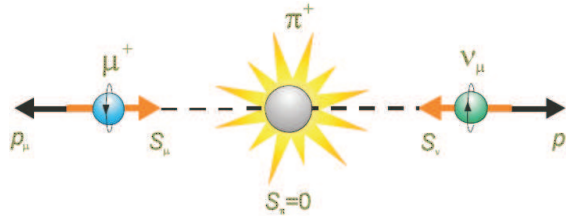


Figure 3.3.1: *The pion decay, which results in the 100 % spin polarized muons. Figure from [180].*

The pion has a spin of 0, and the neutrino and the muon have spin 1/2. Due to parity-breaking the neutrino always has a helicity of -1 and therefore a spin antiparallel to the momentum. The laws of conservation of momentum and angular momentum, therefore dictate that the spin of the muon is 100 % antiparallel to its momentum. Hence we have 100 % spin polarization in the reference frame of the pion [170].

As we are interested in 100 % spin polarized muons, the reference frame chosen is that of the laboratory. Furthermore only surface muons are selected for further use (or equivalently muons with a momentum of  $29.8 \frac{\text{MeV}}{c}$ , corresponding to a kinetic energy of approximately 4.1 MeV [180], as the muon loses energy by travelling through matter).

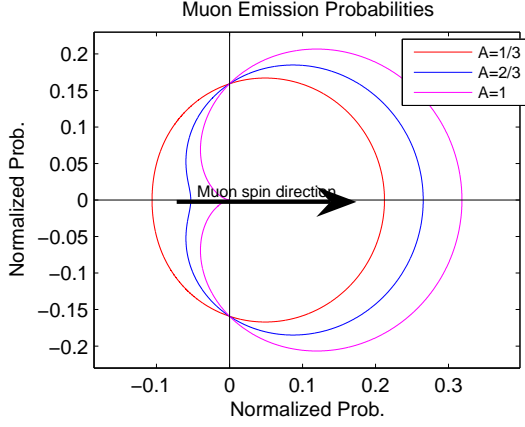


Figure 3.3.2: The angular probability distribution of the muon decay, with constants  $A=\{1/3, 2/3, 1\}$ . The arrow indicates the muon spin direction.

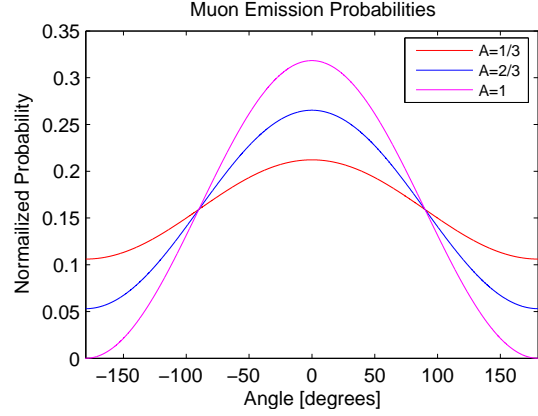


Figure 3.3.3: The angular probability distribution of the muon decay, with constants  $A=\{1/3, 2/3, 1\}$  versus angle in degrees.

### 3.3.2 Muon Decay

After  $2.197 \mu\text{s}$  the muon will decay into a positron and two neutrinos as

$$\mu^+ \rightarrow e^+ + \nu_e + \bar{\nu}_\mu, \quad (3.3.3)$$

where  $e^+$  is a positron,  $\nu_e$  is a electron neutrino and  $\bar{\nu}_\mu$  is an anti-muon neutrino.

Another important property of the muon is that during the decay the positron is preferentially emitted in the spin direction of the muon, as a consequence of the weak interaction, as

$$W(\phi, t) = 1 + A \cos(\phi + \omega_L t), \quad (3.3.4)$$

where  $\phi$  is the phase angle (or angle between polarization and observation direction at  $t = 0$ ),  $\omega_L$  is the Larmor frequency, and  $A$  is a constant. By averaging over all energies  $A$  is found to be  $1/3$ , for the GPS experimental setup.

When directing a muon beam onto a material, the muon will behave as a proton (albeit light, with  $1/9$  of the proton mass  $m_p$ ), and will settle in a negative environment, where there is a local energy minimum. If the  $\mu^+$  is subject to a magnetic field at the site, it will due to its spin be subjected to a torque  $\mathbf{\Gamma}$

$$\mathbf{\Gamma} = \boldsymbol{\mu} \times \mathbf{B}, \quad (3.3.5)$$

where  $\boldsymbol{\mu}$  is the magnetic moment and  $\mathbf{B}$  is the magnetic field. This causes it to Larmor-precess with a Larmor frequency  $\omega_L$  of

$$\omega_L = \gamma B, \quad (3.3.6)$$

where  $\gamma$  is the gyromagnetic ratio, which for the muon is  $0.01355 \text{ MHz/G}$  or  $135.5 \text{ MHz/T}$  (see table 3.3.1).

When the muon decays it will preferentially be emitted in the direction of the  $\mu^+$  spin as described in the emission direction probability expression (3.3.4), and by registering the emission directions of the emitted positrons versus time, and using the asymmetry equation ((3.3.11)-(3.3.15)), one can investigate the local magnetic environment in the sample, in terms of local magnetic fields, different muon sites, muon diffusion and more.

### 3.3.3 Detected Signal

The muon spin direction is detected through the emitted positron ( $e^+$ ), which is a result of the  $\mu^+$  decay, the signal per time (is the number of positrons)  $N(t)$  detected by each detector will be nominally be given as

$$N(t) = N_0 \exp\left(\frac{-t}{\tau_{\mu^+}}\right) + N_{bg}, \quad (3.3.7)$$

where  $N_0$  is the signal amplitude,  $\tau_{\mu^+}$  is the life time of the  $\mu^+$  and  $N_{bg}$  is the background.

If the sample has muon sites which are magnetically ordered, there will be an oscillation/precession signal added to the above expression, which then becomes

$$N(t) = N_0 \exp\left(\frac{-t}{\tau_{\mu^+}}\right) \left(1 + a_0 P(t) \cos(\omega_L t + \varphi)\right) + N_{bg}, \quad (3.3.8)$$

where  $a_0$  is the oscillation amplitude,  $\omega_L = 2\pi\nu_L$  is the Larmor precession frequency induced by the local field,  $\varphi$  is the phase of the precession and  $P(t)$  is the damping function for the oscillating fraction [81]. The damping function  $P(t)$ , is also known as the dephasing function, as it is caused by small variations in the local field experienced by the muons, which over time causes them to precess out of phase. In most cases this function is fitted with an exponential  $\exp(-\lambda t)$ .

However, in some cases the damping function has to be combined with a slow precession function, a Kubo-Toyabe [93], which is a slow precession function caused by the muonic interaction with the nuclear moments.

### 3.3.4 Apparatus

#### 3.3.4.1 The GPS beam line

The muons are produced at a light proton beam ion target (C, Be), where they form from collisions with high-energy protons ( $>500$  MeV). The light elements are chosen as target to maximize pion production and minimizing multiple scattering of the proton beam [180].

A tuned applied field selects through momentum selection, muons which are the product of pions at rest at the surface of the target, as these as mentioned are 100 % spin polarized.

The used instrument, the GPS is located at the end of the  $\pi$ M3 beam line which is equipped with an electromagnetic separator/spin rotator allowing rotation of the muon spin with respect to the muon momentum [142].

The muons have a kinetic energy of 4.1 MeV, and as the stopping power of the muons is around  $150 \text{ mg/cm}^2$  the instrument is capable of investigating materials at depths of several hundred  $\mu\text{m}$ .

Slits are set such as to optimize that that only one muon can enter the target volume within the time frame dictated by the life time of a muon.

Furthermore the usage of electronic logic evaluates the detection events. The passing of a muon into the measurement chamber starts a clock. After this point in time  $t_0$  the actual muon is rejected if a number of events occur, such as:

- A positron is detected within a certain starting time frame.
- A second muon is detected as it enters the chamber, within the given measurement time frame (usually  $10 \mu\text{s}$ ).
- Zero or more than one positrons are detected, within the measurement time frame.

This same electronic logic measures the time of detection, after which a TDC (Time Digital Converter) organizes the detected and accepted events, into time bins which are used in the analysis of the data.

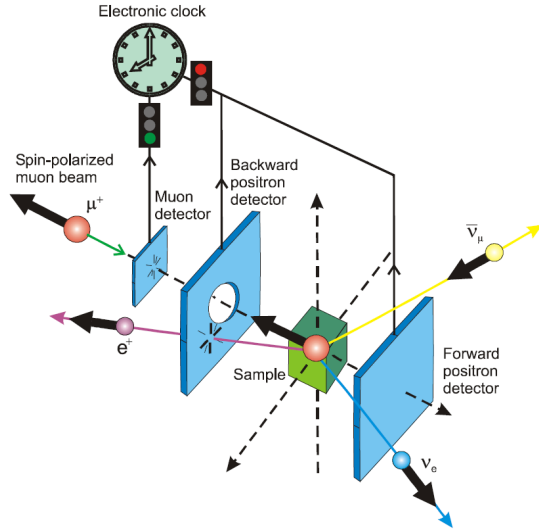


Figure 3.3.4: A schematic of a Zero Field (ZF)  $\mu$ SR setup. The muon comes in from the upper left (green arrow), starts the clock, and settles in the sample (green). The clock stops when the muon decay positron (magenta) is detected in one of the detectors. The forward and backward detectors are included in the schematic. Bold black arrows indicate spin directions. Figure from [180].

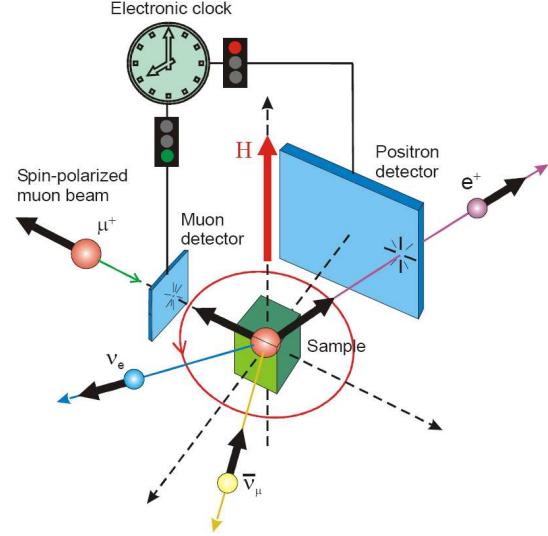


Figure 3.3.5: A schematic of a Transverse Field (TF)  $\mu$ SR setup. The muon comes in from the upper left (green arrow), starts the clock, and settles in the sample (green), which is subject of an applied transverse field (red). The clock stops when the muon decay positron (magenta) is detected in one of the detectors. One of the transverse detectors (left, right, up or down) detectors is included in the schematic. Bold black arrows indicate spin directions. Figure from [180].

### 3.3.4.2 Different Measurement Geometries

To extract information from the  $\mu$ SR measurements, there are mainly four different types of measurements which can be made with [131].

**Zero Field (ZF)** measurements are measurements performed with no applied magnetic field. It is used to study materials in their normal state.

**Transverse Field (TF)** measurements are measurements performed with an applied (non-zero) field perpendicular to the incoming muon spin. It is used to study materials in an applied magnetic field, e.g. vortex lattices in superconductors.

**Weak Transverse Field (wTF)** is very similar to the TF measurements, only the field is much weaker. It is used to determine detector normalization ( $\alpha$ ) fractions, or to study phenomena requiring weak applied fields.

**Longitudinal Field (LF)** measurements are measurements performed with an applied (non-zero) field parallel to the incoming muon spin. In this mode the time evolution of the muon polarization along its original direction. It is used to study dynamics in the magnetic environment in a material.

### 3.3.5 Measurement Time Scales

The time scale for  $\mu$ SR is ranging from approximately the lifetime of the muon, ( $2.197 \cdot 10^{-6}$  s), giving  $\sim 10^{-6}$  s to  $\sim 10^{-10}$  s. The shorter time scale limit is given by the resolution of the detector

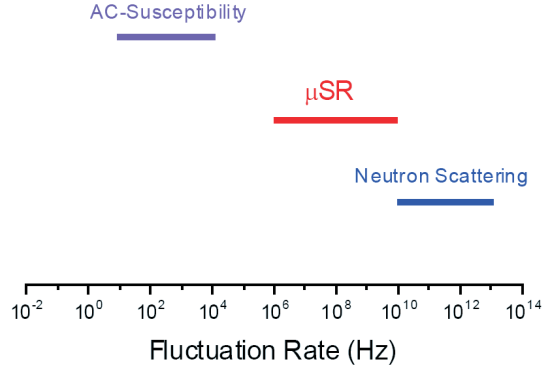


Figure 3.3.6: A comparative plot of the time scale for different measurement techniques. The time scales here are typical for the high- $T_C$  cuprates. Reproduced from [131, 180].

apparatus, which for the GPS is  $\sim 0.01 \mu\text{s}$ . Using this we can write up [131]

$$\tau = \frac{\lambda}{\omega^2}, \quad (3.3.9)$$

where  $\lambda$  is the detector time resolution,  $\omega$  is the Larmor precession frequency of the muons, and  $\tau$  is the time scale that we are interested in. By putting values into (3.3.9) we get

$$\tau = \frac{0.01 \mu\text{s}^{-1}}{(24 \text{ MHz})^2} \simeq \frac{0.01 (\mu\text{s})^{-1}}{(24 \mu\text{s}^{-1})^2} = 1.71 \cdot 10^{-5} \mu\text{s}, \quad (3.3.10)$$

by using a Larmor frequency  $\omega = 2\pi\nu$  of  $\sim 24 \text{ MHz}$ , which is not uncommon. Going to materials with higher internal field, the time scale resolution will improve.

### 3.3.6 Asymmetry

There are two factors in the asymmetry of the spectrum, the asymmetry  $A$ , usually just known as the asymmetry, which is the signal actually being analyzed and the detector efficiency asymmetry factor usually known as  $\alpha$ , which are coupled. The Asymmetry spectrum  $A(t)$  is defined as [91]

$$A_{raw}(t) = \frac{N_f(t) - N_b(t)}{N_f(t) + N_b(t)}, \quad (3.3.11)$$

where  $N_f(t)$  is the count rate at time  $t$  (or in channel  $k$ ) in the forward direction,  $N_b(t)$  is the count at time  $t$  in the backward direction. The  $\alpha$  factor is defined through as the detector efficiency

$$\alpha = \frac{N_{b,0}(t)}{N_{f,0}(t)} \quad (3.3.12)$$

and the detector symmetry  $\beta$  detector asymmetry is defined as the asymmetry between the raw forward and backward asymmetries

$$\beta = \frac{A_{b,0}}{A_{f,0}}. \quad (3.3.13)$$

The expression for reduced asymmetry [91], is given by

$$A_{red}(t) = \frac{\alpha N_f(t) - N_b(t)}{\alpha \beta N_f(t) + N_b(t)}, \quad (3.3.14)$$

and assuming that the detectors are symmetric (and thus  $\beta = 1$ ), this expression can further be reduced, into

$$A(t) \equiv A_{red,\beta=1}(t) = \frac{\alpha N_f(t) - N_b(t)}{\alpha N_f(t) + N_b(t)}. \quad (3.3.15)$$

In the used apparatus (the GPS/PIM3), the forward and backwards detector are different as the beam is coming in through the backward detector [5, 131], and it therefore has a hole for the beam to pass through. The detector area is therefore not the same. Of course this should be corrected with the  $\beta$  parameter, but it can equivalently be corrected through the  $\alpha$  parameter.

An example on a combined asymmetry spectrum is presented in figure 3.3.8 along with the raw and uncombined data in figure 3.3.7.

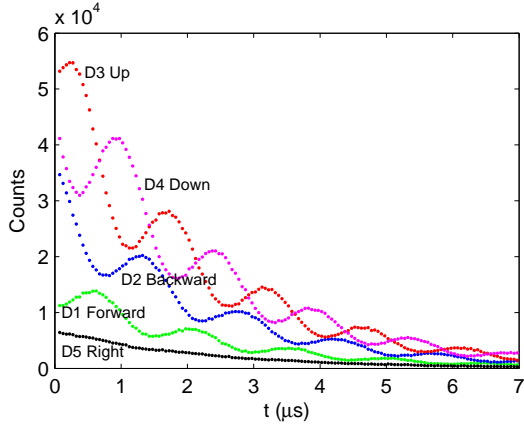


Figure 3.3.7: An example of the raw detector counts in a  $\mu$ SR measurement. In this case calibration data, counts versus time on the individual detectors for YBCO sample Sample 5 ( $x=0.30$ ) at 300 K in a 50 G transverse magnetic field.

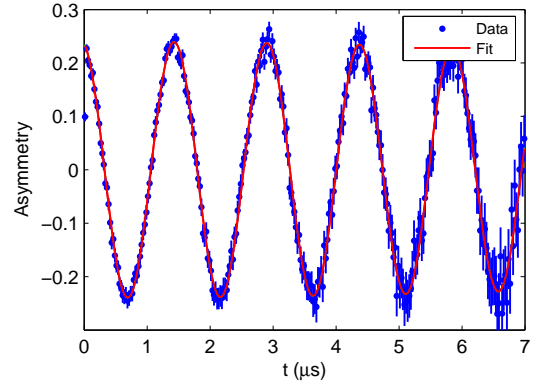


Figure 3.3.8: An example of the combined asymmetry spectrum obtained by combining forward and backward counters. In this case the fitted asymmetry calibration spectrum for the YBCO sample Sample 5 ( $x=0.30$ ) at 300 K in a 50 G transverse magnetic field. Note that the error bars increase with time as the detection rate of muons decreases.

### 3.3.6.1 Calibration

To find the  $\alpha$  parameter for an experiment, we fit a high temperature spectrum with an applied weak transverse field with a single 'Gaussian model'  $M$  of

$$M(\alpha, A_1, \sigma, \omega, \nu, \varphi) = A_1 e^{-\frac{1}{2}(\sigma_1 t)^2} \cos(2\pi\nu t + \varphi), \quad (3.3.16)$$

where the detector asymmetry  $\alpha$  is allowed to vary and  $A_1$  is a constant. The Gaussian term  $e^{-\frac{1}{2}(\sigma_1 t)^2}$  contains a represents a that the muons precessing muons experience a field distribution, which is assumed to be Gaussian. The term  $\cos(2\pi\nu t + \varphi)$  represents the precession of the muons in a field, with a Larmor frequency of  $2\pi\nu$ . The data to be fitted,  $A$ , is also subject to the fitting as the  $\alpha$  is one of the fit parameters (see (3.3.15)). An example of a transverse field fit is displayed in table 5.2.2, and all calibration fits are found in section E.2.1.2.

### 3.3.7 Analysis methods

The fitting of the raw data has primarily been performed using the  $\mu$ SR fitting program WKM [91]. Plotting and second level analysis has been performed using MatLab and the MatLab package Spec1d [116].

#### 3.3.7.1 Fit components

There are a vast number of modelling components which are used to describe and fit the physical data obtained from  $\mu$ SR experiments. To describe all these or even to give an overview is beyond

the scope of this thesis, and I will therefore only briefly present the components which I have used [91]. The components are building blocks, which through addition and multiplication can be combined to a fitting model.

**Constant** ( $A_1$ ) is a simple constant value, which in asymmetry is given by

$$A(t) = A_1. \quad (3.3.17)$$

**Simple exponential** is a simple decaying exponential function with a decay constant of  $\lambda$ ,

$$A(t) = e^{-\lambda t}, \quad (3.3.18)$$

which typically is used to model a muon precession dephasing.

**Cosine** is a cosine with frequency  $\nu$  and  $\varphi$  described by

$$A(t) = \cos(2\pi\nu t + \varphi), \quad (3.3.19)$$

which is used to model the oscillating signal from muons from a specific muon site.

**Simple Gaussian** is a simple Gaussian line shape given by

$$A(t) = e^{-\frac{1}{2}(\sigma_1 t)^2}, \quad (3.3.20)$$

which is typically used to model a field distribution at a specific muon site.

**Internal Field** is often used for fitting powder samples with randomly oriented grains, is given by

$$A(t) = \frac{2}{3} \cos(2\pi\nu_1 t + \varphi) e^{-\lambda_2 t} + \frac{1}{3} e^{-\lambda_1 t}, \quad (3.3.21)$$

where the factors  $\frac{2}{3}$  and  $\frac{1}{3}$  are due to the 2 transverse and 1 parallel axial spin directions with respect to the local magnetic field.  $\nu_1$  and  $\varphi$  are the precession rate and phase, respectively, caused by the transverse field, and  $\lambda_2$  and  $\lambda_1$  are the dephasing rates for muons at muon sites where the local magnetic field is transverse or longitudinal respectively.

The origin of the dephasing is a small variation in the local magnetic fields experienced by the muons, causing them to precess out of phase. The field variation is described by a distribution, usually a Gaussian distribution.

**Static Gauss Kubo Toyabe** describes the non-magnetic sample case where the muons only interact with the nuclear moments which are static and randomly oriented, and where the local field directions can be expressed as

$$\langle H_x^2 \rangle = \langle H_y^2 \rangle = \langle H_z^2 \rangle, \quad (3.3.22)$$

where the  $H_x, H_y, H_z$  are the principal local field directions.

In the zero field power samples spectra 1/3 of the muon sites will be oriented along the  $z$  direction (the direction of muon spin), and the muon will thus not precess. The remaining 2/3 of the muons will precess.

The static Kubo-Toyabe (KT) line shape is commonly used to fit data from non-magnetic samples where the orientation of the individual electronic spins are randomly fluctuating on a time scale much shorter than the characteristic time scale of the  $\mu$ SR measurement technique. The measured field will therefore average out.

The muons will, however, precess in the weak field from the static and randomly oriented nuclear (or atomic) spins (or magnetic dipoles), with a long precession period [68, 93, 131], of which one only sees the very first part, namely the drop-off of the cosine. The static

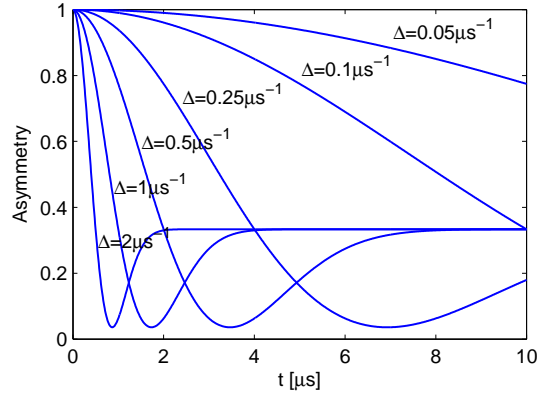


Figure 3.3.9: *Examples of Static Gauss Kubo Toyabe, with different values of the slow Larmor frequency  $\Delta$ .*

Gaussian KT (shown in figure 3.3.9) is used for describing a powder where the concentration of dipoles is high [39]. It is given [91] by

$$A(t) = \frac{2}{3}(1 - \Delta^2 t^2)e^{-\frac{\Delta^2 t^2}{2}} + \frac{1}{3}, \quad (3.3.23)$$

where  $1 - \Delta^2 t^2$  is a cosine approximation modelling a slow precession with Larmor frequency  $\Delta$  and  $e^{-\frac{\Delta^2 t^2}{2}}$  represents a Gaussian field distribution.

These fit components can be combined as one would wish, and the models used while fitting in section 5.2 have been composed from these components.

## Chapter 4

# Sample Preparation and Characterization

Before proceeding to the analysis of the central experiments and measurements performed in the thesis, this chapter will in more detail introduce the studied systems YBCO and CoO through details on the preparation and characterization of the studied samples.

The chapter is divided into three parts. Sections 4.1-4.3, contain general information on the characterization techniques used in the characterization of the studied systems. Sections 4.4-4.7 are on YBCO and sections 4.8-4.9 are on CoO. Part two and three both contain sections on manufacturing, doping and characterization of the two studied systems.

### 4.1 Diffraction

This section is on the aspects of diffraction in general, that I have found relevant to the analysis here and later, in chapters 5 and 6. The content applies to both neutron diffraction and X-Ray diffraction, unless otherwise noted.

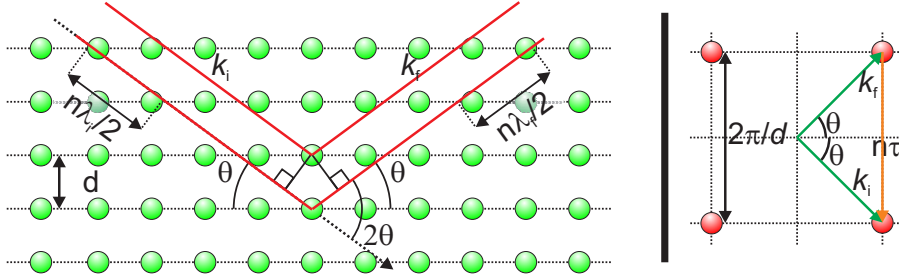


Figure 4.1.1: An illustration of the Bragg law. The incoming radiation with wavelength  $\lambda_i$  and wave vector  $k_i$  is scattered by the lattice planes, at a scattering angle  $2\theta$ . The scattered radiation has wave-length and -vector  $\lambda_f$  and  $k_f$ . Left: Real space lattice. Right: Reciprocal lattice.

**Bragg Scattering** The Bragg equation describes the condition which has to be fulfilled if coherent scattering of a wave is to occur from a crystal. This is illustrated in figure 4.1.1. It can be written in real space as

$$n\lambda = 2d \sin \theta, \quad (4.1.1)$$

where  $n$  is the order (an integer),  $\lambda$  is the wave length,  $d$  is the lattice distance of the given reflection and  $2\theta$  is the scattering angle. Rewriting it in term of reciprocal lattice vector yields

$$n\tau = 2k \sin \theta, \quad (4.1.2)$$

where  $\tau$  is the length of the reciprocal lattice vector, and  $k$  is the length of the wave vector. Bragg scattering will only occur if the scattering vector  $\boldsymbol{\kappa}$  (3.2.5) equals the reciprocal lattice vector  $\boldsymbol{\tau}$ . In order for this condition to be fulfilled we to change  $\boldsymbol{\tau}$  in (4.1.2) to

$$\boldsymbol{\tau}_{hkl} = h\mathbf{a}^* + k\mathbf{b}^* + l\mathbf{c}^*, \quad (4.1.3)$$

where  $h, k, l$  are integer values and are called the Miller indices. The reciprocal lattice will not be described further here, as this is well done in many books, for instance ref. [85].

#### 4.1.1 The Scherrer Formula

When radiation is diffracted from finite size crystals, the Bragg law (4.1.1) and (4.1.2) do not hold exactly, as they assume a delta function shaped response to infinite crystal diffraction. Dealing with bulk samples, this is often a valid approximation. However, when the studied system is finite sized, P. Scherrer found the diffraction line from powder to be broadened [137, 179] as

$$B = \frac{K\lambda}{L \cos(\frac{2\theta}{2})}, \quad (4.1.4)$$

where  $B$  is the FWHM width<sup>1</sup>,  $L$  is the linear size of the particle and  $\theta$  is the Bragg angle (half the scattering angle  $2\theta$ ).  $K$  is a numerical constant found to have the value  $2(\ln(2/\pi))^{1/2} \simeq 0.9394$  for spherical particles. The equation is in units of reciprocal space can in the simplest form be derived as

$$q = 2k \sin \theta \Rightarrow \quad (4.1.5)$$

$$\Delta q = 2k \cos \theta \Delta \theta \quad (4.1.6)$$

$$= kB \cos \theta = \frac{Kk\lambda}{L} = \frac{K2\pi}{L},$$

using that FWHM  $B$  is  $B = 2\Delta\theta$ ,  $k = \frac{2\pi}{\lambda}$  and that  $\Delta q$  is the FWHM peak width in reciprocal space (called  $W$  in the remainder of the thesis). In this approximative derivation it is assumed that we have a single particle size and that the wave length distribution, the beam divergence and the  $d$ -spacing variations are negligible. In the case where one or more of these factors is not negligible, it would also contribute to the peak broadening. The constant  $K$  has a value close to unity (0.8-1.4), but can, however, vary significantly due to several factors, including crystalline shape, crystalline size distribution [100] as well as strain and stress [18, 203]. Furthermore there are different values of  $K$  for different reflections of different particle shapes [100].

This derivation could have been obtained in other ways, *e.g.* through Fourier transformation of a finite size system. For instance, it is known that scattering peaks from finite size systems have finite widths. The question is then what shape the peak has when observed on a spectrometer.

I will not deal further with the different factors skewing the  $K$  factor, but use the original ( $K=0.94$ ) value, as I am interested mainly in a measure of the particle size. However, as seen from the interval of possible  $K$  values, it provides a relative wide margin for error in the particle size estimate, which in worst case can amount up to  $\sim 50\%$ .

#### 4.1.2 The Debye-Scherrer Cone

When neutrons (or any other monochromatic radiation) are Bragg-scattered from a point-sized powder sample, the scattering radiation will be emitted in a Debye-Scherrer cone, as illustrated in figure 4.1.2. The cone is made up of single reflections from the randomly oriented small crystals.

With small samples, the experimental case is often close to ideal. However, when the sample for various reasons is not point-like, but has other forms, *e.g.* cylindrical, the Debye-Scherrer cone will be smeared, as the individual powder grains are displaced from the center of the sample. This will be used further in chapter 6.

<sup>1</sup>There are other definitions of the width  $B$ , which I will not discuss further here, see *e.g.* ref. [100].

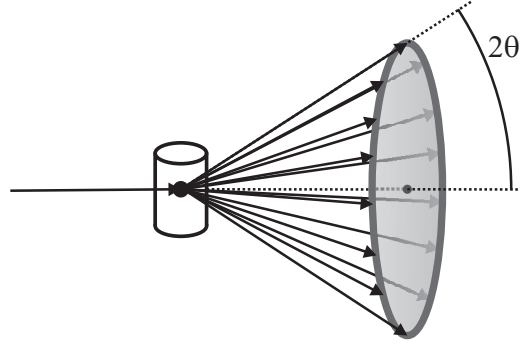


Figure 4.1.2: An illustration of the Debye-Scherrer scattering cone. The incoming neutrons are scattered from a point-sized powder sample, forming a cone of scattered neutrons.

### K- $\alpha$ 1 and K- $\alpha$ 2 issues

All X-Ray diffraction in this thesis is done using Cu-K $\alpha$  radiation with a wavelength of  $\lambda = 1.54184 \text{ \AA}$  [78]. However this radiation is due to the spin-orbit coupling actually a doublet consisting of Cu-K $\alpha$ 1 ( $\lambda = 1.54056 \text{ \AA}$ ) and Cu-K $\alpha$ 2 ( $\lambda = 1.54439 \text{ \AA}$ ). The two wave lengths do not cause problems when measuring on nano-sized materials, as the two resulting peaks are seen as one due to the peak broadening. However, when doing instrument calibration using a well defined material (e.g. Si), the two peaks are separated making an unambiguous determination of the instrument broadening difficult. The ratio of the integrated intensities we find from ref. [22] as

$$\frac{I_{K\alpha 1}}{I_{K\alpha 2}} = \frac{I_{0,K\alpha 1}}{I_{0,K\alpha 2}} \cdot \frac{W_{K\alpha 1}}{W_{K\alpha 2}} = 2.34 \cdot 0.73 = 1.71 \quad (4.1.7)$$

where  $\frac{I_{0,K\alpha 1}}{I_{0,K\alpha 2}}$  and  $\frac{W_{K\alpha 1}}{W_{K\alpha 2}}$  are the ratios between the amplitudes and widths of the peaks respectively.

### Lorentz Factor

The observed intensity from a powder sample is given by the known structure factor  $|F_{hkl}|^2$  (albeit for X-Rays), mentioned in (3.2.19), the reflection multiplicity  $m_{hkl}$  along with the geometry factor known as the Lorentz factor [4]

$$I_{powder} = |F_{hkl}|^2 \frac{m_{hkl}}{2 \sin \frac{2\theta}{2} \sin 2\theta}, \quad (4.1.8)$$

where  $2\theta$  is the scattering angle. In this expression we have ignored polarization effects.

### 4.1.3 Line Shapes

Two of the most common line shapes are the Lorentzian  $L$  and the Gaussian  $G$  which versus  $q$  are given as

$$L(q) = \frac{I_0}{1 + \left(\frac{2(q-q_0)}{W_L}\right)^2}, \quad (4.1.9)$$

$$G(q) = I_0 \cdot \exp\left(-4 \ln(2) \left(\frac{q-q_0}{W_G}\right)^2\right) = I_0 \cdot \exp\left(-\frac{1}{2} \left(\frac{q-q_0}{\sigma}\right)^2\right), \quad (4.1.10)$$

where  $I_0$  is the amplitude,  $\sigma$  is the standard deviation of the Gaussian and  $W_G$  and  $W_L$  are the FWHM widths of the Lorentzian and Gaussian respectively. The Gaussian  $\sigma$  can be converted into FWHM (Full Width at Half Maximum)  $W_G$  using

$$W_G = 2\sqrt{2 \ln(2)} \sigma. \quad (4.1.11)$$

Later in the thesis we will encounter a situation where we have a Gaussian instrumental broadening and a Lorentzian line shape originating from the sample. The resulting line shape from the convolution of these is a Voigtian  $V$  defined as

$$V = L \otimes G = \int_{-\infty}^{\infty} L(\rho)G(q - \rho)d\rho. \quad (4.1.12)$$

The Voigt function, although exact and beautiful, is quite complicated, as it can not be expressed analytically, but only numerically as *e.g.* in ref. [119].

There exist a number of simple approximations to the Voigt function. One is the Pseudo-Voigt ( $pV$ ) line shape [163] which is quite common. It consists simply of a scaled addition of the Lorentzian and the Gaussian

$$pV(q) = \eta L(q) + (1 - \eta)G(q) \quad \text{where} \quad \eta \in [0; 1], \quad (4.1.13)$$

where  $\eta$  is the scaling factor.

In the neutron scattering analysis of YBCO the need for an even more complicated line shape arises, as the instrumental peak broadening is Voigt-like instead of Gaussian. The resulting line shape is Voigtian which is derived as

$$\begin{aligned} V_i(q) \otimes L_s(q) &= (G_i(q) \otimes L_i(q)) \otimes L_s(q) \\ &= G_i(q) \otimes (L_i(q) \otimes L_s(q)) \\ &= G_i(q) \otimes L_{s,i}(q) = V_{i;s,i}(q), \end{aligned} \quad (4.1.14)$$

where the subscripts  $s$  and  $i$  stand for sample and instrument respectively. Here we use that convolution is commutative, and that the convolution of two Lorentzians yields a Lorentzian with a width given by  $W_{1,2} = W_1 + W_2$ . In more detail the line shape is given as

$$V(q, W_{G_i}, W_{L_i}) \otimes L(W_{L_s}) = V(q, W_{G_i}, W_{L_s} + W_{L_i}). \quad (4.1.15)$$

Again, as the Voigtian is troublesome to work with, and in order to ease the separation of the instrumental and sample broadening, I have implemented a linear combination of two Pseudo-Voigtians into the line shape P4-Voigt ( $p4V$ ) which is given by

$$p4V = \alpha pV_1 + (1 - \alpha)pV_2 \quad (4.1.16)$$

where  $I_{P4V}$  is the intensity of the P4-Voigt,  $pV_1$  and  $pV_2$  are the intensity of the Pseudo-Voigt's respectively and  $\alpha$  is given from the area ratios of these two Pseudo-Voigt's as

$$\alpha = \frac{A_{pV1}}{A_{pV1} + A_{pV2}}. \quad (4.1.17)$$

The area (or integrated intensity) of the above line shapes is given by

$$A_L = \frac{I_0 W_L \pi}{2}, \quad (4.1.18)$$

$$A_G = I_0 W_G \sqrt{\frac{\pi}{4 \ln 2}}, \quad (4.1.19)$$

$$A_V = A_L \cdot A_G, \quad (4.1.20)$$

$$A_{pV} = \eta A_L + (1 - \eta)A_G, \quad (4.1.21)$$

$$A_{P4V} = \alpha A_{pV1} + (1 - \alpha)A_{pV2}. \quad (4.1.22)$$

## 4.2 Magnetic Susceptibility

The magnetic susceptibility is defined as the response in magnetization of a material to which an external magnetic field is applied. From the equation

$$\mathbf{B} = \mu_0(\mathbf{H} + \mathbf{M}) = \mu_0(1 + \chi)\mathbf{H} = \mu\mathbf{H}. \quad (4.2.1)$$

which describes the relationship between the applied field  $\mathbf{H}$ , the internal magnetic field  $\mathbf{B}$  and the magnetization  $\mathbf{M}$  of the sample, we can derive the magnetic susceptibility  $\chi$ , *i.e.* the magnetization as function of applied field as

$$\chi = \frac{\mathbf{M}}{\mathbf{H}}. \quad (4.2.2)$$

A positive or negative value of  $\chi$  means that the material is magnetized parallel or antiparallel, respectively, to the applied field. The susceptibility  $\chi$  can be divided into a real  $\chi'$  and a imaginary  $\chi''$  part, or equivalently a magnitude (amplitude)  $|\chi|$  and a phase  $\delta$ . The relations between these is

$$\chi = \chi' + i\chi''. \quad (4.2.3)$$

The total susceptibility is therefore the magnitude  $|\chi|$  of the susceptibility. There are two major cases regarding the above formulas, the case where the imaginary part of (4.2.3) is zero and the case where it is non-zero. A non-zero imaginary part ( $\chi''$ ) means that there is magnetic hysteresis or drag in the material *i.e.* an energy loss. At magnetic phase transitions, such as at the superconducting transition temperature or at the Néel temperature, the imaginary part is often non-zero, and this can be used for determining the transition temperature.

### 4.2.1 Apparatus

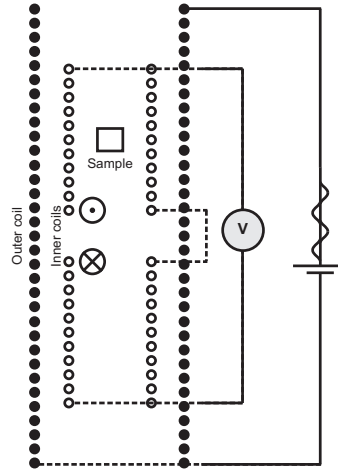


Figure 4.2.1: *Schematic of an AC-susceptometer. An alternating current is applied to the excitation coils (outer coils) (●), generating a magnetic field inside. This field is measured by the inner coils (pick-up coils) (○), which measure only the sample contribution, as they are connected in series (current direction is indicated by ⊙ and ⊗). The voltage across the pick-up coils is measured by a voltmeter.*

Magnetic susceptibility is a quantitative method of probing the magnetic properties of a material. Whether the material is antiferro-, para- or diamagnetic it will respond differently to an applied external magnetic field.

The AC susceptibility measurement apparatus is constructed as an outer coil, the excitation coil, through which an alternating magnetic field is generated. If the coils were ideal, the magnetic field,  $B$ , generated in the excitation coil would be

$$\nabla \times H = j \quad \Rightarrow \quad B = \frac{\mu_0 N i}{2\pi r}, \quad (4.2.4)$$

where the  $B$  is the induced magnetic field,  $j$  is the current density in the coils,  $r$  is the radius of the coil,  $N$  is the number of windings and  $i$  is the current.

Inside the outer coil there are 2 coils, the pickup coils, with the same number of windings or same winding density, connected in series but wound in opposite directions. When applying an excitation field through the outer coils, a field is also generated through the inner coils, and if the inner coils were not connected in series, a voltage would be generated in the circuit connected to these as well. However, since the pickup coils are connected in series, and have opposite winding directions, the voltage generated in one of these is cancelled by the opposite voltage generated in the other.

When a sample is placed inside one of the coils, the electromotive force generated in the pickup circuit will originate only from the sample. The current generated in a pickup coil is calculated below. The mutual inductance between the excitation and pickup coils is given by

$$M_s = \mu_0 A n_{sc}, \quad (4.2.5)$$

where  $A$  is the cross section area of the pickup coils and  $n_{sc}$  is the effective winding number. After some calculation we get an expression for the induced voltage in the pickup coils.

$$U(t) = U_0 e^{i\omega t - \delta} = M_s \frac{\chi V}{A} \frac{\partial H}{\partial t} \quad (4.2.6)$$

$$\begin{aligned} &= M_s \frac{\chi V}{A} H_0 i \omega e^{i\omega t} = M_s \frac{\chi V}{A} H_0 \omega e^{i\omega t + \frac{\pi}{2}} \\ \Rightarrow \chi &= \frac{U_0}{\mu_0 n_{sc} V H_0 \omega} e^{i(\delta + \frac{\pi}{2})}, \end{aligned} \quad (4.2.7)$$

where  $V$  is the sample volume,  $H_0$  is the amplitude of the excitation field,  $\omega$  is the angular frequency and  $\delta$  is the phase shift between the induced pickup voltage  $U(t)$  and the excitation current.

All magnetic AC susceptibility measurements in this thesis were performed in a Physical Properties Measurements System (PPMS) (Quantum Design 6000<sup>2</sup>) at the Paul Scherrer Institute [141].

## 4.2.2 Magnetic Susceptibility of an Antiferromagnet

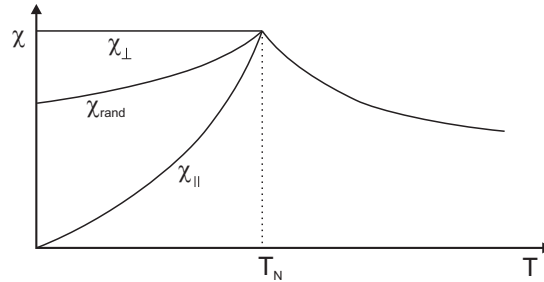


Figure 4.2.2: Schematic of the susceptibility  $\chi$  versus temperature  $T$  of an antiferromagnet. Note the change in the behavior of the susceptibility at  $T_N$ . From ref. [19].

Ideally the AFM-PM transition will be expressed in magnetic susceptibility, as illustrated in figure 4.2.2. The response in susceptibility in an antiferromagnetic particle, depends on the direction of the applied field to that of the spins in the particle. If at low temperatures, the field is parallel or antiparallel to the spins, there will be no response ( $\chi_{\parallel}$ ), or in other words the susceptibility will be zero. At finite temperatures, but below  $T_N$ , thermal fluctuations will cause a finite  $\chi$  increasing with temperature.

If on the other hand, the field is applied perpendicular to the spin direction there will be an response as  $\chi_{\perp}$ , and there will be a finite  $\chi$  constant with temperature.

<sup>2</sup>Website: <http://www.qdusa.com/>

Dealing with a powder (assuming that the grains are randomly oriented) and integrating over all directions, an antiferromagnet will have a response which peaks at  $T_N$  and falls off to a finite value ( $\chi_{rand}$ ) at 0K. Above  $T_N$  the susceptibility will have a Curie-Weiss behavior ( $\chi \propto \frac{1}{T+T_N}$ ).

### 4.3 Transmission Electron Microscopy

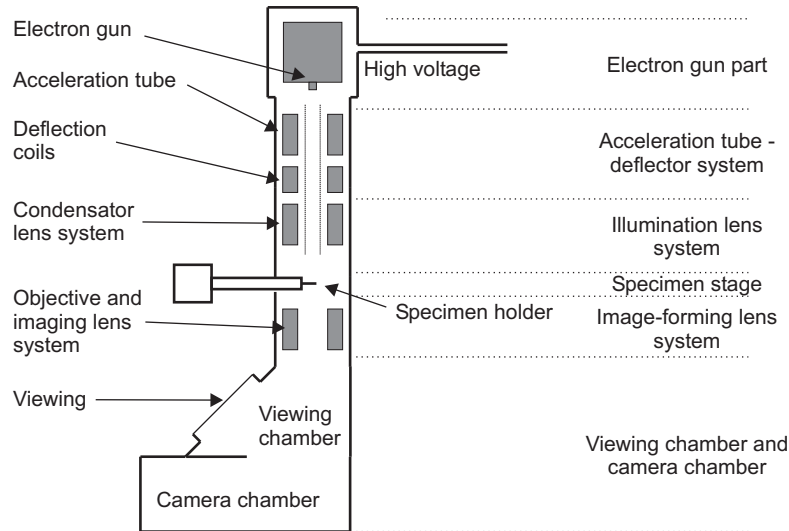


Figure 4.3.1: A schematic illustration of the interior of a transmission electron microscope. Modified from ref. [175].

Without going into details on the workings of a Transmission Electron Microscope (TEM), it will briefly be introduced here. A TEM works in many respects as a classical light microscope, but it uses electrons instead of photons. Turning to the schematic in figure 4.3.1, the electrons are emitted by the electron gun on top of the column, which is kept at high vacuum. The electrons are accelerated through the acceleration tube, and pass through focusing lenses before and after the passing through the sample. The image is viewed on a fluorescent screen, and the image is recorded either on a photographic film or on a CCD (Charge-Coupled Devices) chip [175].

A TEM is very well suited to examine the lateral size and crystalline quality of a sample, but very little information of the horizontal size or thickness of the sample can be extracted, as the image is a 2D projection of the sample.

Without discussing this further, it can be mentioned that techniques exist, from which some information on 3D sizes can be extracted, *e.g.* electron holography.

Size measurements can however, not always stand alone. As previously mentioned, TEM imaging only provides information on the 2D projection of the particle shape. During my Ph.D. time, I have with coworkers looked into this problem, where we have used computer simulations of particle diameter ratios, in order to determine the true shape of the measured particles. A paper on this work has been submitted to European Physics Letters, Applied Physics Section, (see appendix H.1.1 and ref. [72]).

Transmission Electron Microscopy (TEM) imaging has been used to characterize sample the size distribution of the YBCO nanoparticles. The TEM images were obtained in a JEM3000F instrument at Risø.

## 4.4 YBCO Sample Preparation

Different methods of manufacturing small-size YBCO powders exist [136]. For instance, micro-emulsion coprecipitation techniques [96, 136], spray pyrolysis method [184], high energy ball milling [177, 201] or freeze drying [97, 201].

The preparation of bulk YBCO powders is much simpler than the preparation of nano-sized materials, since the only requirement to the procedure is that it yields bulk-sized crystallites and that it structurally and chemically is YBCO.

The nano-sized YBCO particles and the bulk ( $\mu\text{m}$ ) powder were prepared in very different routes. The nano-sized particle powders are the result of the citrate-gel modification of the sol-gel method [146], whereas the bulk powder is manufactured the traditional way through a solid state reaction [53]. In the sections below the manufacturing routes for the two powders will be described.

An isothermal YBCO synthesis phase diagram for the ( $\text{Y}_2\text{O}_3$ ,  $\text{BaO}$ ,  $\text{CuO}$ )-system, showing YBCO and related impurity phases is presented in figure 4.4.1. Although the two synthesis methods presented here differ in the use of reactants, the figure provides an approximate phase diagram for the solid-state and sol-gel techniques.

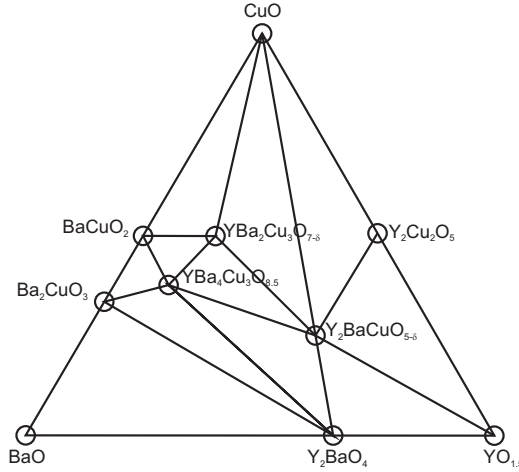


Figure 4.4.1: Isothermal phase diagram for the  $\text{Y}_2\text{O}_3$  -  $\text{BaO}$  -  $\text{CuO}$  system at  $900^\circ\text{C}$  in 1 atmosphere of oxygen. The lines connect phases which exist in equilibrium at this temperature. Figure reproduced from ref. [53], based on calculations in ref. [156].

### 4.4.1 Nanoparticle Preparation

To get insight into the chemistry and manufacturing process, I went to University of Turku, Finland to learn to manufacture the YBCO nano-powder. There I worked with Jussi Raittila [149] and Petriina Paturi, on the manufacturing process.

The raw materials for YBCO are yttriumnitrate ( $\text{Y}(\text{NO}_3)_3$ ), bariumnitrate ( $\text{Ba}(\text{NO}_3)_2$ ) and coppernitrate ( $\text{Cu}(\text{NO}_3)_2$ ), presented in table 4.4.3. Then these are mixed in the ratio 1:2:3 according to the formula  $\text{YBa}_2\text{Cu}_3\text{O}_{6+x}$ . For preparation of the nano-YBCO we used custom mixed stock solutions of chemicals. The chemicals are mixed dissolved in water, for several reasons. Firstly, it is much easier to achieve a homogeneous mixture in liquid form. Secondly, these chemicals always contain some crystal water in solid form, the amount of which may vary. Therefore stock solutions are created and the concentration of these is determined through titration. The stock solutions are prepared from the instructions given in ref. [147].

Three batches of YBCO nano-powder, batch 0-2, have been prepared during this thesis work. These were all prepared following the same procedure. Below I will go through the entire prepa-

ration process of batch 2, since the preparation of batch 1 was made from existing stock solutions. Batch 0 was prepared by J. Raittila. The parameters of the stock solutions used for the batches are found in table 4.4.1 and table 4.4.2.

Compound	Concentration
Y(NO <sub>3</sub> ) <sub>3</sub>	0.111 mol/l
Ba(NO <sub>3</sub> ) <sub>2</sub>	0.243 mol/l
Cu(NO <sub>3</sub> ) <sub>2</sub>	0.382 mol/l

Table 4.4.1: *The stock solutions (solvent is de-ionized water) used in the manufacturing process of batch 1.*

Compound	Concentration
Y(NO <sub>3</sub> ) <sub>3</sub>	0.129 mol/l
Ba(NO <sub>3</sub> ) <sub>2</sub>	0.247 mol/l
Cu(NO <sub>3</sub> ) <sub>2</sub>	0.391 mol/l

Table 4.4.2: *The stock solutions (solvent is de-ionized water) used in the manufacturing process of batch 2.*

**Yttrium stock solution** We are aiming for a solution concentration of 0.125 mol/l. Therefore we mixed 400 ml and 19.5 g of Y(NO<sub>3</sub>)<sub>3</sub>·xH<sub>2</sub>O into the remains of the previous solution (with c(Y)=0.111 mol/l). To determine the exact concentration, we then titrate a small sample of the solution. The titration is performed by adding 100 ml (to a beaker glass) , and then adding a few grams of hexamethylamine (hexamethylenetetramine, C<sub>6</sub>H<sub>12</sub>N<sub>4</sub>) as buffer. Then xylenol is added, which colors the solution red. A titration tube is filled with EDTA<sup>3</sup>, with a concentration EDTA of 0.01 mol/l. EDTA is used as it binds to the metal ions in the solution. A measured amount of the stock solution is added to the solution in the beaker glass. We used 0.5 ml. The EDTA is titrated into the solution until there is a sharp color change to yellow, caused by the binding of all metal ions. During the titration the pH of the solution should be below 6.4, since xylenol colors the solution red at pH>6.4. The amount of used EDTA solution is recorded. This is repeated a few times, and the concentration is the calculated from the mean usage of EDTA per amount of stock solution. The formula used for the calculations is

$$c_0 = \frac{c_1 V_1}{V_0}, \quad (4.4.1)$$

where  $c_0$  is the stock solution concentration,  $c_1$  is the concentration of EDTA,  $V_1$  is the amount of used EDTA and  $V_0$  is the amount of stock solution. The found concentration was  $c_Y = 0.1287$  mol/l. The details of the titration process are found in appendix B.1.1

**Barium stock solution** We are aiming at a barium-concentration of 2 times that of the yttrium solution of

$$c_{Ba} = 2c_Y = 0.257 \text{ mol/l}, \quad (4.4.2)$$

and the approximate amount of material needed can therefore be calculated as

$$m_{Ba} = V_{Ba} \cdot c_{Ba} \cdot M_{Ba} = 0.5 \text{ l} \cdot 0.257 \text{ mol/l} \cdot 261.34 \text{ g/mol} = 33.582 \text{ g}. \quad (4.4.3)$$

What was actually weighed of was 32.73 g. One should at this point keep in mind that the maximum dissolvable concentration of bariumnitrate is  $c_{Ba,max} = 0.28$  mol/l. We dissolved 32.73 g into 500 ml of water.

**Copper stock solution** We are aiming at a copper-concentration of 3 times that of the yttrium solution of

$$c_{Cu} = 3c_Y = 0.386 \text{ mol/l} \quad (4.4.4)$$

and the approximate amount of material needed can therefore be calculated as

$$m_{Cu} = V_{Cu} \cdot c_{Cu} \cdot M_{Cu} = 0.4 \text{ l} \cdot 0.386 \text{ mol/l} \cdot 241.5984 \text{ g/mol} = 37.98 \text{ g}. \quad (4.4.5)$$

<sup>3</sup>EDTA (HO<sub>2</sub>CCH<sub>2</sub>)<sub>2</sub>NCH<sub>2</sub>CH<sub>2</sub>N(CH<sub>2</sub>CO<sub>2</sub>H)<sub>2</sub>

We weighed of the approximate amount and poured this into an old solution (with a concentration of  $c=0.382$  mol/l), and added 400 ml of water. This solution was titrated using EDTA and the concentration of the solution was found to be  $c_{Cu} = 0.391$  mol/l. The details of the titration process are found in appendix B.1.3.

**Mixing of solutions** The chemicals are mixed in the molar ratio 1:2:3 (with respect to Y, Ba, Cu respectively), which for the solutions in table 4.4.2, are 95.7.0 ml, 100.0 ml, 94.8 ml respectively. While monitoring the pH value using an electronic pH-meter, citric acid is added to achieve a pH value of 1.2-1.5. Calculations showed that the amount of citric acid should be around 7.74 g, so the added amount was 7.80 g. The amount of citric acid is calculated by

$$c_{Y,Tot} = \frac{n_Y}{V_{Tot}} = \frac{c_Y \cdot V_Y}{V_Y + V_{Ba} + V_{Cu}} = \frac{0.01235 \text{ mol}}{(95.7 + 100 + 94.8) \text{ ml}} = 0.0425 \text{ mol/l} \quad (4.4.6)$$

$$m_{citric} = 4.333 \cdot M_{citric} \cdot n_Y = 4.3 \cdot 210.14 \text{ g/mol} \cdot 0.0425 \text{ mol/l} \cdot 0.200 \text{ l} = 7.74 \quad (4.4.7)$$

where 4.333 is the scaling factor which comes from the ratio of metal cations to citric acid anions

$$\frac{Y^{3+} + 2 \cdot Ba^{2+} + 3 \cdot Cu^{2+}}{Citric^{3-}} = \frac{13}{3} \sim 4.333. \quad (4.4.8)$$

The function of the citric acid is to act as a chelating agent, forming long chains. After addition of the citric acid, ethyldiamin (99 %,  $H_2NCH_2CH_2NH_2$ ) is titrated into the solution until a pH of 5 is achieved. Then the solution is poured into glasses and put into an oven at 90-100°C over night in order to evaporate the water (see figure 4.4.2(a-b)), forming a gel.

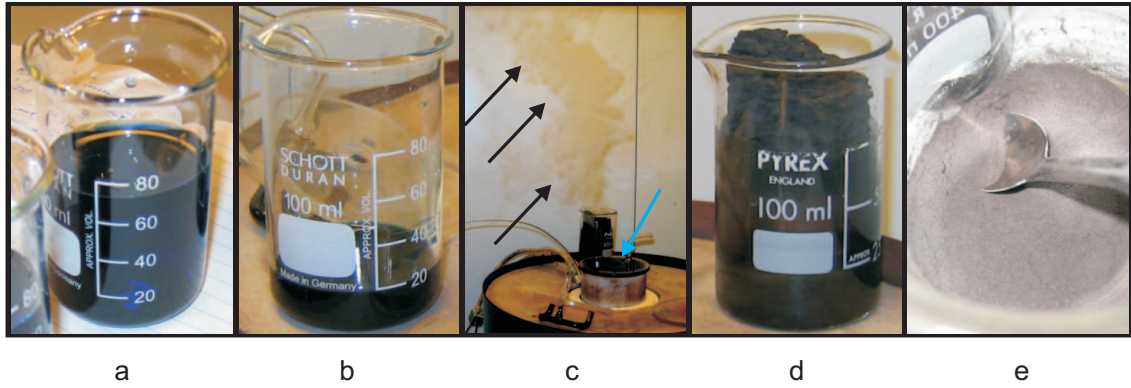


Figure 4.4.2: Images from the manufacturing of the YBCO nanoparticles (Batch 1). (a) Finished solution (Batch 2). (b) Dried solution (gel). (c) The burning of a gel. Note the smoke (black arrows) comes from the closed heat compartment (blue arrow), not the sample in the background. (d) A fired gel (precursor). (e) The pulverized fired precursor.

When the water has evaporated the glasses are taken out and the samples are put into a heat compartment. In the heat compartment the dried solution is fired to remove organic materials (figure 4.4.2(c)). The yield of the firing is the YBCO precursor, which is in a form of a hard, visibly amorphous solid (looking like foam, see figure 4.4.2(d)). The precursor is crushed in a beaker glass (figure 4.4.2(e)), and divided into crucibles for the further calcination. The calcination was performed in a controlled atmosphere of  $P=0.1$  Torr of  $O_2$  at 700 °C for 4 hours, with heating and cooling periods of 30 min as showed in figure 4.4.3. After calcination XRD showed that the sample contained impurities, hence a second calcination was performed (heating for 45 min - 700 °C for 30 min - cooling for 30 min). The XRD of this sample after manufacturing showed close to no impurities.

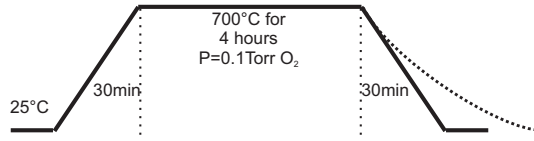


Figure 4.4.3: The calcination procedure of nano-sized YBCO batch 2. The dotted line to the far right show the actual cooling curve.

#### 4.4.2 Bulk Preparation

The bulk powder is in short prepared through mixing stoichiometric fractions of the solid powder compounds containing Y, Ba and Cu, in my case  $Y_2O_3$ ,  $BaCO_3$  and  $CuO$ , and heating this mixture to high temperatures ( $\sim 900^\circ C$ ).

To facilitate complete transformation and homogeneity of the sample the resulting powder is often pressed to a pellet, and sintered further at temperatures similar to the first, before being crushed back into powder. This last step can be repeated to improve the quality of the powder [62, 53]. After sintering, the sample is heated to  $350-500^\circ C$  in order to achieve full oxygen doping.

I will not go further into the chemistry, different routes and procedures that exist regarding the manufacturing of bulk YBCO, nor their advantages or disadvantages, as there are numerous good books such as ref. [53] presenting this nicely. Instead, the procedure which was used to manufacture bulk-sized YBCO powders is presented, with the manufacturing of the bulk Sample 5 ( $x=0.30$ ) as example. The procedure is based on ref. [62].

As raw reactant chemicals I have, as mentioned, used the compounds  $Y_2O_3$ ,  $BaCO_3$  and  $CuO$  (molar weights displayed in table 4.4.4). The procedure started by weighing of plentiful amounts of reactants, which were then placed in an oven for dehydration overnight. This procedure removes the water caught on the particle surfaces, and at the particle interfaces.

The amounts of reactants weighed of for synthesis are listed in (4.4.9)-(4.4.11). The amounts of the reactants needed for 4.0 g of YBCO ( $x=0.5$ ) for  $Y_2O_3$  were calculated (marked by { } brackets in (4.4.9)). The actual amount weighed off ( $\rightarrow$ ) was slightly higher, due to weighing error. The stoichiometric amounts of the other two reactants were adjusted accordingly, which resulted in the numbers marked by [ ] brackets, in (4.4.10) and (4.4.11). The weighed amounts of these reactants was close to the aim, as seen below. As seen from the numbers in (4.4.10)-(4.4.11) great care was taken while weighing of materials, in order to get the 1:2:3 stoichiometry accurate.

$$Y_2O_3: \quad \{0.68611 \text{ g}\} \quad \rightarrow \quad 0.68840 \text{ g}, \quad (4.4.9)$$

$$BaCO_3: \quad [2.40661 \text{ g}] \quad \rightarrow \quad 2.40663 \text{ g}, \quad (4.4.10)$$

$$CuO: \quad [1.45491 \text{ g}] \quad \rightarrow \quad 1.45492 \text{ g}, \quad (4.4.11)$$

During the calculations of reactant amounts, and aiming at 4.00 g of YBCO, it was assumed that the end YBCO powder had a doping of ( $x=0.5$ ). This is not very important, but rather illustrates the doping of the end product is a bit uncertain. Later doping is necessary in any case.

The stoichiometric amounts were very thoroughly mixed and ground in a mortar for  $>20$  min, and then loaded into a Pt-coated crucible, and calcinated in a furnace for  $\sim 120$  hours. The calcination furnace program is displayed in figure 4.4.4.

After calcination, the sample had a yellowish-green color on the surface where it has touched the Pt-foil. However, as this was only the surface layer, the sample was again ground, before being pressed into a pellet <sup>4</sup>. The pellet was sintered according to the program displayed in figure 4.4.5, before again being thoroughly crushed in a mortar, yielding the finished raw YBCO powder. Subsequent XRD analysis showed that the powder is only moderately pure ( $\sim 80\%$ ), containing significant amounts (up  $\sim 20\%$ ) of impurities, however, the amount of impurities is believed to be lower than this, as an inspection of the XRD data only shows very small impurity peaks. The characterization of the samples is provided in section 4.7.

<sup>4</sup>The applied pressure was 100 atm. for 10 min, during which the pressure fell to 80 atm. The pressure was

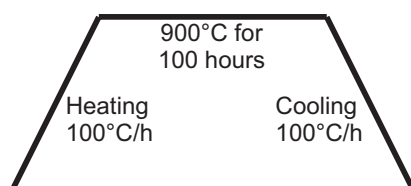


Figure 4.4.4: Schematic of YBCO bulk calcination program.

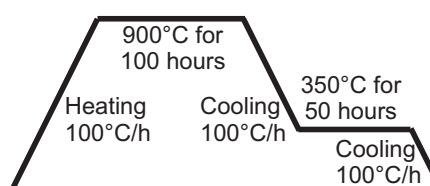


Figure 4.4.5: Schematic of YBCO bulk sintering program.

Compound	Molar mass g/mol
Yttrium nitrate ( $\text{Y}(\text{NO}_3)_3$ )	274.92
Barium nitrate ( $\text{Ba}(\text{NO}_3)_2$ )	261.34
Copper nitrate ( $\text{Cu}(\text{NO}_3)_2$ )	241.5984
Citric acid ( $\text{C}_6\text{H}_8\text{O}_7 \cdot x\text{H}_2\text{O}$ )	210.14

Table 4.4.3: Molar masses of for selected compounds used in the manufacturing of the YBCO nanoparticles.

Compound	Molar mass (g/mol)
Yttrium oxide ( $\text{Y}_2\text{O}_3$ )	225.807
Barium carbonate ( $\text{BaCO}_3$ )	197.348
Copper oxide ( $\text{CuO}$ )	79.539
YBCO ( $x=0.5$ )	658.1985

Table 4.4.4: Molar masses of compounds used in solid state reactions for manufacturing of bulk YBCO powder.

## 4.5 YBCO Doping

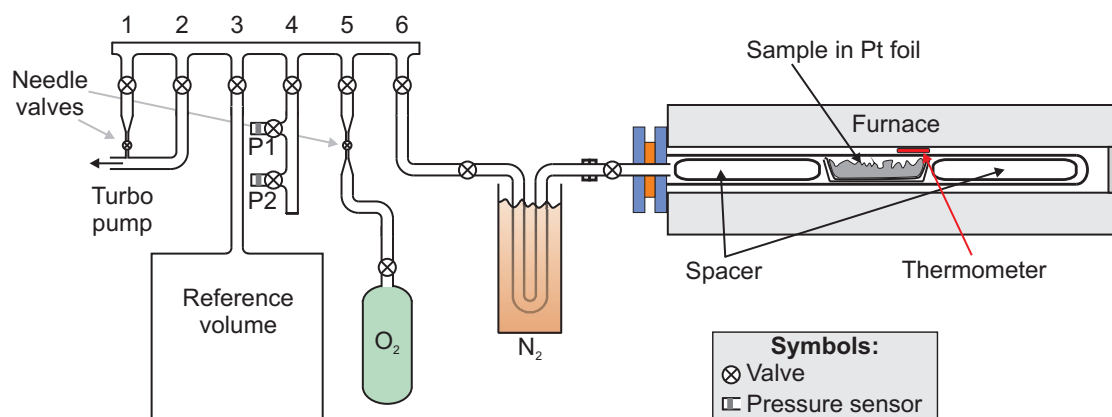


Figure 4.5.1: Schematic of the Gas Volumetric system used for the doping of the YBCO samples. From right: Furnace containing sealable glass tube. The glass tube is connected to the piping system leading to the gas volumetric system itself. The pipe system starts with a water vapor trap (pipe loop in liquid  $\text{N}_2$ ), before leading into the flange. From the flange there are valves (1) and (2) to turbo-pump, to the reference volume (3), to the pressure sensors, P1 and P2 with 1000 Torr and 1 Torr heads respectively (4), to the  $\text{O}_2$  in-let (5) and to the sample and sample environment (6).

The oxygen doping of the YBCO samples (both nano- and bulk-sized) is performed in a high vacuum gas volumetric system, very similar to that described in ref. [7]. A schematic of the system used is presented in figure 4.5.1.

Using the gas volumetric system one can add or remove a very well controlled amount of gas from the sample environment, using a reference volume and a complex valve system.

When YBCO is heated it will, depending on doping, degas or absorb oxygen gas, until an equilibrium pressure with the surroundings is obtained. The higher the temperature and the

momentarily raised to 100 atm., before the pellet was removed from the press.

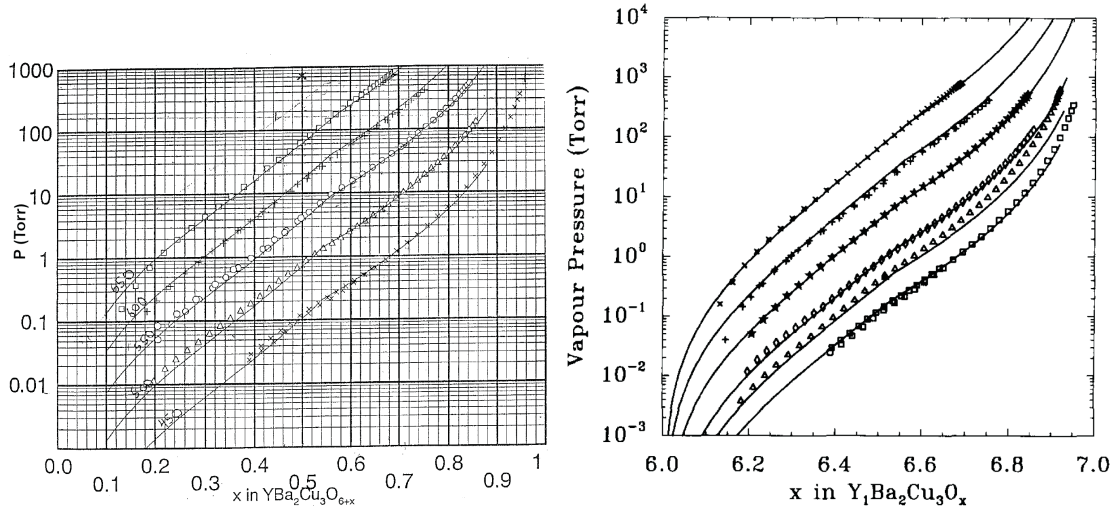


Figure 4.5.2: Vapor pressure of YBCO versus temperature and oxygen doping. Left: Diagram from ref. [8] Right: The curves are results from cluster variation calculations in a quasi-chemical approximation. Modified from ref. [171].

higher the doping, the higher the vapor pressure. The vapor pressure versus temperature and doping has been investigated by Schleger *et al.* [171, 172], resulting in the plots in figure 4.5.2.

Using the gas volumetric system, and knowing the mass and doping of an YBCO sample, the doping can be lowered or raised by removing a calculated amount of oxygen gas from the system at high temperature, and then when the sample is sealed, cool it.

In the present case, however, neither the exact amount of YBCO material nor the exact doping was known at the time of doping. Therefore the above method could not be used. There are several factors making the amount of YBCO unknown. Firstly the exact amount of impurities was unknown. Secondly the material is nanosized, which as mentioned in section 2.5 means that the surface to volume ratio is large. It is unknown how the surface layers of YBCO behave compared to bulk. Third, nanoparticles due to the large surface areas have considerable amounts of condensed water on the surface, which also affect the actual amount of YBCO. On YBCO the water is in the form of  $\text{OH}^-$ .

Taking this into account, I decided to use another approach to dope the samples, namely using the vapor pressure diagrams. Assuming that the (batch) samples had a doping in the vicinity of  $x=1$ , oxygen only has to be removed. For each doping degree I found from the diagrams a temperature which had a suitable vapor pressure. The idea is then to heat the sample to the found temperature, and pump away the excess oxygen until the equilibrium pressure has been lowered to the value found in the diagrams. Then the glass tube containing the sample is sealed, and the sample is slowly (6-18 hours) cooled, to allow the oxygen to be distributed homogeneously within the sample. As seen from the diagrams, YBCO will absorb the gaseous oxygen in the glass tube when cooled, and the doping will be slightly higher than predicted, but with the error of the method. The slow cooling is also important, for the distribution of the extra absorbed oxygen.

The equilibrium pressure must be chosen with some care, since the precision of pressure sensors is poor if the pressure is too low [8], and since the sample will absorb too much extra oxygen if the pressure is too high.

### Sample Dehydration

While heating an effort was put into removing the surface water from the samples. This was done for two reasons:

1. At high temperatures (above  $\sim 600^\circ\text{C}$ ), the  $\text{OH}^-$ , can react with the YBCO, forming un-

wanted impurities.

2. The samples were to be measured upon using neutron scattering. Hydrogen is a source of noise/high background in neutron diffraction, as it has a very high incoherent cross section (see table G.3.1). From previous experiments [94], it was known that the diffraction peak was weak, and that the background was high.

The heating process showed that there were considerable amounts of water on the samples. The water was removed as follows: The samples were heated in steps of 50-100 °C. At each step from 100 °C to ~500 °C, the pressure increases significantly due to water vapor when the set-point temperature is reached. The water-removing procedure described below was repeated at each temperature step until no more water could be removed, before continuing with the heating.

The water vapor was removed by putting a cold-trap of liquid N<sub>2</sub> (displayed in figure 4.5.1) on the pipe-loop. The water vapor then condensed in the loop, and could then be pumped out later, when the loop is heated (and the valve to the sample is closed).

## 4.6 YBCO Sample Doping Overview

Table 4.6.1 contains an overview of the oxygen doping degree  $x$ , and the  $T$ - $P_{O_2}$  parameters used in the doping of the YBCO samples to obtain this doping degree. The errors on the doping values are estimated from the  $T$ - $P_{O_2}$ -diagram (figure 4.5.2) and small experimental details which not mentioned here.

Sample Name	Batch	Oxygen Doping $x$	Doping $P$ (Torr)	Doping $T$ (°C)
Sample 1	Batch 0	0.20±0.025	0.65(5)§	651(5)
Sample 2	Batch 0	0.30±0.025	1.02(5)	600(5)
Sample 3†	Batch 1a	0.35±0.025	2.16(5)	600(5)
Sample 4†	Batch 1a	0.25±0.025	0.55(2)	600(5)
Sample 5‡	Batch 1a <sup>b</sup>	0.30±0.025	0.200(5)	550(5)

Table 4.6.1: *YBCO sample doping overview. Doping pressure and temperature are the  $P$  and  $T$  at which the samples were stabilized. The errors in doping are estimated. Symbols: (†) Bulk- and nano-sized samples were doped together. Doping of bulk was unsuccessful. (‡) Bulk- and nano-sized samples were doped together. Doping of bulk was successful. (§) The pressure was on purpose set too low, to account for reabsorption of O<sub>2</sub> on cooling. (b) Raw material came from Sample 3 and Sample 4.*

## 4.7 YBCO Sample Characterization

In this section I will present the characterization of the YBCO samples which are the subject of studies in this thesis. The samples have been characterized using X-Ray diffraction, magnetic AC susceptibility measurements, transmission electron microscopy and atomic force microscopy.

### 4.7.1 YBCO XRD Phase Characterization

As a part of the characterization, I have using XRD performed a phase characterization of the YBCO samples. The XRD measurements were performed at Risø, on a  $\theta$ - $\theta$  setup (horizontal axis), with Cu K- $\alpha$   $\lambda = 1.54184 \text{ \AA}$  [78] (containing K- $\alpha$ 1 and K- $\alpha$ 2 radiation<sup>5</sup>). Slit settings were

<sup>5</sup> $\lambda_{K\alpha 1} = 1.54056 \text{ \AA}$ ,  $\lambda_{K\alpha 2} = 1.54439 \text{ \AA}$

Phase #	Compound	Crystal system	Space group	ICSD no.	Ref.
1	YBCO	Tetragonal	123 P 4/m m m	83211	[208]
2	BaCuO <sub>2</sub>	Cubic	229 I m -3 m	93655	[42]
3	Y <sub>2</sub> O <sub>3</sub>	Cubic	206 I a -3	155173	[45]
4	CuO	Monoclinic	15 C 1 2/c 1	92368	[209]
5	Y <sub>2</sub> BaCuO <sub>5</sub>	Orthorhombic	62 P n m a	52055	[74]
6	BaCO <sub>3</sub>	Orthorhombic	62 P n m a	91888	[73] <sup>†</sup>
7	Y <sub>2</sub> BaO <sub>4</sub>	Orthorhombic	62 P n m a	89640	[114]
8	Y <sub>2</sub> Cu <sub>2</sub> O <sub>5</sub>	Orthorhombic	33 P n a 21	72058	[2]

Table 4.7.1: XRD properties of selected compounds used in XRD analysis. Symbols: <sup>†</sup>) File slightly modified from reference.

10 mm×0.8 mm on the source side and 10 mm×0.3 mm on the detector side. The XRD data has been analyzed through Rietveld analysis using the Fullprof suite analysis package<sup>6</sup> [157].

Although great care was taken in preparing the XRD samples, many of the diffractograms (*e.g.* Sample 3 ( $x=0.35$ ) in figure E.3.1(3)) are either very noisy or have very strange backgrounds, hampering the analysis significantly. In addition the diffraction lines are broad, due to the finite particle size.

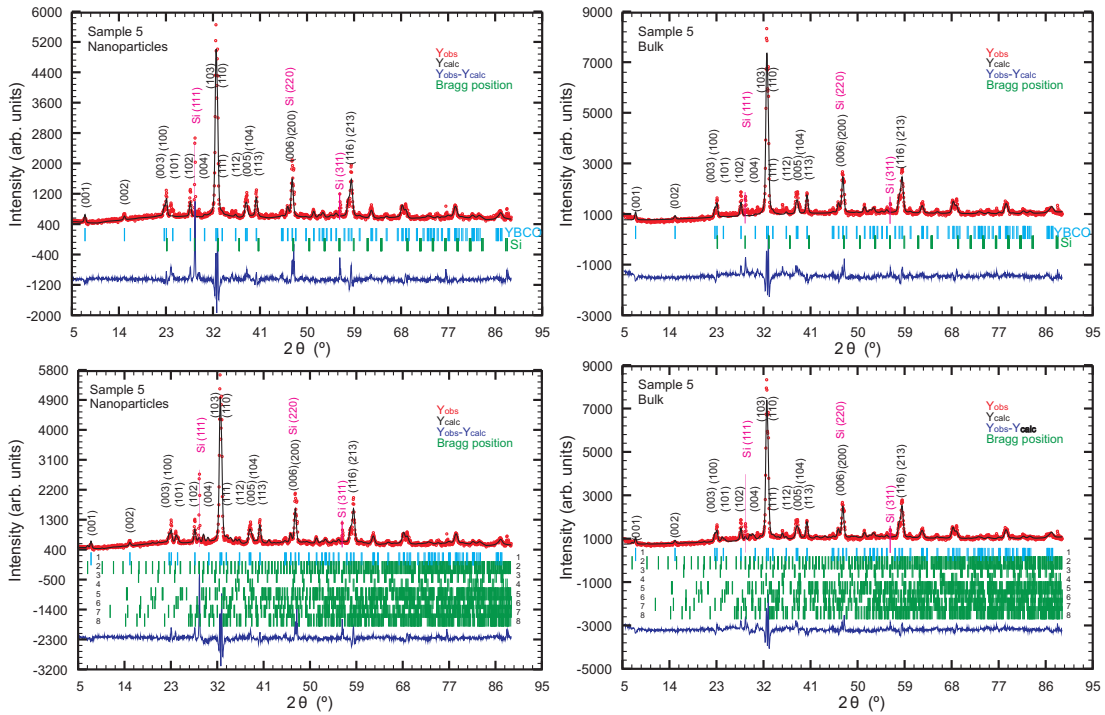


Figure 4.7.1: Examples of fitted XRD data. The blue vertical lines below the diffractogram mark the YBCO peak positions, and the green vertical lines mark the impurity peak positions. The difference between raw data and fit is displayed at the bottom. The phases are marked by numbers. Upper left: Nanosized YBCO (Sample 5 ( $x=0.30$ )) fitted with YBCO and Si. Lower left: Nanosized YBCO (Sample 5 ( $x=0.30$ )) fitted with 8 phases. Upper right: Bulk YBCO (Sample 5 ( $x=0.30$ )) fitted with YBCO and Si. Lower right: Bulk YBCO (Sample 5 ( $x=0.30$ )) fitted with 8 phases.

The analysis revealed that, besides YBCO all the samples contained a relatively large number

<sup>6</sup> Available from the website [www.ill.eu/sites/fullprof/](http://www.ill.eu/sites/fullprof/)

of impurity phases, in rather significant amounts. The phases have been identified from a large number of candidates (similar to section 5.1.8). The identified phases and some properties related to the XRD analysis are listed in table 4.7.1.

Phase no:	1	2	3	4	5	6	7	8
Sample	YBCO %	BaCuO <sub>2</sub> %	Y <sub>2</sub> O <sub>3</sub> %	CuO %	Y <sub>2</sub> BaCuO <sub>5</sub> %	BaCO <sub>3</sub> %	Y <sub>2</sub> BaO <sub>4</sub> %	Y <sub>2</sub> Cu <sub>2</sub> O <sub>5</sub> %
S. 1 ( $x=0.20$ )	78.7(1.4)	7.5(7)	0.4(4)	5.8(7)	0(0.00)	5.7(0.4)	1.8(0.6)	0(0.00)
S. 3 ( $x=0.35$ )	45(2)	0.08(3)	10.2(1.4)	14(2)	0.01(0.00)	21.9(1.5)	8.37( 1.86)	0(0.00)
S. 4 ( $x=0.25$ )	63(2)	0.30(1)	0.42(1)	10.5(1.5)	7.0(1.3)	13.1(9)	6.0(1.4)	0.01(0.00)
S. 5 ( $x=0.30$ )	80.8(1.9)	8.3(1.0)	0(0.00)	5.4(1.0)	0(0.00)	4.7(5)	0.7(8)	0(0.00)
S. 3 ( $x=0.35$ ) B	68(2)	14.3(1.6)	0(0.00)	6.7(1.4)	8.8(1.6)	2.1(6)	0(0.00)	0(0.00)
S. 4 ( $x=0.25$ ) B	62(2)	8.8(1.6)	0(0.00)	9.3(1.6)	7.8(1.6)	3.6(7)	8.7(1.6)	0(0.00)
S. 5 ( $x=0.30$ ) B	80.3(1.6)	5.8(9)	0(0.00)	6.6(8)	0.08(0.00)	2.9(5)	4.2(8)	0(0.00)

Table 4.7.2: *Phase composition of YBCO samples in weight-% found through XRD analysis.* Note: B indicates bulk sample.

As seen from the phase analysis results in table 4.7.2, the samples, according to the XRD analysis contain only 45-80 % (in weight) YBCO. This amount is much lower than expected, considering the size of the YBCO peaks compared to the impurity peaks. Examples of fitted diffractogram are presented in figure 4.7.1. The raw diffractograms are shown in appendix E.3.

What is noticeable in the found compositions is that the content of some of the compounds varies significantly, and some of the results are in my opinion not entirely trustworthy. For instance, Sample 5 which was made from Sample 3 and Sample 4, is found to contain BaCuO<sub>2</sub>, which the other two do not contain. Secondly, Sample 3 is found to contain Y<sub>2</sub>O<sub>3</sub> which the other two do not contain, and thirdly Sample 4 contains according to the XRD Y<sub>2</sub>BaCuO<sub>5</sub> which the other two do not.

Considering that Sample 3 and Sample 4 are made from the same batch and that Sample 5 ( $x=0.30$ ) is made from the other two, it is very unlikely that they should exclusively contain their own impurity phases. On top of that, neutron data clearly show that all samples contain these three impurities. From the found compositions, the quality of the raw data, the fits, and the neutron data, I therefore estimate the impurity content of the samples 3-5 to be equal and to be 3(2) % BaCuO<sub>2</sub>, 2(1) % Y<sub>2</sub>O<sub>3</sub>, 3(2) % CuO, 2(1.5) % Y<sub>2</sub>BaCuO<sub>5</sub>, 5(3) % BaCO<sub>3</sub> and 1(1) % Y<sub>2</sub>BaO<sub>4</sub>, corresponding to ~85 % YBCO.

The last nanosized sample (Sample 1) is accepted to contain approximately the reported YBCO content. However, the bulk sample is most likely cleaner than found from the analysis, as it contains only very small impurity peaks. Common for both of these last two samples is that the actual amounts of the individual impurity phases might differ from the amounts found through the refinement.

## 4.7.2 Magnetic Susceptibility Measurements

All YBCO samples, nanosized and bulk, were subjected to AC susceptibility measurements in order to investigate the macroscopic magnetic properties. These properties are not revealed by neutron diffraction or  $\mu$ SR. Furthermore it was an objective to investigate whether the  $T_N$  could be determined through susceptibility measurements.

All measurements were started at room temperature, and the sample was cooled to 4-8 K, at speeds of 1-4 K/min, taking measurements every 1,2 or 4 K.

A few selected datasets are presented in figure 4.7.2. Displayed are the real and imaginary parts of  $M$ . A larger collection of susceptibility datasets covering most samples is presented in appendix E.4.

Unfortunately the investigations were non-suitable for providing information on the magnetic transition and the Néel temperature. However, some information has been extracted from the data. Common to the nanosized samples is that they have a very low susceptibility from room temperature down to ~100 K where a positive  $\chi'$  signal arises, a signal which diverges at low

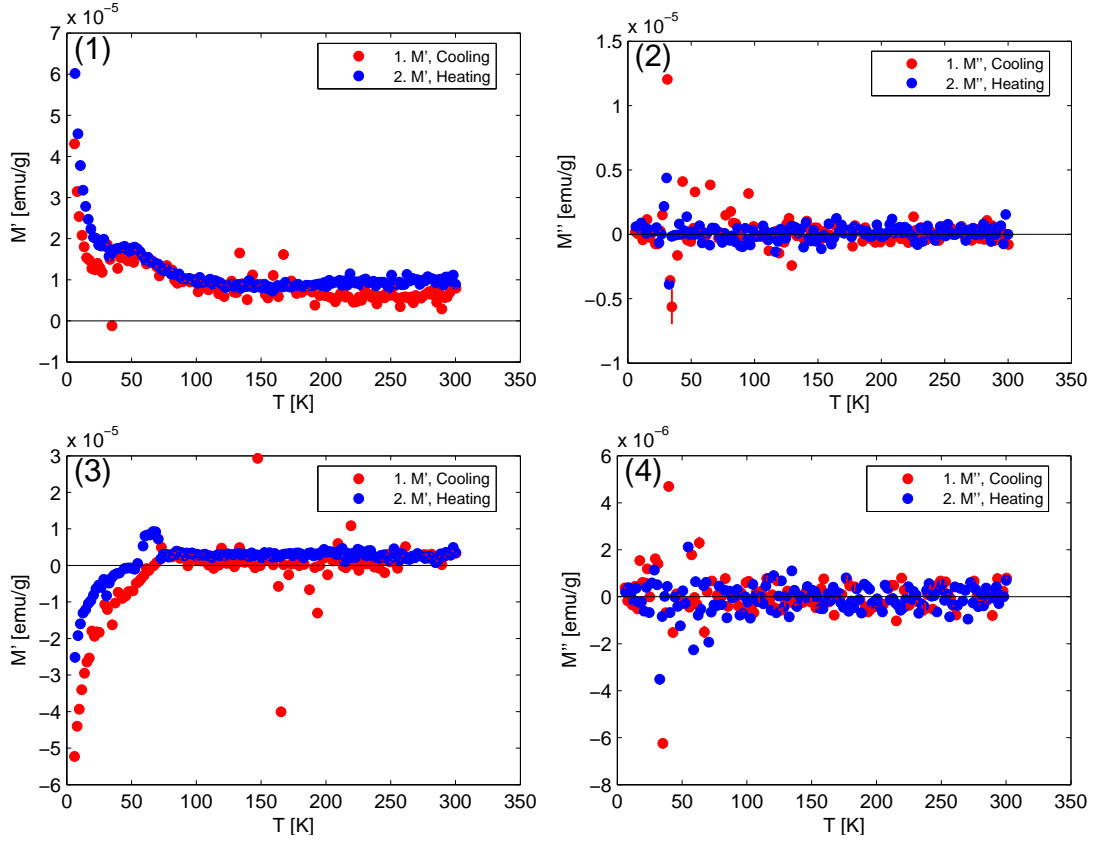


Figure 4.7.2: Selected AC susceptibility data for nanosized YBCO samples. Left plots are the real part of  $M$ . Right plots are the imaginary part of  $M$ . (1-2) Sample 3 ( $x=0.35$ ). (3-4) Sample 4 ( $x=0.25$ ).

temperature ( $\sim 10$  K). The very low signal of the order  $\sim 10^{-5}$  emu/g signifies that YBCO has a very low response to the applied field, compared to the signal of  $\sim 10.7$  emu/g if all spins in YBCO respond fully to the excitation field as calculated in appendix C.1.

The magnetic ordering temperatures of  $\text{BaCuO}_2$ ,  $\text{Y}_2\text{BaCuO}_5$  and  $\text{CuO}$  are 11 K and 15 K and 226 K respectively [197], and the ordering temperature of  $\text{Y}_2\text{Cu}_2\text{O}_5$  is 13 K. In literature both  $\text{BaCuO}_2$  and  $\text{Y}_2\text{Cu}_2\text{O}_5$  are reported to show significant positive  $\chi'$ .

From literature it is known that  $\text{BaCuO}_2$  has a strong paramagnetic signal at low temperature [188, 190, 195], as well as  $\text{Y}_2\text{Cu}_2\text{O}_5$  has a significant signal [190]. I therefore attribute my diverging signal at low temperature to these two phases.

### 4.7.3 TEM Size Measurements

The size of the particles has been done by measurement of the diameter in a vector graphics editor. I have assumed that the particles are disc shaped, and I have therefore measured the in-plane diameter of the particles by drawing a circle around the outer edges of the particle, and the reading the circle diameter, as shown in figures 4.7.5 and 4.7.6. The criterion for usable particles that the edges of the particle could be distinguished in such a degree that a circle could be drawn.

The results of two TEM measurements (presented in table 4.7.9 and figures 4.7.3 and 4.7.3 for measurement 1 and 2 respectively), are consistent. Using measurement no. 1, due to the higher  $N$ , the mean particle diameter is found to be 28(15) nm.

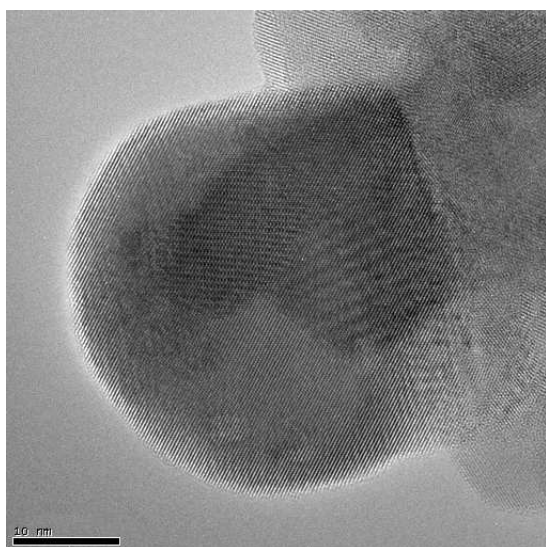


Figure 4.7.3: TEM image of YBCO particle from Sample 2 ( $x=0.30$ ). The bar is 10 nm. Image by C. Bahl.

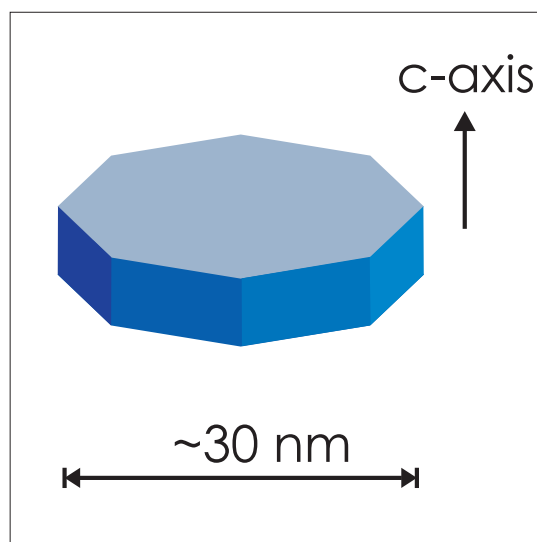


Figure 4.7.4: A schematic of an YBCO disc-shaped nanoparticle. In part reconstructed from ref. [94].

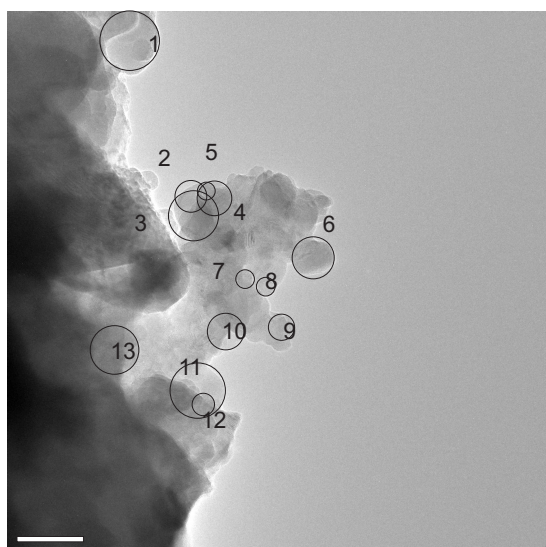


Figure 4.7.5: Example of TEM image of YBCO nano particles from measurement 1. The circles mark measured particles. The bar is 50 nm.

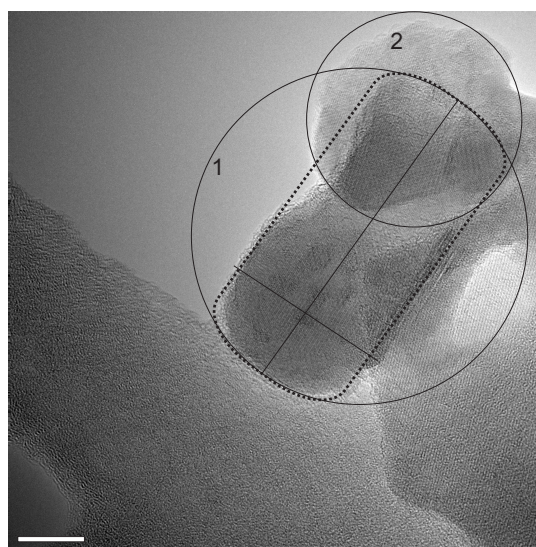


Figure 4.7.6: Example of TEM image of YBCO nano particles from measurement 2. The circles mark measured particles. Notice the long thin particle, which is a particle seen edge-on. The bar is 10 nm.

#### 4.7.4 AFM Size Measurements

An AFM works like a feeling finger on a substrate or sample. Using either contact, non-contact or tapping mode a tip at the end of a vibrating cantilever is moved across the surface, recording the height of the sample. A schematic of an AFM is presented in figure 4.7.10.

I have only used tapping mode in my investigations, and will therefore in the following only

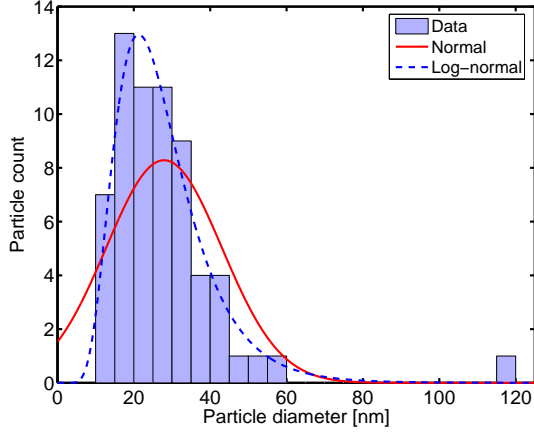


Figure 4.7.7: Size distribution of YBCO particles as measured from TEM measurement no. 1.

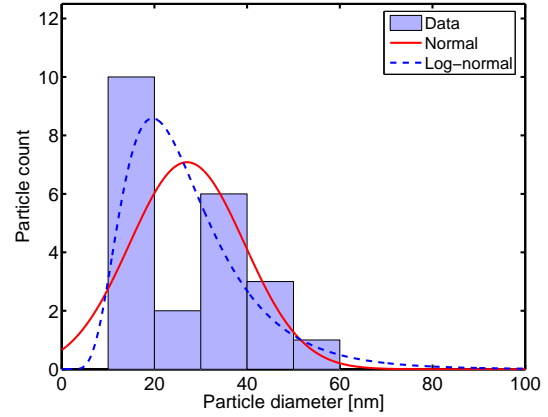


Figure 4.7.8: Size distribution of YBCO particles as measured from TEM measurement no. 2.

Meas. no.	Bin Size	$\langle d \rangle$	$\sigma(d)$	$\exp[\langle \log d \rangle]$	$\exp[\sigma(\log d)]$	Top-point
1	5.0	27.9	15.2	25.3	1.52	21.3
2	10.0	27.0	12.4	24.4	1.60	19.6

Figure 4.7.9: Statistics on YBCO particle size measurement nos. 1 and 2 from TEM images. Symbols:  $\langle d \rangle$  is the average particle diameter with standard deviation  $\sigma(d)$ .  $\exp[\langle \log d \rangle]$ ,  $\exp[\sigma(\log d)]$  and Top-point are the average particle size, standard deviation and the top-point of the log-normal distribution.

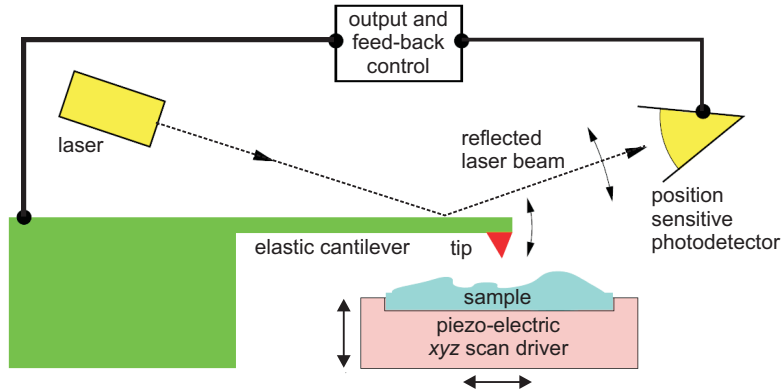


Figure 4.7.10: A schematic illustration of an atomic force microscope, showing the key components. Modified from ref. [26].

deal with this mode, and not go further into the many modes and applications, possible with an AFM.

In tapping mode, the cantilever is vibrating up and down. The oscillations are downwards limited by the substrate/sample which we are measuring upon. The oscillation amplitudes are recorded by the reflection of a laser beam of the cantilever upon a photo detector, as shown in figure 4.7.10.

AFM has a very high resolution in the vertical direction, limited mostly by the resolution

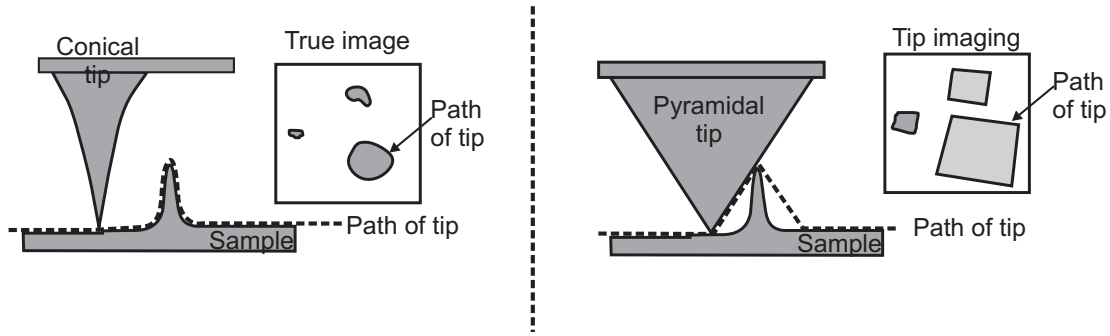


Figure 4.7.11: A schematic illustration of the tip convolution in an AFM. Notice the different paths of the conical and the pyramidal tips, and the different resulting shapes in the images on the right. Modified from ref. [95].

of the photo-detector. In the horizontal direction, the resolution of the AFM is much worse, as the convolution with the tip shape has to be taken into account, when discussing the horizontal size of measured features. In simple terms, one has to have information of the shape and size of the tip in order to very accurately extract horizontal shape information. The most pronounced effect regarding the horizontal resolution is the tip convolution, where in effect the tip shape is convoluted onto the measured features, as illustrated in figure 4.7.11

With the mentioned limitations, I have used AFM to measure the thickness only of the YBCO nano particles on a Si substrate. The measurements were made using a Veeco Dimension 3000 AFM. The tip was presumably rounded and conical, but this was not double-checked.

#### 4.7.4.1 AFM Measurements

The YBCO nanoparticle samples were prepared as follows. A Si substrate was cleaned in a HCl (37%) bath in ultrasound for 4 hours, and was thereafter flushed in ethanol to removed settled impurities and to remove resident HCl.

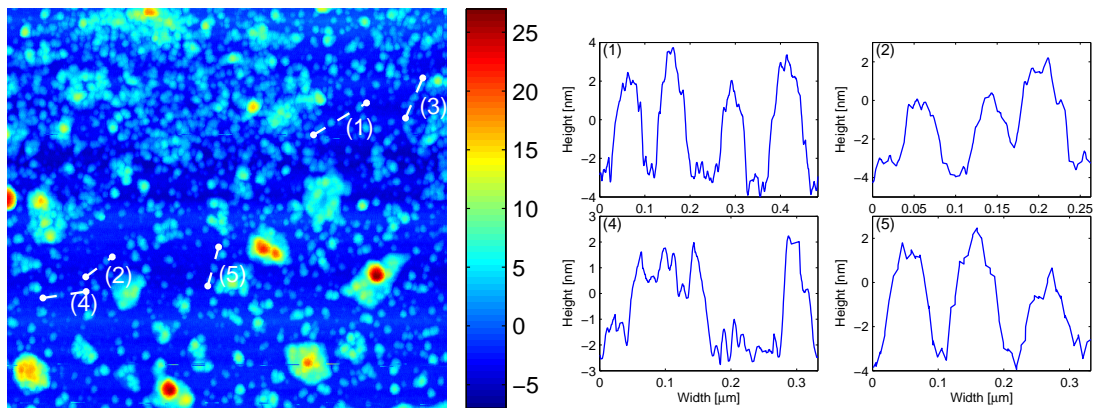


Figure 4.7.12: YBCO Islands on Si substrate. Left: Image is  $3.3 \times 3.3 \mu\text{m}$ . Color scale is in nm. The dashed lines are the cuts used for the cross sections on the right. Right: Cross sections. The number on the individual plot corresponds to the number on the cuts.

A small amount (two tips of small chemistry spoon) of YBCO powder was 'dissolved' into ethanol and subjected to ultrasound for 2 hours to separate particle clusters. Thereafter 3 droplets of the solution were dripped onto the substrate. The solution was clear before ultrasound treat-

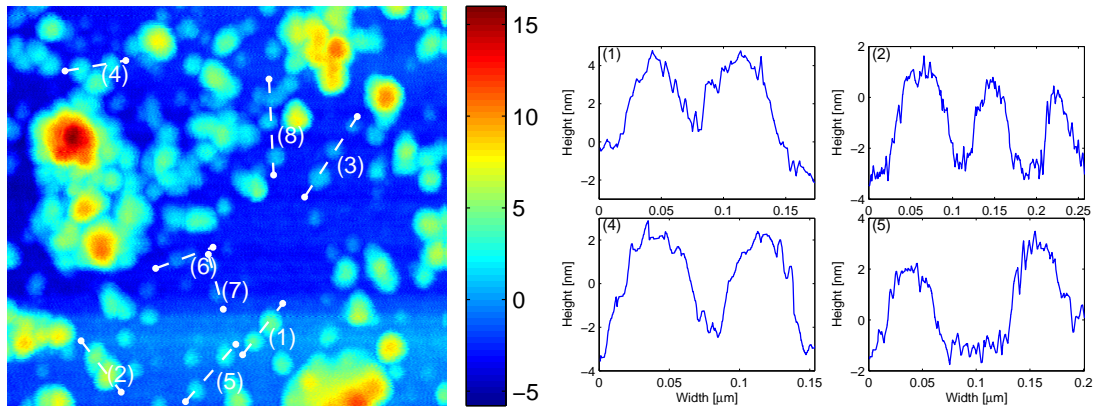


Figure 4.7.13: YBCO Islands on Si substrate. Left: Image is  $1.1 \times 1.1 \mu\text{m}$ . Color scale is in nm. The dashed lines are the cuts used for the cross sections on the right. Right: Cross sections. The number on the individual plot corresponds to the number on the cuts.

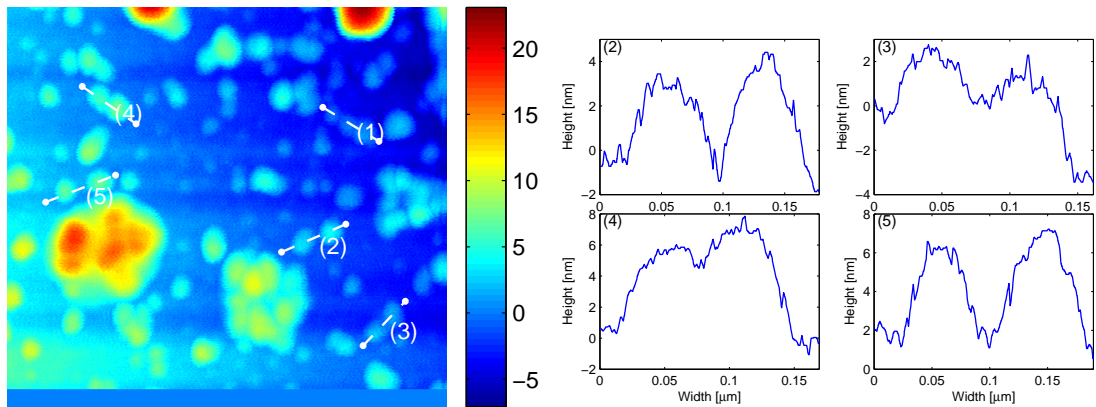


Figure 4.7.14: YBCO Islands on Si substrate. Left: Image is  $1.1 \times 1.1 \mu\text{m}$ . Color scale is in nm. The dashed lines are the cuts used for the cross sections on the right. Right: Cross sections. The number on the individual plot corresponds to the number on the cuts.

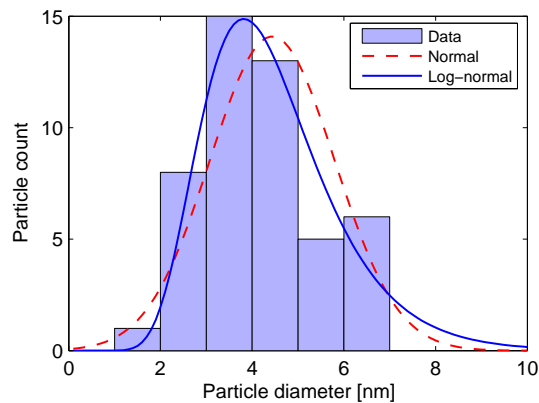


Figure 4.7.15: YBCO nanoparticle thickness distribution extracted from AFM images.

ment, but had changed into opaque black after the treatment, indicating that the particles had

N	Bin size	$\langle d \rangle$	$\sigma(d)$	$\exp[\langle \log d \rangle]$	$\exp[\sigma(\log d)]$	Top-point
48	1.0	4.4	1.4	4.2	1.4	3.8

Table 4.7.3: Thickness distribution data for YBCO nanoparticles. Symbols:  $\langle d \rangle$  is the average particle diameter with standard deviation  $\sigma(d)$ .  $\exp[\sigma(\log d)]$ ,  $\exp[\langle \log d \rangle]$  and Top-point are the average particle size, standard deviation and the top-point in the log-normal distribution.

become well separated.

The measurements were performed as indicated in figures 4.7.12-4.7.14, where suitable particles were selected for a cross section measurement. The criterion for selection of particles, has been that they should be isolated in order to ensure a correct measurement. The particle thickness was then read directly from the cross section, and the thickness distribution in figure 4.7.15 and table 4.7.3 was compiled.

In figure 4.7.15 both a Gaussian and a log-normal distribution are drawn in for comparison. However, as the extracted distribution matches both equally I have chosen to assume that the data are following a Gaussian distribution, giving that the average thickness of the YBCO nanoparticles is 4.4(1.4) nm.

#### 4.7.5 Particle Shape from Neutron Diffraction

Without further introduction I will here present results on the particle shape as derived from the neutron scattering analysis in section 5.1.

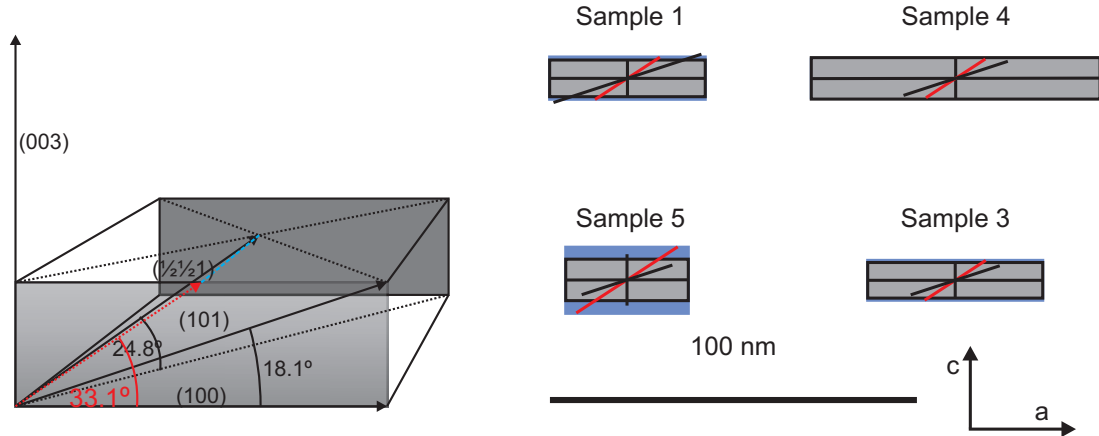


Figure 4.7.16: Left: Schematic of the reciprocal YBCO unit cell, with selected reflections. The red arrow is the projection of the  $(\frac{1}{2} \frac{1}{2} 1)$  reflection onto the  $a, c$  plane. Right: Illustration of the extracted particle dimensions. Solid lines are structural reflections, and the red lines are magnetic reflections projections onto the  $a, c$  plane. A unit cell of  $a = b = 3.84 \text{ \AA}^{-1}$ ,  $c = 11.77 \text{ \AA}^{-1}$  has been used in the calculations.

To elucidate the shape of the particles as found by the neutron diffraction, I have used the Scherrer formula (4.1.4) produced a table (table 4.7.17) of the particle dimensions in the direction of the scattering vectors as seen by the neutrons. The instrumental broadening has been unfolded using

$$\Delta q_s = \left( \Delta q^2 - \Delta q_i^2 \right)^{1/2}, \quad (4.7.1)$$

where  $\Delta q_s$  is the peak broadening originating from particles size,  $\Delta q$  is the measured peak width and  $\Delta q_i$  is the instrumental peak broadening.

Sample	$D(003)$ nm	$D(100)$ nm	$D(101)$ nm	$D(\frac{1}{2}\frac{1}{2}1)$ nm	$H_M(\frac{1}{2}\frac{1}{2}1)$ nm
Sample 1 ( $x=0.20$ ) <sup>‡</sup>	10(2.0)	42.4(8)	21.0(3)	27.5(7)	11.5(3)
Sample 4 ( $x=0.25$ )	11.33(5)	78.7(8)	29.88(16)	25.2(7)	10.6(3)
Sample 5 ( $x=0.30$ )	13.95(18)	33.39(18)	25.95(16)	43(3)	18(1.4)
Sample 3 ( $x=0.35$ )	9.74(6)	47.7(4)	25.19(17)	26(4)	11(1.8)

Figure 4.7.17: Particle width in different directions, calculated from the Scherrer formula.  $D(hkl)$  is the particle size in the  $(hkl)$  direction and  $H_M(\frac{1}{2}\frac{1}{2}1)$  is particle thickness calculated from  $DH_M(\frac{1}{2}\frac{1}{2}1)$ . Symbols: (‡)  $\Delta W(003)$  and therefore  $\Delta D(003)$  are estimated.

A summary of the results is that  $D(003)$  is in most cases small, compared to  $D(100)$  and  $D(101)$  and  $D(100)$  is always largest indicating disc shaped particle.  $D(101)$  has in most cases a value in between the other two, which also is to be expected.

It is noteworthy that the magnetic particle distance  $D(\frac{1}{2}\frac{1}{2}1)$ , and the derived magnetic particle thickness  $H_M(\frac{1}{2}\frac{1}{2}1)$  for Sample 5 ( $x=0.30$ ) are larger than the physical thickness of the particles. This can, however, be explained by magnetic correlations between particles [54], caused by stacking of particles at the  $c$ -axis face.

## 4.8 CoO Nanoparticle Preparation

For the study of CoO several samples with different sizes, listed in table 4.8.1, were produced and characterized. The nano-sized samples have been manufactured using ballmilling and through annealing. Preferably I would have liked to have all samples manufactured using the same method, but this was not possible as the different techniques give different particle sizes. Annealing tends to give increasing particle size with annealing time, whereas ballmilling tends to give very small particles. The samples have therefore been manufactured through the two techniques, which are both described in Frandsen *et al.* (2004) [55].

Description	Size (XRD) nm	Size (ND) nm	Size (TEM) nm	Man. Method
Bulk	-	169(5)	-	Commercial (Alfa, 99.999%).
30 nm sample	29.9(5)	20.05(14)	-	Ann. from CoAT, 44 hours.
20 nm sample	19.3(8)	12.87(11)	-	Ann. from CoAT, 2 and 3 hours, mix.
10 nm sample	11.2(2)	7.89(7)	11(4) / 10(1) <sup>‡</sup>	Ballmilling, Co and Co <sub>3</sub> O <sub>4</sub> , 115 hours.

Table 4.8.1: Overview of the investigated CoO samples. The particle sizes are extracted from the Lorentzian width of on Voigtian fits to XRD and neutron diffraction (ND) data using the Scherrer formula. The neutron data are from section 6. (‡) These values are extracted using Gaussian and log-normal distributions, respectively.

### Ballmilling

The ballmilling technique is quite simple, as it consists of mixing stoichiometric 1:1 amounts of Co and Co<sub>3</sub>O<sub>4</sub>, and ballmilling this in argon atmosphere for  $\sim 160$  hours (in our case 158 hours for the 10 nm sample).

### Annealing

The larger nanoparticle samples have been produced through annealing of cobalt-acetate (CoAT). The manufacturing starts by distributing a homogenous layer of CoAT (Cobalt(II)acetate-4-hydrate, (CH<sub>3</sub>COO)<sub>2</sub>Co·4H<sub>2</sub>O, >99%, Merck), in crucibles. The homogenous distribution is achieved by dispersing CoAT powder in ethanol ( $\sim 5.0$  g in 50 ml), and pouring the solution into

the crucibles, where the CoAT will precipitate. The ethanol is removed by evaporation in a furnace at  $\sim 100^\circ\text{C}$ .

After drying, the crucibles are mounted in another furnace, where the samples are annealed in argon atmosphere. The particle size depends on annealing time and temperature, *e.g.* the 20 nm sample was annealed at  $325^\circ\text{C}$  for 2 and 3 hours (two batches), and the 30 nm sample was annealed at  $325^\circ\text{C}$  for 44 hours.

## 4.9 CoO Sample Characterization

### 4.9.1 XRD Size Determination

I have used XRD to investigate the size of the manufactured samples. Most measurements were performed at the Chemical Institute, DTU<sup>7</sup>, on a commercial  $\theta$ - $\theta$  setup (horizontal axis), with Cu K- $\alpha$  (containing K- $\alpha$ 1 and K- $\alpha$ 2) radiation. The apparatus is built such that the slit settings are adjusted automatically with scattering angle to reduce small angle scattering. However, some measurements were performed at Risø at the apparatus described in section 4.7.1.

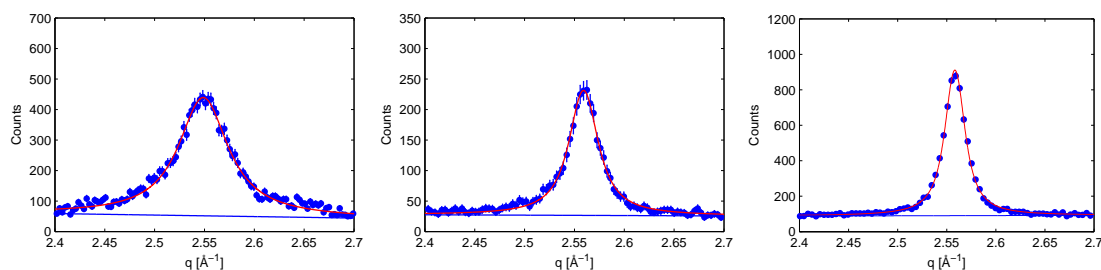


Figure 4.9.1: *CoO* (111) reflections for nanosized samples, measured with XRD, fitted with Voigtians. Notice how the peak width changes according to particle size. Left: 10 nm Center: 20 nm Right: 30 nm.

In the analysis presented, the K- $\alpha$  double line issue is ignored as the Bragg peaks are too broad to distinguish these. However, in the determination of the DTU apparatus resolution (made from  $\text{Al}_2\text{O}_3$ ) the double peaks are well separated, and can hardly be treated as one. Still, I have fitted the double peak with one Voigtian, to facilitate the direct subtraction of instrumental broadening from the sample diffraction peaks.

The extraction of particle size is as in section 4.7.5 done using the Scherrer formula (4.1.6), where I have used the  $K=0.94$ . To be certain of obtaining the size in the magnetic ( $\frac{1}{2}\frac{1}{2}\frac{1}{2}$ ) direction, which is the focus of investigation in chapter 6, I chose to fit the parallel (111) peak. The resulting fitted XRD peaks, which clearly show changes in peak width and thus particle size, are presented in figure 4.9.1.

The XRD analysis also showed that the 30 nm and 20 nm samples contained no impurity peaks. However, the XRD analysis of the 10 nm ballmilled sample, shown in figure 4.9.2, revealed that it contained significant amounts of  $\text{Co}_3\text{O}_4$ . Detailed analysis showed that the sample in weight consisted of  $\sim 91\%$  CoO and  $\sim 9\%$   $\text{Co}_3\text{O}_4$ .

### 4.9.2 TEM Size Measurements

TEM images were obtained in a JEM3000F. Powder was dispersed on standard TEM copper grids with amorphous carbon film, before being inserted into the TEM. The size measurements were performed directly on the images. Observing that most particles have round shapes I have assumed the round shape and fitted all particles with circles. The circle diameter was then taken as the particle size. A TEM image example showing particles is presented in figure 4.9.4. The result

<sup>7</sup>Technical University of Denmark (DTU)

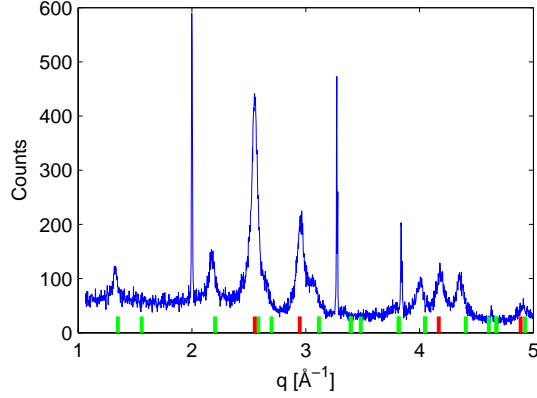


Figure 4.9.2: Raw diffraction pattern in reciprocal space of the CoO 10 nm sample. The red and green lines at the bottom, marks the position of the CoO and Co<sub>3</sub>O<sub>4</sub> reflections, respectively. The narrow reflections are bulk Si peaks used for determination of instrumental resolution.

of the size distribution measurements is presented in figure 4.9.3 and table 4.9.1. An analysis of the particle sizes reveals that the size distribution matches a log-normal distribution well. Unfortunately, it was not possible, due to lack of time and partly due radiation safety issues to get TEM images of other samples than the 10 nm within the time frame of this thesis.

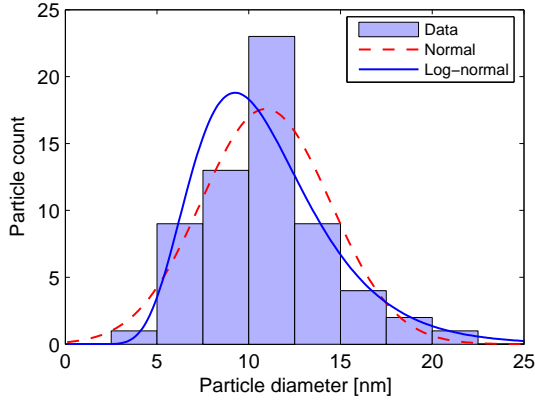


Figure 4.9.3: 10 nm sample measured particle size distribution. The log-normal distribution is calculated from the data, and matches well. The Gaussian distribution is only shown for comparison.

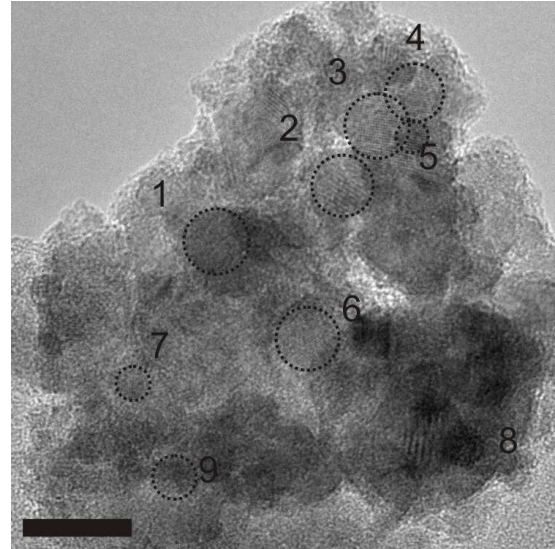


Figure 4.9.4: Example of cluster of particles with measured particles marked. The bar in the lower left is 20 nm.

N	Bin size	$\langle d \rangle$	$\sigma(d)$	$\exp[\langle \log d \rangle]$	$\exp[\sigma(\log d)]$	Top-Point
62	2.5	10.9	3.5	10.4	1.4	9.3

Table 4.9.1: Size distribution data for the 10 nm sample measured using TEM.  $d$  is particle diameter.

### 4.9.3 Magnetic Susceptibility

To investigate the macroscopic magnetic properties of the 10 nm sample it was characterized with magnetic AC susceptibility.

As shown in figure 4.9.5, there is at  $T_N$  ( $\approx 289$  K) no apparent change in  $M'$ . However, around 270 K there is a small change in the slope of  $M''$ , which might indicate a broad phase transition. Differentiating the magnetizations  $dM'/dT$  and  $dM''/dT$ , clearly shows a phase transition feature around 295 K in the  $dM'/dT$  data. It is however too weak and broad, to allow us to determine even  $T_N$  with a reasonable accuracy.

The dominant signal in the dataset, indicating a phase transition is at  $\sim 40$  K, and is most likely an indication of the Néel temperature of the  $\text{Co}_3\text{O}_4$ .  $T_N$  of  $\text{Co}_3\text{O}_4$  is in literature reported as being 30 K [41], 33 K [67] and 40 K [69, 160], of which 40 K is the classic value.

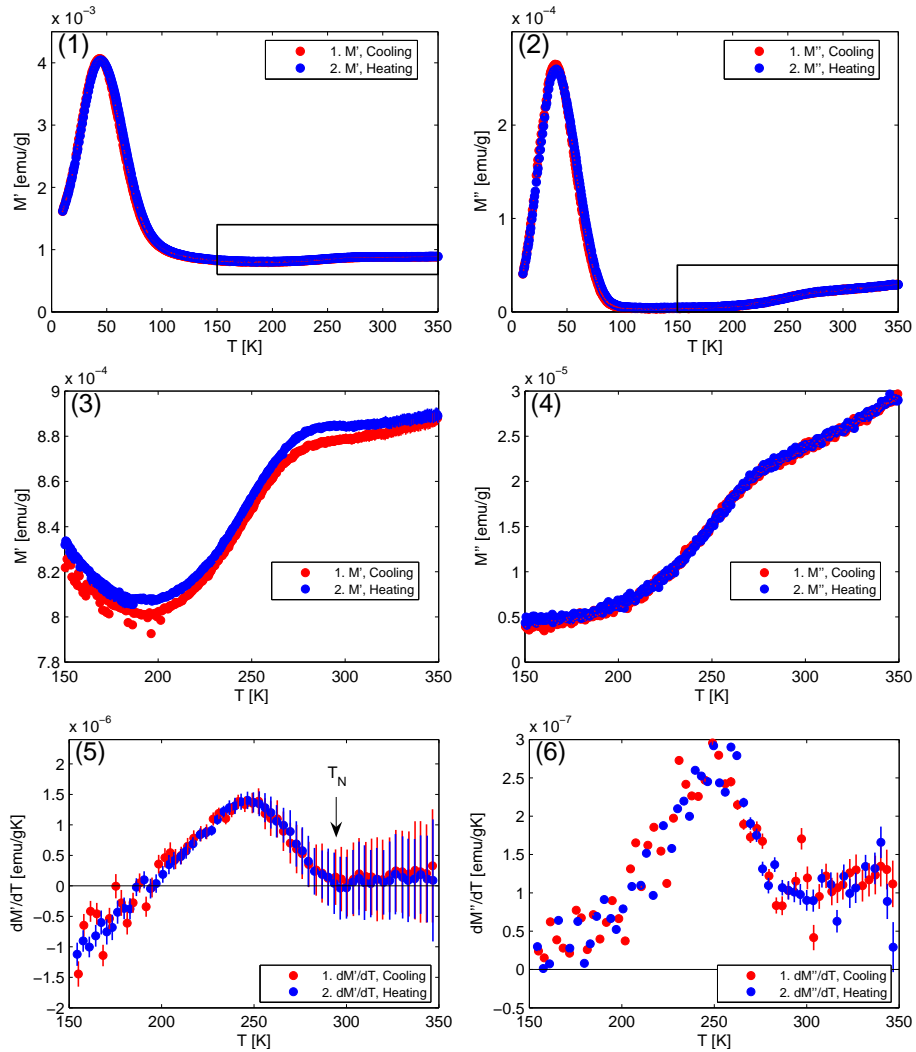


Figure 4.9.5: AC susceptibility data for  $\text{CoO}$  10 nm sample. There are indication of the  $\text{CoO}$   $T_N$  at  $\sim 270$  K in  $M'$  and at  $\sim 295$  K in  $dM'/dT$ . The strong signal at  $\sim 40$  K is likely due to  $\text{Co}_3\text{O}_4$ . (1) Real part susceptibility  $M'$ , 0-350 K. (2) Imaginary part susceptibility  $M''$ , 0-350 K. (3) Real part susceptibility  $M'$ , 150-350 K. (4) Imaginary part susceptibility  $M''$ , 150-350 K. (5) Differentiated real part susceptibility  $dM'/dT$ , 150-350 K. The arrow marks the Néel temperature. (6) Differentiated imaginary susceptibility  $dM''/dT$ , 150-350 K. The boxes in (1) and (2) show the temperature regions magnified in (3) and (4), respectively.

As we from the 10 nm sample could not retrieve information relevant for the studies of critical phenomena, as well as we due to radiation issues<sup>8</sup> were unable to measure susceptibility on the bulk and 20 nm samples, I did not pursue the use of magnetic susceptibility measurements on CoO.

---

<sup>8</sup>The 20 nm and bulk sample had both been inside a neutron beam and had become radioactive, before this project was commenced. Susceptibility measurements on radioactive material – and in particular nanoparticles – was considered too dangerous.



# Chapter 5

## Nano-sized YBCO particles

In this chapter I will analyze the neutron scattering and  $\mu$ SR data obtained on the nanosized YBCO particles. Although the focus is on the results of analysis, and on the discussion of these results, I will also discuss details and considerations concerning the technical side of the analysis.

The outline of this chapter is that section 5.1 contains the neutron diffraction analysis and section 5.2 contains the analysis of the  $\mu$ SR measurements. Each of these sections contains at the end a summarizing discussion, acting as a stepping stone to the conclusion.

In the conclusion, section 5.3, first a comparative discussion of the results from neutron scattering and  $\mu$ SR will be presented, before I will proceed to discuss outlook and perspectives.

### 5.1 Neutron Scattering Data Analysis

The investigations of the magnetic order in YBCO nanoparticles have been done using the RITA-2 instrument, described in section 3.2.5, as a powder diffractometer with energy analysis/selection. Throughout the analysis the flexible Spec1d package [116] for MatLab, for which one can build custom fitting models, has been used as fitting 'machine'.

An overview of the samples studied by neutron scattering are presented in table 5.1.1 and an example of a typical neutron diffraction dataset of nanosized YBCO is presented in figure 5.1.1.

Sample	Oxygen doping $x$	Hole doping $p$	$T_{min}$ K	$T_{max}$ K
Sample 1	$0.20 \pm 0.025$	0.010(2)	8	450
Sample 4	$0.25 \pm 0.025$	0.017(7)	8	300
Sample 5	$0.30 \pm 0.025$	0.044(12)	8	300
Sample 3	$0.35 \pm 0.025$	0.055(6)	8	200
Sample 5 bulk	$0.30 \pm 0.025$	0.044(12)	6	425

Table 5.1.1: *An overview of the neutron scattering measurements performed on  $YBa_2Cu_3O_{6+x}$  (YBCO) nanoparticle and bulk samples (the bulk sample is marked).  $T_{min}$  and  $T_{max}$  indicate the minimum and maximum temperatures during the measurements respectively.*

Prior to the neutron measurements, it was considered which magnetic reflection it would be most feasible to focus on. Tranquada *et al.* (1988) [187, 188] have studied the magnetic structure in YBCO, and determined that the  $(\frac{1}{2}\frac{1}{2}1)$  and  $(\frac{1}{2}\frac{1}{2}2)$  (at  $q \simeq 1.27 \text{ \AA}^{-1}$  and  $q \simeq 1.57 \text{ \AA}^{-1}$ , respectively), are the strongest magnetic reflections (table 5.1.2). Of these the  $(\frac{1}{2}\frac{1}{2}2)$  reflection is stronger by about 35 % [188].

To summarize information on the structural and magnetic reflections of YBCO,  $q$ -values and structure factors for structural and magnetic reflections, for selected reflections and dopings in the

$hkl$	$q(x=0.15)$	$q(x=0.31)$	$q(x=0.34)$	$F^2(x=0.29)$	$I(x=0.15)$	$m$	type
(001)	0.5317	0.5329	0.5327	213.55	-	2	struc.
(002)	1.0634	1.0658	1.0655	12.01	-	2	struc.
$(\frac{1}{2}\frac{1}{2}0)$	1.1511	1.1511	1.1495	$0.00\pm 0.96\ddagger$	$0\pm 100\ddagger$	4	magn.
$(\frac{1}{2}\frac{1}{2}1)$	1.2680	1.2685	1.2670	$12.47\pm 0.67\ddagger$	$1300\pm 70\ddagger$	8	magn.
$(\frac{1}{2}\frac{1}{2}2)$	1.5671	1.5688	1.5674	$16.88\pm 1.06\ddagger$	$1760\pm 110\ddagger$	8	magn.
(003)	1.5951	1.5988	1.5982	79.48	-	2	struc.
(100)	1.6279	1.6279	1.6257	249.14	-	4	struc.
(101)	1.7125	1.7129	1.7107	51.65	-	8	struc.
(102)	1.9444	1.9457	1.9437	0.12	-	8	struc.
$(\frac{1}{2}\frac{1}{2}3)$	1.9671	1.9700	1.9687	$2.01\pm 0.77\ddagger$	$210\pm 80\ddagger$	8	magn.
(004)	2.1268	2.1317	2.1310	657.78	-	2	struc.
(103)	2.2791	2.2817	2.2797	548.48	-	8	struc.
(110)	2.3022	2.3021	2.2990	590.34	-	4	struc.
(111)	2.3628	2.3630	2.3600	175.24	-	8	struc.
$(\frac{1}{2}\frac{1}{2}4)$	2.4183	2.4226	2.4213	$0.86\pm 1.06$	$90\pm 110\ddagger$	8	magn.
(112)	2.5359	2.5369	2.5339	1.04	-	8	struc.
$(\frac{3}{2}\frac{1}{2}0)$	2.5739	2.5739	2.5704	-	-	8	magn.

Table 5.1.2: Table of YBCO structural and magnetic reflections generated from lattice parameters for dopings  $x=\{0.15, 0.31, 0.34\}$ , found in ref. [188]. The values are for room temperature. The values for  $F^2$  have been generated using Crystallographica from ref. [208] and the  $I$  (intensity) values are from ref. [188]. type indicates whether the reflection is structural or magnetic. Symbols: (†) The magnetic  $F^2$  values are measured powder values for  $x=0.15$  from ref. [188]. (‡) Normalized values calculated from the measured.

AFM region are listed in table 5.1.2. From the table it is seen that the structural diffraction peaks from YBCO generally are much stronger than the magnetic peaks.

The Scherrer formula (4.1.6), along with the results from the characterization, predicts that the neutron diffraction peaks from the nanosized particles will be broad, and in some cases overlapping.

Combined, these two observations predict the possibility of having a weak magnetic peak as a shoulder on a strong structural peak, which is difficult to fit. Therefore the magnetic peak chosen as focus of my studies, should be as isolated from structural peaks as possible.

From previous studies [146, 148] and my sample characterization (sections 4.7.3 and 4.7.4), the particles are found to be disc-shaped with the smallest size along the  $c$ -axis. Therefore the strong (003) peak is expected to be broad, (which is confirmed in figure 5.1.1), causing the  $(\frac{1}{2}\frac{1}{2}2)$  to become only a shoulder on the (003) peak.

From the above considerations, the data in table 5.1.2, and by making preliminary measurements similar to those in figure 5.1.1, I chose to focus my studies on the  $(\frac{1}{2}\frac{1}{2}1)$  reflection, as it is isolated, and would therefore give the clearest magnetic signal. It is a bit weaker than  $(\frac{1}{2}\frac{1}{2}2)$ , but this disadvantage is far outweighed by the fact that it is isolated. I will henceforth only refer to the  $(\frac{1}{2}\frac{1}{2}1)$  magnetic peak as *the magnetic peak*.

### 5.1.1 Calibration of Magnetic Scattering Intensity

In contrast to other techniques, which yield an absolute value for the microscopic magnetic field (such as for instance Mössbauer spectroscopy and  $\mu$ SR), neutron scattering is a relative measurement method, which can probe the staggered magnetism of the sublattices in an antiferromagnet.

The neutron data depend on several macroscopic experimental factors besides the physical properties of the sample. Comparisons of measurements on different samples or even different measurements on the same sample, have therefore to take in to account differences in the experimental setup.

When doing triple axis measurements on powder samples, factors affecting the measurement

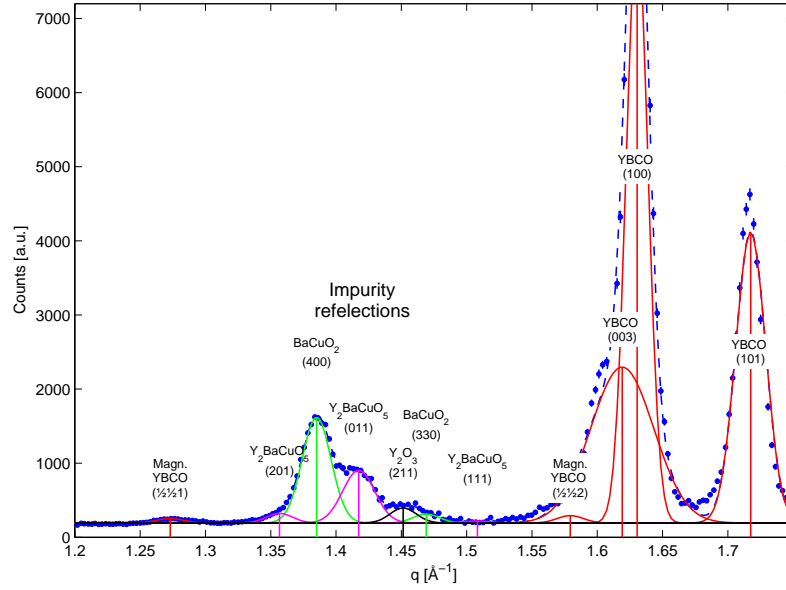


Figure 5.1.1: *Example of neutron diffraction pattern for nanosized YBCO ( $x=0.25$ ) at 100 K. Solid lines are individual peaks and dashed line is the sum of all fitting model components. Note the positions of the magnetic  $(\frac{1}{2}\frac{1}{2}1)$  and  $(\frac{1}{2}\frac{1}{2}2)$  reflections relative to the surrounding peaks, and the widths of the surrounding peaks, in particular the  $(\frac{1}{2}\frac{1}{2}2)$  position relative to the (003) position and width.*

could be the packing of powder, sample container dimensions and differences in instrument settings (in particular slit settings), sample position and detector window settings. Experience shows, that even experimental setups thought to be identical, yield differences in the data. Therefore normalization of the data is crucial in order to compare measurements. This normalization is done by using a structural peak for internal reference.

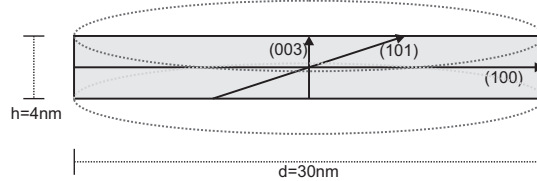


Figure 5.1.2: *Schematic illustration of a typical disc-shaped YBCO particle, showing the calculated scattering thickness (giving the peak width), for the reflections (003), (100) and (101). The gray area is the a-c cross section of a particle.*

Simple structure factor considerations based on structural data from ref. [208] show that several reflections are sensitive to the oxygen content. However, to elucidate further on this calculations have been made on the structure factors of selected YBCO reflections versus doping  $x$  in the doping range where we were planning to measure. These are presented in table 5.1.3 and in figure 5.1.3. From the calculations we see that the reflections (100), (101) and (102) are not changed by doping, whereas all the reflections with non-zero values of at least both the  $a$  and  $b$  axis, or just the  $c$  axis change with doping.

#	$x$	1 (001)	2 (002)	3 (003)	4 (100)	5 (101)	6 (102)	7 (004)	8 (103)	9 (110)	10 (111)	11 (112)
1	0.150	237.8	7.2	66.5	249.1	51.6	0.1	695.4	548.5	625.4	194.4	0.1
2	0.175	233.3	7.9	68.7	249.1	51.6	0.1	688.6	548.5	619.1	190.9	0.2
3	0.200	229.0	8.8	71.0	249.1	51.6	0.1	681.8	548.5	612.8	187.5	0.3
4	0.225	224.6	9.6	73.3	249.1	51.6	0.1	675.1	548.5	606.5	184.0	0.5
5	0.250	220.3	10.5	75.7	249.1	51.6	0.1	668.4	548.5	600.3	180.6	0.7
6	0.275	216.1	11.4	78.0	249.1	51.6	0.1	661.8	548.5	594.0	177.3	0.9
7	0.290	213.5	12.0	79.5	249.1	51.6	0.1	657.8	548.5	590.3	175.2	1.0
8	0.300	211.9	12.4	80.5	249.1	51.6	0.1	655.1	548.5	587.9	173.9	1.1
9	0.325	207.7	13.4	82.9	249.1	51.6	0.1	648.5	548.5	581.7	170.6	1.4
10	0.350	203.6	14.5	85.4	249.1	51.6	0.1	642.0	548.5	575.6	167.3	1.7
11	0.375	199.5	15.6	87.9	249.1	51.6	0.1	635.5	548.5	569.5	164.1	2.1
12	0.400	195.4	16.7	90.5	249.1	51.6	0.1	629.0	548.5	563.5	160.9	2.4

Table 5.1.3: Calculated structure factors for selected reflections versus doping. The values have been calculated using *Crystallographica* and using values from ref. [208]. Tetragonal cell structure and a isotropic displacement parameter have been assumed. A graphic illustration of these data is provided in figure 5.1.3.

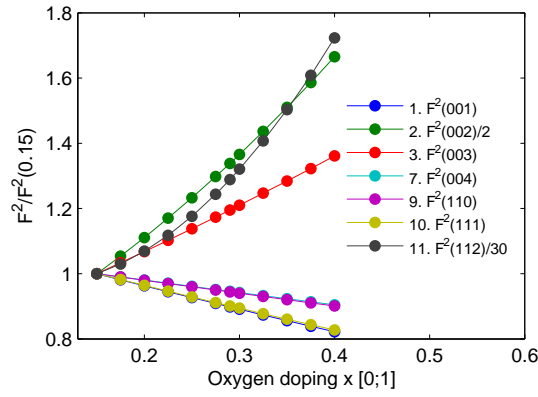


Figure 5.1.3: Calculated YBCO crystal structure factors, normalized to the  $x=0.15$  value. The absolute values are shown in table 5.1.3.

Although both the (003) and (100) peaks are strong (and (100) should be narrow), these peaks are not used as reference. The primary reason is that the (003) peak is very broad, and the second is that they overlap with each other and are therefore difficult to fit. Lastly, as seen from table 5.1.3 and figure 5.1.3, the structure factor of (003) varies with oxygen doping, making it unsuitable for intensity normalization across samples with different dopings. In contrast to these, the (101) peak, although weaker, is isolated and does not vary with oxygen doping, making it the better choice. Furthermore it is expected to always be relatively narrow, as the particles are relatively large along the (101) direction, as illustrated in figure 5.1.2. Conclusively, the (101) peak has been used for inter-sample intensity normalization.

Neutron diffraction measurements in the full temperature range (8-450 K) at RITA-2 has usually been performed using the dispex DIS-E (range 7-325 K [196]) and the furnace CTI-4 (range 30-475 K [196]). Unfortunately these two sample environments do not have the same neutron transparency, and the obtained neutron counts are therefore different. This is corrected through cross-normalizing using one of the large structural peaks (*e.g.* the  $\text{BaCuO}_2$  (400) peak at  $\sim 1.38\text{\AA}^{-1}$  in Sample 1 ( $x=0.20$ )) which is present in two spectra, obtained at the same temperature in the

two sample environments.

### 5.1.2 Analyzer Blade Normalization

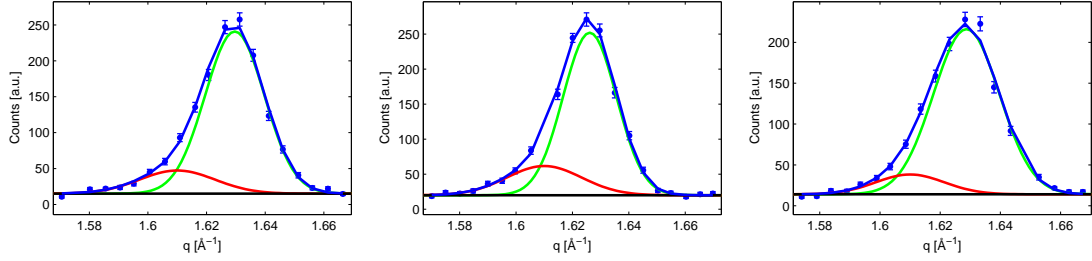


Figure 5.1.4: Examples of fitted blade calibration spectra, here Sample 1 ( $x=0.20$ ). Blue is total fit. Red is (003) Gaussian. Green is (100) Gaussian. Left: Blade 2. Center: Blade 5. Right: Blade 8.

	Blade no.						
Sample	2	3	4	5	6	7	8
Sample 1 ( $x=0.20$ ) (DIS-E)	0.1540	0.1304	0.1549	0.1571	0.1357	0.1255	0.1424
Sample 1 ( $x=0.20$ ) (CTI-4)	0.1406	0.1400	0.1559	0.1544	0.1419	0.1289	0.1384
Sample 4 ( $x=0.25$ ) (DIS-E)	0.1643	0.1316	0.1455	0.1460	0.1360	0.1467	0.1298

Table 5.1.4: Examples of blade normalization factors obtained in measurements. The factors are relative and normalized such that the sum is 1. The first column contains the sample and sample environments (DIS-E and CTI-4) of the measurement.

When measuring in monochromatic imaging mode, the analyzer blades scatter onto different regions of the PSD, as discussed in sections 3.2.5 and 3.2.6. As normalization peaks I have chosen the (003) and (100) peaks. For each blade the peaks are fitted with two Gaussians, and the summed integrated intensity is extracted, yielding the effective reflectivity of the individual blades. The obtained reflectivities are then divided with the summed integrated intensity, yielding the blade normalization factors, the sum of which is normalized to unity.

An example of three fitted blade spectra is plotted in figure 5.1.2, along with some of the found blade normalization factors in table 5.1.4.

### 5.1.3 Discussion of Line Shapes

The result of the size distribution investigations in refs. [146, 148], and of the results from section 4.7.3, show that the particle diameter distribution of the disc-shaped particles is close to log-normal, with some very small and some very large particles. The thickness distribution of the particles is from refs. [146, 148] and from the characterization in section 4.7.4 found to be close-to Gaussian or a narrow log-normal.

Using a simple approach the above information on the particle size distribution is utilized to make the following considerations. The large particle contribution gives rise to a narrow peak and the small particle contribution gives a broad peak. The resulting line shape from the size distribution actually found is therefore likely to be close to Gaussian albeit with small Lorentzian tails, which convoluted with the near-Gaussian instrument broadening, will result in a close-Gaussian Voigt shape.

When fitting data with a model it is of the essence to keep the number of free parameters as small as possible, without compromising the validity of the model. If there are too many parameters, the fitting mechanism will utilize all the free parameters to get as good a fit as

possible, and might in some cases give non-physical parameter values. The case at hand is such a case – the Lorentzian contribution to the line shape is small, but the Lorentz component of the line shape might be used by the fitting mechanism to account for noise, or features in the background, just to minimize the  $\chi^2$ . On the other hand, there are cases where a simple Gaussian is insufficient to account for the line shape and the Lorentzian contribution is important. Also it is important to realize that with a growing number of parameters, the interpretation of the fitting result also might become difficult and ambiguous.

There is therefore no simple answer as to which line shape is the right one to use. It is a matter of estimate and/or test for each sample, for each reflection, and in some cases for each temperature – and then sanity checks for physical consistency.

### 5.1.4 Simulation of Line Shapes

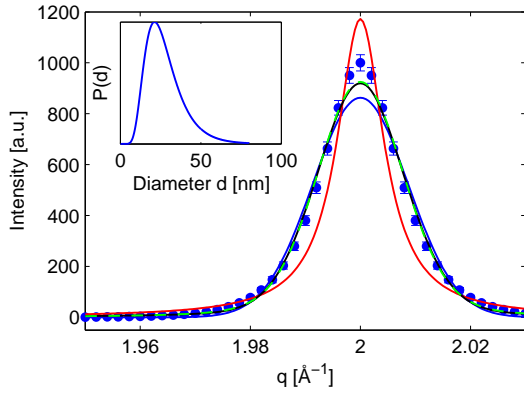


Figure 5.1.5: The simulated line shape in the (100) direction resulting from a log-normal diameter distribution. Blue is the Gaussian fit, red is the Lorentzian fit, black is the Pseudo-Voigt fit and dashed green is the Voigt fit. Inset: The measured diameter distribution. The fit values are found in table 5.1.5.

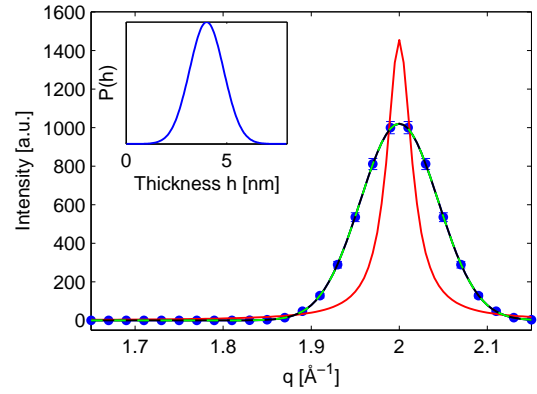


Figure 5.1.6: The simulated line shape resulting from a Gaussian thickness distribution. Blue is the Gaussian fit, red is the Lorentzian fit, black is the Pseudo-Voigt fit and dashed green is the Voigt fit. The Gauss, Pseudo-Voigt and Voigt are nearly coinciding. Inset: The measured thickness distribution. The fit values are found in table 5.1.6.

Line shape	$I_0$ $10^2$	$W$ FWHM	$\eta$	$W_G$ FWHM	$W_L$ FWHM	$\chi^2$
Gauss	8.6(12)	0.02042(18)				7.154
Lorentz	11.7(2)	0.010(16)				25.723
Pseudo-Voigt	9.2(13)	0.019(2)	0.2(13)			2.994
Voigt	11.2(3)			0.017(3)	0.004(3)	2.435

Table 5.1.5: Results of fits to the simulated (100)-line shape.  $I_0$  is the peak amplitude,  $W$  is the FWHM peak width,  $\eta$  is the Pseudo-Voigt scaling factor and  $W_G$  and  $W_L$  are the Voigt Gaussian and Lorentzian FWHM widths. The last column is the  $\chi^2$  value of the fit. Empty spaces indicate non-applicable parameter values.

To elucidate further on the line shape resulting from a size distribution, I have simulated the line shape which emerges from the YBCO size distributions, from the data that I have on the particle shape and size distribution. The line shapes for the (100) and (003) direction, respectively,

Line shape	$I_0$ $10^3$	$W$ FWHM	$\eta$	$W_G$ FWHM	$W_L$ FWHM	$\chi^2$
Gauss	1.020(17)	0.1043(11)				0.021
Lorentz	1.45(5)	0.034(9)				87.150
Pseudo-Voigt	1.021(18)	0.10(12)	0.002(7)			0.017
Voigt	1.02(2)			0.10(14)	0.0003(8)	0.015

Table 5.1.6: Results of fit to simulated (003)-line shape.  $I_0$  is the peak amplitude,  $W$  is the FWHM peak width,  $\eta$  is the Pseudo-Voigt scaling factor and  $W_G$  and  $W_L$  are the Voigt Gaussian and Lorentzian FWHM widths. The last column is the  $\chi^2$  value of the fit. Empty spaces indicate non-applicable parameter values.

are in the simulation given as

$$I_{(100)}(q) = \sum_{d=0}^{\infty} d^2 \cdot P_{(100)}(d)G\left(q, \frac{2\pi K}{d}\right), \quad (5.1.1)$$

$$I_{(003)}(q) = \sum_{h=0}^{\infty} h \cdot P_{(003)}(h)G\left(q, \frac{2\pi K}{h}\right), \quad (5.1.2)$$

where  $P_{(100)}$  as demonstrated in section 4.7.3 is log-normal and  $P_{(003)}$  as it is close-to Gaussian for simplicity is assumed to be Gaussian. Each size is assumed to give rise to a Gaussian contribution  $G(W)$ , where  $W_{(100)} = \frac{2\pi K}{d}$ ,  $W_{(003)} = \frac{2\pi K}{h}$  ( $K=0.94$ ) are the widths found from the Scherrer formula. The values in the distribution functions for  $P_{(100)}$  are those in table 4.7.9, and an estimated mean of 4 nm, with a FWHM of 2 nm is used for  $P_{(003)}$ . The factors  $d^2$  and  $h$  (diameter and height) in (5.1.1)-(5.1.2) are volume weights for the particle sizes.

The result of the calculations is that in the (100) direction the resulting line shape is Voigtian (figure 5.1.5 and table 5.1.5). However in the (003) direction the resulting line shape is close to Gaussian (figure 5.1.6 and table 5.1.6). One could follow the path of using the above line shape, composed from a log-normal distribution. However, this line shape only applies to the (100) direction. Simple considerations of the scattering vector orientations and the particles dimensions, *e.g.* using the directions drawn in figure 5.1.2, yield that the line shape for (101) and more importantly  $(\frac{1}{2}\frac{1}{2}1)$  is the same as that of (003), as the particle height is the limiting factor.

As a starting point, I do therefore not have to take into account any special considerations regarding choice of line shape when fitting the magnetic peak  $(\frac{1}{2}\frac{1}{2}1)$ . Nor will I use the information on the width of the peak, but instead use an effective width found from the data. In the analysis presented in the following sections, I have used both Gauss and Pseudo-Voigt line shapes.

Ideally a Voigt line shape should be used, but since a satisfactory implementation was not available at the time of analysis, the Pseudo-Voigt was used. When a Voigt implementation became available, I decided not to redo the entire analysis as tests show there to be negligible difference between the Pseudo-Voigt and Voigt when the Lorentzian contribution is small, as seen in *e.g.* figure 3.2.11.

### 5.1.5 Preliminary Analysis

After obtaining the first relatively good scattering results (compared to previous attempts [94]), the results were analyzed and the magnetic peak attempted fitted. It soon became clear that there was an impurity Bragg peak present very close to the magnetic peak, as shown in figure 5.1.7. The impurity was identified as the BaCuO<sub>2</sub> (321) peak at  $q \simeq 1.286 \text{ \AA}^{-1}$  [42, 44, 199] (see tables G.5.6 and G.4.1). BaCuO<sub>2</sub> is a common and well known impurity in YBCO [94, 149].

Throughout the following analysis the crystal structure of YBCO will only be considered to be tetragonal, as the doping level  $x$  is below the T/O transition, only just reaching the border region with the  $x=0.35$  sample. Furthermore the broad peaks would make it very difficult to distinguish for instance the adjacent (101) and (011) orthorhombic reflections.

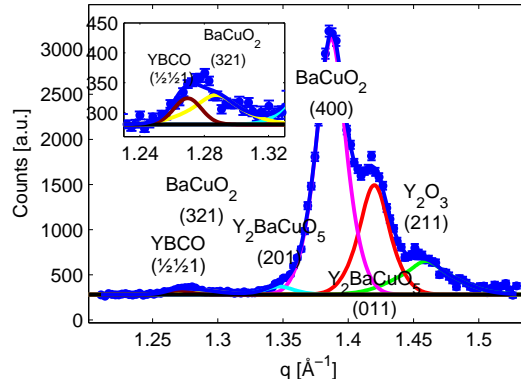


Figure 5.1.7: An example (here Sample 5 ( $x=0.30$ ) at 8K) of the impurity region next to the YBCO ( $\frac{1}{2}\frac{1}{2}1$ ) magnetic peak. Inset: A zoom-in on the region around the magnetic peak.

In the following the two fit approaches which have been applied in the analysis of the neutron scattering measurements data on YBCO nanoparticles, will be presented.

The first, the *Simple Model* (section 5.1.6), uses a simple approach in determining the diffraction peak positions, and the second, the *Advanced Model* or *hkl Model* (section 5.1.8), used a Rietveld-like [4] approach to fit the data.

### 5.1.6 Simple Model Analysis

This model uses a simple approach to determine the peak positions. The focus of the model is to extract the integrated intensity of the magnetic ( $\frac{1}{2}\frac{1}{2}1$ ) peak, and other peaks are fitted only to map the background of the magnetic peak region. The model only makes simple assumptions on the peak positions, in particular impurity peak positions.

Initially, the Gaussian line shape was used to fit the data, but as it was shown to be incapable of fitting the Lorentzian tails of some peaks, a change was made to use the P4-Voigt line shape. The instrumental values of  $W$  and  $\eta$  were found from fitting to an  $\text{Al}_2\text{O}_3$  powder line and are kept constant throughout the analysis.

The fitting procedure applied to every temperature dataset can be described by the 3 following steps.

1. The structural peak positions of YBCO (100) and (101) are found. These are used to calculate the YBCO lattice constants, and hence the magnetic peak position.  
In datasets that do not contain/include the structural peak region, the magnetic peak position is found through extrapolation as described in section 5.1.6.1.
2. To establish a background level for the magnetic peak, the impurity peaks (such as  $\text{BaCuO}_2$  (400)) in the region  $1.35\text{-}1.5 \text{ \AA}^{-1}$  are fitted. All peaks need to be accounted for, as they either by themselves, or via overlaps with the other peaks could influence the shape of the background at the magnetic peak position.
3. The magnetic peak intensity is fitted, using the background found in the step 2, and the position found in the first step.

As mentioned, the magnetic peak ( $\frac{1}{2}\frac{1}{2}1$ ) position is calculated from the (101) and (100) peaks. The (003) peak is not used, as the error on the position of this is large due to the broadness of the peak. The structural peak position fitting in both step 1 and 2 was in many cases an iterative process, manually tweaking the starting values of the fit to obtain valid and trustworthy results. However, in some special cases the (003) and ( $\frac{1}{2}\frac{1}{2}2$ ) peak positions were used as aids for determining the lattice constants.

In some of the measurements, made in an applied/external magnetic field (using the MA-15 15 T magnet (1.6-300 K)), the procedure was a little different from what was described above. Where the structural peaks were available, the magnetic peak position  $q_{hkl}$  was determined from the values found for the structural (100) and (101) peaks, using  $a=b$  in the tetragonal phase as above. However, in the cases where no structural peaks had been recorded, the structural peak positions from zero field measurements were used.

This procedure was followed for each temperature dataset of the samples, and gave nice results, *e.g.* on the magnetic order. The results from the simple analysis model are presented in section 5.1.7.

### 5.1.6.1 Extrapolation of Peak Positions

In datasets where structural peaks are not available, the peak positions are determined by extrapolation, from a model fit, either linear or parabolic, to the temperature development of a structural peak (*e.g.* the  $\text{BaCuO}_2$  (400) peak at  $q \simeq 1.38 \text{ \AA}^{-1}$ ), using the assumption that all lattice expansions are homogeneous (*i.e.*  $\frac{\Delta q(T)}{q_0} = 1/\alpha(T)$  is the same). The linear extrapolation is a valid approximation at high temperature [85], but does not hold at low temperature, where the thermal expansion coefficient  $\alpha(T)$  goes to zero as  $T \rightarrow 0$ , as shown in figure 5.1.8, where it is seen that the expansion becomes linear above  $\sim 100$  K. The low temperature data are therefore extrapolated using an empirical parabolic model  $M(T) = aT^2 + bT + C$ , except for Sample 4 ( $x=0.25$ ) where a linear extrapolation has been used.

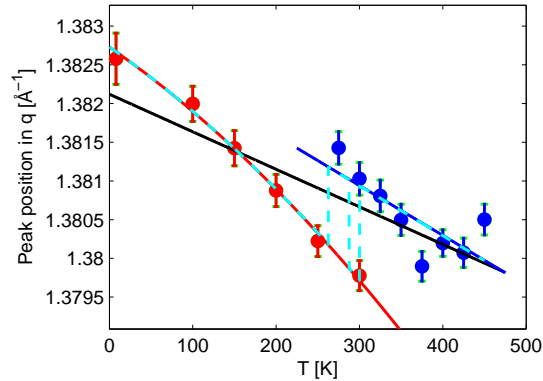


Figure 5.1.8: The measured  $q$  position for the  $\text{BaCuO}_2$  (400) reflection in Sample 1 ( $x=0.20$ ). The red and blue points are measured in the cryostat DIS-E and the furnace CTI-4 respectively. The red line is a parabolic fit to the red points and the blue line is linear fit to the blue points. The dashed cyan line is a function combining the red and blue fits, to match the measured points depending on the sample environment used for this data point. The black line is a linear fit to all measured points, for comparison. The observed difference between the sample environments is most likely due to a small offset in  $2\theta$ .

Having found the coefficients of the extrapolation model through fitting, the extrapolation of the position  $q_{hkl}(T)$  of a particular peak ( $hkl$ ) (including impurity peaks) is done as

$$q_{hkl}(T) = \frac{q_{hkl}(T_0)}{M(T_0)} \cdot M(T), \quad (5.1.3)$$

where  $M(T)$  is the extrapolation model. The extrapolated position is found from the nominal model, and scaled using  $\frac{q_{hkl}(T_0)}{M(T_0)}$ , using the found position  $q_{hkl}(T_0)$  for each reflection. The position is found through fitting at the lowest temperature  $T_0$  (typically 8 K), for each sample, as in practice there are some discrepancies between the extrapolation parameters for the samples.

One could argue that once the position versus temperature has been established (for instance from literature), it should just be a matter of insertion. However, these temperature expansion

coefficients can not be used here, due to uncertainties in the exact instrumental configuration and due to possible sample differences, in combination, with the high relative  $q$ -resolution (which can be seen from *e.g.* figure 5.1.8). Furthermore motors are adjusted, and parts such as analyzer blades are replaced over time, which also contributes to making every measurement setup unique. It is this uniqueness, which forces us to perform the extrapolation uniquely for each measurement data series.

### 5.1.6.2 Determination of Peak Widths

The magnetic peak was as expected most prominent at low temperatures, and disappears towards higher temperatures. As neither the particle size nor instrument broadening change with temperature (neglecting lattice expansions), the width of the magnetic peak is determined at the lowest temperature and thereafter kept fixed for the rest of the analysis.

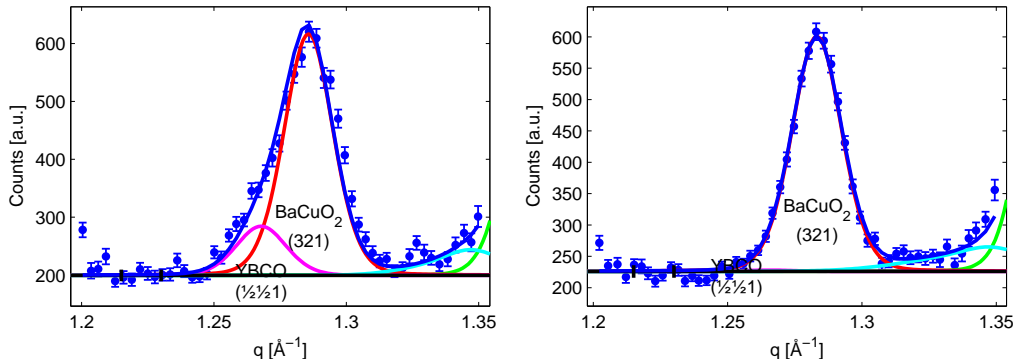


Figure 5.1.9: An example (here Sample 1 ( $x=0.20$ )) of fitting of the widths. The line shape is P4-Voigtian. The black horizontal line shows the background level, determined from the interval marked by the vertical dashed lines. Left: 8 K spectrum, with fitted YBCO ( $\frac{1}{2}\frac{1}{2}1$ ) and BaCuO<sub>2</sub> (321) peaks. Right: 450 K spectrum, with only the BaCuO<sub>2</sub> (321) peak.

I do not have any information on the impurity crystallite size, and therefore it is assumed to differ from that of the magnetic peak. The BaCuO<sub>2</sub> (321) peak width is fitted at high temperature, where I am 'certain' that the magnetic peak has disappeared (figure 5.1.9 (right)).

The P4-Voigt 'sample contribution width' (see section 4.1.3) of the BaCuO<sub>2</sub> (321) peak is fitted with a Pseudo-Voigt, whereas the 'sample contribution' of the magnetic peak is only Gaussian. The distinction is made, as I found the BaCuO<sub>2</sub> (321) to have larger Lorentzian tails than the magnetic peak.

After determination of the impurity peak width, this is reentered into the fit model and the width of the magnetic peak at low temperature is fitted again, with fixed BaCuO<sub>2</sub> width (figure 5.1.9 (left)), whereafter the fitting of the entire dataset can be made.

## 5.1.7 Simple Model Results

In this section I will proceed to present the most important results of the analysis of the samples with dopings  $x=0.20-0.35$ . I will start by giving small details on the fitting of the data before proceeding to present the data.

The peak position determination for the  $x=0.20$  sample has been done through extrapolation (see section 5.1.6.1) as there are no datasets besides the 8 K dataset, which contain the structural peaks (003), (101) and (100).

The data (figure 5.1.10(1-2) and figure 5.1.11) show a clear magnetic peak at low temperature which diminishes towards higher temperature, reaching a minimum level at 325 K. The fitting of the datasets, and in particular the high temperature datasets, is significantly hampered by the

large BaCuO<sub>2</sub> (321) peak. The intensity data points up to 325 K are fitted with a power law, to estimate the Néel temperature. Above 325 K the intensity slope flattens and is close to zero. A part of this behavior, close to  $T_N$ , may be due to critical scattering, but can not account for the intensities at higher temperatures.

The datasets with dopings  $x=0.25-0.35$  were fitted without any noteworthy deviations from the description in section 5.1.6.

To illustrate the fitting of the magnetic peak of individual datasets, fits of the highest and lowest temperature datasets are shown in figure 5.1.10. Additional plots from the fitting of the samples are found in appendix E.1.

$(hkl)$	$F^2$	$m$	Ref. [188] $x=0.31$ $\text{\AA}^{-1}$	Ref. [188] $x=0.34$ $\text{\AA}^{-1}$	Sample 1 $x=0.20$ $\text{\AA}^{-1}$	Sample 4 $x=0.25$ $\text{\AA}^{-1}$	Sample 5 $x=0.30$ $\text{\AA}^{-1}$	Sample 3 $x=0.35$ $\text{\AA}^{-1}$
(003)	79.5	2	1.5988	1.5982	1.6165(12)	1.6009(2)	1.6211(2)	1.6024(5)
(100)	249.1	4	1.6279	1.6257	1.6268(1)	1.6307(1)	1.6338(1)	1.6316(1)
(101)	51.65	8	1.7129	1.7107	1.7119(2)	1.7164(1)	1.7186(1)	1.7175(1)

Table 5.1.7: *Simple Model YBCO structural results. Selected reflection  $q$  values. Sample ( $x=\{0.20, 0.25, 0.30, 0.35\}$ ) values are found from lattice values from 8 K spectra. The comparative values are generated from room temperature lattice parameters for dopings  $x=\{0.31, 0.34\}$  found in ref. [188]. The values for  $F^2$  have been generated using Crystallographica for oxygen doping  $x=0.29$  from ref. [208] and using isotropic ionic displacements. The  $F^2$  values should only be viewed as guiding for the peak intensities, as the (003) reflection is sensitive to oxygen doping and oxygen ordering, as seen in table 5.1.3.  $m$  is reflection multiplicity.*

Sample	$x$	$T_N$ [188] K	$I_0$ a. u.	$M_0$ a. u.	$\beta$	$T_N$ K	$\chi^2$
Sample 1 ( $x=0.20$ )	0.20	385	2.26(14)	1.50(5)	0.31(7)	350(20)	1.393
Sample 4 ( $x=0.25$ )	0.25	373	2.11(19)	1.45(7)	0.34(10)	270(19)	0.691
Sample 5 ( $x=0.30$ )	0.30	353	1.70(13)	1.31(5)	0.20(7)	228(8)	8.163
Sample 3 ( $x=0.35$ )	0.35	310	0.35(8)	0.59(8)	0.25	101(4)	0.024

Table 5.1.8: *Simple Model  $I$  vs.  $T$  data fitted with power laws. The bulk reference values are from Tranquada et al. (1988) [188].  $I_0$  is integrated intensity and  $M_0$  is magnetization derived from  $I_0$ .  $\beta$  (unitless) is the magnetization power law exponent from (5.1.4) and the last column is the  $\chi^2$  value of the fit.*

## Results

Using the Simple Model fitting approach I have successfully extracted information on the magnetic and structural properties from nanosized YBCO powder samples.

The extracted reciprocal lattice parameters are presented in table 5.1.7, and match values apart from the (003) reflection values found in literature for bulk.

The extracted integrated intensities ( $I$  vs.  $T$ ) of the magnetic peak of the individual samples and the staggered magnetism ( $M$  vs.  $T$ ) are shown in figure 5.1.11. The integrated intensities (solid points) have been fitted with power laws

$$I = I_0(1 - T/T_N)^{2\beta}, \quad (5.1.4)$$

shown as solid lines in figure 5.1.11 (left), and the power law fitting of the staggered magnetism  $M$  versus  $T$ , shown in figure 5.1.11 (right), is derived as

$$I = M^2, \quad (5.1.5)$$

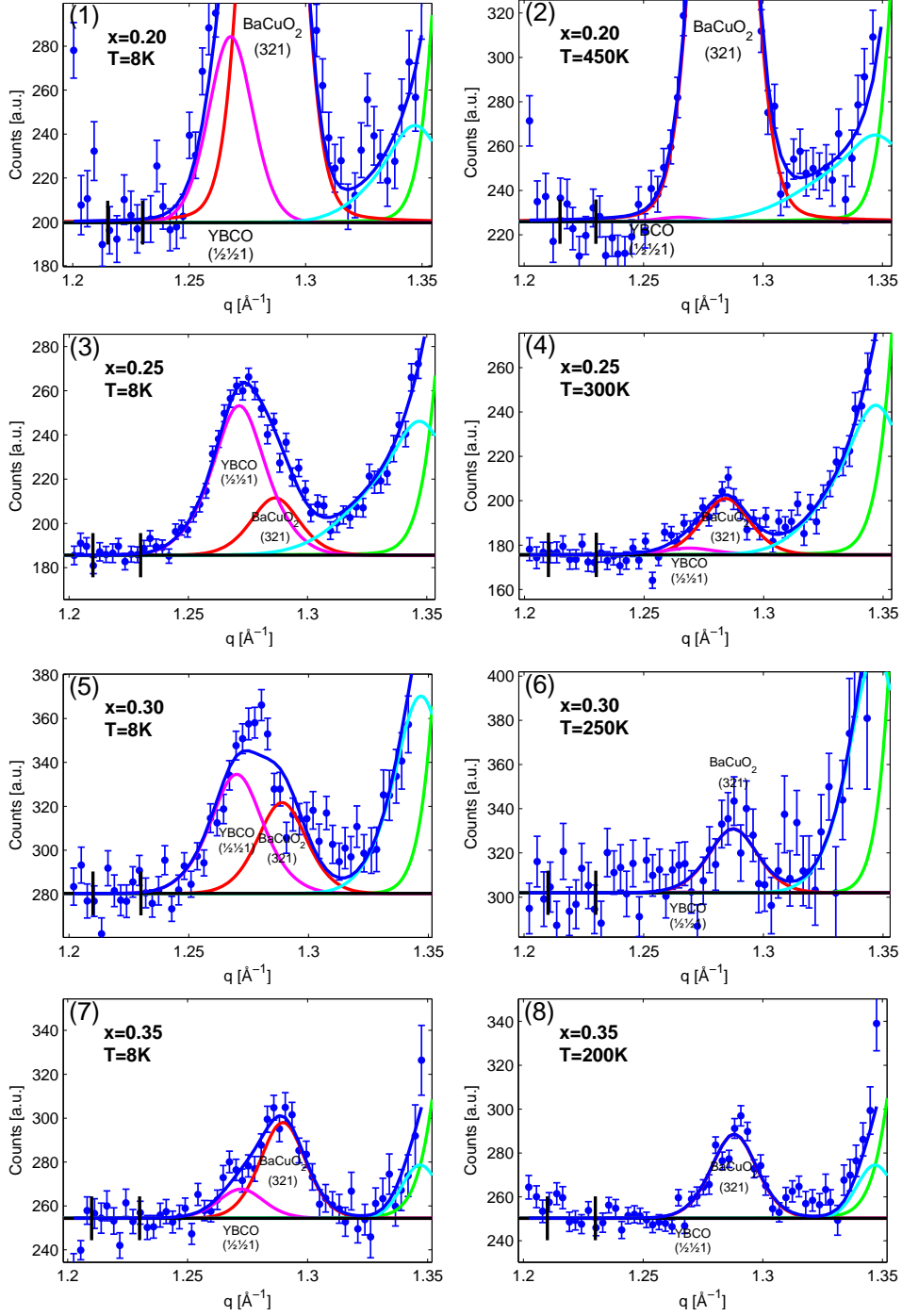


Figure 5.1.10: The development of the magnetic peak versus doping  $x$ , illustrated by the low and high temperature fits for all studied samples. The black horizontal line shows the background level. All plots are to the same scale. (1-2): Sample 1 ( $x=0.20$ ) 8 K and 450 K. (3-4): Sample 4 ( $x=0.25$ ) 8 K and 300 K. (5-6): Sample 5 ( $x=0.30$ ) 8 K and 250 K. (7-8): Sample 3 ( $x=0.35$ ) 8 K and 200 K.

from (3.2.21)-(3.2.22). In this context it is important to point out that the power law fit is an empirical method of finding the Néel temperature, and that it does not represent or include

theoretical considerations such as mean field theory or critical scattering.

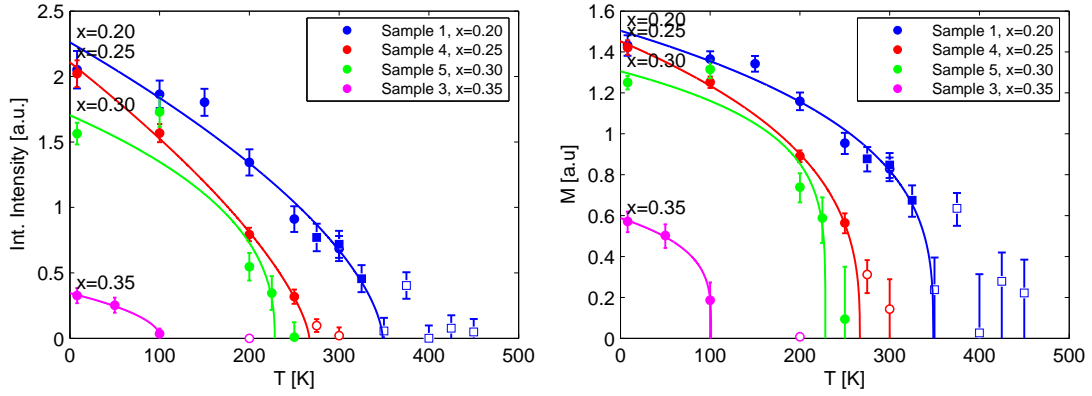


Figure 5.1.11: **Simple Model results.** Integrated intensity,  $I$  vs.  $T$  and staggered magnetism  $M$  vs.  $T$ , for YBCO nanoparticle samples with dopings  $x=\{0.20, 0.25, 0.30, 0.35\}$ . The datasets are normalized to the (101) reflection intensity (as described in section 5.1.1). The lines are fitted power laws (eq. (5.1.4)), and should be considered guides to the eye. However, although empirical, the lines are also the best estimate of the development of the magnetic order versus temperature. Left:  $I$  vs.  $T$ . Right:  $M \propto \sqrt{I}$  vs.  $T$ . Symbols: (●) Data obtained in the DIS-E displex. (■) Data obtained in the CTI-4 furnace. Open Symbols mark points which have been discarded in the power law fitting, since the high value of these points is a peak fitting artifact.

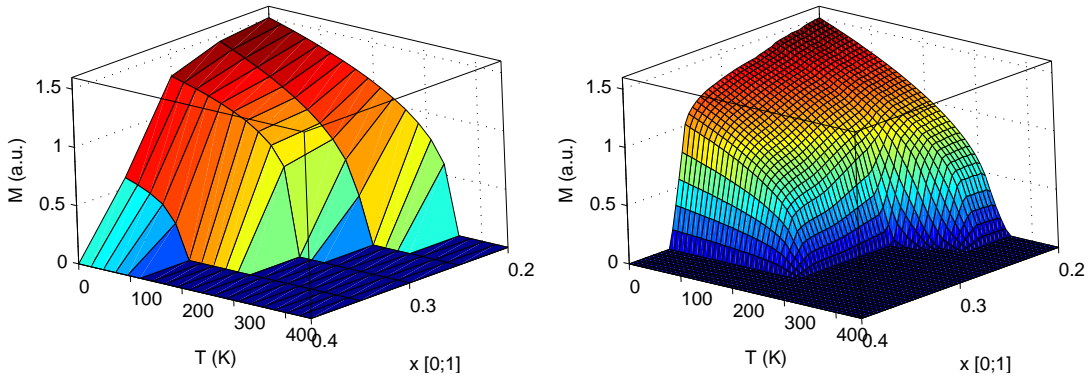


Figure 5.1.12: **Simple Model 3D plot of staggered magnetism versus oxygen doping and temperature ( $M, x, T$ ).** Left: 3D representation of the fits from figure 5.1.11 (right). Right: Fitted and smoothed data.

In general the found Néel temperatures, displayed in table 5.1.8 are significantly lower than those found for bulk powders by Tranquada *et al.* (1988) [188], which will be discussed further in section 5.3.

To answer one of the objectives of the thesis, the first of two contributions to the map of the staggered magnetism in nanosized YBCO versus temperature and oxygen doping is presented in figure 5.1.11. Furthermore a 3D mapping of the staggered magnetism as function of doping and temperature is presented in figure 5.1.12. The smoothed plot above has been made by fitting the power law values in figure 5.1.11 (right), versus  $x$  and  $T$  with power laws in succession, followed by a smoothing of the data points.

### 5.1.8 Advanced Model - $hkl$ Model

Although much work and effort was put into the above model, it still had problems as the positions of the magnetic YBCO peak and the  $\text{BaCuO}_2$  (321) peak could not be determined sufficiently accurately using the Simple Model.

To improve the accuracy I therefore constructed a model containing the compound composition of the sample and the relevant reflections of these.

This involved going through a wide range of known potential impurities and byproducts from the manufacturing of YBCO<sup>1</sup>. The result of this was that the main compounds in the sample besides YBCO were found to be  $\text{Y}_2\text{BaCuO}_5$ ,  $\text{BaCuO}_2$  and  $\text{Y}_2\text{O}_3$ .

Where the Simple Model used standardized fitting functions (*e.g.* Gaussian) containing  $N$  independent line shapes of the same type, the  $hkl$  Model contains crystal structure information *e.g.* lattice constants, and for each reflection an intensity and a width. The method is similar to Rietveld refinement, albeit the intensities and widths are not interlinked. As it is sufficient, I have used Gaussian line shapes in the fitting. The fitting using this model has yielded nice fit results, of which an example is shown in figure 5.1.13.

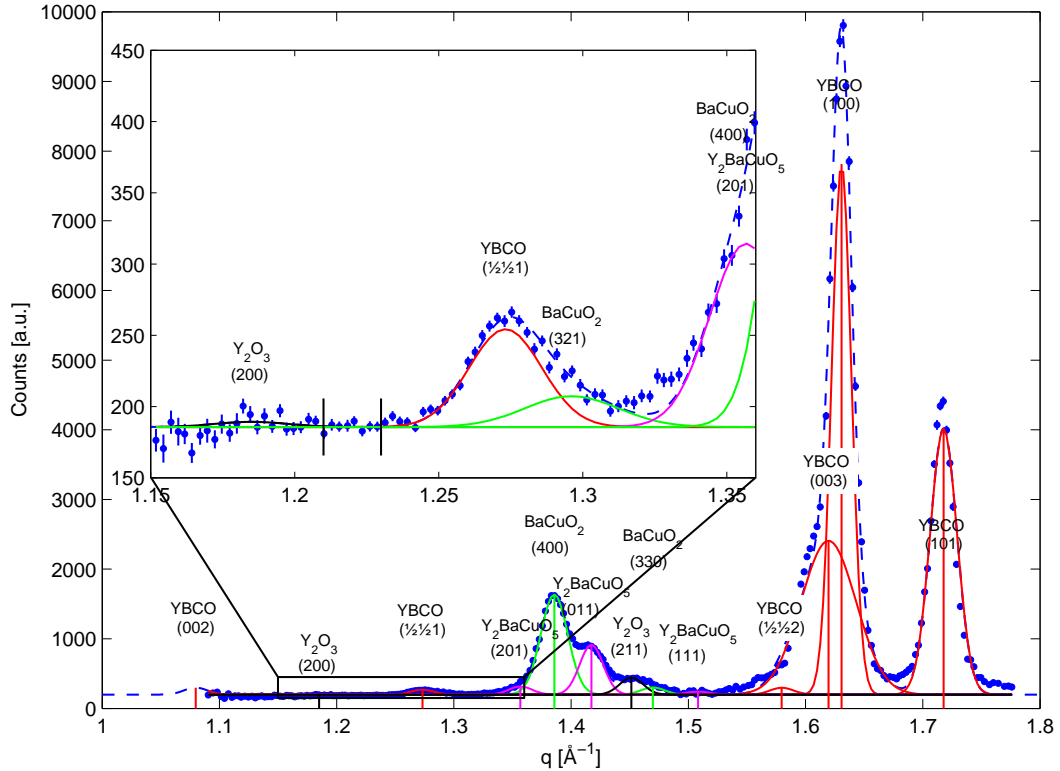


Figure 5.1.13: An example (here Sample 4 ( $x=0.25$ ) at 8 K) of a full data set fitted with the  $hkl$  Model Inset: The fitted  $(\frac{1}{2}\frac{1}{2}1)$  magnetic YBCO, and  $\text{BaCuO}_2$  (321) peaks. Note also the fitted  $\text{Y}_2\text{BaCuO}_5$  (201) and  $\text{BaCuO}_2$  (400) peaks. The vertical lines indicate the background determining interval.

There are 3 main advantages using the  $hkl$  Model:

<sup>1</sup>During the investigations a number of impurities ( $\text{BaO}$ ,  $\text{BaO}_2$ ,  $\text{Cu}_2\text{O}$ ,  $\text{CuO}$ ,  $\text{CuO}_2$ ,  $\text{Y}_2\text{Ba}_4\text{O}_7$ ,  $\text{Y}_2\text{BaCuO}_5$ ,  $\text{Y}_2\text{BaO}_4$ ,  $\text{Y}_2\text{Cu}_2\text{O}_5$ ,  $\text{Y}_2\text{O}_3$ ,  $\text{Y}_3\text{Ba}_3\text{O}_4$ ,  $\text{Y}_3\text{Ba}_3\text{O}_7$ ,  $\text{YBaCuO}_5$ ,  $\text{YCu}_2\text{O}_4$ ,  $\text{YCuO}_2$ ,  $\text{YCuO}_4$ ) have been checked in order to identify the peaks at  $q=1.35\text{-}1.5 \text{ \AA}^{-1}$ .

- By constructing the model such that the crystal structure is an integrated part of the peak fitting, the peak positions are linked to each other, and are thus much less affected by measurement error and noise.
- Through simultaneous fitting of the structural YBCO peaks, the position of the magnetic peak can be established with very good accuracy, as the structural peaks are very strong. Even the broad (003) peak now provides information.
- The peaks from impurities at  $1.35\text{-}1.50 \text{ \AA}^{-1}$ , were previously disturbing in fitting the  $\text{BaCuO}_2$  (321) impurity peak. However using this model, the fitting is easier, as both the  $\text{BaCuO}_2$  (400) and the  $\text{Y}_2\text{BaCuO}_5$  (201) peak positions now can be established through fitting of their other reflections in the mentioned area.

The *hkl* Model has for each temperature two steps. In the first step, the lattice constants of the compounds, the widths and intensities of the reflections are fitted to the full  $q$ -range.

In the second step, after the lattice constants have been found and verified by eye, the positions of YBCO ( $\frac{1}{2}\frac{1}{2}1$ ),  $\text{BaCuO}_2$  (321),  $\text{Y}_2\text{BaCuO}_5$  (201) and potentially other peaks are calculated, and are fitted by Gaussian line shapes. As in the Simple Model case, the widths of the peaks are only allowed to vary at the lowest temperature for each sample. An exception to this is the large  $\text{Y}_2\text{BaCuO}_5$  (400) reflection, in order to optimally compensate for the background.

Without going too much into the details of the fitting of the *hkl* Model, we will in short form present the workings of it here. The input of the fitting procedure is

$$L(q) = L(\hat{d}, \{\hat{S}, \hat{P}\}, \hat{B}) \quad (5.1.6)$$

where  $\hat{d}$  is the data input  $(x, y, \Delta y)$ , and the second parameter  $\{\hat{S}, \hat{P}\}$  contains the crystal structure lattice parameters input in the following format

$$\hat{S} = \left( \underbrace{a_1, c_1}_{\text{YBCO}}, \underbrace{a_2}_{\text{BaCuO}_2}, \underbrace{a_3, b_3, c_3}_{\text{Y}_2\text{BaCuO}_5}, \underbrace{a_4}_{\text{Y}_2\text{O}_3} \right) \quad (5.1.7)$$

and the peak intensity and width parameters

$$\hat{P} = (i_1, w_1, i_2, w_2, \dots, i_{n-1}, w_{n-1}, i_n, w_n). \quad (5.1.8)$$

The last input parameter is an array of boolean's

$$\hat{B} = (s_1, \dots, s_7, b_1, b_2, \dots, b_{2n}), \quad (5.1.9)$$

dictating whether the  $\{\hat{S}, \hat{P}\}$  input parameters are fixed or left free during fitting. Additional reflections of the existing crystal structures are easily added or removed, when needed.

In the model it is built-in that YBCO is in the tetragonal structure phase.  $\text{Y}_2\text{O}_3$  and  $\text{BaCuO}_2$  are cubic, and  $\text{Y}_2\text{BaCuO}_5$  is orthorhombic. The crystal structure data are found in table G.4.1.

The actual peak positions (in  $q$ -space) for each mineral are calculated from the formula

$$q = \left( (ha^*)^2 + (kb^*)^2 + (lc^*)^2 \right)^{1/2}. \quad (5.1.10)$$

One could argue, that from form- and structure factors, the intensity of each reflection can be calculated, which is true, if the crystal grains were bulk-sized. However, the particles are disc-shaped and nanosized, which affects the form-factors and structure factors respectively.

### 5.1.9 *hkl* Model Results

In the following, the results of the *hkl* Model fitting approach are presented. As in the previous results section, I will start by giving minor details on the fitting of the data before proceeding to present the data.

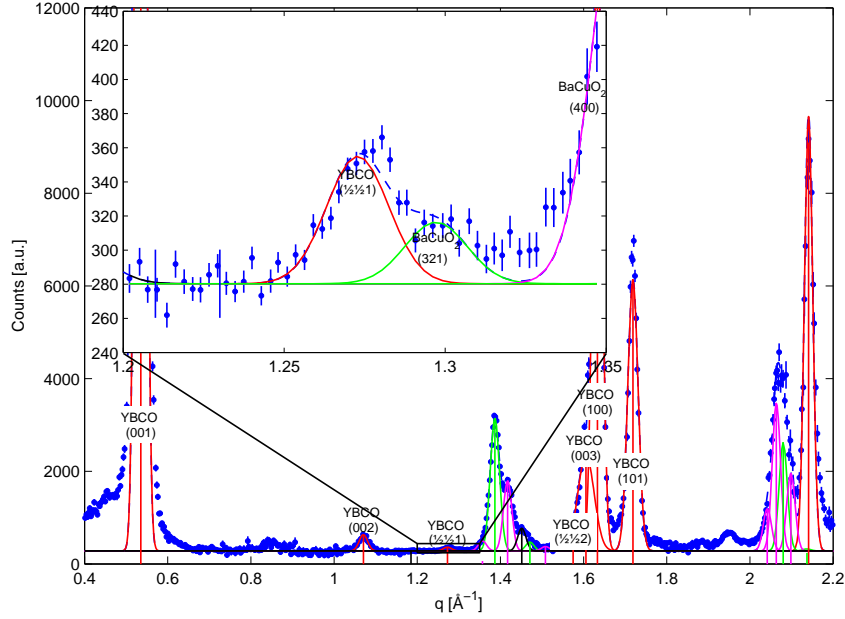


Figure 5.1.14: *hkl*-fitted neutron data of Sample 5 ( $x=0.30$ ) at 8K. Outer plot shows entire  $q$  range, and inset shows the fitted region around the YBCO  $(\frac{1}{2}\frac{1}{2}1)$  peak. The fitted impurity peaks at  $1.3\text{-}1.6\text{ \AA}^{-1}$  and  $2.0\text{-}2.2\text{ \AA}^{-1}$  are plotted with labels in figure 5.1.16. Solid lines are individual peaks and the dashed line represents the full model.

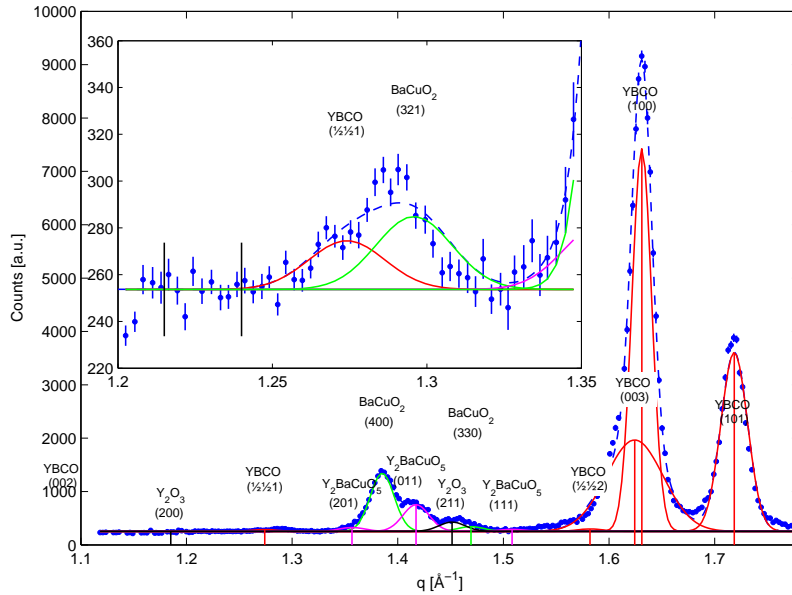


Figure 5.1.15: *hkl*-fitted neutron data of Sample 3 ( $x=0.35$ ) at 8K. Outer plot shows entire  $q$  range, and inset shows the fitted region around the YBCO  $(\frac{1}{2}\frac{1}{2}1)$  peak.

Examples of datasets fitted with this model are shown in figures 5.1.13, 5.1.14 and 5.1.15 for samples with dopings  $x=0.25$ ,  $x=0.30$  and  $x=0.35$  respectively.

The  $hkl$  analysis of the Sample 1 ( $x=0.20$ ) does not entirely follow the course laid out above, as only one of the temperature data sets (8 K) has a scan over the region where (003), (100) and (101) peaks are located, thus making a proper  $hkl$  analysis impossible.

Therefore the  $hkl$  analysis of this sample has been performed similar to the Simple Model, albeit using Gaussian line shapes. The Simple Model results can not be reused directly, as the Lorentzian tails of the P4-Voigt give a slightly, though significantly larger integrated intensity, than a Gaussian.

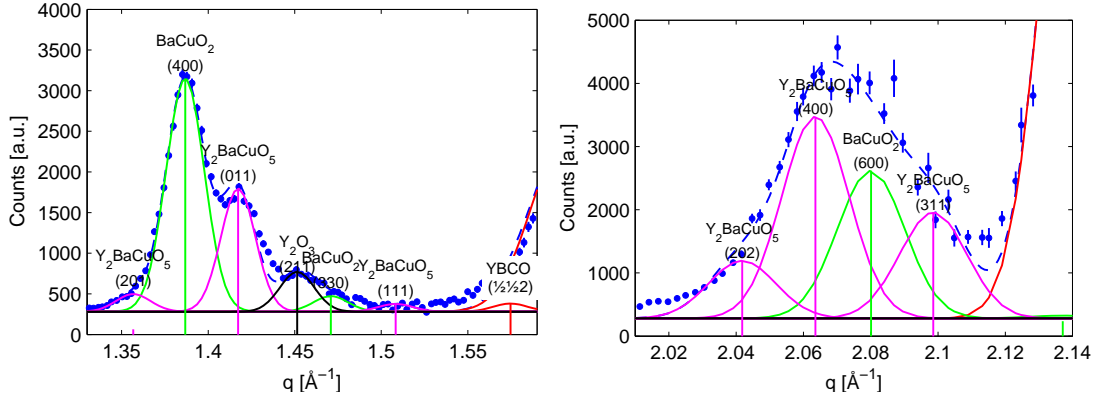


Figure 5.1.16: Example of the impurity peaks fitted using the  $hkl$  Model (Sample 5 ( $x=0.30$ ) at 8 K). Solid line are the individual peaks and dashed lines is the sum of the peaks. Left:  $1.31-1.61 \text{ \AA}^{-1}$ . Right:  $2.01-2.14 \text{ \AA}^{-1}$ .

As mentioned, the impurity peaks were included in the fit model, and the  $hkl$  Model accounts for the reflections very well. To illustrate this, a zoom-in on two regions from figure 5.1.14 is shown in figure 5.1.16.

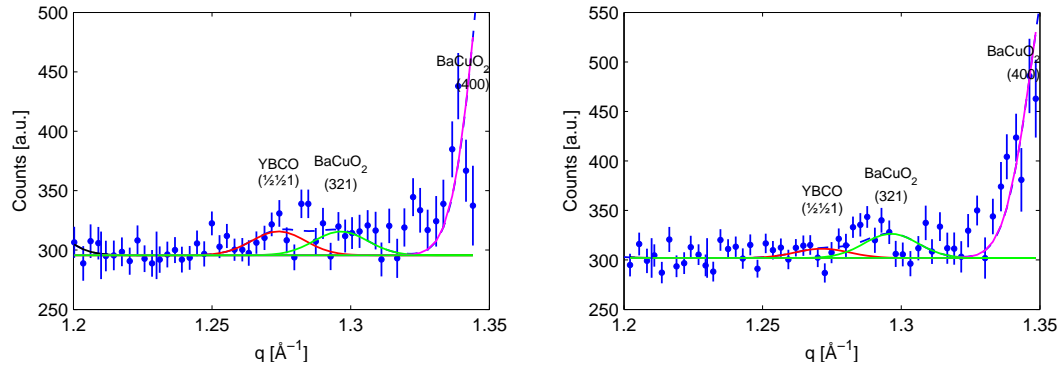


Figure 5.1.17: An example (Sample 5 ( $x=0.30$ )) of the behavior of the fitting algorithm with weak peaks. Left: 225 K, the algorithm fits a peak which is clearly there. Right: 250 K, the algorithm attempts to fit a peak of which there is no clear indication by visual inspection.

From integrated intensity of the magnetic peak versus temperature in figure 5.1.18 (left), it can be seen that the values seldom simply go to zero at high temperature. There are several factors which can explain this behavior. For instance, the background level might have been set a little too low or the  $\text{BaCuO}_2$  (321) position might be slightly off. The fitting algorithm, is always trying

to improve  $\chi^2$ , and will add a small peak if it can improve the fit. An example of this behavior of the fitting algorithm, is shown in figure 5.1.17, where one dataset clearly contains a peak, and where it is questionable whether the other dataset contains a peak. When plotting  $M$  versus  $T$  values, the expression  $I = M^2$  further acts to enhance small peaks.

Sample	$x$	$T_N$ ([188]) K	$I_0$ a.u.	$M_0$ a.u.	$\beta$	$T_N$ K	$\chi^2$
Sample 1 ( $x=0.20$ )	0.20	385	2.37(12)	1.54(4)	0.32(4)	355(7)	1.763
Sample 4 ( $x=0.25$ )	0.25	373	2.29(7)	1.51(2)	0.31(4)	291(8)	13.792
Sample 5 ( $x=0.30$ )	0.30	353	1.93(14)	1.39(5)	0.24(10)	260(20)	19.897
Sample 3 ( $x=0.35$ )	0.35	310	0.63(10)	0.79(7)	0.25	140(30)	0.726

Table 5.1.9: *hkl Model I vs. T data fitted with power laws. The bulk reference values are from Tranquada et al. (1988) [188].  $I_0$  is integrated intensity and  $M_0$  is magnetization derived from  $I_0$ .  $\beta$  (unitless) is the magnetization power law exponent from (5.1.4) and the last column is the  $\chi^2$  value of the fit. Note:  $\beta$  of Sample 3 ( $x=0.35$ ) has been fixed due to the few number of points in the dataset.*

## Results

As done with the Simple Model, the extracted integrated intensity ( $I$  versus  $T$ ), of the magnetic peak of the individual samples has been fitted with power laws (5.1.4), as shown in figure 5.1.18, along with a plot of the staggered magnetization ( $M$  versus  $T$ ), extracted from this. From the fits an estimate of the Néel temperature is found (displayed in table 5.1.9). Consistent with the result from the Simple Model, the found Néel temperatures are significantly lower than those found for the bulk YBCO [188]. 3D mappings of the staggered magnetism, raw data and smoothed fit are presented in figure 5.1.19.

Sample	$x$	$T$ K	$a$ Å	$c$ Å
Ref. [188]	0.31	r.t.	3.8598(4)	11.790(2)
Ref. [188]	0.34	r.t.	3.865(2)	11.794(3)
Sample 4	0.25	300	3.85851(9)	11.665(11)
Sample 5	0.30	250	3.8500(17)	11.7681(9)
Sample 3	0.35	200	3.8546(14)	11.617(17)
Sample 4	0.25	8	3.8531(10)	11.638(10)
Sample 5	0.30	8	3.8471(12)	11.7422(5)
Sample 3	0.35	8	3.8522(14)	11.609(18)

Table 5.1.10: *Selected lattice constants found from hkl Model fitting. Top rows are bulk values for dopings  $x=\{0.31, 0.34\}$  at room temperature from Tranquada et al. (1988) [188]. Upper sample rows contain lattice values found from 200, 250 and 300 K data and lower sample rows contain values found from 8 K data. Sample 1 ( $x=0.20$ ) has not been fitted using the pure hkl approach, and has therefore no values.*

A new result obtained using this analysis approach, is the lattice constants, which are displayed in table 5.1.10. From the data it can be seen that the  $c$ -axis of the unit cell in the nanoparticles is systematically significantly lower than that reported for bulk material by Tranquada et al. (1988) [188].

This might be surprising, but it matches well the findings by Raittila et al. [146, 148], that the disc-shaped nanoparticles have a compressed  $c$ -axis. These investigations were, however, performed on superconducting material, and my observation of a reduced  $c$ -axis in the antiferromagnetic state

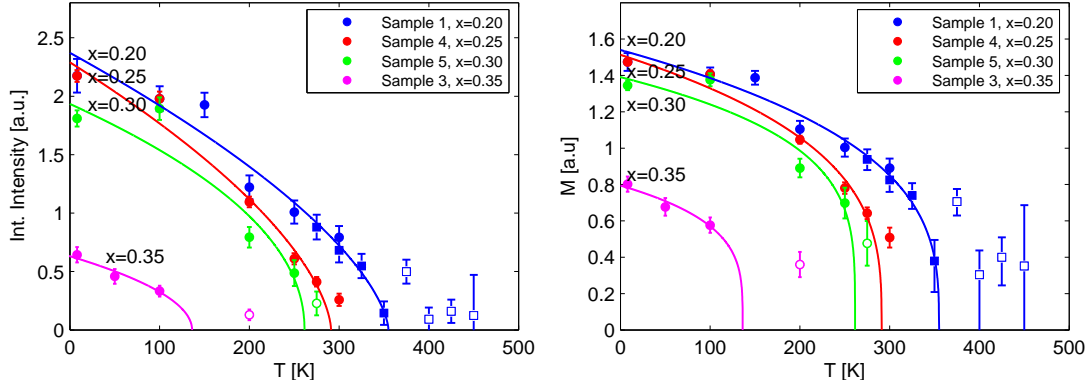


Figure 5.1.18: *hkl Model results*. Integrated intensity  $I$  vs.  $T$  (left) and staggered magnetism  $M$  vs.  $T$  (right) for YBCO nanoparticle samples with dopings  $x = \{0.20, 0.25, 0.30, 0.35\}$ . The datasets are normalized to the (101) reflection intensity (as described in section 5.1.1). The lines are fitted power laws, and should be considered guides to the eye. However, although empirical, the lines are also the best estimate of the development of the magnetic order versus temperature. Symbols: (●) Data obtained in the DIS-E dispex. (■) Data obtained in the CTI-4 furnace. Data points with open symbols have been discarded in the fits. Left:  $I$  vs.  $T$ . Right:  $M$  vs.  $T$ .

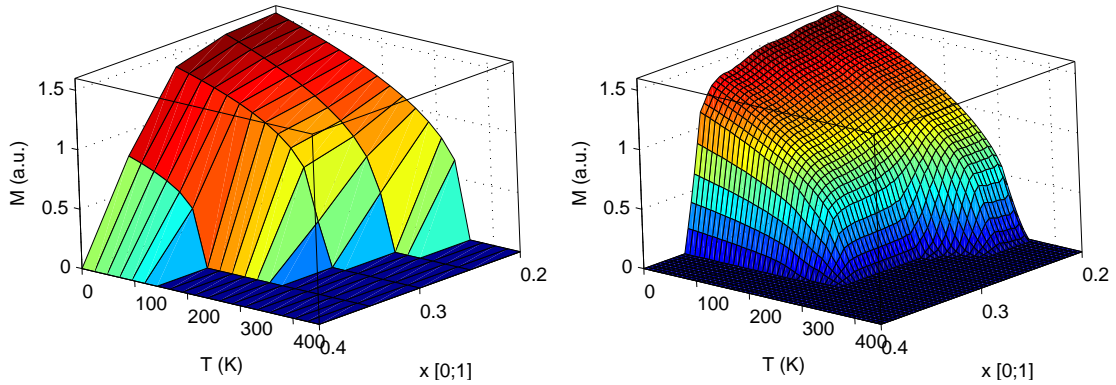


Figure 5.1.19: *hkl Model 3D plot of staggered magnetism versus oxygen doping and temperature ( $M, x, T$ )*. Left: 3D representation of the fits from figure 5.1.18 (right). Right: Fitted and smoothed data.

is thus new.

The results will, as mentioned, be discussed further in section 5.3, where they will be put into context with the results from the  $\mu$ SR measurements and compared to bulk results from literature.

### 5.1.10 Applied Magnetic Field Experiments

Due to finite size effects the staggered magnetism in the nanosized YBCO particles, might be susceptible to an applied magnetic field. To investigate this, neutron scattering experiments have been performed on two of the samples with an applied magnetic field perpendicular to the scattering vector.

The influence of a 13.5 T magnetic field of this magnitude will not be measurable in bulk YBCO, as 1 T roughly corresponds to an energy of the order of 1 meV, and is very small compared to the exchange  $J_{ab}$  of the order 100 meV [181]. However, as mentioned in the section 2.5, finite sized systems do not have periodic boundary conditions, and the spin system might therefore be more

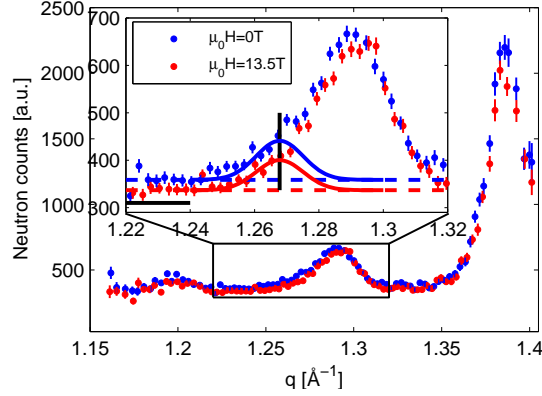


Figure 5.1.20: *Sample 1* ( $x=0.20$ ) neutron scattering data with an applied magnetic field of  $0\text{ T}$  and  $13.5\text{ T}$  at  $8\text{ K}$ . The nominal position of the magnetic peak is marked by the vertical black line. The region used for calculation of the background level is indicated by the horizontal black line. The background levels are indicated by the colored dashed lines

$T$	$\mu_0 H$	$I$
K	T	a.u.
2.7	0.0	1.50(12)
2.7	13.5	1.16(11)

Table 5.1.11: *Sample 1* ( $x=0.20$ ) integrated intensity  $I$  versus applied field  $\mu_0 H$ .

$T$	$\mu_0 H$	$I$
K	T	a.u.
8.0	0.0	0.33(6)
8.1	13.5	0.56(11)

Table 5.1.12: *Sample 3* ( $x=0.35$ ) integrated intensity  $I$  versus applied field  $\mu_0 H$ .

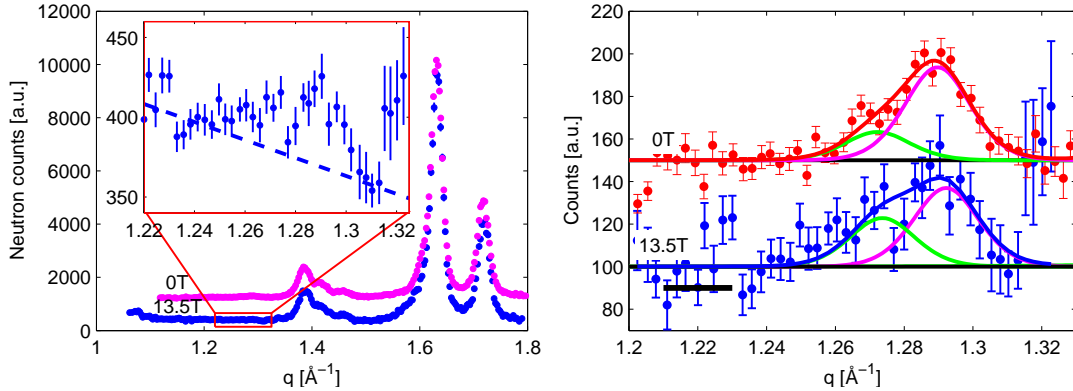


Figure 5.1.21: *Sample 3* ( $x=0.35$ ) neutron scattering data with an applied magnetic field of  $0\text{ T}$  and  $13.5\text{ T}$  at  $8\text{ K}$ . Left: Full dataset. Inset: Fit of background around magnetic peak. Right: Fitted magnetic peak in  $0\text{ T}$  &  $13.5\text{ T}$ . (—) marks the magnetic YBCO peak, and (---) marks the  $\text{BaCuO}_2$  (321) peak.

susceptible to influence by an externally applied magnetic field. For instance it is plausible, that the surface spins in the particle, which have fewer nearest neighbors, might have a lower anisotropy energy, causing them to be more susceptible to an externally applied field.

To investigate whether there is a nanoscale-related field response, we have performed experiments with an applied field perpendicular to the scattering vector  $q$ . Experiments were performed on the samples *Sample 1* ( $x=0.20$ ) and *Sample 3* ( $x=0.35$ ), with  $0\text{ T}$  and  $13.5\text{ T}$  using the MA-15 superconducting magnet.

### The $x=0.20$ Experiment

In the Sample 1 ( $x=0.20$ ) sample there is little difference in the spectra at first glance, but a careful analysis reveals that the integrated intensity of the magnetic peak is diminished, from 0 T to 13.5 T by  $23\pm 15\%$ .

This might be caused by a canting of the spins such that the transverse spin component of the  $(\frac{1}{2}\frac{1}{2}1)$  reflection is diminished. The applied field might thus cause the spins (and more so the surface spins) to cant along the field direction. The spins are as mentioned lying in the  $a, b$ -plane, and canting along the  $c$ -axis would cause the perpendicular component to  $(\frac{1}{2}\frac{1}{2}1)$  to diminish as illustrated in figure 5.1.24.

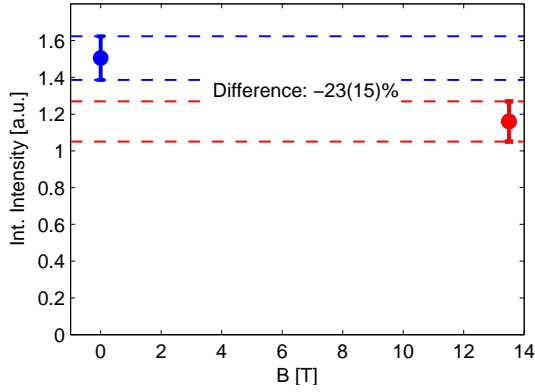


Figure 5.1.22: *Sample 1 ( $x=0.20$ ) integrated intensity versus applied magnetic field,  $I$  vs.  $\mu_0 H$ . Note the significant decrease in intensity.*

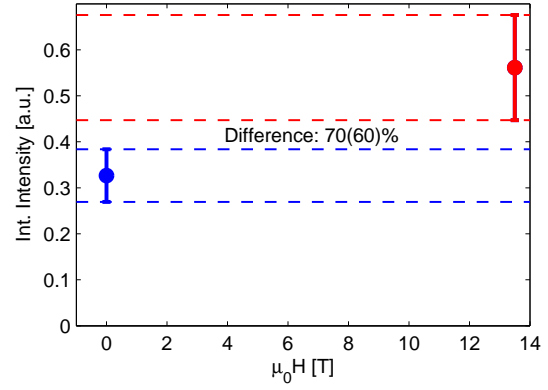


Figure 5.1.23: *Sample 3 ( $x=0.35$ ) integrated intensity versus applied magnetic field,  $I$  vs.  $\mu_0 H$ . Note the significant increase in intensity.*

### The $x=0.35$ Experiment

Performing the same experiment on the higher doping sample, it was expected to exhibit the same behavior as Sample 1 ( $x=0.20$ ).

The data are noisy, but a relatively decent spectrum was extracted using a sloping background fit. The fitted spectra of 0 T and 13.5 T are presented in figure 5.1.21. Surprisingly the fit shows an increase ( $7\pm 6\%$ ) in the integrated intensity, as seen from figure 5.1.23 and table 5.1.12). The cause of this can not be spin canting, as in the previous sample, as simple canting only can diminish the staggered magnetism.

Two possible explanations to this enhanced magnetism are presented. The first is that we have a spin flop transition, which as illustrated by figure 5.1.25, could cause this. For a spin flop to occur we have to have a very low anisotropy energy, which the applied field then overcomes. The anisotropy energy of the surface spins is most likely small compared to that of similar bulk material, and furthermore the doping degree is close to the AFM/SC transition, thus lowering it further. Considering these observations and their potential influence on the anisotropy energy, spin flop can actually be an explanation.

The second possibility is that we have a situation of competing order parameters, magnetism and superconductivity, where the applied field modifies the energy landscape such that the magnetic order is significantly enhanced. This has previously been demonstrated to happen in LSCO in the superconducting state, close to the  $1/8$ th hole doping [29, 84, 98]. This is plausible, as we are close to or even inside, the spin glass like phase and close to the superconducting phase, with the oxygen doping of  $x=0.35$ . The magnetic susceptibility measurements on the sample, shown in figure E.4.1(7-8) do, however, not show any signs of superconductivity.

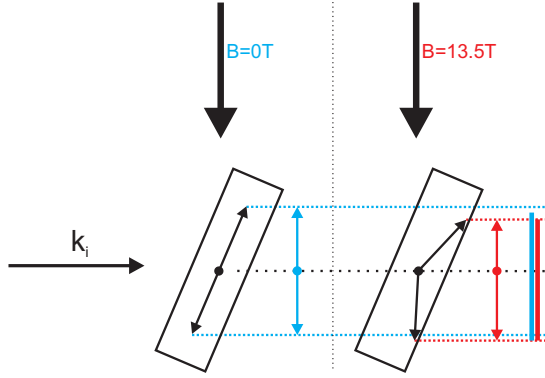


Figure 5.1.24: **Spin Canting.** Schematic illustration of the effect of canting on the neutron scattering cross section. The black box is an outline of the particle shape. The neutron is scattered from the perpendicular component of the spin. With applied field the spins cant, leaving the total perpendicular spin component smaller. The colored arrows are the perpendicular component of the spins. The colored solid bars to the far right represent the measured staggered magnetism. Blue: Zero field. Red: 13.5 T.

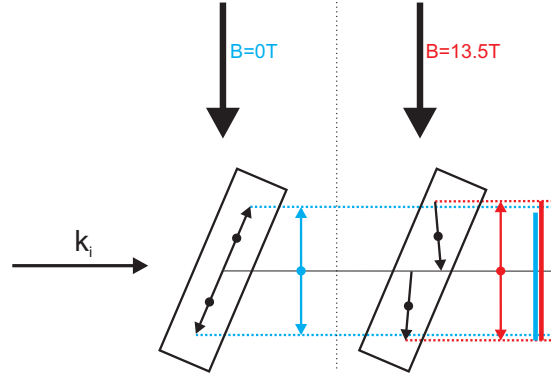


Figure 5.1.25: **Spin Flop.** Schematic illustration of the effect of spin flop on the neutron scattering cross section. The black box is an outline of the particle shape. The neutron is scattered from the perpendicular component of the spin. With applied field some spins flop, thereby yielding the total perpendicular spin component larger. The colored arrows are the perpendicular component of the spins. The colored solid bars to the far right represent the measured staggered magnetism. Blue: Zero field. Red: 13.5 T.

### 5.1.11 Bulk YBCO Analysis

A very important aspect of the investigations of the nanosized YBCO particles, is how the physics in these differ from that of bulk YBCO. As mentioned earlier, there are different opinions in the superconductivity community, on the exact degree of doping at which several phenomena, such as for instance the tetragonal/orthorhombic transition, occur. Some of these differences have their origin in the doping treatment of the samples. When comparing the present results with those from literature, there is always the question of exactly how the samples were doped and treated, and in some cases how clean they are.

Faced with the choice between using results from references or making my own reference samples, I chose to manufacture my own samples. Making my own bulk YBCO had furthermore the advantage, that I could dope the bulk and nanosized samples in the same procedure, and even use the bulk-sized material as a oxygen buffer, ensuring a correct doping degree.

Several attempts ( $x=\{0.25, 0.30, 0.35\}$ ) were made to manufacture and dope the YBCO bulk samples. For reasons still not entirely understood, the oxygen doping procedure was unsuccessful for the samples  $x=\{0.25, 0.35\}$ , and the samples, which prior to the doping procedure had  $x \sim 1$ , did not have their oxygen doping  $x$  as much reduced as was intended. Most likely, the doping procedure resulted in that only a surface layer of the particles had the oxygen content reduced, whereas the bulk of the particles were left with an unchanged value of oxygen doping. The doping procedure is described in detail in section 4.5.

Magnetic susceptibility measurements (see appendix E.4.2), gave a strong diamagnetic signal, indicating superconductivity, shown in figure E.4.3(1-2). A homogenization run, with the sample in a sealed glass vial, resulted in a sample with a smaller diamagnetic signal and a lower  $T_C$  (figure E.4.3(3-4)).

The doping of the  $x=0.30$  sample was successful (albeit it contains a small superconducting component, as shown in figure E.4.3(5-6)), and it was investigated using neutron scattering. An example of the obtained data is shown in figure 5.1.26.

The analysis of the data is extremely difficult as there is a very large impurity Bragg peak on

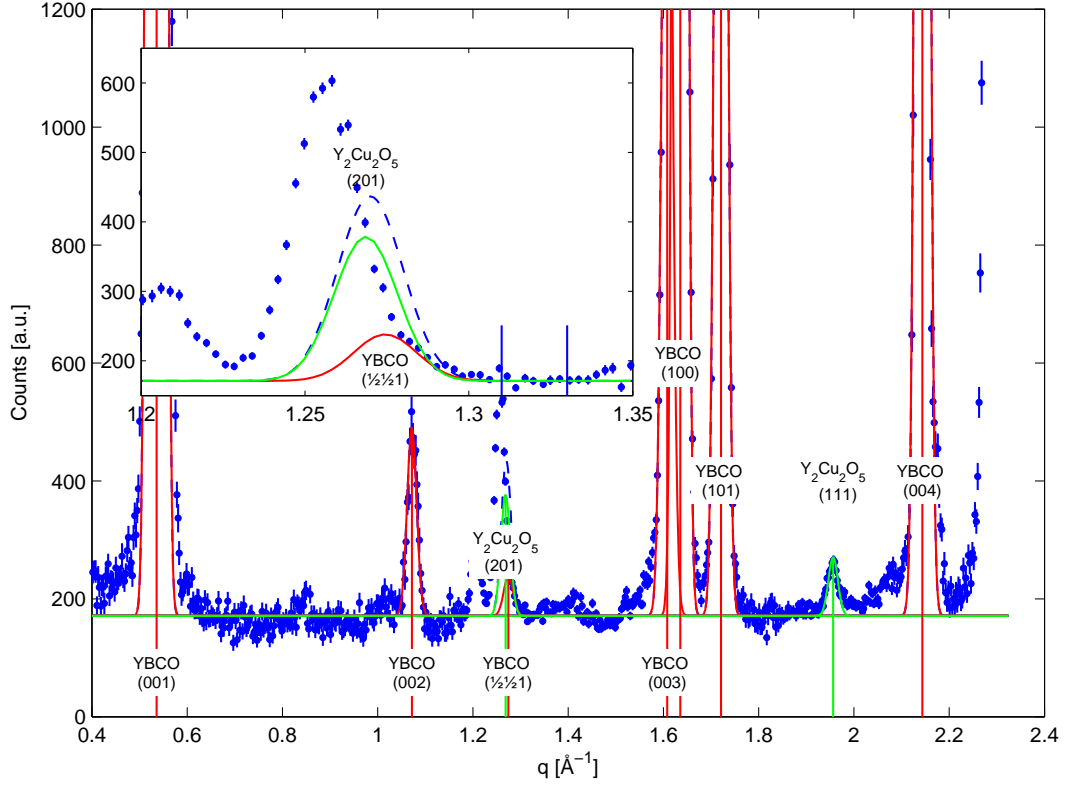


Figure 5.1.26: *hkl*-fitted neutron spectrum of Sample 5 Bulk ( $x=0.30$ ) at 8 K. The outer plot shows entire  $q$ -range, and the inset shows the fitted region around the YBCO ( $\frac{1}{2}\frac{1}{2}1$ ) peak with the impurity peak. From the plot it is apparent that the fit components are unable to account for the entire peak at  $\sim 1.255 \text{ \AA}^{-1}$ .

top of the magnetic peak. Unless accounted for, this impurity peak makes it impossible to fit the magnetic peak. In the search for a matching impurity, a significant number of impurity phases<sup>2</sup> were checked, in addition to the impurities already found in the nano-YBCO analysis. However, during the search only one,  $\text{Y}_2\text{Cu}_2\text{O}_5$ , was found to be partly matching, but unable to account for the full peak, as seen from figure 5.1.26.

Further, the refinement is complicated by the fact that there are very few  $\text{Y}_2\text{Cu}_2\text{O}_5$  peaks to do the refinement on, and the fact that  $\text{Y}_2\text{Cu}_2\text{O}_5$  is orthorhombic with 3 free lattice parameters.

Conclusively, the attempt to compare nanosized and bulk YBCO behavior was therefore unsuccessful, as with the present data I was unable to extract information on the magnetic behavior of the bulk sample. I could not pursue this subject further, as there was no beam time available within the time left in the time allotted to my Ph.D. project.

## 5.2 Muon Spin Rotation Data Analysis

This section covers the analysis of the  $\mu\text{SR}$  data obtained from the nanosized YBCO samples. I will start by describing the calibration of the data, before proceeding to presenting the models employed in the analysis of the  $\mu\text{SR}$  data. Then I will continue to analyze the data before discussing the results of the analysis.

Muon Spin Rotation measurements have been performed on 3 of the nano-YBCO samples.

<sup>2</sup>The checked impurities are among others  $\text{CuO}$ ,  $\text{Cu}_2\text{O}$ ,  $\text{Ba}_2\text{CuO}_3$ ,  $\text{Y}_2\text{BaO}_4$  and  $\text{Y}_2\text{Ba}_4\text{O}_7$ .

The measurements are listed in table 5.2.1. All fitting has been done using the program WKM [143].

Sample	Oxygen doping $x$	Hole doping $p$	$T_{min}$ K	$T_{max}$ K
Sample 4	$0.25 \pm 0.025$	0.017(7)	5	300
Sample 5	$0.30 \pm 0.025$	0.044(12)	10	300
Sample 3	$0.35 \pm 0.025$	0.055(6)	10	125

Table 5.2.1: An overview of the zero field (ZF)  $\mu$ SR measurements performed on YBCO nano particles.  $T_{min}$  and  $T_{max}$  indicate the minimum and maximum temperatures during the measurements respectively.

### 5.2.1 Calibration

Calibration of each sample measurement is performed by going to a temperature where there is no magnetic order in the samples, and there applying a known external weak transverse field (wTF). Transverse should here be understood as transverse to the  $\mu^+$  spin direction. The muons will now precess with a known frequency, and the  $\alpha$  parameter (3.3.12) can be determined through fitting. The model which is being fitted consists of a simple Gaussian (3.3.20) multiplied with a Cosine (3.3.19)

$$A(t) = A_1 e^{-\frac{1}{2}(\sigma t)^2} \cos(2\pi\nu t + \varphi), \quad (5.2.1)$$

where  $\sigma$  is the standard deviation of the Gaussian,  $\nu$  is the precession frequency and  $\varphi$  is the phase. Examples of a raw calibration dataset and a fitted calibration dataset are shown in figure 5.2.1 and figure 5.2.2, respectively. All calibration plots are available in appendix E.2.1, and the calibration results for the 3 samples are presented in tables 5.2.2, E.2.1 and E.2.3.

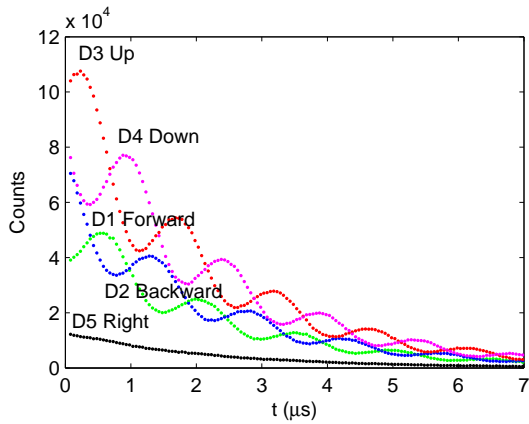


Figure 5.2.1: Raw calibration data, counts versus time on the individual detectors for the  $x=0.25$  sample at 300 K and 50 G.

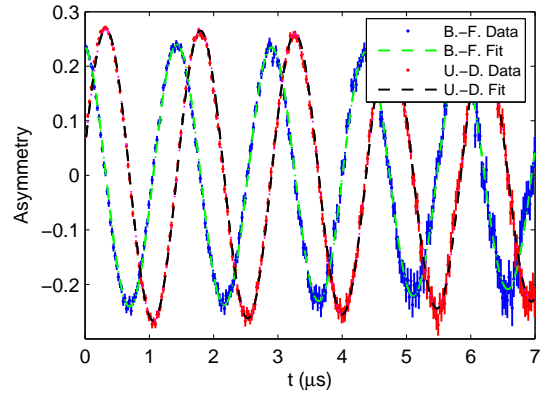


Figure 5.2.2: Fitted calibration dataset for the  $x=0.25$  sample at 300 K and 50 G. Note that the error bars increase with time as the count rate of muons decreases.

### 5.2.2 Fitting models

A preliminary analysis led to the decision to use two different models in the fitting of the data. The first is a general model (model 1) which has the strength of fitting the data relatively well, and being well suited for extracting the precession frequency. However, it does not have many

#	Parameter	Value	Unit
1	$\alpha$	0.8494(8)	
2	$A_1$	0.2414(8)	
3	$\varphi$	10.3(2)	° (degree)
4	$\sigma$	0.082(3)	$\mu\text{s}^{-1}$
5	$\nu$	50.15(2)	G

Table 5.2.2: Calibration parameters found for Sample 4 ( $x=0.25$ ) at 300 K and 50 G.

physical restrictions built-in. The second is a powder model (model 2) which has many built-in physical model restrictions.

### 5.2.2.1 Model 1 - CEE

Model 1, the CEE (Cosine+Exponential+Exponential) model, is based on the ansatz

$$\begin{aligned}
 A(t) &= A_{osc} \cos(2\pi\nu_f t + \varphi) \exp(-\lambda_{osc} t) \\
 &+ A_f \exp(-\lambda_f t) \\
 &+ A_s \exp(-\lambda_s t),
 \end{aligned} \tag{5.2.2}$$

consisting of a damped cosine and two simple decaying exponentials (CEE), all of which are independent.

The most important term is the cosine term, which models the precessing muon signal. Beyond that, the preliminary analysis showed that the spectra contain a least one fast dephasing component, and at least one component, which is close to constant. This last component most likely contains a non-precessing part with a relative asymmetry of 1/3, a so-called 1/3 powder tail. Furthermore the data might also contain a Kubo-Toyabe (KT) line-shape at higher temperatures. In this model I will not distinguish between the KT and the 1/3 powder tail, as it is unneeded for extraction of the precession frequency.

The first term in (5.2.2) is intended to model the precession of the muons, and will give the precession frequency  $\nu$  and phase  $\varphi$ , as well as the dephasing exponent  $\lambda_{osc}$  of the precessing muons. Furthermore the asymmetry  $A_{osc}$  will give the fraction of muon sites with an identical magnetic field.

The second term describes muons with fast dephasing. The fast dephasing described by  $\lambda_f$ , is caused by muons experiencing incoherent local fields or broad local field distributions. These muons are only coherent at  $t = 0$ , and no precession frequency can be detected, as the muons are out of phase within a very short time, making  $\lambda_f$  large. The asymmetry  $A_f$  will as in the previous case, yield the volume fraction of these muon sites.

The third term describes the muons caught in an environment, where the local magnetic field is parallel to the muon spin, or muons at sites where they will experience no or only a very small local magnetic field. These muons will either not precess, or precess very slowly, and the decay positron will be emitted as described in (3.3.4). In an ideal uniformly magnetically ordered powder this fraction would be 1/3 due to the random orientation of the local magnetic field at the muon sites. However, muons will always be affected by the nuclear spins, and slowly precess in the local nuclear field, the so-called Kubo-Toyabe precession (3.3.23). An exponential with a very small  $\lambda_s$  is, however, within the first few  $\mu\text{s}$  a decent to first approximation to the Kubo-Toyabe shape.

The decay rate  $\lambda_s$  should as mentioned be small. Ideally (if no muon sites are dominated by Kubo-Toyabe behavior) the asymmetry  $A_s$  of this term should be 1/3 of the other two as

$$A_s = \frac{A_{osc} + A_f}{3}. \tag{5.2.3}$$

However, this is broken if the muons are captured at sites where the direction of the local magnetic field is fluctuating. Furthermore the relation is broken if the powder is no longer uniformly

magnetically ordered, as there will be non-magnetic regions in the sample contributing with a Kubo-Toyabe term, increasing the  $A_s$ .

The CEE model will be used to fit the precession frequencies up to temperatures, where the model breaks down, close to  $T_N$ . In this high temperature range, the data will be fitted with a Kubo-Toyabe model to investigate whether the assumption is true, that the Kubo-Toyabe contribution in the data, is accounted for by the last term in (5.2.2).

I must stress, that the model does not have all the known physical restrictions of a powder sample in zero field built into it: Rather it is designed with the aim of extracting information on the precession frequency.

As the reader will see in the further analysis, this model can, beyond the precession frequency, also provide information on the distribution of the Néel temperature of the individual muon sites.

### 5.2.2.2 Model 2 - DIN

In order to analyze the general behavior of the samples I have constructed a second model, the DIN (Double INternal field distribution) model. A central issue while constructing this model has been to construct a model, which accommodates and identifies features of the sample  $\mu^+$  behavior in terms of as many significant properties as possible. The preliminary analysis, which was also used in the previous section, identified

- At least one precession component,
- At least one fast decaying component,
- At least one slowly decaying component.

From our knowledge of ideal  $\mu^+$  precession behavior in powders, the precession term (amounting 2/3 of the asymmetry) must have a 1/3 tail term associated with it. Furthermore the fast decay

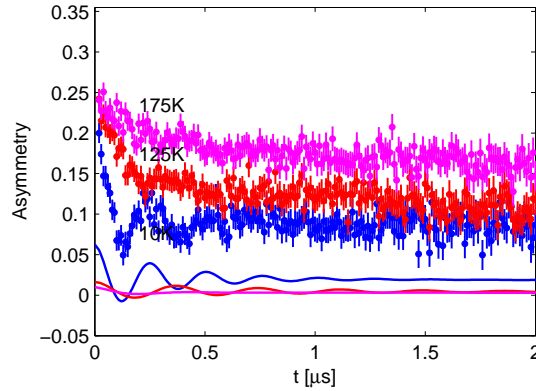


Figure 5.2.3: Example of  $\mu$ SR data (Sample 5 ( $x=0.30$ )) fitted with the DIN model. Solid lines are the fits excluding the fast dephasing component. Note how much is missing for the model to fit the data, compared the full model in figure 5.2.8.

term which is in excess (see figure 5.2.3, showing only the precession component), must also have a 1/3 term.

The DIN model, is a more specific model based on expectations to the physical behavior of the system, than the CEE model. It is given by

$$\begin{aligned}
 A(t) &= A_a \left( \frac{2}{3} \cos(2\pi\nu_a t + \varphi_a) e^{-\lambda_{2a} t} + \frac{1}{3} e^{-\lambda_{1a} t} \right) \\
 &+ A_b \left( \frac{2}{3} \cos(2\pi\nu_b t + \varphi_b) e^{-\lambda_{2b} t} + \frac{1}{3} e^{-\lambda_{1b} t} \right), \quad (5.2.4)
 \end{aligned}$$

where the first line ( $a$ ) is the common part with a decaying cosine term to account for the muonic precession (fraction 2/3), with a 1/3 tail of non-precessing muons. In principle this model is just a restricted version of the CEE model, albeit with only one exponential damping term, and a fixing of the precessing/non-precessing muon ratio.

From the preliminary analysis it was clear that a single IN (INternal field) model was not sufficient to fit the data satisfactorily. In addition to the slow decay and the precessing muons, there was a fast decay, and a 1/3 tail that was not accounted for by the model. However, no precession was detected in this component.

To account for this component, and simultaneously keep the fast (2/3) and slow (1/3) decay ratio, an additional IN term ( $b$ ) with frequency  $\nu=0$  was added to the model. The model expression (5.2.4) therefore became

$$\begin{aligned} A(t) &= A_a \left( \frac{2}{3} \cos(2\pi\nu_a t + \varphi_a) e^{-\lambda_{2a} t} + \frac{1}{3} e^{-\lambda_{1a} t} \right) \\ &+ A_b \left( \frac{2}{3} \cos(\varphi_b) e^{-\lambda_{2b} t} + \frac{1}{3} e^{-\lambda_{1b} t} \right). \end{aligned} \quad (5.2.5)$$

The physical interpretation of the second term, is that the 2/3 sub-term accounts for muons trapped in muon sites with varying magnetic environments, causing their precession to rapidly dephase. This gives rise to a significant signal close to time zero, which thereafter decays rapidly. The 1/3 term muons experience similar variation in the magnetic environment, but as the spin is parallel to the local field direction, they do not precess and only give rise to a tail.

In detail,  $A_a$  is the asymmetry of the magnetic ordered part,  $\nu_{1a}$  is the precession frequency,  $\varphi_a$  is the phase,  $\lambda_{2a}$  is the fast decay rate of the spins, describing the dephasing of the precessing muons in the ordered phase.  $\lambda_{1a}$  is the slow decay rate related to the 1/3 tail. Similarly the  $A_b$  is the asymmetry of the fast decaying component,  $\lambda_{2b}$  is the fast decay rate,  $\lambda_{1b}$  is the slow decay rate and  $\varphi_b$  is the phase.

### 5.2.2.3 Kubo-Toyabe (KT & KTE) Models

As mentioned earlier, a  $\mu$ SR spectrum from a powder sample in the paramagnetic state will have a Kubo-Toyabe shape, due to a (Gaussian/Lorentzian/Voigtian) distribution of randomly oriented local fields. The Gaussian Kubo-Toyabe (KT) model is as in (3.3.23) given by

$$A_{KT}(t) = A_{KT,0} \left( \frac{2}{3} (1 - \Delta^2 t^2) e^{-\frac{\Delta^2 t^2}{2}} + \frac{1}{3} \right) \quad (5.2.6)$$

where  $A_{KT}$  is the asymmetry of the KT part and  $\Delta$  is the KT decay rate.

During the analysis of data it was found that the KT model does not fit most of the data very well, as many of the spectra contain a fast decaying magnetic component. The simple KT model has therefore been extended to yield the Kubo-Toyabe exponential model (KTE) given by an ordinary Kubo-Toyabe added with a simple exponential

$$\begin{aligned} A_{KTE}(t) &= A_{KT,0} \left( \frac{2}{3} (1 - \Delta^2 t^2) e^{-\frac{\Delta^2 t^2}{2}} + \frac{1}{3} \right) \\ &+ A_R e^{-\lambda t}, \end{aligned} \quad (5.2.7)$$

where  $A_R$  is the asymmetry and  $\lambda$  is the decay rate of the magnetic relaxation term.

### 5.2.3 Analysis

I will in this section go through the analysis of the  $\mu$ SR data on the samples with dopings  $x=0.25$ , 0.30 and 0.35, in respective subsections. An example of the  $\mu$ SR data to be analyzed is shown in figure 5.2.4.

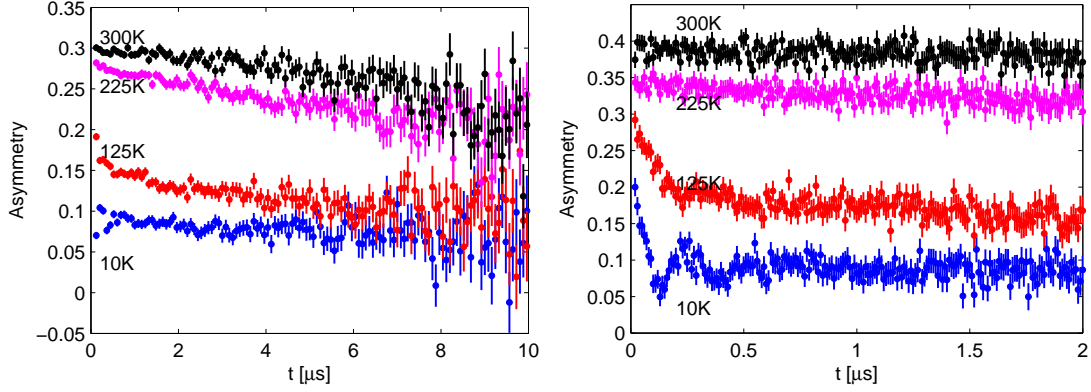


Figure 5.2.4: Examples of  $\mu$ SR raw data (Sample 5 ( $x=0.30$ )) obtained at 10 K, 125 K, 225 K and 300 K. Left: 0-10  $\mu$ s, 64 bins per point. The datasets are shifted 0, 0.02, 0.04 and 0.06 upwards, respectively, for readability. Right: 0-2  $\mu$ s, 8 bins per point. The datasets are shifted 0, 0.05, 0.10 and 0.15 upwards, respectively, for readability.

### 5.2.3.1 $x=0.25$ Analysis Details

The  $\mu$ SR sample data of the lowest doping sample were fitted with the described CEE and DIN models. The CEE fitting was quite smooth, and therefore only DIN details will be discussed here.

At low temperatures the phase  $\varphi$  was kept free during fitting, and was in all cases found to be close to  $0^\circ$ . The phase, which is dependent on the apparatus-sample interaction only, does not change during the measurement series, and the phase was therefore fixed to  $0^\circ$  at higher temperatures, in order to promote convergence of the fits.

The fitting routine converges relatively easy, and gives reasonable results at temperatures up to 100 K. Reasonable results in this context means that the model is able to describe for the entire spectrum shape.

At 125 K this is no longer entirely the case, as the dephasing component at  $t$  close to zero appears to become more linear, and deviating from the exponential shape. It is uncertain what causes this, but the model is unable to accommodate it properly.

The spectra become increasingly difficult to fit, and in order for the DIN fit not only to focus on the dephasing, the first 0.02  $\mu$ s are excluded from the fit interval. Due to the same fit difficulties, the frequency of the 225 K spectrum was fitted by hand from the Fourier Transform of the data, and the error estimated to 0.2 MHz.

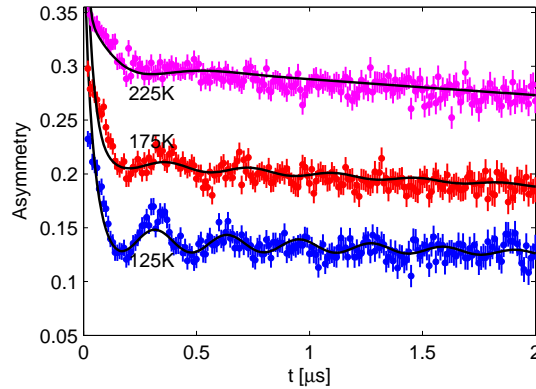


Figure 5.2.5: Example of DIN fits of Sample 4 ( $x=0.25$ ). Notice how the fits at high temperatures are unable to compensate for the fast relaxation at  $t \simeq 0-0.2 \mu$ s.

The reason for the misfit of the DIN model, illustrated in figure 5.2.5, is that the 2/3-1/3 relation that the DIN model is based on, no longer fully applies, as parts of the sample are close to  $T_N$  and exhibit a Kubo-Toyabe-like behavior.

Figure 5.2.15 (top), table 5.2.3 (CEE) and table 5.2.4 (DIN) show the fit results for both CEE and DIN models, obtained from the procedures described above.

### KT & KTE Model

A  $\mu$ SR spectrum from a powder sample in the paramagnetic state will have a Kubo-Toyabe shape, and the high temperature powder datasets (250 K, 275 K and 300 K) have therefore been fitted with a simple KT model. However, only the 300 K dataset can be fitted with this simple model, as the other datasets contain a relaxing magnetically ordered component, as shown in figure 5.2.16.

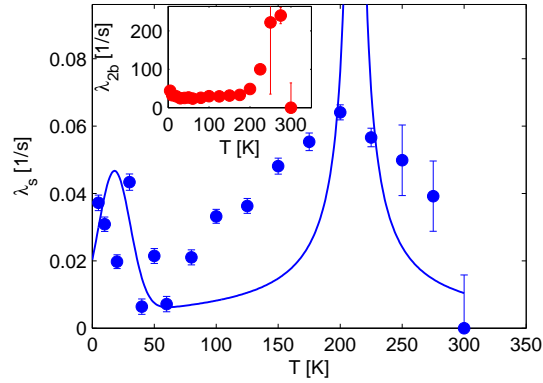


Figure 5.2.6: Sample 4 ( $x=0.25$ )  $\lambda_s$  vs  $T$  for CEE model fits. Inset:  $\lambda_{2b}$  vs  $T$  for DIN model fits. Note the increase around 250 K

The extended KTE model was therefore used for fitting the 250-300 K datasets. The KTE model fits the data quite well, except in the region 8-10  $\mu$ s, which is most likely due to the poor statistics at such high  $t$ . The KTE fit results are shown in figure E.2.7 and table E.2.10.

From the fits, it can be seen that the decay rate slowly decreases with  $T$ , and it would appear that the decline is continuous. More importantly, the magnetic part (the magnetic asymmetry), drops off to zero at 300 K, and the sample is therefore completely paramagnetic at 300 K. On the other hand, the sample is neither completely magnetically ordered nor paramagnetic at 275 K. From these considerations and from the CEE and DIN fit results, the conclusion is that the Néel temperature is lower than 300 K and most likely also lower than 250 K, as there is no uniform long range field at this temperature, but only a fast relaxing component.

### Results

Figure 5.2.15 (top) shows the extracted magnetization  $M$  versus temperature  $T$  curve, which is clearly not a simple  $M$  versus  $T$  curve. Rather the precession frequency is seen to drop rapidly from the 5 K level to a new level around 60-80 K, from where the magnetization curve looks more normal.

A similar behavior has previously been seen in bulk YBCO Sanna *et al.* [164, 165], in bulk  $Y_{1-x}Ca_xBa_2Cu_3O_6$  (YCBCO) by Niedermayer *et al.* [130], and in LSCO by Borsa *et al.* and Chou *et al.* [20, 33], and can be called the reemergence of the native-like Néel state, since the native-like state with a high staggered magnetization, not present at higher temperatures, reemerges at low temperature. This reemergence has been attributed to a freezing of the mobility (a localization) of the charge carriers (holes). The localized holes are by Gooding *et al.* [61] described as skyrmions, which will be discussed further in section 5.2.4.

To analyze this behavior, henceforth referred to as the Low Temperature (LT) phase, the high

temperature curve has been fitted with a common power law,

$$M(T) = M_0 \left( \frac{T_N - T}{T_N} \right)^\beta, \quad (5.2.8)$$

before the LT points have been fitted with a straight line on a background composed of the power law. This gives, without suggesting anything about the behavior in the LT region, an estimate on its staggered magnetism. The fit results for Sample 4 ( $x=0.25$ ) are presented in table 5.2.4 (top).

The normal phase magnetization has been fitted with a power law, although, a power law behavior strictly is only valid in the critical region. However, it provides a good approximation to the actual behavior.

The high temperature points have been selected as being the points that exhibited a regular and continuous behavior. As a consistency check of the power law fits, it is noted that the CEE and DIN models give similar power law results, and that the Néel temperature is found to be  $\sim 250$  K from both models. This finding of  $T_N$  is supported by the finding of a peak in the transverse decay rate  $\lambda_{2b}$  at  $\sim 250$  K, (see figure 5.2.6 (inset)), indicating a phase transition at this temperature.

The peak indicates that a large number of spins exhibit dephasing behavior in this temperature range, which indicates a transition from a homogenous to a non-ordered magnetic environment [131].

However there are fast decaying magnetic components up to at least 275 K, indicating that there are muon sites in the sample, that are slightly magnetically, albeit inhomogeneously, ordered up to this temperature. From it can be concluded that in these samples the concept of a single Néel temperature is not entirely valid and that the particles/regions in the sample rather exhibit a distribution of Néel temperatures. The origin of this phenomena is discussed further in section 5.2.4 and 5.3.

Turning to the asymmetries of the components in the CEE model these can also provide information on the magnetization curve of the sample, in particular in the temperature region 125-225 K. Figure 5.2.14 (top) shows the normalized asymmetries  $A_f/A_N$ ,  $A_2/A_N$  and  $A_1/A_N$ . The normalization asymmetry  $A_N$  and the total asymmetry  $A_{Tot}$  are given as

$$A_N = (A_F + A_2 + A_1) \quad \text{at } (T = 5 \text{ K}) \quad \text{and} \quad (5.2.9)$$

$$A_{Tot} = (A_F + A_2 + A_1). \quad (5.2.10)$$

Several conclusions can be drawn from the plot. The volume fraction of ordered muon sites ( $A_f$ ) drops from low temperature towards high temperature over a broad temperature range. This suggests, in agreement with the results above, that the sample is exhibiting a distribution of Néel temperatures.

$A_2$  and thus the volume fraction of muon sites with broad field distributions is also dropping, albeit at higher temperatures. The behavior of these two asymmetry ratios can be interpreted as that individual muon sites, as the magnetic order is breaking down, are going from being AFM ordered through a broad field distribution, to a paramagnetic state.

As the  $A_f$  and  $A_2$  values decrease, these are compensated by the  $A_1$  asymmetry, as the total muon volume fraction ( $A_{Tot}$ ) is (and should be) relatively constant.  $A_1$  does therefore not only describe the longitudinal muon spins, but does contain the signal from all non-magnetic muon sites, such as KT sites. For instance, KT-like features are observed in the data well below  $T_N$ .

It is noteworthy that the  $A_1$ , even at the lowest temperatures is larger than 1/3, indicating non-magnetic muon sites at all temperatures. Whether these sites are YBCO or impurity sites, can not be said.

### 5.2.3.2 $x=0.30$ Analysis Details

#### CEE Model

The fitting of the CEE model was initiated by finding the phase of the setup, by fitting the CEE

model to the 5 spectra 10-50 K. With one exception (of  $\sim 11^\circ$ ), the phase was in all cases found to be within  $1^\circ$  of zero, whence the phase was fixed to  $0^\circ$  during fitting for all temperatures.

The 10-70 K datasets were easily fitted, whereas there were moderate difficulty in fitting the 80-125 K data, well illustrated in figure 5.2.7. The fitting of the higher temperature data (150-225 K) become increasingly difficult, as the precession signal becomes weaker and the frequency falls off. In the spectra 250-300 K no precession could be identified.

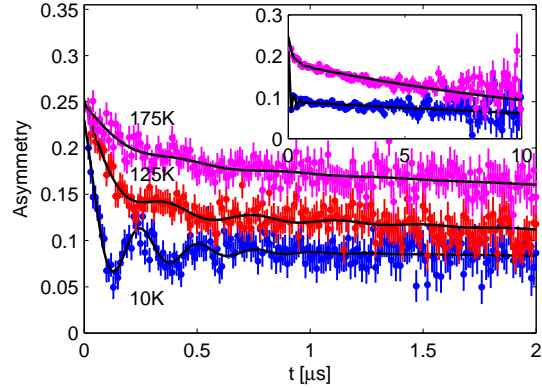


Figure 5.2.7: Selected Sample 5 ( $x=0.30$ ) data (10, 125 and 175 K) fitted with CEE model. For 10 K, note the clarity of the signal and the contrast to the 125 K and 175 K data. Inset: Same data (10 and 175 K), 0-10  $\mu\text{s}$ , showing the behavior of the data over a longer time frame.

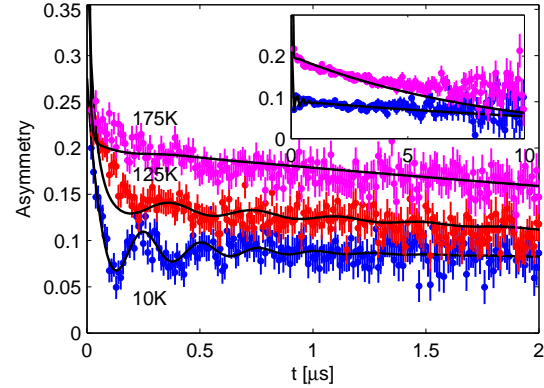


Figure 5.2.8: Selected Sample 5 ( $x=0.30$ ) data (10, 125 and 175 K) fitted with DIN model. Inset: Same data (10 and 175 K), 0-10  $\mu\text{s}$ , showing the behavior of the data over a longer time frame.

### DIN Model

Fitting of the DIN model to the Sample 5 ( $x=0.30$ ) data (see examples in figure 5.2.8) is relatively easy at low temperatures, and the parameters converge rapidly. However, the spectra become increasingly difficult to fit from 100 K and up. To promote convergence, a restriction has been applied to the asymmetry of the precession, forcing it to be smaller than the 80 K value.

The fitting algorithm does not converge on a 'by-eye'-visible frequency in the 125 K and 150 K data (visible in figure 5.2.8), which are thus fitted by hand. The error was in both cases estimated to 0.2 MHz.

The 175 K spectrum has KT-like features, and no frequency is found in the real time data. However, a frequency is visible in the fourier transform at  $\sim 2$  MHz, which is fitted manually. Even though a frequency was found manually, it is clear from the behavior of the fit, that the DIN model is seriously breaking down, as no precession signal is found by the fitting algorithm. This means, that there is no longer any homogeneity in the local magnetic fields at the muon sites, and that the model is not applicable at these temperature.

For consistency, the 200 K data was attempted fitted. No frequency was found, but the data contain instead a small and slow exponential decay on top of a Kubo-Toyabe-like feature.

### KTE Model

The datasets 175-300 K have been fitted with the KTE model. The first three (175 K, 225 K and 250 K) show signs of a dephasing exponential, whereas the 275 K and 300 K data show pure Kubo-Toyabe behavior, indicating a pure paramagnetic state.

During fitting it has been necessary to restrict the exponential  $\lambda$  of most of the spectra to a minimum, as they would go towards zero otherwise, yielding non-physical results. Figure 5.2.11 shows nicely how the volume fraction of the dephasing component  $A_{R,0}$  decreases with temperature.

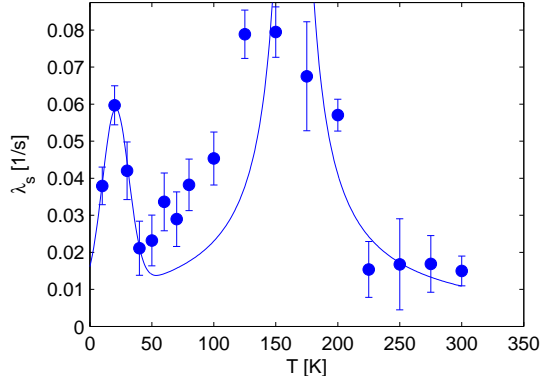


Figure 5.2.9: Sample 5 ( $x=0.30$ )  $\lambda_s$  vs  $T$  for CEE model fits. The low- $T$  peak is fitted with a Gaussian and the upper is fitted with a  $1/(T - T_0)$  model, from ref. [165].

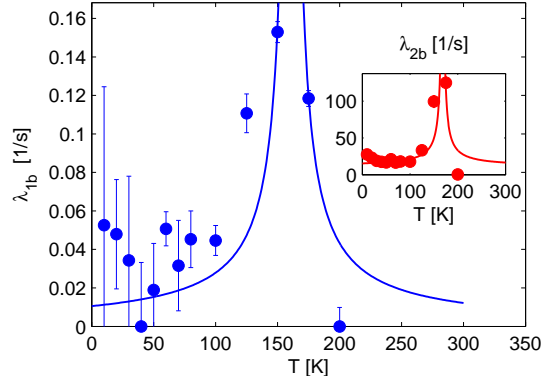


Figure 5.2.10: Sample 5 ( $x=0.30$ )  $\lambda_{1b}$  vs  $T$  for DIN model fits. The lines are guides to the eye based on a  $1/(T - T_0)$  model, from ref. [165]. Inset:  $\lambda_{2b}$  vs  $T$ .

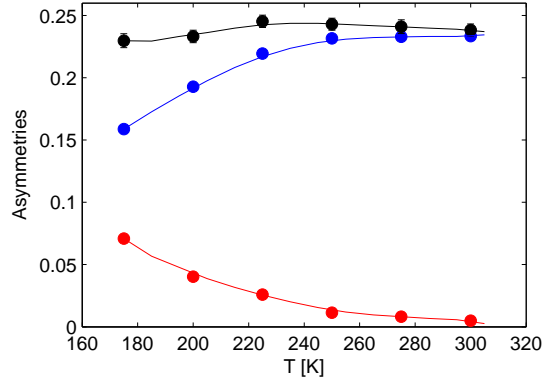


Figure 5.2.11: Sample 5 ( $x=0.30$ ). Kubo-Toyabe asymmetries. The lines are guides to the eye. ( $\bullet$ - $\bullet$ )  $A_{KT,0}$ . ( $\bullet$ - $\bullet$ )  $A_{R,0}$ . ( $\bullet$ - $\bullet$ )  $A_{KT,0} + A_{R,0}$ .

## Results

From the data it is seen that the LT phase is present at 10-50 K and absent above. To elucidate the precession frequency has been fitted with power laws, similar to the procedure in section 5.2.3.1. The results from the fitting are shown in figure 5.2.15 (middle), in table 5.2.3 (middle) and table 5.2.4 (middle).

The points deemed to belong to the LT region are chosen after careful considerations and comparisons with results from Niedermayer *et al.* (1988) [130], where a similar behavior is seen in bulk YBCO ( $Y_{0.94}Ca_{0.06}Ba_2Cu_3O_{6.02}$ ). In this paper the normal phase power law fit has  $\beta=0.2$  which is found to match the  $\beta$  found from our data within errorbars.

Comparison of the 175 K CEE and DIN fits ( figures 5.2.7 and 5.2.8 and figure 5.2.15 (middle)), it is clear that the high temperature fits of the models are quite different. However, rather than being an inconsistency, this is an example of how the CEE model is more flexible and better suited for extracting the precession frequency close to  $T_N$  than the DIN model.

Opposed to the volume fraction results from Sample 4 ( $x=0.25$ ) the  $A_f$  is decreasing and  $A_1$  rising already from low temperatures (from 30 K), as seen from figure 5.2.14 (middle). Furthermore

it is seen that the decrease of  $A_f$  at low temperature, is equally absorbed by  $A_1$  and  $A_2$ . Having noted this, the main change in the volume fractions  $A_f$  and  $A_2$  still occurs in the temperature range 100-200 K. The conclusion of this is that the homogeneity of the local magnetic environments is breaking down, *i.e.* the field distribution is broadening, from low  $T$  to  $\sim 80$  K. At  $\sim 80$  K the increase of  $A_2$  stops, and the increase in  $A_1$  gains momentum.

At 200 K the decrease in magnetically semi-/ordered muon sites ( $A_f + A_2$ ) has stopped and the volume fraction is close to zero. At this temperature, however, the detected frequency is still significant, meaning that the sample still contains some ordered muon sites.

This behavior is very similar to superparamagnetism (eq. (2.5.1)) in magnetic nanoparticles, where the magnetic moment decreases slowly with increasing  $T$ , before collapsing at a certain temperature, specific for the individual particle size.

Applying (2.5.1) to a distribution of particle sizes we get a transition where the fraction of magnetically ordered sites decreases gradually with  $T$ , albeit the magnetization of the ordered sites is still finite.

In the  $\mu$ SR data, this behavior is seen as a very significant decrease in the ordered muon site volume fraction, without a corresponding decrease in precession frequency. This indicates a very broad field distribution, with some sites totally non-ordered and others fully ordered, but does not give information on whether is due to two discrete populations or a continuum of populations.

### 5.2.3.3 $x=0.35$ Analysis Details

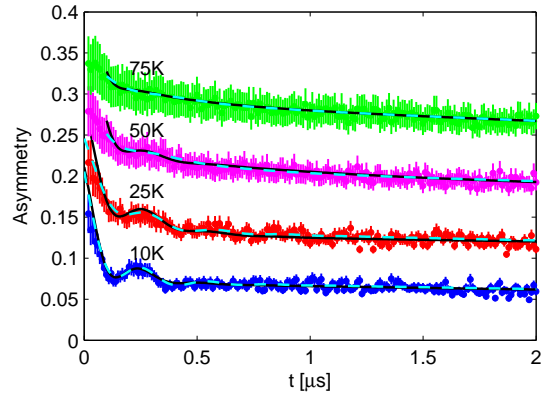


Figure 5.2.12: Raw  $\mu$ SR datasets of Sample 3 ( $x=0.35$ ), 0-2  $\mu$ s. Bin size is 8. The lines are the fitted CEE (---) and DIN (—) models. The fit interval is indicated through the extent of the model curves. The data have been displaced vertically for readability.

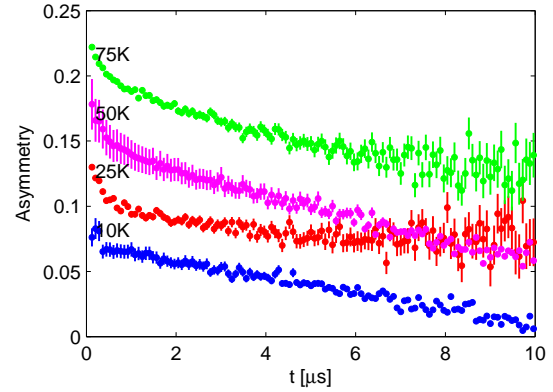


Figure 5.2.13: Raw  $\mu$ SR datasets of Sample 3 ( $x=0.35$ ) (10 K, 25 K, 50 K and 75 K), 0-10  $\mu$ s. Bin size is 64. The data have been displaced vertically for readability.

The CEE model fitting of the Sample 3 ( $x=0.35$ ) data (examples shown in figure 5.2.12) was quite smooth. The only detail worth mentioning is that a fitting interval length of 6 ms, is used for the 50, 75 and 100 K datasets to improve convergence. No information is lost in this, as the data from 6 to 10 ms are very noisy. The found fit parameters are found in table E.2.4.

As above, a reduced fitting interval of 6 ms was used in the DIN model fitting. During the fitting process, however, it was considerably more difficult to obtain convergence using this model than using CEE model. Examples of fitted and raw datasets are shown in figures 5.2.12 and 5.2.13, respectively.

All parameters were left free while fitting the 10 K and 25 K data, except  $\varphi=0$ , and convergence was easily obtained. However, already the 50 K and 75 K datasets were very difficult to fit. Especially, it was difficult to fit the precession frequency, which either tended to go to zero or to

very high values. However, convergence was ultimately achieved by applying some fit parameter restrictions, such as an upper bound for  $\lambda_{2a}$ , by restricting  $\lambda_{2b}$  to  $[20;100] \mu\text{s}^{-1}$  and by omitting to fit to the first  $0.1 \mu\text{s}$  data.

At 100 K precessions can not be identified, and the fit also gives a frequency of close to zero. There are still dynamic phenomena, as there is a fast dephasing component below  $0.1 \mu\text{s}$ . The 125 K dataset contains no detectable frequency, which is therefore set to zero in the fit.

As an observation, it is noted considering the data in figure 5.2.13, that only the 25 K data does not have a slow longitudinal decay ( $\lambda_s$  in CEE and  $\lambda_{1a}$ ,  $\lambda_{1b}$  in DIN), indicating that the sample is in some state of phase transition at the other temperatures. Conclusively it is found that the Néel temperature of the system is close to 100 K.

### KTE Model

Applying the KTE model to temperatures 75 K and 100 K gives good fits. From the fit results (table E.2.6), the KT component accounts for  $\sim 65\%$  and  $\sim 74\%$  respectively of the muon sites, and the dephasing part for  $\sim 35\%$  and  $\sim 26\%$ . Thus the sample is exhibiting an increasing KT behavior with  $T$ .

The fitted KTE datasets (75-125 K) are shown in figure 5.2.17. Of these, 75 K dataset contains a visible precession component around  $t \simeq 1.5 \mu\text{s}$ , which has disappeared at 100 K. Comparing to the Sample 4 ( $x=0.25$ ) KTE fits we are still not entirely in the paramagnetic region at 100 K, as the dephasing component is still present. However, there is no precession, and the sample may therefore be considered paramagnetic, with a  $T_N$  of at most 100 K.

### Results

Considering the extracted fit data shown in figure 5.2.15 (bottom), the field from the reemergence is quite significant, as in the other two samples. However, contrary to the other samples it extends to  $2/3$  of  $T_N$  (in the CEE model). The Néel temperature has been found to be  $\sim 100$  K, which is significantly lower than in the other two samples, but not unexpected considering the high doping.

Fitting the precession frequencies from the CEE and DIN models with power law models (shown in figure 5.2.15 (bottom)), has proved difficult, due to the low number of data points, and a number of restrictions have therefore been applied.

- The normal phase ( $T_N$ ) power law  $\beta$  for the CEE model has been fixed to 0.2 (value from ref. [130]).
- In the data extracted using the DIN model it is very difficult to determine which points belong to the LT phase.  $T_f$  has therefore been restricted to a minimum of 17.5 K, as this is the midpoint between 10 K and 25 K – the only relatively clear LT points in the DIN model results.
- $T_N$  (in CEE and DIN) has been fixed to 100 K, and an error of 10 K has been estimated.

Analyzing the volume fraction behavior of this sample ( figure 5.2.14 (bottom)), it is seen that the precession volume fraction  $A_f$  has a very low value, significantly lower than  $A_2$  at low  $T$ . The non-precessing component  $A_1$  has a value close  $1/3$ , also indicating that most muons sites in the sample have a local magnetic field, albeit the large fast dephasing component also indicates a broad field distribution. As expected, the  $A_f$  and  $A_2$  decrease from low temperature, and the  $A_1$  volume fraction increases, until it reaches a plateau at 100-125 K.

## 5.2.4 Discussion

In this section the results from the  $\mu\text{SR}$  measurements on the nano-YBCO will be discussed. Through the discussion, the focus will be on the behavior of the extracted parameters versus oxygen doping  $x$ .

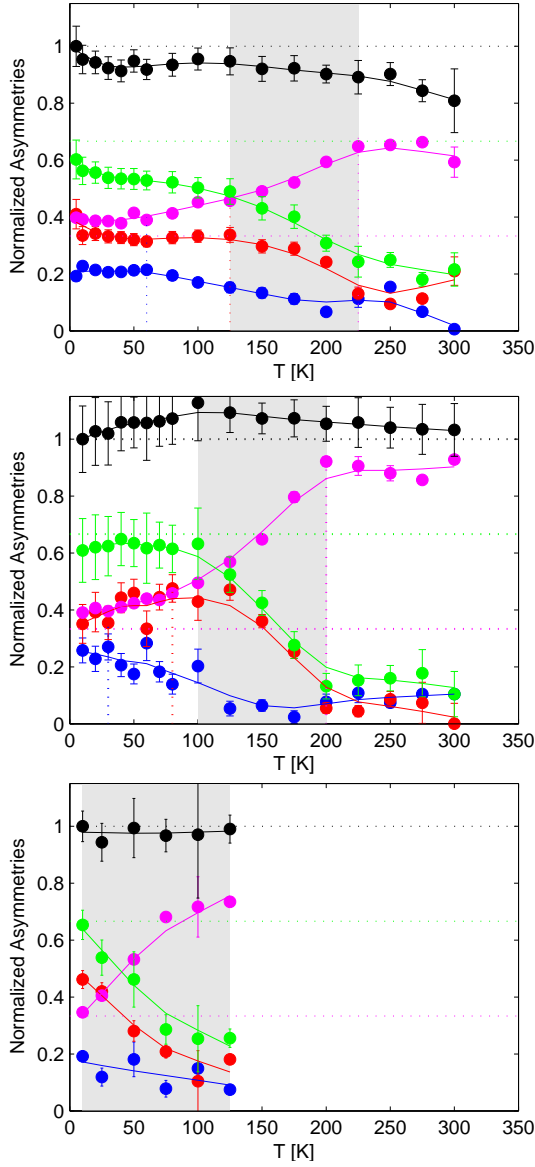


Figure 5.2.14: *Asymmetries ratios vs. temperature for CEE model, normalized to  $A_N$  at 5 K. The dotted lines are guides to the eye at 1/3, 2/3 and 1. The gray areas indicate the transitions temperature range. Top: Sample 4 ( $x=0.25$ ). Middle: Sample 5 ( $x=0.30$ ). NB. The increase in  $A_f$  at higher temperatures is non-physical. Bottom: Sample 3 ( $x=0.35$ ). Symbols: (●)  $A_f/A_N$ . (●)  $A_2/A_N$ . (●)  $A_1/A_N$ . (●)  $(A_f + A_2)/A_N$ . (●)  $A_{Tot}/A_N$ .*

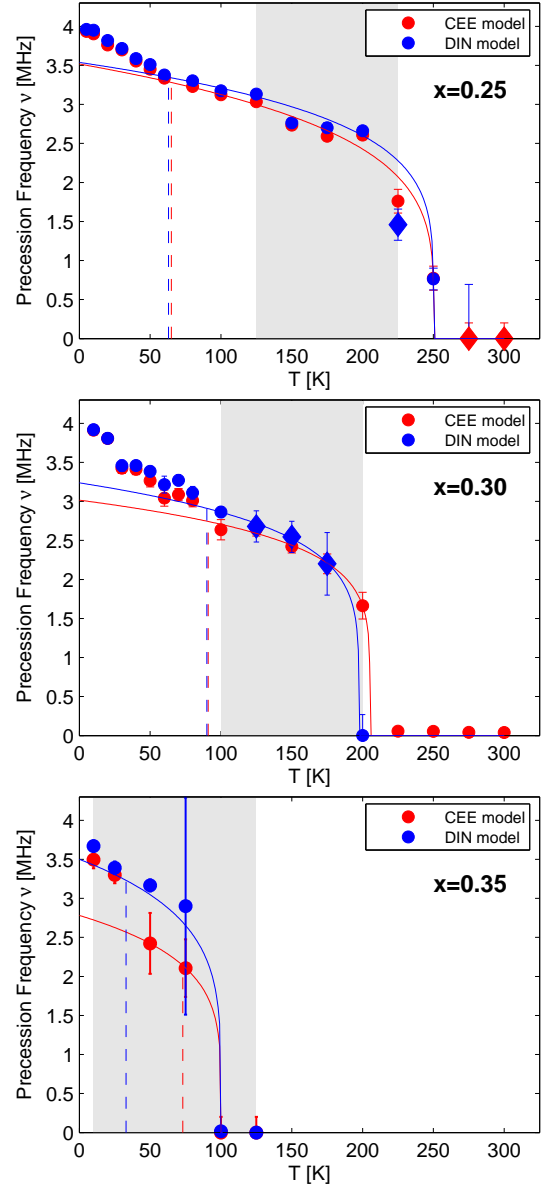


Figure 5.2.15: *Precession frequencies  $\nu_f$  from the CEE model and  $\nu_a$  from the DIN model for the nano-YBCO samples. The diamond marked points are manually fitted. The lines are power law fits to the normal phase magnetization. The gray areas indicate the asymmetry transitions temperature range. Top: Sample 4 ( $x=0.25$ ). Middle: Sample 5 ( $x=0.30$ ). Bottom: Sample 3 ( $x=0.35$ ).*

### Néel Temperature vs. Doping

The data has been fitted and analyzed using two different models, the CEE and DIN models. From the smoothness of the frequency curve, ease of fitting and general behavior it has been chosen

Parameter	Value
$\nu_{g,0}$	0.49(3) MHz
$T_f$	65(3) K
$\chi^2$	0.327
$\nu_{f,0}$	3.52(5) MHz
$T_N^{\dagger}$	250(13) K
$\beta$	0.231(19)
$\chi^2$	4.179

Parameter	Value
$\nu_{g,0}$	0.96(6) MHz
$T_f$	91(7) K
$\chi^2$	1.934
$\nu_{f,0}$	3.0(3) MHz
$T_N$	210(11) K
$\beta$	0.16(10)
$\chi^2$	12.367

Parameter	Value
$\nu_{g,0}$	0.9(2) MHz
$T_f$	70(13) K
$\chi^2$	0.492
$\nu_{f,0}$	2.8(4) MHz
$T_N^{\ddagger}$	100(10) K
$\beta^{\S}$	0.2
$\chi^2$	0.000

Table 5.2.3: CEE model precession frequencies fitted with power law models.  $\beta$  has been fixed to 1 for all LT phase fits. Top: Sample 4 ( $x=0.25$ ). Middle: Sample 5 ( $x=0.30$ ). Bottom: Sample 3 ( $x=0.35$ ). Symbols:  $\dagger$ )  $T_N$  has an estimated error of 12.5 K.  $\ddagger$ )  $T_N$  has an estimated error of 10 K.  $\S$ )  $\beta$  has been fixed to 0.2 (value from ref. [130]).

Parameter	Value
$\nu_{g,0}$	0.494(18) MHz
$T_f$	63(3) K
$\chi^2$	0.661
$\nu_{f,0}$	3.54(3) MHz
$T_N^{\dagger}$	250(13) K
$\beta$	0.191(11)
$\chi^2$	6.545

Parameter	Value
$\nu_{g,0}$	0.71(6) MHz
$T_f$	90(9) K
$\chi^2$	1.676
$\nu_{f,0}$	3.2(8) MHz
$T_N^{\dagger}$	200(13) K
$\beta$	0.2(5)
$\chi^2$	0.025

Parameter	Value
$\nu_{g,0}$	0.3(2) MHz
$T_f$	30(20) K
$\chi^2$	2.377
$\nu_{f,0}$	3.50(11) MHz
$T_N^{\ddagger}$	100(10) K
$\beta^{\S}$	0.2
$\chi^2$	4.782

Table 5.2.4: DIN model precession frequencies fitted with power law models.  $\beta$  has been fixed to 1 for all LT phase fits. Top: Sample 4 ( $x=0.25$ ). Middle: Sample 5 ( $x=0.30$ ). Bottom: Sample 3 ( $x=0.35$ ). Symbols:  $\dagger$ )  $T_N$  has an estimated error of 12.5 K.  $\ddagger$ )  $T_N$  is fixed to 100 K and has an estimated error of 10 K.  $\S$ )  $\beta$  has been fixed to 0.2 (value from ref. [130]).

to rely more on the results from the CEE model. This model was, as mentioned, expected to be more useful in extracting the precession frequency, as it has fewer physical restrictions. However, the DIN results will be used where they are applicable.

From the asymmetries (figure 5.2.14) and the magnetization (figure 5.2.15), it is likely that we have a distribution of Néel temperatures  $T_N$ . This finding is supported by the broadness of the divergence of the  $\lambda$ 's at 150-200 K in figures 5.2.6-5.2.10. Due to the small particle size and the careful doping procedure, which both ensure homogenous doping, the  $T_N$  distribution is not likely to be caused by variation in oxygen content of the particles. Rather it is a finite size effect, since a variation of particle size changes the surface to volume ratio, affecting the number of surface to bulk spins.

It is well known, as discussed in section 2.5, that the behavior of the spins in a magnetic material is very dependent on the particle size. Examples of this are seen in superparamagnetism, and in surface spin canting in nanoparticles, making a significant contribution to the overall magnetic properties of a sample/system.

There are two possible models which can explain the  $T_N$  distribution:

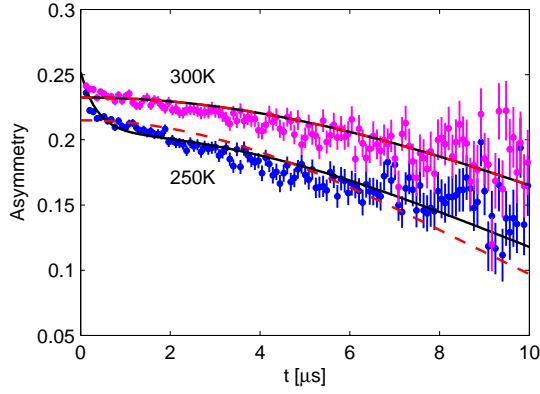


Figure 5.2.16: *Sample 4 ( $x=0.25$ ) KT and KTE fitted data.* Lines: (---) KT model, fitting neither spectrum very well. (—) KTE model, fitting the data better than the KT model at 250 K, whereas the 300 K fit is very similar to that of the KT model. The poor fitting at high  $t$  is due to poor statistics.

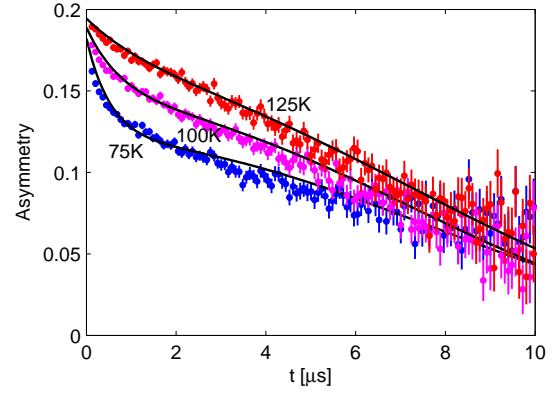


Figure 5.2.17: *Sample 3 ( $x=0.35$ ) KTE model fitted data.* From bottom: 75 K with visible precession and magnetic dephasing components. Only matching the KTE model moderately. Middle: 100 K with magnetic dephasing component visible, and vanishing precession component. Top: 125 K. Almost pure KT, with a decreasing magnetic component.

- Gradual melting of the staggering of the spins in all the particles simultaneous, starting at the surface, working its way towards the center of the particle. This could cause the  $T_N$  distribution, as the particle size distribution would cause the smallest particles to become paramagnetic before the large particles. This has previously been observed in disc-shaped particles by Klausen *et al.* (2002) [86].
- Collective magnetic fluctuations of the spins in the particles, on a time scale faster than measurements' time scale, similar to that seen in superparamagnetism. In this case, the individual particles would appear magnetically ordered when the fluctuations were slow. This effect would occur below the blocking temperature, where the thermal energy is comparable to the anisotropy energy in the particle.

Both of the described models explain the behavior seen in our samples. There are of course differences in the behavior, given the size (diameter and thickness) distributions, but as these are not known in exact detail, it is difficult to determine which model is more correct.

As the high  $T$  of the disappearance of the magnetic order is double that of the onset  $T$ , the Néel-Brown expression (2.5.1) dictates that the largest particles have twice the volume of the smallest - a condition easily fulfilled with the present size distribution, shown in section 4.7.3.

A gradual melting of the spins from the surface and inwards in disc-shaped particles also previously has been reported [86], this scenario is also quite likely, to explain the observed disappearance of the magnetic order, with the found size distribution. I will discuss this matter further in section 5.3.

### $T_f$ vs. Doping

We now consider the reemergence of the staggered magnetization (or native-like Néel state) at low temperatures, which is observed in all the  $\mu$ SR-measured samples. The reemergence temperature or the freezing temperature  $T_f$  is extracted from the precession frequency fits, using the temperature where the reemergence disappears as definition of  $T_f$ . The phase transition of the reemergence is also observed as low- $T$  peaks in the longitudinal  $\lambda_s$ , shown in figures 5.2.6 and 5.2.9. The expression used as guide to the eye in these figures stems from ref. [165].

In opposition to the definition chosen here,  $T_f$  has elsewhere in literature *e.g.* refs. [130, 165], been defined as the top-point of the longitudinal  $\lambda$  peak. I have not chosen this definition, since an

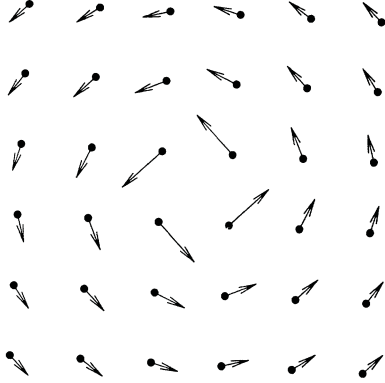


Figure 5.2.18: An example of a skyrmion state. The length of the arrows illustrates the projection of the spin on the paper plane. At infinity the spin point out of the paper. Reproduced from [61].

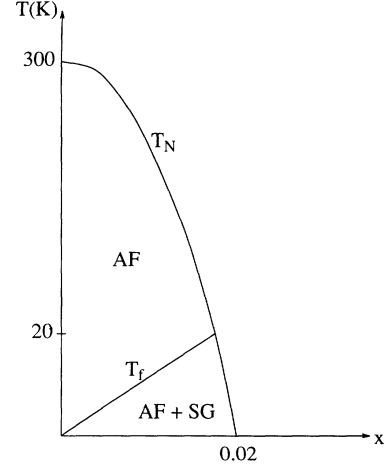


Figure 5.2.19: Schematic phase diagram of the weakly doped LSCO system showing that at temperatures below  $T_f(x)$  ( $x$  is here hole doping) a coexisting antiferromagnetic long range order and a spin-glass-like transverse spin component phase is observed. From [61].

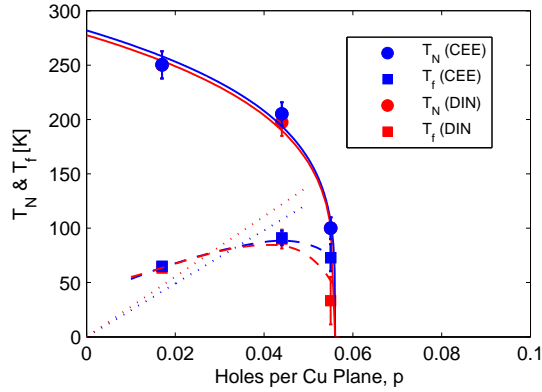


Figure 5.2.20:  $T_N$  and  $T_f$  vs. hole doping  $p$  for nano-YBCO. The (—, —) are guides to the eye for  $T_N$  vs.  $p$  and gives an estimate of transition doping  $p_C$ . (---, ---) are guides to the eye for  $T_f$  vs.  $p$ . (····, ····) are the best linear fit to  $T_f$  points, with fixed  $T_f(p=0)=0$  K.

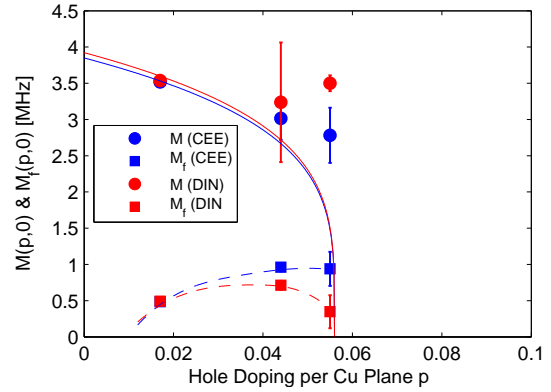


Figure 5.2.21:  $M(p,0)$  and  $M_f(p,0)$  vs.  $p$  for CEE and DIN models. (—, —) are fits to the Borsa model (5.2.17) [20] (see text). The critical doping  $p_C$  being that found from  $M(p,0)$  vs.  $p$  fits. (---, ---) are guides to the eye for  $M_f(p,0)$ .

extraction of such a peak was difficult using my data. The two definitions are, however, compatible as the  $T_f$ 's are proportional.

The reemergence of the native-like Néel state is caused by localization of holes, which at high temperatures are dynamic, *i.e.* the time scale of the hole dynamics, is similar or shorter than that of the experimental technique.

While the holes are dynamic, all spins will be seen as frustrated, yielding a reduced staggered magnetization. The localization creates localized frustrated spins which are canted/have a transverse spin component, but will leave most spins non-frustrated. Thus, the staggered magnetism converges toward the non-doped value at very low temperature, where the hole dynamics become very slow.

On a more theoretical level, Gooding *et al.* (1994) [61] suggest an in-plane (2D) skyrmion model as explanation for the reemergence of the local field observed by Chou *et al.* (1993) [33]. A skyrmion (see figure 5.2.18) is a feature or disturbance in the topology of the spin landscape caused by the presence of an impurity, such as a Sr ion in LSCO just below the spin plane. From this model they find an interaction energy of

$$E_{int} = 2 \cdot 3^2 \frac{1}{2} k_B T_f, \quad (5.2.11)$$

where  $3^2$  is the number of static degrees of freedom and 2 comes from the kinetic and dynamical component of the quantum spins,  $\frac{1}{2} k_B T$  comes from each degree of freedom and  $T_f$  is the spin freezing temperature.

The finding by Keimer *et al.* (1992) [82] that the spin-spin correlation length in LSCO is  $\xi(p, T) \sim 1/\sqrt{p}$  at  $T = 0\text{K}$  supports the assumption made by Gooding, that the separation between Sr defects  $\ell$  is related to the hole doping  $p$  as  $\ell \propto 1/\sqrt{p}$ . Using the assumption that  $T_f \propto |E_{int}|$  and the finding that the interaction energy  $E_{int}$  between two skyrmions with opposite topological charges, is related to  $\ell$  as  $E_{int} \propto 1/\ell^2 \propto 1/p$ , then leads to the expression

$$T_f \propto p. \quad (5.2.12)$$

Which by insertion of values, and under certain assumptions leads to a numerical value of

$$T_f(p) \simeq (784\text{K})p, \quad (5.2.13)$$

which matches the empirical value of

$$T_f(p) \simeq (815\text{K})p, \quad (5.2.14)$$

from ref. [33], found using  $\text{La}^{139}$  nuclear quadrupolar resonance. Here  $p$  is the hole doping or skyrmion concentration per Cu-plane.

Figure 5.2.20 shows my results on the  $T_N$  and  $T_f$  as function of hole doping  $p$ . The  $T_f$  points have been fitted with a line, to provide comparison with (5.2.13) and (5.2.14). The found YBCO reemergence slopes,

$$T_f(p) = 2450(130)\text{K}p \quad (\text{CEE model}), \quad (5.2.15)$$

$$T_f(p) = 2770(150)\text{K}p \quad (\text{DIN model}), \quad (5.2.16)$$

differ somewhat from the values in (5.2.13) and (5.2.14). Furthermore it is clear from the figure, that the linear shape proposed by Gooding *et al.* does not match my data.

On the other hand, my findings with a curved  $T_f$  versus  $p$  matches well the  $T_f$  versus  $p$  curve shape for bulk YBCO found by Sanna *et al.* (2004) [164].

The similar curved behavior of bulk and nano YBCO  $T_f$  stands in contrast to the linear behavior in impurity-doped HTSC's like LSCO [33, 61, 130] and YCBCO [130, 164]. The different behavior could indicate that the mechanism behind the freezing of the holes is affected by the specific location of the dopant within the unit cell and its concomitant influence on the charge carries in the  $\text{CuO}_2$  planes.

### Saturation Magnetization versus Doping.

Borsa *et al.* (1995) [20] discuss a decrease in staggered magnetization  $M(p, T)$  of the YBCO-related LSCO, where  $p$  is the Sr doping factor. They provide the empirical formula for staggered saturation magnetization  $M(p, 0)$  versus doping

$$\frac{M(p, 0)}{M(0, 0)} = \left(1 - \frac{p}{p_c}\right)^n, \quad (5.2.17)$$

where they use  $p_c = 0.023$  and  $n = 0.236$ .

Observing this relation for the staggered magnetism in LSCO, it is tempting to attempt to extend this formula to YBCO as well. Figure 5.2.21 shows the  $M(p, 0)$  of the staggered normal antiferromagnetic phase and the  $M_f(p, 0)$  of the LT phase component, with power law fits to  $M_f(p, 0)$ .

From fitting the data with the empirical power law (5.2.17) (using  $p_c=0.056$ ) a  $M(0, 0)$  of 3.85(6) MHz and 3.92(4) MHz for the CEE and DIN model results respectively, with fixed  $n$ 's. These values lie relatively close to the YBCO( $x=0$ ) value of 4.2 MHz [23, 131, 165]. The  $n$ 's were fixed as my data are too poor to fit the exponent. Instead a comparison is made, concluding that the normal phase points do not match the prediction from Borsa *et al.* well.

There are numerous possible explanations for the mismatch. One could be a poor determination of  $M(p, 0)$  at high  $p$ . Another could be that LSCO and YBCO have significantly different properties *e.g.* being single plane and double plane systems respectively. A third factor, already mentioned, is the different dopants which enter the structures differently.

Lastly, considering the normal phase data in figure 5.2.21, it is not unthinkable that the exchange interaction between the double layers act to stabilize the magnetism, giving high  $M(p, 0)$  values even at high dopings, an effect which would be absent in LSCO.

## 5.3 Conclusion

In this section the results of the present first-ever neutron diffraction and  $\mu$ SR study of nanosized YBCO particles will be discussed, inter-compared and compared with results from literature.

From the focal-point of the studies, the Néel temperature and the magnetization behavior, it will be attempted to draw conclusions, and to draw the results into a broader picture of the physics of the nanosized YBCO particles.

### 5.3.1 Magnetic Field Response

At the present stage, the results of the high field neutron experiments, are not conclusive. While the staggered magnetization in the  $x=0.20$  sample is reduced, it increased in the  $x=0.35$ . Are these results real or not?

As mentioned, one would not expect a response if the sample behaves as a bulk sample. On the other hand, a significant part of the spins are located at the particle surface, and should thus have a lower anisotropy energy.

I have suggested that the response of the sample with low doping is caused by spin canting, and that the response of the sample with high doping is caused either by spin flopping or enhancement of magnetism related to some competition of order parameters.

### 5.3.2 Nano and Bulk Magnetization from Neutron Diffraction

Figure 5.3.1 shows a comparison of  $T_N$  versus oxygen doping  $x$  found for the nano-YBCO using the Simple Model and the  $hkl$  Model approaches, compared to bulk values found by Rossat-Mignod *et al.* [159] and Tranquada *et al.* [188].

A comparison is hampered by the different  $x_C$  found for the nanoparticle- and bulk samples. I find the doping values reported by refs. [159, 188] (both from 1988) a bit high compared to  $x_C$  values found in newer literature, where *e.g.* Stock *et al.* (2002) [182] report 0.35.

Without claiming that my doping values are highly precise, I believe them to be relatively accurate, as they were doped using a well documented and investigated method. The doping accuracy is further enhanced by the nanoscale of the particles, facilitating homogeneity, due to the short diffusion path of the oxygen.

To facilitate a direct comparison the doping value of the Rossat-Mignod and Tranquada data has been scaled down to match the value of the nanosized YBCO (shown with dashed lines in

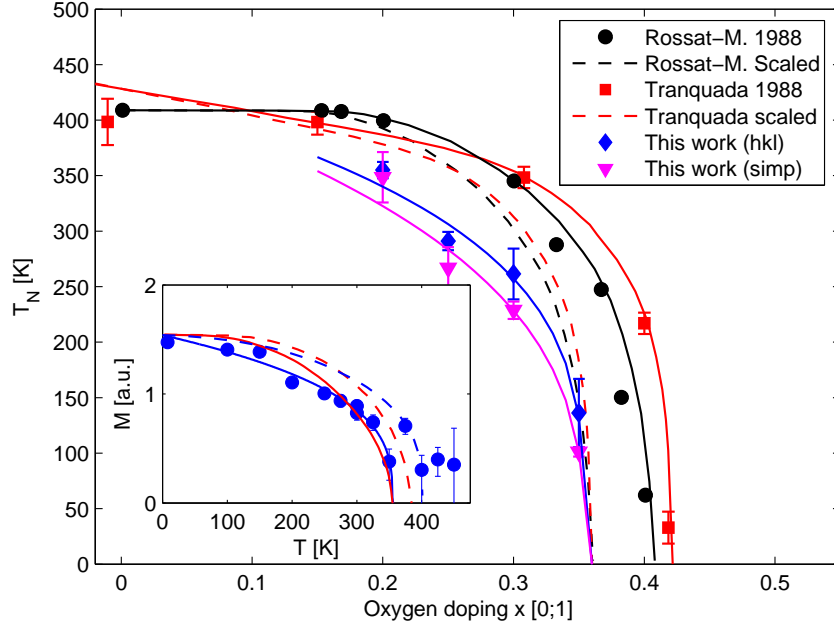


Figure 5.3.1: Comparison of  $T_N$  for the nanosized to bulk samples by refs. [159, 188]. (- $\blacklozenge$ -) is the hkl Model result. (- $\blacktriangledown$ -) is the Simple Model result. (- $\blacksquare$ -) the bulk data from ref. [188]. (- $\bullet$ -) is from ref. [159]. (- -) and (- -) are bulk data scaled to match the  $x_C$  for the nanoparticle samples. Inset:  $M$  vs.  $T$  for (-) nano-YBCO ( $x=0.20$ ) and (- -) bulk ( $x=0.20$ ) [159]. For comparison,  $M$  vs.  $T$  for NiO powders, (-) particle-average  $M$  for a 7 layer disc and for (- -) bulk.  $M_0$  of NiO and bulk YBCO, and  $T_N$  of NiO have been scaled to that of nano YBCO.

figure 5.3.1). The down-scaled  $T_N$  versus  $x$  curve matches well with values found by Lavrov *et al.* (1999) [101].

Using the down-scaled curves for comparison we see that the nanosized samples, at dopings below  $x_C$ , seem to have a lower Néel temperatures than the bulk samples, and that the difference is relatively constant.

The  $M$  versus  $T$  curve also differs from bulk, and seems more linear (larger  $\beta$ ), than that of bulk materials (in ref. [159]) as seen from figure 5.3.1(inset).

Both a reduced  $T_N$  and a more linear-like  $M$  versus  $T$  curve has previously been reported by Klausen *et al.* (2002) [86] for antiferromagnetic disc-shaped NiO particles of thickness 2 nm. The different behavior of the nanoparticles is here attributed to shape, finite size effects and uncompensated surface spins. In particular, the magnetic behavior of the individual layers with temperature is different, as well as the thickness of the particles affects the magnetic behavior.

Besides the similarities in shape, the YBCO and NiO particles both have approximately the same number of magnetic layers. The YBCO particles have a thickness of approximately  $\sim 4.4$  nm giving  $\sim 3.7$  unit cells and  $\sim 7.5$  magnetic layers, which should be compared to 7 layers in the NiO particles.

NiO and YBCO are both Heisenberg antiferromagnets, but differ as they are 3D  $\mathbf{S} = 1$  and 2D  $\mathbf{S} = 1/2$  Heisenbergs [89, 188], with magnetic propagation vectors of  $(\frac{1}{2}\frac{1}{2}\frac{1}{2})$  [155] and  $(\frac{1}{2}\frac{1}{2}1)$  [188], respectively. However, the reduction of  $T_N$  along with the behavior of the magnetization curve of the nanosized YBCO, gives the nano-YBCO system behavior some resemblance to that of the NiO nanoparticle system, indicating that this is a phenomena related to the disc-like shape.

Tranquada *et al.* (1989) [189], have found the exchange interaction in plane to  $J_{a,b} = 80^{+50}_{-30}$  meV, the exchange interaction between nearest neighbor  $\text{CuO}_2$  planes is  $J_c \gtrsim 2$  meV and between the next-nearest neighbor planes to be  $J_{c'} = 0.020(5)$  meV.

It should here be kept in mind, that YBCO is special case compared to other layered structures,

as it has 'isolated' pairs of 2D layers, as illustrated in figure 5.3.2. What is new in the results presented here is that the very weak coupling via the isolating CuO planes seems to be significant, for the overall magnetic order of the planes.

I can not entirely rebut that the reduced magnetization is due to the reduced  $a$ - $b$ -dimensionality, I find it most likely that the reduced magnetization is caused by the reduced  $c$ -axis dimensionality of the particles.

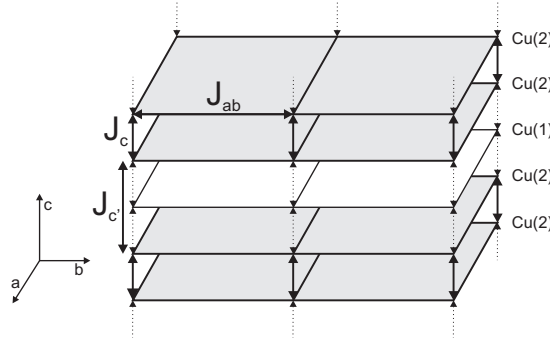


Figure 5.3.2: *Schematic illustration of the strong coupling between the double layers, and the weak coupling to the non-magnetic layer. The values for  $J_{a,b}$ ,  $J_c$  and  $J_{c'}$  are given in the text.*

Which again indicates that the  $J_{c'}$  component (see figure 5.3.2) in the YBCO Heisenberg is significant. This supports previous results [82], which show that there is a small but finite  $c$ -axis coupling, and is a prediction already made by the Mermim-Wagner theorem, as YBCO displays staggered magnetism.

Bozovic (1991) [21] has shown that the behavior of superconductivity in cuprates (YBCO, LSCO etc.) behaves bulk-like if the dimensions of the system is larger than a few (2-5) nm, and that  $T_C$  in YBCO thin films does not scale with number of layers, indicating that the superconductivity is a purely 2D phenomena. However, the above results seem to indicate that this is not the case for the staggered magnetism in YBCO, which seems to be affectable by disc-thickness.

### 5.3.3 Nano and Bulk Magnetization from $\mu$ SR

Figure 5.3.3 shows  $M$  versus  $T$  measured with  $\mu$ SR for the nanosized YBCO samples of this work, for bulk YBCO samples [113, 165], and YCBCO ( $Y_{0.94}Ca_{0.06}Ba_2Cu_3O_{6.02}$ ) [130]. The doping of YCBCO is given as holes per plane and has for comparison been converted to the equivalent oxygen doping using the  $p$ - $x$  relation given through figure 2.4.8.

As seen from the figure, the  $T_N$  versus doping  $x$  for the nano and bulk samples are fairly similar (considering that the doping values of bulk and nano do not match). However, the nanosized samples, have a higher magnetization, and a much steeper drop-off (lower  $\beta$ ) close to  $T_N$ . This is most surprising, and can only be explained by uncertainties/error in the doping degree, such that the supplied bulk doping is too low, or that the nano-sample doping is too high. Indeed comparison of  $T_N$  from ref. [165] to the phase diagram in their later paper [164] (see figure 5.3.7), would indicate that the doping reported in ref. [165] is higher than reported.

Assuming that this is indeed the case, and we instead take the saturation magnetization, excluding reemergence, to represent the doping level, we see that the  $T_N$  of the nanosized samples is systematically  $\sim 30$ -70 K lower than that of bulk. Conclusively also  $\mu$ SR finds nanoparticle  $T_N$  to be lower than bulk  $T_N$ .

### 5.3.4 Magnetization from Neutron Diffraction and $\mu$ SR

Using both neutron diffraction and  $\mu$ SR the Néel temperature of the nano-YBCO samples has been measured, as shown in figure 5.3.4. From the data it is found that the  $T_N$  through  $\mu$ SR is  $\sim 40$ -60 K lower than that found from neutron diffraction.

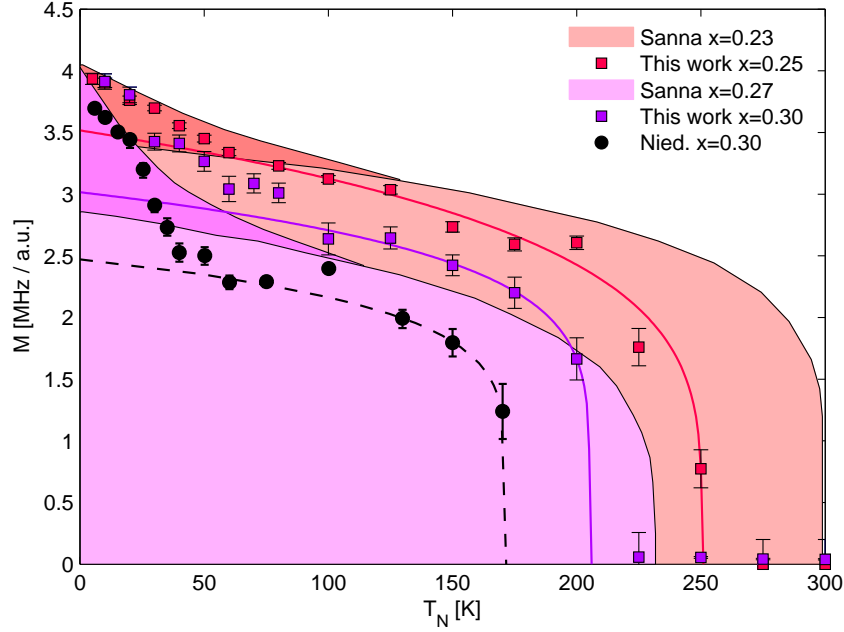


Figure 5.3.3:  $\mu$ SR data (CEE) for nano-YBCO, bulk YBCO [113, 165] and  $Y_{0.94}Ca_{0.06}Ba_2Cu_3O_{6.02}$  [130]. The shaded areas are fits from ref. [165]. The light shaded areas are high temperature  $M$  power law fits, and the darker shaded areas are the fields from the reemergence of the native-like Néel state. The black points and dashed curve are  $Y_{0.94}Ca_{0.06}Ba_2Cu_3O_{6.02}$  ( $\Rightarrow x \sim 0.30$ ) from ref. [130]. The solid colored lines and colored points are fits and data of the nanosized YBCO samples (CEE model).

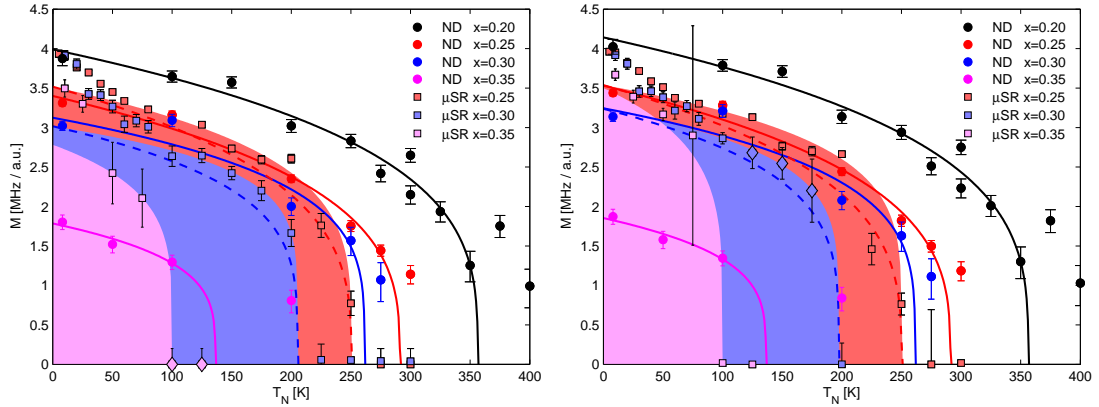


Figure 5.3.4:  $\mu$ SR and neutron data.  $M$  vs.  $T$  measured with neutron diffraction (ND) and  $\mu$ SR. All neutron data are extracted using  $hkl$  Model fitting. Neutron data are scaled to  $\mu$ SR scale. Shaded areas are  $\mu$ SR data power laws. Solid lines are neutron data power laws. Dashed lines are neutron data power laws scaled to  $\mu$ SR results. Left:  $\mu$ SR CEE model data vs. neutron data. Right:  $\mu$ SR DIN model data vs. neutron data.

The neutron magnetization curve is flatter than the  $\mu$ SR curve, which is particularly clear from the dashed curves in figure 5.3.4. As the datasets differ only by measurement technique, the explanation most likely lies here. In this context, the main difference between neutron diffraction and  $\mu$ SR is the measurement time scale and the nature of the measurements. The time scales of neutron scattering and  $\mu$ SR are  $\sim 10^{10}$ - $10^{13}$  Hz and  $\sim 10^6$ - $10^{10}$  Hz, respectively, as seen from figure

3.3.6. The difference in  $T_N$ , is thus likely time-scale related and involves the time scale on which the spins fluctuate.

The difference in the nature of the measurements, long range order versus local order, might also play a role, likely in combination with the time scale issue, as long ranged fluctuating spins can be observed with neutron scattering, but not with  $\mu$ SR.

In the light of the above, I propose two models which both can explain the different behavior observed with neutrons and muons. The first is the *surface spin melting* model where the individual spins of a particle melt from the surface and inwards. The second model is that of *superparamagnetic relaxation*, where all spins in the particle fluctuate collectively.

### Surface Spin Melting

Considering a disc-shaped particle, the local  $M$  will be smallest at the  $c$ -axis surface and increasing inwards, as discussed in the previous section (figure 5.3.1). As we raise the temperature the overall  $M$ , including the 'bulk'-like interior of the particles, decreases. Approaching the critical region,  $\mu$ SR will see a very fast dephasing, representing a broad  $M$ -distribution. At a certain temperature no precession can be seen, due to fast dephasing, yielding  $T_N$ .

In the same temperature region, neutron diffraction will on the other hand measure a gradually decreasing perpendicular spin component, reaching  $T_N$  where the particle core spins are close to paramagnetic.

The observed steep muon curve and flat neutron curve fit rather well with this model, confirming the shape which the model predicts.

### Superparamagnetic Relaxation

It is known (section 4.7.3) that the sample particle sizes are not homogenous. The Néel-Brown expression (2.5.1) predicts that the superparamagnetic relaxation time is very dependent on particle size.

Coupling relaxation time to measurement time scales, it is evident that neutron scattering will yield a higher  $T_N$  than  $\mu$ SR. Furthermore a particle size distribution will give a flatter magnetization curve as measured with neutrons, as the particles of different size become superparamagnetic at different temperatures.

$\mu$ SR will in the same (or slightly lower) temperature region see some spins as ordered and others as paramagnetic, consistent with the observed  $\mu$ SR results (section 5.2.4).

From the data provided, I can not determine which of the proposed models is correct, as they can both explain the observed phenomena. However, personally I believe, that at least a part of the observed is due to *surface spin melting*, since other results (section 5.3.2) indicate a connection to the particle  $c$ -axis dimensionality. In addition to this, a part of the observed might be caused by *superparamagnetism*, blurring the picture further.

## 5.3.5 The $\mu$ SR Magnetization in the General Phase Diagram

Figure 5.3.5 shows the found Néel temperatures for the nanoparticle YBCO compared to bulk YBCO from Sanna *et al.* (2004) [164]. The data comparison shows a distinctly different Néel temperature behavior of the nanoparticle YBCO compared to bulk. At high doping the  $T_N$ 's are similar, and the critical doping  $p_C$  (or  $x_C$ ) is comparable. However, towards lower doping, the nano-YBCO Néel temperature shows a significantly different, almost flat, curve whereas the bulk  $T_N$  continues to rise, as indicated by the arrows in figure 5.3.5.

With few data point as base, it is difficult to conclude decisively, but this strongly indicates that finite size effects alter the  $T_N(p)$  behavior. Compared to the neutron results on Néel temperature versus doping in nano and bulk samples, the difference is more outspoken here.

The different results are most likely related to the techniques, especially considering that the neutron scattering  $T_N$  is higher than that found through  $\mu$ SR.

A possible explanation – related to the *surface spin melting* model – is based on the assumption that the surface spins are very disordered, that the 'core' spins are bulk-like and that there is a gradual transition between these two states.

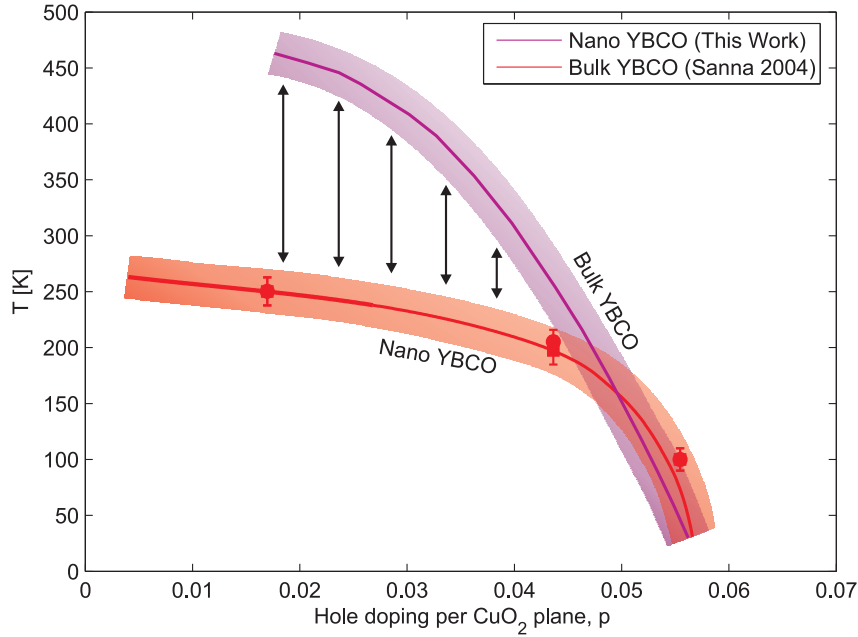


Figure 5.3.5:  $T_N$  versus hole doping  $p$  for nano-sized and bulk YBCO. Solid lines guides to the eye. Symbols: (—) Nanosized YBCO, (●) CEE and (■) DIN models. Bulk YBCO (—) from ref. [164]. The shaded areas indicate the estimated error on the curves.

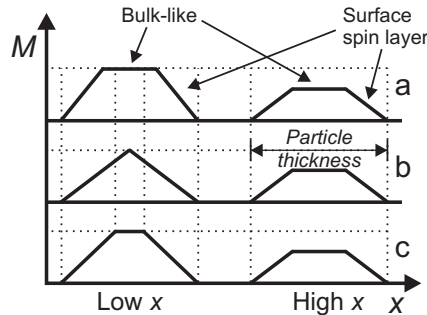


Figure 5.3.6: Schematic of possible developments of the local staggered magnetization with increasing doping. Left particles are low doping and right (all identical) are high doping. (a) Transition zone size constant, slope changes. (b) Transition zone size changes, slope constant. (c) Transition zone and slope change.

At high doping, the saturation staggered magnetism is low and the disorder-order difference between uncompensated surface spins and bulk-like core spins, will be moderate. However, what will the behavior of this system be with changing doping? Possible scenarios are (as illustrated in figure 5.3.6), that the slope of the disorder-order versus  $c$ -axis depth changes, maintaining the size of the transition region (a), that the slope is constant and the transition region expands (b), or the intermediate (c).

Most likely, however, is scenario (c), where the transition region expands some, leaving less volume with a saturation magnetization.

In addition to the presented, it can not be rebutted that the magnetization of some particles or even some  $\text{CuO}_2$  (double-)layers, become superparamagnetic-like and exhibit magnetic fluctuations on the time-scale of  $\mu\text{SR}$ . This would however, only enhance the observed effect.

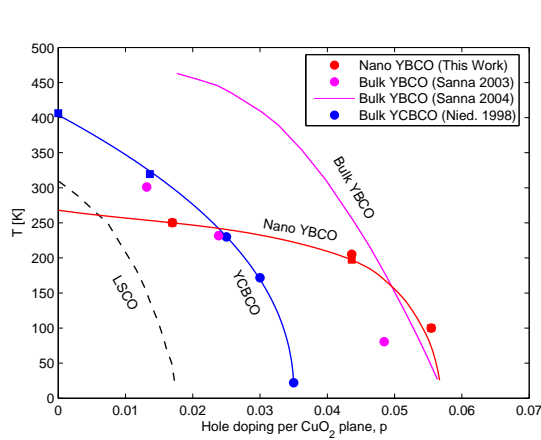


Figure 5.3.7:  $T_N$  versus hole doping for nano-sized YBCO, bulk YBCO and YBCO. Solid lines are fitted power-law guides to the eye. Symbols: (—) Nanosized YBCO, (●) CEE and (■) DIN models. (●) Bulk YBCO [165] and (—) [164]. (●, ■) YBCO. (--) LSCO.

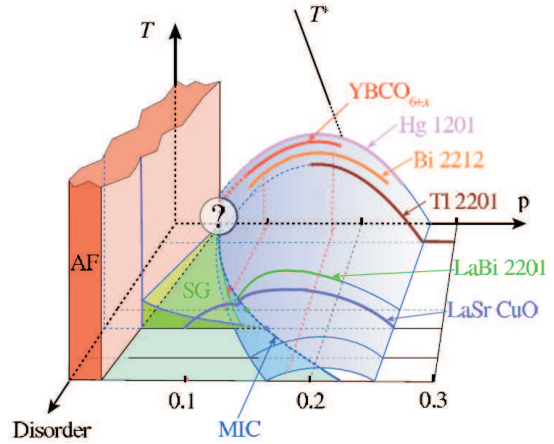


Figure 5.3.8: Extended schematic phase diagram for high- $T_C$  cuprates as a function of temperature  $T$ , hole doping  $p$  and disorder. The shaded orange volume represents the AFM range and the violet volume is the SC dome. A new axis 'Disorder' has been introduced, signifying the intrinsic disorder of the systems. The various systems are ranged with respect to their optimal  $T_C$ . Modified from ref. [161].

Collecting results from refs. [130, 131, 164, 165] and inserting my nano-YBCO  $\mu$ SR results, the  $T_N$  versus  $p$  phase diagram in figure 5.3.7, has been produced. The diagram clearly shows the different critical dopings  $p_C$  for the antiferromagnetic phase of the HTSC's LSCO, YBCO and YBCO<sup>3</sup>. The different  $p_C$  values can be interpreted as a measure of intrinsic disorder in the systems. Similarly we may consider  $T_N$  a measure of tolerance towards frustration and thermal fluctuations in the system.

A disorder-measure definition similar to that of  $p_C$ , however, based on  $T_C$ , is introduced by Rullier-Albenque *et al.* (2008) [161] (figure 5.3.8). According to the disorder-definitions, LSCO is a more disordered system than YBCO. In the same scale, the nanosized YBCO crosses is a relatively clean system. However, not very tolerant to thermal fluctuations and frustration, which most likely is a surface effect caused by missing neighbors.

### 5.3.6 Spin Freezing

One of the main results of the  $\mu$ SR investigations of the nano-YBCO particles is the observation of the reemergence of the staggered magnetization at low temperatures. Although this has previously been observed in bulk systems, it has not been accepted [131] as an intrinsic property of the cuprates. Rather, it has been explained as an effect of dirty samples, and as a feature which will not be present in a sufficiently clean sample.

The additional observation of reemergence in the nano-YBCO is in itself not evidence that the reemergence is intrinsic to the cuprates and as seen from the characterization, the nano-samples do contain some impurities. However, the observation of the reemergence of the Néel-like state in these four different systems (nano-YBCO, bulk YBCO, YBCO and LSCO), manufactured and doped in different ways, supports it. Furthermore, the hole freezing mechanism supports the view

<sup>3</sup>As previously mentioned, the  $T_N$ 's of bulk YBCO by Sanna *et al.* (2004 & 2003) [164, 165] do not match well. However, ref. [164] is newer, and has therefore been used here. However, both datasets are plotted for consistency.

that the reemergence is indeed an intrinsic property of frustrated cuprate superconductors in the antiferromagnetic state.

Regarding impurities, I find it unlikely that the above systems (nano and bulk) should all contain an impurity phase which gave the same signal in measurements, a signal which furthermore is doping dependent and that the precession frequency of this phase should match that of YBCO/YCBCO/LSCO.

In my opinion, the reemergence is intrinsic, as it is related to the same frustration of the spins, just as the doping-induced frustration which eventually causes break-down of the AFM order at higher doping. The reemergence of the native-like staggered magnetization, just arises at the temperature where the holes become localized. Due to the low hole concentration ( $\lesssim 5.5\%$ ), the contribution from the highly frustrated spins (skyrmions) is negligible in measurements.

As a final note, a drop in magnetization observed by neutron scattering is predicted due to the localization of the highly frustrated spins (as the neutrons scatter from the perpendicular spin projection). This is indeed observed by Rossat-Mignod *et al.* (1988) [159] and Tranquada *et al.* (1989) [189] at doping  $x \gtrsim 0.30$ , as well as the neutron data of the nano-YBCO  $x=0.30$  sample in figure 5.3.4 give the same indications.

### 5.3.7 Outlook and Perspectives

In the the above, conclusions have been drawn which shed light upon many questions regarding the physics of the nanoparticle YBCO systems. However, there are still a several issues regarding the detailed physics of the nano-YBCO which are not entirely understood, many of which have arisen during this thesis work. To elucidate these, suggestions to routes and procedures which can be followed are given below.

#### Sample Quality and Reference Samples

During the analysis, it became evident that there are disagreements regarding behavior and properties versus doping. For instance, it seems that there are no recent studies or results regarding the Néel temperature versus oxygen doping. The newest complete results on this [159, 188] are from 1988, and give doping values, which do not agree with values accepted today.

YBCO and variations of YBCO is still today a heavily studied system, and it is therefore important to know the properties of the clean system. A study should therefore be made where well known and accepted techniques are used to prepare very clean bulk samples, before the Néel temperature and magnetization are measured. Once the bulk properties have been well characterized, a similar study of uniform nanosized particle samples could be undertaken to map the size-dependent magnetic properties.

#### Applied Field Response

The two measurements on the applied field response, gave as mentioned very interesting results. That an applied field can cause spin canting is not in itself surprising, but that a limited field could produce measurable lowering of  $M$  at such low temperatures (6 K), is noteworthy and supports the above conclusions that the surface spins in nanoparticles behave significantly different from bulk spins.

Alone the origin of the intriguing enhancement of  $M$ , possibly caused by surface spin-flops, makes this an exciting system.

Similar studies of nano-YBCO close to the AFM/SC transition could provide an opportunity to study the competition of the 2D and 3D order parameters of SC and AFM respectively, exploiting the nano-scale of the system, using techniques where thin films can not be used.

#### Development of Magnetization

The behavior of the surface magnetization and the validity of the the proposed surface spin melting model with increasing in-depth magnetic order, should be further investigated. To elucidate this, the magnetization with both depth and doping, of well controlled particle size samples, would

systematically have to be studied. Particles could be sorted by size through suspension in liquid and a following sedimentation, although the manufacturing technique only yields a fixed particle size and distribution [149].

For directly studying the magnetization versus depth, samples could be prepared through liquid-suspension deposition, where the particles are suspended in a liquid before being dripped onto a wafer. On the wafer, the particles orient with the  $c$ -axis face along the substrate.

Alternatively, recent progress in the growing of YBCO films on semi-conductors, with thickness and orientation control, allow the growing of thin films, in which the magnetization versus depth could be probed [167, 168].

Although it in any case would be a difficult experiment, the in-depth magnetization should be probed with a surface/depth probing technique, such as surface- $\mu$ SR.

However, the most useful technique would still be  $\mu$ SR. Studies of size-homogenized samples could reveal detailed information on the local magnetic field distribution. Careful analysis (considering the  $a$ - $b$  and  $c$  surface-to-volume ratios), complemented with modelling could also reveal information on the dependence of the magnetic properties on the radius of the discs. Furthermore, the experiments could be complemented by both theoretical calculations and numerical simulations on the exchange interactions in finite layered YBCO particles.

## Chapter 6

# Critical Phenomena in Cobalt Oxide Nanoparticles

### 6.1 Critical Fluctuations

As introduced in section 2.1.3, critical phenomena occur in second order phase transitions, close to the critical temperature  $T_N$ . Just below  $T_N$ , the thermal fluctuations almost break the long range order and critical fluctuations will be present in the system.

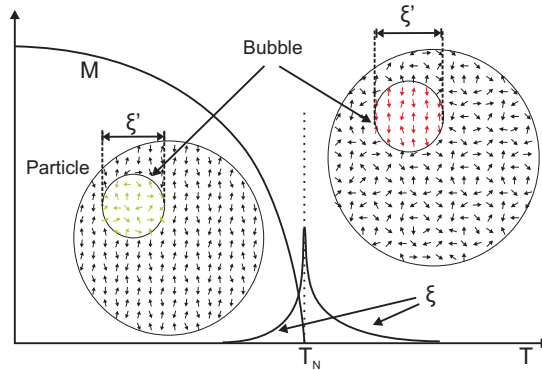


Figure 6.1.1: *Schematic illustration of the correlation length and spin correlations. The spin-particles show the spin order below and above  $T_N$ . The left spin-particle is in the ordered state (below  $T_N$ ) and there is long range order in the particle. The bubble contains locally disordered spins (in green). The locally correlated spins are shown as disordered to illustrate the relative disorder that the local correlations represent. The spin-particle on the right has no long range order, but the bubbles contain correlated spins (in red), and are therefore shown as close to aligned. The diameter of the bubble represents the apparent correlation length  $\xi' = \xi\pi K$  ( $K=0.94$ ), defined in (6.3.7). The staggered magnetism  $M$  and correlation length  $\xi$  curves are not in the same scale or unit.*

The thermal fluctuations may be thought of as bubbles of local disorder, illustrated in figure 6.1.1. In this picture, the system will possess long range order below  $T_N$ , but will contain bubbles of local disorder. In these bubbles, thermal fluctuations have overcome the long range order and the disorder will dominate the long range order. With increasing temperature these bubbles will grow towards infinite size at  $T_N$ , where they thus totally dominate the long range order. A good measure of the range of the local order is the correlation length  $\xi$  which is given (2.1.5-2.1.6, 3.2.31)

as

$$\xi \propto (-\epsilon)^{-\nu'} \quad T < T_N, \quad (6.1.1)$$

$$\xi \propto (\epsilon)^{-\nu} \quad T > T_N \quad (6.1.2)$$

where  $\nu$  and  $\nu'$  are the correlation length exponents and  $\epsilon = \frac{T-T_N}{T_N}$  is the reduced temperature. Above  $T_N$  there is no long range order, but like below  $T_N$  there will be bubbles where local order dominates the paramagnetic disorder of the system, and the spins are thus locally correlated.

The correlation length  $\xi$  is defined through the correlation function (3.2.28), (3.2.31), which for critical fluctuations between individual spins is given by the equations

$$\Gamma_{i,j} = \Gamma(\mathbf{r}_{i,j}, \epsilon, h) = \langle \mathbf{s}_i \cdot \mathbf{s}_j \rangle - \langle \mathbf{s}_i \rangle \cdot \langle \mathbf{s}_j \rangle, \quad (6.1.3)$$

$$\Gamma(\mathbf{r}_{i,j}, \epsilon, 0) \propto \frac{e^{-r_{i,j}/\xi}}{r_{i,j}^{d-2-\eta}}, \quad (6.1.4)$$

and is seen to decay exponentially with distance. We see that at low temperature the correlation function is zero, since the thermal fluctuations do not perturb the spins significantly, and the long range order term  $\langle \mathbf{s}_i \rangle \cdot \langle \mathbf{s}_j \rangle$  balances the short range order term  $\langle \mathbf{s}_i \cdot \mathbf{s}_j \rangle$ . Close to  $T_N$ , however, the long range order term is closer to zero than the short range term. The reason for this is that the long range order term  $\langle \mathbf{s}_i \rangle \cdot \langle \mathbf{s}_j \rangle$  is a product of the individual spin deviations from the long range order spin direction, whereas the short range order term  $\langle \mathbf{s}_i \cdot \mathbf{s}_j \rangle$  is the mean dot product of spins, disregarding the long range order.

At the reciprocal lattice points ( $q'=0$ )<sup>1</sup> [38], however, the correlation function is proportional to the susceptibility (2.1.8-2.1.9), and may therefore be written as

$$\Gamma(\epsilon) \propto (-\epsilon)^{-\gamma'}, \quad T < T_N, \quad (6.1.5)$$

$$\Gamma(\epsilon) \propto (\epsilon)^{-\gamma}, \quad T > T_N, \quad (6.1.6)$$

where  $\gamma'$  and  $\gamma$  are the critical exponents for magnetic susceptibility.

Thus, the correlation function increases with temperature towards  $T_N$  and peaks at  $T_N$ , as the long range order term goes to zero. Above  $T_N$  the correlation function will decrease with increasing temperature, as the long range order term is zero.

### 6.1.1 Studies of Finite-Size Criticality

Theoretical considerations predict that the diverging correlation length  $\xi$  will have a rounded cut-off around the particle size, given by

$$\xi \propto N^{1/d} = L, \quad (6.1.7)$$

where  $N$  is a measure of system volume,  $d$  is the dimensionality of the system and  $L$  is the system size [76]. The behavior of the system starts to exhibit finite size effects when the correlation length approaches the system size [77].

Many experimental studies have been performed on critical phenomena, most of which are performed on bulk systems. There are several reasons for this. Firstly, experiments are easier to carry out on single crystals and the focus has been on confirming the predicted critical exponents. Furthermore, only in recent years the studies of nanosized systems have become common.

Therefore little is known about the critical behavior in small scale systems *i.e.* when the size of the system approaches that of the magnetic correlation length. To elucidate this we have performed a comparative study of CoO nanoparticle powder of particle size 30 nm, 20 nm and 10 nm versus bulk powder using neutron diffraction.

<sup>1</sup> $q'$  is the deviation from reciprocal lattice points, and should not be confused with the scattering vector  $q$  used elsewhere in this thesis.

### 6.1.2 Critical Exponents in CoO

To study finite size critical phenomena we have chosen to study the CoO system. There are several reasons for this choice:

CoO is simple both structurally and magnetically and it is a very 3D Ising-like antiferromagnetic system, which in bulk form has been thoroughly studied through neutron scattering [60, 79, 117, 150, 151, 152, 153, 154, 186, 194], polarized neutron diffraction [83], X-Ray diffraction [79, 186], X-Ray dichroism [51] and AC calorimetry [162].

Very few studies of nanosized CoO have been performed. An exception is, however, Flipse *et al.* [51] who report that very small (4 nm) CoO particles exhibit superparamagnetism and a net magnetic moment due to a large orbital contribution caused by uncompensated spins.

From the structure of CoO (NaCl-like, space group (F m  $\bar{3}$  m)), I have in appendix F.1 calculated that the first allowed structural reflection is (111) and that the allowed structural reflections are located at high  $q$  ( $\approx 2.55 \text{ \AA}^{-1}$ ). Therefore there is little pollution from structural or magnetic CoO peaks at close-by  $q$ 's. Furthermore size controlled CoO nano-particles were available to us through a collaboration with C. Frandsen at the Physics Department at DTU.

### 6.1.3 Critical Exponents in CoO

Thorough studies of the critical phenomena in CoO and extraction of critical exponents, which are introduced in section 2.1.3, have previously been conducted by *e.g.* McReynolds *et al.* (1959) [117], Rehtin *et al.* (1970-1971) [153, 154] (finding  $\beta=0.290\pm 0.025$  and  $\frac{\gamma'}{\gamma} = 1.02 \pm 0.02$ ) and Salamon *et al.* (1970) [162] (reporting  $\alpha'=0.05\pm 0.02$  and  $\alpha=0.12\pm 0.01$ ). As hinted from the few found exponents in each study, the extraction of critical exponents is a difficult task, even though all these studies have been performed on bulk systems.

## 6.2 Strategy of Measurements

As mentioned in section 2.6, the CoO is antiferromagnetic with a  $(\frac{1}{2}\frac{1}{2}\frac{1}{2})$  ordering vector. This reflection has been used to study magnetic order and related critical phenomena.

The measurements have been performed using a novel type of experiment, running RITA-2 in two-axis mode as described in section 3.2.7, and by using the large PSD to collect neutrons around the  $(\frac{1}{2}\frac{1}{2}\frac{1}{2})$  peak and by extracting the diffraction data through subsequent image analysis.

Close to  $T_N$  the extracted diffraction peak will, be composed of two coincident magnetic peaks, a long range order peak with fixed width from the static magnetic order and a short range order peak with varying width from the critical fluctuations. The width of the long range order peak is determined by the 'magnetic particle size' (or magnetic domain size), whereas the width of the short range order is determined by the critical correlation length, which therefore can be extracted from the critical peak width.

In a bulk sample, the  $(\frac{1}{2}\frac{1}{2}\frac{1}{2})$  long range order peak will, apart from instrument broadening, be a  $\delta$ -function, as the length scale of the system is close to infinite. The short range order peak will (excluding instrument broadening) have a Lorentzian line shape, due to the finite length of the critical fluctuations. Therefore, the correlation length  $\xi$  may be extracted from the width of the short range order peak.

### 6.2.1 Two-Axis Measurements and PSD Data Analysis

The analyzed two-axis data were all extracted directly from the individual PSD images, see *e.g.* figure 6.2.1. As the neutrons are scattered in Debye-Scherrer cones from each part of the sample, see section 4.1.2, each pixel in the PSD detects neutrons with a different  $q$ -value. The extraction of a diffraction pattern (an  $I$ - $q$  plot) from a PSD image therefore includes the calculation of the pixel  $q$ -value and a pairing of this with the detector intensity. Examples of diffractograms extracted in this manner are shown in figures 6.3.4 and 6.5.1.

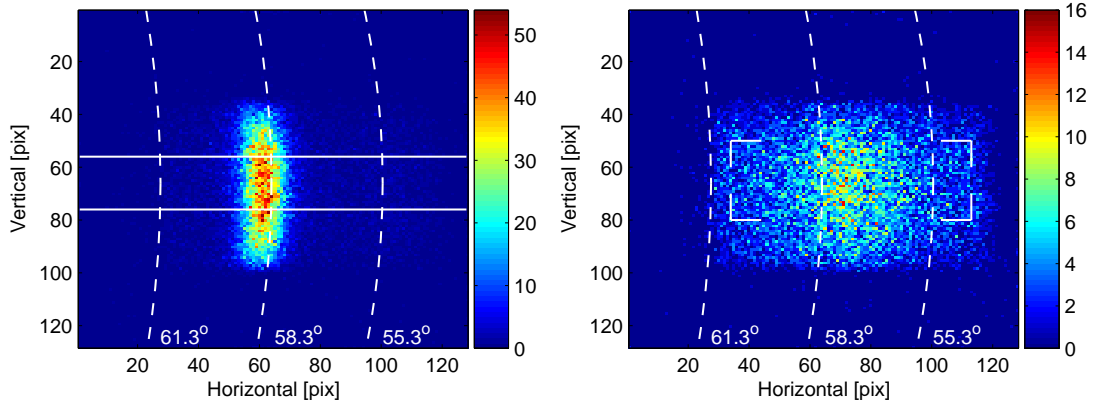


Figure 6.2.1: Examples of PSD images showing the  $(\frac{1}{2}, \frac{1}{2})$  magnetic peak. The dashed lines show the  $2\theta$  angle of the Debye-Scherrer cone at this angle, and the solid lines mark the areas used for data analysis. Left: Bulk sample at 100 K. Right: 20 nm sample at 100 K.

The two-axis setup is intuitively much simpler than the triple-axis experimental setup, and the intensity is markedly enhanced. However, when the data are closely inspected several circumstances appear which are absent in triple-axis measurements.

For instance, as described in section 3.2.7, the setting of the analyzer in TAS mode selects a narrow  $q$  and  $E_f$  region from the scattered beam, whereas in two-axis mode there is no energy filtering of neutrons. Instead, all scattered neutrons within the solid angle of the PSD are detected. The  $q$  value of each pixel on the PSD therefore has to be calculated. For the calculations two approaches have been used. In the first, the shape of the Debye-Scherrer cone is ignored and it is assumed that each column on the PSD has the same  $q$  value. In the second, the Debye-Scherrer cone shape is taken into account and the  $q$  value of each pixels is calculated accordingly. In this approach, a point-like sample is assumed. The details of these calculations are described in appendix F.2.

The calculations rely on a precise knowledge of the geometry of the apparatus, *e.g.* the neutron-sensitive size of the PSD. However, during the analysis, the effective dimensions of the PSD in particular were found to deviate significantly from the data sheet values and were thus derived from comparison of PSD data from different scattering angles.

On the other hand, the calculations do not take into account the smearing of the  $q$ -resolution caused by the instrumental broadening. The instrumental broadening is caused by factors as  $\lambda$ -distribution, beam divergence, finite sample size and detector positioning. Apart from the finite sample size, I will not go further into the details of instrumental broadening factors, as this is outside the scope of this thesis.

During the course of this project there has been significant debate about the shape of the instrumentally broadened Bragg peak on the PSD and whether the Debye-Scherrer cone considerations combined with the finite sample size should be taken into account. Therefore I have chosen to elucidate this by simulating a range of experiments with the neutron ray-tracing package McStas [106, 118, 202]. As the instrumental model, I have used the RITA-2 model by L. Udby [191, 192, 193]. The details of these simulations are presented in appendix F.3.

From the results of the simulations, it is my conclusion that the Debye-Scherrer cone shape indeed is visible and should in some cases be taken into account when extracting data from the PSD images. If only a narrow (21 pixels) vertical strip is used for data extraction, as shown in figure 6.2.1, it is not necessary to compensate for the Debye-Scherrer cone, as it is very close (within 2%) to vertical within this narrow strip. On the other hand, if a larger (47 pixels) vertical area is used, the Debye-Scherrer cone corrections should be used, as there is a  $\sim 5\%$  deviation from the vertical approximation.

### 6.2.2 Choice of Sample Container

Even though the incoming beam is perfectly monochromatic and collimated when measuring neutron scattering from a sample in two-axis mode there will still be smearing on the PSD due to the finite sample size. Therefore the choice of sample container, determining the sample dimensions is important. A narrow sample holder was chosen, giving the sample the shape of a long thin rod and thereby minimizing the sample dimensions in the horizontal plane. This should also give a narrow Bragg peak. A third advantage of the thin-rod shape is a minimized attenuation in the sample, which is highly relevant in this case since Co has a high absorption cross section.

The CoO sample containers used were cylindrical, made from aluminium, with a height of  $\sim 55$  mm and a diameter of  $\sim 6.0$  mm, except for the 30 nm sample which was packed into a 10 mm diameter sample holder.

## 6.3 Preliminary Analysis

In the present and the following two sections, I will proceed to present the analysis of the data, obtained on the 4 mentioned samples. In this section I will go through instrumental and experimental details and considerations, as well as a preliminary analysis. This is done, as the data obtained from a two-axis experiment are raw data and since a rather elaborate procedure is required in order to extract and analyze the obtained data.

I will in section 6.4 continue to present the analysis of the bulk sample data, followed by the analysis of the nano-samples in section 6.5.

### 6.3.1 Detector Normalization

To obtain a good mapping of the background we counted for long periods (2-3 hours in total) at a location in  $q$ -space, with a pure incoherent signal. From these measurements an image of the background variation at the PSD was composed. The typical background variation is presented in figure 6.3.1.

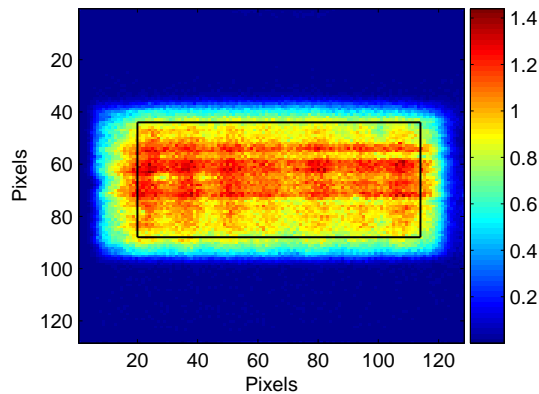


Figure 6.3.1: *An image of the background recorded by the PSD in a region in  $q$ -space with only incoherent scattering. The image has been normalized to an average of unity in the marked region, which is the region used in the analysis.*

During the analysis it was noticed that the background counts varied significantly across the PSD. Initially this was put off as variations in the background radiation, but as the variations are independent of scattering angle, it is related to the experimental setup. Summing the PSD columns (figure 6.3.2) shows a clear wave-pattern, which most likely is caused by the BeO filter collimator. Furthermore the background on average slopes downwards from low to high scattering angle. The origin of this is unknown, but might be pure PSD sensitivity and/or position determination.

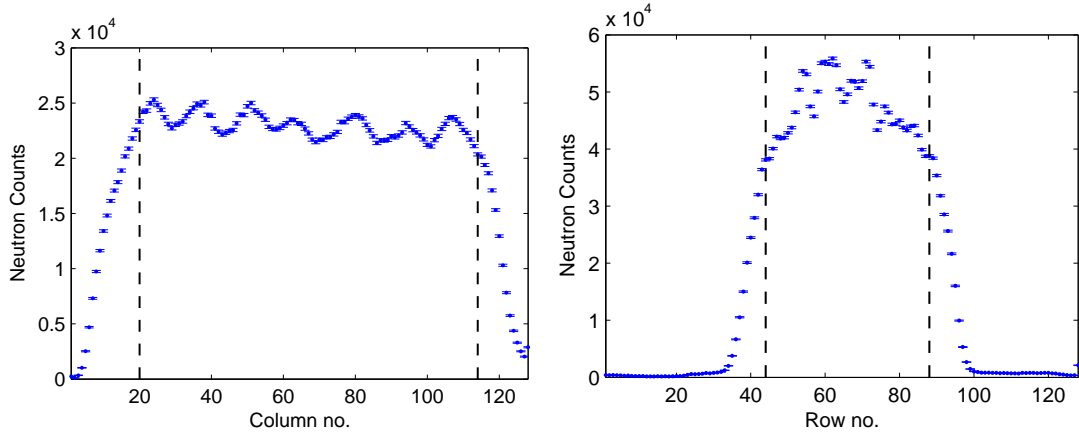


Figure 6.3.2: Plots of the summed background column and row counts obtained from PSD image. The y-axes show actual counts. The dashed lines indicate the regions used in the analysis. Left: Column sums. Right: Row sums.

All measurements were performed in the DIS-E dispex (range 7-325 K [196]), which has a low background contribution.

Turning back to figure 6.3.1 we see variations within each column, as well as horizontal lines in the background. Most likely, these features are due to variations in the PSD sensitivity related to problems with the horizontal detector wires.

With the observed background variations, it was important to establish the details of these, before we commenced the analysis of a dataset. This was done for every experimental setup, as experience shows that the background features vary from experiment to experiment.

In the data analysis, the raw PSD images have been normalized to the background variation per pixel, before they are used in the further analysis.

Other forms of normalization *e.g.* column-normalization, row-normalization, or Debye-Scherrer cone normalization are also possible but not applied here.

### 6.3.2 Observations

Before proceeding to the analysis, we take a look at the raw diffraction data. Figure 6.3.3 shows raw data of the bulk and the 20 nm sample, with subtracted background and normalized to the same amplitude to ease comparison. On the left the raw data with fits are shown and on the right the fits are shown on their own. The model used for the fits is described in section 6.3.3, and consists of Voigt line functions, with a Gaussian instrumental resolution and a particle-size Lorentzian.

From figure 6.3.3 we see that there is a slightly increasing peak broadening from low temperature (100 K and 13 K for bulk and 20 nm, respectively) to a temperature close to  $T_N$  ( $T_N=288(3)$  K and  $T_N=290(4)$  K). Just below  $T_N$  the broadening increases as the peak significantly broadens towards  $T_N$  and further broadens towards higher temperatures, becoming wide at 300 K.

We interpret the peak broadening just below  $T_N$  as a composition of the Lorentzian width from the static magnetism, and an additional width component from the bubbles of disorder which should occur close to  $T_N$ .

Above  $T_N$  the static magnetic order is gone, and we now observe only a Lorentzian from the critically correlated spins. As the correlation length decreases, the Lorentzian becomes broader.

### 6.3.3 Models

The results of the analysis depend is strongly on the construction of a suitable model. It is assumed that:

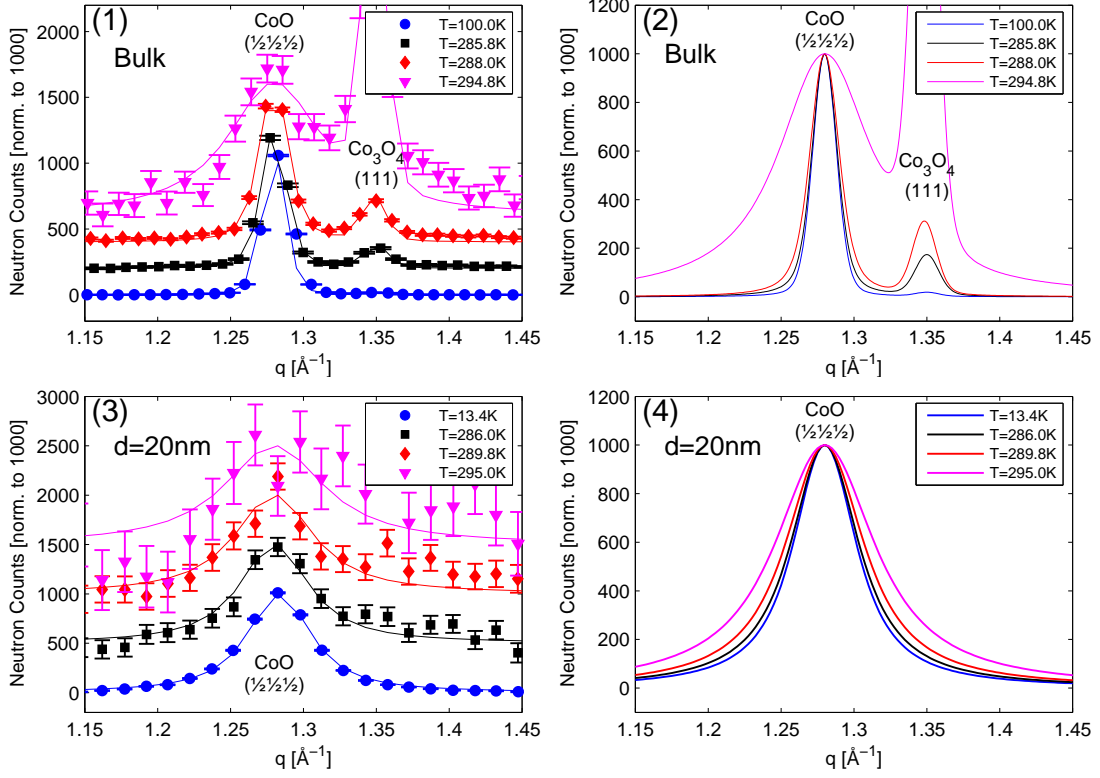


Figure 6.3.3: Comparative plots showing 'raw' data of the  $\text{CoO}(\frac{1}{2}\frac{1}{2}\frac{1}{2})$  peak. The data have been scaled and the background has been subtracted. (1), (2) Bulk raw data and fits at  $T=100.0, 285.8, 288.0$  and  $295\text{ K}$ . The peak at  $\sim 1.35\text{ \AA}^{-1}$ , is the (111)  $\text{Co}_3\text{O}_4$  reflection. (3), (4) 20 nm raw data and fits at  $T=13.4, 286.0, 289.8$  and  $295\text{ K}$ .

- The instrumental broadening is Gaussian.
- The scattering from the static magnetism of a bulk sample is a very narrow peak, approaching the ideal case of a  $\delta$ -function.
- The critical scattering has a Lorentzian shape.

The Gaussian instrumental broadening is determined from fits to the bulk dataset at low temperature with a Voigt. The bulk dataset is utilized as it is assumed to have the narrowest particle size Lorentzian contribution.

The correlation length is proportional to  $e^{-|x|/\xi}$  according to (2.1.7). The Lorentzian shape of the critical scattering peak can be derived from the Fourier transform of this expression as

$$\frac{1}{2\pi} \int_{-\infty}^{\infty} e^{-|x|/\xi} e^{-iqx} dx = \frac{1}{\pi} \frac{1/\xi}{(1/\xi)^2 + q^2} = \frac{1}{\pi} \frac{\gamma}{(\gamma)^2 + q^2}. \quad (6.3.1)$$

This is a Lorentzian, with a HWHM width of  $\gamma = 1/\xi$ . Using FWHM width gives the factor of 2 in (6.3.2), and the correlation length can therefore be calculated from the expression

$$\xi = \frac{2}{W_{Lc}}, \quad (6.3.2)$$

where  $W_{Lc}$  is the critical Lorentzian FWHM.

### Bulk model

From the above considerations and a convolution of the static and critical contributions with the Gaussian instrumental broadening, we arrive at the ideal model for the bulk sample  $M_B$

$$M_B(q) = (\delta_S(q) + L_C(q)) \otimes G(q) = G_S(q) + V_C(q), \quad (6.3.3)$$

where  $G$  is a Gaussian,  $L$  is a Lorentzian,  $V$  is a Voigt line shape and the subscripts  $S$  and  $C$  indicate static magnetism and critical magnetism respectively. Thus the ideal bulk model is a simple Gaussian outside the critical region.

The approach of the data fitting has been to determine the width of static magnetism and instrumental parameters at low temperatures first. These results were then applied in fits to the above model up to close to  $T_N$ . From the extracted fit parameters (integrated intensity) the first critical parameter  $\beta$  was then extracted by fitting with a power law. The obtained  $\beta$ -value was then utilized to give the static magnetism contribution to the measured intensity through extrapolation from (2.1.4)

$$m \propto (-\epsilon)^\beta, \quad (6.3.4)$$

where  $m$  is the order parameter of the staggered magnetism. The critical component parameters may then be extracted as the difference in intensity. Besides the intensity, the Lorentzian width is very interesting as it is inversely proportional to the correlation length  $\xi$  (6.1.1-6.1.2).

### Nano Model

The infinite sized system approximation does not hold for the nanoparticles, where it is limited by the finite particle size. A distribution of finite particle sizes will result in a finite width of the diffraction peak. The peak can have a variety of shapes, but in our case the peak is well described by a Lorentzian. Thus the  $\delta$ -function in (6.3.3) becomes a Lorentzian and the resulting model ( $M_N$ ) for nanoparticles is

$$M_N(q) = (L_S(q) + L_C(q)) \otimes G(q) = V_S(q) + V_C(q). \quad (6.3.5)$$

To confirm this choice, we consider the low temperature data in figure 6.3.3 (3-4), where it is apparent from the tails of the Bragg peak that it contains a Lorentzian component.

The Lorentzian width of the static magnetic peak of each sample is found from fits of the lowest possible temperature dataset for each sample. The results from these fits are found in table 6.3.1 along with examples of fitted datasets in figure 6.3.4.

When utilizing the above model for the analysis, the background is modelled by a linearly sloping background and in the case of present impurity peaks, these are fitted with a similar Voigtian peak.

Sample	$T$ K	Int. Int. $\text{\AA}^{-1}$	$q$ $\text{\AA}^{-1}$	$W_G$ $\text{\AA}^{-1}$	$W_L$ $\text{\AA}^{-1}$	$A_{bg}$ $\text{\AA}$	$B_{bg}$	$\chi^2$
Bulk	100	947(9)	1.28266(4)	0.01714(13)	0.00372(11)	-1.061	12.92	1.1294
30 nm	10.1	3218(13)	1.28118(9)	0.01714	0.0295(2)	-3.6(6)	109.5(8)	2.923
20 nm <sup>‡</sup>	13.4	2656(16)	1.28252(13)	0.01714	0.0459(4)	-42(3)	185.8(7)	1.685
10 nm	6.7	2260(40)	1.2785(5)	0.01714	0.0749(14)	110(30)	1.332	2.181

Table 6.3.1: *Lowest temperature fit results for bulk and 30 nm, 20 nm and 10 nm. Fit model: Voigt with sloping background, as described by (6.3.5). All parameters free, except bulk background found from a prior background fit and Gaussian width in nano-sample fits, found from bulk sample. (‡) 1st experiment. Abbreviations: Int. Int. is integrated intensity.  $A_{bg}$  &  $B_{bg}$  are background line parameters.*

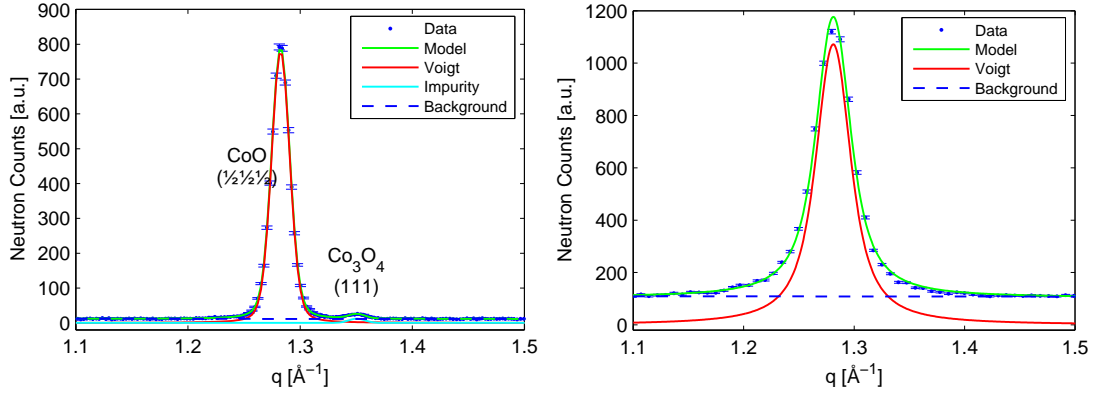


Figure 6.3.4: Voigtian fits of the lowest temperature diffraction peaks for the bulk and 30 nm samples. Fit results are shown in table 6.3.1. Left: Bulk at  $T=100$  K. The dataset contains an impurity at  $q=1.3506(5) \text{ \AA}^{-1}$  with an integrated intensity of  $12.3(7)$ . Right: 30 nm at  $T=10$  K.

### 6.3.4 Particle Length Scales

The structural size of the particles has been extracted from the structural peak width from XRD data using the Scherrer formula (4.1.6) (see table 4.8.1). Similarly, I here introduce the *magnetic size*  $d_m$  of the particles, given by the Scherrer formula (4.1.6) as

$$d_m = \frac{2\pi K}{W_L}, \quad (6.3.6)$$

where  $W_L$  is the Lorentzian width of the static magnetism and  $K=0.94$  is the Scherrer constant value for spherical particles, also used for extracting the structural size from the XRD data.

We do now have three measures of size of the particles, structural size, magnetic size and correlation length, all derived from Lorentzian widths of diffraction peaks. Of these, only the correlation length  $\xi$  is not derived using the Scherrer formula but using (6.3.2), and the value of it can therefore not be directly compared to  $d$  and  $d_m$ , a difference emphasized by the use of  $\text{\AA}$  as unit, where the other two are given in nm.

To facilitate a direct comparison between the correlation length  $\xi$  and  $d$  and  $d_m$ , I introduce the *apparent correlation length*  $\xi'$  which is derived from the Lorentzian width using the Scherrer formula like  $d$  and  $d_m$

$$\xi' = \frac{2\pi K}{W_{Lc}} = \xi \pi K, \quad (6.3.7)$$

where  $W_{Lc}$  is the Lorentzian width of the critical peak, and  $K = 0.94$  is the same Scherrer constant as previously used. In the following, the apparent correlation length, given in units of nm will be used in comparison with the structural and magnetic sizes.

### 6.3.5 Outline of Analysis

There are several steps in the analysis leading to the derivation of the correlation length. For each of the datasets, obtained from the bulk, 10, 20 and 30 nm CoO powders, the following steps are traversed:

1. The instrumental parameters *e.g.* PSD position and dimensions are determined. This has to be done for each sample as minor changes were made to the instrumental setup between each measurement.
2. The PSD normalization is determined by background scans as described in section 6.3.1.
3. The datasets are loaded and are pixelwise normalized. Each pixel is assigned a  $q$ -value calculated as described in section F.2.

4. Using the Gaussian instrumental broadening found from bulk, the static magnetism Lorentzian line width is determined from a fit to the lowest temperature dataset. In case of impurity Bragg peaks, these are fitted at the highest temperature dataset where the magnetic CoO ( $\frac{1}{2}\frac{1}{2}\frac{1}{2}$ ) has negligible intensity.
5. The datasets obtained immediately below the critical temperature region are fitted to the model described in section 6.3.3 (with the critical intensity set to zero), with the Gaussian and static magnetism Lorentzian width kept constant, and the Néel temperature is found from power law fits to the intensity of the static peak. The critical temperature region is in this context considered the region within approximately 10% of  $T_N$ .
6. The entire temperature range is fitted by the described model. Inside the critical region, the static magnetism component is extrapolated from the previously determined power law and above  $T_N$  it is forced to zero, in both cases leaving the critical component free.
7. The correlation length, scattering intensity, and their critical exponents  $\nu$  and  $\gamma$  are extracted.

### 6.3.6 Determining the Néel Temperature

In order to express the correlation length as a power of the reduced temperature,  $T_N$  has to be determined. A task seemingly very simple if not for the critical scattering. The Néel temperature is found through iterative fitting of the intensity within a certain temperature interval and subsequent evaluation of the resulting  $T_N$ . In the evaluation, the fit is reviewed for physical validity and compared to the previous results, as illustrated below. The iteration continues until a physically reasonable result with low  $\chi^2$  is found.

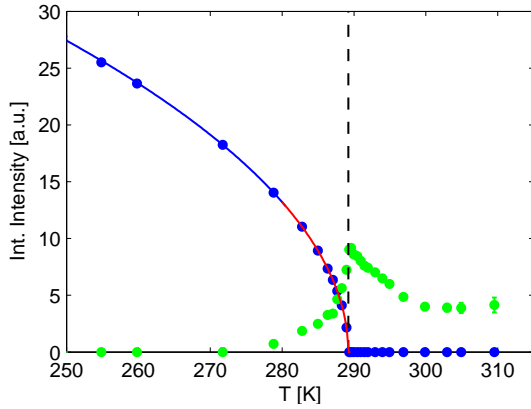


Figure 6.3.5: *Integrated intensity  $I$  vs.  $T$  of the 30 nm sample for the full temperature range. (●) Static  $I$ . (●) Critical  $I$ .*

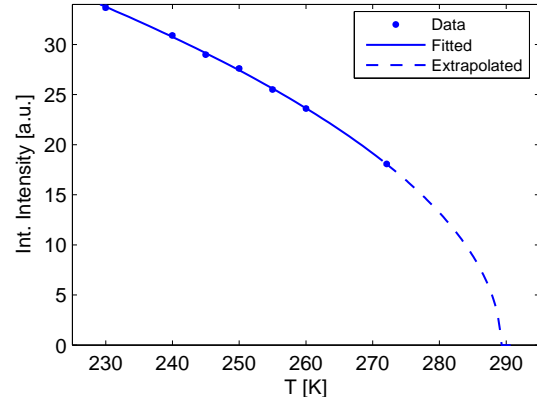


Figure 6.3.6: *Integrated intensity  $I$  vs.  $T$ , fitted and extrapolated to a power law. The fitting range corresponds to bold values in table 6.3.2.*

As an example a more detailed account of the determination of  $T_N$  for the 30 nm sample is provided here.  $T_N$  is found through power law fitting to the integrated intensity of the static magnetism peak. During the fitting only the peak position and intensity (amplitude) of the static magnetism Voigt are allowed to vary whereas the Gaussian and Lorentzian widths are kept constant.

To find a physically reasonable  $T_N$  the lowest and highest temperatures of the temperature interval, which the power law has been fitted to, have been varied. For each temperature interval The results from this process are displayed in table 6.3.2. However, we cannot trust the fit results blindly, as the critical scattering intensity becomes significant close to the Néel temperature. This is unfortunate, considering that the power law model (6.3.4) is only valid close to the transition

$T_{min}$ K	$T_{max}$ K	$T_N$ K	$\beta$ -	$\chi^2$ -
240.0	272.1	291(4)	0.27(4)	0.931
240.0	279.0	291.6(1.9)	0.27(2)	0.721
240.0	282.9	294.4(1.4)	0.301(17)	1.565
230.0	255.0	281(15)	0.20(9)	1.440
230.0	260.0	285(9)	0.23(6)	1.045
<b>230.0</b>	<b>272.1</b>	<b>289(3)</b>	<b>0.25(2)</b>	<b>0.853</b>
230.0	279.0	290.7(1.3)	0.26(14)	0.815
230.0	282.9	293.3(1.0)	0.286(12)	2.02

Table 6.3.2: Result of fitting a power law (6.3.4) to the  $I$  vs.  $T$  dependence just below the critical region for the 30 nm sample. The estimated best fit is emphasized. Abbreviations:  $T_{min}$ =Minimum  $T$  dataset.  $T_{max}$ =Maximum  $T$  dataset.  $T_N$ =The found Néel temperature.  $\beta$ =The found  $\beta$ -value.

temperature. As a rule of thumb, the power law is valid for  $\epsilon$ -values up to 0.1-0.2. To achieve the best estimate for  $T_N$  one therefore needs to find the optimum balance between as many data points as possible and not going too close to the expected  $T_N$ . Considering the results in table 6.3.2, there are several interval candidates for a 'good' result for  $T_N$ , considering the  $\chi^2$ 's.

The intervals [230.0-279.0 K] and [240.0-279.0 K], however, come too close to the  $T_N$  ( $\simeq 289$  K) found in literature, and have to be discarded.

For the intervals [230.0-272.1 K] and [240.0-272.1 K] low  $\chi^2$ 's are achieved and the results agree relatively well on both  $T_N$  and  $\beta$  as well as they have an acceptable distance to the  $T_N$  ( $\simeq 289$  K) from the literature [153]. However, the  $T_N=289(3)$  K value found from the former interval ([230.0-272.1 K]) seems the best choice since it is found from more data points and since the fit has a smaller  $\chi^2$ , and is thus chosen.

Furthermore, as seen later, this Néel temperature gives a flat  $\xi$ -curve for the critical scattering in the cut-off region and it gives a power law-like behavior of  $\xi$  in the sloping region.

## 6.4 Bulk Sample Analysis

In the following, I will go through the main points in the analysis and fitting of the neutron diffraction data obtained on our CoO samples (bulk, 10 nm, 20 nm and 30 nm).

To compare bulk and nanosized system behavior, we performed similar measurements on a bulk powder sample.

The sample is contaminated with  $\text{Co}_3\text{O}_4$ , of which the (111) reflection lies close to the  $(\frac{1}{2}\frac{1}{2}\frac{1}{2})$  CoO reflection, as shown in figure 6.3.4 (left). A list of the  $\text{Co}_3\text{O}_4$  reflections is provided in table 6.4.1.

$h$	$k$	$l$	$m$	$d$ [Å]	$2\theta$ [°]	$q$ [Å <sup>-1</sup> ]	$F^2$
1	1	1	4	4.6563	60.653	1.3494	1010
2	2	0	12	2.8514	111.084	2.2035	686
3	1	1	12	2.4317	150.416	2.5839	600

Table 6.4.1: List of selected  $\text{Co}_3\text{O}_4$  reflections with neutron radiation with  $E=3.7$  meV. Symbols:  $h,k,l$  are Miller indices,  $m$  is multiplicity,  $d$  is lattice spacing,  $2\theta$  is the scattering angle,  $q$  the scattering vector, and  $F^2$  is the structure factor. Generated from ref. [92].

The bulk signal is very clear, and I have therefore abandoned the complicated-character Debye-Scherrer cone correction, and instead only used a narrow horizontal strip (20 pixels high) on the PSD for data. As in the previous fitting procedure the Gaussian width is determined from a low temperature data set (100 K), and thereafter the Néel temperature ( $288.0\pm 2.7$ ) and  $\beta$

( $0.281 \pm 0.047$ ) are determined. Using the found  $T_N$  the critical scattering is then fitted and the correlation length is extracted. The results from this procedure are presented in figures 6.4.1 and 6.4.2. During the fitting, and especially at high temperatures, where the critical signal is weak and broad, I have found the impurity peak to be somewhat disturbing, and better fits could be obtained, were it is not present. Examples of the difference between low and high temperature datasets is shown in figure 6.3.3.

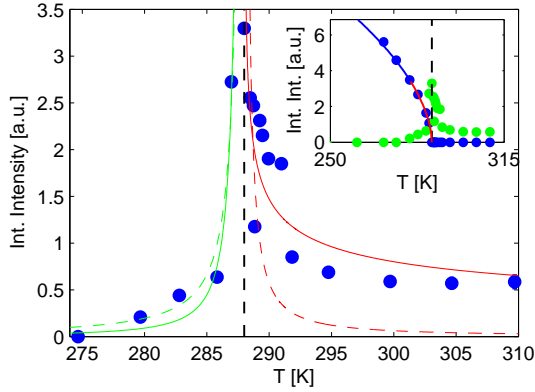


Figure 6.4.1: Bulk critical integrated intensity versus temperature. The lines are power law fits. (—) (—) are free fits, (---) (---) are fixed exponent fits, with the 3D Ising  $\gamma=1.2396(13)$  [64]. Inset: Integrated intensity  $I$  vs.  $T$  for static and critical components.

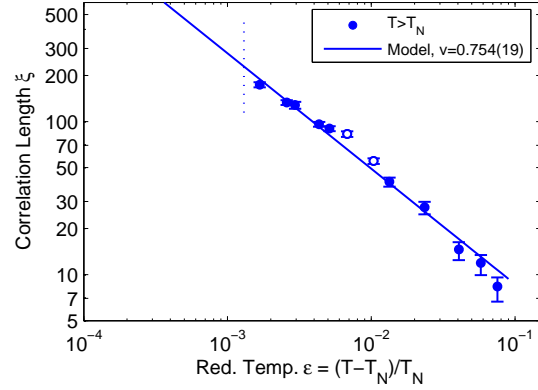


Figure 6.4.2: Bulk  $\xi$  vs.  $\epsilon$ . The solid line is best fit, and the dotted line indicates the lower limit of the fit interval. The open symbols have been ignored in the fit, since they deviate from the general trend of the points.

The  $I$  vs.  $T$  plot (figure 6.4.1) (inset) shows nicely how the static magnetism diminishes, and how the critical scattering tends to diverge at  $T_N$ . The fitted exponent values  $\gamma'=1.62(7)$  and  $\gamma=0.340(10)$  are, however, far from the predicted 3D Ising value of  $1.2396(13)$  [64].

The high temperature intensity in figure 6.4.1 does exhibit a rather strange behavior, as it does not drop off as expected, but rather remains constant. However, this is most likely an artifact caused by the fitting procedure. When reaching temperatures where the critical peak is very broad, and therefore also flat, the fitting algorithm will increase the intensity slightly, to fit the background better, an increase which gives a significant integrated intensity.

Turning to the correlation length in figure 6.4.2, it shows a  $\xi$  development which matches the predicted power law in reduced temperature rather well. While fitting the correlation length exponent  $\nu$ , I have chosen to ignore two points which were deviating from the general trend. Whether these points are included, however, does not affect the error significantly. The found exponent is  $\nu=0.754(19)$ .

Conclusively, the two-axis mode of the RITA-2 spectrometer in combination with the position sensitive detector (PSD) has successfully been applied to investigate critical scattering phenomena in bulk CoO. The results are consistent with literature, the found  $\beta$  value confirms predicted values, whereas the  $\nu$  value lies within a fair distance to predicted value.

To analyze the PSD-image data, an advanced method of extracting  $I$  versus  $q$  values, taking into account the shape of the Debye-Scherrer scattering cone on the PSD, has been developed and successfully applied.

After confirming that the concept of the experiment works, and having implemented the analysis tools, we then continued to perform experiments on nanosized samples.

## 6.5 Nanosized Sample Analysis

Following the successful analysis of the bulk sample I will in this section present the analysis of the nanosized samples with sizes 10 nm, 20 nm, and 30 nm.

Of the nanosized samples, the 20 nm sample has received most attention, as it is clean and as it furthermore was the first nanosized sample we had at our disposal. After comparison of the result to bulk, we decided to attempt to manufacture samples, with different sizes, smaller and larger, to study the systematics in particle size. I will therefore in the analysis of these samples focus on the results and only discuss sample specific issues.

### 6.5.1 20 nm Sample Analysis Details

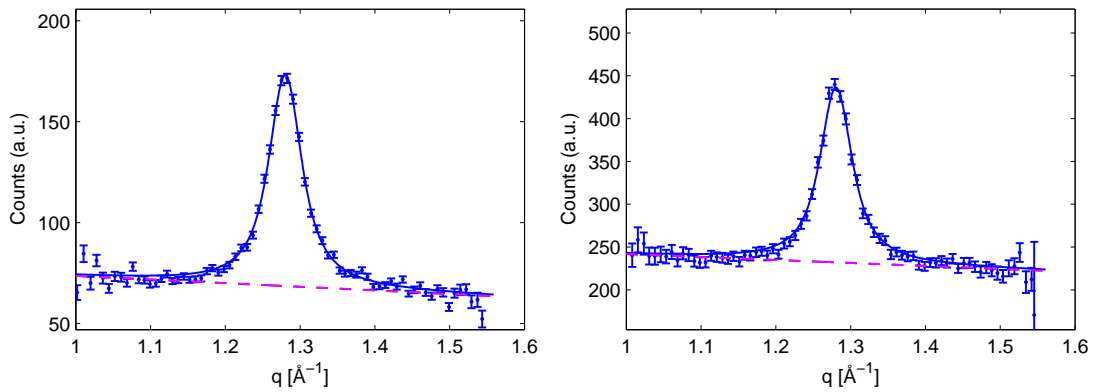


Figure 6.5.1: Comparison of data from different PSD load methods. Here the 20 nm sample at 250 K. Left: Each column has same  $q$  value, and the full pixel-rows 54-74 (2688 pixels total) are used. Right: Each pixel has a unique  $q$  value, and data are extracted from pixels  $x=33-115$  and  $y=43-89$  (3901 pixels total). The difference in signal to background ratio is discussed in the text.

The analysis of the 20 nm acts as a model to the analysis of the other two nano-sized samples (10 nm and 30 nm). Several lessons were learned through the experiment and the following data analysis, some of which are already presented *e.g.* detector normalization (section 6.3.1) and the Debye-Scherrer cone considerations (section F.2).

The measurements on this sample were conducted in two rounds, a preliminary (marked 1st exp.) covering the temperature range (13-310 K) and a later (marked 2nd exp.), concentrating on the critical region just above  $T_N$ . Both experiments were performed using the DIS-E displex, shown in figure 6.5.6. However, the conditions were different, as the first was conducted with two heat shields since we needed to go to low temperatures, and the second was conducted with no heat shields, as we were close to room temperature. Thus the temperature calibration may differ between the two experiments.

#### The Full Temperature Range

The data loading takes the Debye-Scherrer cones into account as described in appendix F.2. It was initially constructed such, that it loaded the data from each column on the PSD as having the same  $q$ , an approximation which gave close to the same result as the Debye-Scherrer correction with regard to peak shape, as seen from figure 6.5.1. However, the Debye-Scherrer cone load method has the advantage that it allows for a larger area on the PSD to be used for data collection (21 vs. 47 rows), giving better statistics.

On the other hand, the Debye-Scherrer cone load method gives a significantly higher background, as shown from figure 6.5.1. This is caused by the larger background-collecting area included in the Debye-Scherrer load routine, as can be seen from figure 6.2.1 (right).

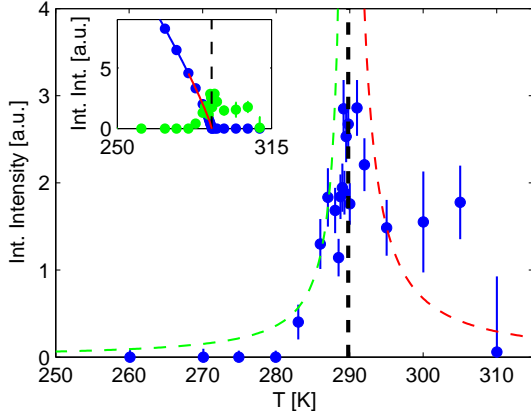


Figure 6.5.2: Critical integrated intensity  $I$  vs. temperature  $T$  of 20 nm particles (1st exp.). The dashed lines are guides to the eye, with 3D Ising  $\gamma=1.2396(13)$  from ref. [64]. Inset: Static magnetism integrated intensity  $I$  vs. temperature  $T$  fitted with power law. (●) static magnetism data points, (●) critical scattering data points, (—) static magnetism power law fit, (—) extrapolated power law behavior of the static magnetism.

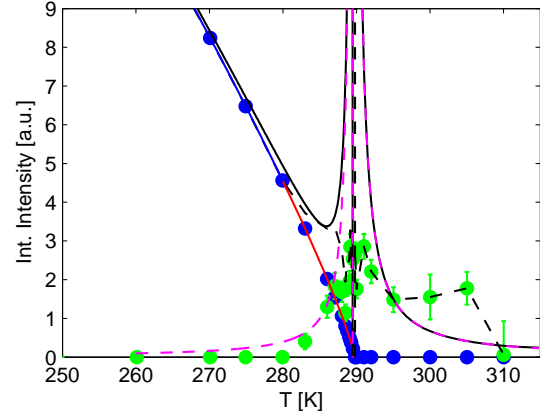


Figure 6.5.3: Integrated intensity  $I$  vs. temperature  $T$  of 20 nm particles (1st exp.) fitted with a power law. (—) is the power law fit, (—) is the behavior extrapolated from the fit, (---) is static+critical intensity, (---) is fitted critical intensity (see also figure 6.5.2) and (—) is summed fit of static and critical intensity.

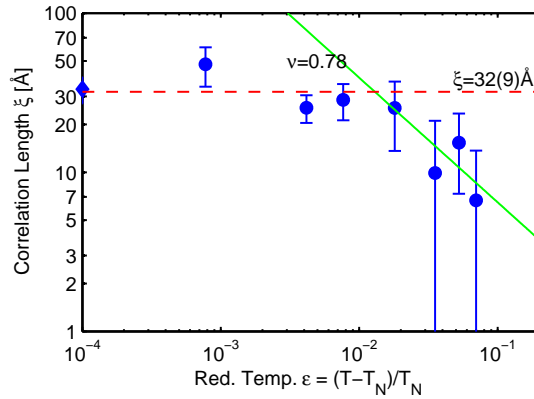


Figure 6.5.4: 20 nm (1st exp.) correlation length  $\xi$  vs. reduced temperature  $\epsilon = \frac{T-T_N}{T_N}$  of 20 nm particles (1st exp.) in log-log scale.  $T_N=289.8$  K.

From power law fitting to the integrated intensity of the Bragg peaks (and considerations like those described in section 6.3.6), the Néel temperature is found to be  $289.8 \pm 3.8$  K for the 1st experiment. The corresponding values from bulk and literature [153] are 288(3) K and 288.98(10) K, respectively. The  $I$  vs.  $T$  plot is presented in figure 6.5.3.

### The Critical Region

In the second experiment we only focused on the region  $T > T_N$ . The temperatures were selected with a log-log plot in mind, and the measured datasets are therefore very close in  $T$  near  $T_N$ , and are farther apart further from  $T_N$ , ensuring that the points are equidistant on a logarithmic scale.

In the calculation of the reduced temperature, I have, despite the  $T_N$  found in the first experiment, decided a value of 289.0 K. This is done as this (2nd exp.), was performed without heat

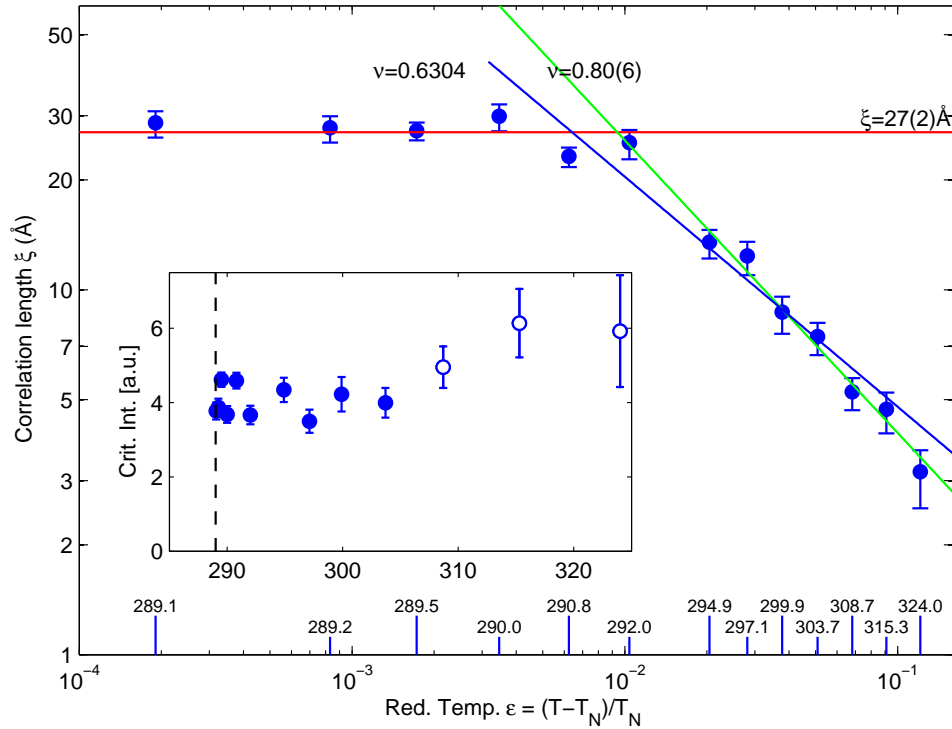


Figure 6.5.5: Correlation length  $\xi$  vs. reduced temperature  $\epsilon = \frac{T-T_N}{T_N}$  of 20 nm particles (2nd exp.) in log-log scale, with  $T_N=289\text{K}$ . The red line is the cut-off correlation length found as mean of the first 6 points. The solid lines are power law fits to the sloping points, (—) with 3D Ising  $\nu=0.6304(13)$  as predicted in literature [64], and (—) with all parameters free, giving  $\nu=0.80(6)$ . Inset: Critical intensity vs. temperature in the same region.

shields in the dispex, where the 1st experiment was performed with 2 heat shields in the dispex. The arguments for using a slightly reduced  $T_N$  are found below.

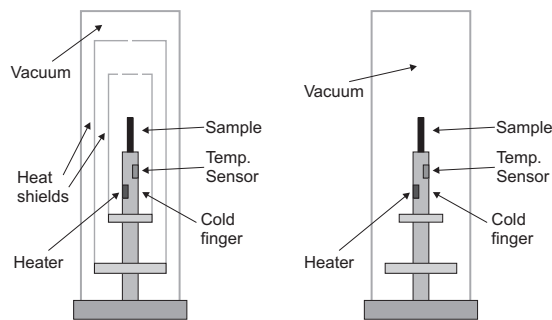


Figure 6.5.6: Schematic of dispex DIS-E with and without heat shields.

The setup of the dispex with and without heat shield is shown in figure 6.5.6. The sample is mounted on a cold-finger, on which there is a heater. The sample can be encased in cooled heat shields, which do not radiate heat. Continuous cooling and controlled heating, enables temperature control of the cold-finger and thereby of the sample. As the temperature sensor as seen from the figure is mounted on the cold finger, it will actually measure the temperature of the cold-finger and not the sample. In the setup with heat shields and operating close to room temperature, the sample and temperature sensor will only radiate away heat, and the sample might actually have

a slightly lower temperature than the sensor, as it is farther from the heat element. In the setup without heat shields, and close to room temperature, both sensor and sample will receive similar amount of heat radiation and will therefore be more likely to have the same actual temperature. The net effect of this is that for a given temperature close to room temperature, the temperature of the sample will be lower when the heat shields are installed, than without them.

With this in mind, one can argue that it actually is reasonable to use a  $T_N$  value lower than that found from the 1st experiment. It is, however, difficult to estimate exactly how large the offset is.

Even though there is some uncertainty in  $T_N$ , using a slightly different  $T_N$  only changes the value of the found  $\nu$ , but does not change the fact that there is a cut-off in the correlation length, as shown in figure 6.5.7.

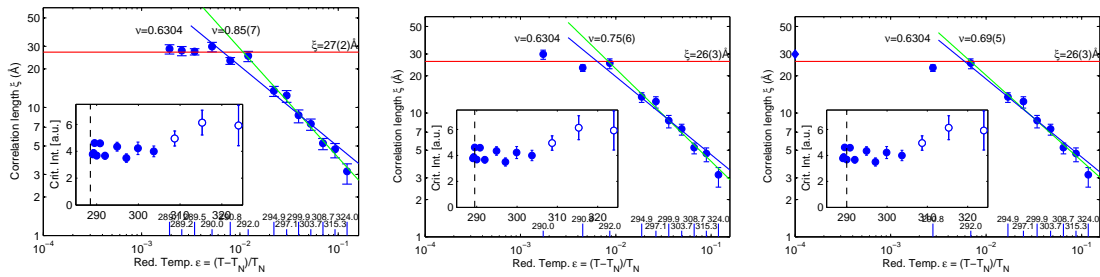


Figure 6.5.7: Correlation length  $\xi$  vs. reduced temperature  $\epsilon = \frac{T - T_N}{T_N}$  of 20 nm particles (2nd exp.) in log-log scale with different values of  $T_N$ . Left:  $T_N = 288.5$  K. Center:  $T_N = 289.5$  K. Right:  $T_N = 290.0$  K. Points marked with  $\blacklozenge$  are outside scale.

Results of the fitting of the critical peaks and subsequent extraction of the correlation length versus temperature is presented in figure 6.5.5. The plot shows as expected the points to lie on a line (on double-logarithmic scale) at large  $\epsilon$ , but at low  $\epsilon$  the correlation length does not increase above a level of  $\sim 27$  Å. The existence of a cut-off, is in itself not surprising, as the correlation length is limited by the particle size. On the other hand, a flat  $\xi$  level over such a wide temperature range ( $\sim 3$  K) is unexpected. In a temperature region where the bulk system is in the middle of a phase transition and  $\xi$  is predicted (and observed) to be very temperature sensitive, we have a system which does not change over a wide temperature range.

It should in this context be considered, whether there could be error in the determination of temperature. I find it, however, very unlikely that the observed cut-off is due to significant errors in temperature determination and control.

Firstly, the temperature controller uses an intelligent feedback circuit to control the temperature and will adjust heating according to the temperature response of the cold-finger. The temperature controller has a temperature accuracy better than 0.1 K [131], and there have been no reports or signs of malfunction.

Secondly, the cut-off is also observed in the 1st experiment (see figure 6.5.4) at close-to the same reduced temperature, showing that the observation of the cut-off is independent of use of heat shields.

Just as strange as the correlation length cut-off is the behavior of the critical scattering intensity (and thus the correlation function  $\Gamma$ ) versus temperature, shown in figure 6.5.5(inset). The intensity remains constant over a wide temperature range, even wider than that of the flat correlation length region, and there are no signs of obedience towards the critical exponents power laws. Besides a slight divergence very close to  $T_N$  in the critical intensity, nor does the first experiment (figure 6.5.2(inset)) show any significant divergence in the intensity, only a slight increase very close to  $T_N$ .

### 6.5.2 30 nm Sample Analysis Details

The analysis of this sample partly presented in section 6.3.6, follows the course of action laid out in section 6.3.5. The critical properties  $\Gamma$  and  $\xi$  are presented in figures 6.5.8 and 6.5.9. Considering the plots, the critical scattering intensity, rises from low levels (below and above  $T_N$ ) to high levels at  $T_N$ , seemingly diverging. However, on closer inspection, just above  $T_N$  the slope is finite (marked in figure 6.5.8), and does not follow the power law model close to  $T_N$ .

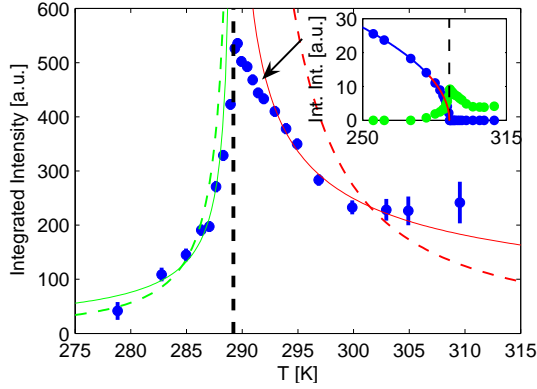


Figure 6.5.8: Critical scattering intensity vs. temperature of the 30 nm particles. The dashed lines are power law decays with 3D Ising  $\gamma=1.2396(13)$  [64]. The solid lines are fitted power laws. The arrow indicates where the intensity starts to deviate from the exponential model. Inset: Static magnetism integrated intensity  $I$  vs. temperature  $T$  fitted with power law. ( $\bullet$ ) static magnetism data points, ( $\circ$ ) critical scattering data points, (—) static magnetism power law fit, (---) extrapolated power law behavior of the static magnetism.

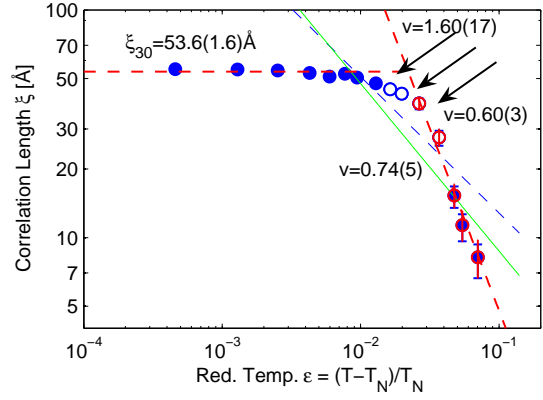


Figure 6.5.9: Correlation length  $\xi$  vs.  $\epsilon = \frac{T-T_N}{T_N}$  of the 30 nm particles. The cut off level and the power law decays are indicated by dashed lines. The arrows indicate the region with unexpected behavior. The power laws fits are: (—) is fitted to selected sloping points (marked with solid face color). (---) is fitted to all points above cut-off temperature. (---) is fitted to highest temperature points (marked with red).

The correlation length behaves as expected (from the 20 nm sample) with an increasing correlation length from high towards lower temperatures.

However, compared to the 20 nm sample data, the 30 nm sample dataset has a series of points close to the cut-off (marked by arrows in figure 6.5.9), which have an unexpected behavior. These points deviate from a power law curve, and have larger values than expected, forming a bulge-like shape. The bulge makes the analysis extra complicated, especially in regard to the extent of the cut-off and to the extraction of the critical exponents. For instance, if all data points in the bulge are used, a  $\nu=0.60(3)$  of the slope is obtained, which is significantly lower than that of the 20 nm sample.

Reviewing the details on the heating of the sample, it was discovered that the heating of the sample had been conducted relatively fast compared to other samples *e.g.* the 20 nm sample. The average time allowed for heating and thermal equilibrium to be reached in this region is 13 min, where *e.g.* the 20 nm sample was given an average of 24 min<sup>2</sup>.

Thermal equilibrium is an issue in this region, as the sample is very temperature-sensitive. Furthermore the sample powder is loosely packed and has thus not good thermal contact. The mentioned time difference thus seems to be crucial, in order for the samples to reach thermal equilibrium.

A different possibility is that the Néel temperature has been erroneously determined and

<sup>2</sup>Although the difference may seem small, the difference is quite significant.

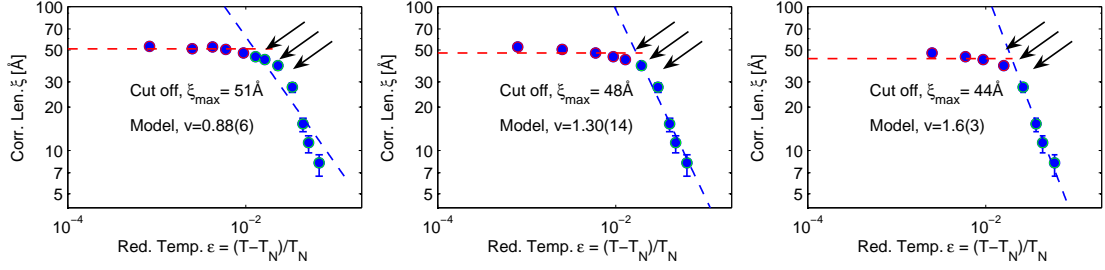


Figure 6.5.10: Correlation length  $\xi$  vs. reduced temperature  $\epsilon = \frac{T - T_N}{T_N}$  of the 30 nm particles, with different values of  $T_N$ . From left,  $T_N = 290.2\text{K}$ ,  $291.2\text{K}$  and  $292.2\text{K}$ . As seen, the most notable difference when changing  $T_N$ , is an increase in  $\nu$ . Red-edged points are used for calculation of the cut-off level, and green edged-points are used for  $\nu$  extraction.

should actually be higher. To test this, a series of plots with different Néel temperature values,  $T_N = T_{N_{org}} \pm \{1, 2, 3\}\text{K}$  was produced. Examples of these are shown in figure 6.5.10. However, as also seen from the plots, the bulge-like feature is not due to an incorrectly determined Néel temperature. Below the original Néel temperature,  $T_{N_{org}} = 289.2 \pm 2.7\text{K}$ ,  $\nu$  is very low,  $\sim 0.55$ , and above  $T_{N_{org}}$ ,  $\nu$  increases dramatically, and reaches values of more than 2.5 times the predicted 3D Ising value  $\nu = 0.6304(13)$  [64] at  $T_N = T_{N_{org}} + 3\text{K}$ ! Simultaneously the cut-off value  $\xi_{max}$  is lowered with increasing  $T_N$ .

Conclusively, it is very likely that the sample was not in thermal equilibrium and that the mean sample temperature, over the measurements in the bulge-like shape, thus was lower than reported by the temperature control. A temperature lower than reported would exactly give the bulge-feature, if one compares to the 20 nm sample behavior.

### 6.5.3 10 nm Sample Analysis Details

The scans early in the analysis showed that the sample is contaminated by  $\text{Co}_3\text{O}_4$ . In the fitting of the critical scattering, the fitting is significantly hampered by the  $\text{Co}_3\text{O}_4$  (111) peak, lying close to the  $\text{CoO}$   $(\frac{1}{2}\frac{1}{2}\frac{1}{2})$  position, as evident from figure 6.5.13 (inset). The proximity of the (111), means that it has to be taken into account in the fitting. Therefore the highest (324 K) and lowest temperature (6.8 K) datasets are fitted to find the instrumental broadening, the static magnetic peak width and the Lorentzian width of the  $\text{Co}_3\text{O}_4$  (111) peak. The Néel temperature is found as described earlier.

Secondly the analysis is hampered by the  $\text{Co}_3\text{O}_4$  (220) peak at  $\sim 2.20\text{\AA}^{-1}$ , obstructing the background at high  $q$ , and by the small angle scattering from the direct beam at low  $q$ , which gives a significant rise of the of the background at  $\sim 0.6\text{\AA}^{-1}$ . These two background disturbances limit the range in which we can find a flat background.

From fitting the integrated intensity in the region 215-279 K, the Néel temperature is found to  $T_N = 287(2)\text{K}$ , and the critical scattering is fitted using this value. The result of the fitting is that the critical scattering (figure 6.5.11) rises to a maximum level around  $T_N$ , as expected from theory (2.1.5)-(2.1.7) and (2.1.13). However, there are 3 points above  $T_N$  where the intensity is unexpectedly high, raising the suspicion that  $T_N$  has been erroneously determined. However, considering the large error bars on these deviating points, and the smaller error bars on the surrounding points following a regular trend, I dismiss these points as fitting errors.

The correlation length, on the other hand, behaves more like the other nanosized samples, and does not exceed a certain level. However, as seen from figure 6.5.12 in this sample, the error bars on  $\xi$  are quite significant, and it can be questioned whether a slope can be seen at high  $\epsilon$ . The data show, however, an upper limit to the correlation length, which is not higher than  $\sim 32\text{\AA}$  and most likely not higher than  $\sim 20\text{\AA}$ .

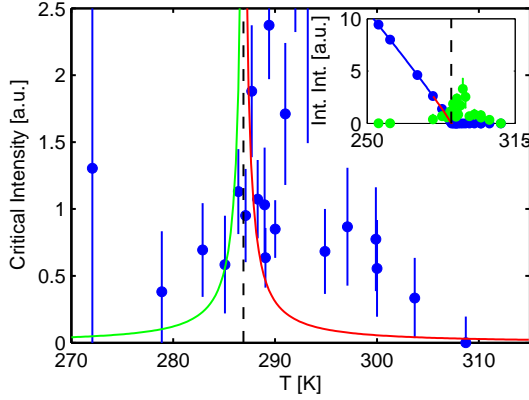


Figure 6.5.11: Critical scattering integrated intensity  $I$  vs.  $T$  of the 10 nm particles. The solid lines are guides to the eye and follow the 3D Ising  $\epsilon^{-\gamma}$  ( $\gamma=1.24$ ).  $T_N$  is indicated by the dashed line. Inset: Static magnetism integrated intensity  $I$  vs. temperature  $T$  fitted with power law. (●) static magnetism data points, (●) critical scattering data points, (—) static magnetism power law fit, (—) extrapolated power law behavior of the static magnetism.

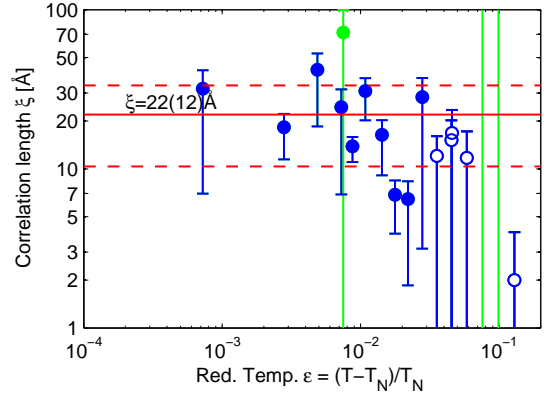


Figure 6.5.12: Correlation length  $\xi$  vs. reduced temperature  $\epsilon = \frac{T-T_N}{T_N}$  of the 10 nm particles. The (—) and (---) are the mean and standard deviation, respectively, of the cut-off  $\xi$ , extracted from the points marked as (●). (●) represents points deemed invalid.

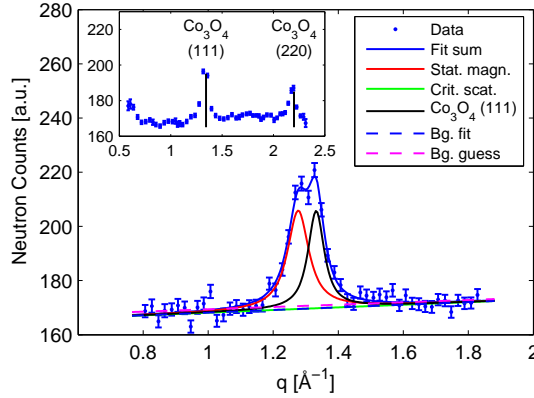


Figure 6.5.13: Fitting of  $\text{CoO}$  ( $\frac{1}{2}\frac{1}{2}\frac{1}{2}$ ) and  $\text{Co}_3\text{O}_4$  (111) Bragg peaks in the 10 nm particles at 272 K. Inset: Full  $q$  range raw data with visible  $\text{Co}_3\text{O}_4$  peaks (marked) at 315 K.

## 6.6 Discussion and Conclusion

In the following I will discuss the results of the neutron diffraction investigations of the critical phenomena in CoO nanoparticles.

### 6.6.1 Consistency Check

One could argue that the cut-off in correlation length is an artifact of a wrongly determined Néel temperature. A wrong determination of  $T_N$  would cause points which truly are close in reduced temperature, to appear well separated, giving an illusion of a cut-off like shape. However, I will in the following provide considerations and arguments, for that I have chose correct Néel temperatures.

Firstly, all Néel temperatures have been found using the same method, and mistakes are thus likely to appear as systematic errors.

In the bulk sample, with the found  $T_N$ , the correlation length diverges, and follows a power law (*i.e.* a line in a log-log plot) as shown in figure 6.4.2.

Using a Néel temperature found through the same method, I find in the 20nm sample a  $\nu$  value of the slope similar to that found for bulk.

Furthermore the high temperature data (outside the cut-off) follow a power law nicely, which would not be the case if a incorrect  $T_N$  was used.

Turning to the intensity, the critical intensity at  $T_N$  is constant. If a too low  $T_N$  had been chosen, the long range order power law would not account for all the long range order intensity. This would therefore be detected as a sloping critical intensity, with negative slope as the long range order went to zero, on the other hand, if  $T_N$  was too high, the critical intensity would be zero or close to zero.

The last argument for a correct  $T_N$ , is the observation that there is a broadening of the critical peak component to both lower and higher temperatures, from  $T_N$  – indicating a correct  $T_N$  with minimal peak broadness.

## 6.6.2 The Cut-Off in the Correlation Length

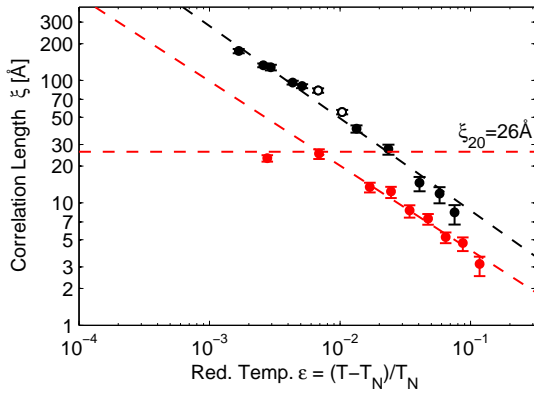


Figure 6.6.1:  $\xi$  vs.  $\epsilon$  for samples bulk and 20 nm. The dashed horizontal lines are the found cut-off correlation lengths, and the sloping dashed lines are power law fits to the data. (●) Bulk sample. (●) 20 nm sample.

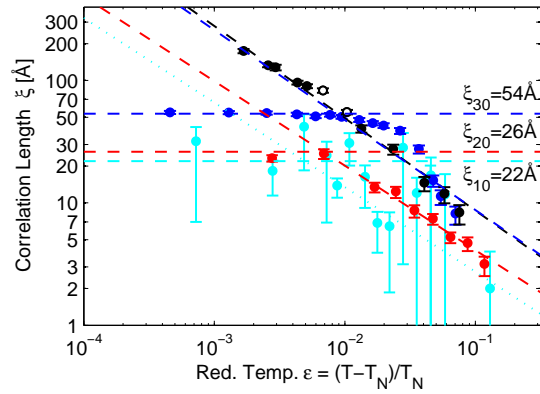


Figure 6.6.2:  $\xi$  vs.  $\epsilon$  for all samples. The dashed horizontal lines are the found cut-off correlation lengths, and the sloping dashed lines are power law fits to the data. The dotted sloping lines are coarse fits made by eye. (●) Bulk sample. (●) 30 nm sample. (●) 20 nm sample. (●) 10 nm sample.

Comparing the development of the correlation length with temperature, in the bulk and the 20 nm samples, the most distinct and significant result of the experiments is that there is a cut-off in the correlation length in the 20 nm sample of  $\xi_{20}=27(2)$  Å and no cut-off in the bulk sample, which is particularly clear from figure 6.6.1. The physical interpretation of this is, that it is caused by the finite size of the 20 nm particles, which sets an upper limit for the correlation length.

Similarly the cut-offs  $\xi_{max}$  of the correlation length of the 30 nm and 10 nm samples are  $\xi_{30}=53.6(1.6)$  Å and  $\xi_{10}=22(17)$  Å, respectively.

The error on the 10 nm sample correlation length cut-off is large and the found value should rather be considered an upper limit for the correlation length cut-off. There is only a weak indication of a slope above the cut-off temperature, marked with a dotted line in figure 6.6.2.

As seen from the sloping part of the correlation length in figures 6.6.1 and 6.6.2, there seems to be an vertical offset between the individual datasets. The trend is that at given temperature,

the correlation length increases with increasing particle size.

In particular, the difference between the bulk and the 20 nm data is clear. The 30 nm sample data appears to be similar to the bulk data (apart from the non-physical points in the bulge-like shape), while the 10 nm data show a correlation length smaller than the 20 nm data.

The development of correlation length with particle size is most likely a finite size effect, and could be an indication that the surface-close spins have a reduced contribution to the measured correlation length, which is consistent with that surface-close spins have a larger volume fraction, with decreasing particle size. This will be discussed further later in this section.

The behavior of the surface spins can also be regarded as a pure temperature activation phenomena, in which the surface spins, due to the reduced number of neighbors are more susceptible to thermal fluctuations, and therefore do not contribute to the correlation length. The system is thus approaching bulk behavior with increasing particle size, as there are more 'bulk' spins with larger particle size.

To illustrate the impact of surface contribution in small particles, we can as an example consider a surface layer of fixed thickness  $a=2$  nm in a spherical particle with radius  $r$ .  $r$  then has to be larger than  $\sim 9.7$  nm (or 19.4 nm in diameter) for the core volume to exceed the surface volume. Similarly, the surface to core volume ratio is  $\sim 3.6$  and  $\sim 0.53$  for  $r=5$  and 15 nm, respectively.

Sample	$d$ nm	$W_L$ $\text{\AA}^{-1}$	$d_m$ nm	$W_{L,min}$ $\text{\AA}^{-1}$	$\xi_{max}$ $\text{\AA}$	$\xi'_{max}$ nm
Bulk	-	0.00372(11)	169(5)	-	-	-
30 nm	29.9(5)	0.0295(2)	20.05(14)	0.0374(12)	53.6(1.6)	15.8(5)
20 nm ‡	19.3(8)	0.0459(4)	12.87(11)	0.074(7)	27(2)	8.0(7)
10 nm	11.2(2)	0.0749(6)	7.89(7)	0.09(4)	22(17)	6.6(5.0)

Table 6.6.1: *CoO* sample list of measured length scales. Details of how these were achieved are described in the text.  $d$  is the structural particle size,  $W_L$  is the static magnetism long range order Lorentzian width,  $d_m = 2\pi K/W_L$  ( $K=0.94$ ) is the magnetic particle size (or magnetic domain size) found from  $W_L$  using the Scherrer formula.  $W_{L,min}$  is the minimal Lorentzian width of the critical scattering,  $\xi_{max} = 2/W_{L,min}$  and  $\xi'_{max} = 2\pi K/W_{L,min}$  are the corresponding correlation length cut-off and apparent correlation length cut-off, respectively.

### Structural and Magnetic Size

Table 6.6.1 shows the structural size, the magnetic size and the critical correlation lengths found for the investigated samples. As mentioned, the structural size is found from XRD, the magnetic size from the low temperature neutron data and the correlation length from the cut-off in the width of the critical Lorentzian.

Comparing the structural and the magnetic particle sizes, it appears that there is an offset between the structural size and the magnetic size. This offset appears to increase with particle size. Applying the core-shell model, shown in figure 6.6.3, there is a non-magnetic shell  $\frac{d-d_m}{2}$  of 9.9(6)/2=5.0(3) nm, 6.4(9)/2=2.7(5) nm and 3.3(3)/2=1.7(2) nm on the 30 nm, 20 nm and 10 nm particles respectively. Considering the error bars, the found values are significantly different.

This is most likely caused by finite size effects in the magnetic order, uncompensated surface spins, which are 'invisible' to the neutron scattering, leaving the magnetically ordered part of particle size smaller than the physical particle size. The difference is illustrated in figure 6.6.3.

However, a magnetically disordered layer of 5 nm (for the 30 nm particles) seems a rather large value, compared to that the 10 nm particles, which are 11.2(2) nm in diameter and have a disordered layer of 1.7 nm. From these results it looks like the disorder-layer thickness is not constant, but maybe grows with particle size. An explanation could be that the particles are not spherical as indicated in the figure, but more irregular, giving rise to the large difference between structural and magnetic size. Given the method of preparation, annealing, it can be questioned whether the

particles have a regular shape, and to which degree the core shell model applies.

An alternative to the core shell model, is that the discussed length scales scale with particle size. The source of this scaling could lie in the applied experimental setups and methods. These have, however, been carefully reviewed to ensure a correct procedure.

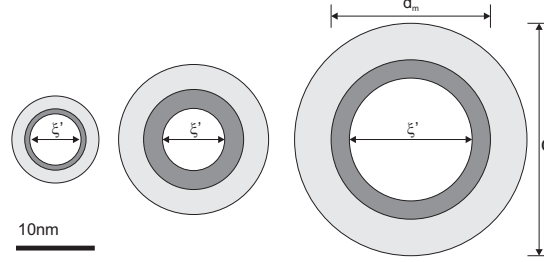


Figure 6.6.3: Schematic illustration of the core-shell model. Drawn in are the 10 nm, 20 nm and 30 nm particles with found correlation lengths. For each particle the outer-most light-gray circle represents the structural size, the middle dark-gray circle the 'magnetic size' and the inner-most white the apparent correlation length.

### Magnetic Size and Correlation Length

Studying the *magnetic* correlation length, the *magnetic* particle size is more important than the physical particle size. Comparison of the magnetic size and the apparent correlation length, yields that the apparent correlation length is smaller than the magnetic size by 4.3(6) nm, 4.9(8) nm and 1.2(5.1) nm for the 30 nm, 20 nm and 10 nm particles respectively. In the core-shell model this corresponds to a 'shell' thickness of 2.2(3) nm, 2.5(4) nm and 0.6(2.6) nm, respectively, meaning that the 30 nm and 20 nm samples have the same apparent correlation length 'shell' thickness, and where it can be significantly questioned whether the 10 nm data show a 'shell' at all.

Where the difference in physical size and 'magnetic size' is relatively easy to explain, the explanation for the difference between the apparent correlation length and magnetic size is more elusive. The magnetic size represents the size of the particles where the magnetic environment is 'stable' enough for long range order to form *i.e.* where there are (close-to) magnetic periodic boundary conditions. Within this (below  $T_N$ ) magnetically ordered region, the apparent correlation length should intuitively, behave bulk-like.

Considering the above the core-shell model, the 20 nm and 30 nm particles apparently contain a layer of  $\sim 2.5$  nm in the magnetically ordered region, where no correlation length is detected.

As a model for the 'dead' apparent correlation length layer, I propose that the contribution to the total correlation function from the outer parts of the 'magnetically ordered' particle, are dominated by the contribution from the core of the magnetically ordered particle.

As previously mentioned, the correlation function (3.2.28), (3.2.31) between individual spins is given as

$$\Gamma_{i,j} = \Gamma(\mathbf{r}_{i,j}, \epsilon, h) = \langle \mathbf{s}_i \cdot \mathbf{s}_j \rangle - \langle \mathbf{s}_i \rangle \cdot \langle \mathbf{s}_j \rangle, \quad (6.6.1)$$

$$\Gamma(\mathbf{r}_{i,j}, \epsilon, 0) \propto \frac{e^{-r_{i,j}/\xi}}{r_{i,j}^{d-2-\eta}}, \quad (6.6.2)$$

is exponentially decaying with distance. The total correlation function  $\Gamma$  for a full particle is given

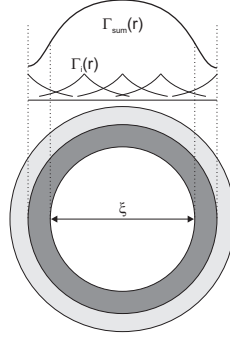


Figure 6.6.4: Schematic illustration of the total correlation function of a nano-particle. The top curve is the total correlation function  $\Gamma$ , versus particle  $\mathbf{r}$ . The individual exponentials are the individual spin-spin correlation functions  $\Gamma(\mathbf{r}_{i,j}, \epsilon, 0)$  (6.6.2). The exponents of the exponentials are not to scale.

as

$$\Gamma = \sum_{\langle i,j \rangle} \Gamma(\mathbf{r}_{i,j}, \epsilon, h) = \sum_{\langle i,j \rangle} \langle \mathbf{s}_i \cdot \mathbf{s}_j \rangle - \langle \mathbf{s}_i \rangle \cdot \langle \mathbf{s}_j \rangle, \quad (6.6.3)$$

$$\Gamma(\epsilon, 0) \propto \sum_{\langle i,j \rangle} \frac{e^{-r_{i,j}/\xi}}{r_{i,j}^{d-2-\eta}}, \quad (6.6.4)$$

where  $\sum_{\langle i,j \rangle}$  mean a sum over all combinations of spins  $i$  and  $j$ .

The surface-close spins have fewer 'close' neighbors (having fewer neighbors outwards), than the core spins, and give thus a reduced contribution to the total correlation function, and thus to the scattering intensity, as illustrated in figure 6.6.4.

This model can explain the observed phenomena, as the inner parts of the sample will give a dominating contribution to the scattering, yielding an apparent correlation length smaller than particle size.

The 10 nm sample is different from the other two samples with a 'dead' apparent correlation length layer less than 1 nm. The 10 nm sample differs from the other samples in manufacturing method, but I do not believe this to be the origin of this difference, since the origin of both the magnetic size and the apparent correlation length values is magnetic scattering.

Rather, in the very small particle size case (10 nm), the weak scattering from the spin-spin correlations in the surface-close regions is observable, as the core contribution, if existent, is not large enough to dominate it. The low contribution to the correlation function from the individual parts of the magnetic sample is consistent with the large errors on the apparent correlation length.

However, the above equations (6.6.1-6.6.2) are not necessarily valid close to the surface of the magnetic part of the particle. The net effect would, however, be similar, namely a similar effect with a reduced contribution from the outer spins.

Another explanation for the reduced correlation length is the experiment itself. Measuring in a two-axis setup mode, with no energy selection, the experiment automatically integrates over all available energies [15]. Therefore we have to integrate the scattering function  $S(\mathbf{q}, \omega)$  (3.2.12), over all available energies, that is, up to the incoming energy  $E_i=3.7$  meV. The scattering function therefore becomes [158]

$$S(\mathbf{q}, E_i) = \int_{-\infty}^{E_i} \frac{\mathbf{k}_f}{\mathbf{k}_i} S(\mathbf{q}, \omega) d\omega \simeq S(\mathbf{q}). \quad (6.6.5)$$

This means that if there is inelastic scattering, there will be a fraction which lies outside of what we can measure, as the incident energy is too low.

The point is that as there is some inelastic scattering not detected by our experimental setup and therefore that the measured correlation length will not be exactly what is usually understood by correlation length, namely the size of a typical correlated region in a snapshot ( $\mathbf{s}_0(t=0) \cdot \mathbf{s}_r(t=0)$ ).

Without going further into this, it is sufficient to conclude that the found correlation length will be a measure of the correlation length, and most likely lie close to the true value, as  $S(\mathbf{q}, E_i) \simeq S(\mathbf{q})$ .

### 6.6.3 Néel Temperature and Critical Exponents

Sample	$T_N$ (K)	$\beta$	$\nu$	$\gamma'$	$\gamma$
3D Heisenberg [64]	-	0.3662(25)	0.7073(35)	-	1.3895(50)
3D Ising [64]	-	0.3258(14)	0.6304(13)	-	1.2396(13)
CoO bulk [153]	288.98(10)	0.290(25)	-	-	-
Bulk	288(3)	0.28(5)	0.754(19)	1.62(7)	0.340(10) <sup>†</sup>
30 nm <sup>†</sup>	289(3)	0.25(2)	0.74(5)	0.87(7)*	0.47(4)*
20 nm <sup>‡</sup>	290(4)	0.43(8)	0.80(6)	-	-
10 nm	287(2)	0.46(3)	-	-	-

Table 6.6.2:  $T_N$  and critical exponents found from the investigated samples. For comparison numerically and experimentally found values are also listed. (<sup>†</sup>) 30 nm  $\nu$  is extracted from selected points on the log-log slope. (<sup>‡</sup>) 20 nm  $\beta$  is from 1st experiment, and  $\nu$  is from 2nd experiment. (\*) These values are invalid, see text.

Where the data have been suitable, I have extracted the critical exponents  $\beta$ ,  $\nu$ ,  $\gamma'$  and  $\gamma$ , in order to compare them to the previously found values and simulation results. The obtained results are listed in table 6.6.2.

#### Extraction of Néel Temperatures

All samples are found to have a  $T_N$  similar to that reported by Rehtin *et al.* (1971) [153], and only the 10 nm sample has a tendency towards slightly lower values.

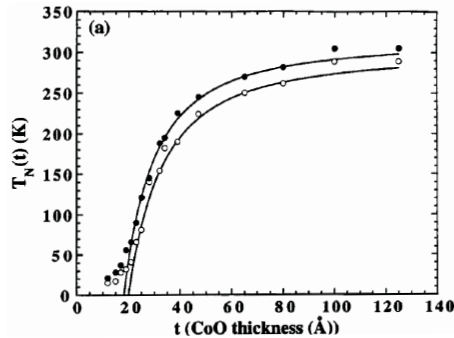


Figure 6.6.5:  $T_N(t)$  vs. CoO film thickness  $t$ . These data were measured using DC susceptibility, and the solid and open points are obtained from the peak in  $\chi(T)$  and  $d\chi(T)/dT$ , respectively. From ref. [6].

A reduction of the Néel temperature is not unexpected, as it is commonly reported in nano-sized samples *e.g.* in refs. [48, 49]. From the results, it seems that the critical size for reduction of the Néel temperature in CoO is  $\sim 10$  nm.

Ambrose *et al.* (1996) [6] report for CoO films, measured with DC susceptibility, a decreasing  $T_N$  with decreasing CoO film thickness from  $\sim 120$  Å, and indicate that it is unchanged for larger

thicknesses, in good agreement with our data (see figure 6.6.5). They find slightly higher values of  $T_N$  (300 and 315 K), than otherwise reported in literature, which, however, most likely can be attributed to the technique used.

A significantly lower  $T_N$  of 278(0.5) K, is reported for porous CoO with particle sizes of 100(5) Å [60]. The porous nature of this sample, might, however, have influence on this result.

A reduced  $T_N$  is also found by Klausen *et al.* (2002) [86], for the CoO-related compound NiO, where disc-shaped nanoparticles (12 nm wide and 2 nm thick), exhibit a reduced  $T_N$  from 523 K to  $\sim$ 460 K.

In their work on CoO films, Ambrose *et al.* [6] present the finite-size effects on the ordering temperature as

$$\frac{T_N(\infty) - T_N(t)}{T_N(\infty)} = \left(\frac{\xi_0}{t}\right)^\lambda, \quad (6.6.6)$$

where  $T_N(\infty)$  and  $T_N(t)$  are the Néel temperatures at infinite film thickness and  $t$  thickness, respectively.  $\xi_0$  is the extrapolated correlation length at  $T=0$  K and  $\lambda$  is the shift exponent for the finite size scaling ( $\lambda = 1/\nu$ ). They fit the found  $T_N$  to the finite-size scaling relation, and find shift exponent values of 1.54(5) and 1.55(5) using two different approaches, which matches the theoretical estimate for a 3D Ising by Ferrenberg *et al.* (1991) [46] of 1.5587(4) well. Considering the points of similarity between behavior by CoO particle  $T_N$ , in particular the 10 nm, and the CoO films, I find it very likely that our measurements and determination of the  $T_N$  of the CoO particles is correct, and that a significant reduction of  $T_N$  only occurs for smaller particle sizes.

### Extraction of Critical Exponents

Figure 6.6.6 shows the fitted integrated intensity versus temperature for all samples, illustrating

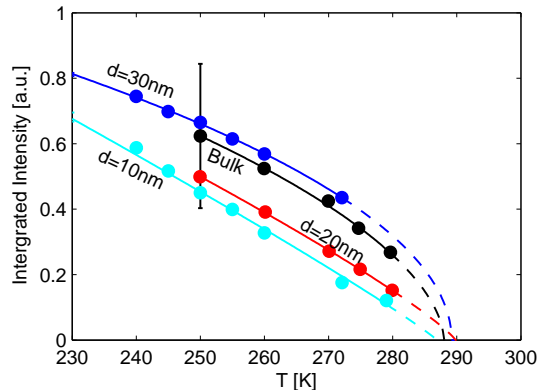


Figure 6.6.6: *Integrated intensity  $I$  vs.  $T$ , for all samples, illustrating the different  $\beta$ 's of the samples.  $I$  is normalized to the 200 K value. (●) Bulk. (●) 30 nm. (●) 20 nm. (●) 10 nm.*

the  $\beta$  values. From the found values it seems that the 30 nm  $\beta$  is bulk-like, whereas the  $\beta$  values for the 20 nm and 10 nm samples are increasing with decreasing particle size, showing an increasing deviation from the predicted 3D Ising values. This is not entirely unexpected, considering nano-scale effects in general, the results from chapter 5 and even results in literature *e.g.* in NiO particles as reported by Klausen *et al.* (2002) [86], which have a flatter magnetization curve and hence a larger  $\beta$ .

The exponent  $\nu$  of the correlation length, has been extracted from the sloping part of the  $\xi$  vs.  $\epsilon$  data in *e.g.* figure 6.6.1. The found value for  $\nu$  is for all samples deviating significantly from the 3D Ising value 0.6304(13) predicted by Guida *et al.* (1998) [64]. The bulge-like shape in  $\xi$  in the 30 nm data casts doubt on the validity of this  $\nu$ , but the bulk and 20 nm values are similar, suggesting similar behavior. Considering the errors on these two values, my estimate of

the critical  $\nu$  for CoO is thus 0.78(4) – a value valid for bulk CoO, as the slope (of the sloping part) of the  $\xi$  versus  $\epsilon$  plot are similar (figure 6.6.1).

As mentioned the found  $\nu$  value is very high compared to the predicted values for a 3D Ising system, and are close to the predictions for a 3D Heisenberg, shown in table 6.6.2.

I have attempted to fit the critical intensity exponent  $\gamma'$  and  $\gamma$  (table 6.6.2). The found values show a large variation, and large deviations from the predicted values. In the light of the large variations I will not claim that the found values represent the true  $\gamma'$ ,  $\gamma$  exponents of the CoO system, except the bulk  $\gamma'$  value which combined with  $\nu$ , and using  $\gamma'=\gamma$  (see section 2.1.3), is close to fulfilling the Fisher scaling law (2.1.16),

$$\frac{\gamma'}{\nu} = (2 - \eta) \simeq 2, \quad (\eta \simeq 0) \quad (6.6.7)$$

$$\Rightarrow \frac{1.62(7)}{0.754(19)} = 2.15(5) \simeq 2. \quad (6.6.8)$$

The remaining  $\gamma'$  and  $\gamma$  values, deviate from the predicted values by a factor of 2-4, and significantly violate the  $\gamma'=\gamma$  relation for 3D Ising systems. Deviations of this size in systems which otherwise behave 'similar' (regarding  $\beta$  and  $\nu$ ) to bulk systems, deem these values useless. However, for documentation these values (marked with (\*)) are presented in table 6.6.2.

#### 6.6.4 Mesoscopic Range Order

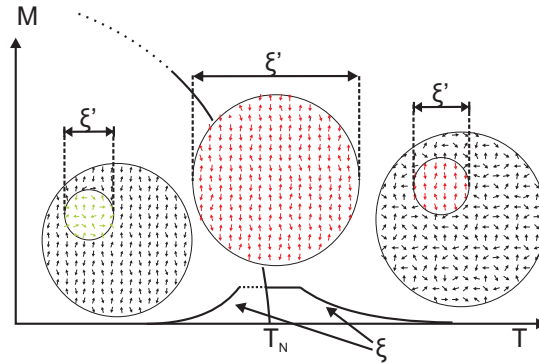


Figure 6.6.7: Schematic illustration of the behavior of the correlation length  $\xi$  and the apparent correlation length  $\xi'$  around the correlation length cut-off. On the left, a long range ordered particle, with small domains of disorder. In the center, a particle in the cut-off region above  $T_N$ . In the right, a particle with only small domains of correlated spins. The dashed  $\xi$  below  $T_N$  has not been studied, but observed as a peak broadening below  $T_N$ . The curves, staggered magnetism  $M$  and correlation length  $\xi$  are not in the same scale or unit.

As mentioned, the most prominent feature of the data on the nanosized systems, is that in the region just above  $T_N$ , it shows a constant correlation length over a  $\epsilon$ -region 0 to  $\sim 10^{-2}$ , corresponding to a temperature region of  $\sim 3$  K, as illustrated schematically in figure 6.6.7.

At high  $T$ 's with low  $\xi$ -values, the system behaves bulk-like, since the correlation length (and the apparent correlation length) – is much smaller than the particle size, meaning that most spins can not see the finiteness of the system.

Cooling towards  $T_N$ , the correlation length of the magnetic fluctuations increases reaching the maximum dictated by the particle size. At this temperature  $\xi'$  has risen to  $\xi'_{max}$ , all the spins are correlated, and the apparent correlation length spans the entire particle.

A bulk system is in this region very temperature sensitive, and it is therefore stands in stark contrast, that the nanosized system is invariant to variation in  $T$ , and only changes when the nominal bulk  $\xi$  is below  $\xi_{max}$ .

To understand this behavior we consider the correlations in a single particle. When the apparent correlation length reaches the particle size, it can not grow anymore and the particle does not have further degrees of freedom to become further correlated, except inter-particle correlations. Inter-particle correlations, however, have not been observed. In this state all spins in the particle are correlated, but static long range order can not form, as  $T$  is above  $T_N$ . Considering the system size, the state is an effective long range order, independent on temperature, which might be called a mesoscopic range order (MRO) state.

It has during this thesis work been discussed if the MRO state was a new phase. However, there is neither evidence nor indications that the MRO state should be a new phase. Rather, it is a temperature regime, where an 'ideal' system ceases to be ideal, and responds to the spatial limitations applied to it.

### 6.6.5 Perspectives and Outlook

From the results of these experiments, very interesting new questions emerge. In the above section I propose the possible existence of a new mesoscopic range order (MRO) regime. With the present knowledge on this system, this proposition can neither be shown not rejected, and further investigations of the thermodynamic properties should be conducted.

#### Critical Exponents

There are several characteristics of phase transitions, including abrupt changes in thermodynamic properties such as heat capacity. Finite systems are, however, known to exhibit phase transitions, where the change in thermodynamic quantities is rounded [76, 77]. If the MRO is new phase, it should have phase transitions to both the paramagnetic state and the antiferromagnetic state.

From the observation that  $\nu$  becomes zero in the MRO state, and by using the Josephson scaling law (2.1.17) we get that  $\alpha$  changes value abruptly from  $\alpha = 2 - d\nu = -0.40(18)$  to 2 ( $d$  is system dimensionality). This causes a dramatic change in heat capacity at the onset of the  $\xi$  cut-off, which may signify a phase transition. This is of course only valid, provided that the power laws do not break down entirely. In principle the scaling laws are valid only for infinite systems, and may therefore be invalid as an argument for characterization of MRO as a new phase.

In context of the Josephson scaling law, the value of system dimensionality  $d$  may be explored. In an infinite system, or a very large system the value would be 3 for a 3D Ising, but is this also the case in a finite system as the present? One could argue that in a system, finite in all directions, the dimensionality is 0. A measurement of the heat capacity critical exponent  $\alpha$  would determine this, as the only unknown parameter in the Josephson scaling law would then be the system dimensionality  $d$  – again provided that the scaling law hold in this regime.

#### Collective Magnetic Excitations

There is no conventional long range order in the MRO state, and conventional magnons, understood as spin-deviations from the equilibrium long-range order orientation, can therefore not form. It is therefore possible that a state arises here, where there is no normal magnon dispersion relation.

The found  $\nu$  value indicates that the spin system is more Heisenberg-like than Ising-like, and therefore that the spin-orbit coupling is significantly weakened. If this is the case, and observing that the system in the MRO state, where all spins are correlated, the possibility for collective magnetic fluctuations similar to those observed in hematite [66], could arise.

The constant correlation length in the MRO state, over a relatively large temperature interval, can possibly be explained by the existence of collective magnetic fluctuations. These collective spin fluctuations of the correlated spins could possibly absorb the difference in thermal energy while the system is in the MRO state.

The existence of collective spin fluctuations, has recently been indicated [16, 17, 107] in preliminary results from inelastic neutron scattering measurements in the range  $[T_N-30\text{ K}, T_N+30\text{ K}]$ . In these measurements an inelastic signal is observed at both  $T_N$  and at 310 K, at  $\sim 0.5\text{ meV}$  from

the elastic ( $\frac{1}{2}\frac{1}{2}$ ) peak. As  $T$  is above  $T_N$ , this can not be attributed to magnons, as can thus be interpreted as a sign of a collective spin excitation.

### Understanding the Correlation Length

Although the correlation length has a simple definition, the understanding of exactly how the correlation length and the correlation function relates to the physical size of the spins system, is elusive.

The definition of the correlation length from (6.1.4) has the unit of length, but as demonstrated earlier, it differs from the expression for physical size, when put in relation to the Scherrer formula.

The correlation length has an exponentially decaying nature, given as the value of  $r_{i,j}$  where the term  $e^{-r_{i,j}/\xi}$  is  $1/e$ . This definition is valid in infinite systems, but the question remains, how it should be understood in a finite size system. As a prerequisite for this definition is a infinite (or large) system, how does the correlation function and hence the correlation length behave close to the system border?

This question can be elucidated through computer simulations, as the number of spins in a typical CoO particle can be modelled using modern computers. In fact, there is work in progress [16, 17], where computer simulations are used to simulate the individual spin-spin correlations, in order to extract the correlation function. These results may for instance be used to extract the shape of the Bragg peak and the maximum correlation length as a function of particle size.

### Further Investigations

With the many open questions regarding the MRO regime, and the properties of this state, further investigations of the thermodynamic properties should be performed. The indications that the  $\nu$  is Heisenberg-like, is also a motivation for further investigations.

These measurements have to include careful mapping of the heat capacity, optionally the magnetic susceptibility, as well as further neutron scattering studies, both elastic and inelastic.

However, the first prerequisite for a further elucidating study on CoO nanosized particles is that clean and well characterized samples are available. A homogenous particle size is in this context important, and to optimize a size sorting technique could for instance be applied.

The purpose of the elastic measurements would be to obtain better data, by improving the experimental setup by *e.g.* using triple axis mode.

Inelastic measurements should be used to investigate possible changes in the elastic response, a possible lifetime peak broadening, as well as to investigate the existence of the suggested collective spin fluctuation state.

High quality temperature control is crucial for making successful measurements of critical exponents and critical phenomena. In future experiments, great care should therefore be taken to ensure high precision temperature control as well as thermal equilibrium conditions. For instance, a temperature sensor inside the sample container could be applied.

# Chapter 7

## Summary and Outlook

This section contains a brief summary of the results obtained in this thesis and of the outlook of these results. The results and outlooks have already been discussed thoroughly in the conclusions of chapter 5 and 6, and this chapter is only intended as a summing up. In addition to the above a new subject is discussed in the outlook, since it has not been treated earlier.

### 7.1 Summary

The magnetic properties of YBCO and CoO nanoparticles have been thoroughly investigated by means of a variety of complementary experimental techniques. The use of different techniques allows verification and validation of the results of the individual techniques.

The samples were manufactured through a sol-gel method (nano-YBCO), solid state calcination (bulk YBCO), ball-milling (CoO), annealing (CoO). After preparation the YBCO samples have been annealed in oxygen at various partial pressures and temperatures to achieve specific oxygen content and doping state.

The particles have been characterized using Transmission Electron Microscopy, Atomic Force Microscopy (YBCO only), X-Ray Diffraction and magnetic AC-susceptibility.

Our experiments show that it is possible to study the magnetic order in YBCO nanoparticles using triple-axis neutron scattering as well as muon spin rotation. Furthermore, it is proven possible to study critical phenomena in both bulk and nanosized CoO and to extract critical exponents.

The investigation of disc-shaped YBCO nanoparticles,  $\sim 30$  nm in diameter and  $\sim 4$  nm thick, reveals that nearly all physical properties of the system exhibit finite-size effects. Utilizing neutron scattering the magnetization curve is from power law fitting found to have a higher  $\beta$ -value, which makes it flatter than for bulk YBCO. Through both neutron scattering and muon spin rotation measurements the Néel temperature  $T_N$  is found to be lower than the bulk value. Furthermore, different values of  $T_N$  are found through muon spin rotation and neutron scattering, indicating that there is a distribution of  $T_N$  values within the individual samples. The question whether the  $T_N$  distribution is due to superparamagnetism (time-scale related) or due to a distribution of the magnetic order parameter within the individual particles (surface spin melting) has yet to be determined.

The exciting reemergence of the native-like Néel state in doped nano-YBCO is observed through muon spin rotation, observations which are supported by indications from neutron scattering measurements. The reemergence is most likely caused by slowing and eventual freezing of the hole dynamics. At low temperatures the doped holes are immobile and therefore only have a small effect on the magnetic properties of the system and one observes an internal field characteristic for the undoped compound. Mobile holes will frustrate the magnetic order and will be seen as a reduction of the internal magnetic field.

Applied field experiments on the YBCO nanoparticles showed signs of spin canting and spin

flop phenomena at low and high dopings, respectively, strongly related to the dimensionality of the system. These results are controversial, as the applied field is too low to cause a response in bulk YBCO and might prove to be an nice example of a rare direct observation of surface spin effects.

The investigation of critical phenomena in CoO nanoparticles showed that the correlation length in nanoparticles behaves similar to bulk at temperatures where the bulk correlation length is smaller than the magnetic particle size. However, when the correlation length becomes similar to the magnetic particle size, a cut-off in the correlation length is observed, which remains unchanged over a temperature range of several degrees. The correlation length cut-off temperature regime is interpreted as an effect of a short ranged magnetic order covering all spins in the system.

In accordance with results in literature, the Néel temperature does not vary with particle size, for particles of diameter larger than  $\sim 12$  nm.

The critical scattering intensity in the nanoparticles is found to exhibit a weak divergence only, in contradiction to theoretical predictions. The lack of dispersion is probably also a finite-size effect, as even the bulk-sized sample (with magnetically ordered diameter  $\sim 160$  nm) in our study did not exhibit a full divergence.

The correlation length cut-off temperature regime is found probably not to be a new phase, but a mesoscopic range order regime with short range order, covering all spins in the system.

## 7.2 Outlook

The controversial applied field response to YBCO nanoparticles should be investigated further regarding the possible surface spin canting and surface spin-flop.

The connection between particle size distribution, Néel temperature, possible superparamagnetism and possible surface spin melting should also be further examined and modelled to determine the physical behavior and properties of the nanosized samples. These investigations could be supplemented by investigations on YBCO thin films and by numerical modelling.

The most important remaining question regarding CoO is on the proposed mesoscopic range order regime, which should be elucidated further. In this context, it is important to examine the existence and potential properties of the suggested collective fluctuation spin state.

Further investigations of the thermodynamic properties and the critical phenomena should also be performed, herein heat capacity, magnetic susceptibility and neutron scattering measurements. The indications, that the CoO system is more Heisenberg-like than Ising-like above  $T_N$ , could in this context also be examined further.

An effort should be put into understanding the relation between measurable quantities and the theoretical correlation length, particularly in nanosized systems, which could be done through computer simulations and theoretical calculations.

### Superconductors on Semiconductors

Present day microprocessor technology is relies heavily on semiconducting materials. Unfortunately with the increasing clock-frequencies and higher demands for speed, the excess heat from ohmic resistance has become a barrier, not easily overcome.

However, after learning about our work with nanosized superconductors, Professor G. Aeppli approached us with the idea of integrating superconducting in semiconductor devices. Preliminary investigations were made to deposit YBCO islands on semiconducting materials of Si and SrTiO<sub>3</sub> (STO) using PLD. These two materials were chosen since Si is the basis in most present day microelectronic devices, but unfortunately does not have YBCO-matching lattice parameters. STO on the other hand has matching lattice parameters, whence it has been used.

The aim by depositing the YBCO islands on semiconductor substrates was to measure the conductance both vertically and horizontally through the YBCO islands and therethrough to assess the possibility of incorporation into semiconductor devices.

I performed preliminary AFM investigations of the deposited YBCO islands on the substrates, which showed that YBCO on Si seemed to behave as water droplets on an oily surface, forming a landscape where larger roundish droplets had absorbed the smaller droplets in the close vicinity, leaving it droplet free. This behavior indicated that the YBCO droplets, due to the lattice mismatch, were freely floating around on the substrate, held only on the surface by van der Waals forces.

The YBCO islands on STO were much smaller, more irregular and were more homogeneously distributed, indicating a much better match with the YBCO lattice parameters. Examples of AFM images of YBCO islands on these two substrates are found in appendix D. The very promising preliminary results make further studies highly desirable.

Recently, homogenous YBCO films have successfully been deposited on STO and NGO ( $\text{NdGaO}_3$ ) substrates [168], of sufficiently high quality for Arpes (Angle Resolved PhotoEmission Spectroscopy) investigations, again giving hope of studying the interaction phenomena between superconductors and semiconductors.



# Appendix A

## SICS Implementation

### A.1 Implementation of SICS on RITA-2

For many years the control software running the RITA-2 spectrometer, was the Risø invented TASCUM [87]. As a part of a larger instrumentation software strategy, it was decided that the SINQ Instrument Control Software (SICS) system [70, 90] should be implemented on RITA-2 as control software. SICS is a common software package used on all neutron scattering instruments as the Paul Scherrer Institute, mainly maintained and developed by Mark Könnecke. A schematic of the functionality and communications of SICS is shown in figure A.1.1.

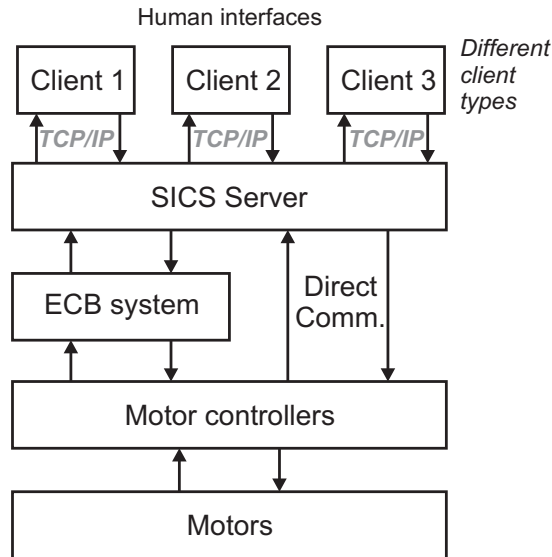


Figure A.1.1: Schematic illustration of the communication from human to instrument motors. The human send commands through a client to the SICS server, via various TCP/IP based protocols. The SICS server evaluates the new motors positions against limits and present positions, and decides whether the motors should be driven. Depending on instrument mode, and which motors are to be driven, the SICS server either sends the commands to the ECB system or directly to the motor controllers. The ECB system accepts the new position and through the motor controllers, sends signal to the motors to drive to the new position. In some cases (e.g. if there are several motors on the same controller) the ECB system it not intelligent enough to handle the driving of motors, and the SICS server will communicate directly to the motor controller with the operation instructions. As the figure indicates, all communication is of course two-way, supplying the SICS server and eventually the user with feedback on the operation of the instrument.

As SICS is common at PSI, and as SICS already had been implemented on the TASP triple axis spectrometer, the implementation of control software for standard TAS's had already been done, and was merely inherited. Lacking was, however, the implementation of control software for the RITA-2 specific functionality (see section 3.2.4.3) [36, 104]. As part of my Ph.D. work, it was assigned to me to implement the RITA-2 functionality.

SICS is implemented in part in C, and in part in TCL [198]. My work mainly concerned the implementation and testing of the code controlling the motor positions, data acquisition and data saving. Furthermore I worked with user I/O writing convenient user procedures and commands. The motor positions as function of scattering vectors  $h$ ,  $k$ ,  $l$ ,  $q$ ,  $E_i$ ,  $E_f$  and  $E_n$  are in part given by standard scattering and trigonometric equations (see for instance section 3.2.1).

Turning to the three implemented RITA-2 modes, flat, focusing and monochromatic imaging (as described in section 3.2.5), the flat mode simply involves setting the analyzer blades flat. The focusing and monochromatic imaging modes are a bit more complicated. The equations for the position of the RITA-2 analyzer blade rack and of the individual analyzer blade positions in these two modes, has been calculated by Bahl *et al.* (2004) [10].

During the implementation of RITA-2 SICS, the properties and functionality of the software was discussed by Christof Niedermayer and Niels B. Christensenm, instrument responsables, Mark Könnecke and I. These discussions were the basis on which the implementation of the software built on.

The implementation of SICS introduced some new features compared to the old TASCOS system:

- The data format was changed from old text based to the newer NeXus format [88], which introduced a hierarchical data structure, which has been tailored for triple axis spectroscopy. Among other features, all PSD images are now saved within one file, as well as all configurations are saved for each scan point.
- The inter-analyzer blade distances and inter-data window distances are now customizable, as well as there is support for increasing the number of analyzer blades from the present seven to nine. The number of data windows has been increased from 9 to 12, to provide operators with more freedoms during experiments and in data analysis.
- A special `none` mode has been installed for aligning and for running in special configurations.
- The operation of the spectrometer is now in real-time, meaning that *e.g.* a drive command or a change of RITA-2 mode will actually drive the spectrometer to this position/configuration.
- During a scan, all motor positions are set for each scan point from SICS, always ensuring a correct instrument configuration. As SICS communicates with the motor hardware-controllers, only motors which are not within the tolerance of the desired position, are driven.

After implementation, the system was thoroughly tested, errors were corrected and eventually a manual for the operation of RITA-2 was written [132]. The RITA-2 instrument has been running SICS since the fall of 2006.

# Appendix B

## YBCO Preparation Logs

### B.1 Nano YBCO Fabrication Logs

This section contains selected section transcript of the manufacturing logs of the YBCO nanoparticle sample batch, 'batch 2'. The manufacturing was made in Turku, Finland in March 2006, and the log below is a log of part of the procedure.

#### B.1.1 Titration of Yttrium solution

- 
- 
- Aiming for 0.125 mol/l solution.
  - 400 ml deionized water +19.15 g of  $Y(NO_3)_3 + xH_2O$ .
  - Then we titrate to determine concentration, using EDTA on xylenol (look for color change red->orange). (in our case it was violet->light/pinkish red) (maybe the xylenol was old).
  - Buffer (Hexamethylenetetraamine)(there is a photo)(pH 5.5) 1-2 small spoons is poured into 100 ml of deionized water.
  - Add Color (xylenol-solution).
  - Titration is performed with EDTA ( $c=0.1$  mol/l).
  - Titration of Yttrium (in 100 ml water+buffer)

#	Yttrium	EDTA	divided by #
1	0.5 ml	1.31 ml	1.31
2	1.0 ml	2.58 ml	1.29
3	1.5 ml	3.82 ml	1.273
4	2.0 ml	5.15 ml	1.288
5	2.5 ml	6.46 ml	1.292
6	3.0 ml	7.67 ml	1.278
7	3.5 ml	8.94 ml	1.277
		$\langle c \rangle =$	0.128 mol/l

since  $c_0 = \frac{c_1 V_1}{V_0}$  and  $c_1 = c_{EDTA} = 0.05$  mol/l

---

---

Table B.1.1: *Log for titration of yttrium nitrate for batch 2.*

### B.1.2 Titration of Barium solution

- 
- 
- Aiming at a barium concentration of 2 times that of Y:  
 $C_{Ba} = 2c_Y = 0.257 \text{ mol/l}$   
 $M_{Ba(NO_3)_2} = 261.34 \text{ g/mol}$   
 $m_{Ba(NO_3)_2} = V \cdot c_{Ba} \cdot M_{Ba(NO_3)_2} = 0.51 \cdot 0.257 \text{ mol/l} \cdot 261.34 \text{ g/mol} = 33.582 \text{ g}$
  - We weighed of 32.73 g.
  - Max.  $c_{Ba} \simeq 0.28 \text{ mol/l}$
  - Mixed 32.73 g into 500 ml of deionized water.
  - It will dissolve slowly, therefore we add stirring magnet and put glass on stirrer.
  - Added 10 ml 0.1 mol/l Mg-EDTA.
  - Add 0.5 ml of Ba-solution.
  - Add 3 tips of Erio-T:NaCl (ratio 1:100)
  - Add pH-10 buffer  $\sim 2 \text{ ml}$ . - Sharp color change (light blue to red)
  - Titration of barium-solution:

#	Barium	EDTA	divided by #
1	0.5 ml	2.48 ml	2.48 ml
2	1.0 ml	4.92 ml	2.46 ml
3	1.5 ml	7.40 ml	2.466 ml
4	2.0 ml	9.88 ml	2.47 ml
		$\langle c \rangle =$	0.247 mol/l

since  $c_0 = \frac{c_1 V_1}{V_0}$  and  $c_1 = c_{EDTA} = 0.05 \text{ mol/l}$

---



---

Table B.1.2: Log for titration of barium nitrate for batch 2.

### B.1.3 Titration of Copper solution

- 
- 
- Aiming at  $c_{Cu} = 3c_Y = 0.386 \text{ mol/l}$ .
  - $Cu(NO_3)_2 \cdot 3H_2O \Rightarrow M = 241.5984 \text{ g/mol}$

#	Barium	EDTA	divided by #
1	0.5 ml	3.94 ml	3.94 ml
2	1.0 ml	7.75 ml	3.875 ml
		$\langle c \rangle =$	0.39075 mol/l

since  $c_0 = \frac{c_1 V_1}{V_0}$  and  $c_1 = c_{EDTA} = 0.05 \text{ mol/l}$

---



---

Table B.1.3: Log for titration of copper nitrate for batch 2.

# Appendix C

## Calculations and Implementations

### C.1 Calculations of Magnetic Moments in YBCO

To calculate the fully saturated magnetic moment of YBCO, we calculate the number of formula units  $n_{YBCO}$  in a specific amount of material. The molar mass of YBCO  $N_{YBCO}$ <sup>1</sup> is

$$N_{YBCO} = m_Y + 2m_{Ba} + 3m_{Cu} + 7m_O = 666.2197 \text{ g/mol}, \quad (\text{C.1.1})$$

and the number of Cu ions per gram is

$$n_{YBCO} = \frac{m_{YBCO}}{N_{YBCO}} \quad (\text{C.1.2})$$

$$= \frac{1 \text{ g}}{666.2197 \text{ g/mol}} = 1.501 \cdot 10^{-3} \text{ mol}, \quad (\text{C.1.3})$$

where  $m_{YBCO}$  is the YBCO sample mass. The number of Cu atoms per gram is

$$n_{Cu} = 3 \cdot n_{YBCO} \cdot N_A \quad (\text{C.1.4})$$

$$= 3 \cdot 1.501 \cdot 10^{-3} \text{ mol} \cdot 6.022 \cdot 10^{23} \text{ mol}^{-1} = 2.71 \cdot 10^{21} \quad (\text{C.1.5})$$

where  $n_{Cu}$  is the number of Cu atoms in the amount of YBCO in question,  $n_{YBCO}$  is the number of YBCO formula units,  $N_A$  is Avagadros number (see table G.1.1).

Rossat-Mignod *et al.* [159] find that only the conduction layer Cu-ions have a magnetic moment, and therefore the ratio of magnetically ordered Cu-ions is  $2/3$ . Furthermore each magnetic Cu-ion has an ordered moment of  $\sim 0.6\mu_B$ , ( $0.64(3)\mu_B$  in ref. [159] and  $0.66(7)\mu_B$  in ref. [188]) due to quantum fluctuations. The magnetic moment  $M_{YBCO}$  of fully ordered YBCO is therefore (using the value from ref. [159])

$$M_{YBCO} = n_{Cu} \cdot \mu_B \cdot 2/3 \quad (\text{C.1.6})$$

$$= 2.71 \cdot 10^{21} \cdot 9.274 \cdot 10^{-24} \text{ J/T} \cdot 2/3 \cdot 0.64(3) = 1.07(5) \cdot 10^{-2} \text{ J/T} \quad (\text{C.1.7})$$

$$= 10.7(5) \text{ emu/g}. \quad (\text{C.1.8})$$

In these calculations ref. [126] has been used for unit conversion.

---

<sup>1</sup>Usually the symbol  $M$  is used for molar mass, but to avoid confusion with magnetic moment,  $N$  is used here instead.



## Appendix D

# YBCO Islands on Semiconductor Substrates

This section contains details on the deposition of the YBCO islands on semiconductor substrates as discussed in section 7.2, as well as it contains AFM images on the resulting samples.

The deposition of YBCO islands was made in Turku, Finland on the 23-34th of March 2006 by Jari í Hjöllum and Hannu Huhtinen, using Pulsed Laser Deposition (PLD).

The used PLD target was an YBCO pellet pressed from powder, manufactured through the sol-gel method as described in section 4.4.1. Two types of substrates were used:

- A SrTiO<sub>3</sub> substrate with a (001) face, doped with 0.5 % Nb, making it conductive (SrTiO<sub>3</sub>:Nb 0.5 % (001)).
- A Si-wafer p-type doped, with a (100) face, 0.01 Ωcm.

### **The parameters in the PLD process were:**

- Laser energy: beam limiter, filter conversion (2.92 V/J)  
Size of the beam = (16 × 6.6) mm<sup>2</sup>, on the target = 4.224 mm<sup>2</sup>  
Used filters: Nro 1 (transmittance = 0.56%), Nro3 (transmittance = 16 %).
- O<sub>2</sub> pressure = 0.3 Torr (fixed)
- Lens distance = 80 mm, Target-substrate distance = 35 mm (fixed)

### **Manufactured Samples:**

- Sample B, substrate Si  
Energy : 60 mV, filter no. 1  
Temperature: 780 °C  
Pulses: 200, 5 Hz
- Sample D, substrate STO:Nb  
Energy 60 mV, filter no 1  
Temperature 780 °C  
Pulses: 200, 5 Hz

As mentioned, the samples were afterwards investigated using AFM, yielding the images shown in sections D.1 and D.2.

## D.1 YBCO Islands on Si Substrate

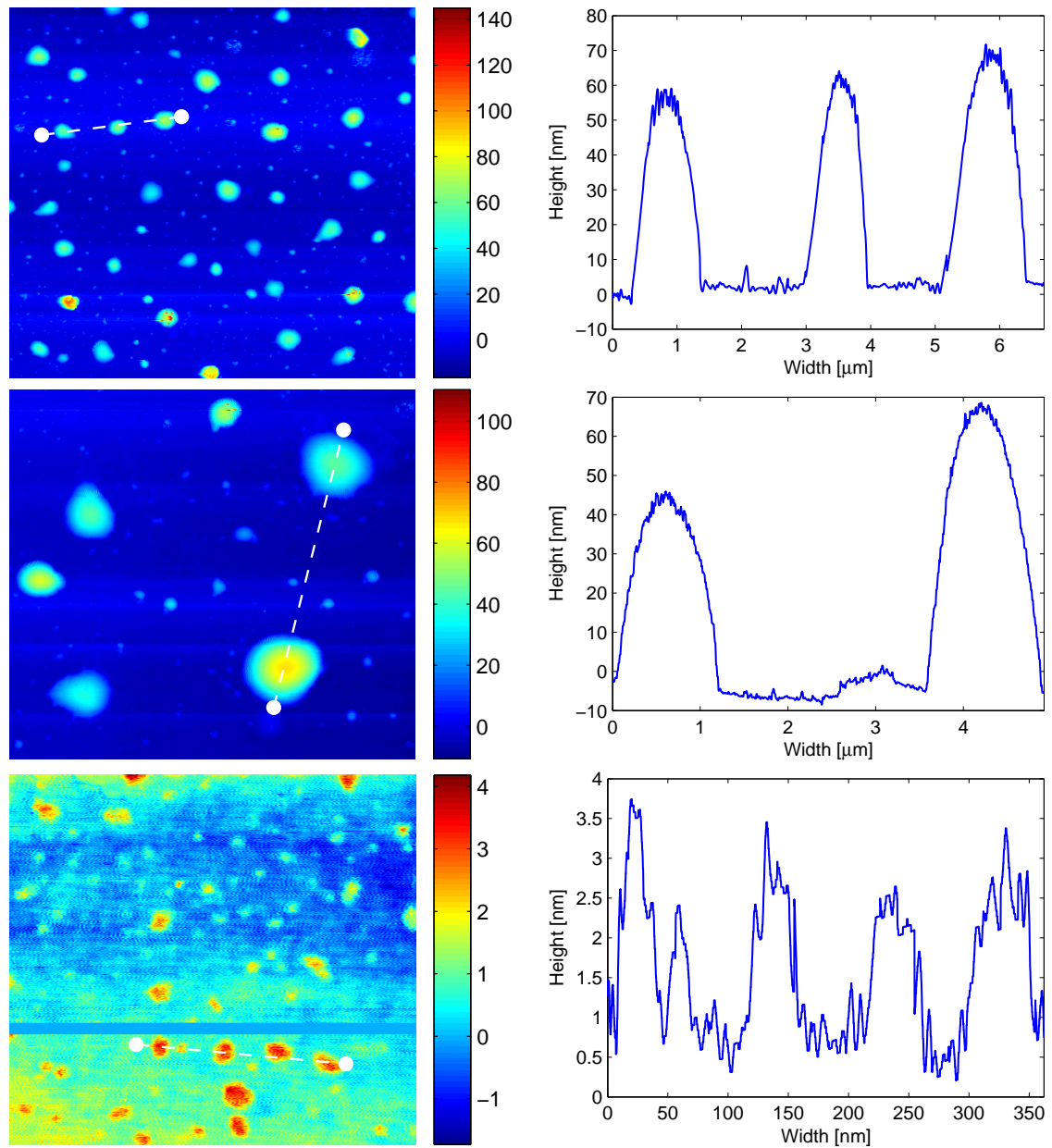


Figure D.1.1: YBCO Islands on Si (B) substrates. Left column contains raw AFM images, with the paths of the cross sections marked. The color scale is in nm. Right column contains cross section height curves. Top row: Image is  $20 \times 20 \mu\text{m}$ . Middle row: Image is  $6.6 \times 6.6 \mu\text{m}$ . Bottom row: Image is  $3.3 \times 3.3 \mu\text{m}$ .

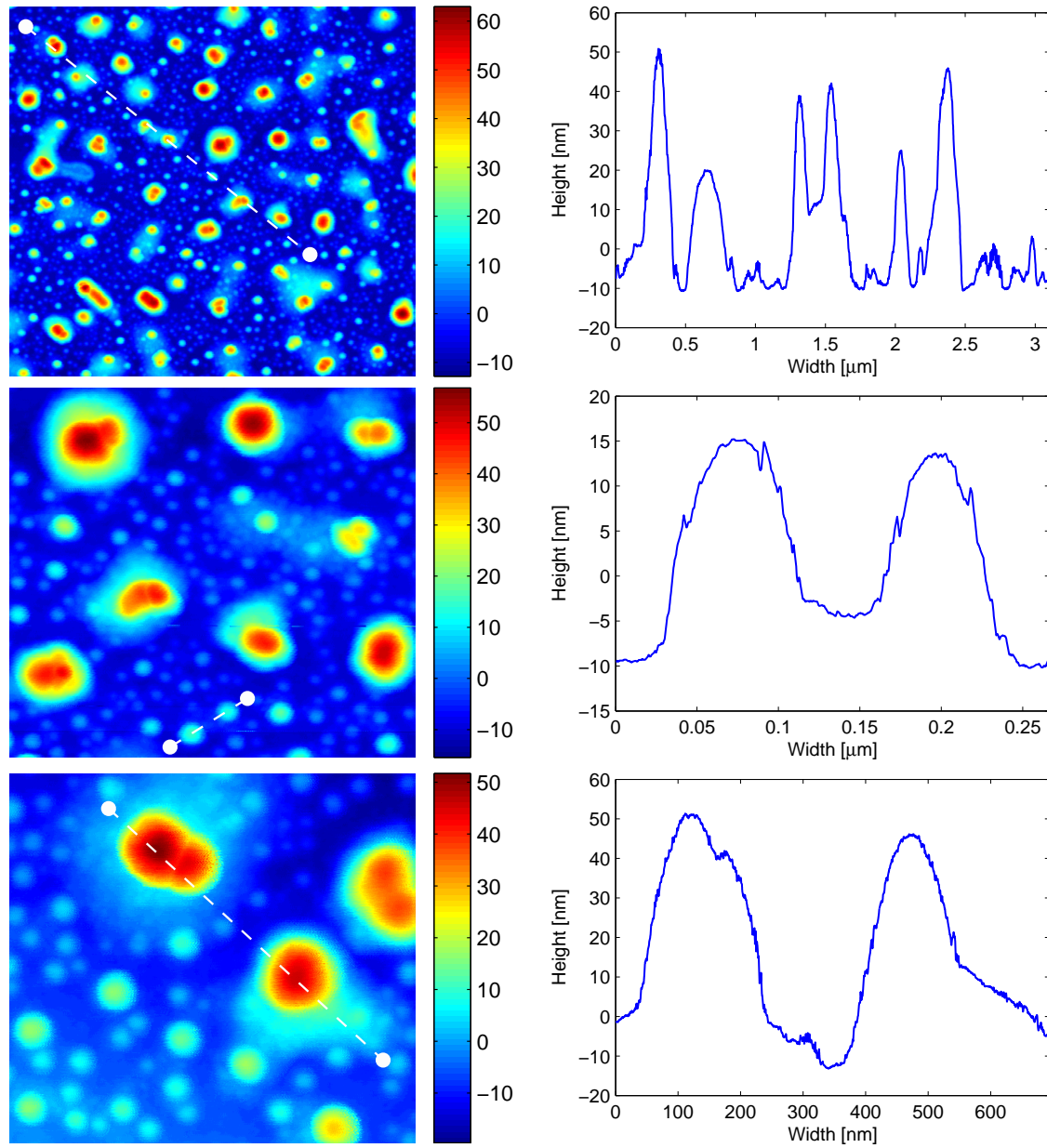
D.2 YBCO Islands on SrTiO<sub>3</sub> Substrate

Figure D.2.1: YBCO Islands on STO (D) substrates. Left column contains raw AFM images, with the paths of the cross sections marked. The color scale is in nm. Right column contains cross section height curves. Top row: Image is  $3.3 \times 3.3 \mu\text{m}$ . Middle row: Image is  $1.2 \times 1.2 \mu\text{m}$ . Bottom row: Image is  $723 \times 723 \text{ nm}$ .



# Appendix E

## YBCO Extra Analysis Material

This chapter contains the analysis material which I have deemed not essential for the thesis, but which contains relevant material for further reading.

### E.1 Neutron Scattering Data

#### E.1.1 Sample 1 ( $x=0.20$ ) - Simple Model Details

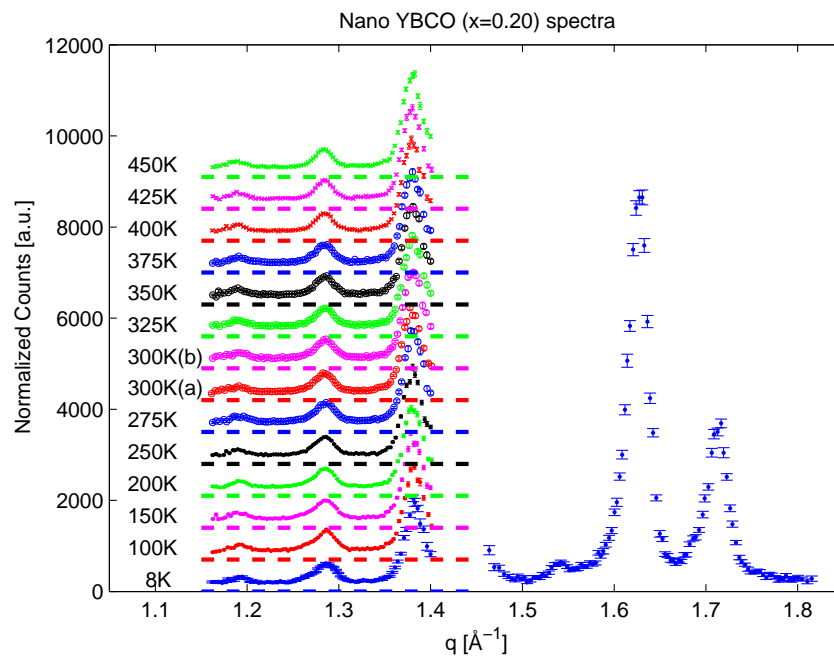


Figure E.1.1: Overview of the Sample 1 ( $x=0.20$ ) sample neutron diffraction spectra. The horizontal dotted lines mark 0.

### E.1.2 Sample 3 ( $x=0.35$ ) - Simple Model Details

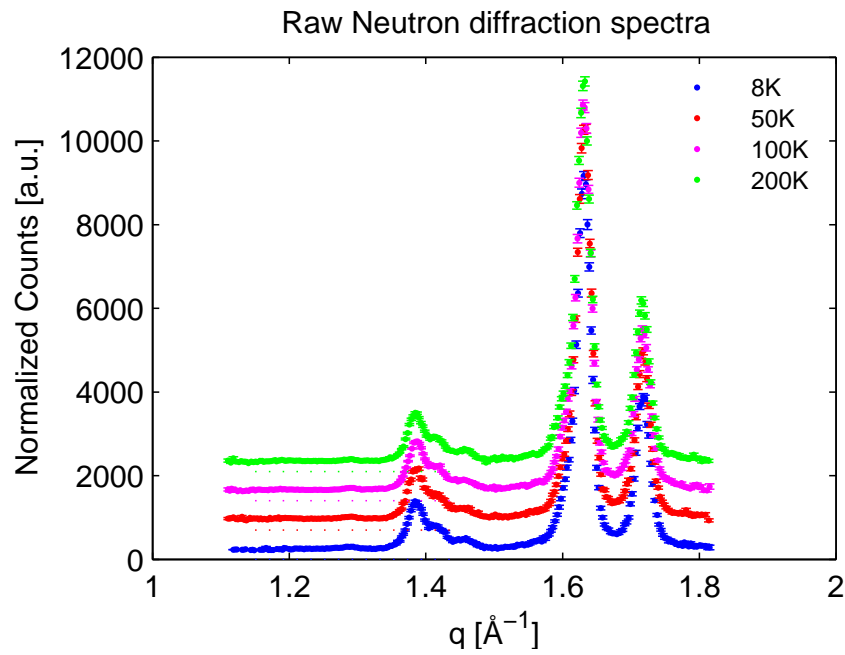


Figure E.1.2: Overview of the Sample 3 ( $x=0.35$ ) sample neutron diffraction spectra.

### E.1.3 Sample 4 ( $x=0.25$ ) - Simple Model Details

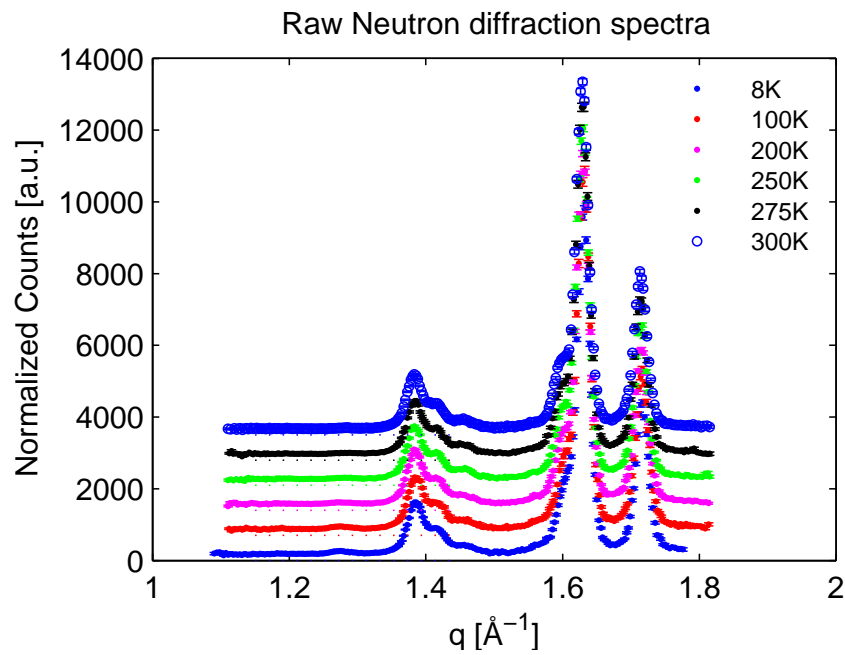


Figure E.1.3: Overview of the Sample 4 ( $x=0.25$ ) sample neutron diffraction spectra.

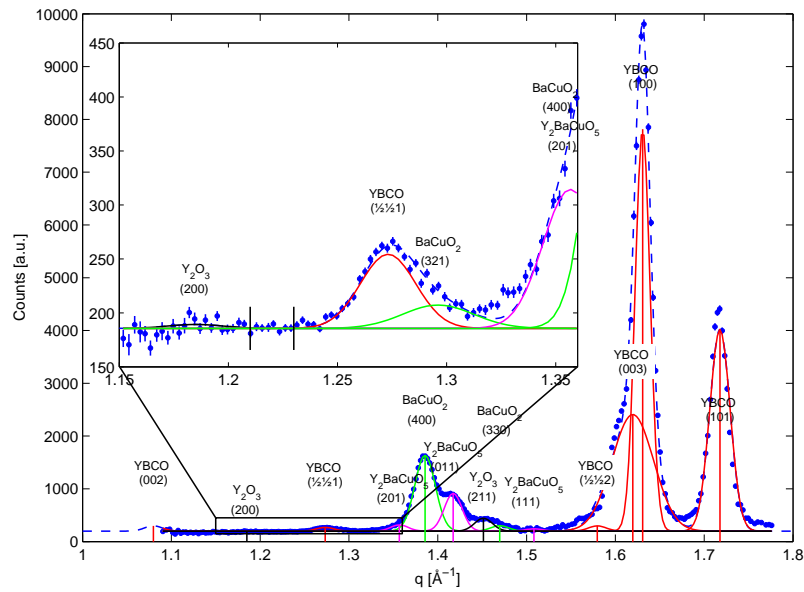


Figure E.1.4: *hkl*-fitted neutron spectrum of Sample 4 ( $x=0.25$ ) at 8 K. Outer plot shows entire  $q$  range, and inset shows the fitted region around the YBCO ( $\frac{1}{2}\frac{1}{2}1$ ) peak.

#### E.1.4 Sample 5 ( $x=0.30$ ) - Simple Model Details

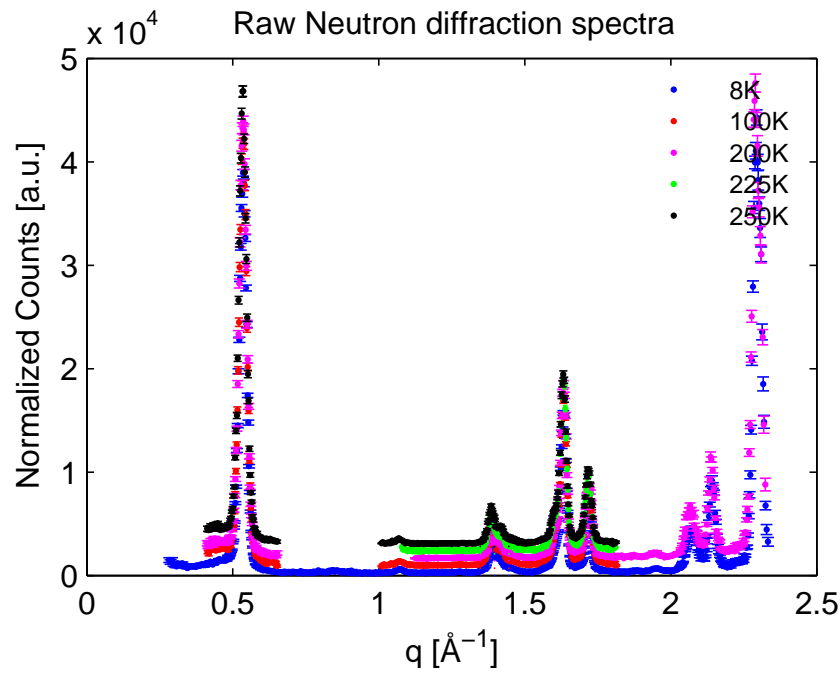


Figure E.1.5: Overview of the Sample 5 ( $x=0.30$ ) sample neutron diffraction spectra.

## E.2 $\mu$ SR Data

### E.2.1 Calibration

#### E.2.1.1 Sample 3 ( $x=0.35$ ) Calibration

#	Parameter	Value	Unit
1	$\alpha$	0.9590(7)	
2	$A_1$	0.1599(6)	
3	$\varphi$	4.1(3)	$^\circ$ (degree)
4	$\sigma$	0.164(3)	$\mu\text{s}^{-1}$
5	$\nu$	99.49(3)	G

Table E.2.1: Calibration parameters found for Sample 3 ( $x=0.35$ ) at 100 K and 100 G transverse field (using up and down detectors).

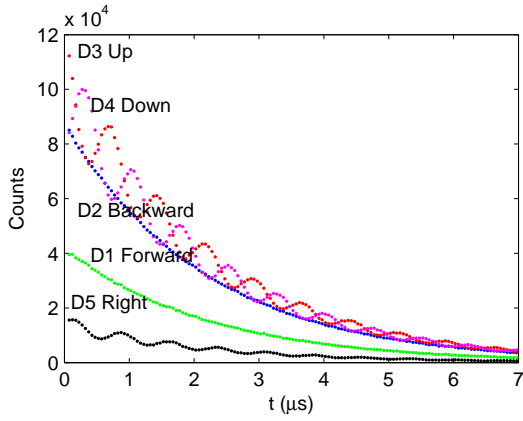


Figure E.2.1: Raw calibration data, counts versus time on the individual detectors for the  $x=0.35$  sample at 300 K and 100 G.

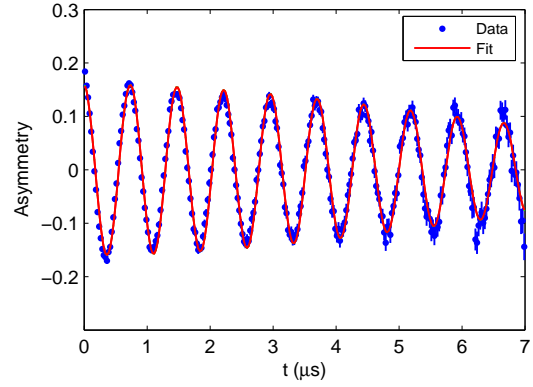
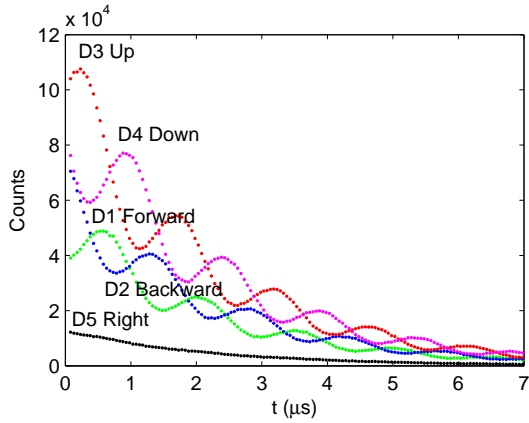
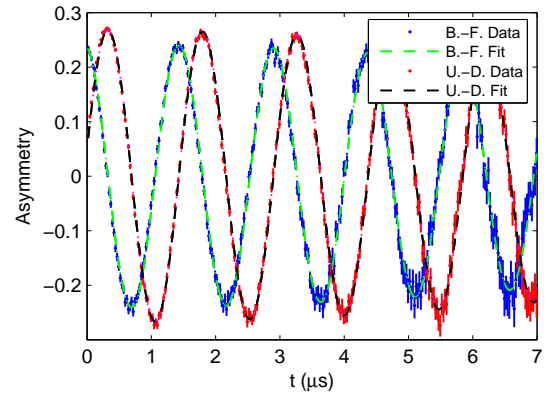


Figure E.2.2: Fitted calibration dataset for Sample 3 ( $x=0.35$ ) at 300 K and 100 G. Note that the error bars increase with time as the count rate of muons decreases.

E.2.1.2 Sample 4 ( $x=0.25$ ) Calibration

#	Parameter	Value	Unit
1	$\alpha$	0.8494(8)	
2	$A_1$	0.2414(8)	
3	$\varphi$	10.3(2)	$^\circ$ (degree)
4	$\sigma$	0.082(3)	$\mu\text{s}^{-1}$
5	$\nu$	50.15(2)	G

Table E.2.2: Calibration parameters found for Sample 4 ( $x=0.25$ ) at 300 K and 50 G.Figure E.2.3: Raw calibration data, counts versus time on the individual detectors for the  $x=0.25$  sample at 300 K and 50 G.Figure E.2.4: Fitted calibration dataset for the  $x=0.25$  sample at 300 K and 50 G. Note that the error bars increase with time as the count rate of muons decreases.

### E.2.1.3 Sample 5 ( $x=0.30$ ) Calibration

#	Parameter	Value	Unit
1	$\alpha$	0.4871(8)	
2	$A_1$	0.2397(13)	
3	$\varphi$	10.7(4)	$^\circ$ (degree)
4	$\sigma$	0.04804(10)	$\mu\text{s}^{-1}$
5	$\nu$	50.15(3)	G

Table E.2.3: Calibration parameters found for Sample 5 ( $x=0.30$ ) at 300 K and 50 G.

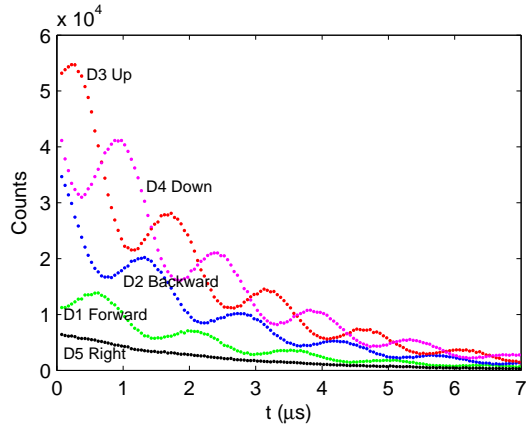


Figure E.2.5: Raw calibration data, counts versus time on the individual detectors for Sample 5 ( $x=0.30$ ) at 300 K and 50 G.

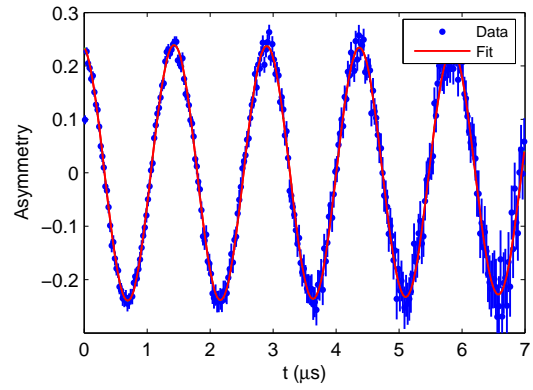


Figure E.2.6: Fitted calibration dataset for Sample 5 ( $x=0.30$ ) at 300 K and 50 G. Note that the error bars increase with time as the count rate of muons decreases.

## E.2.2 Sample 3 ( $x=0.35$ ) Fit Results

### E.2.2.1 Sample 3 ( $x=0.35$ ) CEE Model Results

T K	#	$\varphi$ °	$A_{osc}$	$\nu$ MHz	$\lambda_{osc}$ $\mu s^{-1}$	$A_f$	$\lambda_f$ $\mu s^{-1}$	$A_s$	$\lambda_s$ $\mu s^{-1}$
	1	2	5	6	7	8	9	10	
10	4674	17(8)	0.040(4)	3.50(11)	5.2(6)	0.096(7)	9.7(7)	0.0718(5)	0.070(3)
25	4678	1(9)	0.025(7)	3.30(11)	4(1.5)	0.087(6)	6.0(6)	0.0840(9)	0.079(4)
50	4675	0	0.038(13)	2.4(4)	9(3)	0.058(8)	3.4(6)	0.1103(14)	0.081(4)
75	4679	0	0.016(6)	2.1(4)	7(2)	0.043(5)	3.7(6)	0.1412(12)	0.093(3)
100	4676	0	0.0309(19)	0(9)	6.3(7)	0.02(2)	0.01(9)	0.15(2)	0.113(13)
125	4680	0	0.015(3)	0(1.8)	11(4)	0.038(3)	0.09(3)	0.152(3)	0.089(7)

Table E.2.4: CEE model fit results for Sample 3 ( $x=0.35$ ).

### E.2.2.2 Sample 3 ( $x=0.35$ ) DIN Model Results

T K	#	$A_a$	$\varphi$ °	$\nu_a$ MHz	$\lambda_{2a}$ $\mu s^{-1}$	$\lambda_{1a}$ $\mu s^{-1}$	$A_b$	$\lambda_{2b}$ $\mu s^{-1}$	$\lambda_{1b}$ $\mu s^{-1}$
	2	3	4	5	6	7	10	11	
10	4674	0.094(9)	0	3.67(7)	8.4(9)	0.06(3)	0.117(9)	7.8(7)	0.06(2)
25	4678	0.091(4)	0	3.39(8)	7.00(3)	0.06(2)	0.145(6)	5.2(4)	0.055(15)
50	4675	0.099(6)	0	3.17(8)	9.0(6)	1.0(6)	0.294(4)	13.5(3)	0.053(4)
75	4679	0.103(8)	0	3(1.4)	16(1.3)	3(3)	0.421(2)	29(1.8)	0.091(2)
100	4676	0.157(3)	0	0.016(6)	0.14(2)	0.01(3)	0.035(6)	4(1.5)	0.028(14)
125	4680	0.0725(14)	0	0	70(10)	0.09(6)	0.500(9)	10(9)e2	0.091(9)

Table E.2.5: Sample 3 ( $x=0.35$ ) DIN model fit results.

### E.2.2.3 Sample 3 ( $x=0.35$ ) KTE Model Results

T	#	$\alpha$	$A_{KT,0}$	$\Delta$ $\mu s^{-1}$	$A_R$	$\lambda$ $\mu s^{-1}$
1	2	3	4	5	6	7
75	4679	0.959	0.1182(9)	0.0959(20)	0.0639(11)	1.82(11)
100	4676	0.959	0.1401(12)	0.1022(18)	0.0487(11)	1.22(9)
125	4680	0.959	0.154(4)	0.098(3)	0.041(3)	0.66(11)

Table E.2.6: Sample 3 ( $x=0.35$ ) KTE model fit parameters.

### E.2.3 Sample 4 ( $x=0.25$ ) Fit Results

#### E.2.3.1 Sample 4 ( $x=0.25$ ) CEE Model Results

T K	#	$\varphi$ °	$A_{osc}$	$\nu$ MHz	$\lambda_{osc}$ $\mu s^{-1}$	$A_f$	$\lambda_f$ $\mu s^{-1}$	$A_s$	$\lambda_s$ $\mu s^{-1}$
	1	2		5	6	7	8	9	10
5	4620	5(6)	0.057(5)	3.94(5)	2.5(2)	0.122(15)	27(5)	0.1183(7)	0.037(2)
10	4619	6(3)	0.068(5)	3.90(4)	3.1(2)	0.100(9)	15(1.7)	0.1164(7)	0.031(2)
20	4621	6(3)	0.064(4)	3.76(3)	2.9(2)	0.102(7)	12(1.0)	0.1151(6)	0.020(2)
30	4626	0	0.061(4)	3.70(2)	2.9(2)	0.099(7)	12(1.1)	0.1147(7)	0.043(2)
40	4627	0	0.062(4)	3.56(2)	2.9(2)	0.097(6)	9.9(9)	0.1126(7)	0.006(2)
50	4622	0	0.063(5)	3.45(3)	3.1(3)	0.095(6)	9.9(9)	0.1234(7)	0.021(2)
60	4628	0	0.064(4)	3.34(2)	3.0(2)	0.093(6)	8.2(7)	0.1160(8)	0.007(2)
80	4629	0	0.058(5)	3.23(3)	2.9(3)	0.097(6)	8.9(8)	0.1228(8)	0.021(2)
100	4623	0	0.051(4)	3.12(3)	2.5(2)	0.099(6)	9.9(9)	0.1346(7)	0.033(2)
125	4630	0	0.045(6)	3.04(3)	2.6(4)	0.100(8)	9.0(10)	0.1361(8)	0.036(2)
150	4631	0	0.040(5)	2.73(4)	2.9(4)	0.088(7)	8.2(9)	0.1458(9)	0.048(2)
175	4632	0	0.033(5)	2.59(5)	3.0(5)	0.086(7)	7.4(8)	0.1551(10)	0.055(3)
200	4624	0	0.020(4)	2.61(5)	2.1(5)	0.072(5)	6.5(7)	0.1767(10)	0.064(2)
225	4633	0	0.034(9)	1.76(15)	5(1.2)	0.039(7)	3.6(9)	0.1929(15)	0.057(3)
250	4625	0	0.046(4)	0.77(15)	7(1.2)	0.028(4)	0.05(7)	0.194(4)	0.050(10)
275	4634	0	0.020(3)	0	6(1.6)	0.034(4)	0.04(6)	0.197(4)	0.039(10)
300	4635	0	0.002(3)	0	3(3)	0.062(15)	0.12(4)	0.176(16)	0.000(16)

Table E.2.7: CEE model fit results for Sample 4 ( $x=0.25$ ).

#### E.2.3.2 Sample 4 ( $x=0.25$ ) DIN Model Results

T K	#	$A_a$	$\varphi$ °	$\nu_a$ MHz	$\lambda_{2a}$ $\mu s^{-1}$	$\lambda_{1a}$ $\mu s^{-1}$	$A_b$	$\lambda_{2b}$ $\mu s^{-1}$	$\lambda_{1b}$ $\mu s^{-1}$
		2	3	4	5	6	7	10	11
5	4620	0.075(5)	0(1.2)	3.961(19)	2.21(18)	0.23(4)	0.281(5)	44(2)	0.000(20)
10	4619	0.068(4)	0(2)	3.95(2)	2.28(17)	0.0(2)	0.283(4)	32(1.4)	0.03(4)
20	4621	0.058(3)	0(4)	3.819(19)	1.90(15)	0.17(20)	0.295(5)	29(1.6)	0.01(2)
30	4626	0.056(4)	0(3)	3.72(2)	1.93(18)	0.04(15)	0.286(5)	25(1.1)	0.04(3)
40	4627	0.050(3)	0	3.59(2)	1.79(16)	0.0(6)	0.299(4)	25(1.1)	0.03(3)
50	4622	0.047(4)	0.0(6)	3.51(3)	1.78(19)	0.03(17)	0.328(5)	26(1.1)	0.03(2)
60	4628	0.048(4)	0(1.2)	3.38(3)	1.83(17)	0.0(10)	0.312(5)	23.5(10)	0.030(5)
80	4629	0.037(3)	0.0(5)	3.30(3)	1.51(17)	0.0(10)	0.341(4)	25.7(10)	0.04(8)
100	4623	0.033(3)	0.0(3)	3.17(3)	1.33(16)	0.04(16)	0.377(4)	30(5)	0.043(13)
125	4630	0.021(3)	0.0(4)	3.13(3)	0.89(16)	0.00(17)	0.397(3)	29(1.0)	0.052(4)
150	4631	0.016(3)	0.0(8)	2.76(5)	1.2(3)	0.00(9)	0.437(3)	31(1.1)	0.069(4)
175	4632	0.008(2)	0(1.2)	2.70(6)	0.7(3)	0.00(15)	0.476(3)	33(1.1)	0.075(3)
200	4624	0.006(2)	0	2.66(3)	0.4(3)	0.000(4)	0.554(3)	48(1.5)	0.092(3)
225	4633	0.0649(7)	0	1.46	6.0(5)	0.000(10)	0.548(2)	100(7)	0.094(3)
250	4625	0.06(6)	0	0.76(14)	6.8(7)	0	0.602(3)	220(190)	0.055(2)
275	4634	0.051(6)	0	0.0(7)	0.00(3)	0	0.552(19)	240(20)	0.05977
300	4635	0.199(16)	0	0.017(5)	0.0(2)	0.0(3)	0.042(8)	0(60)	0.9(8)

Table E.2.8: DIN model fit results for Sample 4 ( $x=0.25$ ).

E.2.3.3 Sample 4 ( $x=0.25$ ) KT Model Results

T	#	$\alpha$	$A_{KT,0}$	$\Delta$ $\mu s^{-1}$
1	2	3	4	5
250	4625	0.8494	0.2150(4)	0.0862(10)
275	4634	0.8494	0.2251(4)	0.0811(10)
300	4635	0.8494	0.2325(4)	0.0577(11)

Table E.2.9: *KT model fit parameters for Sample 4 ( $x=0.25$ ).*E.2.3.4 Sample 4 ( $x=0.25$ ) KTE Model Results

T	#	$\alpha$	$A_{KT,0}$	$\Delta$ $\mu s^{-1}$	$A_R$	$\lambda$ $\mu s^{-1}$
1	2	3	4	5	6	7
250	4625	0.8494	0.2047(11)	0.0726(18)	0.047(2)	2.6(4)
275	4634	0.8494	0.2148(13)	0.0685(18)	0.0290(14)	1.4(2)
300	4635	0.8494	0.2325(4)	0.0577(13)	0.00(10)	0(70)

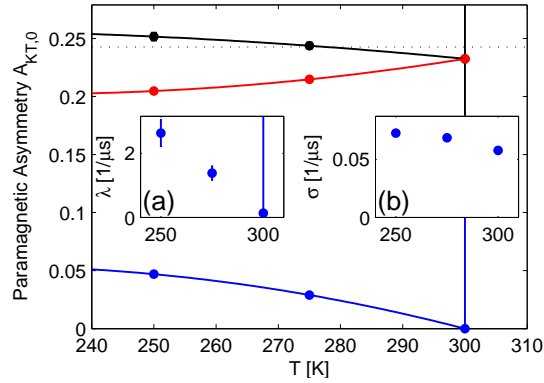
Table E.2.10: *KTE model fit parameters for Sample 4 ( $x=0.25$ ).*

Figure E.2.7:  $x=0.25$  KTE asymmetries, ( $\bullet$ ) magnetic relaxation asymmetry  $A_R$ , ( $\bullet$ ) Kubo-Toyabe asymmetry  $A_{KT,0}$  versus temperature  $T$  and ( $\bullet$ )  $A_R + A_{KT,0}$ . The lines are guides to the eye. Insets: (a) Magnetic relaxation  $\lambda$ .  $\lambda$  appears unexpectedly to be falling with increasing temperature. However this is most likely a fitting artifact, caused by the falling asymmetry of the component, giving room for a dropping  $\lambda$  with very large error bars. (b) Kubo-Toyabe decay rate  $\sigma$ .

## E.2.4 Sample 5 ( $x=0.30$ ) Fit Results

### E.2.4.1 Sample 5 ( $x=0.30$ ) CEE Model Results

T K	#	$\varphi$ °	$A_{osc}$		$\nu$	$\lambda_{osc}$	$A_f$	$\lambda_f$	$A_s$	$\lambda_s$
			1	2	MHz	$\mu s^{-1}$	7	$\mu s^{-1}$	8	9
10	5030	0	0.059(10)		3.91(6)	4.0(7)	0.081(16)	15(3)	0.0901(12)	0.038(5)
20	5031	0	0.053(10)		3.81(6)	3.7(7)	0.090(16)	14(3)	0.0937(12)	0.060(5)
30	5032	0	0.062(11)		3.42(7)	4.2(7)	0.082(13)	10(2)	0.0913(15)	0.042(8)
40	5033	0	0.048(9)		3.41(7)	3.6(8)	0.102(12)	10(1.6)	0.0945(15)	0.021(7)
50	5034	0	0.040(8)		3.27(8)	3.2(7)	0.106(11)	10(1.4)	0.0977(14)	0.023(7)
60	5035	0	0.065(14)		3.04(10)	5(1.0)	0.077(14)	8(1.9)	0.1014(18)	0.034(8)
70	5036	0	0.042(8)		3.09(8)	3.2(7)	0.103(10)	8(1.2)	0.1003(17)	0.029(7)
80	5037	0	0.032(8)		3.01(8)	2.7(8)	0.110(11)	9(1.3)	0.1055(16)	0.038(7)
100	5038	0	0.047(14)		2.64(13)	4(1.1)	0.099(15)	7(1.4)	0.1142(19)	0.045(7)
125	5039	0	0.012(6)		2.65(9)	2(1.1)	0.109(8)	7.4(9)	0.1312(18)	0.079(7)
150	5040	0	0.015(5)		2.42(8)	1.8(7)	0.083(5)	4.7(6)	0.149(2)	0.079(7)
175	5041	0	0.005(5)		2.20(13)	2(2)	0.058(6)	5(1.1)	0.184(4)	0.068(15)
200	5042	0	0.018(6)		1.66(17)	4(2.0)	0.013(4)	1.4(8)	0.213(4)	0.057(4)
225	5043	0	0.025(8)		0.057(12)	0.11(7)	0.010(5)	4(3)	0.209(8)	0.015(8)
250	5044	0	0.017(4)		0.054(8)	0.0(4)	0.020(6)	0.0(2)	0.203(6)	0.017(12)
275	5045	0	0.024(2)		0.041(6)	0.000(7)	0.017(17)	0.02(8)	0.1975(12)	0.017(8)
300	5046	0	0.0240(18)		0.039(5)	0.000(5)	0.000(17)	0(70)	0.214(3)	0.015(4)

Table E.2.11: CEE model fit results for Sample 5 ( $x=0.30$ ).

### E.2.4.2 Sample 5 ( $x=0.30$ ) DIN Model Results

T K	#	$A_a$		$\varphi$	$\nu_a$	$\lambda_{2a}$	$\lambda_{1a}$	$A_b$	$\lambda_{2b}$	$\lambda_{1b}$
		2	3	°	MHz	$\mu s^{-1}$	$\mu s^{-1}$	7	$\mu s^{-1}$	$\mu s^{-1}$
10	5030	0.062(9)		0(11)	3.92(7)	3.1(5)	0.1(5)	0.213(10)	28(3)	0.05(7)
20	5031	0.050(9)		0	3.81(7)	2.6(5)	0.05(12)	0.228(10)	23(2)	0.05(3)
30	5032	0.056(10)		0	3.46(7)	3.0(6)	0.03(19)	0.216(12)	19(2)	0.03(4)
40	5033	0.039(9)		0	3.46(7)	2.2(5)	0.3(2)	0.248(14)	18(2)	0.00(3)
50	5034	0.031(9)		0	3.38(7)	1.8(7)	0.0(6)	0.260(11)	17(1.5)	0.02(2)
60	5035	0.028(8)		0	3.21(11)	2.3(8)	0.0(9)	0.282(9)	21(1.5)	0.051(9)
70	5036	0.024(7)		0	3.27(7)	1.3(6)	0.0(8)	0.279(10)	16(1.4)	0.03(2)
80	5037	0.016(5)		0	3.11(8)	1.2(4)	0.0(5)	0.302(7)	18(1.3)	0.045(15)
100	5038	0.008(4)		0	2.86(7)	0.7(6)	0.00(5)	0.334(7)	18(1.1)	0.045(8)
125	5039	0.01625		0	2.68	1.415	0.10(7)	0.404(8)	33(4)	0.111(10)
150	5040	0.009044		0	2.546	0.6744	0.00(7)	0.509(4)	99(8)	0.153(5)
175	5041	0.0100(12)		0	2.2	6(4)	0.05	0.593(4)	125(8)	0.118(4)
200	5042	0.100(6)		0	0.0(3)	0.000(6)	0.000(12)	0.1248(14)	0.277(15)	0.000(10)

Table E.2.12: DIN model fit results for Sample 5 ( $x=0.30$ ).

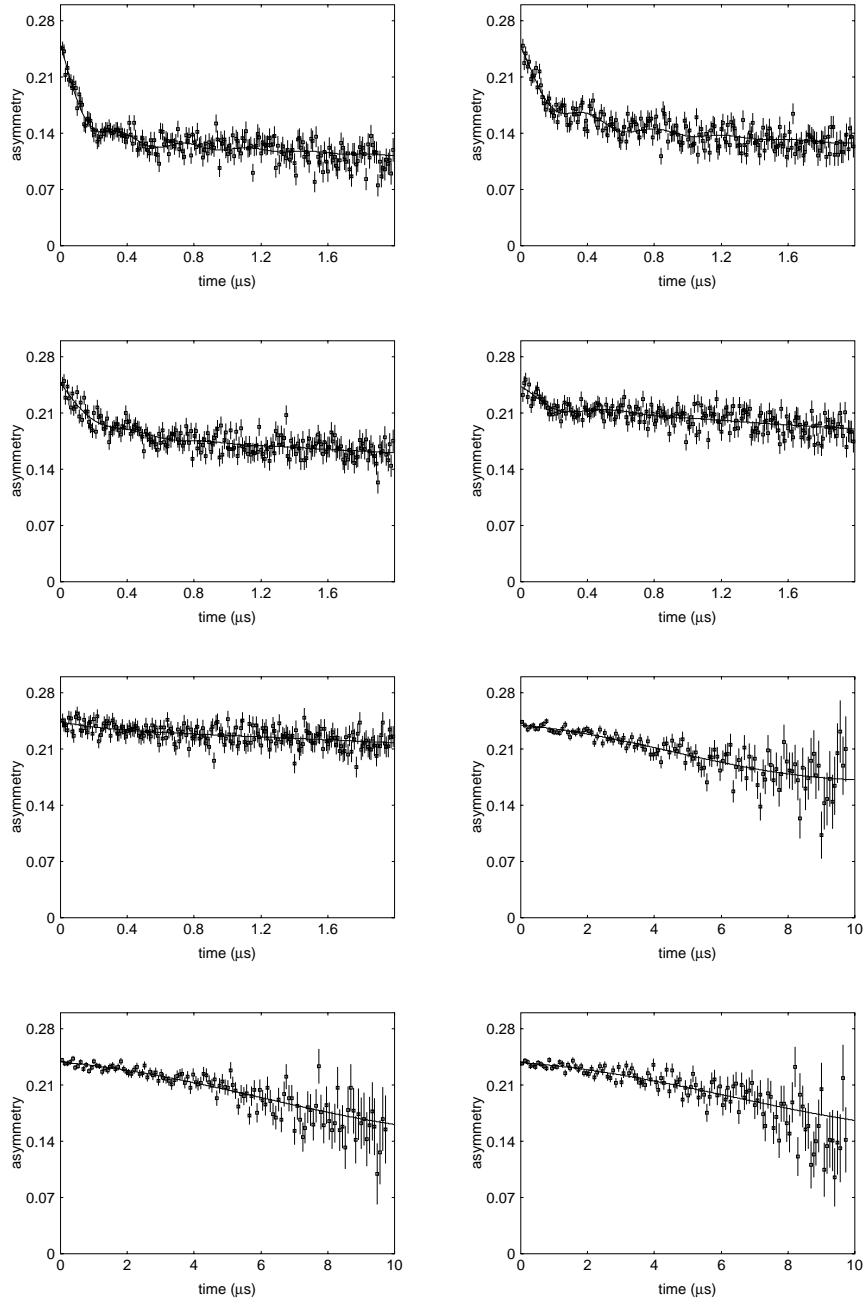
E.2.4.5 Sample 5 ( $x=0.30$ ) CEE Plots

Figure E.2.8: Sample 5 ( $x=0.30$ ) CEE model fitted  $\mu$ SR spectra. 1st row: 125 K and 150 K. 2nd row: 175 K and 200 K. 3rd row: 225 K and 250 K. 4th row: 275 K and 300 K. Note different  $t$ -scale in the last 4 plots.

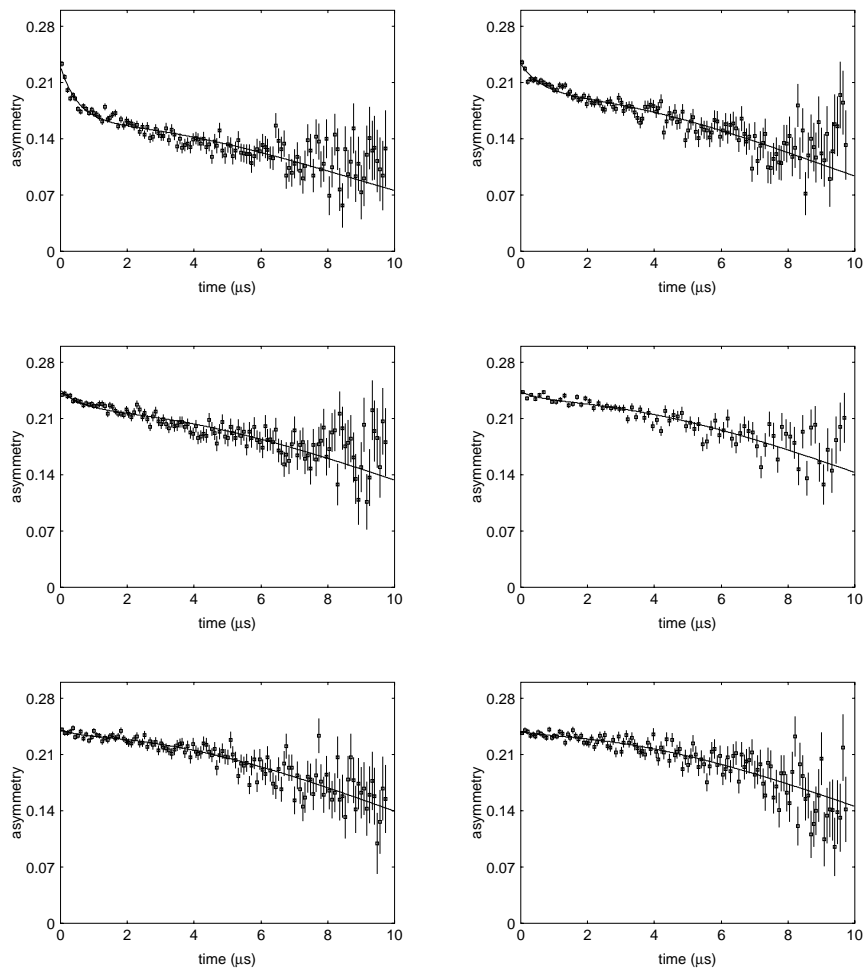
E.2.4.6 Sample 5 ( $x=0.30$ ) KTE Plots

Figure E.2.9: *Sample 5 ( $x=0.30$ ) KTE model fitted  $\mu$ SR spectra.* 1st row: 175 K and 200 K. 2nd row: 225 K and 250 K. 3rd row: 275 K and 300 K.

**E.2.4.3 Sample 5 ( $x=0.30$ ) KT Model Results**

T	#	$\alpha$	$A_{KT,0}$	$\Delta$ $\mu s^{-1}$
1	2	3	4	6
175	5041	0.4871	0.1807(7)	0.107(2)
200	5042	0.4871	0.2073(7)	0.0934(18)
225	5043	0.4871	0.2286(7)	0.0743(18)
250	5044	0.4871	0.2357(7)	0.0711(17)
275	5045	0.4871	0.2354(7)	0.0669(18)
300	5046	0.4871	0.2355(7)	0.0635(19)

Table E.2.13: *KT model fit parameters for Sample 5 ( $x=0.30$ ).***E.2.4.4 Sample 5 ( $x=0.30$ ) KTE Model Results**

T	#	$\alpha$	$A_{KT,0}$	$\Delta$ $\mu s^{-1}$	$A_R$	$\lambda$ $\mu s^{-1}$
1	2	3	4	5	6	7
175	5041	0.4871	0.159(2)	0.083(4)	0.071(3)	1.8(3)
200	5042	0.4871	0.1929(11)	0.082(2)	0.040(3)	1.50(4)
225	5043	0.4871	0.2194(11)	0.069(2)	0.026(2)	1.50(5)
250	5044	0.4871	0.2317(11)	0.068(2)	0.011(2)	1.50(17)
275	5045	0.4871	0.2329(16)	0.070(2)	0.008(3)	2(1.8)
300	5046	0.4871	0.2334(11)	0.067(2)	0.005(2)	2(6)

Table E.2.14: *KTE model fit parameters for Sample 5 ( $x=0.30$ ).*

### E.3 XRD Data

Below are presented the raw XRD data on the YBCO samples contained in this thesis.

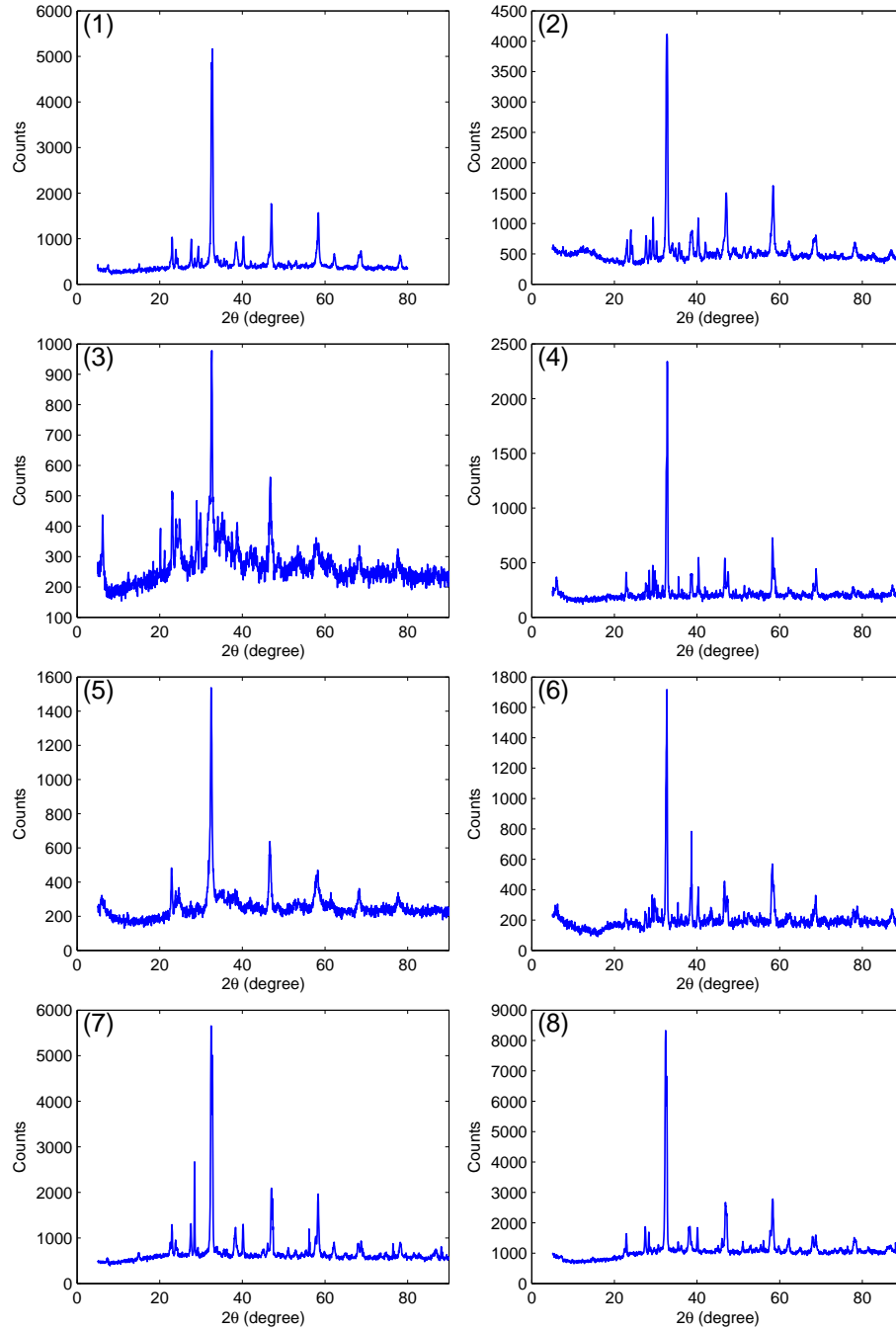


Figure E.3.1: Raw X-Ray diffractograms of YBCO samples. (1) Nanosized Sample 1 ( $x=0.20$ ). (2) Nanosized Sample 2 ( $x=0.30$ ). (3) Nanosized Sample 3 ( $x=0.35$ ). (4) Bulk Sample 3 ( $x=0.35$ ). (5) Nanosized Sample 4 ( $x=0.25$ ). (6) Bulk Sample 4 ( $x=0.25$ ). (7) Nanosized Sample 5 ( $x=0.30$ ). (8) Bulk Sample 5 ( $x=0.30$ ).

## E.4 Susceptibility Data and Measurements

As mentioned in section 4.7.2 the magnetic susceptibility of all YBCO samples was investigated. Although the data revealed little of interest relevant for the magnetic properties of samples, susceptibility data for the samples investigated through neutron scattering and  $\mu$ SR are presented in figure E.4.1.

The strange behavior, and the negative value of the susceptibility in the Sample 4 ( $x=0.25$ ) data is caused by nitrogen gas in the sample chamber and treated further in appendix E.4.3.

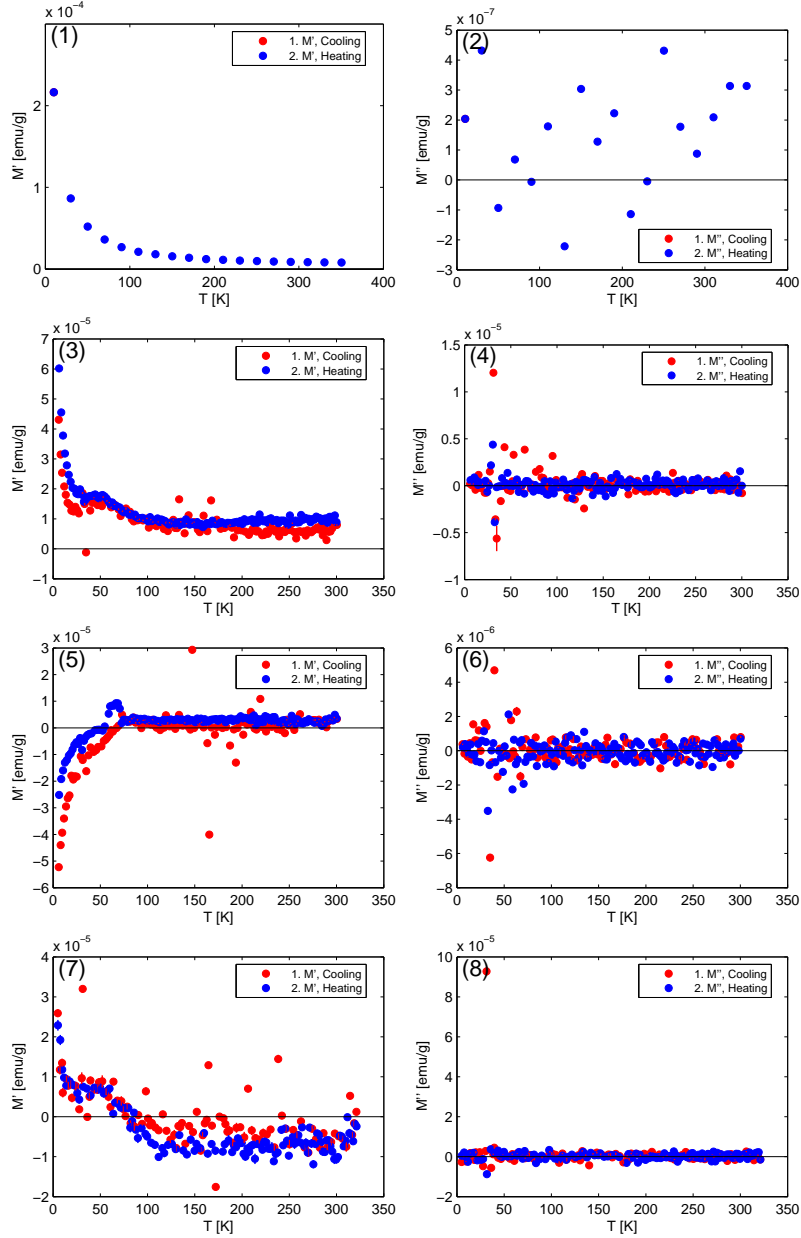


Figure E.4.1: *AC* susceptibility data for nanosized YBCO samples. Left plots are the real part of  $M$ . Left plots are the imaginary part of  $M$ . (1-2) Sample 1 ( $x=0.20$ ). (3-4) Sample 3 ( $x=0.35$ ). (5-6) Sample 4 ( $x=0.25$ ). (7-8) Sample 5 ( $x=0.30$ ).

### E.4.1 Sample 5 ( $x=0.30$ ) Applied Field Dependence

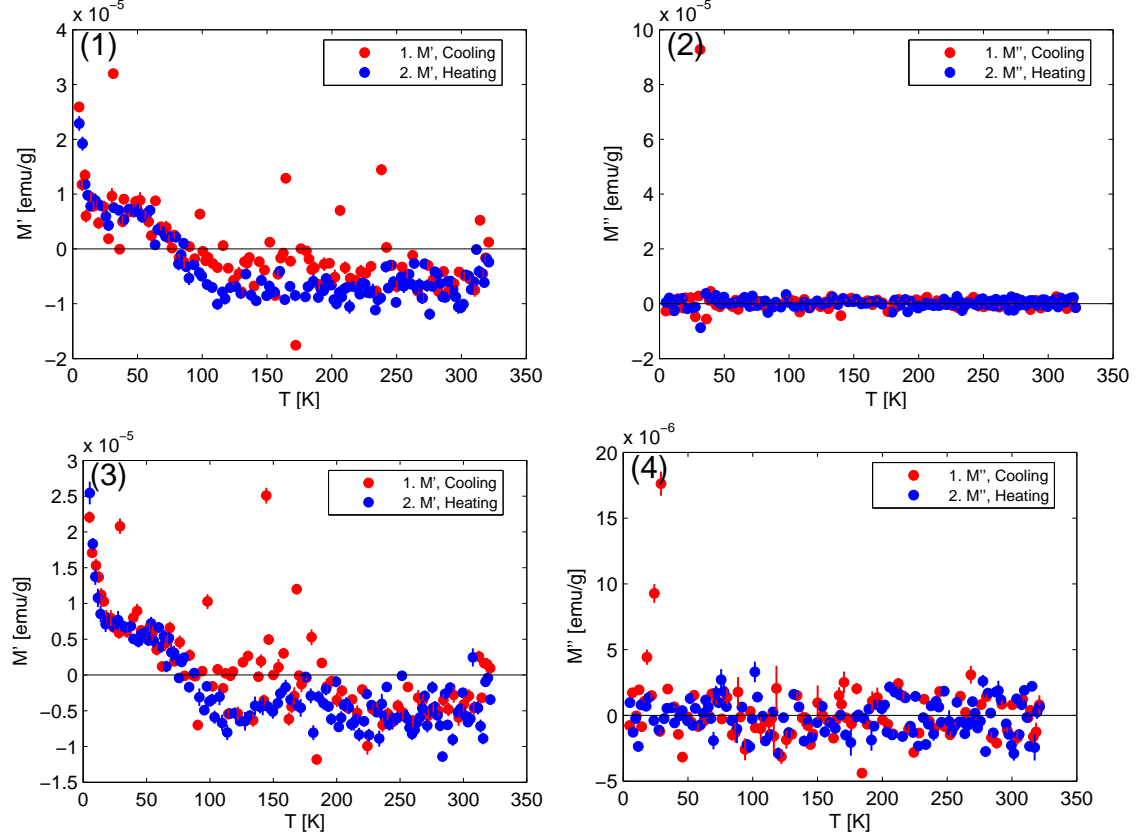


Figure E.4.2:  $M'$  and  $M''$  of Sample 5 ( $x=0.30$ ) with and without applied field. (1-2)  $B=0$  Oe. (3-4)  $B=100$  Oe.

Investigations of the susceptibility on Sample 5 ( $x=0.30$ ) did, as shown in figure E.4.2, not show any significant difference. An exception is a small increase in  $\chi'$  at 120-150 K while cooling and at 150-200 K while heating in applied field, which is absent in the zero field measurement. Considering the heat transport in the sample, and averaging over the cooling and heating data, this increase occurs at 130-170 K, which is a bit below  $T_N$  for this sample found through neutron diffraction and  $\mu$ SR. The feature might still indicate the  $T_N$  position, and be lowered due to the much longer time scale (frequency  $\nu=1$  kHz, corresponding to  $1 \text{ ms}^{-1}$ ) of susceptibility measurements.

### E.4.2 Bulk Doping Problems

As mentioned in section 5.1.11, there was a problem with the first two dopings of the bulk samples of Sample 3 and Sample 4, but not with Sample 5. To illustrate this, I present in the figure E.4.3 magnetic susceptibility measurements of selected samples Sample 3 and Sample 5. The data in (1-2) show the Sample 3 just after doping, where it exhibits a continuous superconducting phase transition. After the homogenization, where the sample is heated to approx.  $700^\circ\text{C}$  in a sealed ampoule, the susceptibility had changed into that in (3-4). After homogenization the  $T_C$  is lower, but the superconducting transition is narrower. In the imaginary data there are now two distinct phase transition temperatures of  $\sim 26$  K and  $\sim 60$  K.

The data in (5-6), show nothing but an expected increase of  $\chi'$  with decreasing temperature, until  $\sim 28$  K, where a part of the sample becomes superconducting. This fraction is however

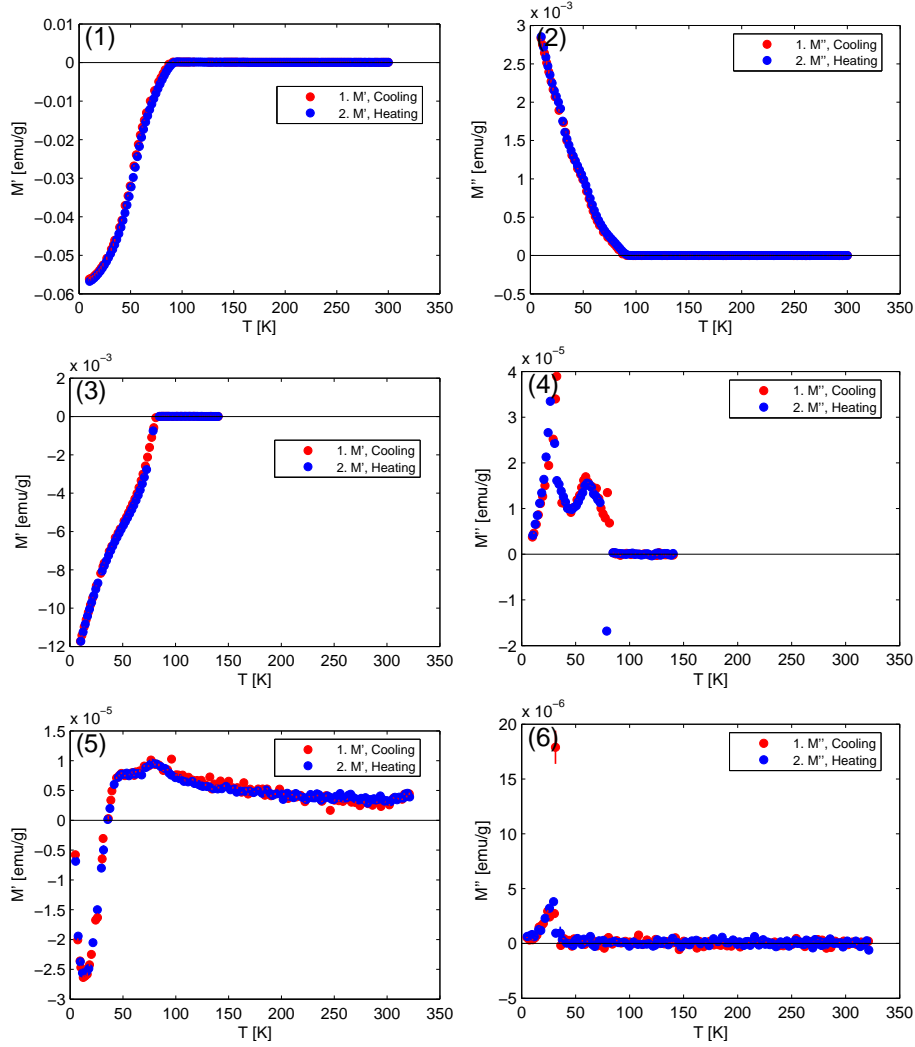


Figure E.4.3: Selected AC susceptibility data for bulk YBCO samples. The plot on the left contain the real part of  $M$ . The plots on the right contain the imaginary part of  $M$ . (1-2) Sample 3 ( $x=0.35$ ) after first doping. (3-4) Sample 3 ( $x=0.35$ ) after homogenization. (5-6) Sample 5 ( $x=0.30$ ).

very low, as the increase of  $\chi'$  from other parts of the sample (most likely impurities), is able to overcome it, and raise  $\chi'$  it significantly at very low temperatures.

### E.4.3 Chasing a Phantom...

As seen from figure E.4.1 (5-6) there is a strange increase in  $\chi'$  around 50-90 K when heating from low temperatures. This feature was further investigated and a series of datasets, shown in figure E.4.4. The data show nothing when cooling from high temperatures, but when heating the feature showed up again. In the following cooling, the feature is again gone. Next I tried stopping the heating in the middle of the feature (at 75 K), and cool from there, which caused the susceptibility to increase again. Further repetitions of these last steps showed similar behavior.

All in all I could not explain this behavior, but it looked very interesting and new and we were very excited about and were looking into different phenomena as Paramagnetic Meissner [58] which occurs in small superconducting particles.

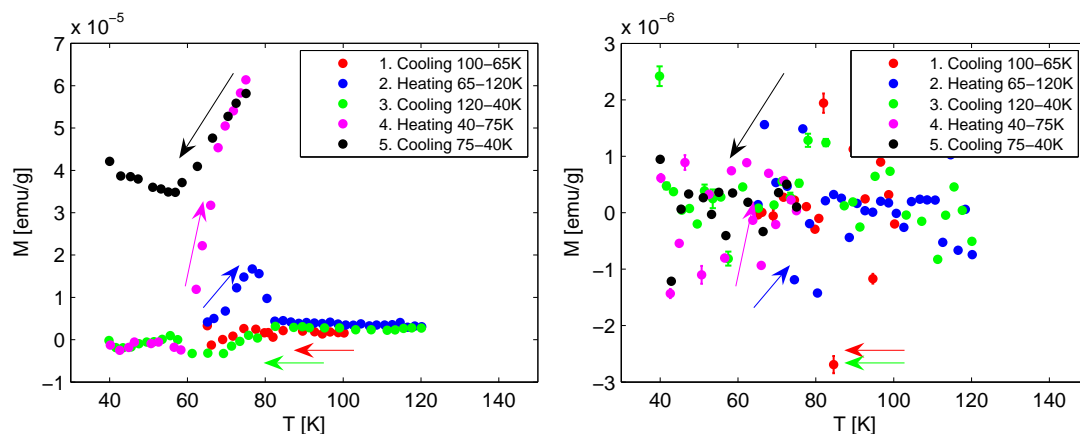


Figure E.4.4: *Strange feature in the susceptibility data.*

However, at the end of the day, we could not explain the feature, until that it was a problem with the apparatus in use. The cause was a gas leak in the system, causing nitrogen to be present in the sample chamber. The nitrogen present would then condensate and evaporate around temperatures 50-90 K, giving this pronounced signal while heating [141]. After becoming aware of this I abandoned the chase of this phenomenon. The negative susceptibility signal is most likely due to nitrogen gas, which is a diamagnetic [19].

## Appendix F

# Calculations and Simulations on CoO

### F.1 Structure Factor Calculations for CoO

To calculate the structure factors we first establish the generators for the unit cell. The Co atoms are placed on a simple fcc lattice and the O atoms are placed on an identical fcc lattice displaced  $(\frac{1}{2}, \frac{1}{2}, \frac{1}{2})$  from the origin. The fcc unit cell can be written as  $(0, 0, 0)$ ,  $(\frac{1}{2}, \frac{1}{2}, 0)$ ,  $(\frac{1}{2}, 0, \frac{1}{2})$ ,  $(0, \frac{1}{2}, \frac{1}{2})$ .

The integrated intensity of a Bragg peak can (in simplified form) be written as [103]

$$I_{hkl} \propto \frac{\lambda^3 m_{hkl} |F_{hkl}|^2}{V_c^2} P(\theta_B) L(\theta_B) \Omega, \quad (\text{F.1.1})$$

where  $m_{hkl}$  is the multiplicity,  $V_c^2$  is the volume of the crystallographic unit cell,  $\Omega$  the sample volume and  $P(\theta_B)$  and  $L(\theta_B)$  are the polarization and Lorentz factors respectively. The unit cell structure factor  $|F_{hkl}|^2$  is given by

$$|F_{hkl}|^2 = \left| \sum_j^N b_j \exp(2\pi i(hx_j + ky_j + lz_j)) \right|^2, \quad (\text{F.1.2})$$

where  $b_j$  is the scattering amplitude for, and  $x_j, y_j, z_j$  are the coordinates of, the  $j$ 'th atom in the unit cell [103]. The CoO structure can therefore be written as

$$(\text{fcc}) \cdot \begin{pmatrix} b_{Co}(0, 0, 0) \\ b_O(\frac{1}{2}, \frac{1}{2}, \frac{1}{2}) \end{pmatrix} = (\text{fcc}) \cdot (\text{dd}). \quad (\text{F.1.3})$$

To calculate the geometrical structure factor  $|G_{hkl}|^2$  we set  $b_j$  in (F.1.2) to 1. Inserting into the (fcc) part of (F.1.3) we get:

$$\begin{aligned} |G_{hkl}|_{fcc}^2 &= |F_{hkl}(b_j = 1)|_{fcc}^2 & (\text{F.1.4}) \\ &= |\exp(2\pi i \cdot 0) + \exp(2\pi i(\frac{h+k}{2})) \\ &\quad + \exp(2\pi i(\frac{h+l}{2})) + \exp(2\pi i(\frac{k+l}{2}))|^2 \\ &= |1 + \exp(2\pi i(\frac{h+k}{2})) + \exp(2\pi i(\frac{h+l}{2})) + \exp(2\pi i(\frac{k+l}{2}))|^2. \end{aligned}$$

Inserting into the (dd) part of the (F.1.3) we get similarly

$$\begin{aligned} |G_{hkl}|_{dd}^2 &= |F_{hkl}(b_j = 1)|_d^2 & (\text{F.1.5}) \\ &= |1 + \exp(2\pi i(\frac{h+k+l}{2}))|^2. \end{aligned}$$

Inserting  $h, k, l$  either all even or all odd, gives

$$|G_{hkl}|_{fcc}^2 = |F_{hkl}(b_j = 1)|_{fcc}^2 = |4|^2. \quad (\text{F.1.6})$$

Insertion of all other combinations of odd and even  $h, k, l$ 's gives  $|G_{hkl}|_{fcc}^2 = 0$ , therefore the only allowed reflections are those where the  $h, k, l$ 's are all even or all odd. Insertion of the values for  $b_j, b_{Co}$  and  $b_O$  gives

$$|G_{hkl}|_{dd}^2 = |F_{hkl}|_{fcc}^2 = |b_{Co} + b_O|^2 \quad h, k, l \text{ even} \quad (\text{F.1.7})$$

$$|G_{hkl}|_{dd}^2 = |F_{hkl}|_{fcc}^2 = |b_{Co} - b_O|^2 \quad h, k, l \text{ odd} \quad (\text{F.1.8})$$

$$|G_{hkl}|^2 = 1101.84 \text{ fm}^2 \quad h, k, l \text{ even} \quad (\text{F.1.9})$$

$$|G_{hkl}|^2 = 176.199 \text{ fm}^2 \quad h, k, l \text{ odd}, \quad (\text{F.1.10})$$

where the  $b_{Co}$  and  $b_O$  values are the  $b_c$  values from table G.3.1.

In the above calculation of the structure factors, the Debye-Waller factor and the Lorentz factor section 4.1.2 have not been taken into account.

## F.2 PSD Debye-Scherrer Calculations

As a first approximation, one can consider the all pixels in a column on the PSD as having the same  $q$  value. However, to improve precision and the  $q$  resolution, I have taken into account the Debye-Scherrer cone, and for each pixel calculated the ideal  $q$  value. This procedure is repeated for each scan-point, since the radius of the cone changes with scattering angle. The calculations of the  $q$  are presented below, and are illustrated in figure F.2.1.

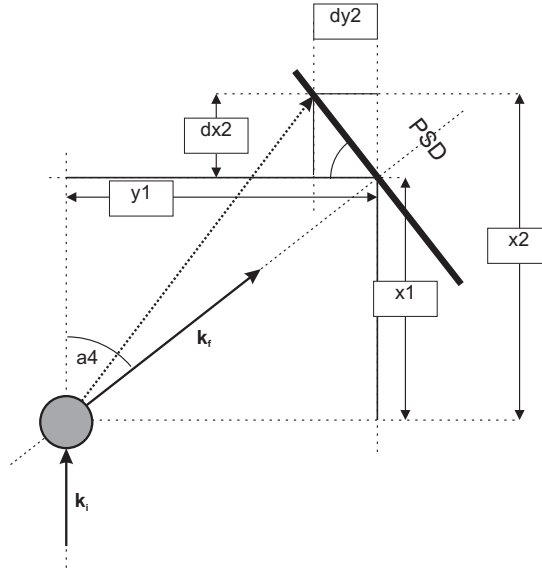


Figure F.2.1: A graphical illustration of the  $q$ -calculations on the Debye-Scherrer cone on the PSD.

The calculations are performed in loops. For each scan point the calculations

$$\phi = a4 \quad (\text{F.2.1})$$

$$x_1 = d_{sd} \cdot \cos(\phi), \quad (\text{F.2.2})$$

$$y_1 = d_{sd} \cdot \sin(\phi), \quad (\text{F.2.3})$$

are performed (in the instrument plane), where  $d_{sd}$  is the distance from sample to detector and  $a4$  is the  $a4$  motor position.

Then we continue to the calculations performed for each column  $i$  (1-128)

$$x_2 = x_1 + dx_2 = x_1 + \sin(\phi) \cdot (i - i_0) \cdot \Delta w \quad (\text{F.2.4})$$

$$y_2 = y_1 + dy_2 = y_1 + \cos(\phi) \cdot (i - i_0) \cdot \Delta w, \quad (\text{F.2.5})$$

where  $i_0$  is the horizontal pixel center of the PSD,  $i$  is the current pixel column and  $\Delta w$  is the width per pixel of the PSD. For every pixel  $j$  in the individual column we calculate the  $q$  value

$$l = \sqrt{x_2^2 + y_2^2 + ((j - j_0)\Delta h)^2} \quad (\text{F.2.6})$$

$$\theta = \arccos\left(\frac{x_2}{l}\right) \quad (\text{F.2.7})$$

$$q_{i,j} = \sin(\theta/2) \cdot k_i \cdot 2, \quad (\text{F.2.8})$$

where  $l$  is the total length from sample to intersection point on the PSD,  $j_0$  is the vertical pixel center on the PSD,  $\Delta h$  is the height per pixel on the PSD,  $k_i$  is the  $k$ -vector of the incoming neutrons. This is all shown graphically in figure F.2.1, and in figure F.2.2 there are examples of the calculated Debye Scherrer cones on the PSD.

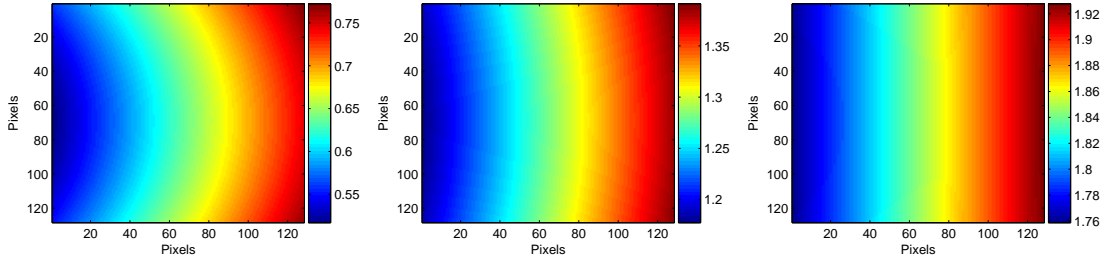


Figure F.2.2: *Examples of  $q$  values on the PSD.  $q$ -values are displayed on the color scale. Left: Scan point no. 31.  $2\theta=27.3^\circ$ ,  $q=0.63$ . Center: Scan point no. 16.  $2\theta=57.3^\circ$ ,  $q=1.28$ . Right: Scan point no. 1.  $2\theta=87.3^\circ$ ,  $q=1.84$ .*

### F.3 PSD Debye-Scherrer Simulations

The results of the simulations are shown in figure F.3.1, where I have varied the sample dimensions. The sample has the shape of a cylinder and I have run simulations with diameters 1, 3, 6 and 10 mm in combination with heights 10, 55 and 110 mm.

The real sample sizes are as mentioned in section 6.2.2,  $h \sim 55$  mm and  $d=6$  mm (30 nm:  $d=10$  mm). My interpretation of the simulation results, is that the optimum method of data loading depends on whether the data window is narrow or broad vertically.

As seen from all images in figure F.3.1, the Debye-Scherrer cone can inside the narrow box be approximated with a vertical line, as the deviation is negligible compared to the horizontal distribution. When using the larger box, it should be considered to use the Debye-Scherrer cone calculations, which I have chosen to do.

However, the sample container size, as seen from the simulations, does affect the shape and width of the Bragg peak on the PSD. For the used sample sizes (diameters 6 mm and 10 mm), a difference in the Bragg peak width can not be demonstrated.

To elucidate on the effect of sample holder width on the instrumental resolution, the Bragg peaks from the 6 mm x 55 mm and the 10 mm x 55 mm simulations have been extracted and fitted with Gaussians, as shown in figure F.3.2.

As pixel position and reciprocal lattice position, within a narrow angle are approximately proportional, I have analyzed the intensity as a function of (horizontal) pixel position.

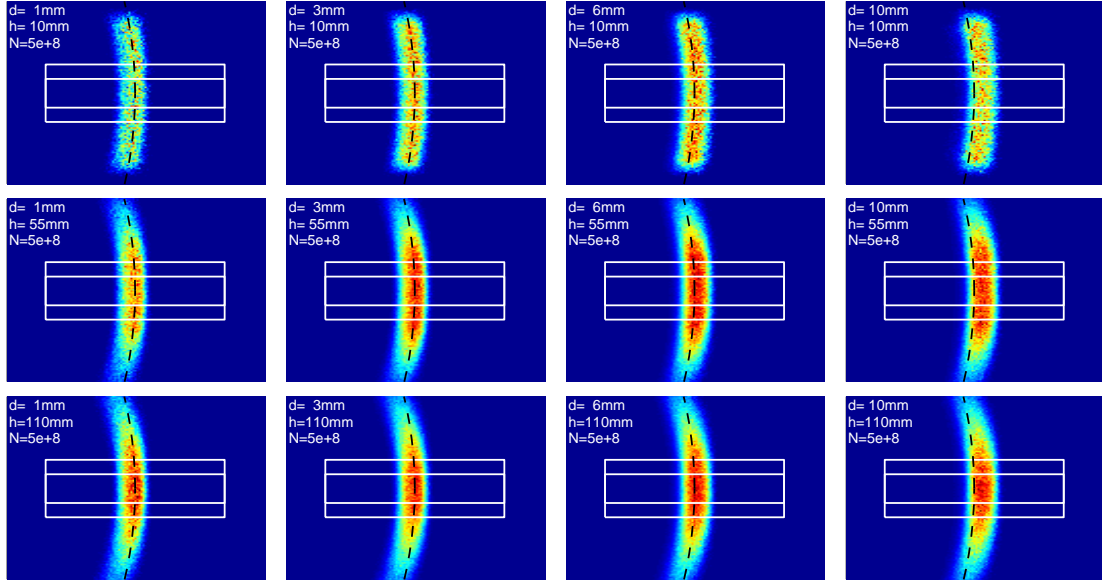


Figure F.3.1: Simulated PSD images of the  $\text{CoO}$  ( $\frac{1}{2} \frac{1}{2} \frac{1}{2}$ ) reflection at  $2\theta=57.1^\circ$  with neutron absorption enabled. Width and height of the PSD is 30 cm and 50 cm respectively. The analyzer slit slit opening is 80x80 mm. The white boxes indicate the typical areas used for data analysis, with heights of 20 and 40 pixels. The dashed line shows the calculated Debye-Scherrer cone. Columns from left: Sample diameter: 1. 1 mm, 2. 3 mm, 3. 6 mm, 4. 10 mm. Rows from top: Sample height: 1. 10 mm 2. 55 mm, 3. 110 mm.

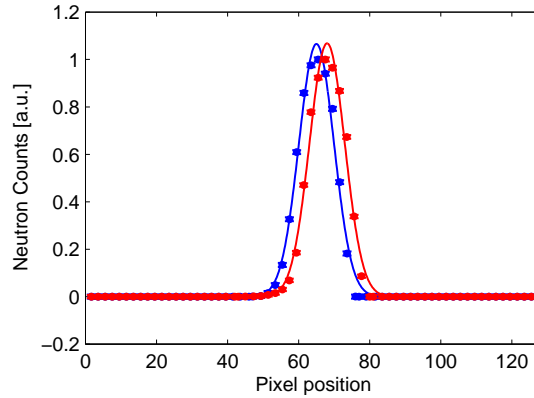


Figure F.3.2: Bragg peaks extracted from *McStas* simulations. (●) simulation with 6 mm x 55 mm sample holder. (●) simulation with 10 mm x 55 mm sample holder.

The Gaussian widths found from the fits are 4.94(3) and 4.96(2) pixels for the 6 mm x 55 mm and 10 mm x 55 mm simulations, respectively. That is, the widths are identical within error-bars, and hence a change in instrumental resolution is unneeded when switching between sample containers of diameters 6 mm and 10 mm.

## Appendix G

# Physical and Chemical data tables

### G.1 Fundamental Physical Constants

Name	Symbol	Value	Unit
Molar Gas Constant	$R$	8.314 472	J/(mol · K)
Boltzmann Constant	$k_B$	1.380 650 4 · 10 <sup>-23</sup>	J/K
Avogadro Constant	$N_A$	6.022 141 79 · 10 <sup>23</sup>	mol <sup>-1</sup>
The Bohr Magneton	$\mu_B$	9.274 009 15 · 10 <sup>-24</sup>	J/T
The Nuclear Magneton	$\mu_N$	5.050 783 24 · 10 <sup>-27</sup>	J/T

Table G.1.1: *Selected physical constants used. From [127]*

### G.2 Properties of Selected Elements

Atom	Molar mass (g/mol)
O	15.9994
Cu	63.546
Y	88.9059
Ba	137.34

Table G.2.1: Physical properties of selected elements.

### G.3 Neutron Scattering Properties for Selected Elements

Z	Isot.	P	I	$b_c$	$b_+$	$b_-$	c	$\sigma_{coh}$	$\sigma_{inc}$	$\sigma_{scatt}$	$\sigma_{abs}$
1	H			-3.7409(11)				1.7568(10)	80.26(6)	82.02(6)	0.3326(7)
5	B			5.30(4)				3.54(5)	1.70(12)	5.24(11)	767.0(8.0)
6	C			6.6484(13)				5.551(2)	0.001(4)	5.551(3)	0.00350(7)
8	O			5.805(4)				4.232(6)	0.000(8)	4.232(6)	0.00019(2)
23	V			-0.443(14)				0.01838(12)	5.068(6)	5.10(6)	5.08(4)
27	Co <sup>59</sup>	100	7/2	2.49(2)	-9.21(10)	3.58(10)	±	0.779(13)	4.8(3)	5.6(3)	37.186(6)
29	Cu			7.718(4)				7.485(8)	0.55(3)	8.03(3)	3.78(2)
39	Y <sup>89</sup>	100	1/2	7.75(2)	8.4(2)	5.8(5)	±	7.55(4)	0.15(8)	7.70(9)	1.28(2)
56	Ba			5.07(3)				3.23(4)	0.15(11)	3.38(10)	1.1(1)

Table G.3.1: *The most used neutron scattering properties of selected isotopes.* Abbreviations:  $Z$  = Nuclide;  $Isot.$  = Isotope;  $P$  = Abundance;  $I$  = Nuclear spin;  $b_c$  = bound coherent scattering length (in fm);  $b_+$  = spin-dependent scattering length for  $I+1/2$  (in fm);  $b_-$  = spin-dependent scattering length for  $I-1/2$  (in fm);  $c$  = indication whether separate ( $b_+$ - $b_-$ ) values are available (+/-);  $\sigma_{coh}$  = coherent cross section in barn;  $\sigma_{inc}$  = incoherent cross section in barn;  $\sigma_{scatt}$  = total cross section in barn;  $\sigma_{abs}$  = thermal absorption cross section in barn for 0.0253 eV. From [43].

### G.4 Crystal Data for Selected Compounds

Material	T(K)	ICSD #	a	b	c	Ref.
YBa <sub>2</sub> Cu <sub>3</sub> O <sub>6</sub>	-	41645	3.84	3.84	11.77	[30, 31]♣
YBa <sub>2</sub> Cu <sub>3</sub> O <sub>7</sub>	-	41646	3.8178	3.8839	11.6828	[30, 31]♣
Y <sub>2</sub> Cu <sub>2</sub> O <sub>5</sub>	20	63306	10.796(2)	3.494(1)	12.457(2)	[50]
Y <sub>2</sub> Cu <sub>2</sub> O <sub>5</sub>	50	67119	10.805(1)	3.4955(2)	12.4605(7)	[9]
Y <sub>2</sub> Cu <sub>2</sub> O <sub>5</sub>	80	79429	10.796(2)	3.494(1)	12.4546(2)	[57]
Y <sub>2</sub> Cu <sub>2</sub> O <sub>5</sub>	296	72058	10.805(1)	3.4955(2)	12.4605(7)	[2]
Y <sub>2</sub> BaCuO <sub>5</sub> <sup>†</sup>	293	52055	12.1793(7)	5.6591(5)	7.1323(4)	[74]
BaCuO <sub>2</sub>	-	65801	18.2772(2)	18.2772(2)	18.2772(2)	[199]
BaCuO <sub>2</sub>	-	93655	18.261	18.261	18.261	[42]
Y <sub>2</sub> O <sub>3</sub>	-	155173	10.60389(1)	10.60389(1)	10.60389(1)	[45]
BaCO <sub>3</sub>	-	91888	5.316(1)	8.892(2)	6.428(2)	[73]
CuO <sup>‡</sup>	-	92368	4.6894(7)	3.4222(7)	5.1299(8)	[209]
Co <sub>3</sub> O <sub>4</sub>	-	9362	8.065(5)	8.065(5)	8.065(5)	[92]

Table G.4.1: *Cell parameters of YBa<sub>2</sub>Cu<sub>3</sub>O<sub>6</sub> and YBa<sub>2</sub>Cu<sub>3</sub>O<sub>7</sub> and selected YBCO impurities.* The angles  $\alpha$ ,  $\beta$  and  $\gamma$  are in all cases 90°. From [44]. Symbols: (†) Green phase. (‡) CuO is monoclinic ( $\alpha, \beta, \gamma$ ) = (90, 99.591(14), 90). (♣) The ICSD reference is erroneous. The second quoted reference is probably the correct one, although one value differs slightly.

## G.5 Tables of Reflections for Selected Materials

### G.5.1 $Y_2Cu_2O_5$ at 20 K

$h$	$k$	$l$	$m$	$q$ ( $\text{\AA}^{-1}$ )	$2\theta$ ( $^\circ$ )	$d$ ( $\text{\AA}$ )	$F^2$
2	0	0	2	1.16398	51.641	5.398000	13.0532
2	0	1	4	1.26857	56.678	4.952970	250.2960
2	0	2	4	1.54029	70.390	4.079220	370.5390
0	1	1	4	1.86767	88.672	3.364170	2727.1600
1	1	0	4	1.89011	90.025	3.324240	495.2550
2	0	3	4	1.90906	91.180	3.291230	1478.7400
1	1	1	8	1.95625	94.110	3.211850	440.0520
0	0	4	2	2.01755	98.042	3.114250	825.5870
2	1	0	4	2.14211	106.558	2.933170	3166.5000
1	1	2	8	2.14246	106.583	2.932690	425.6580
2	1	1	8	2.20069	110.869	2.855090	4921.2600
4	0	0	2	2.32797	121.174	2.699000	1559.4300
2	0	4	4	2.32925	121.286	2.697510	3390.6100
0	1	3	4	2.35021	123.146	2.673460	331.4360
2	1	2	8	2.36776	124.748	2.653640	2541.5000
4	0	1	4	2.38197	126.077	2.637800	313.6870
1	1	3	8	2.42119	129.913	2.595070	283.0380
3	1	0	4	2.50643	139.398	2.506820	276.6300
4	0	2	4	2.53713	143.380	2.476490	327.3070
3	1	1	8	2.55668	146.149	2.457550	387.0430
2	1	3	8	2.62265	157.847	2.395730	61.1216

Table G.5.1: Reflection data for  $Y_2Cu_2O_5$  at 20 K. Generated from [50] with neutron radiation ( $E_i=3.7\text{ meV}$ ).

### G.5.2 $Y_2Cu_2O_5$ at 50 K

$h$	$k$	$l$	$m$	$q$ ( $\text{\AA}^{-1}$ )	$2\theta$ ( $^\circ$ )	$d$ ( $\text{\AA}$ )	$F^2$
2	0	0	2	1.16301	51.594	5.402500	13.6384
2	0	1	4	1.26762	56.632	4.956670	219.2200
2	0	2	4	1.53937	70.342	4.081650	282.3210
0	1	1	4	1.86689	88.625	3.365580	2244.9700
1	1	0	4	1.88922	89.971	3.325800	365.1700
2	0	3	4	1.90813	91.124	3.292830	1110.1500
1	1	1	8	1.95536	94.054	3.213310	472.4590
0	0	4	2	2.01699	98.005	3.115120	589.8040
2	1	0	4	2.14094	106.474	2.934780	3013.6700
1	1	2	8	2.14155	106.518	2.933940	124.2020
2	1	1	8	2.19952	110.780	2.856610	3911.3400
4	0	0	2	2.32602	121.004	2.701250	656.7810
2	0	4	4	2.32826	121.200	2.698640	2889.4700
0	1	3	4	2.34934	123.068	2.674440	172.5210
2	1	2	8	2.36657	124.638	2.654960	1884.3200
4	0	1	4	2.38005	125.895	2.639930	201.2970
1	1	3	8	2.42023	129.816	2.596100	284.7080
3	1	0	4	2.50487	139.205	2.508390	139.3220
4	0	2	4	2.53524	143.122	2.478330	270.4680
3	1	1	8	2.55512	145.920	2.459050	290.8540
2	1	3	8	2.62145	157.579	2.396830	61.4875

Table G.5.2: Reflection data for  $Y_2Cu_2O_5$  at 50 K. Generated from [9] with neutron radiation ( $E_i=3.7\text{ meV}$ ).

G.5.3  $Y_2Cu_2O_5$  at 80 K

$h$	$k$	$l$	$m$	$q$ ( $\text{\AA}^{-1}$ )	$2\theta$ ( $^\circ$ )	$d$ ( $\text{\AA}$ )	$F^2$
2	0	0	2	1.16398	51.641	5.398000	5.4422
2	0	1	4	1.26861	56.680	4.952820	255.9750
2	0	2	4	1.54041	70.397	4.078880	329.6980
0	1	1	4	1.86770	88.674	3.364130	2643.3200
1	1	0	4	1.89011	90.025	3.324240	602.7260
2	0	3	4	1.90929	91.195	3.290830	1308.7200
1	1	1	8	1.95627	94.112	3.211800	382.6780
0	0	4	2	2.01794	98.067	3.113650	766.5250
2	1	0	4	2.14211	106.558	2.933170	3244.7000
1	1	2	8	2.14256	106.590	2.932560	441.6810
2	1	1	8	2.20072	110.871	2.855060	4984.2000
4	0	0	2	2.32797	121.174	2.699000	1670.3400
2	0	4	4	2.32958	121.315	2.697120	3374.0300
0	1	3	4	2.35040	123.163	2.673240	272.7380
2	1	2	8	2.36784	124.755	2.653540	2460.5400
4	0	1	4	2.38199	126.079	2.637770	243.7300
1	1	3	8	2.42137	129.931	2.594880	252.9770
3	1	0	4	2.50643	139.398	2.506820	179.1830
4	0	2	4	2.53721	143.390	2.476410	279.9550
3	1	1	8	2.55670	146.152	2.457530	305.6670
2	1	3	8	2.62282	157.884	2.395580	46.5969

Table G.5.3: Reflection data for  $Y_2Cu_2O_5$  at 80 K. Generated from [57] with neutron radiation ( $E_i=3.7\text{meV}$ ).G.5.4  $Y_2Cu_2O_5$  at 296 K

$h$	$k$	$l$	$m$	$q$ ( $\text{\AA}^{-1}$ )	$2\theta$ ( $^\circ$ )	$d$ ( $\text{\AA}$ )	$F^2$
2	0	0	2	1.16366	51.625	5.399500	43.0429
2	0	1	4	1.26824	56.662	4.954250	237.0240
2	0	2	4	1.53994	70.371	4.080150	335.2240
0	1	1	4	1.86518	88.522	3.368670	2617.8200
1	1	0	4	1.88761	89.874	3.328630	509.5140
2	0	3	4	1.90867	91.156	3.291900	1383.1900
1	1	1	8	1.95382	93.957	3.215840	550.1210
0	0	4	2	2.01723	98.021	3.114750	703.7620
2	1	0	4	2.13978	106.391	2.936360	3139.5900
1	1	2	8	2.14018	106.420	2.935810	453.7600
2	1	1	8	2.19840	110.696	2.858060	4839.3700
4	0	0	2	2.32731	121.117	2.699750	1697.5700
2	0	4	4	2.32880	121.247	2.698030	3411.4500
0	1	3	4	2.34808	122.955	2.675870	335.7220
2	1	2	8	2.36557	124.546	2.656080	2388.1600
4	0	1	4	2.38133	126.016	2.638510	189.9250
1	1	3	8	2.41910	129.701	2.597320	385.9500
3	1	0	4	2.50425	139.129	2.509000	195.2990
4	0	2	4	2.53647	143.290	2.477130	304.8080
3	1	1	8	2.55452	145.833	2.459620	404.3540
2	1	3	8	2.62061	157.395	2.397600	50.2103

Table G.5.4: Reflection data for  $Y_2Cu_2O_5$  at 296 K. Generated from [2] with neutron radiation ( $E_i=3.7\text{meV}$ ).

G.5.5  $Y_2BaCuO_5$  (Green Phase)

$h$	$k$	$l$	$m$	$q$ ( $\text{\AA}^{-1}$ )	$2\theta$ ( $^\circ$ )	$d$ ( $\text{\AA}$ )	$F^2$
2	0	0	2	1.03178	45.422	6.089650	447.8740
2	0	1	4	1.35670	61.017	4.631220	519.1650
0	1	1	4	1.41732	64.058	4.433150	97.4177
1	1	1	8	1.50828	68.719	4.165770	365.4750
2	1	0	4	1.51568	69.104	4.145450	1761.7200
2	1	1	8	1.75310	81.990	3.584040	27.6230
0	0	2	2	1.76189	82.490	3.566150	575.5720
3	0	1	4	1.78082	83.575	3.528230	3.7506
1	0	2	4	1.83586	86.780	3.422460	7.5142
2	0	2	4	2.04177	99.638	3.077310	292.4260
4	0	0	2	2.06356	101.097	3.044830	129.8480
3	1	1	8	2.09858	103.491	2.994000	1638.0200
1	1	2	8	2.14549	106.801	2.928550	1315.8200
0	2	0	2	2.22056	112.385	2.829550	1657.0000
4	0	1	4	2.24373	114.192	2.800320	126.0760
2	1	2	8	2.32412	120.839	2.703460	402.8480
4	1	0	4	2.34329	122.526	2.681350	1189.0400
3	0	2	4	2.34510	122.688	2.679270	3318.0200
1	2	1	8	2.44399	132.274	2.570870	1029.7700
2	2	0	4	2.44856	132.761	2.566070	51.4609
4	1	1	8	2.50341	139.026	2.509850	477.7560
3	1	2	8	2.59466	152.286	2.421580	642.5730
2	2	1	8	2.60221	153.671	2.414550	340.9390

Table G.5.5: Reflection data for  $Y_2BaCuO_5$  (green phase) at 293K. Generated from [74] with neutron radiation ( $E_i=3.7\text{meV}$ ).

G.5.6 BaCuO<sub>2</sub> #1

$h$	$k$	$l$	$m$	$q$ (Å <sup>-1</sup> )	$2\theta$ (°)	$d$ (Å)	$F^2$
2	1	1	24	0.84206	36.733	7.461640	93.0069
2	2	0	12	0.97233	42.672	6.461970	1164.3600
3	1	0	24	1.08710	48.006	5.779760	3245.0400
2	2	2	8	1.19086	52.924	5.276170	4855.5100
3	2	1	48	1.28627	57.542	4.884790	29829.0000
4	0	0	6	1.37508	61.934	4.569300	17807.1000
3	3	0	12	1.45850	66.153	4.307980	22475.4000
4	1	1	24	1.45850	66.153	4.307980	6884.3200
4	2	0	24	1.53739	70.238	4.086910	7061.3800
3	3	2	24	1.61243	74.221	3.896710	2663.0100
4	2	2	24	1.68413	78.127	3.730820	34467.9000
5	1	0	24	1.75289	81.978	3.584450	2560.9000
4	3	1	48	1.75289	81.978	3.584450	21.9643
5	2	1	48	1.88291	89.589	3.336950	1250.0500
4	4	0	12	1.94466	93.383	3.230980	1453.5700
4	3	3	24	2.00451	97.193	3.134510	12125.1000
5	3	0	24	2.00451	97.193	3.134510	404.0580
6	0	0	6	2.06262	101.034	3.046200	239861.0000
4	4	2	24	2.06262	101.034	3.046200	26570.8000
5	3	2	48	2.11915	104.927	2.964950	45220.7000
6	1	1	24	2.11915	104.927	2.964950	3594.1200
6	2	0	24	2.17420	108.891	2.889880	344.1070
5	4	1	48	2.22789	112.952	2.820230	2362.9000
6	2	2	24	2.28032	117.139	2.755390	6.1130
6	3	1	48	2.33157	121.489	2.694830	11.8251
4	4	4	8	2.38171	126.052	2.638090	68342.5000
5	4	3	48	2.43083	130.898	2.584790	9606.7800
5	5	0	12	2.43083	130.898	2.584790	4268.4000
7	1	0	24	2.43083	130.898	2.584790	2650.4800
6	4	0	24	2.47897	136.129	2.534590	26669.0000
6	3	3	24	2.52619	141.914	2.487210	51104.6000
5	5	2	24	2.52619	141.914	2.487210	11621.0000
7	2	1	48	2.52619	141.914	2.487210	283.1880
6	4	2	48	2.57254	148.570	2.442390	1184.2800
7	3	0	24	2.61808	156.848	2.399910	61764.5000

Table G.5.6: Reflection data for BaCuO<sub>2</sub>. Generated from [199] with neutron radiation ( $E_i=3.7$  meV).

G.5.7 BaCuO<sub>2</sub> #2

$h$	$k$	$l$	$m$	$q$ ( $\text{\AA}^{-1}$ )	$2\theta$ ( $^\circ$ )	$d$ ( $\text{\AA}$ )	$F^2$
1	1	0	12	0.48660	20.982	12.912500	23448.4000
2	0	0	6	0.68815	29.844	9.130500	17145.6000
2	1	1	24	0.84281	36.767	7.455020	171.3400
2	2	0	12	0.97320	42.712	6.456240	39.2948
3	1	0	24	1.08807	48.051	5.774630	5040.2300
2	2	2	8	1.19192	52.975	5.271500	4764.0100
3	2	1	48	1.28742	57.598	4.880460	28232.9000
4	0	0	6	1.37631	61.995	4.565250	20552.4000
3	3	0	12	1.45979	66.219	4.304160	11463.4000
4	1	1	24	1.45979	66.219	4.304160	7633.0500
4	2	0	24	1.53876	70.310	4.083280	11559.0000
3	3	2	24	1.61386	74.298	3.893260	5316.7000
4	2	2	24	1.68563	78.210	3.727510	26175.5000
5	1	0	24	1.75445	82.067	3.581280	1766.7600
4	3	1	48	1.75445	82.067	3.581280	645.1380
5	2	1	48	1.88458	89.690	3.333990	2644.2500
4	4	0	12	1.94639	93.491	3.228120	835.2530
4	3	3	24	2.00629	97.308	3.131740	2445.7700
5	3	0	24	2.00629	97.308	3.131740	968.0220
6	0	0	6	2.06446	101.158	3.043500	286980.0000
4	4	2	24	2.06446	101.158	3.043500	19440.4000
5	3	2	48	2.12103	105.059	2.962330	39127.4000
6	1	1	24	2.12103	105.059	2.962330	9106.3100
6	2	0	24	2.17613	109.034	2.887320	21.4075
5	4	1	48	2.22987	113.106	2.817730	0.3192
6	2	2	24	2.28235	117.305	2.752950	2493.7600
6	3	1	48	2.33364	121.671	2.692440	52.5437
4	4	4	8	2.38383	126.253	2.635750	157928.0000
5	5	0	12	2.43299	131.121	2.582500	13090.0000
7	1	0	24	2.43299	131.121	2.582500	4030.2700
5	4	3	48	2.43299	131.121	2.582500	2631.6700
6	4	0	24	2.48117	136.382	2.532350	19956.3000
6	3	3	24	2.52843	142.210	2.485010	34533.2000
5	5	2	24	2.52843	142.210	2.485010	8655.5400
7	2	1	48	2.52843	142.210	2.485010	0.1552
6	4	2	48	2.57483	148.934	2.440230	1.3556
7	3	0	24	2.62041	157.350	2.397790	43033.4000

Table G.5.7: Reflection data for BaCuO<sub>2</sub>. Generated from [42] with neutron radiation ( $E_i=3.7\text{meV}$ ).G.5.8 Y<sub>2</sub>O<sub>3</sub>

$h$	$k$	$l$	$m$	$q$ ( $\text{\AA}^{-1}$ )	$2\theta$ ( $^\circ$ )	$d$ ( $\text{\AA}$ )	$F^2$
2	0	0	6	1.1851	5.30195	52.6473	31.8506
2	1	1	24	1.4514	4.32902	65.7901	272.28
2	2	0	12	1.6759	3.74904	77.676	44.8696
2	2	2	8	2.0526	3.06108	100.36	1.40137
3	2	1	24	2.2171	2.83401	112.116	4777.82
3	1	2	24	2.2171	2.83401	112.116	2785.84
4	0	0	6	2.3701	2.65097	124.968	46842.6
4	1	1	24	2.5139	2.49936	140.332	311.415
4	0	2	12	2.6499	2.3711	165.105	75.1308
4	2	0	12	2.6499	2.3711	165.105	16.8642

Table G.5.8: Reflection data for Y<sub>2</sub>O<sub>3</sub>. Generated from [45] with neutron radiation ( $E_i=3.7\text{meV}$ ).



# Appendix H

## Publications

### H.1 Submitted Papers

#### H.1.1 Paper I

**Size Controlled Fabrication of Stoichiometric Magnetite Nanoparticles  
by Reverse Micelles**

*by*

J. í Hjøllum, L. Theil Kuhn, E. E. Carpenter, E. Johnson, M. B. Madsen, and K. Bechgaard

*In revision for the European Physical Journal - Applied Physics. Referee reports positive.*



# Size Controlled Fabrication of Stoichiometric Magnetite Nanoparticles by Reverse Micelles

J. í Hjøllum<sup>1,2</sup>, L. Theil Kuhn<sup>3</sup>, E. E. Carpenter<sup>4</sup>, E. Johnson<sup>1,2</sup>, M. B. Madsen<sup>1</sup>, and K. Bechgaard<sup>5</sup>

<sup>1</sup> Niels Bohr Institute, University of Copenhagen, Juliane Maries Vej 30, DK-2100 Copenhagen Ø, Denmark

<sup>2</sup> Materials Research Department, Risø National Laboratory, Technical University of Denmark, Fredriksborgvej 399, DK-4000 Roskilde, Denmark

<sup>3</sup> Fuel Cells and Solid State Chemistry Department, Risø National Laboratory, Technical University of Denmark, Fredriksborgvej 399, DK-4000 Roskilde, Denmark

<sup>4</sup> Virginia Commonwealth University, Department of Chemistry, 1001 West Main Street, P.O. Box 842006, Richmond, Virginia 23284-2006, USA

<sup>5</sup> Department of Chemistry, University of Copenhagen, Universitetsparken 5, DK-2100 Copenhagen Ø, Denmark

the date of receipt and acceptance should be inserted later

**Abstract.** We report on the successful implementation of the reverse micellar technique as a tool for controlled preparation of nano-sized, crystalline stoichiometric magnetite particles in the size range 12-25 nm. Through variation of the macroscopic synthesis parameters we were able to control the average size of the nanoparticles. The chemical composition and the magnetic properties of the particles have been explored using Mössbauer spectroscopy on samples where in-situ and post-synthesis oxidation was prevented. The particle size distributions have been determined from transmission electron microscopy images and a truncated octahedral shape of the particles was found from application of projection analysis of 3D numerical shape simulations.

**PACS.** 76.30.Fc Iron group (2d) ions and impurities – 75.75.+a Magnetic properties of nanostructures – 68.37.Lp Transmission electron microscopy (TEM) – 81.07.Wx Nanopowder

## 1 Introduction

Nanoparticles are the subject of interest in many fields of science and technology due to their unique physical and chemical properties.

Iron oxide nanoparticles are used in pigments, in magnetic storage media, in sensors, as catalysts, in medicine, as coatings etc. Particularly, magnetic iron oxide nanoparticles are being used in large quantities in magnetic storage devices, and as an emerging application as controllable drug delivery agent in medical treatment[1].

For most applications of iron oxide nanoparticles, control of chemical composition and size distributions of the nanoparticles is crucial, as inhomogeneity in size and composition may change their properties radically. The iron oxide magnetite ( $\text{Fe}_3\text{O}_4$ ) is a widely used ferrimagnetic material. For instance magnetite has potential as a candidate for use in spintronics[2].

A range of methods exist for preparation of magnetite nanoparticles such as co-precipitation[3–5], a sol-gel method[6], high-temperature reactions[7] and microemulsion/micellar precipitation[8–11].

However, final composition and size distribution of the produced powders are varying, and there are only few reports of successful size controlled manufacturing of stoichiometric magnetite particles, for instance demonstrated for 3-9 nm  $\text{Fe}_3\text{O}_4$  nanoparticles in [12]. In many cases composition control of the resulting nanoparticles is lacking. Either the composition has not been thoroughly examined or the nanoparticles actually consist of mixtures of magnetite and the end oxidized product maghemite ( $\gamma\text{-Fe}_2\text{O}_3$ )[5–8, 13, 14].

For characterization of nanoparticles the standard bulk methods of X-ray powder diffraction (XRD), magnetization and susceptibility can not always be applied due to stress/strain effects, defects, non-periodic boundary conditions, surface layer properties such as uncompensated surface spins and surface oxidation, and stoichiometric effects on the formfactor. A thorough investigation of magnetite nanoparticles therefore requires a technique that locally probes the oxygen environment of the Fe-ions. We have chosen Mössbauer spectroscopy for this purpose.

In the AOT reverse micellar systems, there is a linear relation between the solution dependent parameter  $\omega$  and the water droplets radius, and in some cases a simple and almost linear relation between the water pool size and the particle size. However, a straightforward droplet to particle size correlation is rare. It is found to depend on reactant concentration, concentration balancing, sur-

factant film flexibility and micellar droplet size. Even the shape of the produced particles is dependent on various manufacturing conditions such as pH and surfactant[15, 16].

In the present paper we demonstrate that by applying a reverse micellar method and working in a partly deoxygenated atmosphere we can fabricate stoichiometric single crystalline  $\text{Fe}_3\text{O}_4$  nanoparticles and control the average particle size in the range 12-25 nm. To our knowledge this covers sizes larger than previously reported[12].

### 1.1 Magnetite nanoparticle synthesis

The reverse micellar technique[9–11] utilizes that soap and water in an excess of oil will self arrange into a microemulsion system, which consists of water droplets with a shell of soap, a so-called micelle, within the oil bulk. Chemical reactions giving off nanoparticles can take place inside the micelle by dynamic fusion. The micelle size and concentration of reactants within the micelle sets an upper limit for the size of the manufactured particles.

To describe the micelles one defines  $\omega$  as the molar ratio of water to surfactant,

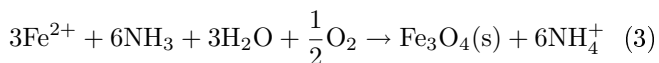
$$\omega = \frac{M_{\text{H}_2\text{O}}}{M_{\text{S}}}, \quad (1)$$

where  $M_{\text{H}_2\text{O}}$  and  $M_{\text{S}}$  are the apparent molar concentrations of water and surfactant, respectively, in the solutions. The radius of the water droplet,  $R_w$ , is given by

$$R_w = 3 \frac{v_{\text{H}_2\text{O}} M_{\text{H}_2\text{O}}}{\sigma M_{\text{S}}} = 3 \frac{v_{\text{H}_2\text{O}}}{\sigma} \times \omega, \quad (2)$$

where  $v_{\text{H}_2\text{O}}$  is the volume of a water molecule and  $\sigma$  is the area of a surfactant polar head group. The droplet radius determines the amount of reactants available for nanoparticle formation and this is therefore controlled by the concentration of the reactants. We employed mixing of equal volume of inverse micelle solutions of equal  $\omega$  assuming that each fusion event of micelles carrying iron salt and ammonia, respectively, would lead to magnetite formation whereas fusion events of micelles carrying identical chemical load in turn regenerate the original micelles[9, 17, 18, 15].

The chemical reaction employed is given in (3):



As seen it is thus important to use excess ammonia to completely transform  $\text{Fe}^{2+}$  to magnetite and also a small amount of excess oxygen is needed.

## 2 Experimental

The  $\text{Fe}_3\text{O}_4$  particles were prepared in part as suggested in[11]. By controlling  $\omega$ , we aimed at obtaining particle

sizes in the range 10-30 nm. AOT (Sodium 1,2-bis(2-ethylhexyloxycarbonyl)-ethanesulfonate,  $\text{C}_{20}\text{H}_{37}\text{NaO}_7\text{S}$ , Sigma-Aldrich) was used as surfactant, iso-octane(Aldrich) as oil phase and  $\text{Fe}_2\text{SO}_4 \cdot 7\text{H}_2\text{O}$  (Aldrich) and 25% ammonia were used as reactants. Solutions were prepared and sonicated in Ar atmosphere for several minutes to remove dissolved oxygen. On the basis of those we have synthesized several different samples to investigate the control parameters for the chemical composition and stability of the nanoparticles. Here we present the results for a stoichiometric sample (sample 1) supplemented with some post synthesis oxidation observations for sample 2.

Sample 1 ( $\omega = 6.0 \pm 0.2$ ) 0.2836 g of  $\text{Fe}_2\text{SO}_4 \cdot 7\text{H}_2\text{O}$  was dissolved in 1.25 ml of water with a droplet of conc. sulphuric acid, and mixed with 22 ml of pure AOT/iso-octane stock solution (conc. 0.53 M). A clear solution is normally formed but depending on the quality of the iron salt used it may be necessary to centrifuge the solution to remove turbidity. 22.5 ml of AOT/iso-octane stock solution was mixed with 1.25 ml of 25 %  $\text{NH}_3$  to form a second solution containing ammonia.

The solutions were sonicated under Ar, and the iron solution was poured into a tall measurement glass (100 ml, sealable). The ammonia solution was then added quickly while stirring and still keeping all operations under Ar. The mixed solutions had identical  $\omega$  (with dissolved iron and ammonia, respectively), and therefore the final solution also retained  $\omega$ .

After mixing the solution instantly became green, after 2 secs it changed color to black and 15 secs later it turned black-green. The solution was left sealed and stirred overnight, after which the color had become black. The material was strongly magnetic.

The solution was then transferred to a separation funnel, and the micelles were destroyed by adding 110 ml of acetone ( $\text{C}_3\text{H}_6\text{O}$ ). The magnetic powder was collected with a strong permanent magnet ( $\sim 1$  T), while decanting. The remaining powder-solution was washed with methanol ( $\text{CH}_3\text{OH}$ ) ( $\sim 100$  ml) several times using mechanical stirring and magnetic filtering to remove residual surfactant. The resulting powder-liquid was split in a liquid which was frozen in liquid  $\text{N}_2$ , and a powder fraction which was dried in a desiccator under vacuum.

Sample 2 ( $\omega = 11.2 \pm 0.2$ ) was prepared and purified as sample 1. However, to observe the effects of  $\omega$  and post-synthesis oxidation, sample 2 was prepared with  $\omega = 11.2 \pm 0.2$  and was after synthesis and purification exposed to air, which added traces of brownish to the black powder.

It is crucial to use a protective Ar atmosphere and deoxygenate solvents for hindering formation of the end oxidation product  $\gamma\text{-Fe}_2\text{O}_3$ . The samples were also kept in an Ar atmosphere during transfer from the synthesis laboratory to the Mössbauer spectrometer, and to the transmission electron microscope (TEM).

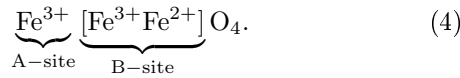
Mössbauer spectra were obtained at temperatures in the range 20-300 K using custom built transmission spectrometers. Mössbauer spectroscopy was performed on both samples in both powder and liquid form. The samples were

cooled using a closed cycle liquid He cryostat. The spectra were calibrated from a spectrum of a thin ( $12.5 \mu\text{m}$ )  $\alpha\text{-Fe}$  foil. For fitting the Mössbauer spectra the computer program Fit;o)[19,20] has been used. For obtaining TEM images the powder was dispersed on standard Cu grids with lacey amorphous carbon film. A Philips CM20 and a JEM3000F were used to acquire the images.

### 3 Results and discussion

#### 3.1 Mössbauer analysis

Magnetite is an inverse spinel in which the iron is located at the tetrahedral (A-site) and octahedral (B-site) sites. The ratio between A and B occupation for stoichiometric magnetite at room temperature is 1:2. The extended formula for magnetite is:



In Mössbauer spectroscopy the two oxidation sites are seen as the states  $\text{Fe}^{3+}$  (A) and  $\text{Fe}^{2.5+}$  (B). The  $\text{Fe}^{2.5+}$  is caused by a delocalized electron on the octahedral sites, and is an average of the octahedral  $\text{Fe}^{2+}$  and  $\text{Fe}^{3+}$  ions. Magnetite has a transition, the so-called Verwey transition[21] below which the delocalized electron becomes localized.

In the magnetically ordered state above the Verwey transition the Mössbauer spectrum of magnetite consists of two sextets with different isomer shifts and hyperfine fields. According to literature[21] the Verwey transition occurs in bulk stoichiometric magnetite at 118 K. When considering non-stoichiometric magnetite, the transition may either be totally suppressed or may occur at lower temperature[21–24], which may be countered when considering non-stoi nanoparticles[25]. Below the Verwey transition the Mössbauer spectrum of magnetite is complicated to model as it consists of at least five sextets[26].

The Mössbauer spectra of samples 1 and 2 are presented in Figs. 1 and 3, respectively, and the fitted parameters are listed in tab. 1. Further, in fig. 2 the temperature dependence of the hyperfine field and isomer shift of sample 1 are shown.

All samples contain poorly crystalline iron oxide residues from the synthesis process. This does not influence the properties of the ordered nanoparticles. It contributes as a background signal (observed as a doublet) in the Mössbauer spectra. This phase of Fe-ions is disordered above 40 K, as it is observed as a temperature independent doublet, which only below 40 K disappears and develops into sextets with broad absorption lines.

The temperature series of sample 1 (fig. 1) shows a sextet component at 295 K spectrum, which is asymmetric and can be fitted well to yield the characteristic parameters of magnetite (refer to tab. 1). The room temperature A to B site ratio is found to be

$$\frac{[A]}{[B]} = \frac{14.6}{34.1} \simeq 0.43. \quad (5)$$

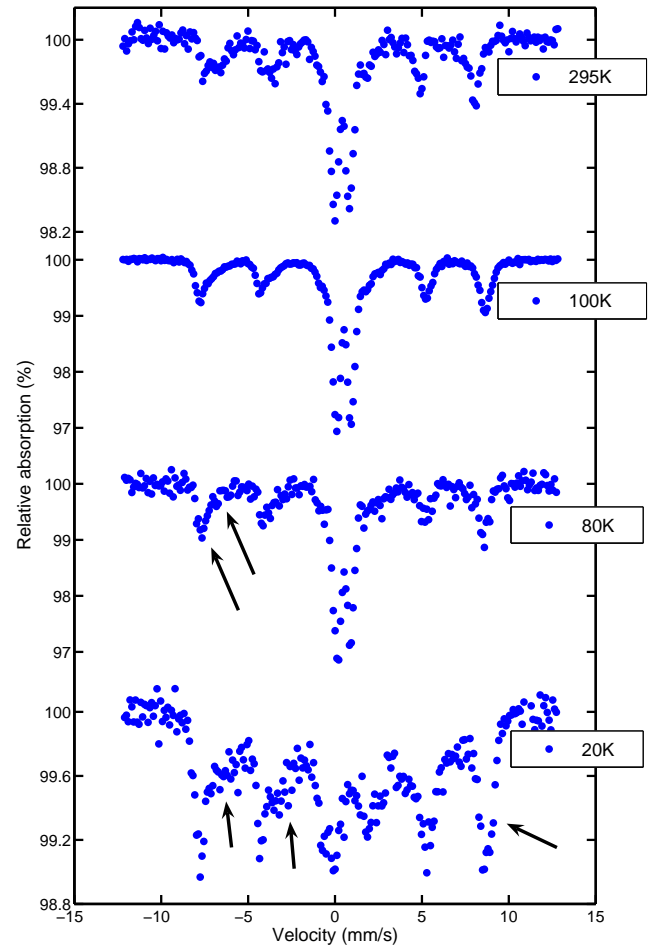


**Fig. 1.** A selection of Mössbauer spectra as a function of temperature of sample 1 (powder). The Verwey transition signs in the 80 K spectrum are marked. Signs of the complex magnetite spectrum are marked in the 20 K spectrum.

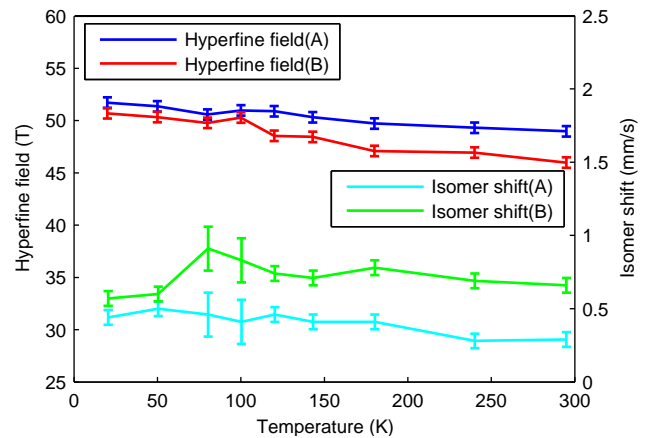


**Fig. 2.** Hyperfine fields and isomer shifts of the A and B magnetite components as function of temperature in sample 1. Notice the change in hyperfine field and the isomer shift in the range 80-120 K.

#	T	Co	HF	QS	IS	Area
	K		T	$\frac{mm}{s}$	$\frac{mm}{s}$	%
1	295	MaA	49.0	<i>-0.02</i>	0.29	14.6
1	295	MaB	46.0	<i>-0.03</i>	0.66	34.1
1	295	Do1	-	0.86	0.40	51.3
1	100	MaA	51.0	<i>0.00</i>	0.41	26.2
1	100	MaB	50.3	<i>0.00</i>	0.83	20.5
1	100	Do1	-	0.85	0.51	53.2
1	80	MaA	50.6	<i>-0.01</i>	0.44	29.5
1	80	MaB	49.8	<i>0.00</i>	0.91	19.0
1	80	Do1	-	0.77	0.50	51.5
1	20	Se1	51.7	<i>0.00</i>	0.57	22.7
1	20	Se2	50.7	<i>0.00</i>	0.44	33.4
1	20	Si2	-	-	<i>0.00</i>	4.5
1	20	Se3	37.1	<i>0.00</i>	0.21	39.4
2	295	MaA	49.1	<i>-0.01</i>	0.36	47.3
2	295	MaB	46.0	<i>0.00</i>	0.72	23.5
2	295	Do1	-	0.54	0.40	16.0
2	295	Do2	-	1.07	0.43	13.3
2	80	Se1	51.0	<i>0.00</i>	0.44	39.8
2	80	Se2	51.0	<i>0.00</i>	0.54	28.7
2	80	Do1	-	0.84	0.62	10.8
2	80	Do2	-	0.76	0.34	20.7
2	20	Se1	50.6	<i>0.00</i>	0.45	39.1
2	20	Se2	52.5	<i>0.00</i>	0.54	27.2
2	20	Se3	46.2	<i>-0.21</i>	0.81	22.7
2	20	Do1	-	1.63	0.91	3.9
2	20	Do2	-	1.54	0.10	7.1

**Table 1.** Mössbauer fit results for sample 1 and 2. Numbers in *italic* were fixed during the fitting process. The relative areas of the A and B components have been allowed to vary during fitting at temperatures below 295 K to accommodate the Verwey transition. Abbreviations: #=Sample number, T=Temperature, Co=Component, HF=Hyperfine Field, QS=Quadrupole shift/split, IS=Isomer Shift, Area=Relative area of component to total model area, Ma=Magnetite, Se=Sextet, Do=Doublet, Si=Singlet.

In the 100 K and 80 K spectra of sample 1 the first indications of the onset of the Verwey transition are seen as a gradual disappearance of the distinct magnetite sextets and at 20 K the two-sextet magnetite spectrum has changed into a very complex spectrum described by several sextets. Fig. 2 shows the variation in hyperfine field and isomer shift as a function of temperature. In this plot the onset of the Verwey transition can be seen at 80-120 K. While cooling to 100 K the hyperfine field of the B component changes considerably, and the hyperfine fields of the A and B components become comparable at lower temperatures. Similarly, the isomer shifts of the sextets are increasing with decreasing temperature down to 100 K. Below 80 K the B component value drops towards that of the A component. These observations indicate breakdown of the room-temperature magnetite model and are clear signs of the Verwey transition. The transition temperature,  $T_v$ , is estimated to be  $\sim 90$  K. This is consistent with the Verwey transition being very sensitive to the degree of stoichiometry[23,24] and the nanoparticle size[25]. From comparison with [27], and in particular with [28],

and applying the method of [3] we estimate the  $x$  parameter for sample 1 to  $x = 0.05 \pm 0.05$ , where  $x$  describes the degree of stoichiometry, i.e.  $\text{Fe}_{3-x}\text{O}_4$  ( $0 < x < 1/3$ ). We therefore conclude that sample 1 consists of stoichiometric magnetite.

We have consistently found the hyperfine field of the iron oxides in the samples to be slightly lower than for bulk material. This is expected and can be attributed to a hyperfine field distribution due to canting of the surface spins in the nanoparticle surfaces[29].

The 295 K spectrum of sample 2 shows characteristic features of non-stoichiometric magnetite (marked in fig. 3), with two distinct sextets with an area ratio deviating from 1 : 2[28]. The other fitted sextet parameters match those of magnetite very well[27]. The 80 K spectrum of sample 2 also contains two sextets. However, the parameters are quite different from the 295 K spectrum, and this indicates that there is a partly onset of the Verwey transition. At lower temperature (20 K) the spectrum shows evidence of maghemite ( $\gamma\text{-Fe}_2\text{O}_3$ ) features[30]. These maghemite features are primarily a narrow component line 1 compared to line 6 (see arrows in fig. 3).

The 295 K area ratio of the A and B components in sample 2 is

$$\frac{[A]}{[B]} = \frac{[\text{Fe}^{3+}]}{[\text{Fe}^{2.5+}]} = \frac{47.3}{23.5} \simeq 2. \quad (6)$$

Further, we estimate the  $x$  parameter to  $x = 0.15 \pm 0.05$ . Sample 2 therefore contains non-stoichiometric magnetite.

### 3.2 TEM analysis

To demonstrate the particle size control, we have investigated the particle sizes and shapes using TEM, examples are shown in Figs. 4 and 5.

We observe that the particles of samples 1 and 2 have cubic/rectangular/trapezoid shapes, however, the particles in sample 1 appear about half the size of those in sample 2.

We have measured the crystal planar spacing of the particles in sample 1 in the (222) direction. Comparing the experimental planar distance of  $2.4 \pm 0.1 \text{ \AA}$  with the table values of bulk magnetite and maghemite of  $2.42198 \text{ \AA}$  and  $2.4097 \text{ \AA}$ , respectively, from [31,32], we find good agreement. However, the experimental uncertainty does not allow a distinction between magnetite and maghemite nanocrystals.

We have extracted the particle size distributions (tab. 2 and fig. 6) for sample 1 and sample 2. The images reveal that the manufactured particles are not mono-disperse. Both size distributions can be fitted well with a log normal distribution.

When evaluating the size distributions we assume that those observed by TEM reflect the actual size distribution of the synthesis. This may, however, not be entirely true. The observed size distributions may have been distorted since small particles ( $d < 3 \text{ nm}$ ) with poor contrast were difficult to observe. Further the magnetic filtering of particles

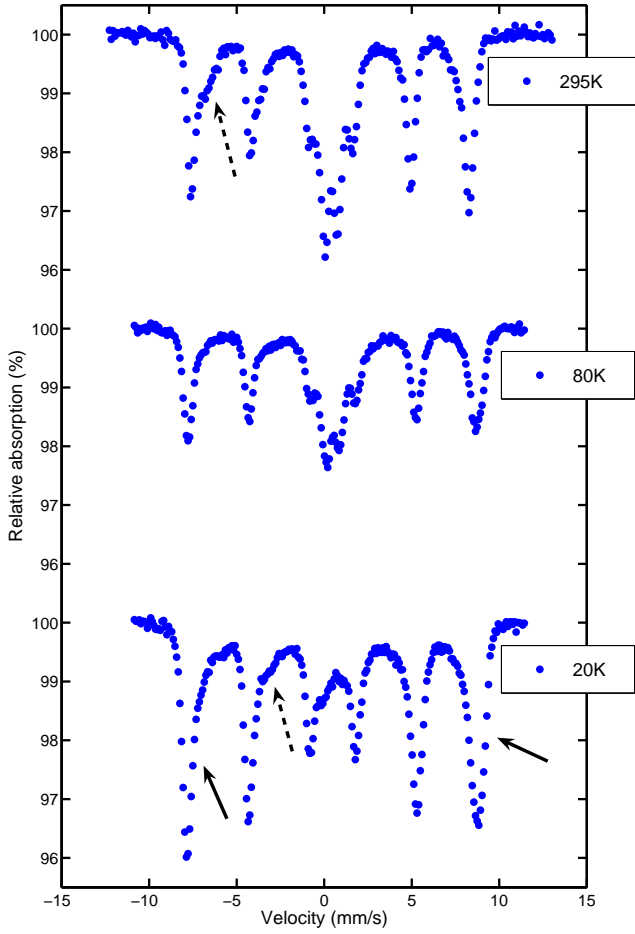


**Fig. 3.** Mössbauer spectra as a function of temperature of sample 2 (powder). Marked features: Non-stoichiometric magnetite: dashed arrows. Maghemite: solid arrows.

Sample #	$d$ nm	$\sigma$ nm	$d_{fit}$ nm	$\sigma_{fit}$ nm
1	12.9	1.4	13.1	1.4
2	23.4	1.4	23.4	1.4

**Table 2.** Size distribution data measured from TEM images.  $\bar{d}$  is the calculated top-point of the fitted log-normal distribution, and  $\sigma = \exp(\sigma(\log(x)))$  is the corresponding deviation.  $\bar{d}_{fit}$  and  $\sigma_{fit}$  are defined similarly for the fitted values.

from the solution favors larger particles, due to the surface to volume ratio. We estimate that leaving out a possible fraction of small particles with sizes less than 3 nm only affects the shape of the size distribution and would not significantly change the mean particle size, which is the focus point of this study.

Samples 1 and 2 are synthesized under identical conditions, with the parameter  $\omega$  as the only variable, which according to [9] determines the particle size. To show that the particle size is proportional to  $\omega$ , we compare the ratios between  $\omega$ 's and between particle sizes of the samples.

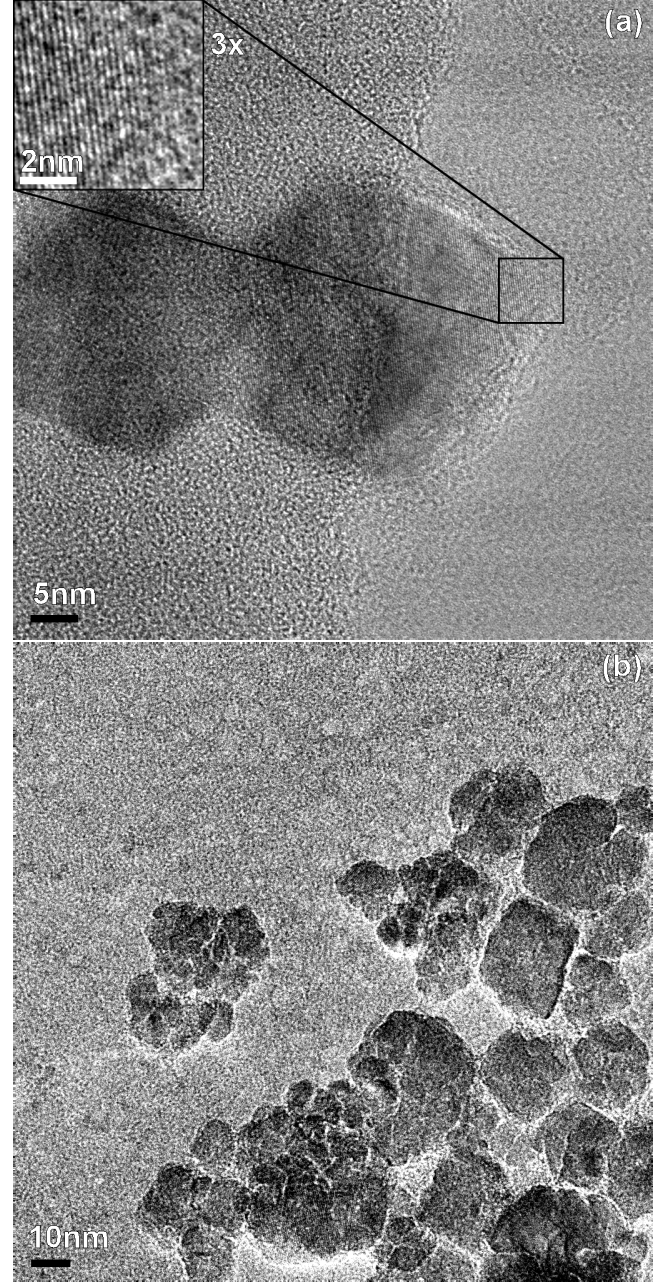


**Fig. 4.** TEM images of sample 1. (a) The enlarged insert shows lattice planes. (b) Clusters of particles.

Ratio	$\omega_{S1}$ $6.0 \pm 0.2$	$\bar{d}_{S1}$ (nm) $12.9 \pm 0.8$
$\omega_{S2}$ $11.2 \pm 0.2$	$1.9 \pm 0.10$	-
$\bar{d}_{S2}$ (nm) $23.4 \pm 0.5$	-	$1.8 \pm 0.16$

**Table 3.** Ratios  $a_\omega$  and  $a_{\bar{d}}$ , between  $\omega$ 's and  $\bar{d}$ 's respectively of sample 1 and sample 2.

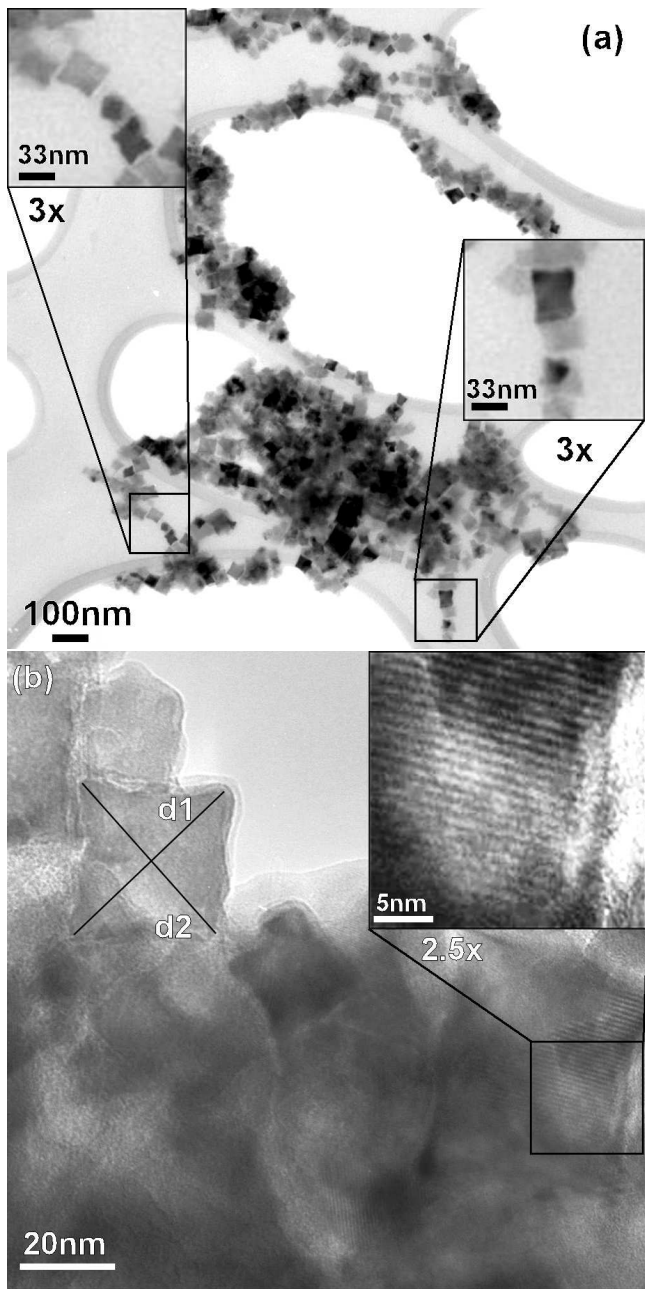


**Fig. 5.** TEM images of sample 2. (a) The magnified insert in (a) show chain formation typical for ferri/ferromagnetic nanoparticles. (b) The black lines labelled d1 and d2 indicate how the size measurements of the nanocrystals have been made. The magnified insert in (b) shows the lattice planes.

The ratio,  $a_\omega$ , between the  $\omega$ 's of the samples is calculated as  $a_\omega = \omega_{S2}/\omega_{S1}$ , and the ratio,  $a_{\bar{d}}$ , between the calculated log-normal top-points of the curves is calculated as  $a_{\bar{d}} = \bar{d}_{S2}/\bar{d}_{S1}$ . The uncertainties on  $\omega$  and  $\bar{d}$  are estimated. The comparison of  $a_\omega$  to  $a_{\bar{d}}$  (see tab. 3) reveals a good correspondence between the ratios and shows that we have succeeded in controlling the particle size.

The TEM images show many chain-like structures of particles in sample 2, most likely caused by dipolar in-

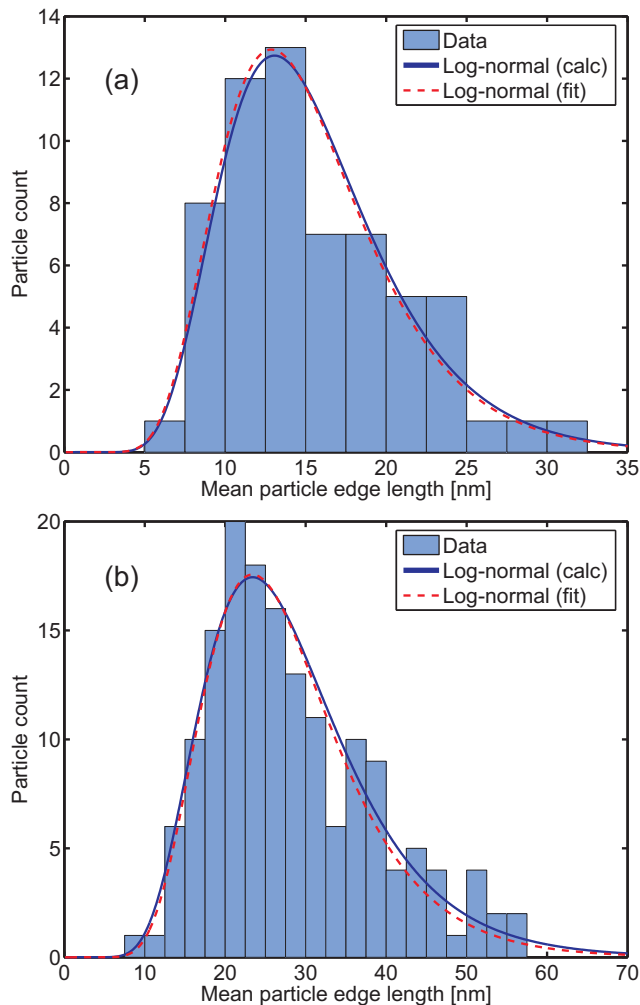


**Fig. 6.** Particle size distributions for samples 1 (a) and 2 (b). Both calculated and fitted log-normal distributions are shown to demonstrate the good agreement. The populations are 61 and 158 counted particles for samples 1 and 2, respectively.

teraction which can lead to chain formation and uniform orientation[33], some are framed in fig. 5. The smaller particle sample 1 (fig. 4) does not show the same chain formation. This is likely due to that chain formation requires at least a physical rotation, if not a displacement. As the rotating/displacing forces are proportional to the volume and the frictional forces are proportional to the surface area, the larger particles are more likely to agglomerate in general.

Determining the shapes of the particles is important since it influences the determination of the particle size distribution, and thus the extracted average size. Further it contributes information on the synthesis, since the equilibrium shape of magnetite is dependent on the pH value of the solution[26]. It is not trivial to extract 3D information on the particle shape from the TEM images, which contain the information projected on 2D.

If regular particles are ordered randomly they have many shapes in TEM images, for instance squares, hexagons

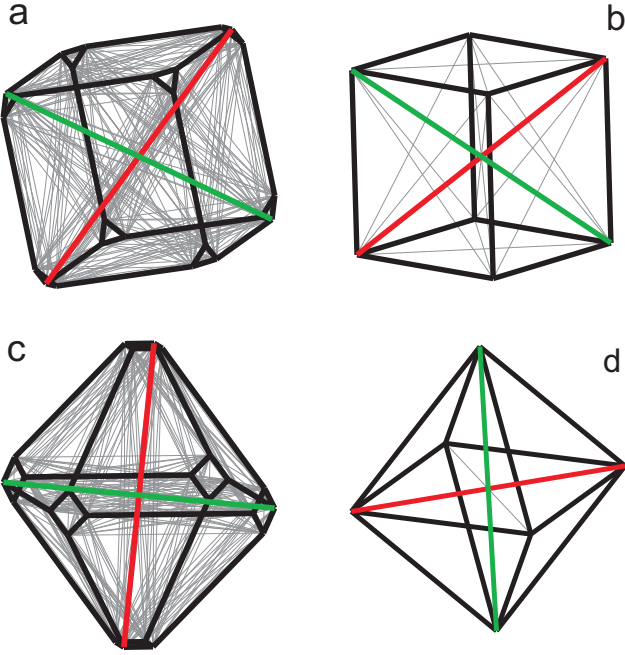


**Fig. 7.** Simulated particle shapes in random orientations. **a)** Iso-cube  $\alpha=1/10$ , **b)** regular cube, **c)** iso-octahedron  $\alpha=0.13$  and **d)** regular octahedron, e.g. appearing as squares, hexagons and trapezoids. The red line is the longest diagonal  $d_1$  and the green diagonal is  $d_2$ , which gives the largest spanned area.

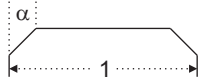


**Fig. 8.** Illustration of the definition of  $\alpha$ .

$N_{\text{Measured}} = 158$	$\sigma(f_m) = 0.0933$
<i>Simulations:</i>	
Iso-Cube, $\alpha=1/5$	0.0515
Iso-Cube, $\alpha=1/10$	0.0588
Iso-Cube, $\alpha=1/20$	0.0651
Cube	0.0703
Iso-Octa., $\alpha=1/3$	0.0553
Iso-Octa., $\alpha=1/5$	0.0708
Iso-Octa., $\alpha=0.13$	0.0934
Iso-Octa., $\alpha=1/10$	0.104
Iso-Octa., $\alpha=1/20$	0.123
Octahedron	0.144

**Table 4.** Measured (sample 2) and simulated data. The simulations of the  $f$ -distribution have been conducted with a particle population of  $N=10000$  and a blurring of edge lengths of 5%. The parameter of comparison  $\sigma(f_m)$ , is the standard deviation of the mirrored  $f$ -distribution, in mathematical notation written as  $f_m = (f) \cup (-f)$ .

and trapezoids (fig. 7). We have observed shapes similar to these, although, most particles appear as squares and very few as hexagons. Both are expected to be very com-

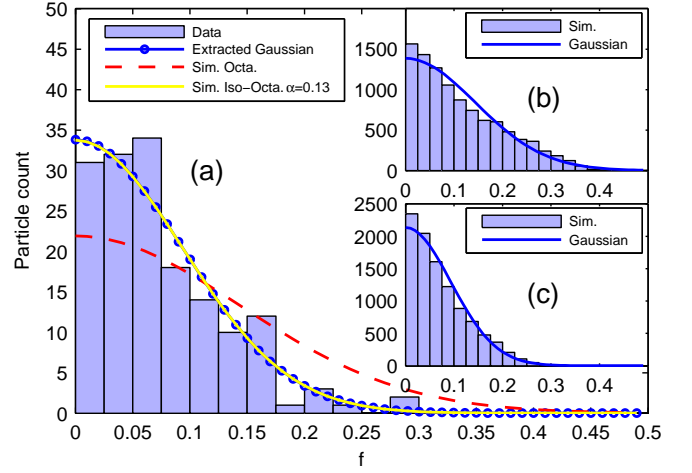


**Fig. 9.**  $f$ -distributions from measurements (sample 2) and simulations (see tab. 4). The normal distributions with the standard deviation are displayed for comparison. **(a)** Measured  $f$  for sample 1. **(b)** Simulated  $f$  for regular octahedron. **(c)** Simulated  $f$  for iso-octahedron  $\alpha=0.13$ .

mon due to the cubic crystal structure of maghemite/magnetite.

To explore the effect of the 2D projection on the shape and size analysis we have performed simulations of 2D projections of various 3D particle shapes. Simulations of cubes and octahedra show that cubes are most likely (>80%) to appear as hexagons and octahedra are most likely (>85%) to appear as squares/trapezoids. The TEM images of the larger particles in sample 2 illustrate the particle shapes in the most clear fashion, therefore results for sample 2 are presented here to demonstrate the analysis.

From measuring the diagonals  $d_1$  (longest corner-to-corner diagonal) and  $d_2$  (giving the largest cross-product with  $d_1$ ) of the particles as indicated in fig. 5 and fig. 7, the aspect ratio  $f$  of the particles is defined as

$$f = \frac{2|d_1 - d_2|}{d_1 + d_2}, \quad (7)$$

providing a useful measure of the particle shape.

Before calculating  $f$  the length of the diagonals are blurred with a random 5% uncertainty to simulate the uncertainty in the image-measurements. The truncation of a corner is defined by the parameter  $\alpha$  ( $0 < \alpha < 0.5$ ), which is the fractional part of the adjacent edges being truncated (fig. 8).

Numerical simulations have been performed to test whether any of the shapes cube, octahedron, iso-cube or iso-octahedron<sup>1</sup>, matches the observed  $f$ -distribution.

Fig. 9 shows the measured  $f$ -distribution of sample 2, the simulated  $f$ -distributions for  $\alpha = 0$  and  $\alpha = 0.13$ . The simulations show that the iso-octahedron with  $\alpha = 0.13$  is the best match for the measured distribution in tab. 4.

<sup>1</sup> Iso-cube and iso-octahedron are cubes and octahedron with truncated corners respectively.

## 4 Conclusion

We have implemented the inverse micellar technique to manufacture nanoparticles of stoichiometric magnetite, and we have demonstrated control of the average particle size in the range 12-25 nm using the AOT/iso-octane system. This expands the available particle size range as compared to previous publications [12].

From the particle size distributions extracted from TEM images, we have shown that particle size control using this particular synthesis technique is possible, and that the particle size is proportional to the water-to-surfactant ratio  $\omega$ . This is very useful as this in general is not the case for the reverse micellar technique [15, 16, 18].

We found that the particles differ in shape. From TEM images we conclude that sample 2 with the larger particles with sizes about 20-40 nm consists of octahedral particles, and sample 1 with smaller particles with sizes around 15-25 nm contains a wide variety of shapes.

Mössbauer analysis reveals that the manufactured nanoparticles are composed of stoichiometric magnetite. The samples exhibit clear signs of the Verwey transition as expected in stoichiometric magnetite. The occurring non-stoichiometry of sample 2 is attributed to post-synthesis oxidation and emphasizes that when handling stoichiometric magnetite nanoparticles, it is crucial to protect them against partly conversion into maghemite.

## Acknowledgments

We would like to thank C. Bahl for his help with TEM and comments on the manuscript, H. Rasmussen for help with operating the Mössbauer equipment, F. C. Krebs for assistance in the chemistry lab, and to K. Hansen, P. Christiansen, S. Mørup and K. Lefmann for valuable discussions.

This work was partly supported by the framework programme on nanomagnetism funded by the Danish Research Council.

## References

1. *Proceedings of Fifth International Conference on Fine Particle Magnetism*. (Editor: Q. Pankhurst) (2005)
2. W. Wang, Phys. Rev. B **73**, 134412 (2006)
3. I. Nedkov, J. Magn. Magn. Mater. **300**, 358 (2006)
4. R. Vandenberghe, Hyperfine Interact. **165**, 267 (2005)
5. R. Hong, J. Magn. Magn. Mater. **310**, 37 (2007)
6. J. Xu, J. Magn. Magn. Mater. (309), 307 (2007)
7. S. Sun, J. Am. Chem. Soc. (124), 8204 (2002)
8. T. Koutzarova, Phys. Stat. Sol (c) (5), 1302 (2005)
9. E.E. Carpenter, Ph.D. thesis, University of New Orleans (1999)
10. C.J. O'Connor, Nanostruct. Mater. **12**, 65 (1999)
11. C.T. Seip, IEEE Trans. Magn. **34**(4), 1111 (1998)
12. Y. Lee, Adv. Func. Mater. **15**(3), 503 (2005)
13. D.K. Kim, J. Magn. Magn. Mater. **225**, 30 (2001)
14. Y. h. Zheng, Mater. Research Bullet. **41**, 525 (2006)
15. D. Mathew, Chem. Eng. Jour. **129**, 51 (2007)
16. A.E. Palmqvist, Current Opinion in Colloid and Interface Science **8**, 145 (2003)
17. M.P. Pileni, Chem. Phys. Lett. **118**(4), 414 (1985)
18. M.P. Pileni, Nat. Mat. **2**, 145 (2003)
19. J. í Hjöllum, In preparation (2008)
20. J. í Hjöllum, *Fit;o*, www.hjollum.com/zzbug/fit/ (2004)
21. E.J.W. Verwey, Nature **144**(3642), 327 (1939)
22. J.B. Yang, J. Appl. Phys. **95**(11), 7540 (2004)
23. R. Aragón, J. Appl. Phys. **57**(8), 3221 (1985)
24. R.J. Aragón, Phys. Rev. B **31**(1), 430 (1985)
25. N. Guigue, Phys. Rev. B **64**(012402), 1 (2001)
26. R.M. Cornell, U. Schwertmann, *The Iron Oxides, Structure, Properties, Occurrence and Uses*. (VCH Publishers, 1996)
27. M.B. Madsen, Nature **321**(6069), 501 (1986)
28. A. Ramdani, J. Phys. Chem. Solids **48**(3), 217 (1987)
29. S. Mørup, Hyperfine Interactions **60**, 959 (1990)
30. S. Mørup, Phys. Rev. B **52**(1), 287 (1995)
31. F. de Boer, J. Chem. Phys. **18**, 1032 (1950)
32. A.N. Shmakov, J. Appl. Cryst. **28**, 141 (1995)
33. A. Eggeman, J. Magn. Magn. Mater. **301**, 336 (2006)

### H.1.2 Paper II

#### Overview of the Magnetic Properties Experiments on the Mars Exploration Rovers

*by*

M.B. Madsen, P. Bertelsen, C.S. Binau, F. Folkmann, W. Goetz, H.P. Gunnlaugsson, J. í Hjølum, S.F. Hviid, J. Jensen, K.M. Kinch, K. Leer, D.E. Madsen, J. Merrison, M. Olsen, H.M. Arneson, J.F. Bell III, R. Gellert, K.E. Herkenhoff, J.R. Johnson, M.J. Johnson, G. Klingelhöfer, E. McCartney, D.W. Ming, R.V. Morris, J.B. Proton, D. Rodionov, M. Sims, S.W. Squyres, T. Wdowiak, A.S. Yen, and the Athena Science Team.

*In revision for Journal of Geophysical Research. Referee reports positive.*



# Overview of the Magnetic Properties Experiments on the Mars Exploration Rovers

M.B. Madsen<sup>1\*</sup>, P. Bertelsen<sup>1</sup>, C.S. Binau<sup>1</sup>, F. Folkmann<sup>2</sup>, W. Goetz<sup>3</sup>, H.P. Gunnlaugsson<sup>2</sup>, J. í Hjöllum<sup>4</sup>, S.F. Hviid<sup>3</sup>, J. Jensen<sup>2</sup>, K.M. Kinch<sup>5</sup>, K. Leer<sup>1</sup>, D.E. Madsen<sup>6</sup>, J. Merrison<sup>2</sup>, M. Olsen<sup>1</sup>, H.M. Arneson<sup>5</sup>, J.F. Bell III<sup>5</sup>, R. Gellert<sup>7</sup>, K.E. Herkenhoff<sup>8</sup>, J.R. Johnson<sup>8</sup>, M.J. Johnson<sup>5</sup>, G. Klingelhöfer<sup>9</sup>, E. McCartney<sup>5</sup>, D.W. Ming<sup>10</sup>, R.V. Morris<sup>10</sup>, J.B. Proton<sup>5</sup>, D. Rodionov<sup>9</sup>, M. Sims<sup>11</sup>, S.W. Squyres<sup>5</sup>, T. Wdowiak<sup>12</sup>, A.S. Yen<sup>13</sup>, and the Athena Science Team

**To be submitted to Journal of Geophysical Research. Draft, January. 31st, 2008.**

---

<sup>1</sup> *Niels Bohr Institute, University of Copenhagen, Copenhagen, DK-2100, Denmark*

<sup>2</sup> *Institute of Physics and Astronomy, University of Aarhus, Aarhus, DK-8000, Denmark*

<sup>3</sup> *Max-Planck-Institut für Sonnensystemforschung, Katlenburg-Lindau, D-37191, Germany*

<sup>4</sup> *Materials Research Department, Risø National Laboratory, Roskilde, DK-4000, Denmark*

<sup>5</sup> *Department of Astronomy, Cornell University, Ithaca, NY 14853-6801, USA*

<sup>6</sup> *Department of Physics, Technical University of Denmark, Kgs. Lyngby, DK-2800, Denmark*

<sup>7</sup> *Department of Physics, University of Guelph, Ontario, Canada*

<sup>8</sup> *U.S. Geological Survey, Astrogeology Team, Flagstaff, AZ, 86001, USA*

<sup>9</sup> *Johannes Gutenberg-Universität, Mainz, D-55128, Germany*

<sup>10</sup> *NASA Johnson Space Center, Houston, TX 77058, USA*

<sup>11</sup> *Planetary Systems Branch, Space Science Division, NASA Ames Research Center, Moffett Field, CA 94035-1000, USA*

<sup>12</sup> *Astro and Solar System Physics Program, Department of Physics, University of Alabama, AL 35294, USA*

<sup>13</sup> *Jet Propulsion Laboratory, California Institute of Technology, Pasadena, CA 91109, USA*

\*To whom correspondence should be addressed. Email: [mbmadsen@fys.ku.dk](mailto:mbmadsen@fys.ku.dk)

## **Abstract**

240 words: This is close to the JGR limit (250 words)!

The Mars Exploration Rovers have accumulated airborne dust that could be studied by a variety of instruments onboard the rovers. Panoramic Camera (Pancam) and Microscopic Imager (MI) data reveal that different magnets (differing in field strength and field gradient) attract different (magnetic) subsets of the airborne dust: Pancam images demonstrate their difference in color, whereas MI images reveal the formation of magnetic chains diagnostic of magnetite-rich grains with substantial magnetization ( $> 8 \text{ Am}^2/\text{kg}$ ). Such images (both Pancam and MI) also show the dynamics of dust capture. Magnetite is clearly identified by the MB spectra and makes up more than 40% of the total fit area. MB spectra also provide evidence for the presence of olivine and pyroxene. APXS data show a correlation between the elements Fe, Ti and Cr, indicative of chromium-substituted titanomagnetite. The presence of titanomagnetite, olivine and pyroxene is suggestive for a basaltic origin of the dust. Mössbauer spectra also indicate a larger ratio  $\text{Fe}^{3+}/\text{Fe}_{\text{tot}}$  for airborne dust (0.6~0.7) than for average Gusev soil (~0.3). The higher degree of oxidation is consistent with the smaller grain size of the airborne dust, favoring alteration by solar UV radiation and/or atmospheric oxidants. In addition, a strong correlation between the elements calcium and sulfur (as inferred from APXS data) is interpreted as presence of  $\text{CaSO}_4$  (any gypsum-related phase with unknown water content) in the airborne dust. This may be the record of extended volcanic periods in the history of Mars.

## **1. Introduction**

The Mars Exploration Rovers [Squyres et al., 2003] carry three different sets of magnets for investigation of magnetic properties of airborne dust and of rock dust generated by the action of the Rock Abrasion Tool [Gorevan et al., 2003; Madsen et al., 2003]. Also some of the previous missions to the surface of Mars, Viking 1 and 2 [Petersen et al., 1974; Hargraves et al., 1976], and Mars Pathfinder [Gunnlaugsson et al., 1997; Smith et al., 1997], carried magnetic properties experiments. While the Pathfinder lander had only magnets for capture of airborne dust, both Viking landers carried a soil sampler by which they were able to actively sample surface material for further investigation by instrumentation inside the landers [Soffen, 1977]. The soil sampler of the Viking missions carried additional magnets that were automatically inserted into the surface soil while sampling the material. Results from Viking showed that the airborne dust and the soil on Mars contain a substantial fraction of material that is sufficiently magnetic to be attracted to the magnets [Hargraves et al., 1979]. In particular, the backhoe magnets were saturated with adhering material after only a few soil insertions. Based on comparison with terrestrial samples it was estimated that the saturation magnetization of the soil was between 1 and 7 Am<sup>2</sup>kg<sup>-1</sup> [Hargraves et al., 1979].

These observations in themselves were not sufficient to unambiguously identify the nature of the strongly magnetic phase in Martian soil and dust. However, one of the Viking biology experiments [Levine et al., 1979] showed that the soil is not only highly oxidized, but also sufficiently oxidizing to degrade organic material when the mixture was incubated with water. These results suggested that the strongly magnetic mineral should be a highly oxidized phase. Given the reddish color of soil and dust, it was advocated that this mineral could be maghemite ( $\gamma$ -Fe<sub>2</sub>O<sub>3</sub>, [Hargraves et al., 1979]), although the absorption spectra of airborne dust, in particular their minimum near  $\lambda \sim 800$  nm, seemed to indicate the presence of

magnetite ( $\text{Fe}^{2+}\text{Fe}^{3+}_2\text{O}_4$ ) in the dust [Pollack et al., 1979]). From a geological point of view, magnetite should have been *the* obvious magnetic mineral phase, due to its widespread occurrence in (terrestrial) basalts. However, the question arose, how magnetite would be able to withstand oxidation over billions of years in a strongly oxidizing environment. This became the origin of a decade-long controversy on the strongly magnetic phase in Martian surface material. Also Mars Pathfinder (July-Sept. 1997) carried permanent magnets, this time including magnets substantially weaker than the Viking magnets. From the results of the experiments on Pathfinder it was concluded that at least most of the airborne dust particles are not very strongly magnetic [Hviid et al., 1997, Madsen et al., 1999]). The question on maghemite versus magnetite remained unresolved: Both magnetite covered by a thin ferric-oxide coating and „fully oxidized magnetite“ (maghemite) would be consistent with the observations.

The science payload onboard the Viking Landers allowed only visual observation of the magnetic material by the means of cameras, but for Pathfinder also observation in the near-infrared wavelength range was possible. Some color information on the material adhering to the magnets could be obtained by acquiring images through different filters. The Mars Pathfinder mission was equipped to provide also information on the chemical composition of magnetic material [Hviid et al., 1997]. However, unfortunately, this mission ended before such data could be acquired.

Finally, the Athena science payload onboard the Mars Exploration Rovers allowed studies of the magnetic fraction of airborne dust by a variety of techniques. In addition, different types of magnets allowed the capture of different magnetic subsets of the airborne dust [Madsen et al., 2003].

Finally the Athena science payload onboard the Mars Exploration Rovers allowed to study the magnetic fraction of airborne dust by a variety of techniques. In addition, different types of

magnets (fig.1.1) allowed the capture of different magnetic subsets of the airborne dust [Madsen et al., 2003].

Briefly, two large magnets of different strengths, termed „Capture magnet“ and „Filter magnet“, respectively, are mounted to the rover deck in front of the camera mast (fig.1.1).

They owe their name to their ability to either „capture“ most of the magnetic particles, or to act as a magnetic „filter“ such that only the most strongly magnetic particles will be selected.

The surface normal of the active surface of the magnets is tilted by 45 degrees away from the camera mast for best exposure of these surfaces to the dust-laden atmosphere and to provide easy access by the instruments that are mounted on the „Instrument Deployment Device“

(IDD) for analysis of the thin dust layer on these magnets. These instruments consist of a

Mössbauer spectrometer (MB) [Klingelhöfer et al., 2003], an Alpha-Particle X-ray

Spectrometer (APXS) [Rieder et al., 2003] and a Microscopic Imager (MI) [Herkenhoff et al.,

2003]. The magnets were also imaged through thirteen interference bandpass filters [Bell et

al., 2003, 2006] from above by a pair of cameras (Pancam) that are mounted on a boom at the

top of the camera mast. The interference filters have a bandpass of typically 20-40 nm width.

Thus 13-point VIS/NIR reflectance spectra (extending over the spectral range 400 – 1000 nm) can be derived from a full set of Pancam images of the magnets.

spectral In addition a small ring magnet, termed the „sweep magnet“, is mounted to the rear part of the solar panels nearby the Pancam calibration target (fig.1.1). Magnet and calibration target fit into a small Pancam subframe (320 x 272 pixels, < 10% of full frame). The sweep magnet is designed to “sweep” magnetic dust off the central region of the ring magnet as a result of the geometry of the magnetic field lines and associated field gradients [Madsen et al., 2003]. The „sweeping magnetic force“ is so strong that only non-magnetic (diamagnetic) particles can settle in the central region of the magnet, while the trajectories of para- or ferrimagnetic grains will be deflected to the ring zone.

Table 1.1 specifies the location of the magnets, their purpose (by design) and the instruments that could be used to characterize the material adhering to these magnets. The present paper summarizes the principal scientific results that were obtained from these experiments.

It should be noted that a set of magnets were also built into the revolve housing of the Rock Abrasion Tool (RAT) in order to extract strongly magnetic grains that may be liberated during grinding operations [fig.1.1; Madsen et al., 2003]. The results from these experiments fall in a different category and were published in a separate paper [Goetz et al., 2008b].

name	location on rover	purpose of the magnet (by design)	instruments for dust analysis
Capture Magnet	front of camera mast	capture all magnetic particles	MB, APXS, MI, Pancam
Filter Magnet		capture the strongly magnetic particles preferentially	
Sweep Magnet	remote edge of rear solar panel	search for non-magnetic particles	Pancam

**Table 1** Magnets onboard the Mars Exploration Rovers. The Mössbauer spectrometer (MB) provides information on the (iron) mineralogy. Data from the Alpha-Particle X-ray Spectrometer (APXS) contain information on the chemical elements present in the dust. The Microscopic Imager (MI) delivers high resolution (30  $\mu\text{m}/\text{px}$ ), monochrome images of dust grains and their distribution on the surface of the magnets. The panoramic cameras (Pancam) provide spectral information on the dust in the VIS/NIR range (400-1000 nm) that is diagnostic for certain types of minerals, in particular for iron oxides in the visible and for selected silicates in the near-infrared range.

## **2. Dust Activity at Both Landing Sites – Gusev Crater and Meridiani Planum**

Dust activity can be tracked by monitoring the magnets over time. Here we focus on other methods that are suitable for dust tracking and describe results of these alternative measurement campaigns, as far as they help for a better understanding of the magnet data. Pancam disposes of two filters that allow for direct imaging of the solar disk in two different spectral regions:  $\lambda = 440$  nm (left eye) and  $\lambda = 880$  nm (right eye). For both filters the bandwidth is about 20 nm [Bell et al., 2006]. By imaging the solar disk and correcting for the varying path of the solar incident light through the atmosphere, the normal optical depth (also referred to as “opacity” or “dust opacity”, usually denoted as  $\tau$ ) can be determined. This quantity is defined by the following relation:

$$\frac{I}{I_0} = e^{-\tau}, \quad (\text{equation 2.1})$$

where  $I$  and  $I_0$  are the ground and top-of-atmosphere radiances, respectively, that would be measured at solar zenith. The optical depth defined in that way is essentially a dust optical depth, since its Rayleigh scattering component (0.001~0.01, depending on wavelength and atmospheric pressure) is always negligible.

The optical depth is a useful measure of the dust activity at both landing sites. Another approach for measuring the amount of dust in the atmosphere is based on the radiance from the Pancam caltarget. This caltarget consists of a shadow post that is placed in the center of three concentric rings of different albedo (from inside to outside: a black, a grey and a white ring; cf. inset of fig.1.1). Dust addition and removal have been monitored on a sol-by-sol basis by comparing the radiances from each albedo ring [Kinch et al., 2007]. While the optical

depth is a powerful quantity characterizing the *regional* atmospheric dust loading, the radiances of the Pancam albedo rings provide information on the dust events that occur *right at the rover's position on a given sol*. Both data sets turn out to be very important to understand the dust dynamics on the magnets.

Fig. 2.1 plots the optical depth (measured at  $\lambda = 440$  nm) as a function of sol number at both landing sites. Fig. 2.2 plots the ratio of the radiances of the black and the grey ring relative to that of the white ring for both rovers. Obviously, these ratios must increase towards unity, as more and more airborne dust is accumulated on the caltarget. A decrease of these ratios reveals dust removal.

Let us outline a few characteristics of these figures. Fig. 2.1 displays seasonal patterns of dust activity: The first opacity spikes appear at A-sol  $\sim 351$  and B-sol  $\sim 330$  (corresponding to  $L_S \sim 136^\circ$ ) and persist over several hundred sols. Next onset of such spikes is one Martian year later at A-sol  $\sim 1011$  and B-sol  $\sim 990$  ( $L_S \sim 132^\circ$ ). As mentioned above, fig. 2.2 shows dust activity at the rovers' position, and we notice strong differences between figs. 2.1 and 2.2. A few dust activity events (such as the one at A-sol 419) show up in both figures. However, most such events can only be seen in the caltarget radiances, not in the opacity data. Two features are very important for the understanding of the dust dynamics on the magnets: NIR Pancam images reveal an overall decrease of the caltarget radiance ratios in the A-sol range 400-600 showing that the opacity spikes observed in the same sol range did effectively remove dust from the caltarget. This is consistent with the strong magnetic selection of airborne dust that was observed on the magnets at around A-sol 600 (cf. subsequent sections). On MER-B the radiance ratios increased from landing up to B-sol  $\sim 165$  (monotonous dust accumulation), then decreased in the B-sol range 165-300 (corresponding to net dust removal). This observation is consistent with MI and APXS data (section 6): Sulfur is found to be an element that does *not* belong to the strongly magnetic phase in the dust. And indeed,

the sulfur peak is largest around B-sol 168 (figs. 6.1 and 6.3), while the magnetic chains first appeared around B-sol 330 (fig. 4.1).

### **3. Dust Properties as Inferred from Panoramic Camera Data**

Pancam images and spectra provide evidence that the airborne dust is magnetically separable. The correlation between optical and magnetic properties can be seen on the Filter and Capture magnets [Bertelsen et al., 2004] as well as on the Sweep magnet. In this section Pancam images will be presented that support other data presented in later MI, MB and APXS sections. In addition focus will be on the dynamics of dust accumulation on the magnets.

#### **3.1 Filter and Capture Magnet**

The following sols have been selected for the discussion of Pancam data of the Filter and Capture magnets: A184 and A425, and B198 and B350. Refer to fig.2.2 that describes the dust contamination of the caltarget: A184 marks the late part of a steady accumulation of dust, while A425 postdates events of strong winds (observed around A419). Similar statements apply to B198 and B350 that pre- and postdate events of strong winds around sol 331.

Fig.3.1 shows false-color images of Filter and Capture magnets before and after such events. These images have been generated such that they are inter-comparable in terms of color. We note that the dust pattern is sensitive to wind gusts. In addition the over-all color of the dust adhering to the magnets changes from light brown to dark brown (Capture) and from brown to almost black (Filter), according to the false color images shown. Fig. 3.2 shows a zoom of the Capture magnet shown in fig. 3.1.

Reflectance spectra are shown in fig.3.3. The A184 spectra are I/F data as read from the IOF calibrated images (Bell et al., 2006) except that the right-eye IOF data have been scaled by a constant (wavelength independent) factor, such that they match the left-eye IOF data at 754 nm. The A425 spectra have been obtained in a similar way, but additionally scaled down by a

constant factor (C: 0.7542, F: 0.7607), so that the A425 reflectance of the border regions of each magnet matches the A184 reflectance in the NIR region ( $\lambda = 1001 \text{ nm}$ ), where the dust is weakly absorbing. In fact, the different shadows around the A184 and A425 magnets (fig.3.1) indicate different local incidence angles and, accordingly, different amounts of incident/reflected light. The Pancam calibration pipeline cannot take these differences into account, in particular due to the tilt (45 deg.) of the magnets with respect to the Pancam calibration target and due to the partly specular reflection of light by the magnet surfaces. The scaling is intended to make the A184 and A425 dust units on the Capture magnet comparable in terms of their VIS/NIR reflectance spectra.

The reflectance spectra of the dust-free magnets are rather flat across the VIS/NIR spectral range, with a maximum near 670 nm and a dip near 800 nm (according to preflight data). The spectra of the magnet borders, as acquired during the mission (cf. e.g. fig.3.3), are similar, but often have a reddish slope due to contamination with dust. In general that reddish slope is smaller for the border regions of Filter and Capture magnets than for the outer region of the sweep magnet, not surprisingly caused by the tilt of the former magnets with respect to horizontal [Madsen et al., 2003].

Two aspects of the dust spectra (shown in fig.3.3) shall be commented further:

a) Difference between Filter and Capture magnet dust:

This feature is most obvious in the A184 spectra and the following discussion will largely refer to these data. In the beginning of the mission the active surfaces of the magnets were clean (as confirmed by images acquired early after landing). As dust accumulated, the central part of the Filter magnet became darker, while the central part of the Capture magnet became, brighter in the NIR spectral range (as compared to the border regions). This observation clearly demonstrates the accumulation of different spectral/magnetic subsets on Filter and

Capture magnet and confirms similar findings (based on A071 Pancam images) that were reported in an earlier paper [Bertelsen et al, 2004]. Those earlier data have been acquired at a time, when the dust layer was still quite thin ( $< 50 \mu\text{m}$ , see below): As a result the blue reflectance ( $\lambda = 440 \text{ nm}$ ) of the Filter magnet was somewhat higher than that of the Capture magnet, indicating that these early Pancam images (A071) did not actually represent the reflectance of Filter magnet dust, but the overall-reflectance of a thin translucent dust veneer on a bright (aluminum) support. The later data that are presented here (A184) show that Filter and Capture magnet dust have a similar reflectance in the blue part, but differ from each other in the NIR part of the spectrum. The similarity of the blue reflectance, in turn, indicates that a semi-infinite layer thickness has been achieved for blue light incident on/reflected by the magnet dust, while that same layer is (likely) still translucent in the NIR.

During the Mössbauer Filter magnet integration (A243-258) a soil clod (adhering to the contact plate of the Mössbauer spectrometer) was accidentally deposited onto the Filter magnet (fig.3.4). Roughly 100 sols later, and likely as a result of rover motion, the soil clod fell off the magnet surface. The images of the soil clod on the Filter magnet provide a unique opportunity to compare optically thick material to thin layers in terms of their reflectance spectra that were acquired at the very same lighting/viewing geometry: The soil clod spectrum has a maximum at  $\lambda = 900 \text{ nm}$  similar to spectra of thick dust layers on the sweep magnet (section 3.2), while the spectra of (thin) dust layers on the Filter/Capture magnets are basically flat in the NIR spectral range (although slightly tilted with higher reflectance as the wavelength increases).

The translucency of the dust layer provides constraints on the dust layer thickness. Following Hapke (1993) the dust layer thickness ( $h^*$ , also referred to as *radiolith thickness*) that effectively controls the reflectance is given by:

$$h^* \cong \frac{D}{f} \cdot \frac{1+r}{1-r}, \quad (\text{equation 3.1})$$

where  $D$  is the effective particle diameter,  $f$  is the filling factor (dimensionless quantity) and  $r$  is the reflectance. The formula is only a very rough approximation. The dependence on the reflectance is weak for Martian dust in the VIS/NIR wavelength range ( $r < 0.3$ ) and can almost be neglected near the blue end of the spectrum. Let us choose  $D = 3.2 \mu\text{m}$  (mean particle diameter of airborne dust, [Tomasko et al, 1999]),  $r = 0.04$  at  $\lambda = 440 \text{ nm}$  and  $r = 0.30$  in the NIR range (these are the I/F values plotted in fig. 3.3). The filling factor is a poorly known quantity that ranges from typically 5% for loosely aggregated wind-blown dust, and up to 50% for accumulations of sand-sized particles. Here we will assume a filling factor of 5-10%. With these values  $h^* \sim 50 \mu\text{m}$  at  $\lambda = 440 \text{ nm}$  and  $h^* \sim 80 \mu\text{m}$  at NIR wavelengths. As a result, the A184 dust layer thickness (Capture or Filter magnet) should be in the range 50-80  $\mu\text{m}$  (as purely inferred from reflectance properties).

The A425 dust spectra (open symbols in fig. 3.3) all share the characteristic features of the blank aluminum spectra, implying that these dust layers are *not* semi-infinite in an optical sense and should have a thickness below 50  $\mu\text{m}$ .

b) Existence of two different dust units on the Capture magnet:

Fig. 3.3 shows the reflectance spectra of two distinct (dust covered) regions of the Capture magnet, a brighter and a darker region. During the period of continuous dust accumulation (up to  $\sim$  A400) these regions have (almost) similar reflectance. After events of strong wind (observed around sol 419) the spectra become very different, indicating that two distinct dust units have been separated and confined in adjacent concentric ring-shaped regions of the Capture magnet (cf. figs. 3.1b and 3.2b). The dark and bright dust units correspond to more strongly and more weakly magnetic material, respectively. The dark unit is preferentially accumulated near the outer edges of the ring-shaped samarium-cobalt magnets that are positioned below the protective aluminum cover of the magnet device (Madsen et al., 2003) in accordance with CFD-simulations of the interaction between magnetic dust and the magnets

[Kinch et al., 2006] . The cleaning event around A419 has removed considerable amounts of dust from both magnets. As a result the border regions have a flatter (less reddish) spectrum indicative of a rather clean aluminum surface post A419. Flatter dust spectra are interpreted as being reflectance spectra of magnetite rich dust (as opposed to ferric-oxide rich dust). However, some of the A425 dust spectra (from the Filter magnet and the bright regions of the Capture magnet) may also bear signs of a two-layer reflectance (with the underlying aluminum surface shining through).

The above described observations clearly demonstrate the magnetic separability of the airborne dust. The question, how many different magnetic subsets have been extracted from the airborne dust, will be addressed in section 3.2. Figs. 3.1 and 3.2 also show magnet images from B198 and B350. It can be seen that the magnetic selection on the MER-B magnets is not as pronounced as for MER-A. The weaker magnetic selection on the MER-B magnets is also apparent in the Mössbauer spectra (cf. section 5) and this apparent difference between the two landing sites will be further discussed in following sections.

The B198 reflectance spectra are of lower quality due to shadowing of the Filter magnet in the right-eye images (not shown in this paper). Despite these effects the available MER-B reflectance spectra clearly support the above conclusions on the correlated optical and magnetic properties of the dust.

## 3.2 Sweep Magnet

Intercomparable false-color images of the Sweep magnet (generated from Pancam images acquired on A206 / A425 and B207 / B350) are presented in fig. 3.5.

The B350 image of the Sweep magnet (fig. 3.6) has been acquired late during the day (LST 16:47) at grazing solar incidence ( $i \sim 74$  deg.): The dust layer casts shadows, and the extension of these shadows as well as the variation in brightness across the dust pattern allows an estimation of the height of the dust ring. Applying similar methods as used for analysis of data from the RAT magnet experiments [Goetz et al ., 2008b] provide evidence that the dust layer thickness is in the range 120 to 160 microns. This value is somewhat larger than the dust layer thicknesses inferred for the Capture/Filter magnet dust (section 3.1), likely a result of the tilt of these magnets with respect to horizontal.

Figs. 3.7-3.9 show selected IOF spectra before and after events of strong wind. The spectra shown in figs. 3.7-3.8 are calibrated and scaled as described earlier for the case of Capture/Filter magnet dust spectra (section 3.1): The A206 spectra are again I/F data as read from the IOF calibrated image except the scaling of the right-eye data, such that left- and right-eye I/F agree at  $\lambda = 754$  nm. The A425 data have been processed in the same way, but additionally have been scaled down by a constant factor (0.7240) so that these data agree in the center region (the cleanest region of the sweep magnet) and at  $\lambda = 1001$  nm with the corresponding data from A206. The scaling procedure is directly inherited from that applied for the Capture/Filter magnet spectra (fig.3.3) and should allow for direct comparison of sweep magnet spectra on a relative scale. Fig. 3.9 focuses on spectral shape: Therefore all spectra shown (Capture, Filter and Sweep magnet) have been scaled to 0.04 at  $\lambda = 440$  nm.

Refer to fig.3.7. Border and center region spectra of the Sweep magnet have a reddish slope that is more pronounced than that of the corresponding spectra from the Filter/Capture

magnets (fig.3.3). This is likely (and intentionally) caused by the tilt of the latter magnets that – presumably assisted by the vibrations due to rover motion - cannot hold as much of the weakly/non-magnetic material. The significant difference between the A206 center and border spectra of dust on the Sweep magnet cannot be explained by a difference in layer thickness (as it becomes apparent when comparing these spectra to the pre-flight BUG spectrum). The spectral differences between center and border regions are therefore interpreted as being caused by a different mineralogy of the dust adhering to these respective regions.

Fig. 3.7 also provide clues on the dynamics of dust accumulation on the Sweep magnet: While the A206 border region spectrum of the Sweep magnet strongly mimics an ordinary Martian dust spectrum (like e.g. that of Laguna Hollow), the corresponding A425 spectrum of the border region is indistinguishable from the center region spectrum. We conclude that the events of strong wind that took place around A419 removed most of the weakly magnetic, reddish dust from border and center regions, leaving behind a very thin (incomplete, almost transparent) layer that adheres to the rough (glass-bead blasted) aluminum surface of the magnet.

Fig.3.8 shows again the very same reflectance spectra of the center regions (A206, A425) for reference. These spectra are now compared to spectra of the dusty regions on the Sweep magnet. As in the case of the Capture/Filter magnets the events of strong wind (prior to A425) remove bright material. As a result the dusty ring region (referred to as “d1”) becomes darker and the corresponding reflectance spectrum has a significantly lowered red-to-blue slope (fig.3.8, also fig. 3.9). In addition, substantial stretching of the NIR image of the A206 Sweep magnet shows the appearance of a bright annulus (referred to as “d2”) around the darker center. The reflectance spectra of that particular region is very similar to those of the thick dust region, however moved to higher values of reflectance both in the blue and the NIR part of the spectrum. If that region was just a transition from the thick dust ring to the (potentially) clean center area, the reflectance should be more intense near the blue end and less intense in

the NIR range as compared to the spectrum of the dust ring (d1). We conclude that this shift in spectral properties reflect a change in mineralogy. The bright NIR annulus is invisible in the A425 image of the Sweep magnet, implying that the material that caused the annulus is weakly magnetic and was removed by these events of strong wind. The MER-B sweep magnet dust has similar spectra as corresponding MER-A dust. However, the bright NIR ring is far less pronounced at the B site providing another clue to the subtle differences between the airborne dust at the two sites.

One aspect of the spectra shown in fig. 3.8 has not yet been addressed, i.e. the particular shape of these spectra in the NIR spectral range: The center-region spectrum of the sweep magnet has a clear NIR minimum around 850 nm, while the dust spectrum has a maximum at that wavelength. This feature turns out to express the layer thickness of the adhering dust: The soil clod spectrum shown in fig. 3.4 already provided a clue to the NIR shape of the reflectance spectrum of thick dust layers (whatever may be the magnetic properties of this material). The soil clod may well be close to bulk airborne dust (in terms of mineralogy, magnetic properties and grain size), otherwise this sample could not have stuck to the lower side of the Mössbauer contact plate. The reflectance spectrum of the soil clod has a maximum near 850 nm, indicating that the particulate material that has this reflectance spectrum has a minimum absorption at that wavelength. This result is consistent with the absorption spectra that have been inferred for airborne dust from light scattering experiments [Goetz et al., 2008a, and references therein]. Contrary to the soil clod spectrum, the magnet dust spectra shown by [Bertelsen et al., 2004] still had the NIR inflection that is characteristic for thin (translucent) dust layers.

This discussion leads to fig.3.9, where a number of spectra (both MER-A and MER-B, all spectra scaled to 0.04 at  $\lambda = 440$  nm) are shown in one diagram: The Sweep magnet dust spectra all have a NIR maximum, while the Capture/Filter magnet spectra are flat in the NIR region. By comparison with the soil clod spectrum (fig. 3.4) we now understand this feature

as being controlled by the dust layer thickness. In particular, we conclude that the dust ring of Sweep magnet is thicker than the dust layer on the Filter/Capture magnets. This result is consistent with earlier estimations on the layer thickness that were based on the reflectance properties alone: Below 50  $\mu\text{m}$  for A425/Capture/Filter, 50-80  $\mu\text{m}$  for A184/Filter/Capture and 120-160  $\mu\text{m}$  for B350/Sweep.

Fig. 3.9 shows both MER-A and MER-B spectra: Although B dust may be brighter in an absolute sense the B spectra have a lower red-to-blue ratio (750 nm/440 nm). Both results are consistent with results obtained in other work [e.g., Yen et al., 2005]. The differences between pre- and post-wind gust spectra are larger for MER-A as compared to MER-B. We conclude that MER-A dust is more separable from a magnetic point of view (and/or that wind gusts in Gusev crater were significantly stronger than on Meridiani Planum). Already the color images shown in figs. 3.1-3.2 suggested such a difference.

So far we have seen that different regions on the sweep magnet turn out to map to different subsamples of the airborne dust.

The center of the sweep magnet is preferentially reached by (virtually) non-magnetic particles [Madsen et al., 2003]. Has there been accumulation of such dust in the center of the sweep magnet? Obviously non magnetic particles must be present in the airborne dust, at least at low concentration. However, whatever this concentration may be, the amount of dust in the center of the sweep magnet must remain comparatively small. Therefore the reflectance of dust in the center of the sweep magnet is necessarily a complex 2-layer problem and Pancam spectra of the sweep magnet can only set an upper bound to the potential presence of dust at that location.

Thus all three dust units are more or less reddish, with the ring region being most reddish, followed by border and center regions. The same statement may not be made on the individual dust units themselves due to the 2-layer characteristics of the reflectance. There is no clear correlation between these dust units. We conclude that these dust units react

differently to the action of wind and must therefore have different magnetic properties. The center region becomes gradually more contaminated by reddish dust, although at a very low pace. This indicates the presence of at least some virtually non magnetic (though probably iron-bearing) particles in the airborne dust. At sols beyond A1100/B1100 the data become less reliable due to possible contamination of the Pancam optics.

#### **4. Dust Properties as Inferred from Microscopic Imager Data**

The images obtained by the Microscopic Imager documents the dynamics of the process of accumulation and removal of dust on the magnets. Figure 2.1 shows the magnets close in time, when the Pancam data discussed earlier were acquired. The amount of dust adhering to the magnets has varied substantially over the course of the mission. The long-lasting stand-down of Spirit during the first Martian winter encountered allowed the accumulation of substantial amounts of both weakly and strongly magnetic dust particles on the active surface of both magnets. Because of the amount of dust accumulated the characteristic pattern of the dust on the Capture magnet from early in the mission (composed of a central spot and three concentric rings) had almost disappeared on sol 963 ( $L_S = 109^\circ$ ). This is consistent with both Pancam (section 3) and APXS data (section 6). Besides magnetic dust the Capture magnet (as imaged on A963) also attracted a number of (magnetic) sand grains, up to 50 grains, typically 100 – 300  $\mu\text{m}$  in diameter).

Wind gusts at the Meridiani site (in particular a wind gust recorded on sol 331) favored the selection of strongly magnetic grains such that millimeter-long magnetic chains (oriented along the magnetic field lines) could be formed as observed on the image from sol 337 (fig. 4.1).

## **5. Dust Properties as Inferred from Mössbauer Data**

In general  $^{57}\text{Fe}$  Mössbauer (MB) spectra obtained from  $\gamma$ -photons resonantly backscattered from thin layer of dust (such as found on the MER Filter and Capture magnets) will be inherently noisy. However, useful MB spectra have been acquired of Capture magnet dust on sols A505-507, A594-597 and B328-330. The last of these data sets has already been discussed in some detail by [Goetz et al., 2005]. Filter magnet dust spectra are of limited quality due to poor statistics.

Figure 5.1 shows two spectra of Capture magnet dust, obtained on sols A594-597 and B328-330. Due to the experimental statistics, fits of these data are not unique. In order to narrow down the parameter space, we have fitted both dust spectra (MER-A and MER-B) with the same set of MB components (but allowed for different abundances of the different components). In addition, for a given mineral component, we constrained the fit to allow only a limited range of MB parameters around a central value that was inferred from good statistics soil spectra. Laguna Hollow soil is believed to be representative for a larger area around the Spirit landing site (and possibly even for a substantially larger fraction of the Martian surface) and is therefore considered to be a good soil counter part of the airborne dust. Table 5.1 lists the MB parameters of Laguna Hollow soil, as well as the parameters found for Capture magnet dust.

The dust spectra are rather complex. However, by applying the fit procedure described above, we found evidence for presence of the following mineral components in the airborne dust (or more precisely: the magnetic sub-set of airborne dust that had accumulated and remained on the Capture magnet at these particular points in time in spite of dust removal events having occurred): Olivine, pyroxene, paramagnetic oxides and oxyhydroxides or nano-phase oxides (ferric doublet) and magnetite. The implications of these findings are summarized in the conclusions (section 7). Because of the constraints inherent in our fitting procedure and since

we are using the same fit components for both spectra, we will not be able to detect small differences between mineral components, such as e.g. the iron content of the olivine.

However, we are able to distinguish different characteristics of the magnetite, since the relative area of the two sextets (caused by tetrahedrally and octahedrally coordinated iron, respectively) can be freely varied in our fits.

A careful inspection of Fig. 5.1 shows that the total fit does not fully account for the data. Especially for the spectra A594-597 it is clear that the spectrum does have components not accounted for in the fit and further (minor) mineral components (in particular magnetically ordered mineral(s), i.e., with MB sextets are present in the dust. However, further discussion of this or these components is part of ongoing work and will be published in a subsequent paper. For the same reason and because of the evidence for strong dynamics of the experiment because of the action of winds, the areas of the component sub-spectra (listed in table 5.1) should not be taken too literally. Nevertheless some preliminary conclusions can be drawn from the results of the fits. First, there is a larger degree of average oxidation of iron in the airborne dust ( $\text{Fe}^{3+}/\text{Fe}_{\text{tot}} \sim 0.6-0.7$ ) as compared to the Laguna Hollow soil ( $\sim 0.3$ ).

Next we discuss some differences between MER-A and MER-B spectra. Visual inspection of the spectra reveals the difference in the narrow velocity range near the center, between -2 and +4 mm/s. The ratio of the summed olivine/pyroxene doublets to the ferric doublet is significantly smaller in the A spectrum as compared to B (table 5.1). As pointed out in the next section (section 6) the amount of iron on the magnets (APXS-Fe signal  $\sim 2.0 \sim 2.5$  counts per second, fig.6.2) is similar (say within 20%) at the time, when the discussed MB spectra were acquired (A594-597 and B328-330, respectively). It appears that the A spectrum is indicative of less olivine/pyroxene with respect to ferric doublet component (or -inversely- more ferric doublet component with respect to olivine/pyroxene) than the B spectrum.

Another difference between A and B can be quantified by the ratio of all doublets (olivine, pyroxene, and the ferric doublet component) to all sextets: Based on MB data the A dust

seems to contain significantly more magnetite relative to the amount of doublet-generating minerals than B dust, but as mentioned this may well be caused alone by the differences in wind interactions encountered at the two sites. Finally the spectra suggest that the magnetite is different in A and B dust: The area ratio of the two sextets is very different for both dust spectra (table 5.1) that – in turn – may indicate different Fe/Ti and/or  $\text{Fe}^{3+}/\text{Fe}^{2+}$  ratios for the magnetite-related phase (may that be titanomagnetite or magnetitic maghemite (somewhat oxidized magnetite) – and this observation does not depend on different wind environments at the two sites.

So far we have been discussing some differences between A and B spectra. Given the available data we cannot claim that these differences reflect true (permanent) differences between airborne the dust at the two landing sites. However, what these differences with certainty do tell us, is that the composition of the subset of airborne dust that is held on the magnets varies within rather large ranges, depending on the wind regime. At this point we should go back to fig. 2.2 showing the dust contamination of the Pancam caltarget. In particular these figures tell us that the Mössbauer spectra that are discussed in this section have been acquired at the end of a dust cleaning period (A400–600, B160–300). However, the dust cleaning was more efficient at the A-site than at the B-site in these time periods. In particular, the black-to-white (B/W) ratio of the rings of the MER Pancam calibration target (as monitored through the 753-nm filter (L2)) decreased from ~0.7 to ~0.4 in the sol range A400-600 whereas the same ratio decreased from ~0.55 to ~0.4 in the time frame B160-300. Thus the above noted differences in relative magnetite abundance are consistent with a more efficient wind-controlled selection of strongly magnetic (i.e. magnetite-rich) particles at the A site. In general fig. 2.2 suggests that the cleaning events at the B-site are not as powerful as the events occurring at the A-site. This can be an explanation of the comparatively stronger magnetite signal in the Mössbauer spectra obtained at Gusev crater.

MB properties	A, Capture	B, Capture	Gusev soil* *Morris et al., 2007, tables 1+3
<i>Mössbauer parameters:</i>			
<i>olivine:</i>			
IS [mm s <sup>-1</sup> ]	1.18+/- 0.04		1.15 +/- 0.02
QS [mm s <sup>-1</sup> ]	3.05+/- 0.08		2.97 +/- 0.02
<i>pyroxene:</i>			
IS [mm s <sup>-1</sup> ]	1.19+/- 0.04		1.14 +/- 0.02
QS [mm s <sup>-1</sup> ]	2.09+/- 0.08		2.10 +/- 0.02
<i>ferric doublet:</i>			
IS [mm s <sup>-1</sup> ]	0.40+/- 0.06		0.40 +/- 0.02
QS [mm s <sup>-1</sup> ]	0.95+/- 0.12		0.83 +/- 0.04
<i>magnetite (tetrahedral):</i>			
IS [mm s <sup>-1</sup> ]	0.30+/- 0.02		0.31 +/- 0.02
QS [mm s <sup>-1</sup> ]	0.08+/- 0.02		0.06 +/- 0.02
B <sub>hf</sub> [T]	50.3+/- 0.8		50.1 +/- 0.8
<i>magnetite (octahedral):</i>			
IS [mm s <sup>-1</sup> ]	0.61+/- 0.02		0.64 +/- 0.02
QS [mm s <sup>-1</sup> ]	-0.03+/- 0.02		0.00 +/- 0.02
B <sub>hf</sub> [T]	46.5+/- 0.8		46.9 +/- 0.8
<i>hematite:</i>			
IS [mm s <sup>-1</sup> ]			0.37 +/- 0.02
QS [mm s <sup>-1</sup> ]			-0.16 +/- 0.02
B <sub>hf</sub> [T]			51.7 +/- 0.8
<i>Areas of component subspectra (%):</i>			
olivine, Fe <sup>2+</sup>	4	16	35 +/- 5
pyroxene, Fe <sup>2+</sup>	7	14	33 +/- 4
ferric doublet, Fe <sup>3+</sup>	21	23	21 +/- 6
magnetite (tetrahedral), Fe <sup>3+</sup>	24	32	4 +/- 2
magnetite (octahedral), Fe <sup>2.5+</sup>	44	14	5 +/- 2
hematite, Fe <sup>3+</sup>	0 (?)	0 (?)	2 +/- 1
-----	-----	-----	-----
sum	100	100	100
<i>Characteristics inferred from the sub-spectral areas:</i>			
Fe <sup>3+</sup> /Fe <sub>tot</sub>	0.67	0.62	0.30 +/- 0.06
(oliv.+pyr.) / ferric doublet component	0.5	1.3	3.2
all doublets / all sextets	0.5	1.2	8.1
magnetite: tet. / oct.	0.5	2.3	0.8

**Table 5.1** Capture magnet dust (A594-597, B328-330; summed without any f-factor or temperature correction) and Laguna hollow soil (A047-A050) as characterized by Mössbauer spectroscopy [Morris *et al.*, 2006]. IS [mm s<sup>-1</sup>], QS [mm s<sup>-1</sup>] and B<sub>hf</sub>[T] are the isomer shift,

the quadrupole shift or quadrupole splitting, and the magnetic hyperfine field strength, respectively.

## **6. Dust Properties as Inferred from X-Ray Fluorescence Data**

The APXS magnet spectra are much less affected by the small sample mass than the MB spectra. Therefore good spectra could be acquired of both Filter and Capture magnet dust. Examples (MER-B Capture magnet spectra) are presented in fig. 6.1.

In fig. 6.2 the area of the iron peaks is plotted as a function of sol number for both missions. As expected, the rate of dust accumulation is higher on the Capture magnet than on the Filter magnet. Furthermore the dust accumulation was faster on MER-B than on MER-A, likely caused by the higher atmospheric dust loading at the MER-B landing site (fig. 2.1).

Fig. 6.3 plots the peak areas of major elements on the Capture magnet as a function of sol number. It turns out that iron, titanium and chromium follow each other, and these have been drawn as thick solid lines in fig. 6.3. The amount of these elements has been increasing throughout the sol range presented, though at different rates. Obviously, we always may have some dynamic equilibrium between removal of already accumulated material and addition of new particles. Yet, there is no net removal of these elements, except for titanium in the time frame A597 to A968. This data point also deviates from the general correlation between iron and titanium (point marked by arrow in fig. 6.4c) and this is not fully understood at present. It should be pointed out, however, that this data point represents a strong titanium peak and has been inferred from a good APXS spectrum. Therefore it may not be considered as a statistical outlier. One possible explanation could be that the airborne dust contained less titanium at A-sol 968 than before, be that caused by local differences or by changes over time. New APXS spectra may resolve this issue in the future.

Fig. 6.3 also plots the amount of a variety of other elements (Si, S, Ca, Cl, P, and K) as a function of sol number. These elements (except phosphorus) must be present in minerals forming weakly magnetic (or non-magnetic) particles, since they are effectively removed from the magnet in the time frame A308-597.

In the time frame A597-968, the amount of iron, titanium and chromium on the magnet is basically stable, while the amount of the second element group (Si, S, Ca, Cl, P, and K) typically increases by a factor of two. We conclude that the magnetic selection was not very efficient in this time frame. In other words, both strongly and weakly magnetic (and -perhaps- non-magnetic) particles were accumulated during this period of time that included part of the Spirit stand down during southern-hemisphere winter (A-sol 968 corresponds to  $L_S = 111^\circ$ ). This interpretation is strongly supported by the corresponding MI images (fig. 4.1).

The dust on the MER-B Capture magnet shows a similar behavior. Again the elements iron, titanium and chromium follow each other and appear to belong to the strongly magnetic phase. These elements cannot be removed easily, and the amount of these elements actually increases over the sol range shown in fig. 6.3 (B-sol 53-337).

In the time frame B-sol 53-168 the amount of all elements on the Capture magnet (with the exception of phosphor and chlorine) increases at approximately the same rate, implying that all kinds of particles (strongly magnetic, weakly magnetic, non-magnetic) were accumulated on the magnet. This interpretation is supported by the MI image from B168 (fig. 4.1): The dust cover is almost homogenous and has lots of weakly magnetic (or non-magnetic) in-fill between the concentric rings that likely contain the most strongly magnetic particles.

Obviously, the (almost) homogeneous appearance of the dust cover is favored by the broadband sensitivity of the MI. Pancam images of the MER-B Capture magnet that were acquired through a blue filter (e.g. L7,  $\lambda = 440$  nm) and close in time to the B168 MI image do show a more pronounced ring pattern (section 3).

In the time frame B168 -337 the amount of iron, titanium and chromium continues to grow, while the amounts of the second element group (again with the exception of P and Cl) decreases. This evolution is interpreted as enhanced magnetic selection of magnetic dust particles and, indeed, the associated MI images (fig. 4.1) show that the formation of magnetic chains has taken place.

The evolution of the dust deposition on the MER-B Capture magnet (as described so far) implies that the amount of Si, S, Ca and K was at a (local) maximum at B-sol 168. This can be nicely seen in fig. 6.3 and (for the case of S and Ca) also in fig. 6.1.

Let us emphasize that chlorine (in the case of MER-B) and phosphor (MER-A and MER-B) apparently do not belong to either one of the (above defined) two element groups indicating that our picture of the separability of airborne dust into two major groups is somewhat oversimplified.

Finally we will address correlations between different elements (fig. 6.4). The one between titanium and iron as well as the one between chromium and iron have already been mentioned and are presented in figs. 6.4c and 6.4d, respectively. We conclude that the magnetite (as identified by MB spectroscopy; section 5) is actually titano-magnetite and, in addition, does contain some chromium. Fig.6.1 shows clearly that iron does *not* correlate with sulfur. Thus - in agreement with MB data- the strongly magnetic phase is not an iron sulfide, such as pyrrhotite ( $\text{Fe}_{1-x}\text{S}$ ,  $x = 0$  to 0.2) or greigite ( $\text{Fe}_3\text{S}_4$ , a common magnetic bio-mineral on Earth).

Let us go back to fig. 6.1: These spectra suggest the already much discussed correlation between titanium and iron. However, they also suggest a correlation between sulfur and calcium. The latter one is plotted in fig. 6.4a, including all data (Capture and Filter magnets) from MER-A and MER-B. It turns out that this correlation is very strong indicating that Ca and S not only belong to the same magnetic sub-group, but most probably are also part of the same mineral component. Given the high degree of oxidation of airborne dust (section 5, table 5.1) we suspect that this mineral component may be related to  $\text{CaSO}_4$  with an unknown amount of crystal water (gypsum, anhydrite etc.).

Fig. 6.4b shows the correlation between silicon and sulfur. Plotting the abundance of two anion-forming elements against each other may appear somewhat strange. However, there is a clear correlation, indicating that these two elements are part of intergrown mineral phases and

belong to the same magnetic sub-group that has accumulated on the magnets. Si is most commonly present in silicates, which are more or less paramagnetic with a low net attraction to permanent magnets. If, say, S was present in either greigite or pyrrhotite, we would have expected an anti-correlation between Si and S. So from these observations we conclude that greigite or pyrrhotite is not part of the magnetic sub-group of minerals in the airborne dust on Mars. Obviously, the correlations between Ca and S on the one hand and between Si and S on the other hand imply some correlation between Ca and Si. Therefore, the APXS data considered here are certainly also consistent with the presence of some of the calcium in a silicate phase.

## **7. Conclusions**

The magnets on board the Mars Exploration Rovers (Filter magnet, Capture magnet and Sweep magnet) have been attracting two different magnetic subsets of the airborne dust (referred to as *group 1* and *group 2*).

*Group 1* is composed of weakly magnetic, rather bright particles that have a high abundance in the elements Si, S, Ca and K. *Group 2* contains more strongly magnetic, lower-albedo particles that are dominated by the elements Fe, Ti and Cr. The role of Cl and P is not well understood. The magnetization of particles in *group 2* is large enough, so that these particles can form millimeter-long magnetic chains. The accumulation of dust on the magnets is not a continuously ongoing process, but displays strong dynamics.

MB spectra reveal the presence of magnetite, olivine, pyroxene and some (poorly constrained) ferric oxides or oxyhydroxides (ferric doublet component) in the airborne dust, indicating that this dust was derived from basaltic rocks as a result of slow, essentially dry weathering processes. The MB spectra indicate that there may be some mineralogical differences between airborne dust at both landing sites. The APXS data show in addition that the magnetite identified by MB spectroscopy is actually titanomagnetite with an associated low content of chromium. APXS data show that greigite or pyrrhotite are not part of the dust particles and the data also show a good correlation between calcium and sulfur, which suggest the presence of  $\text{CaSO}_4$  in the dust.. This finding may be a record of earlier volcanic activity and thus may provide a constraint on the average age of the dust particles.

## Acknowledgements

Danish participation in the MER missions was supported by the Danish Science Agency, by Thomas B. Thrige's foundation and by DELTA Danish Electronics, Light & Acoustics in Hørsholm, Denmark. Support from the University of Copenhagen for C.S.B. and W.G. is gratefully acknowledged.

## References

- Allen, C. C., et al. (1997), JSC-Mars-1: Martian Regolith Simulant, Proc. Lunar Planet. Sci. Conf. 28, Abstract # 1797.
- Ashcroft, N. W., and Mermin, N. D. (1976), Solid State Physics, Saunders College Publishing.
- Bell III, J.F., T.B. McCord and P.D. Owensby, Observational Evidence of Crystalline Iron Oxides on Mars, *J. Geophys. Res.* 95(B9), 14447-14461, 1990.
- Bell III, J.F., S.W. Squyres, K.E. Herkenhoff, J.N. Maki, H.M. Arneson, D. Brown, S.A. Collins, A. Dingizian, S.T. Elliot, E.C. Hagerott, A.G. Hayes, M.J. Johnson, J.R. Johnson, J. Joseph, K. Kinch, M.T. Lemmon, R.V. Morris, L. Scherr, M. Schwochert, M.K. Shepard, G.H. Smith, J.N. Sohl-Dickstein, R. Sullivan, W.T. Sullivan, and M. Wadsworth, The Mars Exploration Rover Athena Panoramic Camera (Pancam) Investigation, *J. Geophys. Res.*, 108 (E12), doi:10.1029/2003JE002070, 2003.
- Bell III, J.F., J. Joseph, J.N. Sohl-Dickstein, H.M. Arneson, M.J. Johnson, M.T. Lemmon, and D. Savransky, In-flight calibration and performance of the Mars Exploration Rover Panoramic Camera (Pancam) Instruments, *J. Geophys. Res.*, 111, E02S03, doi:10.1029/2005JE002444, 2006.
- Bertelsen, P., et al. (2004), Magnetic Properties Experiments on the Mars Exploration Rover Spirit at Gusev Crater, *Science*, 305, 827-829.
- Cabrol, N. A., et al., Exploring Gusev Crater with Spirit: Review of science objectives and testable hypotheses, *J. Geophys. Res.*, 108, 8076, doi:10.1029/2002JE002026, 2003.
- Coey, J. M. D. (1988), Magnetic Properties of Iron in Soil Iron Oxides and Clay Minerals, edited by J. W. Strucki, et al., pp. 397-466, D. Reidel Publishing Company, Dordrecht.
- Coey, J. M. D., et al. (1990), Titanomaghemite in magnetic soils on Earth and Mars, *J. Geophys. Res.*, 95, 14423-14425.
- Connerney, J. E. P., Acuña, M. H., Wasilewski, P., Ness, N. F., Rème, H., Mazelle, C., Vignes, D., Lin, R. P., Mitchell, D. and Cloutier, P., Magnetic Lineations in the Ancient Crust of Mars, *Science* 284, 794-798, 1999.
- Craddock, R.A., T.A. Maxwell and A.D. Howard, Crater morphometry and modification in the Sinus Sabaeus and Margaritifer Sinus regions of Mars, *J. Geophys. Res.*, 102 (E6), 13321-13340, 1997.
- Criddle, A.J. and C.J. Stanley (1993), Quantitative Data File for Ore Minerals (QDF3), 3rd edition, Chapman & Hall, London.

- Davies, C.N., Definitive equations for the fluid resistance of spheres, *The Proceedings of the Physical Society*, 57 (4), 259-270, 1945.
- Davis, P.A. and L.A. Soderblom, Modeling Crater Topography and Albedo From Monoscopic viking Orbiter Images, *J. Geophys. Res.*, 89 (B11), 9449-9457, 1984.
- de Wys, J. N. (1969), Magnet Data, In Surveyor: Program Results, NASA SP-184, 223.
- Dunlop, D. J., and Özdemir, Ö. (1997), Rock Magnetism, Fundamentals and Frontiers., Cambridge University Press.
- Dunlop, D.J. and Ö. Özdemir, Rock Magnetism, Fundamentals and Frontiers, *Cambridge University Press*, 1997.
- Farrand, W.H., J.F. Bell III, J.R. Johnson, B.L. Jolliff, A.H. Knoll, S.M. McLennan, S.W. Squyres, W.M. Calvin, J.P. Grotzinger, R.V. Morris, J. Soderblom, S.D. Thompson, W.A. Watters and A.S. Yen, Visible and Near-Infrared Multispectral Analysis of Rocks at Meridiani Planum, Mars, by the Mars Exploration Rover Opportunity, *J. Geophys. Res.* (submitted), 2006.
- Gellert, R., R. Rieder, R.C. Anderson, J. Brückner, B.C. Clark, G. Dreibus, T. Economou, G. Klingelhöfer, G.W. Lugmair, D.W. Ming, S.W. Squyres, C. d'Uston, H. Wänke, A. Yen and J. Zipfel, Chemistry of Rocks and Soils in Gusev Crater from the Alpha Particle X-ray Spectrometer, *Science*, 305, 829-832, 2004.
- Goetz, W., The Optical Properties of Martian Dust, Ph. D. Thesis thesis, Center for Planetary Science, University of Copenhagen, 2002.
- Goetz, W., P. Bertelsen, C.S. Binou, H.P. Gunnlaugsson, S.F. Hviid, K.M. Kinch, D.E. Madsen, M.B. Madsen, M. Olsen, R. Gellert, G. Klingelhöfer, D.W. Ming, R.V. Morris, R. Rieder, D.S. Rodionov, P.A. de Souza Jr., C. Schröder, S.W. Squyres, T. Wdowiak and A. Yen, Indication of drier periods on Mars from the chemistry and mineralogy of atmospheric dust, *Nature*, 436, 62-65, 2005.
- Goetz, W., S.F. Hviid, K.M. Kinch, and M.B. Madsen, "16. Magnetic Properties Results from Surface Landers and Rovers", in: J.F. Bell III (ed.), "The Martian Surface: Composition, Mineralogy and Physical Properties", Cambridge University Press, accepted for publication, 2008a.
- Goetz, W., K. Leer, H.P. Gunnlaugsson, P. Bartlett, B. Basso, J.F. Bell III, P. Bertelsen, C.S. Binou, P.C. Chu, S. Gorevan, M.F. Hansen, S.F. Hviid, K.M. Kinch, G. Klingelhöfer, A. Kusack, M.B. Madsen, D.W. Ming, R.V. Morris, E. Mumm, T. Myrick, M. Olsen, S.W. Squyres, J. Wilson, and A. Yen, The Search for Magnetic Minerals in Martian Rocks: Overview of the RAT Magnet Investigation on Spirit and Opportunity, *J. Geophys. Res.*, doi: 10.1029/2006JE002819, 2008b.
- Golombek, M. P., et al., Selection of the Mars Exploration Rover landing sites, *J. Geophys. Res.*, 108, 8072, doi:10.1029/2003JE002074, 2003.
- Gorevan, S.P., T. Myrick, K. Davis, J.J. Chau, P. Bartlett, S. Mukherjee, R. Anderson, S.W. Squyres, R.E. Arvidson, M.B. Madsen, P. Bertelsen, W. Goetz, C.S. Binou and L. Richter, Rock Abrasion Tool: Mars Exploration Rover mission. *J. Geophys. Res.*, 108 (E12), 8068, doi:10.1029/2003JE002061, 2003.
- Greeley, R., et al. (2006), Gusev Crater: Wind-related features and processes observed by the Mars Exploration Rover Spirit, *J. Geophys. Res.*, 111.
- Gunnlaugsson, H.P., S.F. Hviid, J.M. Knudsen, M.B. Madsen, Instruments for the Magnetic Properties Experiments on Mars Pathfinder, *Planet. Space Sci.* 46, 449-459, 1998.

- Gunnlaugsson, H. P., Analysis of the magnetic properties experiment data on Mars: Results from Mars Pathfinder, *Planetary and Space Science*, 48, 1491-1504, 2000.
- Hapke, B., *The Theory of Reflectance and Emittance Spectroscopy*, Cambridge University Press, 1993.
- Hargraves, R. B., Collinson, D. W., and Spitzer, C. R., Viking Magnetic Properties Investigation: Preliminary Results, *Science*, 194, 84-86, 1976a.
- Hargraves, R. B., et al., Viking Magnetic Properties Investigation: Further Results, *Science*, 194, 1303, 1976b.
- Hargraves, R. B., et al., The Viking Magnetic Properties experiment: Primary Mission results, *J. Geophys. Res.*, 82, 4547-4558, 1977.
- Hargraves, R. B., et al., Viking Magnetic Properties Experiment - extended mission results, *J. Geophys. Res.*, 84, 8379-8384, 1979.
- Hargraves, R. B., et al., Magnetic enhancement on the surface of Mars?, *J. Geophys. Res. - Planets*, 105, 1819-1827, 2000.
- Horn, B.K.P. and M.J. Brooks (eds.), *Shape from Shading*, MIT Press, Cambridge, MA, 1989.
- Huffmann, D. R., and Stapp, J. L., Optical Measurements on Solids of Possible Interstellar Importance, in *Interstellar dust and Related Topics*, edited by Greenberg and V. d. Hulst, p. 297, 1973.
- Hviid, S. F., et al., Magnetic Properties experiments on the Mars Pathfinder Lander: Preliminary Results, *Science*, 278, 1768-1770, 1997.
- Jackson, J. D., *Classical Electrodynamics*, 3rd ed., Page 189 pp., John Wiley & Sons, 1999.
- J. Jensen, F. Folkmann, H.P. Gunnlaugsson, J.P. Merrison, K.M. Kinch, J. M. Knudsen, P. Nørnberg, M.B. Madsen: "Analysis of Magnetic Dust Layers on Mars by PIXE and XRF", *X-Ray Spectrometry* 34, 359-362, 2005.
- Johnson, J. R., Grundy, W. M., and Lemmon, M. T., Dust deposition at the Mars Pathfinder landing site: observations and modeling of visible/near-infrared spectra, *Icarus*, 163, 330-346, 2003.
- Kinch, K.M., *Numerical Modeling of Magnetic Capture of Martian Atmospheric Dust*, Ph.D. thesis, University of Aarhus, Denmark, 2005.
- Kinch, K. M., et al., Preliminary analysis of the MER magnetic properties experiment using a computational fluid dynamics model, *Planetary and Space Science*, 54, 28-44, 2006.
- Kinch K.M., J. Sohl-Dickstein, J.F. Bell III, J.R. Johnson, E. Guinness, M.B. Madsen and W. Goetz, A preliminary radiative transfer analysis of dust deposition on the Mars Exploration Rover Panoramic Camera (Pancam) calibration targets, *J. Geophys. Res.* (accepted), 2007.
- Kletetschka G., P.J. Wasilewski, P.T. Taylor, Hematite vs. magnetite as the signature for planetary magnetic anomalies?, *Physics of the Earth and Planetary Interiors*, 119, 259-267, 2000a.
- Kletetschka, G., P.J. Wasilewski and P.T. Taylor, Mineralogy of the Sources for Magnetic Anomalies on Mars, *Meteoritics & Planetary Science* 35, 895-899, 2000b.
- Kletetschka, G. and P.J. Wasilewski, Grain size limit for SD hematite, *Physics of the Earth and Planetary Interiors* 129, 173-179, 2002.

- Klingelhöfer, G. *et al.* Athena MIMOS II Mössbauer spectrometer investigation. *J. Geophys. Res.* 108, 8067-8084, 2003.
- Klingelhöfer, G., R.V. Morris, B. Bernhardt, C. Schröder, D.S. Rodionov, P.A. de Souza Jr., A. Yen, R. Gellert, E.N. Evlanov, B. Zubkov, J. Foh, U. Bonnes, E. Kankeleit, P. Gütlich, D.W. Ming, F. Renz, T. Wdowiak, S.W. Squyres and R.E. Arvidson, Jarosite and Hematite at Meridiani Planum from Opportunity's Mössbauer Spectrometer, *Science*, 306, 1740-1745, 2004.
- Knudsen, J. M., et al., Mössbauer Spectroscopy on the Surface of Mars. Why?, *Hyperfine Interactions*, 68, 83-94, 1991.
- Landis, G. A., and Jenkins, P. J., Measurement of the settling rate of atmospheric dust on Mars by the MAE instrument on Mars Pathfinder. *J. Geophys. Res.*, 105, 1855-1857, 2000.
- Landis, G. A., et al., Dust and Sand Deposition on the MER Solar Arrays as Viewed by the Microscopic Imager, *Proc. 37th Lunar and Planetary Science Conference*, 2006.
- Larsen, L.M. and A.K. Pedersen, Processes in high-Mg, high-T magmas: Evidence from olivine, chromite and glass in Palaeogene picrites from West Greenland, *Journal of petrology*, 41, 7, 1071-1098, 2000.
- Leer K., B. Basso, C. Binau, W. Goetz, S. Gorevan, S.F. Hviid, A. Kusack, M.B. Madsen, S.W. Squyres, J. Wilson, Simulating collection of dust on the RAT magnets onboard the Mars Exploration Rovers, *LPSC XXXVII*, abstract #1784, 2006.
- Lemmon, M., Wolff, M.J., Smith, M.D., Clancy, R.T., Banfield, D., Landis, G.A., Ghosh, A., Smith, P.H., Spanovich, N., Whitney, B., Whelley, P., Greeley, R., Thompson, S., Bell, J.F., and Squyres, S.W., Atmospheric Imaging Results from the Mars Exploration Rovers: Spirit and Opportunity, *Science*, 306, 1753-1756, 2004.
- Levin, G. V., and Straat, P. A. Viking labeled release biology experiment: Interim results. *Science* 194, 1322-1329, 1976.
- Madsen, M. B., et al., The magnetic properties experiments on Mars Pathfinder, *J. Geophys. Res.*, 104, 8761-8779, 1999.
- Madsen, M.B., P. Bertelsen, W. Goetz, C.S. Binau, M. Olsen, F. Folkmann, H.P. Gunnlaugsson, K.M. Kinch, J.M. Knudsen, J. Merrison, P. Nørnberg, S.W. Squyres, A. Yen, J. Rademacher, S. Gorevan T. Myrick and P. Bartlett, Magnetic Properties Experiments on the Mars Exploration Rover Mission, *J. Geophys. Res.*, 108 (E12), 8069, doi:10.1029/2002JE002029, 2003.
- Maki, J.N., J.F. Bell III, K.E. Herkenhoff, S.W. Squyres, A. Kiely, M. Klimesh, M. Schwochert, T. Litwin, R. Willson, A. Johnson, M. Maimone, E. Baumgartner, A. Collins, M. Wadsworth, S.T. Elliot, A. Dingizian, D. Brown, E.C. Hagerott, L. Scherr, R. Deen, D. Alexander, and J. Lorre, Mars Exploration Rover Engineering Cameras, *J. Geophys. Res.*, 108 (E12), 8071, doi:10.1029/2003JE002077, 2003.
- Markiewicz, W. J., et al., Optical properties of the Martian aerosols as derived from imager for Mars Pathfinder midday sky brightness data, *J. Geophys. Res.*, 104, 9009-9017, 1999.
- McSween, H.Y., SNC meteorites: clues to martian petrologic evolution?, *Reviews of Geophysics* 23, 391-416, 1985.
- McSween, H.Y., M. B Wyatt, R. Gellert, J.F. Bell III, R. V. Morris, K. E. Herkenhoff, L. S. Crumpler, K. A. Milam, K. R. Stockstill, and L. L. Tornabene, R. E. Arvidson, P. Bartlett, D. Blaney, N. A.

Cabrol, P. R. Christensen, B. C. Clark, J. A. Crisp, D. J. Des Marais, T. Economou, J. D. Farmer, W. Farrand, A. Ghosh, M. Golombek, S. Gorevan, R. Greeley, V. E. Hamilton, J. R. Johnson, B. L. Joliff, G. Klingelhöfer, A. T. Knudson, S. McLennan, D. Ming, J. E. Moersch, R. Rieder, S. W. Ruff, C. Schröder, P. A. de Souza Jr., S. W. Squyres, H. Wänke, A. Wang, A. Yen, J. Zipfel, Characterization and petrologic interpretation of olivine-rich basalts at Gusev Crater, Mars, *J. Geophys. Res.*, 111, E02S10, doi:10.1029/2005JE002477, 2006.

Merrison, J. P., et al., Capture of magnetic dust in a simulated Martian aerosol: the importance of aerodynamics, *Planetary and Space Science*, 50, 371-374, 2002a.

Merrison, J. P., et al., Simulation of the Martian Dust Aerosol at Low Wind Speeds, *J. Geophys. Res.*, 107, 5133, 2002b.

Metzger, S. M., et al., Dust devil vortices seen by the Mars Pathfinder camera, *Geophysical Research Letters*, 26, 2781-2784, 1999.

Mogensen, C. T., et al., Magnetic properties Experiments on the Mars Polar Lander, *J. Geophys. Res.*, 106, 1759-17588, 2001.

Morris, R. V., H. V. Lauer Jr., C. A. Lawson, E. K. Gibson Jr., G. A. Nace, and C. Stewart, Spectral and other physiochemical properties of submicron powders of hematite (?-Fe<sub>2</sub>O<sub>3</sub>), maghemite (?-Fe<sub>2</sub>O<sub>3</sub>), magnetite (Fe<sub>3</sub>O<sub>4</sub>), goethite (?-FeOOH), and lepidocrocite (?-FeOOH), *J. Geophys. Res.*, 90, 3126–3144, 1985.

Morris, R. V., and Singer, R., Origins of Marslike spectral and magnetic properties of a Hawaiian Palagonitic soil., *J. Geophys. Res.*, 95, 14427-14434, 1990.

Morris, R. V., et al., Mineralogy, composition, and alteration of Mars Pathfinder rocks and soils: Evidence from multispectral, elemental, and magnetic data on terrestrial analogue, SNC meteorite, and Pathfinder samples., *J. Geophys. Res.*, 105, 1757-1818, 2000.

Morris, R. V., Graff, T. G., and Mertzman, S. A., Phyllosilicate-poor palagonitic dust from Mauna Kea Volcano (Hawaii): A mineralogical analogue for magnetic Martian dust?, *J. Geophys. Res.*, 106, 5057-5084, 2001.

Morris, R.V., G. Klingelhöfer, B. Bernhardt, C. Schröder, D.S. Rodionov, P.A. de Souza, Jr., A. Yen, R. Gellert, E.N. Evlanov, J. Foh, E. Kankeleit, P. Gütllich, D.W. Ming, F. Renz, T. Wdowiak, S.W. Squyres, R.E. Arvidson Mineralogy at Gusev Crater from the Mössbauer Spectrometer on the Spirit Rover, *Science*, 305, 833-836, 2004.

Morris, R.V., G. Klingelhöfer, C. Schröder, D.S. Rodionov, A. Yen, D.W. Ming, P.A. de Souza Jr., I. Fleischer, T. Wdowiak, R. Gellert, B. Bernhardt, E.N. Evlanov, B. Zubkov, J. Foh, U. Bonnes, E. Kankeleit, P. Gütllich, F. Renz, S.W. Squyres and R.E. Arvidson, Mössbauer mineralogy of rock, soil, and dust at Gusev Crater, Mars: Spirit's journey through weakly altered olivine basalt on the Plains and pervasively altered basalt in the Columbia Hills, *J. Geophys. Res.*, accepted for publication, 2006.

Morris, R.V., G. Klingelhöfer, C. Schröder, D.S. Rodionov, A. Yen, D.W. Ming, P.A. de Souza Jr., T. Wdowiak, I. Fleischer, R. Gellert, B. Bernhardt, U. Bonnes, B.A. Cohen, E.N. Evlanov, J. Foh, P. Gütllich, E. Kankeleit, T. McCoy, D.W. Mittlefehldt, F. Renz, M.E. Schmidt, B. Zubkov, S.W. Squyres, and R.E. Arvidson, Mössbauer mineralogy of rock, soil, and dust at Meridiani Planum, Mars: Opportunity's journey across sulfate-rich outcrop, basaltic sand and dust, and hematite lag deposits, *J. Geophys. Res.*, accepted for publication, 2007.

Mustard, J.F. and J.F. Bell, New Composite Reflectance Spectra of Mars from 0.4 to 3.14  $\mu$ m, *Geophys. Res. Lett.* 21(5), 353-356, 1994.

- Nørnberg, P. et al., Mineralogy of a burned soil compared with four anomalously red Quaternary deposits in Denmark, *Clay Minerals*, *Clay Minerals*, 39, 85-98, 2004.
- Ockert-Bell, M. E., et al., Absorption and scattering properties of the Martian dust in the solar wavelengths, *J. Geophys. Res.*, 102, 9039-9050, 1997.
- O'Reilly, W., Magnetic Minerals in the Crust of Earth, *Rep. Prog. Phys.*, 39, 857-908, 1976.
- O'Reilly, W., *Rock and Mineral Magnetism*, Blackie and son Limited, Glasgow, 1984.
- Pollack, J. B., et al., Properties of aerosols in the Martian atmosphere as Inferred from Viking Lander Imaging Data, *Journal of Geophysical Research*, 82, 4479-4496, 1977.
- Pollack, J. B., et al., Properties and effects of dust suspended in the Martian atmosphere, *J. Geophys. Res.*, 84, 2929-2945, 1979.
- Pollack, J. B., Ockert-Bell, M. E., and Shepard, M. K., Viking Lander image analysis of Martian atmospheric dust, *Journal of Geophysical research*, 100, 5235, 1995.
- Rieder R, Gellert R, Brückner J, Klingelhöfer G, Dreibus G, Yen A, Squyres SW. *J. Geophys. Res.*, 108(E12): 8066, 2003.
- Rieder, R. *et al.* Chemical Composition of Martian Rocks and Soils at Meridiani Planum from the Alpha Particle X-ray Spectrometer. *Science* 306, 1746-1749, 2004.
- Roberts, A.P., Y.L. Cui and K.L. Verosub, Wasp-waisted hysteresis loops – mineral magnetic characteristics and discrimination of components in mixed magnetic systems, *J. Geophys. Res.*, 100 (B9), 17909-17924, 1995.
- Schlegel, A., Alvarado, S. F., and Wachter, P., Optical Properties of Magnetite (Fe<sub>3</sub>O<sub>4</sub>), *J. Phys. C: Solid State Phys.*, 12, 1157-1164, 1979.
- Schofield, J. T., et al., The Mars Pathfinder Atmospheric Structure Investigation/Meteorology (ASI/MET) Experiment, *Science*, 278, 1752-1758, 1997.
- Rochette P., J.P. Lorand, G. Fillion and V. Sautter, Pyrrhotite and the Remanent Magnetization of SNC Meteorites: A Changing Perspective on Martian Magnetism, *Earth Planet. Sci. Lett.*, 190, 1-12, 2001.
- Schröder, C., Klingelhöfer, G. and Tremel, W. Weathering of Fe-bearing minerals under Martian conditions, investigated by Mössbauer spectroscopy. *Planet. Space Sci.* 52, 997-1010, 2004.
- Singer R.B., T.B. McCord, R.N. Clark, J.B. Adams and R.L. Huguenin, Mars Surface Composition from Reflectance Spectroscopy: A Summary, *J. Geophys. Res.* 84(B14), 8415-8426, 1979.
- Smith, P. H., M. G. Tomasko, D. Britt, D. G. Crowe, R. Reid, H. U. Keller, N. Thomas, F. Gliem, P. Rueffer, R. Sullivan, R. Greeley, J.M. Knudsen, M. B. Madsen, H. P. Gunnlaugsson, S. F. Hviid, W. Goetz, L. A. Soderblom, L. Gaddis, and R. Kirk, The Imager for Mars Pathfinder experiment, *J. Geophys. Res.*, 102, 4003-4025, 1997.
- Soffen, G.A., The Viking Project, *J. Geophys. Res.*, 82(28), 3959-3970, 1977.
- Squyres, S.W., R.E. Arvidson, E.T. Baumgartner, J.F. Bell III, P.R. Christensen, S. Gorevan, K.E. Herkenhoff, G. Klingelhöfer, M.B. Madsen, R.V. Morris, R. Rieder, R.A. Romero, Athena Mars rover science investigation, *J. Geophys. Res.* 108 (E12), 8062, doi:10.1029/2003JE002121, 2003.

Squyres, S.W., R. Arvidson, J.F. Bell III, J. Brückner, N.A. Cabrol, W. Calvin, M.H. Carr, P.R. Christensen, B.C. Clark, L. Crumpler, D.J. Des Marais, C. d'Uston, T. Economou, J. Farmer, W. Farrand, W. Folkner, M. Golombek, S. Gorevan, J.A. Grant, R. Greeley, J. Grotzinger, L. Haskin, K.E. Herkenhoff, S.F. Hviid, J. Johnson, G. Klingelhöfer, A. Knoll, G. Landis, M. Lemmon, R. Li, M.B. Madsen, M.C. Malin, S.M. McLennan, H.Y. McSween, D. W. Ming, J. Moersch, R.V. Morris, T. Parker, J. W. Rice Jr., L. Richter, R. Rieder, M. Sims, M. Smith, P. Smith, L.A. Soderblom, R. Sullivan, H. Wänke, T. Wdowiak, M. Wolff, A. Yen: "The Spirit Rover's Athena Science Investigation at Gusev Crater, Mars", *Science* 305, 794-799, 2004.

Squyres, S.W., R.E. Arvidson, J.F. Bell III, J. Brückner, N.A. Cabrol, W. Calvin, M.H. Carr, P.R. Christensen, B.C. Clark, L. Crumpler, D.J. Des Marais, C. d'Uston, T. Economou, J. Farmer, W. Farrand, W. Folkner, M. Golombek, S. Gorevan, J.A. Grant, R. Greeley, J. Grotzinger, L. Haskin, K.E. Herkenhoff, S. Hviid, J. Johnson, G. Klingelhöfer, A. Knoll, G. Landis, M. Lemmon, R. Li, M.B. Madsen, M.C. Malin, S.M. McLennan, H.Y. McSween, D. W. Ming, J. Moersch, R.V. Morris, T. Parker, J.W. Rice Jr., L. Richter, R. Rieder, M. Sims, M. Smith, P. Smith, L.A. Soderblom, R. Sullivan, H. Wänke, T. Wdowiak, M. Wolff, A. Yen, The Opportunity Rover's Athena Science Investigation at Meridiani Planum, Mars, *Science*, 306, 1698-1703, 2004.

Tanaka, T., Optical Constants of Polycrystalline 3d Transition Metal Oxides in the Wavelength Region 350 to 1200 nm, *Japanese Journal of Applied Physics*, 18, 1043, 1979.

Tauxe, L., T.A.T. Mullender and T. Pick, Potbellies, wasp-waists, and superparamagnetism in magnetic hysteresis, *J. Geophys. Res.*, 101 (B1), 571-583, 1996.

Tomasko M.G., Doose, L.R., Lemmon, M., Smith, P.H., Wegryn, E., Properties of dust in the Martian atmosphere from the Imager on Mars Pathfinder, in *Journal of Geophysical Research – Planets*, 104 (E4), 8987-9007, 1999.

Yen, A. *et al.* Subsurface Weathering of Rocks and Soils at Gusev Crater. LPSC XXXVI 1571, 2005a.

Yen, A.S., R. Gellert, C. Schröder, R.V. Morris, J.F. Bell III, A.T. Knudson, B.C. Clark, D.W. Ming, J.A. Crisp, R.E. Arvidson, D. Blaney, J. Brückner, P.R. Christensen, D.J. DesMarais, P.A. de Souza Jr., T.E. Economou, A. Ghosh, B.C. Hahn, K.E. Herkenhoff, L.A. Haskin, J.A. Hurowitz, B.L. Joliff, J.R. Johnson, G. Klingelhöfer, M.B. Madsen, S.M. McLennan, H.Y. McSween, L. Richter, R. Rieder, D. Rodionov, L. Soderblom, S.W. Squyres, N.J. Tosca, A. Wang, M. Wyatt and J. Zipfel, An Integrated View of the Chemistry and Mineralogy of Martian Soils, *Nature* 436, 49-54, 2005b.

## Figures

NB: All figures designed for either 80 mm (1 JGR column) or 160 mm (2 JGR columns) full width. We have systematically tried to minimize color, when designing the figures. For MB spectra, we would prefer 160 mm full width (otherwise we kill the resolution that is in these spectra).

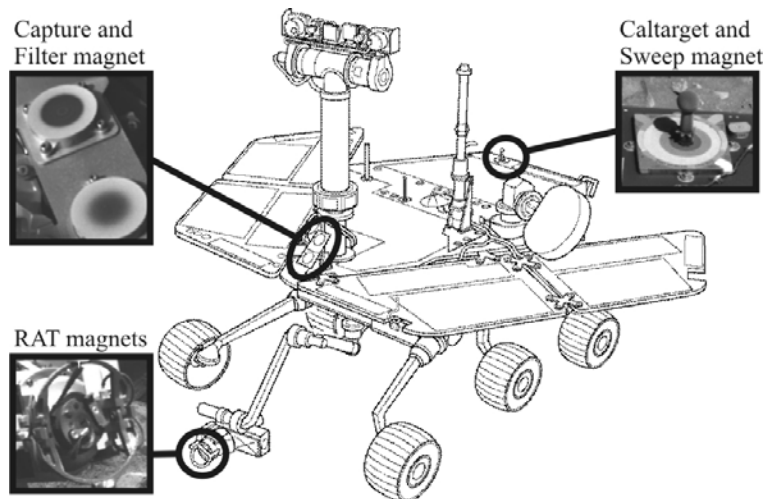


**Fig.1.1** Permanent magnets onboard the Mars Exploration Rovers. The insets show images of the magnets acquired by the panoramic camera (Pancam) that is mounted on top of the camera mast. *Top left* (image obtained on sol A206, at 440 nm): Capture and Filter magnet (45 mm in diameter). These magnets are mounted obliquely in front of the camera mast. The lower magnet is the Capture magnet and is located furthest away from the mast. *Bottom left* (sol A068, 440 nm): The image is about 100 mm across and shows the butterfly structure of the Rock Abrasion Tool (RAT) with four magnets (5.9 mm in diameter) built into its revolving base plane (33.4 mm in diameter). *Top right* (sol A149, 440 nm): Pancam image of the caltarget and the Sweep magnet. The latter has an elongated shape and is found to the right of the caltarget. The long axis of the Sweep magnet measures 20 mm.

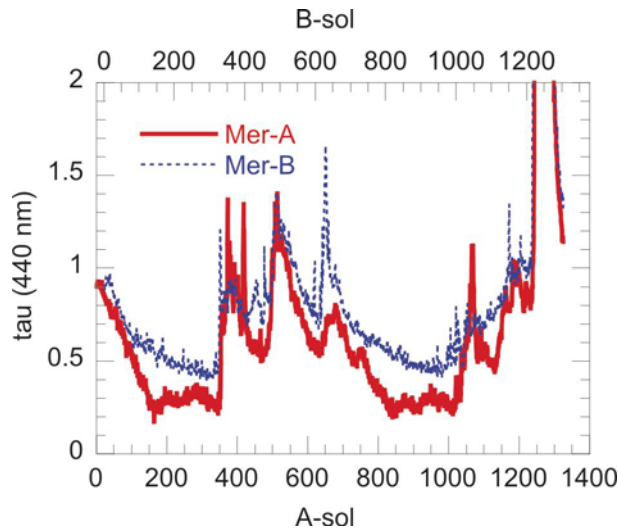


**Fig.2.1** Atmospheric dust opacity (measured at  $\lambda = 440$  nm) at both landing sites. Throughout the entire mission the opacity was higher at the MER-B site. The top abscissa (referring to MER-B) has been shifted by 21 sols with respect to the bottom abscissa (MER-A), in order to clearly display the seasonal behavior: Sol 1 corresponds to  $L_S = 327.5^\circ$  (MER-A) and  $338.9^\circ$  (MER-B), i.e. late southern-hemisphere summer. The first opacity spikes appear at A-sol  $\sim 351$  and B-sol  $\sim 330$  ( $L_S \sim 136^\circ$ , mid southern-hemisphere summer) and persist over several hundred sols. Next onset of such spikes is one Martian year later at A-sol  $\sim 1011$  and B-sol  $\sim 990$  ( $L_S \sim 132^\circ$ ). Unusual high opacities (greater than 4 and at the time record-breaking) are measured at A-sol  $\sim 1240$  and B-sol  $\sim 1260$ .

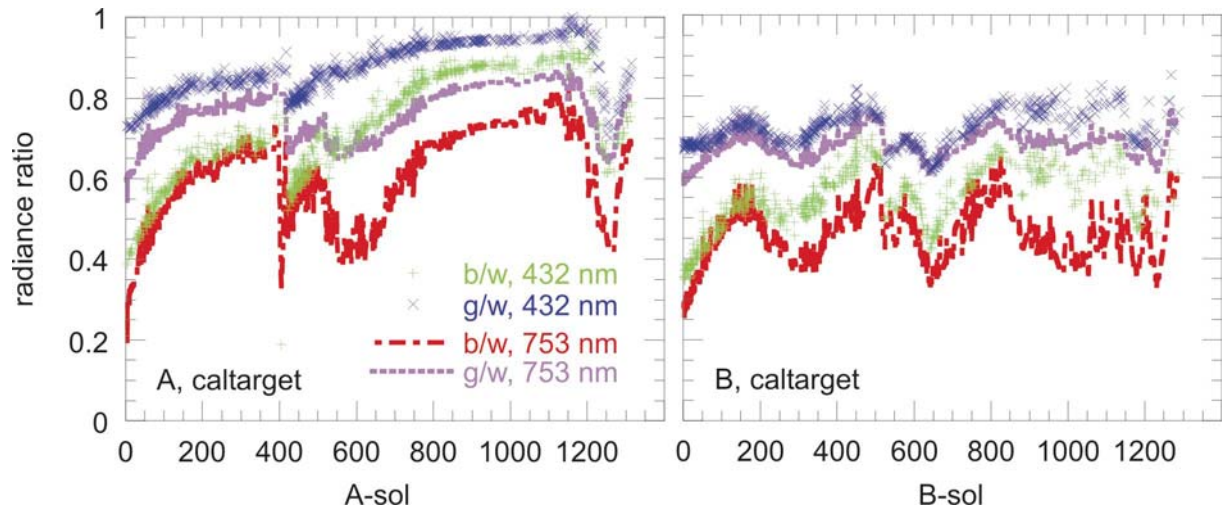


**Fig.2.2** Contamination of the Pancam caltargets by airborne dust: The radiant power of grey (g) and black regions (b) on the caltarget as ratioed to the white region (w). Strong contamination of the caltargets by airborne dust lets these ratios tend to unity. Green and blue crosses are based on images acquired through the blue Pancam filters ( $\lambda = 432$  nm). Red and magenta lines are based on NIR Pancam images ( $\lambda = 753$  nm).

Left: MER-A: A prominent dust cleaning event occurred at sol  $\sim 19$ . A moderate dust cleaning period in the sol range 500-600 can only be seen in the NIR data, indicating that the dust layer is optically semi-infinite in the blue, but not in the NIR region. Strong dust cleaning has been observed in the sol range 1200-1260.

Right: MER-B: Periods of dust accumulation on the caltarget (sols 1-165, 300-500, 640-830) and gentle gradual cleaning (sols 165-300, 500-640) follow each other. A prominent dust cleaning event occurred at sol  $\sim 510$ . The overall caltarget dust contamination on MER-B is smaller than that on MER-A.

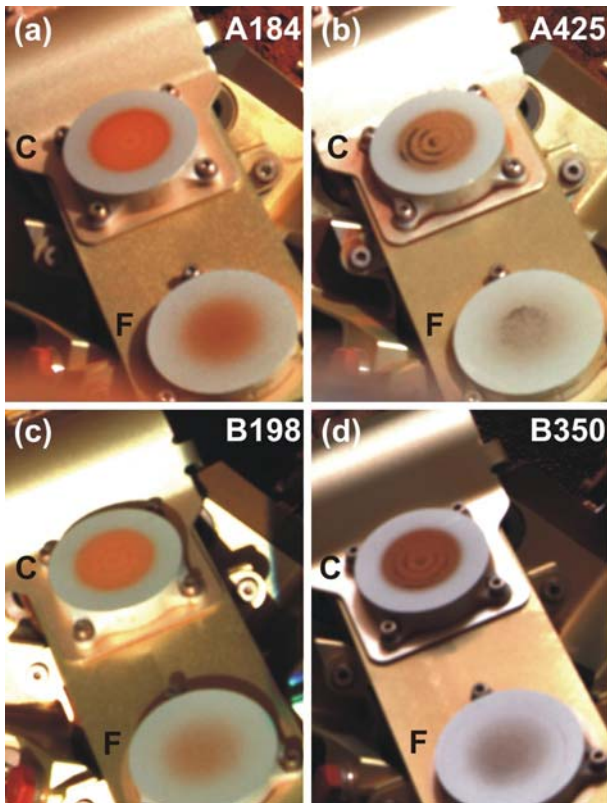


**Fig.3.1** False-color images of the Capture (C) and filter (F) magnets before and after events of strong winds. Both dust pattern and color change significantly after such events. The RGB color images are composed of three equally weighted IOF-calibrated, left-eye Pancam images (440 nm, 535 nm, 750 nm) and should be intercomparable in terms of color. The images are stretched from 0 to 0.30 (A184, B198) and from 0 to 0.35 (A425, B350).

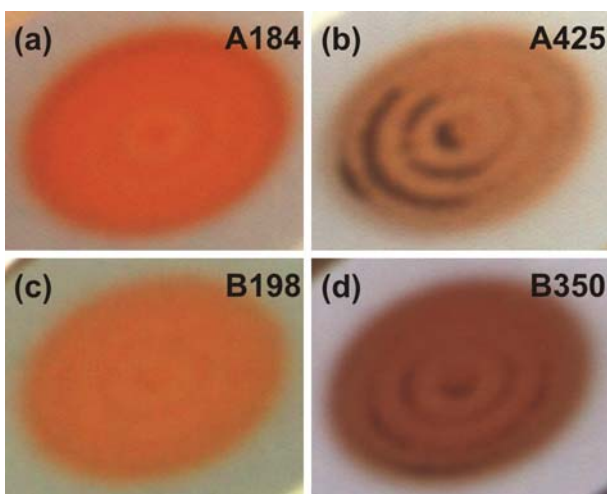


**Fig.3.2** Zoom of Capture magnet in fig. 3.1.

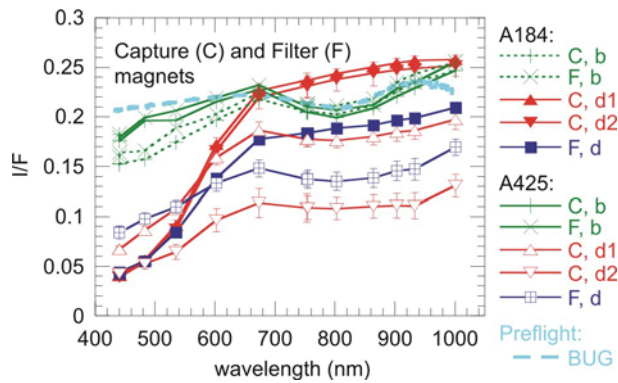


**Fig.3.3** Reflectance spectra (I/F) of dust on the MER-A Capture (C) and Filter (F) magnets before (A184) and after (A425) events of strong wind. Green crosses/lines refer to the border (b) region outside the circular dust (d) cover. Filled and empty symbols refer to A184 and A425, respectively. Red triangles and blue squares refer to Capture and Filter magnet, respectively. The reflectance spectra of two distinct (dust covered) regions of the Capture magnet (denoted d1 and d2, respectively) are shown. During the period of continuous dust accumulation (up to A-sol ~ 400) these regions have almost similar reflectance. After events of strong wind (observed around sol 419) the spectra are very different, indicating that two distinct dust units (a bright one (d1) and a dark one (d2), interpreted as weakly and strongly magnetic, respectively) have been accumulated in different regions on the active surface of the Capture magnet. Also shown: Reflectance data as recorded by the Bloomsburg University Goniometer (BUG) of a flight-like witness piece of the Filter magnet surface.

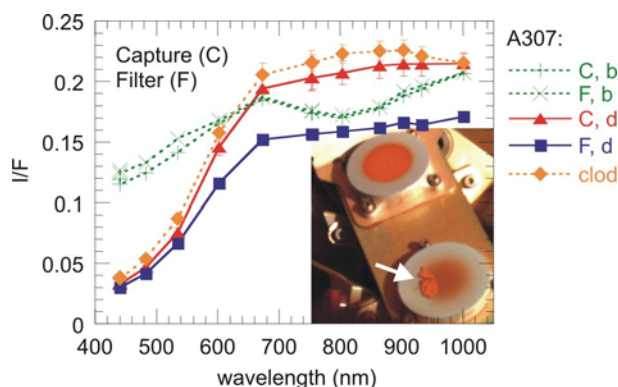


**Fig. 3.4** Thick versus thin layers on the A307 Capture/Filter magnets: The soil clod (marked by a white arrow) was brought to the magnets by IDD motion around A243 and provides a unique opportunity to compare optically thick material to thin layers in terms of their reflectance spectra that were acquired at the very same lighting/viewing geometry. It can be seen that the soil clod spectrum nicely matches the one of thick dust layers on the sweep magnet, while the spectra of (thin) dust layers on the Filter/Capture magnets are basically flat in the NIR region. The false-color image has been generated from IOF-calibrated left-eye Pancam images (440 nm, 535 nm, 750 nm, equally stretched from 0 to 0.25) as in figs. 3.1-3.2.

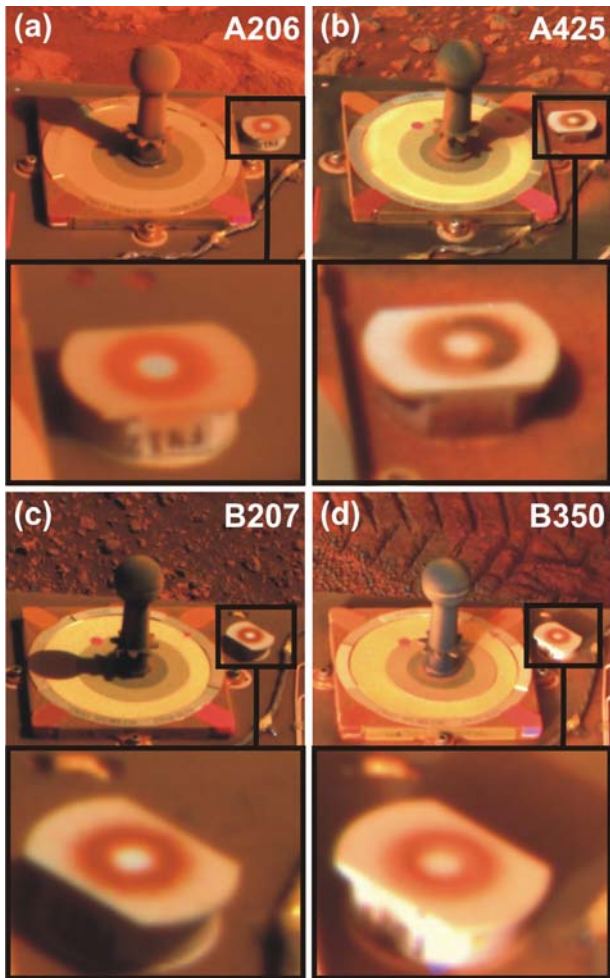


**Fig.3.5** False-color images of Pancam caltarget and sweep magnet before and after events of strong winds. Dust pattern and color change after such events, especially in the case of MER-A. Image B350 has been acquired late (16:46 LST) with grazing solar incidence (note the long shadows cast by caltarget mast and sweep magnet housing). Even the B350 dust ring on the sweep magnet casts a clear shadow that allows a rough estimation of dust layer thickness. The RGB color images are generated as described in the caption to fig.3.1 with following stretching parameters: 0 - 0.23 (A206), 0 - 0.26 (A425), 0 - 0.30 (B207) and 0 - 0.08 (B350).

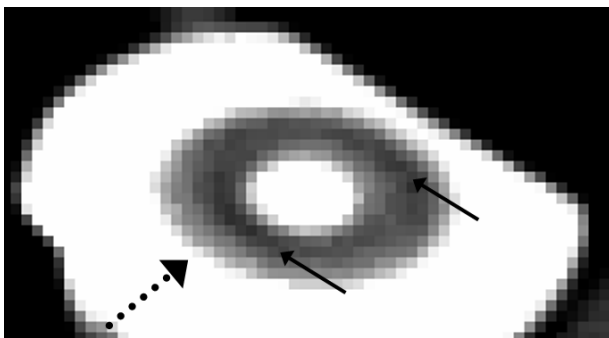


**Fig. 3.6** B350 sweep magnet (RAD calibrated L7 image stretched from 0.0015 to 0.0040). Solid arrows indicate the darker parts due to shading by the topography of the dust ring. The dotted arrows indicate the direction of the incident sun light as projected onto the surface of the sweep magnet.

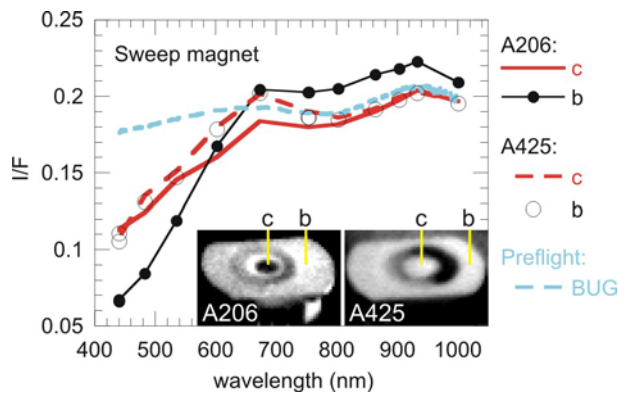


**Fig.3.7** Reflectance spectra ( $I/F$ ) of border (b) and center (c) region the MER-A sweep magnet before (A206) and after (A425) events of strong wind. The insets are RAD calibrated L2 ( $\lambda = 754$  nm) Pancam images stretched from 0.025 to 0.029 (A206) and 0.025 to 0.044 (A425). Also shown: Reflectance data as recorded by the Bloomsburg University Goniometer (BUG) of a flight-like witness piece of the Sweep magnet surface.

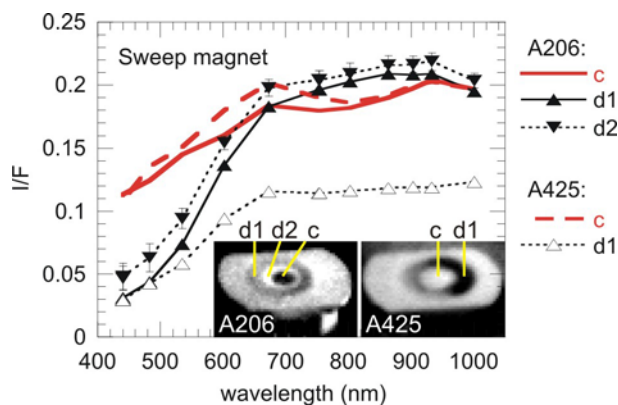


**Fig.3.8** Reflectance spectra ( $I/F$ ) of ring regions (dust covered, labeled: d1, d2) and center region (c) of the MER-A sweep magnet before (A206) and after (A425) events of strong wind. The insets are stretched as in fig. 3.7. The d2 spectrum refers to the bright ring that can be seen in L2 Pancam images of the sweep magnet.

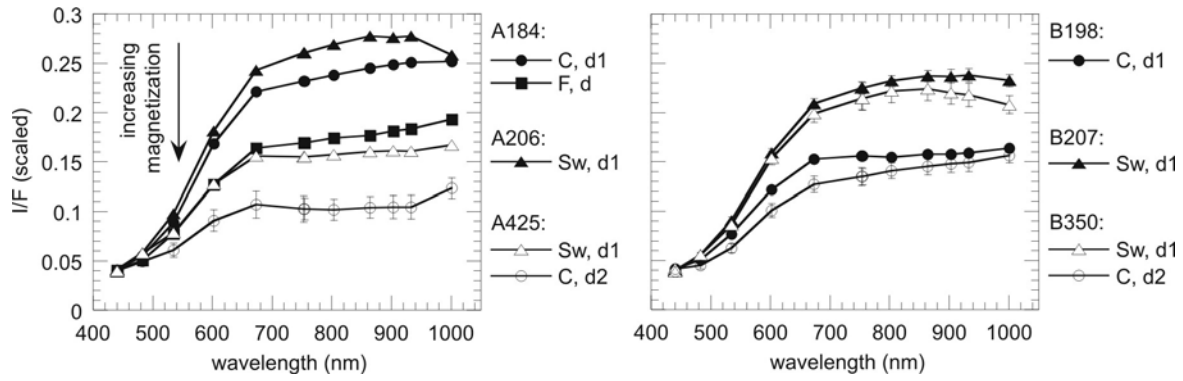


**Fig.3.9** Reflectance spectra ( $I/F$ , scaled to 4% at  $\lambda = 440$  nm) of dust units on the MER-A Capture, Filter and Sweep magnets before (A184, A206) and after (A425) events of strong wind. This diagram provides information on the shape of the spectra, since all spectra are scaled to the same value at 440 nm. The Capture magnet labels “d1” and “d2” refer to the regions defined in fig. 3.3. The sweep magnet label “d1” refers to the region designated in fig. 3.8. MER-B dust is seen to be less reddish than MER-A dust. The NIR shape of the spectra are controlled by layer thickness. Thin layer spectra are dominated by the underlying aluminum surface, while thick layers have reflectance spectra with a maximum near 800-900 nm. The strong NIR maximum of the B350 Sweep magnet spectrum (d1) may, however, be partially caused by the grazing incidence that (in addition to backscattering geometry) certainly minimizes the impact of the underlying aluminum layer on the “2-layer spectrum”. The particular NIR shape of the B350 Capture magnet spectrum (d2) is not understood.



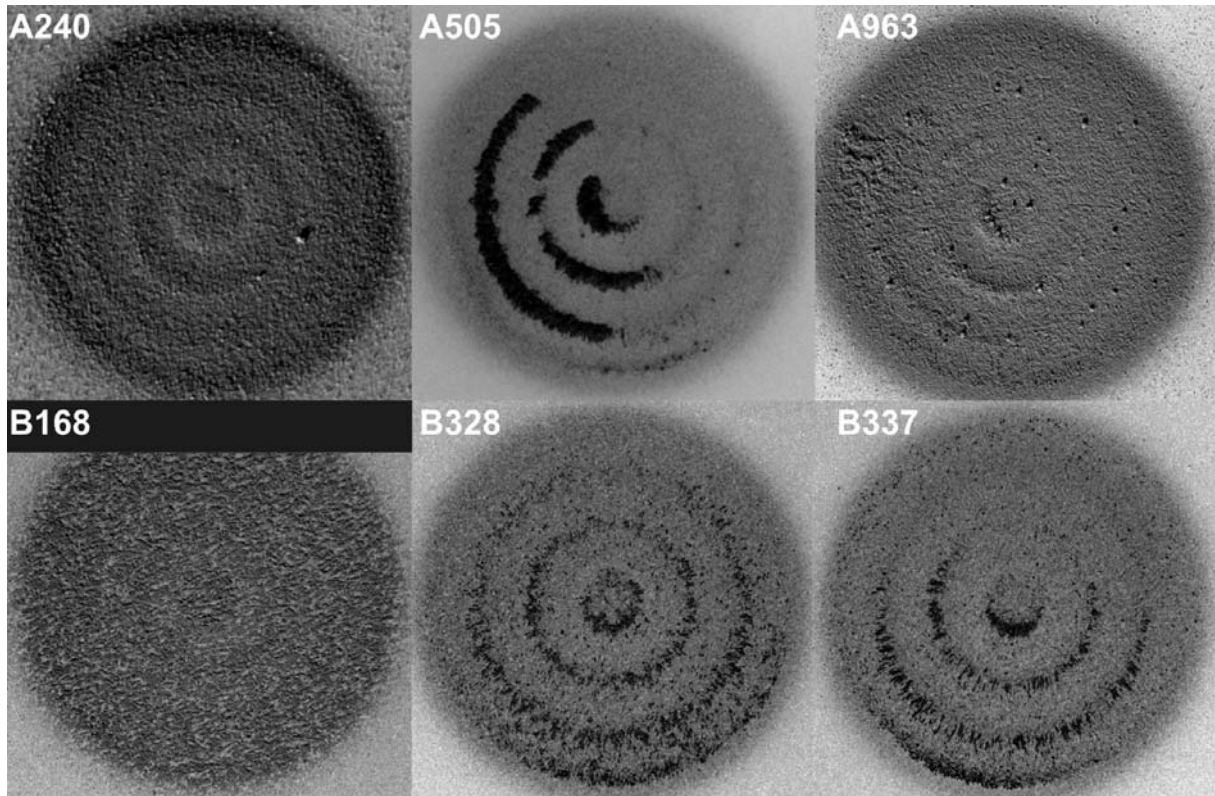


**Fig.4.1** Dynamics of dust capture on the Capture magnet as documented by the Microscopic Imager. Top row: Spirit, sols A240, A505 and A963. A strong wind event was seen around sol 419. The A963 ( $L_S = 109^\circ$ ) image shows a thick dust layer that has accumulated after extended stand down during southern hemisphere winter. Bottom row: Opportunity, B168, B328 and B337. The dust in the center and on the outermost ring is considerably re-distributed over a short period of time (less than 10 sols). The particle chains in the image from sol 337 reveal a strong magnetic selection that may have been caused by a strong wind event on sol 331 [Kinch et al., 2007]. The B168 image does not cover the entire dust pattern. Each image is about 25 mm across.

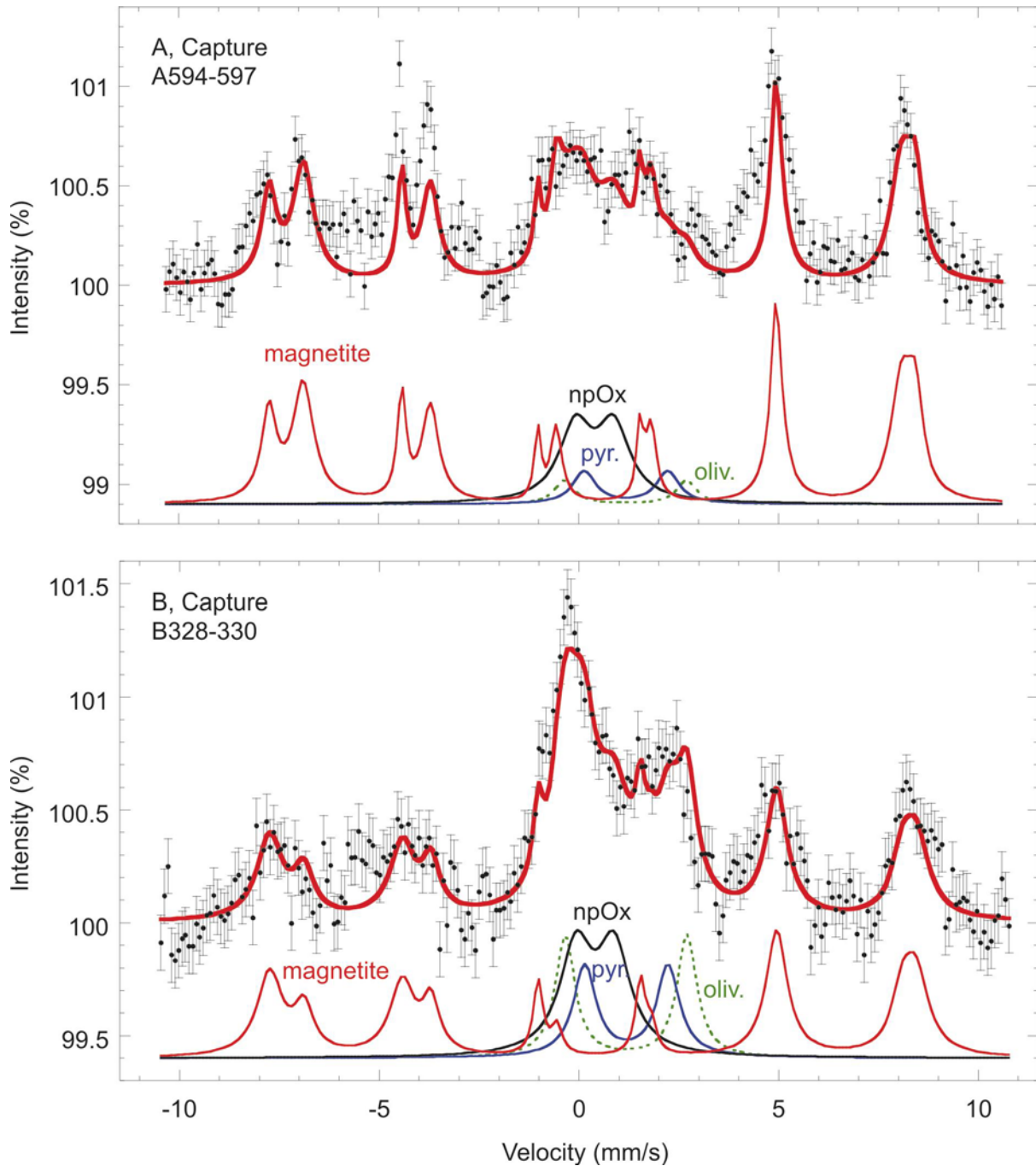


**Fig.5.1** Mössbauer spectra of Capture magnet dust on both rovers. The spectra have been acquired when the dust layer on the Capture magnet on both rovers was of comparable net "iron-thickness" (giving rise to an APXS-Fe signal of 2.0 ~ 2.5 cps; cf. fig.6.2). Differences between these spectra reveal substantial differences between dust units at the two landing sites (cf. main text). Despite the poor statistics (caused by the thin dust layer) magnetite is clearly identified in both spectra. The MER-B spectrum (lower diagram), though with a slightly different fit, has been published earlier by [Goetz et al., 2005].

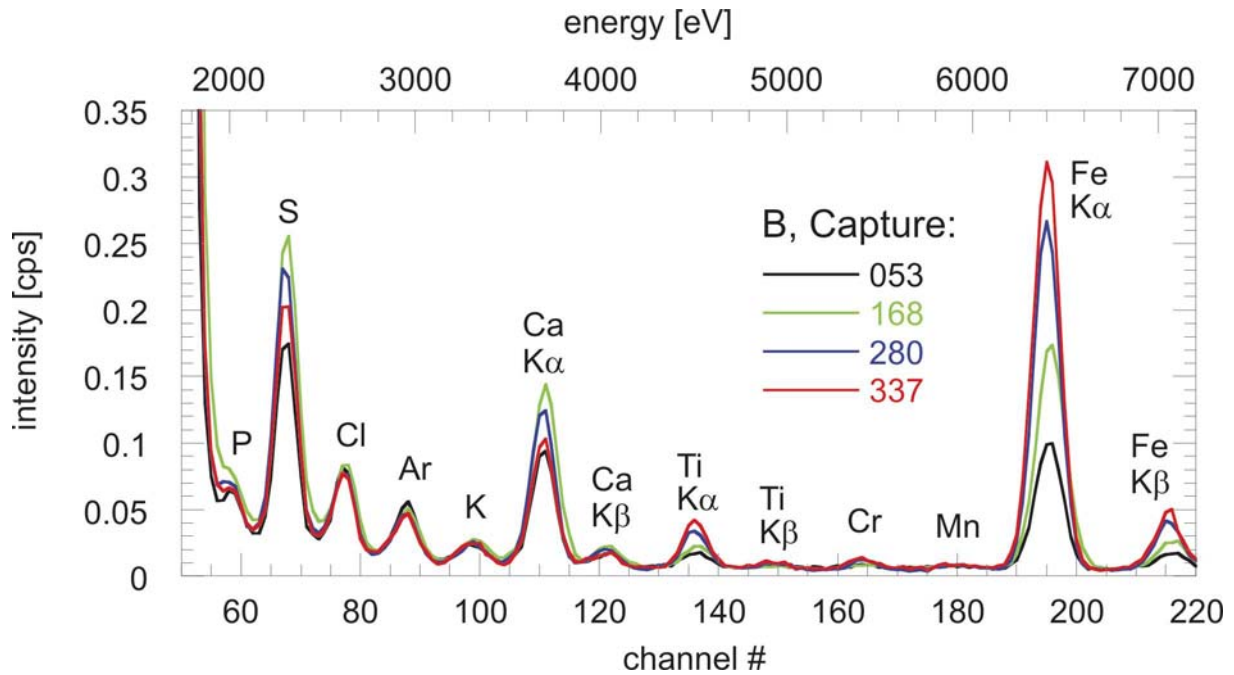


**Fig.6.1** APXS spectra of MER-B Capture magnet dust acquired on sols 53, 168, 280 and 337. Energy (top abscissa) and channel number (bottom abscissa) are related to each other by  $E(\text{eV}) \sim 136.18 + 32.12 \cdot \text{channel\#}$ . The steep increase at small energies is due to the strong aluminum peak centered at around 1.5 keV that in turn is caused by the aluminum cover of the magnet. Visual inspection of these spectra suggests a correlation between Ti and Fe, as well as a correlation between S and Ca. Note the particular high abundance of sulfur at sol 168 (further discussed in the text).

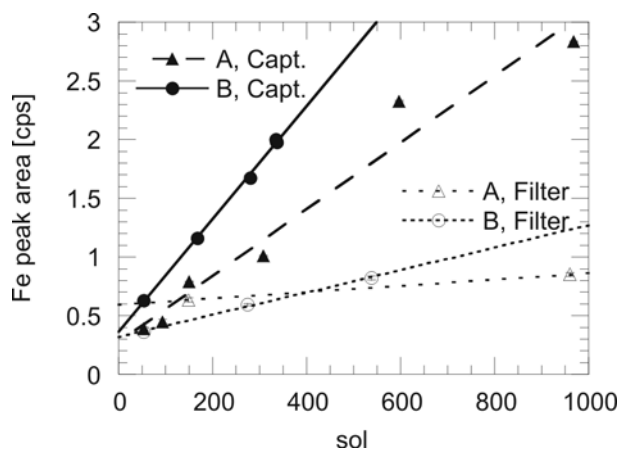


**Fig.6.2** Accumulation of the element iron on the magnets as a function of the sol number. Error bars are drawn, but they are smaller than the plot symbol in all cases. The higher accumulation rate on MER-B magnets (as compared to MER-A) is likely related to the higher atmospheric dust loading at the B site. The straight-line fits shall guide the eye: There is no physical reason to expect a linear dependence. The MER-A Capture magnet shows a significant deviation from linearity implying a different – or substantially varying – dynamics of the dust accumulation. The ability of the magnets to accumulate iron can be ordered as follows: A, Filter < B, Filter < A, Capture < B, Capture, where each un-equality sign (<) stands for a factor 2~3.

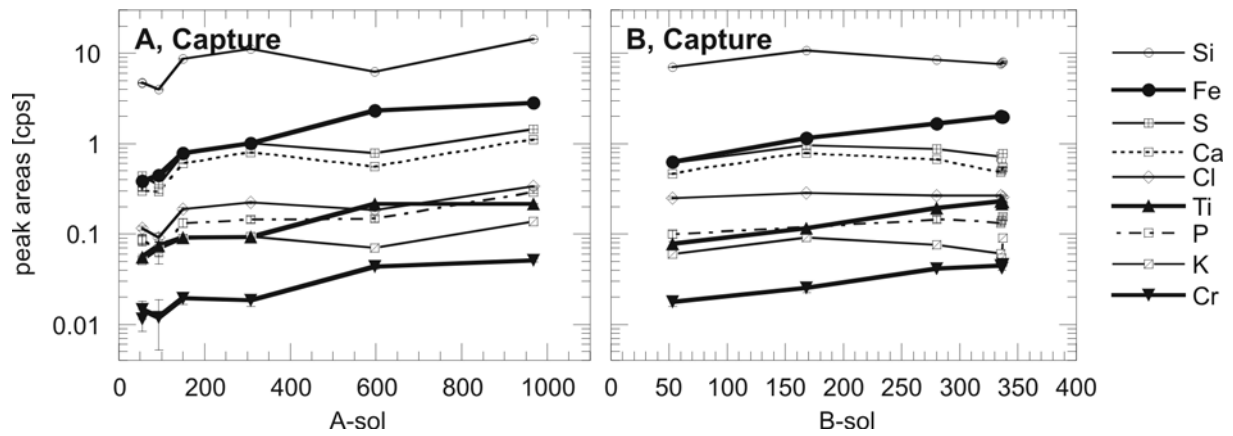


**Fig. 6.3** Accumulation of major elements onto the magnets (expressed as APXS counts per second (cps)). The curves for Fe, Ti and Cr are highlighted by thick lines, and visual inspection of these data suggest that these three elements are correlated and belong to the (strongly) magnetic phase. All other elements (Si, S, Ca, Cl, P, and K) belong to a weakly magnetic (or non-magnetic) phase and belong to particles that can be removed by events of strong winds. The minimum for the abundance of these elements on the MER-A Capture magnet reveals one or several dust cleaning events in the time frame sol 305 to 597.

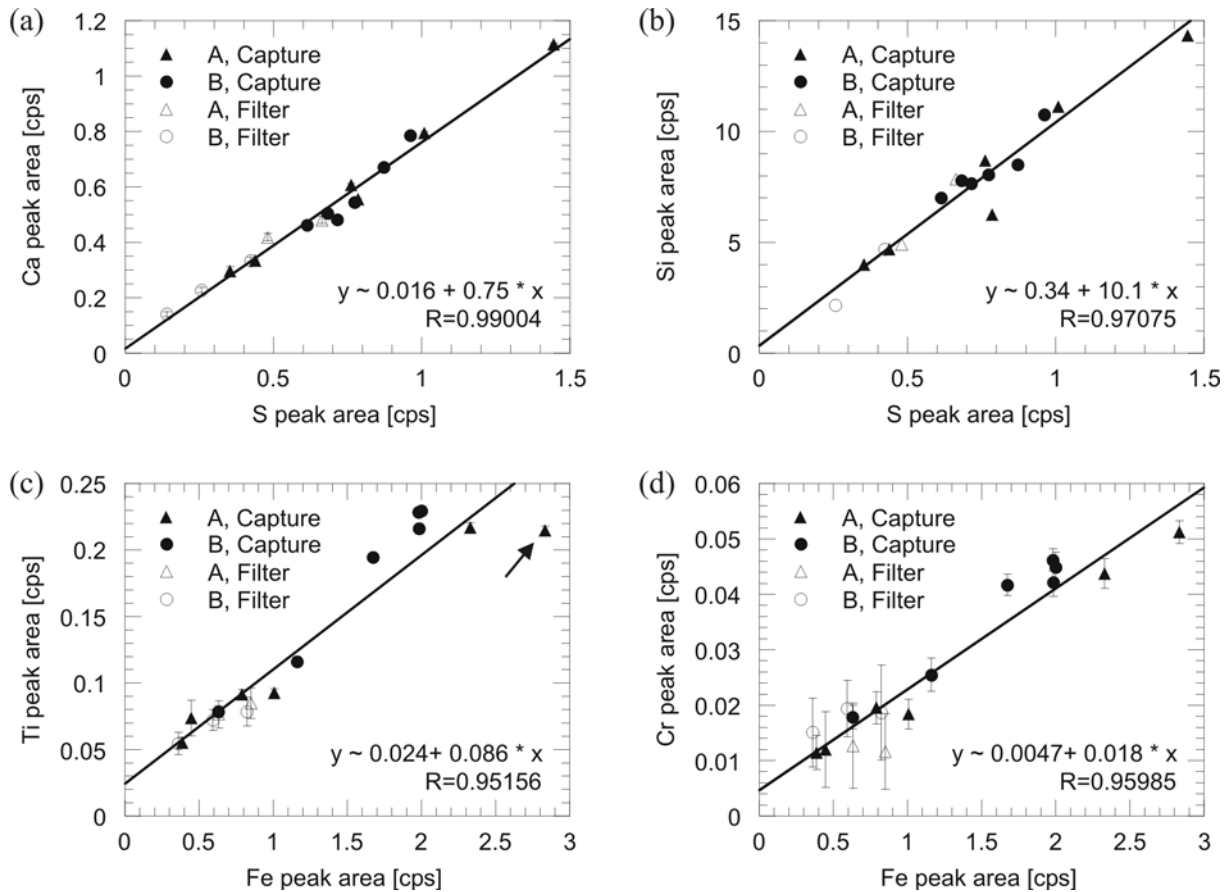


**Fig.6.4** Correlation between abundances of selected elements. Filled and empty symbols refer to Capture and Filter magnets, respectively. The low-abundance part of these diagrams is dominated by Filter magnet data - as expected. Straight-line fits are drawn through all data (Capture and Filter magnets on both rovers) without weighting. (a) Ca versus S: The excellent correlation suggests that these two elements actually appear within the same mineral phase that may be related to  $\text{CaSO}_4 \cdot n\text{H}_2\text{O}$  (such as anhydrite or gypsum). (b) Si versus S: This (somewhat unusual) plot shows the correlation between two anion-forming elements. The correlation is of lower quality as compared to the previous case (Ca versus S) implying that Si and S belong to the same weakly magnetic (or non-magnetic) subgroup of dust particles that is captured/released by the magnets. (c) Ti versus Fe: Clearly a correlation between these two elements implying the occurrence of titano-magnetite in the airborne dust. The A968 data point (marked with black arrow) is not understood. (d) Cr versus Fe: The clear correlation between these two elements implies that the titano-magnetite (or a mineral closely associated with this mineral) in the dust contains chromium.

### H.1.3 Paper III

#### Fit;o) - A Mössbauer spectrum Fitting program

*by*

Jari í Hjöllum and Morten Bo Madsen

*In submission to Nuclear Instruments and Methods in Physics, Section B.*



# Fit;o) - A Mössbauer spectrum fitting program

Jari í Hjøllum <sup>a,b</sup>, Morten Bo Madsen <sup>a</sup>,

<sup>a</sup>*Earth and Planetary Physics, Juliane Maries vej 30, Niels Bohr Institute,  
University of Copenhagen, Denmark.*

<sup>b</sup>*Materials Research Department, Building 775, Risø National Laboratory,  
Technical University of Denmark, Fredriksborgvej 399, DK-4000 Roskilde,  
Denmark.*

---

## Abstract

Fit;o) is a Mössbauer fitting and analysis program written in Borland Delphi. It has a complete graphical user interface that allows all actions to be carried out via mouse clicks or key shortcut operations in a WYSIWYG fashion. The program does not perform complete transmission integrals, and will therefore not be suited for a complete analysis of all types of Mössbauer spectra and e.g. low temperature spectra of ferrous silicates. Instead, the program is intended for application on complex spectra resulting from typical mineral samples, in which many phases and different crystallite sizes are often present at the same time. The program provides the opportunity to fit the spectra with Gaussian, Lorentzian, Split-Lorentzian, Pseudo-Voigt, Pseudo-Lorentz and Pearson-VII line profiles for individual components of the spectra. This feature is particularly useful when the sample contains components, that are affected by effects of either relaxation or interaction among particles. Fitted spectra may be printed, fits saved, data files exported for graph creation in other programs, and analysis tables and reports may be exported as plain text or L<sup>A</sup>T<sub>E</sub>X files. With Fit;o) even an inexperienced user will soon be able to analyze and fit relatively complex Mössbauer spectra of mineralogical samples quickly without programming knowledge.

PACS: 33.45.+x , 82.80.Ej , 61.18.Fs

### *Key words:*

Mössbauer spectra, Mössbauer fitting, mineralogical analysis, <sup>57</sup>Fe, complex mixture

---

---

*Email addresses:* jari.hjoellum@risoe.dk (Jari í Hjøllum),  
mbmadsen@fys.ku.dk (Morten Bo Madsen).

## 1 Introduction

During work with analysis of Mössbauer spectra we found that existing analysis software packages however competent (i.e. Mfit [1], Recoil [2], MacFit [3], MossWinn[4]) could not fulfill our needs of being simple and yet very flexible. For fitting of spectra with many components, as is typical for samples with complex mineral assemblies, advanced programs are in many cases too detailed to be really useful.

We therefore developed this program package which attempts to mitigate these issues, and thus provides a powerful tool for rapid fitting of complex Mössbauer spectra.

The program has been downloaded around 100 times in several versions, and an estimate of regular users is around 20. The program package has been used in the preparation of several articles or talks [5–9].

## 2 Program summary

Fit;o) is a program for fitting and analyzing transmission and scattering geometry  $^{57}\text{Fe}$  Mössbauer spectra of metals, alloys and mixtures of ferric oxides, oxyhydrates and silicates. The program can be expanded to handle other Mössbauer isotopes as well. It has a complete graphical user interface, which allows all actions to be performed via mouse clicks or key shortcuts. The program accepts currently both particular plain text files (.exp-files, see [10,11] for a definition) and comma-separated files e.g. counts vs. velocity (velocity;counts) as data input. It is the intention to release the source code under an open license.

Mössbauer spectra can be fitted using singlets, doublets and sextets (all with a selection of line profiles of which Lorentzian is default) and the fit model can be saved for later reloading for example for further refinement of the fit. Fitted and unfitted spectra can be saved as reports and saved as both plain text and in customizable L<sup>A</sup>T<sub>E</sub>Xformat, and spectra can be printed with a fit report.

The program contains a precompiled list of Mössbauer data of many common iron compounds with an option for the user to edit or add new compounds.

Calibration data for Mössbauer experimental setups can be extracted from calibration spectra, and saved in separate calibration .cal-files (see [10,11] for a description).

The settings window contains a wide range of customizable settings through which the user may customize the appearance and behavior of the program. Backwards compatibility is ensured, as file formats are kept unchanged and user-changed files are not overwritten.

The web update option provides an easy and automated way to keep the software updated with the latest program version.

The program does not perform complete transmission integrals, and will therefore not be suited for a complete analysis of all types of Mössbauer spectra. Also the fitting does not use the complete spin-Hamiltonian (but approximations) so for example magnetic (low-temperature) spectra of silicates cannot be analyzed by the programme.

Some of Fit;o)'s main features are:

- Microsoft Windows 2000/XP compatible.
- Easy to install, no external dependencies, and safe uninstallation/removal.
- Complete point-and-click graphical user interface.
- Easy saving and loading of fit models.
- Most program parameters as customizable.
- Working with several spectra (MDI<sup>1</sup>) at a time is possible.
- Created with object-oriented programming.

### 3 Description

#### 3.1 Prerequisites

As noted in the introduction, execution of Fit;o) requires an updated Microsoft Windows 2000, Microsoft Windows XP operating system. A screen resolution of a least 1024x768 with a 16 bit color depth is recommended.

#### 3.2 Installation and execution

The program is available at <http://hjollum.com/jari/zzbug/fit/>. After installation and execution the main options are:

- Open the selected type spectrum by selecting an appropriate icon in File menu.

---

<sup>1</sup> Multi Document Interface

- To open a file in text mode, use the `Open text file` option and to view the application log, use the `Open log` option.

A more detailed description of the program interface can be found in the manual [10] or the web site [11].

### 3.3 *The layout of the graphical user interface*

After the first execution of the program the user is presented to the graphical user interface shown in figure 1. The main window of Fit;o) is divided into five areas (listed from top down), the menu bar, the tool bar, the work area, the window panel and the status panel.

### 3.4 *Fitting*

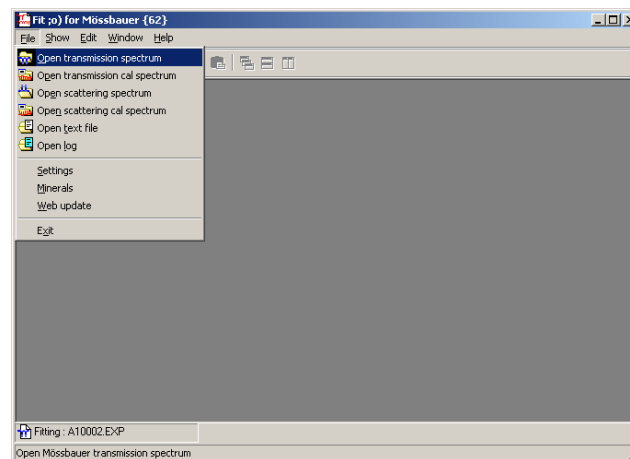


Fig. 1. *Opening a spectrum file.*

When choosing to open a spectrum for fitting, the open spectrum form (figure 2) appears, in which the spectrum to be loaded is chosen. After choosing a spectrum the fit form (figure 3) is opened and the spectrum is loaded.

As fitting components, it is possible to insert either simple (fundamental) components (singlets, doublets, sextets), or to insert predefined mineral components.

Simple components are inserted by clicking one of the spectrum icons in the toolbar, and then marking, position, intensity and width of the components on the graph. The parameter that the user is expected to mark is indicated at the cursor.

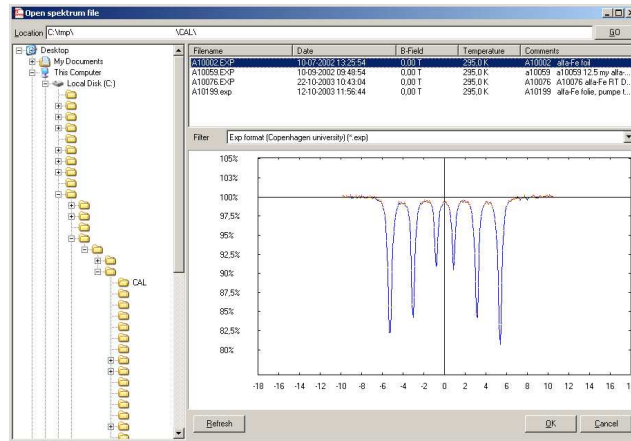


Fig. 2. Choosing the spectrum to open.

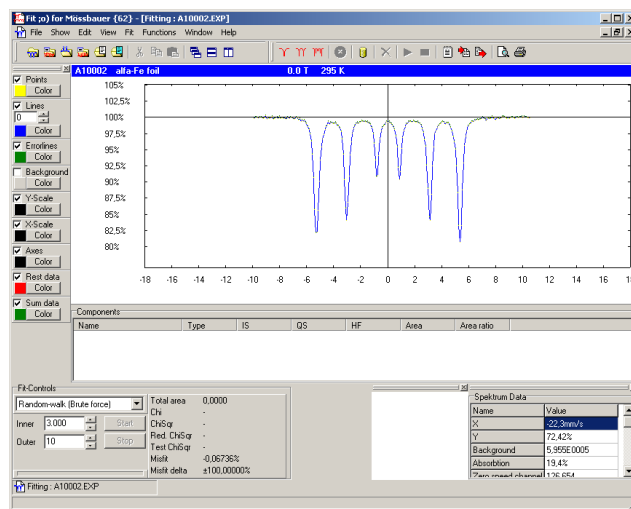


Fig. 3. The fit form with a loaded spectrum.

Predefined (but editable) mineral components are inserted by clicking the cylinder icon in the toolbar, and choosing the mineral. After choosing, one has to mark the intensity of the component on the graph using the mouse cursor.

The fitting algorithm is chosen in the **Fit Controls** combobox in the lower left corner of the form. The fitting process is started and aborted by using the adjacent start and stop.

### 3.5 Calibration

Fitting components are inserted by clicking the button in the toolbar with the sextet icon (see figure 5). When the components have been inserted, either a single fitting run or a series of repetitive fitting runs can be started, through

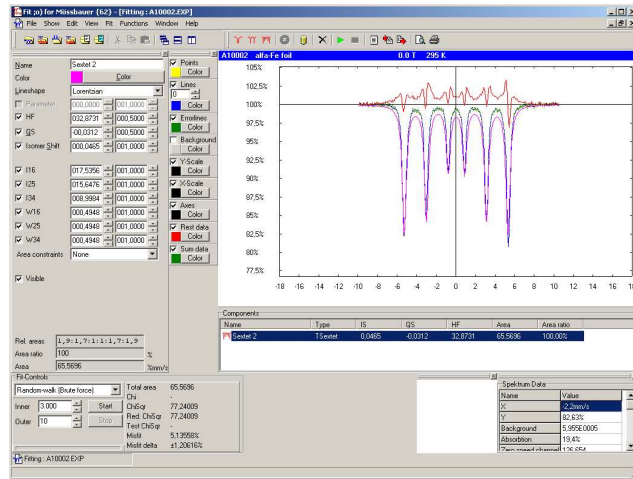


Fig. 4. The fit form with an inserted component.

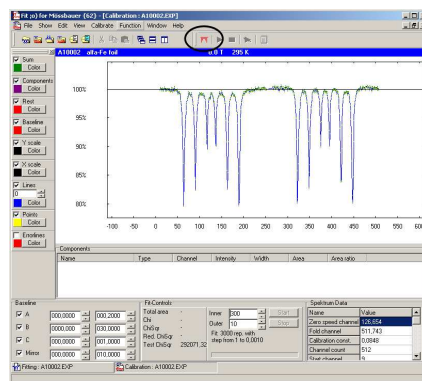


Fig. 5. The calibration form before inserting the calibration fit components. The insert button is marked.

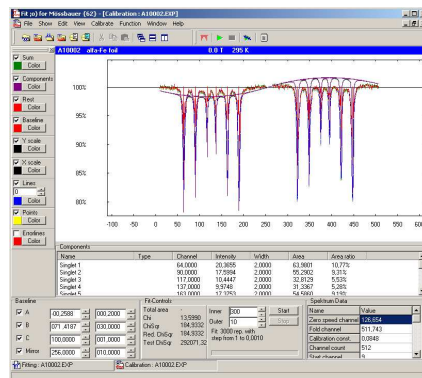


Fig. 6. The calibration form after insertion of the calibration fit components.

the start icons. The result can be saved and exported by clicking the 'notepad' icon.

Name	Temp	Field	Type	IS	QS	HF	Date
Y Iron a-Fe (superparamag...	295.0	0.00	TMSinglet	0.0000			01-04-2003
YY Lepidocrocite g-FeOOH	295.0	0.00	TMDoublet	0.3000	0.9500		01-04-2003
YY Pyrite	80.0	0.00	TMDoublet	0.4200	0.6100		01-04-2003
YY Pyrite	295.0	0.00	TMDoublet	0.3100	0.6100		01-04-2003
YY Wustite A Fe <sub>1-x</sub> O (x=...	295.0	0.00	TMDoublet	0.8100	0.4600		01-04-2003
YY Wustite B Fe <sub>1-x</sub> O (x=...	295.0	0.00	TMDoublet	0.8500	0.7800		01-04-2003
YY Ilmenite FeTiO <sub>3</sub>	295.0	0.00	TMDoublet	1.0700	0.6800		01-04-2003
YY Ulvospinel Fe <sub>2</sub> TiO <sub>4</sub>	295.0	0.00	TMDoublet	1.0700	1.8500		01-04-2003
YY Ferrosulfite a-FeSO <sub>4</sub>	4.2	0.00	TMSextet	0.4900	0.0000	52.5000	01-04-2003
PI Goethite a-FeOOH	4.2	0.00	TMSextet	0.4900	-0.1300	50.6000	01-04-2003
PI Goethite a-FeOOH	80.0	0.00	TMSextet	0.4900	-0.1300	50.1000	01-04-2003
PI Goethite a-FeOOH	295.0	0.00	TMSextet	0.3700	-0.1300	38.1000	01-04-2003
PI Hematite	4.2	0.00	TMSextet	0.4900	0.2000	54.2000	01-04-2003
PI Hematite	80.0	0.00	TMSextet	0.4900	0.2000	54.2000	01-04-2003
PI Hematite	295.0	0.00	TMSextet	0.3700	-0.1000	51.7000	01-04-2003
PI Ilmenite FeTiO <sub>3</sub>	4.2	0.00	TMSextet	1.2200	1.4300	4.8000	01-04-2003
PI Iron a-Fe	4.2	0.00	TMSextet	0.1200	0.0000	34.0000	01-04-2003
PI Iron a-Fe	80.0	0.00	TMSextet	0.1200	0.0000	33.9000	01-04-2003
PI Iron a-Fe	295.0	0.00	TMSextet	0.0000	0.0000	33.0200	01-04-2003
PI Lepidocrocite g-FeOOH	4.2	0.00	TMSextet	0.4700	0.0000	45.8000	01-04-2003
PI Magnetite	4.2	0.00	TMSextet	0.4400	0.0000	52.6000	01-04-2003

Fig. 7. The minerals administration window.

### 3.6 Minerals

The program contains a list of common and well-known minerals (figure 7), which can be used for as starting point fitting. The mineral data are from [12]. It is possible to edit the listed minerals and save these modifications, and to enter new minerals. This can be done either through the **New**, **Edit** or **Delete** options, or by editing the minerals file manually. The name and location of the minerals file is displayed in top of the window.

## 4 Project planning

In the following we discuss the properties of the program as used for analysis of a transmission/absorption spectrum. However, the discussion is completely valid also for scattering/emission spectroscopy, since there will be only few details differentiating these.

### 4.1 Line shapes

Ideally each Mössbauer absorption line has a Lorentzian line shape, (see table 1). However, there are physical effects that might disrupt or distort the ideal case. For these cases other line shapes are necessary.

In practice most absorption lines are Lorentzians, which may be slightly smeared by a Gaussian due to for instance temperature fluctuations, leading to the Voigt line shape. The Voigt line shape is a convolution of a Lorentzian

and a Gaussian and can be expressed as [13]

$$L_{Voigt}(v) = \int_{-\infty}^{\infty} L_{Gau}(v')L_{Lor}(v - v')dv'. \quad (1)$$

However, this can not be solved analytically, and therefore several approximations to this profile exist. We have implemented three of these: Pseudo-Voigt, Pseudo-Lorentz and Pearson-VII, which are listed in table 1. Especially the Pearson-VII line shape is difficult to implement, since it involves the implementation of the Gamma function [14], which was implemented using Stirlings approximation [15]

$$\Gamma_{Stirling}(z) \cong \sqrt{\frac{2\pi}{z}} \left( \frac{z}{e} \sqrt{z \sinh \frac{1}{z} + \frac{1}{810z^6}} \right)^z, \quad (2)$$

which is accurate to a least 5 digits for  $z > 1$ .

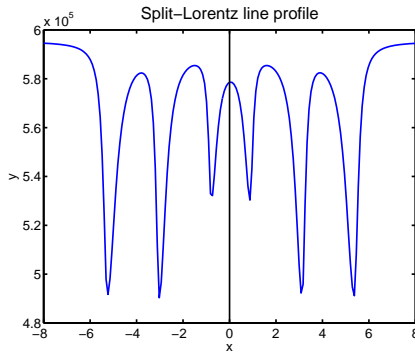


Fig. 8. An example of a spectrum with Split-Lorentzian line profiles. The outer slope of an absorption line is defined as the slope farthest from the center of the component. This of course only applies to doublets and sextets.

The Split-Lorentzian (see figure 8) line shape is commonly used for samples in which small-particle effects or interactions distort the line shapes in such a way that the outer slope is steeper than the inner slope. The Split-Lorentzian line shape is made up of the outer side using one Lorentzian line shape, and the inner side using another shape. The amplitude and center of the two line shapes are kept equal, but the widths vary. The relationship between the widths is usually controlled by defining a width parameter and an asymmetry parameter. The asymmetry parameter is usually known as  $b$ .

When using the Split-Lorentzian line shape in doublets and sextet (see section 4.2) the line shapes are mirrored with respect to the center of the component, and the left side of a line shape is identical to the right side of its mirrored twin.

The line shapes implemented for the Mössbauer analysis and the properties of these are presented in table 1.

Name	Formula	Area	Additional parameters
Lorentzian	$L_{Lor}(v) = I_0 \left( 1 + \left( \frac{2(v-v_0)}{W} \right)^2 \right)^{-1}$	$A_{Lor} = \frac{I_0 W \pi}{2}$	-
Gaussian	$L_{Gau}(v) = I_0 \exp \left( - \left( \frac{2(v-v_0)}{W} \right)^2 \right)$	$A_{Gau} = \frac{I_0 W \sqrt{\pi}}{2}$	-
Split-Lorentzian	$L_{S-L}(v) = \begin{cases} L_{Lor}(W_1) , & v < v_0 \\ L_{Lor}(W_2) , & v \geq v_0 \end{cases}$	$A_{S-L} = \frac{1}{2} \sum_{i=1}^2 A_{Lor}(W_i)$	$b \equiv \frac{W_1}{W_2} - 1$ $W_1 \geq W_2$
Pseudo-Voigt	$L_{Pseu}(v) = \eta \cdot L_{Lor} + (1 - \eta) \cdot L_{Gau}$	$A_{Pseu} = \eta \cdot A_{Lor} + (1 - \eta) \cdot A_{Gau}$	$\eta \in [0; 1]$
Pseudo-Lorentz	$L_{PLor}(v) = I_0 \left( 1 + \left  \frac{2(v-v_0)}{W} \right ^{2+\alpha} \right)^{-1}$	$A_{PLor} = \frac{I_0 W \pi}{2} \frac{2 \sin(\frac{\pi}{2+\alpha})}{2+\alpha}$	$\alpha \in [0; 1.45]$ $\alpha = 0$ Lorentz
Pearson-VII	$L_{PVII}(v) = I_0 \left( 1 + \left( \frac{2(v-v_0)}{W} \right)^2 \frac{1}{m} \right)^{-m}$	$A_{PVII} = \frac{I_0 W \sqrt{m\pi}}{2} \frac{\Gamma(m - \frac{1}{2})}{\Gamma(m)}$	$m \geq 1$ $m = 1$ Lorentz $m \rightarrow \infty$ Gauss

Table 1

*Line shapes used for Mössbauer analysis. Reproduced from [16].*

#### 4.2 Fit components

The three fundamental Mössbauer fitting components are the singlet, the doublet and the sextet with 1, 2 and 6 absorption lines, respectively. All of these components are characterized by their isomer shift (IS).

The splitting of the doublet depend on the quadrupole interaction, and is in the doublet quadrupole splitting (QS).

The singlet, doublet and the sextet have furthermore the line shape a parameter ( $b$ ,  $\eta$ ,  $\alpha$  and  $m$  in table 1) in common. The Split-Lorentzian, Pseudo-Voigt, Pseudo-Lorentz and Pearson-VII line shapes use this property.

The magnetic Zeeman interaction, the magnetic hyperfine field (HF), is only used in the sextet, and needs only to be implemented in the sextet. For sextets this software - presently - can handle only spectra in which the magnetic Zeeman interaction is dominant, so that the quadrupole interaction can be treated as a small perturbation on the magnetic interaction. In the case of the sextet QS indicates the quadrupole shift in contrast to the doublet quadrupole split.

However, since the properties HF, and QS, are the only properties which do not apply to all components, we have provided an interface to them in all components, but disabled them where they are not needed. As mentioned, we

do not use the complete spin-Hamiltonian for calculations of the line positions in the, but rather approximate expressions, which however, have been quite sufficient in most all cases.

The singlet consists of a single line, and the position of the single line is the same as the isomer shift. The expression for the singlet is given by

$$y_i = L(v_i - v_0), \quad (3)$$

where  $L$  is the line shape function providing the value of  $y_i$  as a function of  $v_i$ , and  $v_0$  is the value of the isomer shift.

The doublet consists of two lines, and the centers of the lines are placed at a distance of  $QS$  apart, around the isomer shift. The expression for the doublet is given by

$$y_i = L(v_i - v_0 - \frac{v_0}{2}) + L(v_i - v_0 + \frac{v_{QS}}{2}), \quad (4)$$

where  $v_{QS}$  is the value of the quadrupole splitting.

The sextet consists of six lines, and the centers of the lines are placed at positions dictated by the isomer shift, quadrupole shift and hyperfine field.

The expression for the sextet is given by

$$y_i = \sum_{i=1}^6 L(v_i - v_0 + (-1)^{(1+\delta_{2345})} \frac{v_{QS}}{2} + (-1)^{(1+\delta_{456})} k_{q,w} \cdot B_{HF}), \quad (5)$$

where  $\delta_{mnl}$  is a delta function, which is 1 when  $i$  has one of its values.  $k_{q,w}$  is a Mössbauer proportionality factor, composed of several physical constants. The three values that apply are  $k_{1,6}$ ,  $k_{2,5}$ ,  $k_{3,4}$  for the paired lines.  $B_{HF}$  is the hyperfine field. The  $k_{i,j}$  values are calculated from the general expression for the sextet energy levels, which is given by

$$E_m = -g\beta_n mB, \quad (6)$$

where  $g$  is the Landé factor,  $\beta_n$  is the nuclear magneton, and  $m$  is the m-quantum number. The energy splitting is calculated by

$$|\Delta E_{(i,j)}| = |\Delta E_i| + |\Delta E_j| = 2|\Delta E_i|, \quad (7)$$

where  $(i, j) = (1, 6), (2, 5), (3, 4)$ . Applied to the line pairs  $(1,6)$ ,  $(2,5)$ ,  $(3,4)$  then energy splitting is calculated from

$$|\Delta E_{(i,j)}| = -2(\beta_n B (g_e \frac{3}{2} - g_g \frac{1}{2})) = \beta_n B \cdot g_{ij}, \quad (8)$$

where  $g_g = 0.181208$  and  $g_e = -0.10355$  are the g-factors for the ground state and the excited state respectively, values from [12], and the  $g_{ij}$  factors,

$$g_{16} = -2(g_e \frac{3}{2} - g_g \frac{1}{2}) = 0.491858, \quad (9)$$

$$g_{25} = -2(g_e \frac{1}{2} - g_g \frac{1}{2}) = 0.284758, \quad (10)$$

$$g_{34} = -2(g_e \frac{-1}{2} - g_g \frac{1}{2}) = 0.077658, \quad (11)$$

$$(12)$$

are g-factors extracted from the g-factor for the excited and ground state and  $E_0$  is the transition energy from  $I = \frac{3}{2}$  to  $I = \frac{1}{2}$  for  $^{57}\text{Fe}$  Mössbauer spectroscopy.

The actual calculation being performed is

$$v_{HF} = g_{ij} \beta_n B_{HF} \cdot \frac{c}{2E_0}, \quad (13)$$

using unit conversion this becomes

$$v_{HF} = g_{ij} B_{HF} \frac{\beta_n \cdot c \cdot k}{2E_0 e} \quad (14)$$

$$= g_{ij} B_{HF} \frac{5.0505 \cdot 10^{-27} \text{ J/T} \cdot 3.0 \cdot 10^{11} \text{ mm/s}}{2 \cdot 14.41 \text{ keV} \cdot 1.6022 \cdot 10^{-19} \text{ J/eV}} \quad (15)$$

$$= g_{ij} B_{HF} \cdot 0.32794 \text{ mm/sT}, \quad (16)$$

where  $e$  is the elementary charge. Now the  $k_{q,w}$ 's can be calculated as

$$k_{1,6} = 1.61299 \cdot 10^{-1} \text{ mm/sT}, \quad (17)$$

$$k_{2,5} = 9.33835 \cdot 10^{-2} \text{ mm/sT}, \quad (18)$$

$$k_{3,4} = 2.54672 \cdot 10^{-2} \text{ mm/sT}. \quad (19)$$

### 4.3 Fitting spectra

The program will analyze Mössbauer spectra by fitting a model set by the user, and it will report the result of the fit.

Before any analysis can commence, a background level has to be established/calculated. The background level is calculated as the mean of the value of the outermost 8 channels on each side of the spectrum. Transmission spectra contain absorption lines, which have fewer counts than the background level. The expression for components provided above has to be subtracted from the background to produce a model data series.

The program can also be used for analysis of reflection spectra. Reflection spectra also contain a background level, to which the reflection lines are added. To produce a fitting model, the fitting components are added to the background level.

#### *4.4 Calibration spectra*

The program derives the calibration parameters of the spectrometer from automatic analysis of calibration spectra. The found calibration parameters are then used in the analysis of spectra obtained under circumstances identical to those of the calibration spectrum. In this program version (1.0.0.63) only calibration of linear velocity profiles are implemented. We are well aware that sinusoidal velocity profiles are common in the Mössbauer community, and a later version may be adapted for spectra obtained in the mode.

Contrary to a normal spectrum for Mössbauer analysis, a calibration spectrum is analyzed unfolded with the channel numbers used as reference.

The calibration spectrum usually consists of the spectrum of a thin iron ( $\alpha$ -Fe) foil (12.5  $\mu\text{m}$ ) at 295 K. But other calibration materials can also be used, such as stainless steel and other well characterized iron compounds.

The unfolded calibration spectrum consists of a background level, and 12 absorption lines on the background level figure 5. The calibration is used for finding 3 unknown parameters of the experimental setup, and to provide information on any imperfections of the source/drive system i.e. increased line widths, nonlinearity etc. The three unknown parameters are listed below:

**The folding channel** is the channel (integer) around which the data channels are folded. Operationally (for historic reasons and backwards compatibility) it is defined as the channel number, which is added to channel number 1, e.g. it is the double of the actual folding channel. In a 512 channel setup, it has typically a value of 510-514. It is found by calculating the mean of positions of the lines (1,12), (2,11), etc.

**The zero velocity channel** is defined as the detector channel position (decimal, 5 digits), of the symmetry center of the 295 K spectrum of a thin foil of  $\alpha$ -Fe. It is found in each of the spectrum halves separately. It is found

by locating the mean center of the lines (1,6), (2,5) and (3,4) pairwise, and correspondingly for the second half of the spectrum, and then finding the common center.

**The calibration constant** is the link between the channel number and the source velocity. It is found as the mean value of the known hyperfine field of the absorber material ( $B_{HF} = 33.02$  T for  $\alpha$ -Fe at 295 K) divided by the distances between the transition pairs,  $(i, j) = (1, 6), (2, 5), (3, 4)$ , and scaled by the Mössbauer constants (17). The exact formula is

$$c_{cal} = \frac{1}{6} \sum \frac{g_{ij} \beta_n B_{HF}}{E_0 \cdot c} \left( \frac{1}{P_j - P_i} + \frac{1}{P_{j+6} - P_{i+6}} \right), \quad (20)$$

where  $P_i$  is the channel position of the  $i$ 'th absorption line.

The background line has a shape that is dependent on the mode of operation of the spectrometer (e.g. frequency and velocity range) and geometry of the experimental setup. The radioactive source is placed inside a collimator, and since the source is oscillating with near constant acceleration, the solid angle seen by the source will vary as a function of position. The radiation detected is proportional to the angular area. The baseline shape is approx. that of two parabolas in succession with positive and negative  $a$  values:

$$A = +a \cdot (v - c_M)^2 - b(v - c_M) + c, \quad 1 \leq v \leq c_M, \quad (21)$$

$$A = -a \cdot (v - c_M)^2 - b(v - c_M) + c, \quad c_M \leq v \leq N, \quad (22)$$

where  $A$  is the angular area,  $c_M$  is the mirror channel,  $v$  is the channel number,  $N$  is the number of channels, and  $a$ ,  $b$  and  $c$  are the parabola parameters.

Besides the above calculations, the calibration is able to find the 12 absorption lines ( $^{57}\text{Fe}$ ), and fit these and the baseline to find the calibration constants.

As the equipments available during the development only used a linear velocity drives, only this case has been implemented in the program, but this is easily expanded, when the apparatus data are available.

## 5 The program structure

The program is built entirely on object oriented technology (OOT). There are several advantages in using OOT:

- Inheritance makes it easy to create a child class, which inherits most of its properties and methods from its ancestor, but introduces some new, or changes the internal behavior in some areas.

- Isolation makes it easy to correct errors or undesirable behavior, without affecting other parts of the program, thereby minimizing program errors. Furthermore it makes it easy to extend functionality.

There are also disadvantages in choosing OOT:

- Processing speed will in most cases be lower than that of a procedural program since the overhead will be larger, and the amounts of data manipulated in most cases will be larger.
- The implementation process will take longer and the source code will be larger, since similar behavior may have to be implemented several times in order to avoid code shared between classes.

The program was implemented using Borland Delphi 5, 6 and 7, and should be executed on a PC running Microsoft Windows 2000 or Microsoft Windows XP. During implementation the built-in classes of Delphi have been used as programming base. For increased flexibility the program is designed to be a multiple document interface (MDI) program, meaning that it would be possible to work with several 'documents' (spectra) simultaneously.

### 5.1 *The fitting form*

The Mössbauer fitting form is implemented as the class `TdfmFitForm` (see figure 9). It is the graphic user interface, through which the user makes input to and receives output from the spectrum analysis. It contains two very important classes `TGraph` and `TFitGraph`.

After the `FitForm` has been created and initialized, it loads a data-file (which the user has chosen), and calculates the Mössbauer spectrum background level. The spectrum is folded during loading.

Whenever a change has been made to one of the fitting components, or a new fitting component has been inserted, several calculations have to be performed:

- The sum data, `SumData`, which contains the sum of the fitting components is calculated as

$$S_i = \sum_{j=1}^{N_{tet's}} T_{j,i}, \quad (23)$$

where  $S_i$  is the sum at the  $i$ 'th point,  $T_{j,i}$  is the value of the  $j$ 'th fit component (singlet, doublet, sextet), at the  $i$ 'th point.

- The rest data, `RestData`, which contains the difference between the spectrum data and the sum is calculated as

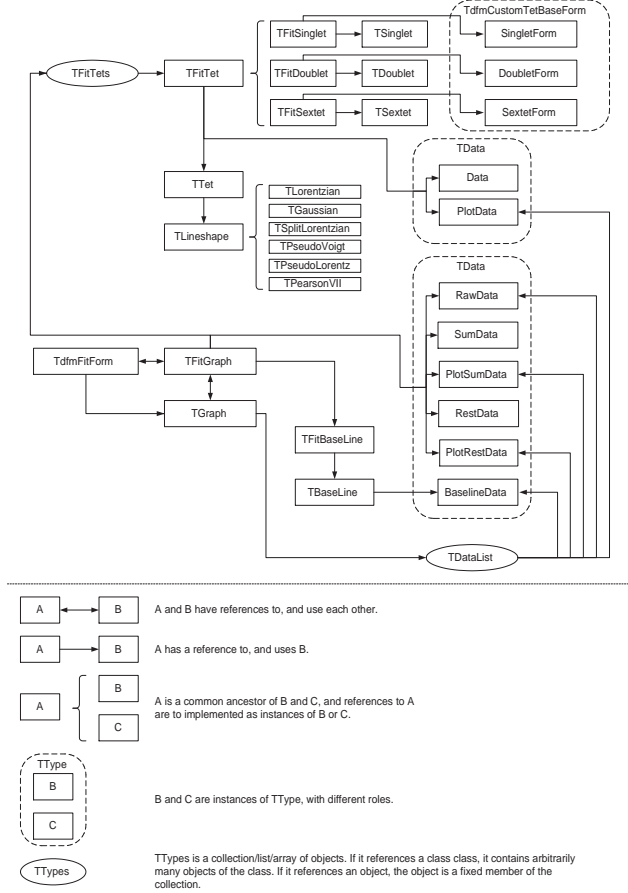


Fig. 9. The logical/workflow diagram of the *TdfmFitForm* class, used for fitting Mössbauer spectra. The upper part is the logical/workflow diagram, and the symbol explanations are shown in the lower part.

$$R_i = D_i - (B_i - S_i) = D_i - M_i \quad \text{for transmission spectra,} \quad (24)$$

$$R_i = D_i - (B_i + S_i) = D_i - M_i \quad \text{for scattering spectra,} \quad (25)$$

where  $R_i$  is the rest at the  $i$ 'th point,  $D_i$  is the  $i$ 'th data point of the spectrum data,  $B_i$  is the  $i$ 'th point in the baseline and  $M_i$  is the model data at the  $i$ 'th point.

- The  $\chi^2$ , **ChiSqr**, and  $\tilde{\chi}^2$  which are indicators for difference between the model and the data, and used for fitting, is calculated. The misfit is also given as an output parameter. It can be summarized mathematically to

$$\chi^2 = \frac{1}{n_{valid}} \sum_{i=1}^{n_{valid}} \frac{R_i^2}{D_i} = \frac{1}{n_{valid}} \sum_{i=1}^{n_{valid}} \frac{(D_i - M_i)^2}{E_i^2}, \quad (26)$$

since  $E_i = \sqrt{D_i}$  and  $n_{valid}$  is the number of valid channels in the spectrum. Furthermore we calculate the reduced chi-squared  $\tilde{\chi}^2$  by

$$\tilde{\chi}^2 = \frac{1}{n_{valid} - n_{free}} \sum_{i=1}^{n_{valid}} \frac{R_i^2}{D_i}, \quad (27)$$

where  $n_{free}$  is the number of free fit parameters. As a goodness of fit parameter we use the misfit  $m$  [17] defined by

$$m = \frac{n(\chi^2 - 1)}{\sum_{i=1}^{n_{valid}} \frac{(B_i - D_i)^2}{D_i}}. \quad (28)$$

Two fitting algorithms, random walk [16] and amoeba [18], have been implemented in the fitting form. First we will go through the random walk algorithm.

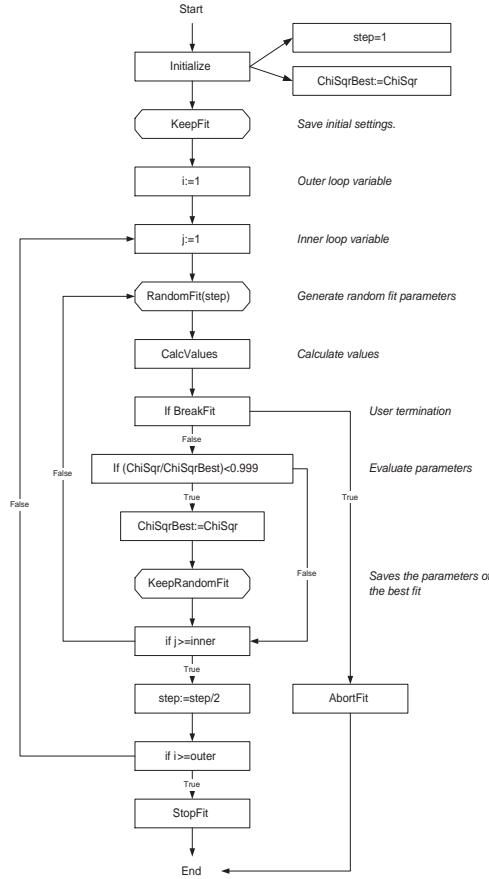


Fig. 10. A graphical illustration of the *RandomFit* fitting algorithm. The steps marked with octagonal boxes indicate that this step iterates through all *TFitTet*'s in the fit.

The random walk algorithm is a variant of the "simulated annealing"-algorithm used in many areas of physics. It differs however, in that the tunneling possibility has been eliminated. The *RandomFit* algorithm is presented graphically in figure 10. The algorithm is based on two loops, the outer and the inner. The core of the algorithm is thus run

$$N = n_{outer} \cdot n_{inner} \quad (29)$$

times. The algorithm starts with setting the variable `step` to 1. Each time the

outer loop is traversed once, **step** is set to one half of its previous value. The philosophy is to find the hitherto best fit for each time the outer loop has been traversed, and thereafter to narrow the interval in which the parameters are allowed to vary, before traversing to the outer loop again.

The algorithm is based on the assumption that the best fit after  $n_{inner}$  guesses, lies in the vicinity of the best fit. The fitting parameters all have an interval to which they are restricted during fitting. Using the result of the sum

$$\sum_{i=0}^{\infty} 2^{-i} = 2, \quad (30)$$

this can be maintained/fulfilled. If  $\Delta$  is the fitting variation interval of a fitting parameter, the following formula

$$\sum_{i=0}^{n_{outer}-1} \Delta \cdot 2^{-i} < 2 \cdot \Delta \quad (31)$$

provides a way to implement our version of the random walk algorithm without violating the restrictions:

$$\sum_{i=0}^{n_{outer}-1} 1/2 \cdot \Delta \cdot 2^{-i} < 1/2 \cdot 2 \cdot \Delta = \Delta. \quad (32)$$

Before the first traversal of the inner loop, the variation intervals are therefore set to half of the original, corresponding to the formula above. This guarantees that the fit parameters are kept within the allowed fit interval.

The amoeba algorithm [18] works in many areas much like the random-walk algorithm. It has an outer loop, which repeats  $n_{outer}$  times, or until the improvements are no longer significant. The inner loop basically works same way as in random walk.

Besides the evaluation of the improvements mentioned, the difference between the random walk and amoeba is that after the best fit has been found using the inner loop, some preprogrammed variations of the best fit are tried. For all parameters the following is tried individually: Try to the fit parameter value in the opposite direction, with the same amount. If this gives a better fit, it tries to shift the parameter value a step further in the same direction, to see if it should give an even better fit. This tests if the point of origin was a local maximum, and if the fit has found the worst local minimum. If so, the algorithms tries if a further step in the same direction gives a better fit.

If the opposite step did not yield a better result, the algorithm tests to see if

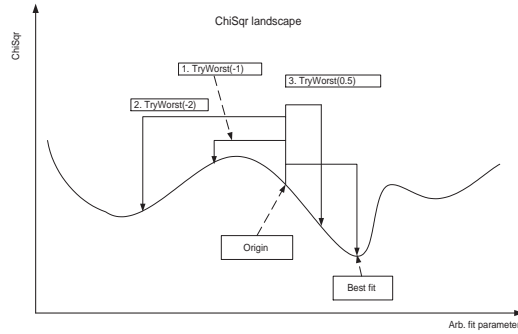


Fig. 11. A graphical illustration of the preprogrammed steps in the amoeba fitting algorithm.

it has stepped too far to find the currently best fit, and tries to see if there is a better point halfway between the origin and the currently best fit. If all of these attempt do not result in a better fit the `step` variable is divided by 2, and the content of the outer loop is traversed again. If a better fit is found `step` is not changed. The preprogrammed steps are illustrated in figure 11.

The outer loop will terminate when it has been traversed 20 times, terminated by the user or when the `rtol` variable is larger than the `ftol`. `ftol` is a measure of the minimum relative improvement required, for improvements to be considered significant. `rtol` is a measure of the improvement of the best fit compared to the worst fit in the current traversal of outer loop. `rtol` is calculated from:

$$rtol = 2 \frac{|\chi_{worst}^2 - \chi_{best}^2|}{|\chi_{worst}^2| + |\chi_{best}^2|}. \quad (33)$$

The source code is presented graphically in figure 12.

## 5.2 The calibration form

The Mössbauer calibration form is the graphic user interface, through which the user makes input to and receives output from the calibration process. Generally it resembles the fitting form in many points, and the description of common features will not be repeated. The data files are, however, loaded unfolded.

Whenever a change has been made to one of the fitting parameters, the same calculations as in the fitting form have to be performed. `SumData`, `PlotSumData`, `RestData` and `PlotRestData`, are calculated in the same way. The only difference with regards to the fitting form is the variable baseline in the calibrations form, which has to be taken into account.

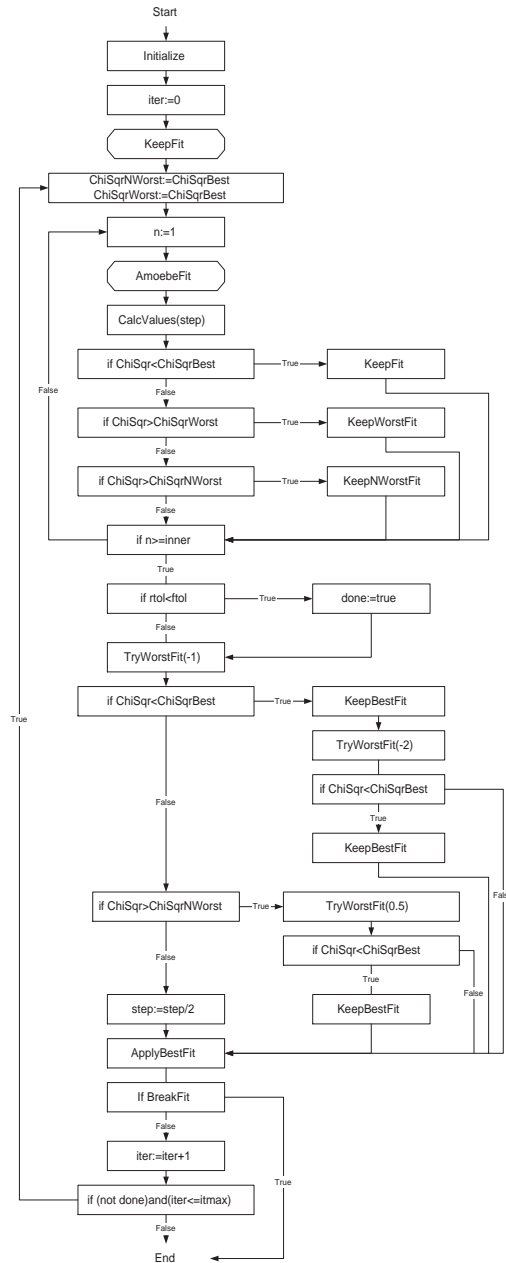


Fig. 12. A graphical illustration of the *AmoebaFit* fitting algorithm. The steps marked with octagonal boxes indicate that this step iterates through all *TFitTet*'s in the fit.

Before the calibration process can commence, the fitting components have to be inserted, and the baseline parameters defined. The baseline is initially fixed, but is allowed to vary during the calibration. The 12 components are inserted at the 12 local extrema with the largest 'magnitude'.

The local minima are found by traversing through the data points of the data, and for each data point it checks whether the current point is a local extremum by comparing it to its neighboring points. If the point is a local extremum the

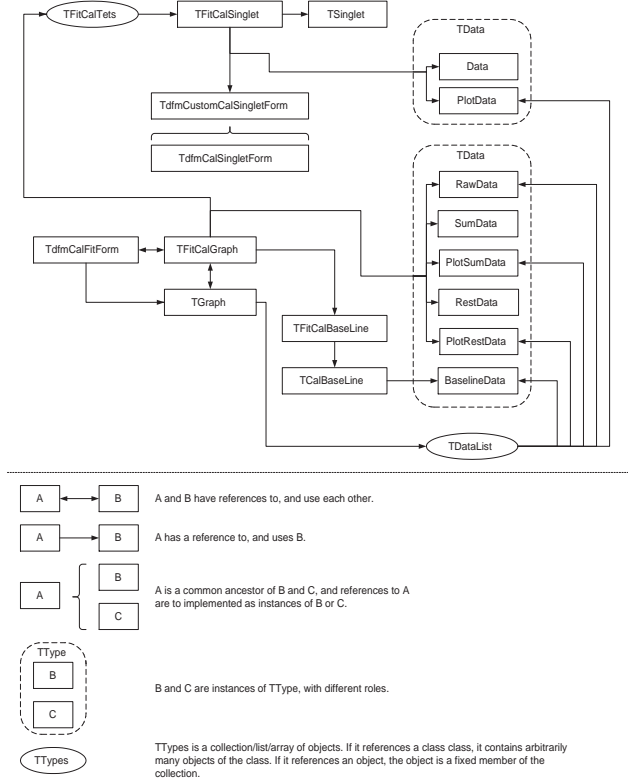


Fig. 13. The logical/workflow diagram of the *TdfmCalForm* class, used for fitting Mössbauer spectra. The upper part is the logical/workflow diagram, and the symbol explanations are shown in the lower part.

magnitude is calculated as

$$M_{pivot} = \frac{y_{i+2} + y_{i+1} + y_{i-1} + y_{i-2}}{4} - y_i, \quad (34)$$

where  $y_i$  is the  $i$ 'th point. After finding the all local extrema, the list of extrema is sorted, so the local extrema with the largest magnitude are placed first in the list, and the predefined number of largest local extrema are returned, and used for inserting the fitting components.

The random walk in the calibration form is very similar to that of the fitting form. The only difference lies in that the inner loop fits the components parameters when the inner loop counter  $j$  is even and the baseline parameters when it is odd. This is done since experiments during programming shows that this improves the intelligence and speed of the calibration procedure.

## **6 Conclusion**

We have presented the functionality and the basic principles behind the Fit;o) program. We believe that by the program we have made available a valuable tool for general simple Mössbauer analysis of complex samples.

## **7 Acknowledgements**

We would like to thank Preben Bertelsen and Kristoffer Leer of the Mars/Mössbauer group at The Niels Bohr Institute at Copenhagen University for testing and suggestions. From Risø National Laboratory, Roskilde, Denmark we would like to thank Peter Kjær Willendrup, Kim Lefmann for comments, and Luise Theil Kuhn for comments, suggestions and testing.

## **8 Additional information**

The program is available from the Fit;o) homepage at [11]. There is a forum section, a FAQ, as well as a short manual available.

## A Examples

There are a few .exp-files included in the installation package. These are test spectra, which can be used for practicing. A description of the contents of the files is given below:

- A10000.exp, A10000el.exp, A10000er.exp are simulated/generated testing spectra. They contain a perfect  $\alpha$ -Fe sextet on both, right and left side respectively.
- A10001.exp is a spectrum of soil from Salten Skov, Århus, Denmark.
- A10002.exp is an  $\alpha$ -Fe transmission calibration spectrum from a Fe foil.
- B10001.exp is an  $\alpha$ -Fe scattering calibration spectrum from a Fe foil.
- B10105A.exp B10001.exp is an  $\alpha$ -Fe scattering calibration spectrum from a  $25\ \mu$  Fe foil, with an perpendicularly applied magnetic field.
- B10106a.exp is an  $\alpha$ -Fe scattering calibration spectrum from a  $25\ \mu$  Fe foil.
- HA668.exp, HA679.exp, HA869.exp, HA900.exp, HB300.exp, HB506.exp, HB522.exp and HE0195.exp are real spectra of various samples, both natural and synthesized.

## References

- [1] K. Jónsson, Mfit : A program for fitting Mössbauer spectra, Website, <http://www.raunvis.hi.is/~kj/mfit/>.
- [2] I. S. A. Inc., Recoil, Website, <http://www.isapps.ca/recoil/index.html>.
- [3] A. R. Dinesen, C. T. Pedersen, CanArd MacFit.
- [4] Z. Klencsár, Mosswinn 3.0i, Website, <http://www.mosswinn.com/english/index.html>.
- [5] E. Carpenter, J. Long, D. Rolison, M. Logan, K. Pettigrew, R. Stroud, L. T. Kuhn, B. R. Hansen, S. Mørup, Magnetic and Mössbauer spectroscopy studies of nanocrystalline iron oxide aerogels, Journal of Applied Physics.
- [6] H. I. Duprat, P. M. Holm, M. B. Madsen, K. Leer, Ferric iron in clinopyroxene as a redox-meter for primitive magmas, In preparation.
- [7] J. í Hjöllum, L. Kuhn, M. B. Madsen, E. E. Carpenter, E. Johnson, K. Bechgaard, Magnetic Properties of Magnetite Nano-Particles Manufactured by Reverse Micelles, To be submitted to Journal of Applied Physics.
- [8] W. Goetz, M. Madsen, S. Hviid, R. Gellert, H. Gunnlaugsson, K. Kinch, G. Klingelhöfer, K. Leer, M. Olsen, and the Athena Science Team, The nature of martian airborne dust. indication of long-lasting dry periods on

the surface of mars, Seventh International Mars Conference, 2007, website, <http://www.lpi.usra.edu/meetings/7thmars2007/pdf/3104.pdf>.

- [9] M. B. Madsen, P. Bertelsen, C. S. Binau, F. Folkmann, W. Goetz, H. P. Gunnlaugsson, J. i. Hjøllum, S. F. Hviid, J. Jensen, K. M. Kinch, K. Leer, D. E. Madsen, J. Merrison, M. Olsen, H. M. Arneson, J. F. B. III, R. Gellert, K. E. Herkenhoff, J. R. Johnson, M. J. Johnson, G. Klingelhöfer, E. McCartney, D. W. Ming, R. V. Morris, J. B. Proton, D. Rodionov, M. Sims, S. W. Squyres, T. Wdowiak, A. S. Yen, and the Athena Science Team, Overview of the magnetic properties experiments on the mars exploration rovers, *Journal of Geophysical Research* (to be submitted 2007).
- [10] J. i Hjøllum, A Mössbauer Spectra Fitting program, Internal Report, Niels Bohr Institute, University of Copenhagen (2004).
- [11] J. i Hjøllum, Web Page of Fit ;o), Website, <http://www.hjollum.com/jari/zzbug/fit/>.
- [12] S. Mørup, Mössbauer spectroscopy and its applications in materials science, Physics dep. DTU, 1994.
- [13] Wikipedia, Voigt profile, Website, [http://en.wikipedia.org/wiki/Voigt\\_profile](http://en.wikipedia.org/wiki/Voigt_profile).
- [14] Wikipedia, Gamma function, Website, [http://en.wikipedia.org/wiki/Gamma\\_function](http://en.wikipedia.org/wiki/Gamma_function).
- [15] Wikipedia, Stirling's approximation, Website, [http://en.wikipedia.org/wiki/Stirling%27s\\_approximation](http://en.wikipedia.org/wiki/Stirling%27s_approximation) (March 2006).
- [16] M. F. Hansen, Superparamagnetism in Martian dust-analogies (In Danish), Master's thesis, HCØ, Niels Bohr Institute, University of Copenhagen (August 1995).
- [17] G. A. Waychunas, *American Mineralogist* 71 (1986) 1261–1265.
- [18] W. H. Press, S. A. Teukolsky, W. T. Vetterling, B. P. Flannery, *Numerical Recipes in Fortran 77*, Cambridge University Press, 1996.

## H.2 Papers in Preparation

### H.2.1 Paper IV

#### Investigations of the Antiferromagnetic Order Parameter in Nano-Sized YBCO Particles

*by*

Jari í Hjøllum, Ch. Niedermayer, K. Lefmann, L. Theil Kuhn, J. Raittila, P. Paturi, N. B. Christensen, N. H. Andersen and B. Lebech

*In preparation*

#### **Abstract**

YBCO ( $\text{YBa}_2\text{Cu}_3\text{O}_{6+x}$ ) is maybe the best known high-temperature superconductor (HTSC), being the first superconductor with a  $T_C$  above the boiling point of liquid  $\text{N}_2$ . It is as the other cuprate HTSC antiferromagnetically ordered at low doping, and a superconductor at high doping. The superconductivity of YBCO is a two-dimensional phenomenon, existing even in materials only one unit cell high. However, it is well known that the dimensionality of the system affects the magnetic order in a material, with for instance a changed magnetization curve. We have manufactured disc-shaped YBCO with a diameter of 30 nm and a height of 4 nm, and using neutron diffraction (ND) and Muon Spin Rotation ( $\mu\text{SR}$ ) we have measured the staggered magnetization in the YBCO particles versus doping and temperature. The results show a significant lowering of both the Néel temperature and of the staggered magnetic order parameter compared to bulk. This shows that the magnetic order parameter in YBCO is a 3D phenomenon, in opposition to the superconducting order parameter. Furthermore the  $\mu\text{SR}$  results show the reemergence of the native-like Néel state in the magnetic order parameter at low temperature, previously only reported in bulk-sized systems. This observation strongly supports the view that the reemergence is an intrinsic property of the cuprate systems.

## H.2.2 Paper V

### Nano-criticality in small CoO particles

*by*

Jari í Hjøllum, Jonas O. Birk, Kim Lefmann, Christof Niedermayer, Niels B. Christensen and Cathrine Frandsen

*In preparation*

#### **Abstract**

Through a neutron scattering study of CoO bulk and nanoparticle powders, we have measured the critical magnetic scattering at temperatures below and above their Néel temperatures,  $T_N$ . From the integrated intensity and the width of the  $(\frac{1}{2} \frac{1}{2} \frac{1}{2})$  antiferromagnetic diffraction peak, we extract the magnetic order parameter,  $M \propto (-\epsilon)^\beta$  (where  $\epsilon = T/T_N - 1$  is the reduced temperature, and  $\beta$  is the magnetic order parameter exponent), and the magnetic coherence length  $\xi \propto (-\epsilon)^{-\nu}$ , where  $\nu$  is the coherence length exponent.

We have found a magnetic order parameter exponent with tendency to change with particle size. Close to  $T_N$ , we observe critical scattering in both bulk and nanoparticles. This is seen as an increase in peak width. The measurements confirm the predicted behavior of the correlation length. In the nanosized samples we find a cut-off in the correlation length which scales with the particle size, in large- $\xi$  regions of  $T$ , whereas the behavior is bulk-like where in small- $\xi$  regions.

The measurements have been conducted in a novel type of experimental set-up by running a triple-axis spectrometer in two-axis mode, and by using a large 2-D Position Sensitive Detector collecting neutrons with scattering vectors around the  $(\frac{1}{2} \frac{1}{2} \frac{1}{2})$  peak. The diffraction data was revealed by subsequent image analysis.

## H.3 Conference Contributions

I have enjoyed summer schools/workshops in Anglet, France, in June 2005 and on Crete, Greece in October/November 2006, and at PSI in Switzerland in October 2006. In Crete I presented the poster:

J. í Hjøllum, L. Theil Kuhn, K. Lefmann, J-C. Grivel, A. B. Abrahamsen, B. Lebech, N. H. Andersen, J. Raittila, Ch. Niedermayer, N. B. Christensen and P. Paturi. Investigations of the antiferromagnetic phase of YBCO nano-particles. *Poster, First CoMePhS Workshop on Phase Separation In Electronic Systems, Crete - Greece, November 2006.*

I have attended the following Conferences:

- The International Conference on Neutron Scattering 2005 (ICNS2005) in Sydney, Australia, where I presented the poster:

Jari í Hjøllum, Luise Theil Kuhn, Kim Lefmann, Asger Bech Abrahamsen, Bente Lebech, Niels Hessel Andersen, Jussi Raittila, Christof Niedermayer, Niels Bech Christensen and Petriina Paturi. Neutron scattering investigations of the antiferromagnetic phase of YBCO nano-particles. *Poster, ICNS 2005, Aus, nov-dec 2005, 2005.*

- The European Conference on Neutron Scattering 2007 (ECNS2007), in Lund, Sweden where I presented the poster:

Jari í Hjøllum, Jonas O. Birk, Kim Lefmann, Christof Niedermayer, Niels B. Christensen and Cathrine Frandsen. Nano-criticality in small CoO particles. *Poster, European conference on neutron scattering (ECNS 2007), Lund (SE), 25-29 Jun 2007, 2007.*

- The annual meetings of the Danish Physical Society 2005-2007 (DFS2005-07), where I have among others have presented:

Jari í Hjøllum, Kim Lefmann, Jonas O. Birk, Niels B. Christensen and Cathrine Frandsen. Criticality in CoO nanoparticles. *Talk, Danish Physical Society annual meeting 2007, Nyborg (DK), 18-20 June 2007. Unpublished, 2007.*

## H.4 Awards

During my Ph.D. I have been awarded the following prizes:

- The prize for best Ph.D. talk at the DFS2007 for the talk '*Nano-criticality in small CoO particles*'
- The best poster at the ECNS2007 for the poster '*Nano-criticality in small CoO particles*'.



# Bibliography

- [1] E. N. Abarra, A. Inomata, H. Sato, I. Okamoto, and Y. Mizoshita. Longitudinal magnetic recording media with thermal stabilization layers. *Applied Physics Letters*, 77(16):2581–2583, 2000.
- [2] R.D. Adams, J.A. Estrada, and T. Datta. Crystal structure analysis of Y2Cu2O5. [*ICSD 72058*], *Journal of Superconductivity*, 5(1):33–38, 1995.
- [3] J. Als-Nielsen, S.T. Bramwell, M.T. Hutchings, G. J. McIntyre, and D. Visser. Neutron scattering investigation of the static critical properties of Rb<sub>2</sub>CrCl<sub>4</sub>. *Journal of Physics: Condensed Matter*, 5:7881–7892, 1993.
- [4] Jens Als-Nielsen and Des mcMorrow. *Elements of Modern X-Ray Physics*. Wiley, 2001.
- [5] A. Amato. General Purpose Surface-Muon Instrument (GPS) and GPS User Guide. PSI website: <http://lmu.web.psi.ch/facilities/gps/gps.html> and [http://lmu.web.psi.ch/facilities/gps/User\\_Guide\\_version\\_march\\_2006.pdf](http://lmu.web.psi.ch/facilities/gps/User_Guide_version_march_2006.pdf), 2007.
- [6] T. Ambrose and C. L. Chien. Finite-Size Effects and Uncompensated Magnetization in Thin Antiferromagnetic CoO Layers. *Physical Review Letters*, 76(10):1743–1746, 1996.
- [7] N. H. Andersen, B. Lebech, and H. F. Poulsen. The structural phase diagram and oxygen equilibrium partial pressure of YBa<sub>2</sub>Cu<sub>3</sub>O<sub>6+x</sub> studied by neutron powder diffraction and gas volumetry. *Physica C*, 172:31–42, 1990.
- [8] Niels Hessel Andersen. Private communications, 2004-2008.
- [9] J. Aride and S. Flandrois. New investigations on magnetic and neutron diffraction properties of Y2Cu2 O5 and related oxides. [*ICSD 67119*], *Solid State Communications*, 72(5):459–463, 1989.
- [10] C. R. H. Bahl, P. Andersen, S. N. Klausen, and K. Lefmann. The monochromatic imaging mode of a RITA-type neutron spectrometer. *Nuclear Instruments and Methods in Physics Research B*, 226:667–681, 2004.
- [11] Christian Robert Haffenden Bahl. *The Magnetic properties of antiferromagnetic nanoparticles: NiO and  $\alpha$ -Fe<sub>2</sub>O<sub>3</sub>*. PhD thesis, Materials Research Department, Risø National Laboratory & Department of Physics, Technical University of Denmark, 2006.
- [12] J. Bardeen, L. N. Cooper, and J. R. Schrieffer. Theory of superconductivity. *Physical Review*, 108(5):1175–1204, 1957.
- [13] D. P. Belanger and H. Yoshizawa. Neutron scattering and the critical behavior of the three-dimensional Ising antiferromagnet FeF<sub>2</sub>. *Physical Review B*, 35(10):4823–4830, 1. April 1987.
- [14] J.J. Binney, N.J Dowrick, A.J. Fisher, and M.E.J. Newman. *The Theory of Critical Phenomena*. Oxford University Press, 1992.

- [15] R. J. Birgeneau, M. Greven, M. A. Kastner, Y. S. Lee, B. O. Wells, Y. Endoh, K. Yamada, and G. Shirane. Instantaneous spin correlations in  $\text{La}_2\text{CuO}_4$ . *Physical Review B*, 59(21):13788–13794, 1999.
- [16] Jonas Okkels Birk. Private communications, 2006-2008.
- [17] Jonas Okkels Birk. A study of critical systems. Master’s thesis, Niels Bohr Institute, University of Copenhagen, In preparation, 2008.
- [18] C. Biselli and D. G. Morris. Microstructure and strength of Cu-Fe *In Situ* composites after very high drawing strains. *Acta Materialia*, 44(2):493–504, 1996.
- [19] S. Blundell. *Magnetism in Condensed Matter*. Oxford University Press, 2001.
- [20] F. Borsa, P. Caretta, J. H. Cho, F. C. Chou, Q. Hu, D. C. Johnston, A. Lascialfari, D. R. Torgeson, R. J. Gooding, N. M Salem, and K. J. E. Vos. Staggered magnetization in  $\text{La}_{2-x}\text{Sr}_x\text{CuO}_4$  from  $^{139}\text{La}$  NQR and  $\mu\text{SR}$ : Effects of Sr doping in the range  $0 < x < 0.02$ . *Physical Review B*, 52(10):7334–7345, 1995.
- [21] I. Bozovic. Effective dimensionality of cuprate superconductors. *Journal of Superconductivity*, 4(2):193–197, 1991.
- [22] J. Bremer, T. Johnsen, and H. Sørum. The  $\text{Cu}\alpha\text{K}_{1,2}$  spectrum as measured with a curved-crystal spectrometer. *X-Ray Spectrometry*, 11(3):149–152, 1981.
- [23] J.H. Brewer, J. Carolan, W.N. Hardy, H. Hart, R. Kadono, J. Kempton, R.F. Kiefl, S.R. Kreitzman, G.M. Luke, T.M. Riseman, P. Schleger, B.J. Sternlieb, Y.J. Uemura, D.Li. Williams, and B.X. Yang. Magnetic Ordering in  $\text{YBa}_2\text{Cu}_3\text{O}_x$  Studied by  $\mu^+$  Spin Rotation. *Physica C*, 162-164:157–158, 1989.
- [24] B. N. Brockhouse. in *Inelastic Scattering of Neutrons in Solids and Liquids*, IAEA Vienna, 113, 1961.
- [25] Stephen G. Brush. History of the Lenz-Ising Model. *Reviews of Modern Physics*, 39(4):883–893, 1967.
- [26] Henrik Bruus. Introduction to nanotechnology. Lecture Notes, Mikroelektronik Centret, Technical University of Denmark, 2003.
- [27] R. J. Cava, B. Batlogg, C. H. Chen, E. A. Rietman, S. M. Zahurak, and D. Werder. Single-phase 60-K bulk superconductor in annealed  $\text{Ba}_2\text{YCu}_3\text{O}_{7-\delta}$  ( $0.3 < \delta < 0.4$ ) with correlated oxygen vacancies in the Cu-O chains. *Physical Review B*, 36(10):5719–5722, 1987.
- [28] R.J. Cava, A.W. Hewat, E.A. Hewat, B. Batlogg, M. Marezio, K.M. Rabe, J.J. Krajewski, W.F. Peck Jr., and L.W. Rupp Jr. Structural Anomalies, Oxygen Ordering and Superconductivity in Oxygen Deficient  $\text{Ba}_2\text{YCu}_3\text{O}_x$ . *Physica C*, 165:413–419, 1990.
- [29] J. Chang, Ch. Niedermayer, R. Gilardi, N.B. Christensen, H.M. Rønnow, D.F. McMorrow, M. Ay, J. Stahn, O. Sobolev, A. Hiess, S. Pailhes, C. Baines, N. Momono, M. Oda, M. Ido, and J. Mesot. Tuning competing orders in  $\text{La}_{2-x}\text{Sr}_x\text{CuO}_4$  cuprate superconductors by the application of an external magnetic field. *arXiv*, 0712.2181v2, 2007.
- [30] S.L. Chaplot, W. Reichardt, L. Pintschovius, and N. Pyka. Common interatomic potential model for the lattice dynamics of several cuprates. [*Erroneous ref.*] *ICSD 41645,41646*, *Journal of Physics and Chemistry of Solids*, 53(6):761–770, 1992.
- [31] S.L. Chaplot, W. Reichardt, L. Pintschovius, and N. Pyka. Common interatomic potential model for the lattice dynamics of several cuprates. *Physical Review B*, 52(10):7230–7242, 1995.

- [32] S-W. Cheong, G. Aeppli, T. E. Mason, H. Mook, S. M. Hayden, P. C. Canfield, Z. Fisk, K. N. Clausen, and J. L. Martinez. Incommensurate magnetic fluctuations in  $\text{La}_{2-x}\text{Sr}_x\text{CuO}_4$ . *Physical Review Letters*, 67(13):1791–1794, 1991.
- [33] F. C. Chou, F. Borsa, J. H. Cho, D. C. Johnston, A. Lascialfari, D. R. Torgeson, , and J. Zibold. Magnetic phase diagram of lightly doped  $\text{La}_{2-x}\text{Sr}_x\text{CuO}_4$  from  $^{139}\text{La}$  nuclear quadrupole resonance. *Physical Review Letters*, 71:2323–2326, 1993.
- [34] N. B. Christensen, Ch. Niedermayer, K. Lefmann, and H. M. Rønnow *et al.*. Blade Runner - from Risø to PSI and beyond... Talk, Grenoble, 2006.
- [35] H. Claus, S. Yang, A. P. Paulikas, J. W. Downey, and B. W. Veal. Atomic short-range order in oxygen deficient  $\text{YBa}_2\text{Cu}_3\text{O}_{7-\delta}$ . *Physica C*, 171:205–210, 1990.
- [36] Kurt Nørgaard Clausen, Bente Lebech, Desmond F. McMorrow, Steen Aagaard Sørensen, Gabriel Aeppli, and Thomas E. Mason. Instrument development at Risø - The RITA neutron spectrometer and the germanium monochromator facility. Website, [http://www.risoe.dk/afm/external/bele/Neutrons/RITA\\_article.pdf](http://www.risoe.dk/afm/external/bele/Neutrons/RITA_article.pdf), 1996.
- [37] Kurt Nørgaard Clausen, Bente Lebech, Desmond F. McMorrow, Steen Aagaard Sørensen, Gabriel Aeppli, and Thomas E. Mason. The RITA spectrometer at Risø. *Neutron News*, 7(4):21–24, 1996.
- [38] M. F. Collins. *Magnetic Critical Scattering*. Oxford University Press, 1989.
- [39] M. R. Crook and R. Cywinski. Voigtian Kubo-Toyabe muon spin relaxation. *J. Phys.: Condens. Matter*, 9:1149–1158, 1997.
- [40] Pengcheng Dai, H. A. Mook, , and F. Doğan. Incommensurate Magnetic Fluctuations in  $\text{YBa}_2\text{Cu}_3\text{O}_{6.6}$ . *Physical Review Letters*, 80(8):1738–1741, 1998.
- [41] P. Dutta, M. S. Seehra, S. Thota, and J. Kumar. A comparative study of the magnetic properties of bulk and nanocrystalline  $\text{Co}_3\text{O}_4$ . *Journal of Physics: Condensed Matter*, 20(015218), 2008.
- [42] N.N. Eremin, L.I. Leonyuk, and V.S. Urusov. Interatomic potentials for structure simulation of alkaline-earth cuprates. [ICSD #93655] *Journal of Solid State Chemistry*, 158:162–168, 2001.
- [43] H. Börner *et al.* Neutron data booklet, 2003.
- [44] Fachinformationszentrum (FIZ) Karlsruhe. ICSD - Inorganic Crystal Structure Database. (c)2007 FIZ Karlsruhe.
- [45] F.F. Ferreira, E. Granado, W.jr Carvalho, S.W. Kycia, D. Bruno, and R.jr Droppa. X-ray powder diffraction beamline at D10B of LNLS: application to the  $\text{Ba}_2\text{FeReO}_6$  double perovskite. [ICSD #65801], *Journal of Synchrotron Radiation*, 13:46–53, 2006.
- [46] Alan M. Ferrenberg and D. P. Landau. Critical behavior of the three-dimensional Ising model: A high-resolution Monte Carlo study. *Physical Review B*, 44(10):5081–5091, 1991.
- [47] Michael E. Fisher. Correlation functions and the critical region of simple fluids. *Journal of Mathematical Physics*, 5(7):944–962, 1964.
- [48] M. R. Fitzsimmons, J. A. Eastman, and R. A. Robinson. The Néel temperature of nanocrystalline chromium. *Journal of Applied Physics*, 78(2):1364–1366, 1995.
- [49] M.R. Fitzsimmons, S.D. Bader, J.A. Borchers, G.P. Felcher, J.K. Furdyna, A. Hoffmann, J.B. Kortright, Ivan K. Schuller, T.C. Schulthess, S.K. Sinha, M.F. Toney, D. Weller, and S. Wolf. Neutron scattering studies of nanomagnetism and artificially structured materials. *Journal of Magnetism and Magnetic Materials*, 271:103–146, 2004.

- [50] H. Fjellvag, P. Karen, and A. Kjekshus. Crystal Structure of Y<sub>2</sub> Cu<sub>2</sub> O<sub>5</sub> Refined from Powder Neutron Diffraction Data. [*ICSD 63306*], *Acta Chemica Scandinavica, Series A:*, (28, 1974-)(42):144–147, 1988.
- [51] C.F.J. Flipse, C.B. Rouwelaar, and F.M.F.de Groot. Magnetic properties of CoO nanoparticles. *European Physical Journal D*, 9:479–481, 1999.
- [52] H. Fogedby. Complexity. Lecture notes, Website, <http://www.phys.au.dk/~fogedby/statphysII/complexity.pdf>, <http://www.phys.au.dk/~fogedby/statphysII06.html>, 2005.
- [53] Kristian Fossheim and Asle Sudbø. *Superconductivity : Physics and Applications*. Wiley, 2004.
- [54] C. Frandsen, C. R. H. Bahl, B. Lebech, K. Lefmann, L. Theil Kuhn, L. Keller, N. H. Andersen, M. v. Zimmermann, E. Johnson, S. N. Klausen, and S. Mørup. Oriented attachment and exchange coupling of  $\alpha$ -Fe<sub>2</sub>O<sub>3</sub> nanoparticles. *Physical Review B*, 72(214406), 2005.
- [55] C. Frandsen, C. W. Ostefeld, M. Xu, C. S. Jacobsen, L. Keller, K. Lefmann, and S. Mørup. Interparticle interactions in composites of nanoparticles of ferrimagnetic ( $\gamma$ -Fe<sub>2</sub>O<sub>3</sub>) and antiferromagnetic (CoO,NiO) materials. *Physical Review B*, 70:134416, 2004.
- [56] Eric E. Fullerton, D. T. Margulies, M. E. Schabes, M. Carey, B. Gurney, A. Moser, M. Best, G. Zeltzer, K. Rubin, and H. Rosen. Antiferromagnetically coupled magnetic media layers for thermally stable high-density recording. *Applied Physics Letters*, 77(23):3806–3808, 2000.
- [57] J.L. Garcia-Munoz and J.Rodriguez-Carvajal. Structural characterization of R<sub>2</sub> Cu<sub>2</sub> O<sub>5</sub> (R=Yb,Tm,Er,Y and Ho) oxides by neutron diffraction. [*ICSD 79429*], *Journal of Solid State Chemistry*, 115:324–331, 1995.
- [58] A. K. Geim, S. V. Dubonos, J. G. S. Lok, M. Henini, and J. C. Maan. Paramagnetic Meissner effect in small superconductors. *Nature Letters*, 396:144–146, 1998.
- [59] Marcelo Gleiser. Phase transitions in the universe. *arXiv:hep-ph*, 9803291v1, 1998.
- [60] I. V. Golosovsky, I. Mirebeau, G. André, D. A. Kurdyukov, Y. A. Kumzerov, M. Tovar, and D. M. Többens. Magnetic phase transition in CoO confined to a vycor type porous glass. Neutron diffraction study. *arXiv:cond-mat*, 0506483v1, 2005.
- [61] R. J. Gooding, N. M. Salem, and A. Mailhot. Theory of coexisting transverse-spin freezing and long-ranged antiferromagnetic order in lightly doped La<sub>2-x</sub>Sr<sub>x</sub>CuO<sub>4</sub>. *Physical Review B*, 49(9):6067–6073, 1994.
- [62] Jean-Claude Grivel. Conversation and discussion, 2007.
- [63] R. Guida and J. Zinn-Justin. 3D Ising model: The scaling equation of state. *Nuclear Physics B*, 489(3):626–652, 1997.
- [64] R. Guida and J. Zinn-Justin. Critical exponents of the N-vector model. *Journal Of Physics A*, 31(8103-8121), 1998.
- [65] Henning Haack. Distribution of minerals in primitive meteorites detection and characterization of the first solids to form in the Solar System. Experimental report, Danish Geological Museum and Paul Scherrer Institute, 2005.
- [66] Mikkel F. Hansen, Franz Bødker, Steen Mørup, Kim Lefmann, Kurt N. Clausen, and Per-Anker Lindgård. Dynamics of magnetic nanoparticles studied by neutron scattering. *Physical Review Letters*, 79(24):4910–4913, 1997.

- [67] Yuko Hayakawa, Shigemi Kohiki, Michi Sato, Yuko Sonda, Tomohiro Babasaki, Hiroyuki Deguchi, Akiko Hidaka, Hirokazu Shimooka, and Seiji Takahashi. Magnetism of diluted  $\text{Co}_3\text{O}_4$  nanocrystals. *Physica E*, 9:250–252, 2001.
- [68] R. S. Hayano, Y. J. Uemura, J. Imazato, N. Nishida, T. Yamazaki, and R. Kubo. Zero- and low-field spin relaxation studied by positive muons. *Physocal Review B*, 20(3):850–859, 1979.
- [69] Lin He, Chinping Chena, Ning Wang, Wei Zhou, , and Lin Guo. Finite size effect on Néel temperature with  $\text{Co}_3\text{O}_4$  nanoparticles. *Journal of Applied Physics*, 102(103911), 2007.
- [70] H. Heer, M. Konnecke, and D. Maden. The SINQ instrument control software system. *Physica B*, 241:124–126, 1998.
- [71] V. Hinkov, D. Haug, B. Fauqué, P. Bourges, Y. Sidis, A. Ivanov, C. Bernhard, C. T. Lin, and B. Keimer. Electronic Liquid Crystal State in the High-Temperature Superconductor  $\text{YBa}_2\text{Cu}_3\text{O}_{6.45}$ . *Science*, 319:597–600, 2008.
- [72] J. í Hjøllum, L. Theil Kuhn, E. E. Carpenter, E. Johnson, M. B. Madsen, and K. Bechgaard. Size Controlled Fabrication of Stoichiometric Magnetite Nanoparticles by Reverse Micelles. *European Physical Journal, Applied Physics*, In revision, 2008.
- [73] C.M. Holl, J.R.Smyth, H.M.S. Laustsen, S.D. Jacobsen, and R.T. Downs. Compression of witherite to 8 GPa and the crystal structure of  $\text{BaCO}_3\text{II}$ . [*ICSD 91888*], *Physics and Chemistry of Minerals*, 27:467–473, 2000.
- [74] R. Hsu, E.N. Maslen, and N. Ishizawa. A synchrotron x-ray study of the electron density in  $\text{Y}_2\text{BaCuO}_5$ . [*ICSD 52055*], *Acta Crystallographica B*, 39, 1983-(52):569–572, 1996.
- [75] Y. Ijiri, J. A. Borchers, R. W. Erwin, S.-H. Lee, P. J. van der Zaag, and R. M. Wolf. Perpendicular Coupling in Exchange-Biased  $\text{Fe}_3\text{O}_4/\text{CoO}$  Superlattices. *Physical Review Letters*, 80(6):608 – 611, 1998.
- [76] Y. Imry and D. Bergman. Critical Points and Scaling Laws for Finite Systems. *Physical Review A*, 3(4):1416–1418, 1971.
- [77] Yoseph Imry. Finite-size rounding of a first-order phase transition. *Physical Review B*, 21(5):2042–2043, 1980.
- [78] Oxford Cryosystems Inc. Crystallographica. Computer program.
- [79] W. Jauch, M. Reehuis, H. J. Bleif, and F. Kubanek. Crystallographic symmetry and magnetic structure of  $\text{CoO}$ . *Physical Review B*, 052102, 64.
- [80] J. D. Jorgensen, B. W. Veal, A. P. Paulikas, L. J. Nowicki, G. W. Crabtree, H. Claus, and W. K. Kwok. Structural properties of oxygen-deficient  $\text{YBa}_2\text{Cu}_3\text{O}_{7-\delta}$ . *Physical Review B*, 41(4):1863 – 1877, 1990.
- [81] Erik B. Karlsson. *Solid State Phenomena: As Seen by Muons, Protons, and Excited Nuclei*. Clarendon Press - Oxford, 1st edition, 1995.
- [82] B. Keimer, N. Belk, R. J. Birgeneau, A. Cassanho, C. Y. Chen, M. Greven, , M. A. Kastner, A. Aharony, Y. Endoh, R. W. Erwin, and G. Shirane. Magnetic excitations in pure, lightly doped, and weakly metallic  $\text{La}_2\text{CuO}_4$ . *Physical Review B*, 46(21):14034–14053, 1992.
- [83] N. Kernavanois, E. Ressouche, P.J. Brown, J.Y. Henry, and E. Lelièvre-Berna. Magnetization distribution in paramagnetic  $\text{CoO}$ : a polarized neutron diffraction study. *Journal of Physics: Condensed Matter*, 15:3433–3443, 2003.

- [84] B. Khaykovich, S. Wakimoto, R. J. Birgeneau, M. A. Kastner, Y. S. Lee, P. Smeibidl, P. Vorderwisch, and K. Yamada. Field-induced transition between magnetically disordered and ordered phases in underdoped  $\text{La}_{2-x}\text{Sr}_x\text{CuO}_4$ . *Physical Review B*, 71(220508), 2005.
- [85] Charles Kittel. *Introduction to Solid State Physics*. Wiley, 8th edition, 2005.
- [86] S. N. Klausen, P.-A. Lindgård, K. Lefmann, F. Bødker, and S. Mørup. Temperature Dependence of the Magnetization of Disc Shaped NiO Nanoparticles. *Physica Status Solidi A*, 189(3):1039–1042, 2002.
- [87] Stine Nyborg Klausen. *Manual for the RITA2 spectrometer*. Risø and PSI, version 0 edition, 2001.
- [88] P. Klosowski, M. Koennecke, J. Z. Tischler, and R. Osborn. NeXus: A common format for the exchange of neutron and synchrotron data. *Physica B*, 241-243:151–153, 1998.
- [89] D. Ködderitzsch, W. Hergert, Z. Szotek, and W. M. Temmerman. Electronic structure of 3d-transition-metal monoxides: surface and bulk-point-defects. *Journal of Magnetism and Magnetic Materials*, 272-276:E253–E254, 2004.
- [90] Mark Könnekce and Heinz Heer. SICS: SINQ Instrument Control Software. Webpage: <http://lns00.psi.ch/sics/design/sics.html>.
- [91] Wolfgang Kopmann. WKM Einführung und technische Referenz. Website, <ftp://ftp.psi.ch/psi/musr/software/wkm-handbuch.pdf>, 2000.
- [92] I. S. Kotousova and S. M. Polyakov. Electron-diffraction study of  $\text{Co}_3\text{O}_4$ . [*ICSD 9362*] *Kristallografiya*, 17:661–663, 1972.
- [93] R. Kubo and T. Toyabe. *A stochastic model for low field resonance and relaxation in Magnetic Resonance and Relaxation*, Session 19, no. 1, pages 810–823. North-Holland, Amsterdam, 1967.
- [94] L. Theil Kuhn, P. Andersen, K. Lefmann, N. H. Andersen, M. Meedom Nielsen, P. Paturi, and J. Raittila. Antiferromagnetism in  $\text{YBa}_2\text{Cu}_3\text{O}_{6+x}$  nanoparticles studied by elastic neutron scattering. Poster, Risø international symposium on materials science, Risø (DK), 10-13 Sep 2003, 2003.
- [95] Luise Theil Kuhn. AFM i praksis. Lecture notes in the Nano2 course at Univ. of Copenhagen, 2006.
- [96] P. Kumar, V. Pillai, S. R. Bates, and D. O. Shah. Preparation of  $\text{YBa}_2\text{Cu}_2\text{O}_{7-x}$  superconductor by coprecipitation of nanosize oxalate precursor powder in microemulsions. *Materials Letters*, 16(2-3):68–74, 1993.
- [97] C. Lacour, F. Laher-Lacour, A. Dubon, M. Lagues, and Ph. Mocaër. Freeze drying preparation of  $\text{YBaCuO}$  - Correlations between electrical and microstructural properties. *Physica C*, 167:287–290, 1990.
- [98] B. Lake, H.M. Rønnow, N. B. Christensen, G. Aeppli, K. Lefmann, D. F. McMorrow, P. Vorderwisch, P. Smeibidl, N. Mangkorntong, T. Sasagawa, M. Nohara, H. Takagi, and T. E. Mason. Antiferromagnetic order induced by an applied magnetic field in a high-temperature superconductor. *Nature*, 415:299–302, 2002.
- [99] D.P. Landau. Computer simulation studies of magnetic phase transitions. *Journal of Magnetism and Magnetic Materials*, 200:231–247, 1999.
- [100] J.I. Langford and J.C. Wilson. Scherrer after Sixty Years: A Survey and Some New Results in the Determination of Crystallite Size. *J. Appl. Cryst.*, 11:102–113, 1978.

- [101] A. N. Lavrov, Yoichi Ando, Kouji Segawa, and J. Takeya. Magnetoresistance in Heavily Underdoped  $\text{YBa}_2\text{Cu}_3\text{O}_{6+x}$ : Antiferromagnetic Correlations and Normal-State Transport. *Physical Review Letters*, 83(7):1419–1422, 1999.
- [102] Bente Lebech. Conversation and discussion, 2005-2008.
- [103] Bente Lebech. Exercise 2: X-ray diffraction of  $\text{YBa}_2\text{Cu}_3\text{O}_{6+x}$ . Exercise notes, Superconductivity course website, 2007.
- [104] K. Lefmann, D. F. McMorrow, H. M. Rønnow, K. Nielsen, K. N. Clausen, B. Lake, and G. Aeppli. Added flexibility in triple axis spectrometers: the two RITAs at Risø. *Physica B*, 283:343–354, 2000.
- [105] K. Lefmann, Ch. Niedermayer, A.B. Abrahamsen, C.R.H. Bahl, N.B. Christensen, H.S. Jacobsen, T.L. Larsen, P. Häfliger, U. Filges, and H.M. Rønnow. Realizing the full potential of a RITA spectrometer. *Physica B*, 385-386:1083–1085, 2006.
- [106] K. Lefmann and K. Nielsen. Mcstas, a general software package for neutron ray-tracing simulations. *Neutron News*, 10(20), 1999.
- [107] Kim Lefmann. Conversations and discussions, 2004-2008.
- [108] Chun Li, A. J. Freeman, H. J. F. Jansen, and C. L. Fu. Magnetic anisotropy in low-dimensional ferromagnetic systems: Fe monolayers on Ag(001), Au(001), and Pd(001) substrates. *Physical Review B*, 42(9):5433 – 5442, 1990.
- [109] Ruixing Liang, D. A. Bonn, and W. N. Hardy. Evaluation of  $\text{CuO}_2$  plane hole doping in  $\text{YBa}_2\text{Cu}_3\text{O}_{6+x}$  single crystals. *Physical Review B*, 73(180505(R)), 2006.
- [110] C. Liu and S. D. Bader. Morphology of Fe/Pd(100) films studied using photoemission from physisorbed Xe. *Physical Review B*, 44(5):2205 – 2208, 1991.
- [111] Shang-Keng Ma. *Modern Theory of Critical Phenomena*. Addison-Wesley Publishing Company, 1976.
- [112] P. Manca, S. Sanna, , G. Calestani, A. Migliori, S. Lapinskas, and E. E. Tornau. Orthorhombic low-temperature superstructures in  $\text{YBa}_2\text{Cu}_3\text{O}_{6+x}$ . *Physical Review B*, 63(134512), 2001.
- [113] P. Manca, S. Sanna, G. Calestani, A. Migliori, R. De Renzi, and G. Allodi. Critical chain length and superconductivity emergence in oxygen-equalized pairs of  $\text{YBa}_2\text{Cu}_3\text{O}_{6.30}$ . *Physical Review B*, 61(22):15450–15453, 2000.
- [114] V. Massarotti, D. Capsoni, M. Bini, A. Altomare, and A.G.G. Moliterni. X-ray diffraction study of polycrystalline  $\text{Y}_2\text{BaO}_4$ : a test of the new EXPO program. [*ICSD 89640*] *Zeitschrift fuer Kristallographie (149,1979-)*, 214:200–204, 1999.
- [115] D. F. McMorrow, N. Hamaya, S. Shimomura, Y. Fujii, S. Kishimoto, and H. Iwasaki. On the length scales of the critical fluctuations in  $\text{SrTiO}_3$ . *Solid State Communications*, 76(3):443–448, 1990.
- [116] Des McMorrow, Henrik Rønnow, Emmanuel Farhi, and Peter K. Willendrup. Spec1d - matlab data analysis package.  
[wwwold.ill.fr/Computing/resources/software/matlab/doc/spec1d/spec1d.html](http://wwwold.ill.fr/Computing/resources/software/matlab/doc/spec1d/spec1d.html).
- [117] A. W. McReynolds and T. Riste. Critical Scattering of Neutrons from  $\text{CoO}$ . *Le Journal de Physique et le Radium*, 20:175–177, 1959.
- [118] McStas.org. McStas - Monte Carlo simulation of neutron instruments. Website: [www.mcstas.org](http://www.mcstas.org).

- [119] Marcus H. Mendenhall. Fast computation of voigt functions via fourier transforms. *arXiv:Physics*, 060713v1, 2006.
- [120] N. D. Mermim and H. Wagner. Absence of Ferromagnetism or Antiferromagnetism in One- or Two-Dimensional Isotropic Heisenberg Models. *Physical Review Letters*, 17(22):1133–1136, 1966.
- [121] H. A. Mook, Pengcheng Dai, F. Doğan, and R. D. Hunt. One-dimensional nature of the magnetic Fluctuations in  $\text{YBa}_2\text{Cu}_3\text{O}_{6.6}$ . *Nature*, 404:729–731, 2000.
- [122] H. A. Mook, Pengcheng Dai, S. M. Hayden, G. Aeppli, T. G. Perring, and F. Doğan. Spin fluctuations in  $\text{YBa}_2\text{Cu}_3\text{O}_{6.6}$ . *Nature*, 395:580 – 582, 1998.
- [123] H. A. Mook, Pengcheng Dai, S. M. Hayden, A. Hiess, J. W. Lynn, S.-H. Lee, and F. Doğan. Magnetic order in  $\text{YBa}_2\text{Cu}_3\text{O}_{6+x}$  superconductors. *Physical Review B*, 66(144513), 2002.
- [124] S. Mørup, F. Bødker, P. V. Hendriksen, and S. Linderoth. Spin-glass-like ordering of the magnetic moments of interacting nanosized maghemite particles. *Physical Review B*, 52(1):287–294, 1995.
- [125] Steen Mørup. Mössbauer effect in small particles. *Hyperfine Interactions*, 60:959–974, 1990.
- [126] Bruce M. Moskowitz. *Global Earth Physics: A Handbook of Physical Constants*. AGU Reference Shelf 1. American Geophysical Union, 1995.
- [127] National Institute of Standards and Technology. The NIST Reference on Constants, Units, and Uncertainty. Website, <http://physics.nist.gov/cuu/index.html>.
- [128] L. Néel. *Ann. Geophysics*, 5(99), 1949.
- [129] L. Néel. Superparamagnetisme des grains tres fins antiferromagnetiques. *Comptes Rendus Hebdomadaires Des Seances De L'Academie Des Sciences*, 252(26), 1961.
- [130] Ch. Niedermayer, C. Bernhard, T. Blasius, A Golnik, A. Moodenbaugh, and J. I. Budnick. Common Phase Diagram for Antiferromagnetism in  $\text{La}_{2-x}\text{Sr}_x\text{CuO}_4$  and  $\text{Y}_{1-x}\text{Ca}_x\text{Ba}_2\text{Cu}_3\text{O}_6$  as Seen by Muon Spin Rotation. *Physical Review Letters*, 80(17):3843–3846, 1998.
- [131] Christof Niedermayer. Conversations and discussions, 2005-2008.
- [132] Christof Niedermayer and Jari í Hjöllum. Quick helper for RITA-2 and SICS. Website, Wiki: <http://lns00.psi.ch/sinqwiki/Wiki.jsp?page=RITA2SpecialCommandsAndProcedures>, 2005-2007.
- [133] Nobel Foundation Website. Nobelprize.org. <http://nobelprize.org/>.
- [134] M. R. Norman, D. Pines, and C. Kallin. The pseudogap: friend or foe of high  $T_c$ ? *Advances in Physics*, 54(8):715 – 733, 2005.
- [135] Lars Onsager. Crystal Statistics. I. A Two-Dimensional Model with and Order-Disorder Transition. *Physical Review*, 65(3/4):117–149, 1994.
- [136] L. C. Pathak and S. K. Mishra. A review on the synthesis of Y-Ba-Cu-oxide powder. *Superconductor Science and Technology*, 18(R67-R89), 2005.
- [137] A.L. Patterson. The scherrer formula for x-ray particle size determination. *Physical Review*, 56(15):978–982, 1939.
- [138] P. Paturi, J. Raittilaa, H. Huhtinen, V.-P. Huhtala, and R. Laiho. Size-dependent properties of  $\text{YBa}_2\text{Cu}_3\text{O}_{6+x}$  nanopowder. *Journal of Physics: Condensed Matter*, 15(12):2103–2114, 2003.

- [139] Paul Scherrer Institute. The Megapie Experiment - Facts & Figures. Media Report, Website, [http://www.psi.ch/medien/Medienmitteilungen/mm\\_megapie\\_jan07/PSI\\_MM\\_Megapie\\_Jan07\\_BgInfo\\_E.pdf](http://www.psi.ch/medien/Medienmitteilungen/mm_megapie_jan07/PSI_MM_Megapie_Jan07_BgInfo_E.pdf), January 2007.
- [140] Henning Friis Poulsen, Niels Hessel Andersen, Jørgen Vitting Andersen, Henrik Bohr, and Ole G. Mouritsen. Relation between superconducting transition temperature and oxygen ordering in  $\text{YBa}_2\text{Cu}_3\text{O}_{6+x}$ . *Nature*, 349(6310):594–596, 1991.
- [141] Krunoslav Prsa. Private communications, 2006-2008.
- [142] PSI. GPS User Guide. Booklet at GPS, PSI.
- [143] PSI. WKM - Analysis in time-space, analysis software. Website, [http://lmu.web.psi.ch/facilities/software\\_wkm.html](http://lmu.web.psi.ch/facilities/software_wkm.html), <http://lmu.web.psi.ch/facilities/software.html>.
- [144] PSI. RITA-II at SINQ. Website: <http://spectroscopy.web.psi.ch/rita2/>, 2007.
- [145] P. G. Radaelli. *Neutron Scattering in Layered Copper-Oxide Superconductors*, chapter Structural Anomalies, Oxygen Ordering and Superconductivity in  $\text{YBa}_2\text{Cu}_3\text{O}_{6+x}$ , pages 23–83. Kluwer Academic Publishers, 1998.
- [146] J. Raittila, H. Huhtinen, P. Paturi, and Yu. P. Stepanov. Preparation of superconducting  $\text{YBa}_2\text{Cu}_3\text{O}_{7-\delta}$  nanopowder by deoxydation in Ar before final oxygenation. *Physica C*, 371:90–96, 2002.
- [147] Jussi Raittila. *Titration of yttrium in aqueous solution/Titration of barium in aqueous solution/Titration of copper in aqueous solution*. University of Turku. Recipe for stock solutions.
- [148] Jussi Raittila. *Synthesis and Applications of YBCO Nanopowder*. Phd thesis, University of Turku, 2003.
- [149] Jussi Raittila. Private communications, 2005-2007.
- [150] M.D. Reichtin and B. L. Averbach. Tetragonal Elongation in CoO near the Néel Point. *Physical Review Letters*, 26(24):1483–1485, 1971.
- [151] M.D. Reichtin and B. L. Averbach. Long-Range Magnetic Order in CoO. *Physical Review B*, 6(11):4294–4300, 1972.
- [152] M.D. Reichtin and B. L. Averbach. Short-Range Magnetic Order in CoO. *Physical Review B*, 5(7):2693–2704, 1972.
- [153] M.D. Reichtin and B.L. Averbach. Critical Magnetic Scattering from CoO. *Physical Review Letters*, 26(24):1480–1483, 1971.
- [154] M.D. Reichtin, C.S. Moss, and B.L. Averbach. Influence of Lattice Contraction on Long-Range Order in CoO near  $T_N$ . *Physical Review Letters*, 24(26):1485–1489, 1970.
- [155] Eric Ressouche, Nolwenn Kernavanois, Louis-Pierre Regnault, and Jean-Yves Henry. Magnetic structures of the metal monoxides NiO and CoO re-investigated by spherical neutron polarimetry. *Physica B*, 385-386:394–397, 2006.
- [156] G. Rian. *A thermodynamic study of the phase stability regions in the system  $\text{Y}_2\text{O}_3 - \text{BaO} - \text{CuO}_x$* . PhD thesis, Norwegian Institute of Technology, 1992.
- [157] Juan Rodríguez-Carvajal. Recent advances in magnetic structure determination by neutron powder diffraction. *Physica B*, 192:55–69, 1993.

- [158] H. M. Rønnow, D. F. McMorrow, and A. Harrison. High-Temperature Magnetic Correlations in the 2D  $S = 1/2$  Antiferromagnet Copper Formate Tetradeuterate. *Physical Review Letters*, 82(15):3152–3155, 1999.
- [159] J. Rossat-Mignod, P. Burlet, M. J. Jurgens, C. Vettier, L. P. Regnault, J.Y. Henry, C. Ayaiche, L. Forro, H. Noel, M. Potel, P. Gougeon, and J.C. Levet. Antiferromagnetic Ordering and Phase-Diagram of  $\text{YBa}_2\text{Cu}_3\text{O}_{6+x}$ . *Journal de Physique*, 4-9(C-8):2119–2124, 1988.
- [160] W. L. Roth. The magnetic structure of  $\text{Co}_3\text{O}_4$ . *Journal of Physics and Chemistry of Solids*, 25(1):1–10, 1964.
- [161] F. Rullier-Albenque, H. Alloul, F. Balakirev, and C. Proust. Disorder, metal-insulator crossover and phase diagram in high- $T_c$  cuprates. *Europhysics Letters*, 81(37008), 2008.
- [162] M.B. Salamon. Specific Heat of  $\text{CoO}$  near  $T_N$ : Anisotropy Effects. *Physical Review B*, 2(1):214–220, 1970.
- [163] F. Sánchez-Bajo and F. L. Cumbreira. The Use of the Pseudo-Voigt Function in the Variance Method of X-ray Line-Broadening Analysis. *Journal of Applied Crystallography*, 30:427–430, 1997.
- [164] S. Sanna, G. Allodi, G. Concas, A. D. Hillier, and R. De Renzi. Nanoscopic Coexistence of Magnetism and Superconductivity in  $\text{YBa}_2\text{Cu}_3\text{O}_{6+x}$  Detected by Muon Spin Rotation. *Physical Review Letters*, 93(20), 2004.
- [165] S. Sanna, G. Allodi, and R. De Renzi. The freezing of spin and charge at low temperature in  $\text{YBa}_2\text{Cu}_3\text{O}_{6+x}$ . *Solid State Communications*, 126:85–91, 2003.
- [166] S. Sasaki, K. Fujino, and Y. Takeuchi. X-ray determination of electron-density distributions in oxides,  $\text{MgO}$ ,  $\text{MnO}$ ,  $\text{CoO}$ , and  $\text{NiO}$ , and atomic scattering factors of their constituent atoms. [*ICSD 9865*] *Proceedings of the Japan Academy (1979)*, 55, 43-48. *Phase Transition (1992)*, 38, 127-220.
- [167] Yasmine Sassa. Private communications, 2008.
- [168] Yasmine Sassa and Milan Radović. Growth of YBCO films on STO and NGO, on systems suitable for in-situ ARPES measurements. *In preparation*, 2008.
- [169] D. J. Scalapino, Jr. E. Loh, and J. E. Hirsch.  $d$ -wave pairing near a spin-density-wave instability. *Physical Review B*, 34(11):8190–819, 1986.
- [170] G. Schatz and A. Weidinger. *Nukleare Festkörperphysik*. Teubner Studienbücher, Physik, 1992.
- [171] P. Schleger, W. N. Hardy, and B. X. Yang. Thermodynamics of oxygen in  $\text{Y}_1\text{Ba}_2\text{Cu}_3\text{O}_x$  between  $450^\circ\text{C}$  and  $650^\circ\text{C}$ . *Physica C*, 176:261–273, 1991.
- [172] Paul Richard Schleger. *Thermodynamics of Oxygen Ordering in  $\text{YBa}_2\text{Cu}_3\text{O}_{6+x}$* . PhD thesis, The Faculty of Graduate Studies, Physics, The University of British Columbia, Vancouver, Canada, 1992.
- [173] Ivan K. Schuller, S. Kim, and C. Leighton. Magnetic superlattices and multilayers. *Journal of Magnetism and Magnetic Materials*, 200:571–582, 1999.
- [174] R. Sellmann, H. Fritzsche, H. Maletta, V. Leiner, and R. Siebrecht. Spin-reorientation transition and magnetic phase diagrams of thin epitaxial  $\text{Au}(111)/\text{Co}$  films with W and Au overlayers. *Physical Review B*, 64(054418), 2001.
- [175] D. Shindo and T. Oikawa. *Analytical Electron Microscopy for Materials Science*. Springer.

- [176] Gen Shirane, Stephen M. Shapiro, and John M. Tranquada. *Neutron Scattering with a Triple Axis Spectrometer*. Cambridge University Press, 1st edition, 2002.
- [177] M. Simoneau, G. L'Espérance, and R. Schulz. Formation by ball milling and recrystallization of Y-Ba-Cu-O nanocrystalline phases. *Journal of Applied Physics*, 16(1):163–171, 1994.
- [178] Z. Slanič, D. P. Belanger, and J. A. Fernandez-Baca. Equilibrium Random-Field Ising Critical Scattering in the Antiferromagnet  $\text{Fe}_{0.93}\text{Zn}_{0.07}\text{F}_2$ . *Physical Review Letters*, 82(2):426–429, 1999.
- [179] Robert L. Snyder, Jaroslav Fiala, and Hans J. Bunge. *Defect and Microstructure Analysis by Diffraction*. Oxford University Press, 1999.
- [180] Jeff E. Sonier. Muon Spin Rotation/Relaxation/Resonance ( $\mu\text{SR}$ ). Simon Fraser University, Department of Physics, Burnaby, British Columbia, Canada.
- [181] G. L. Squires. *Introduction to the Theory of Thermal Neutron Scattering*. Dover Publications Inc., 1996.
- [182] C. Stock, W. J. L. Buyers, Z. Tun, R. Liang, D. Peets, D. Bonn, W. N. Hardy, and L. Taillefer. Neutron scattering search for static magnetism in oxygen ordered  $\text{YBa}_2\text{Cu}_3\text{O}_{6.5}$ . *Physical Review B*, 66(024505):1–5, 2002.
- [183] C. Stock, W. J. L. Buyers, Z. Yamani, C. L. Broholm, J.-H. Chung, Z. Tun, R. Liang, D. Bonn, W. N. Hardy, and R. J. Birgeneau. Central mode and spin confinement near the boundary of the superconducting phase in  $\text{YBa}_2\text{Cu}_3\text{O}_{6.353}$  ( $T_c=18$  K). *Physical Review B*, 73(100504), 2006.
- [184] H. Stroumbos, A. Laroui, P. Monod, B. Decamps, J. P. Dubois, and P. Odier. London penetration depth determination from ultrafine particles of  $\text{YBa}_2\text{Cu}_3\text{O}_7$ . *Physica C*, 167:375–387, 1990.
- [185] J. L. Tallon, C. Bernhard, H. Shaked, R. L. Hittermann, and J. D. Jorgensen. Generic superconducting phase behavior in high- $T_c$  cuprates:  $T_c$  variation with hole concentration in  $\text{YBa}_2\text{Cu}_3\text{O}_{7-\delta}$ . *Physical Review B*, 51(18):12991–12913, 1 May 1995.
- [186] K. Tomiyasu, T. Inami, and N. Ikeda. Magnetic structure of CoO studied by neutron and synchrotron x-ray diffraction. *Physical Review B*, 70(184411), 2004.
- [187] J. M. Tranquada, D. E. Cox, W. Kunnmann, H. Moudden, G. Shirane, M. Suenaga, P. Zolliker, D. Vaknin, S. K. Sinha, M. S. Alvarez, A. J. Jacobson, and D. C. Johnston. Neutron-Diffraction Determination of Antiferromagnetic Structure of Cu Ions in  $\text{YBa}_2\text{Cu}_3\text{O}_{6+x}$  with  $x=0.0$  and  $0.15$ . *Physical Review Letters*, 60(2):156–159, 1998.
- [188] J. M. Tranquada, A. H. Moudden, A. I. Goldman, P. Zolliker, D. E. Cox, and G. Shirane. Antiferromagnetism in  $\text{YBa}_2\text{Cu}_3\text{O}_{6+x}$ . *Physical Review B*, 38(4):2477–2485, 1988.
- [189] J. M. Tranquada, G. Shirane, B. Keimer, S. Shamoto, and M. Sato. Neutron scattering study of magnetic excitations in  $\text{YBa}_2\text{Cu}_3\text{O}_{6+x}$ . *Physical Review B*, 40(7):4503–4516, 1989.
- [190] R. Troć, Z. Bukowski, R. Horyń, and J. Klamut. Possible Antiferromagnetic Ordering In  $\text{Y}_2\text{Cu}_2\text{O}_5$ . Paramagnetic Behaviour Of  $\text{BaCuO}_2$ . *Physics Letters A*, 125(4):222–224, 1987.
- [191] Linda Udby. Personal communication, 2004–2008.
- [192] Linda Udby. *Superoxygenated LSCO - theory, simulation and experiment*. PhD thesis, Niels Bohr Institute, University of Copenhagen, In preparation, 2009.
- [193] Linda Udby, Peter Kjær Willendrup, Kim Lefmann, Jari í Hjøllum, and Niels Hessel Andersen. Using McStas Sample Components for Virtual Experiments. *In preparation*, 2008.

- [194] B. van Laar, J. Schweitzer, and R. Lemarie. Neutron-Diffraction Investigation of CoO Single Crystals. *Physical Review*, 141(2):538–540, 1966.
- [195] D. C. Vier, S. B. Oseroff, C. T. Salling, J. F. Smyth, S. Schultz, Y. Dalichaouch, B. W. Lee, M. B. Maple, Z. Fisk, and J. D. Thompson. Precautions when interpreting EPR and dc magnetization measurements of high-T<sub>c</sub> RBa<sub>2</sub>Cu<sub>3</sub>O<sub>9-x</sub>-phase superconducting materials. *Physical Review B*, 36(16):8888–8891, 1987.
- [196] Paul Scherrer Institute Website. Website: [www.psi.ch](http://www.psi.ch).
- [197] Alois Weidinger, Joseph I. Budnick, Burt Chamberland, Andrzej Golnik, Christof Niedermayer, Ekkehard Recknagel, Manfred Rossmannith, and De Ping Yang. Magnetic Ordering In High-T<sub>c</sub>-Related Compounds. *Physica C*, 153-155:168–169, 1988.
- [198] Brent B. Welch and Ken Jones with Jeffrey Hobbs. *Practical Programming in Tcl and Tk*. Prentice Hall PTR, 2003.
- [199] M.T Weller and D.R. Lines. Structure and oxygen stoichiometry in Ba Cu O<sub>2+x</sub>. [ICSD #65801], *Journal of the Chemical Society. Chemical Communications (1972-)*, pages 484–485, 1989.
- [200] B. O. Wells, Y. S. Lee, M. A. Kastner, R. J. Christianson, R. J. Birgeneau, K. Yamada, Y. Endoh, and G. Shirane. Incommensurate Spin Fluctuations in High-Transition Temperature Superconductors. *Science*, 277(1067-1071), 1997.
- [201] C. Weyl, J. Zhao, C. Lacour, F. Laher-Lacour, and P. Thuery. Investigation of a nanocrystalline YBa<sub>2</sub>Cu<sub>3</sub>O<sub>7-δ</sub> powder by neutron and electron diffractions. *J. Phys. Chem. Solids*, 56(9):1211–1221, 1995.
- [202] Peter Willendrup, Uwe Filges, Lukas Keller, Emmanuel Farhi, and Kim Lefmann. Validation of a realistic powder sample using data from DMC at PSI. *Physica B*, 385-386:1032–1034, 2006.
- [203] G. K. Williamson and W. H. Hall. X-ray line broadening from filed aluminium and wolfram. *Acta Metallurgica*, 1(1):22–31, 1953.
- [204] Kenneth G. Wilson. Renormalization Group and Critical Phenomena. I. Renormalization Group and the Kadanoff Scaling Picture. *Physical Review B*, 4(9):3174–3183, 1971.
- [205] Kenneth G. Wilson. Renormalization Group and Critical Phenomena. II. Phase-Space Cell Analysis of Critical Behavior. *Physical Review B*, 4(9):3184–3205, 1971.
- [206] Kenneth G. Wilson and J. Kogut. The Renormalization Group and the  $\epsilon$  Expansion. *Physics Reports (Section C Of Physics Letters)*, 12(2):75–200, 1974.
- [207] M. K. Wu, J. R. Ashburn, C. J. Torng, P. H. Hor, R. L. Meng, L. Gao, Z. J. Huang, Y. Q. Wang, and C.W. Chu. Superconductivity at 93 K in a New Mixed-Phase Yb-Ba-Cu-O Compound System at Ambient Pressure. *Physical Review Letters*, 58(9):908–910, Mar 1987.
- [208] X.S. Wu, W.M. Chen, X. Jin, and S.S. Jiang. Mechanochemical effects of grinding on the Y Ba<sub>2</sub> Cu<sub>3</sub> O<sub>x</sub> superconductor. [ICSD #83211], *Physica C*, 273:99–106, 1996.
- [209] H. Yamada, Y. Soejima, X.G. Zheng, and M. Kawaminami. Structural study of CuO at low temperatures. [ICSD 92368], *Transaction of the Material Research Society of Japan*, 25(4):1199–1202, 2000.
- [210] J. Zinn-Justin. Determination of critical exponents and equation of state by field theory methods. *arXiv:hep-th*, 9810193v1, 1998.
- [211] J. Zinn-Justin. Precise determination of critical exponents and equation of state by field theory methods. *arXiv:hep-th*, 0002136v1, 2000.





